Pb-isotopic Insights into the Late Palaeoproterozoic Crustal Evolution and Metallogenesis of the Gawler Craton, South Australia

Nathan D. Chapman

B.Sc. (Hons.) University of New England

ARC Centre of Excellence in Ore Deposits (CODES)

School of Natural Sciences (Earth Sciences)

Submitted in fulfillment of the requirements for the degree of Doctor of Philosophy

University of Tasmania

September 2020

Dedicated to my beautiful Audrey –
The PhD I never knew I needed, and my lighthouse in the storm.

Table of Contents

List of Figures

List of Tables

List of Appendices

Abstract

Pb-isotopes present a powerful tool to investigate ancient crustal evolution and metallogenesis. When coupled with an analytical techniques such as laser ablation inductively-coupled plasma mass spectrometry (LA-ICP-MS) which yield high analytical throughput and high-spatial resolution at a level of precision which is fit-for-purpose, Pb-isotopes represents a cost-effective method through which to conduct large-scale, regional studies. This study examines the late Paleoproterozoic Pb-isotopic evolution of the Gawler Craton, South Australia in order to investigate igneous petrogenesis and ore deposit metallogenesis.

The late Paleoproterozoic-Early Mesoproterozoic period (1690 – 1590 Ma) represents an important period for metallogenesis (i.e. Olympic Dam, Prominent Hill, Carapateena and Tarcoola) and igenous crustal evolution in the Gawler Craton. However, like many of Australia's Paleoproterozoic terranes, extensive Neoproterozoic and younger cover sequences largely obscure the geological relationships of the underlying igneous basement, limiting straightforward geodynamic and petrogenetic interpretations. Isotopic investigations are ideal in such situations, providing a great deal of constraint on melt-sources and the tectonic regimes driving magmatism. New Pb-isotopic results presented here, are integrated with extant geochemical, geochronlogical and Sm-Nd isotopic data to provide new insights in the igneous crustal evolution and metallogensis of the Gawler Craton.

The tectonic setting of 1690 – 1670 Ma Tunkillia Suite remains unclear, and has been variably attributed to both arc and continental-collisional/ post-collisional tectonic environments. In situ Pb-isotopic results from alkali feldspars reveal a complex petrogenesis, instigated by mantle-driven magmatism, but with dramatic differences between the crustal-Pb components of the eastern and western Tunkillia Suite. The crustal Pb component in the western Tunkillia Suite is particularly noteworthy as it records a rare occurrence of retarded Pb-isotopic behaviour (i.e. less radiogenic than predicted by growth models), caused by significant, ancient, U-depletion related to granulite-facies metamorphism. Similarities between the geochemical and Pb-isotopic compositions of the eastern Tunkillia Suite and the nearby 1630-1600 Ma St Peters Suite which are considered to represent island

arc-style magmatism, demonstrates some inconsistencies in the way igneous suites of the Gawler Craton have been previously classified. Comparison between the Pb-isotopic, Nd-isotopic and geochemical characteristics of the Tunkillia Suite shows that it has a greater similarity with modern-day continental arc-style granitoids than either continental-collisional or post-tectonic granitoids. It is therefore suggested that the late Paleoproterozoic (<1700 Ma) crustal evolution of the Gawler Craton is dominated by subduction-related tectonics, beginning around ~1690 Ma with the Tunkillia Suite and terminating around ~1600 Ma with the St Peters Suite.

Less than 13 Ma after the completion of the St Peters Suite subduction cycle, high-temperature (~870°C), volumetric (100 000 km^3), A-type (K-HFSE-REE-rich) felsic magmas of the 1595-1575 Ma Hiltaba Suite/ Gawler Range Volcanics (GRV) were emplaced across the Gawler Craton. Recent high-precision geochronological data on the GRV provides constraints on how the Hiltaba-GRV magmatic event evolved through time. The dominantly mantle-like Pb-isotopic signatures in the 1592 Ma Lower GRV contrast strongly with the high-μ signature in the 1589 Ma Upper GRV, suggesting that either the GRV may not have been co-magmatic *sensu stricto*. Alternatively, the Upper GRV may reflects a period of the Hiltaba-GRV magmatic event characterised by large-scale crustal melting (4200 km^3). Isotopic (Pb-Pb, Sm-Nd), geochemical, and physicochemical (T°C, aH_2O etc) similarities between the GRV and modern-day volcanic terranes which have generated large volumes of felsic volcanics (e.g. Basin and Range Province), suggest that the Hiltaba/ GRV event may have developed in an intracontinental, back-arc tectonic setting, consistent with the interpretation of the late Paleoproterozoic Gawler Craton tectonic regime presented here.

Initial Pb-isotopic compositions from alkali feldspars belonging to the widespread Hiltaba Suite granitoids show a diverse range of melt-sources identical to the GRV, from enriched-mantle to U-Th-enriched lower crust. Mantle-like signatures are limited to the Hiltaba Suite granites in proximity of the Nuyts Terrane, highlighting a possible geodynamic link between the subduction-related paradigm interpreted for the Tunkillia and St Peters Suites. To the north-northwest of the Nuyts Terrane, Hiltaba Suite granites have incorporated weakly-retarded, high-κ, Pb-isotopic signatures, demonstrating that

U-depleted granulites are an extensive component of the western Gawler Craton lower crust. In contrast, Hiltaba Suite granites in the eastern Gawler Craton contain high-μ, high-κ Pb-isotopic signatures indicating that crust underlying the IOCG province contains U and Th concentrations which are anomalously enriched compared to average crust.

A particular emphasis was placed on acquiring the initial Pb-isotopic signature of the Roxby Downs Granite (RDG), a member of the Hiltaba Suite which hosts the world-class Olympic Dam Cu-Au-U-Ag deposit. Complex textural, paragenetic and crystallographic features of alkali feldspars from the RDG has inhibited previous initial Pb-isotopic determinations using conventional dissolution-based methods. A series of high-spatial resolution geochemical and crystallographic techniques (SC-XRD, SEM-WDS and synchrotron) were employed to determine pristine, orthomagmatic domains in least-altered alkali feldspar phenocrysts, and were crucial in validating the authenticity of the initial Pb-isotopic signatures determined by LA-MC-ICP-MS. The initial Pb-isotopic signature shows that the RDG was partially-derived from a crustal source (20:80 crust:mantle melt) that was ~14% more enriched in U and ~7% more enriched in Th than average crust. Growth curve modelling suggests that the U-Th-enriched crustal reservoir was formed at 3.2-3.1 Ga, which is consistent with the age of the Cooyerdoo Granite – a known U-Th-rich granite. It is therefore likely that U-contribution from an enriched crustal melt represents a first-order explanation for the anomalously U-rich mineralisation of Olympic Dam. Pb-isotopic variations between high-temperature (830-870°C) alkali feldspars, and low-temperature (300-400°C), paragenetically-later K-feldspars indicates that some open-system Pb-exchange occurred between the RDG and surrounding country rock during the transition from orthomagmatic conditions, to magmatic-hydrothermal conditions, consistent with the fluid-mixing model invoked by previous studies for the formation of Olympic Dam.

The Olympic Dam Cu-Au-U-Ag deposit is one of the largest polymetallic resource currently known, however, little is understood about how it formed. A growing body of evidence suggests that the deposit has a protracted history of reworking. 397 analyses of Pb-rich mineral species from across the deposit were analysed for their Pb-isotopic compositions, in order to constrain potential

disturbances to the U-Th-Pb system of the deposit. Calcite veins in the deepest part of the deposit, and galena from the highest-Pb zone of the deposit contains the least radiogenic signatures encountered. The galena Pb-isotopic compositions form linear arrays which intersect the RDG initial Pb-isotopic signature demonstrating that most primary Pb (and possibly other metals) were contributed by the RDG itself. The high-μ trajectory of the array suggests that high U/Pb conditions were already established within the deposit from at least 1527 ± 147 Ma, and therefore there is no Pb-isotopic requirement to introduce U after initial formation of the deposit. However, Pb-isotopic signatures from across the deposit show no relationship with U, Th or Pb concentrations suggesting that U and Pb have been redistributed to some degree. Strong, uranogenic departures in the Pb-isotopic signatures from bornite and chalcocite zones of the deposit indicates that at least one major reworking event has dramatically affected U-mineralisation. Radiogenic Pb-isotopic signatures show a positive correlation with modal % bornite, yet reflect a negative relationship with modal % chalcopyrite, suggesting that the U-disturbance event recorded by Pb-isotopic compositions may have also upgraded chalcopyrite to bornite. Pb-Pb isochrons from bornite and chalcocite-rich areas of the deposit yield repeatable radiogenic Pb ages of av. 664 ± 66 Ma (MSWD = 2.3, n = 7) which is consistent with the depositional age of Ediacaran sediments (~676 Ma) above the unconformity which unroofs the Olympic Dam deposit. To explain these phenomena, it is suggested that Cryogenean-Ediacaran marine transgression following the Marinoan Glaciation, led to the ingress of oxidised marine fluids into the Olympic Dam breccia complex, remobilising some U and forcing the Cu-sulphide stability field from chalcopyrite-stable to bornite-stable conditions. It is therefore considered likely that reworking of Olympic Dam during the Neoproterozoic upgraded some Cu-U mineralisation, ultimately contributing to the economic tenor of its world-class resource.

Statements and Declarations

Declaration of originality

This thesis contains no material which has been accepted for a degree or diploma by the University or any other institution, except by way of background information and duly acknowledged in the thesis, and to the best of my knowledge and belief no material previously published or written by another person except where due acknowledgement is made in the text of the thesis, nor does the thesis contain any material that infringes copyright.

Signed: **Date:** 02/02/2020

Authority of access

This thesis may be made available for loan and limited copying and communication in accordance with the Copyright Act 1968.

Signed: **Date:** 02/02/2020

Statement regarding published work contained in this thesis

The publishers of the paper comprising Chapters 4 hold the copyright for that content and access to the material should be sought from the corresponding journals. The remaining non-published content of the thesis may be made available for loan and limited copying and communication in accordance with the Copyright Act 1968.

Signed: **Date:** 02/02/2020

Statement of authorship – List of authors

The following people contributed to the publication and submission of work undertaken as a part of this thesis:

Candidate, Author 1: Nathan Chapman, ARC Centre of Excellence in Ore Deposits (CODES), School of Natural Sciences, University of Tasmania

Author 2: Sebastien Meffre, Primary Supervisor, CODES-TMVC, School of Natural Sciences, University of Tasmania

Author 3: Kathy Ehrig, BHP Olympic Dam

Author 4: Roland Maas, School of Earth Sciences, University of Melbourne

Author 5: Matthew Ferguson, ARC Centre of Excellence in Ore Deposits (CODES), School of Natural Sciences, University of Tasmania

Author 6: Aleksandr Stepanov, CODES, School of Natural Sciences, University of Tasmania

Author 7: Michael Gardiner, School of Chemistry, University of Tasmania

Proportion of Work Undertaken Towards Manuscripts

Manuscript 1 - The Bearing of Pb-Isotopic Compositions on the Petrogenesis of the Tunkillia Suite, Gawler Craton

- Located in Chapter 3 (to be submitted to *Precambrian Research*)
- Candidate was the primary author. Author 2 contributed to conception and analytical work. Author 3 contributed financial support and manuscript revision. Author 4 contributed to analytical work (MC-ICP-MS) and manuscript revision. The candidate collected samples, data and contributed to its interpretation.

Candidate contributed approximately 90% to the planning, execution, and preparation of the manuscript.

Manuscript 2 - Pb-isotopic constraints on the source of A-type Suites: Insights from the Hiltaba Suite - Gawler Range Volcanics Magmatic Event, Gawler Craton, South Australia

- Located in Chapter 4 (published in *Lithos, Vol. 346*)
- Candidate was the primary author. Author 5 contributed to some ideas in manuscript. Author 2 contributed to technical conception, interpretation and financial support. Author 6 contributed to ideas and manuscript framework. Author 4 contributed to analytical work (MC-ICP-MS). Author 3 contributed financial support.
- The candidate collected samples, undertook most analytical work and interpretation. Manuscript revisions were provided by authors 2, 3, 4, 5 and 6.

Candidate contributed approximately 90% to the planning, execution, and preparation of the manuscript.

Manuscript 3 - Integrating Pb-Isotopic And Crystallographic Analyses On Alkali Feldspar Of The Roxby Downs Granite – Constraints On The Melt-Source And Cooling History Of The Host To Olympic Dam

- Located in Chapter 5 (to be submitted to *Contributions to Mineralogy and Petrology*)
- Candidate was the primary author. Author 2 contributed to conception, interpretation and financial support. Author 7 contributed to crystallography work, including data acquisition, reduction and in-kind financial support. Author 4 contributed technical expertise with data collection (LA-MC-ICP-MS, MC-ICP-MS). Author 3 contributed financial support and access to samples.
- Candidate collected samples, undertook analytical work, and interpretation. Manuscript revisions were provided by Authors 2 and 7.

Candidate contributed approximately 85% to the planning, execution, and preparation of the manuscript.

Manuscript 4 - Pb-Isotope Systematics Of The Olympic Dam IOCG-U: Evidence For A Protracted History Of Modification

- Located in Chapter 6 (to be submitted to *Economic Geology*)
- Candidate was the primary author. Author 2 contributed to conception and interpretation.

- Candidate contributed to analytical work, data reduction of legacy data set, and interpretation. Manuscript revisions were provided by Author 2.

Candidate contributed approximately 85% to the planning, execution, and preparation of the manuscript.

We the undersigned agree with the above stated "proportion of work undertaken" for each of the above published or submitted peer-reviewed papers contributing to the thesis:

Signed: _____

Sebastien Meffre	David Cooke	Nathan Chapman
Supervisor/Head of Discipline (Earth Sciences)	Director of CODES	PhD Candidate
School of Natural Sciences/CODES/TMVC	School of Natural Sciences/CODES/TMVC	School of Natural Sciences
University of Tasmania	University of Tasmania	University of Tasmania
Date: 12/02/20.	12/2/20	23/09/2020

Publications during course of thesis

Journal articles

Chapman, N. D., Ferguson, M., Meffre, S. J., Stepanov, A., Maas, R., and Ehrig, K. J., 2019, Pb-isotopic constraints on the source of A-type Suites: Insights from the Hiltaba Suite - Gawler Range Volcanics Magmatic Event, Gawler Craton, South Australia: Lithos, v. 346-347, p. 105156.

Conference presentations

Chapman, N. D., Meffre, S. J., Kamenetsky, V.S., Ehrig, K., and Kontonikos-Charos, A. 2016, Pb-isotopes of Olympic Dam and Beyond: The Uranium Story of the Gawler Craton, in AESC 2016 – Australian Earth Sciences Convention abstracts, 26-30 June 2016, Adelaide, Australia.

Chapman, N. D., Meffre, S. J., Maas, R., Kamenetsky, V.S., and Ehrig, K., 2018, Linking the Pb-isotopic Evolution of the Roxby Downs Granite and the Supergiant Olympic Dam Cu-Au-U, in SEG 2015 – Society of Economic Geologists Conference Abstracts, 22-25 September 2018, Keystone, CO, U.S.A.

Acknowledgements

Funding was received primarily from BHP Olympic Dam Operations, but also from the CODES/ TMVC hub. These contributions are gratefully acknowledged.

Sebastien Meffre, my primary supervisor and possibly the busiest man in the Geology Department, made this project possible. The project was fluid, full of setbacks, and began with little-to-no assured funding - the faith he showed in me and my tangents is a testament to his character. The support, both financial and scientific, from Kathy Ehrig (BHP Olympic Dam Operations) is duly acknowledged. The tight-line she walks between curiosity and pragmatism was an inspiration. Roland Maas (University of Melbourne) is thanked for his general guidance, hospitality while I was in Melbourne, and for being open and willing to indulge in any topic of discussion. His lightning-fast ability to answer emails at 11 pm on a Saturday night is a rare skill indeed. Michael Gardiner (School of Chemistry, UTas) provided immense assistance in crystallographic work and is gratefully thanked. It takes a special person to be willing to help a random PhD from another faculty, on a random project with no funding and which you will gain little from. This research profited hugely from conceptual discussions and long tennis matches with Sasha Stepanov. Leonid Danyushevsky taught me a great deal about the nuances of LA-ICP-MS, and showed an admirable amount of patience while we worked on the LA-ICP-MS model. The input from Dima Kamanetsky during the earlier stages of this PhD is thanked. Shaun Barker in his role as GRC is thanked for his level-headed guidance during the difficulties faced at the latter part of this project.

The interpretations in Chapter 6 build on data and ideas generated by a team of students, postdoctoral researchers s and investigators who have worked on the following projects:

- Mafic-Ultramafic Igneous Facies at Olympic Dam (2008 - 2009 McPhie J; Kamenetsky VS; funded by BHP)
- Research on the Setting, Age and Architecture of the Olympic Dam Cu-U-Au-Ag Deposit, South Australia (2010 – 2014, McPhie J; Kamenetsky VS; funded by BHP).
- Stable isotopes (C, S and O) and halogens (CI, F) at Olympic Dam: Evaluation of mantle and crustal contributions to mineralisation (2012 Kamenetsky VS; McPhie J; funded by BHP)
- "The supergiant Olympic Dam U-Cu-Au-REE ore deposit: towards a new genetic model" (LP130100438, 2013 – 2017, Kamenetsky VS; Ehrig, K; McPhie J; Meffre S; Maas R; funded by BHP and the Australian Research Council)
- Sedimentary units within the Olympic Dam deposit: Provenance and implications to metal sources (2016 Kamenetsky VS; Grant-Hugh McKinstry Fund)

In addition to the investigators listed above, the team included the following Master and PhD students, and postdoctoral fellows: Glen Diemar, Alex Cherry, Matt Ferguson, Qiuyue Huang, Olga Apukhtina, Andrea Agangi, Karin Orth and Isabelle Chambefort.

The technical staff from the CODES LA-ICP-MS labs (Jay Thompson, Paul Olin and Ivan Belousov) and the CSL SEM lab (Karsten Goemann and Sandrin Feig) are absolute legends, capable of superhuman feats of patience, support and guidance. Each one of them has gone above and beyond the call of duty at some point during this research, and I thank each one of them from the bottom of my heart.

During my time at UTas I have had the opportunity to enjoy the company of many amazing people. Many terrific conceptual discussions were had with “Bloody Matt Ferginsuns” and Alex Cherry (Olympic Dam research group) over Monday Coffees. The camaraderie of Brian, Cass, Sean, Naomi, Adam and Joe, and many others made the tough slog of a PhD bearable. Geology is a small world and I hope to see you all again some time.

Last but not least, this work would not have been possible without the support and patience of my partner-in-crime, Imogen. From Knoppies to parenthood, it’s been a wild few years.

Chapter 1: Introduction

1.1 Preamble

Put simply, the Pb-isotopes ($^{204, 206, 207 \text{ and } 208}$Pb) present an opportunity to observe the ancient abundances, behaviours and residencies of U, Th and Pb throughout the Earth, and assign a model age to these geochemical behaviours. Subsequently, Pb-isotopes represent a powerful tool through which to investigate geological processes, and ancient crustal evolution. Pb-isotopes have played a crucial role in the development of fundamental geological concepts such as;

- The age of the Earth
- Differentiation of the crust, mantle and core
- Orogenesis and crustal recycling vs geosyncline theory
- Mantle heterogeneity
- Mantle plume theory

Nonetheless, Pb-isotopes are often considered a "dark-art" by many geologists – even by those who are experts in radiogenic isotopic systems. While some of the issues relate to the complexities inherent in the open-system behaviour of the Pb-isotopic system, at least part of the problem resides in the deficiency of *a priori* constraints and ways to objectively validate Pb-isotopic results. Despite continuing advances in analytical technology, we are still no closer than Hart (1964) in understanding the exact mechanism for Pb-isotopic exchange in alkali feldspars – a study published just two years after Harry Hess' 1962 seminal paper on continental drift! Understanding the crystallographic changes in alkali feldspar that lead to Pb-isotopic exchange is a crucial *a priori* constraint, if we are to be able to differentiate genuine accelerated Pb-signatures in granites, from incursion of post-formational radiogenic Pb. Considerable effort was made during the course of this research to constrain genuine initial Pb-isotopic signatures based on alkali feldspar crystallography (Chapter 5), however more work is needed. At present the merit and validity of initial Pb-isotopic

signatures obtained from alkali feldspars is largely judged based on high-analytical precision of unknowns and performance of standard reference material (SRM's), rather than objective constraints on the authenticity of the alkali feldspar being analysed. Hopefully, the increasing focus on in situ Pb-isotopic analyses (such as LA-ICP-MS), as opposed to dissolution-based sampling techniques, will improve our understanding of this fundamental aspect of Pb-isotopic geochemistry – the outcome of which could lead to profound discoveries about our Earth's crustal evolution. As a closing remark, this preamble will finish with a quote which remains poignant to this day;

"*The time has come for geologists to face up to the fact that in Pb-isotope studies, the weak link has been geology. Too few geologists have devoted time to Pb-isotope research. The geologist has not yet assumed his proper share of responsibility … many more geologists must make the effort to understand the simple principles that underlie Pb-isotope geology.*"

- *Cannon et al. (1961)*

1.2 Significance, Aims and Thesis Structure

The Gawler Craton represents an important temporal link in the crustal evolution of the Australian continent; between the Archean crustal components of Western Australia (i.e. Yilgarn and Pilbara Cratons) and the Proterozoic terranes and inliers of central and northern Australia (Fig. 1.1). The period in which this research focusses (1690 – 1590 Ma) contains some of the most hotly-debated igneous suites of the Gawler Craton (i.e. the 1690 - 1669 Ma Tunkillia Suite, 1630-1608 Ma St Peters Suite, ~1590 Ma Hiltaba Suite/ Gawler Range Volcanics), as well as some of the most-cryptic, yet economically-lucrative, mineral deposits in Australia and the world (e.g. Olympic Dam). The ~1590 Ma temporal-link between the poorly-understood iron oxide-copper-gold (IOCG) deposits (i.e. Olympic Dam, Prominent Hill, Carrapateena, Oak Dam) and equally-enigmatic igneous suites (i.e. Hiltaba Suite) suggests crustal development of the Gawler Craton during this period was particularly unique.

Figure 1.1: The location of the Gawler Craton with respect to other Paleoproterozoic crustal components of the Australian continent.

In order to better understand the link between crustal evolution and metallogenesis in the Gawler Craton, in situ Pb-isotopic techniques (LA-ICP-MS) will be applied to a variety of regional- and deposit-scale studies. The initial Pb-isotopic signatures determined from alkali feldspars of the Tunkillia Suite and St Peters Suite, supplemented by whole-rock geochemistry, will attempt to explore the Late Paleoproterozoic (1690 - 1608 Ma) geodynamic setting of the Gawler Craton (Chapter 3). Initial Pb-isotopic signatures of the regionally-expansive 1590 Ma Hiltaba Suite/ GRV will provide an insight into the range of Pb-isotopic reservoirs located throughout the Mesoproterozoic Gawler Craton, and investigate the genesis of A-type magmas in general (Chapter 4). Particular emphasis will be placed on determining the melt-sources and magmatic conditions of the 1593 Ma Roxby Downs Granite, a member of the Hiltaba Suite, which hosts the supergiant Olympic Dam Cu-Au-Ag-U deposit (Chapter 5). The focus will then turn to Olympic Dam itself, where Pb-isotopic signatures of Pb-rich sulfides and carbonates will be used to tie the Roxby Downs Granite petrogenesis to metallogenesis, and investigate the potential for economically-significant post-formational modification. Thus, this thesis has three-broad aims;

1) Demonstrate the accuracy and effectiveness of the LA-ICP-MS Pb-isotopic method to both regional and deposit-scale studies.
2) Contribute to the understanding of Late Paleoproterozoic – Early Mesoproterozoic crustal evolution in the Gawler Craton.
3) Provide a link between the crustal evolution of the Gawler Craton and IOCG metallogenesis.
4) Investigate the potential for post-formational modification of the world-class Olympic Dam ore deposit.

In the following introductory chapter, the reader will be introduced to a brief geological framework of the Gawler Craton leading up to 1690 – 1590 Ma with the aim of providing context for the range of crustal Pb-isotopic reservoirs referred to throughout this thesis. The second half of this chapter will provide a short overview of the Pb-isotopic system with a particular focus on the concept of Pb-isotopic growth curves as well as a discussion on the effectiveness of alkali feldspars as a host for magmatic Pb-isotopic signatures.

1.3 Pre-1690 to 1590 Ma Geological History of the Gawler Craton

1.3.1 Introduction

The Gawler Craton is a major crustal component of the Australian landmass (Fig. 1.1), and covers much of the state of South Australia. It temporally links the development of Earth's crust, from the Archean cratons of Western Australia, with the Proterozoic inliers of central and northern Australian (Fig. 1.1). It has been subdivided into a number of domain components on the basis of major structural features, geophysical characteristics and lithologies (Fig. 1.2). In order to contextualise some of the major crustal reservoirs and geodynamic processes discussed throughout the body of this work this thesis, this section aims to provide a brief overview of the geological history of the Gawler Craton leading up to the time-period which this work focusses on (1690 – 1590 Ma).

1.3.2 Archean-Early Paleoproterozoic Crustal Evolution (3150 – 2440 Ma)

The Archean-Early Paleoproterozoic history of the Gawler Craton is poorly-understood, with interpretation inhibited by scant outcrop, thickcover sequences and overprinting by successive, deformation events resulting in the paragneisses, orthogneisses and granulites which comprise the Mulgathing, Sleaford and Nawa Complexes (Fig. 1.2)

The oldest rocks identified in the Gawler Craton belong to the Mesoarchean Cooyerdoo Granite (3157 Ma; Fraser et al. (2010)), which is located near Whyalla and the township of Iron Knob (Fig. 1.2). Interestingly, the occurrence of the Mesoarchean crust was predicted 17 years before its discovery by the occurrence of strongly-evolved Nd-isotopic signatures (εNd_t= -14.3) in the much-younger, c.1590 Ma Charleston Granite which had intruded through, and assimilated part of it (Creaser and Fanning, 1993). Inherited cores within zircons of the Cooyerdoo Granite yield ages between 3310 Ma and 3215 Ga (Fraser et al., 2010), suggesting older crust may still be present within the vicinity of the Cooyerdoo Granite. The geochemical similarities the Cooyerdoo Granite

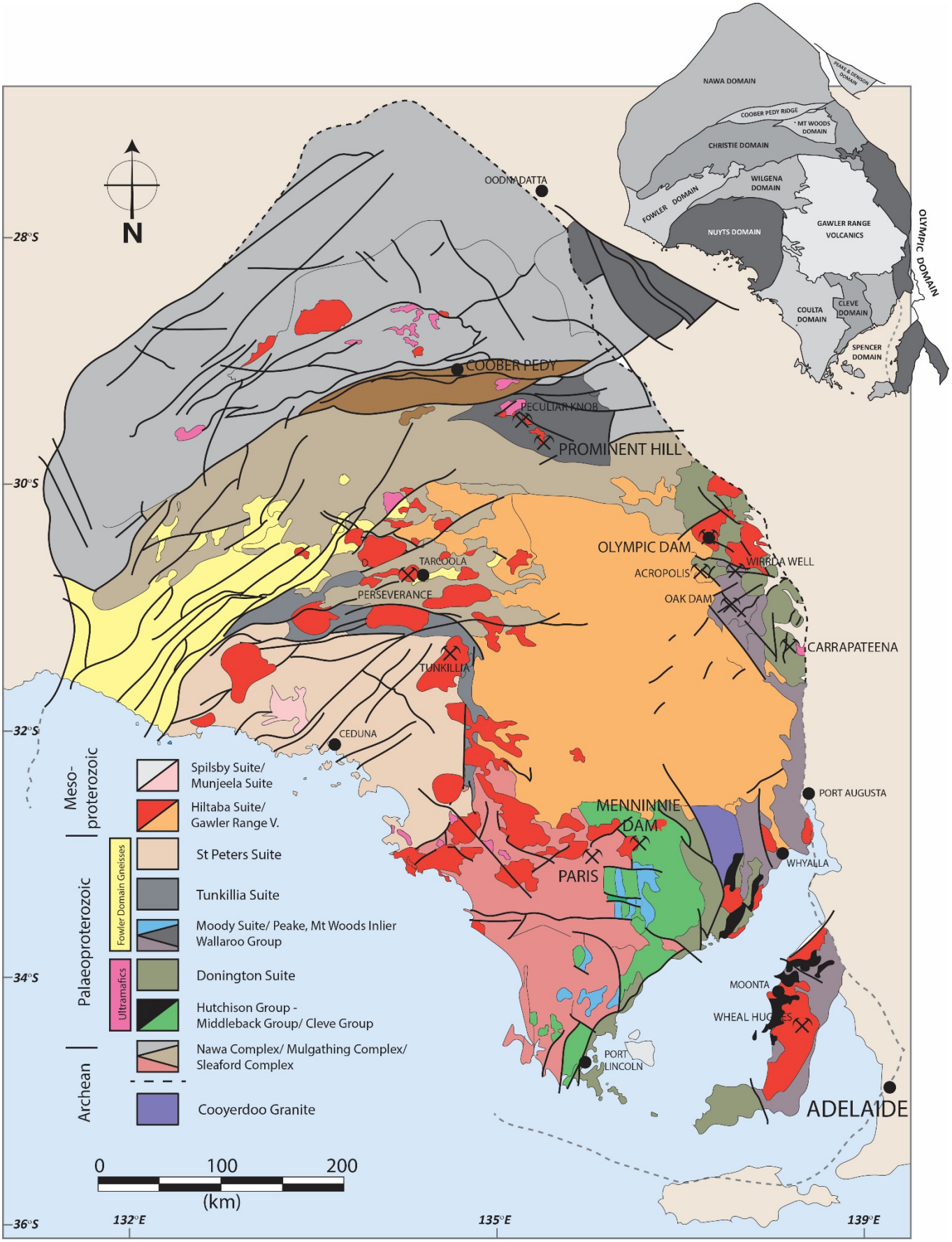

Figure 1.2: Schematic outline of the Mesoarchean – Mesoproterozoic Gawler Craton. Colour-coded based on the distribution of major igneous/ volcano-sedimentary units. Mineral deposits thought to be temporally-associated with the period 1690 – 1590 Ma also shown. Inset (top, right) shows simplified crustal domains. Diagram and domain nomenclature after Daly et al. (1998) and Ferris et al. (2002).

and low-Ca tonalite-trondhjemite-granodiorites (TTGs) within the Yilgarn and Pilbara Cratons led Fraser et al. (2010) to suggest that the Archean nucleus of the Gawler Craton may be genetically related to these ancient crustal components. The geographical extent of Cooyerdoo-aged crust within the Gawler Craton is largely unknown, with geophysical insights obscured by coverage of the Gawler Range Volcanics to the north. However, the high U-Th concentrations of the Cooyerdoo Granite, coupled with the spatial coincidence of it with the South Australian Heat Flow Anomaly (Neumann et al., 2000) which extend beyond Olympic Dam in the north, suggest radiogenic Mesoarchean crust may comprise a significant portion of the Olympic Domain (Fraser et al., 2010; McAvaney, 2012). The antiquity and U-Th-rich nature of the Cooyerdoo Granite represents an important, potential radiogenic Pb-isotopic reservoir within the Gawler Craton crust.

The bimodal 2558 ± 6 Ma (Cowley and Fanning, 1991) Devils Playground Volcanics are located approximately half-way between the Olympic Dam and Prominent Hill mine sites. Curiously, the evolved εNd(t) signatures in some basalts of the Devils Playground Volcanics suggest some potential for assimilation/ contamination from Mesoarchean crust (T_{DM} = 3.19 Ga). The calc-alkaline geochemistry and generally juvenile εNd(t) signatures (+2.61 to -1.1) suggest they may have formed in an arc-like environment, although the geodynamic significance of calc-alkaline igneous geochemical signatures in Archean rocks is a source of constant disagreement (van Hunen and Moyen, 2012). High-grade metasedimentary paragneisses and syn-sedimentary tonalitic intrusive from near the Challenger deposit in the Christie Domain, have been interpreted as forming in a long-lived, arc-like tectonic regime (Reid et al., 2014). Further south, the eruption of mafic and ultramafic lavas such as the 2520 Ma Lake Harris Komatiite (Hoatson et al., 2005) within the Wilgena Domain, suggesting only relatively thin crust was present in the Gawler Craton at this time.

Emplacement of major batholiths along the western Eyre Peninsula containing relatively juvenile εNd_t signatures (+0.5 to -2.1; Swain et al. (2005)) such as the 2520 Ma Dutton Suite and 2520 Ma Glenloth Granite (Fanning et al., 2007), occurred penecontemporaneously with granite formation in the central Eyre Peninsula with evolved εNd(t) signatures (+2.8 to -6.8) such as the

Carpa Granite (Wade and McAvaney, 2017). It remains unresolved whether the difference in Nd-isotopic signatures between these coeval granite suites represents increased crustal melt proportions in central Eyre Peninsula region, or an older isotopic component. The granodioritic composition of some members of the Dutton Suite, compared with the monzogranitic composition of the Carpa Granite advocate strongly for different proportions of crustal and mantle-derived melt components.

The 2480 – 2420 Ma Sleafordian Orogeny affected much of the Mesoarchean - Neoarchean nucleus of the Gawler Craton, peaking at granulite facies (850°C, 7-9 kbars; Reid and Hand (2012); Teasdale (1997)). Most of the granites generated syn- and post-Sleafordian Orogeny are weakly-peraluminious monzogranite-granodiorites considered to be derived from the partial melting of supracrustal TTG sources (Swain et al., 2005; Wade and McAvaney, 2017). Examples include the 2462 Ma Kiana Granite of the Dutton Suite and 2440 Ma Glenloth Granite of the Sleaford Complex and 2465 Ma Mobella Tonalite of the Mulgathing Complex (Fanning et al., 2007).

1.3.3 Middle Paleoproterozoic Crustal Evolution

Few examples of rocks have been dated between the Sleafordian Orogeny and the emplacement of the Donington Suite, representing a major tectono-thermal hiatus in the Gawler Craton of ~600 Ma. The Miltalie Gneiss (2002 Ma) and other undifferentiated orthogneisses of the Central Eyre Peninsula represent the limited examples of such rocks, and have been interpreted to represent a localised event, related to extension and formation of volcano-sedimentary depocentres of the Hutchison Group (Daly et al., 1998).

The 1860 – 1847 Ma Donington Suite is a bimodal suite, dominated by felsic batholiths which extend from the southern tip of the Yorke Peninsula, all the way to the Olympic Dam area – a distribution in excess of ~600km. The tholeiitic chemistry of co-magmatic dolerites and gabbronorites, relatively juvenile εNd_t signatures of the granites, coeval formation of charnockites on the south Eyre Peninsular and pervasive post-magmatic deformation fabric dated to ~1827 Ma by

syn-tectonic monazites led Reid et al. (2008) to suggest that emplacement of the Donington Suite occurred within a short-lived extensional-compressional cycle, possibly related to the far-field effects related to similar-aged convergent margins of the Halls Creek and Capricorn Orogen (Mortimer et al., 1988). The similarity of trace-element and REE geochemical signatures of the Donington Suite to those of the temporally-equivalent 1870 - 1840 Ma Kalkadoon Suite of the Mt Isa Inlier (Ba-Nb-Sr-P-to depletion; Fig. 1.3)) imply they both share a similar petrogenetic origin, suggested by Wyborn and Page (1983) to be the result of partial melting of 2100 – 1900 Ma-aged lower crustal TTG's. However, higher abundances of LILE-REE-HFSE in the Donington Suite (Fig. 1.3) does imply a greater crustal melt component (possibly metasedimentary in origin) was involved in its formation relative to the Kalkadoon Suite.

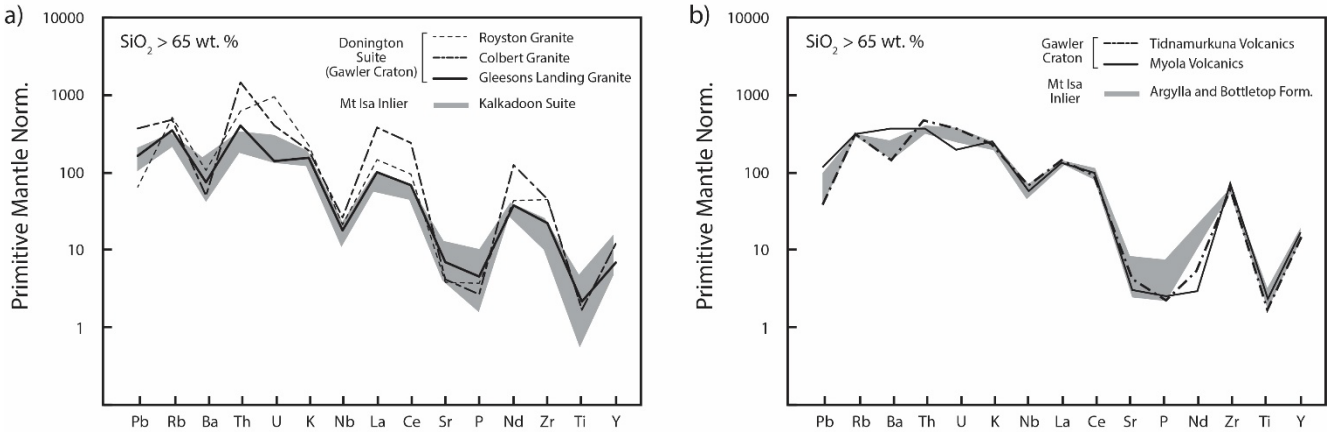

Figure 1.3: Primitive mantle normalised (McDonough and Sun (1995) geochemical signatures of the a) ~1850 Ma Donington Suite and b) ~1790 Ma Tidnamurkuna Volcanics and Myola Volcanics. Both igneous suites show broad geochemical similarities with temporally-equivalent igneous suites in the Mt Isa Inlier. Data compiled from Hopper (2001), Szpunar and Fraser (2010), Schaefer (1998) and Wyborn et al., (1987).

1.3.4 Late Paleoproterozoic Crustal Evolution

The geological history of the Gawler Craton during the Late Paleoproterozoic (1792 - 1700 Ma) leading up to 1690 – 1590 Ma, is thought to be dominated by intracontinental, extension-related volcanism and sedimentation, followed by craton-wide, compressional tectonics and crustal shortening of the 1730 – 1700 Ma Kimban Orogeny. Due to the vastly different geodynamic

paradigms invoked for rocks formed between 1792 -Ma 1730 Ma (extensional) and 1730 - 1700 Ma (compressional), they will be discussed separately below.

- Pre-Kimban Period (1792 - 1735 Ma)

Intracontinental, extensional tectonics led to the widespread formation of discrete depocentres across the Gawler Craton between 1792 – 1735 Ma. The earliest, magmatism associated with the Pre-Kimban periods is represented by the 1792 Ma (Fraser and Neumann, 2010) Myola Volcanics in the eastern Eyre Peninsula and the 1789 Ma Tidnamurkuna Volcanics/ 1787 Ma Wirriecurrie Granite (Fanning et al., 2007) of the Peake and Denison Inlier. Both the Myola Volcanics and Tidnamurkuna Volcanics share a number of similarities – they are both weakly-metaluminious to weakly-peraluminous, LILE-LREE-HFSE-enriched, bimodal but dominantly felsic (SiO_2 av. ~70 wt. %), rhyolites-rhyodacites, with a plagioclase (-hornblende) phyric mineralogy (Parker, 1993; Wyborn et al., 1987). Previous workers suggested that both the Tidnamurkuna Volcanics and Myola Volcanics formed in response to incipient intracontinental rifting (Parker, 1993). More recently, Reid et al. (2017) has suggested 1790 Ma volcanism is the result of far-field back-arc basin extension. Geochemical similarities (Fig. 1.3b) between the ~1790 Ma volcanism of the Gawler Craton and temporally-equivalent volcanism in the Mt Isa Inlier (1800 – 1790 Ma Argylla and Bottletree Formation; Wyborn et al. (1987), suggest extensional, within-plate volcanism was widespread across the Australian continent at this time.

The slightly younger, 1772 – 1735 Ma volcano-sedimentary package of the Wallaroo Group and equivalents which extended throughout the Olympic Province and into the My Woods Domain (Fig. 1.2), are also thought to have formed during within-plate extension. Despite an apparent 22 Ma age difference, the 1772 Ma Wardang Volcanics and 1755 Ma Moonta Porphyry of the Yorke Peninsula are geochemically very similar (Parker, 1993; Zang, 2006). They display notable enrichments in alkalis, LREE's and HFSE's, which led to their classification as A-type volcanics (Parker, 1993; Zang, 2006).

The geochronology and Sm-Nd isotopic signatures of granites such as the 1773 Ma Tip Top Granite (McAvaney et al., 2016) and 1768 Ma Wertigo Granites (Fraser and Neumann, 2010) imply that crustal melting was an increasingly important aspect of magmatism during the Pre-Kimban Period. Both contain ~1790 Ma inherited zircon age populations, similar in age to the Myola-Tidnamurkuna Volcanics. Likewise, both the Tip Top and Wertigo Granites contain εNd(t) signatures of ~-5, which are consistent with direct isotopic inheritance from crustal sources such as the Myola-Tidnamurkuna Volcanics (McAvaney et al., 2016).

- Syn-Kimban Period (1730 - 1700 Ma)

The 1730 - 1700 Ma Kimban Orogeny is widespread through the Gawler Craton, being observed in from the Eyre Peninsula in the southern Gawler Craton, to the Peak and Denison Inlier in the northern Gawler Craton, and Fowler Domain in the west (Hand et al., 2007). Widespread, east-verging, thrust-fold style deformations imply that the Kimban Orogeny reflects crustal shortening similar to continental-continental collision (Dutch, 2009; Tong et al., 2004). Crustal strain was controlled by movement along steeply-dipping, N-S faults such as the Kalinjala Mylonite Zone (Vassallo and Wilson, 2002), which separates the Spencer Domain from the Cleve Domain (Fig. 1.2). Regional metamorphism peaked at granulite-facies (850°C and 9 kbar; Tong et al. (2004)) in the southern Eyre Peninsula, and Amphibolite Facies (650°C and 7 kbar; Dutch (2009)) in the northern Eyre Peninsula region. Contemporaneous orogenesis in the Arunta Inlier (1740 – 1715 Ma Strangways Orogeny; Scrimgeour et al. (2005)) is characterised by similar peak metamorphic P-T conditions (750 – 950°C, 7.5 - 9 kbar; Norman and Clarke (1990)), and has been interpreted to represent collision between the Gawler Craton and Northern Australian Component (Betts and Giles, 2006).

High metamorphic temperatures during the peak-Kimban Orogeny (1730 – 1720 Ma) led to widespread crustal melting through the Eyre Peninsula. Subsequently, much of the magmatism associated with the Syn-Kimban period (monzogranites-syenogranites) are characterised by

peraluminious and alkali-rich geochemical composition (Fig. 1.4), and highly-evolved Sm-Nd isotopic signatures (Fig. 1.4) typical of supracrustal melts. Examples include the 1726 Ma Middle Camp Granite (Fanning et al., 2007), 1720 Ma Carappee Granite (Fraser and Neumann, 2010) and 1722 Ma Paxton Granite (Budd, 2006b).

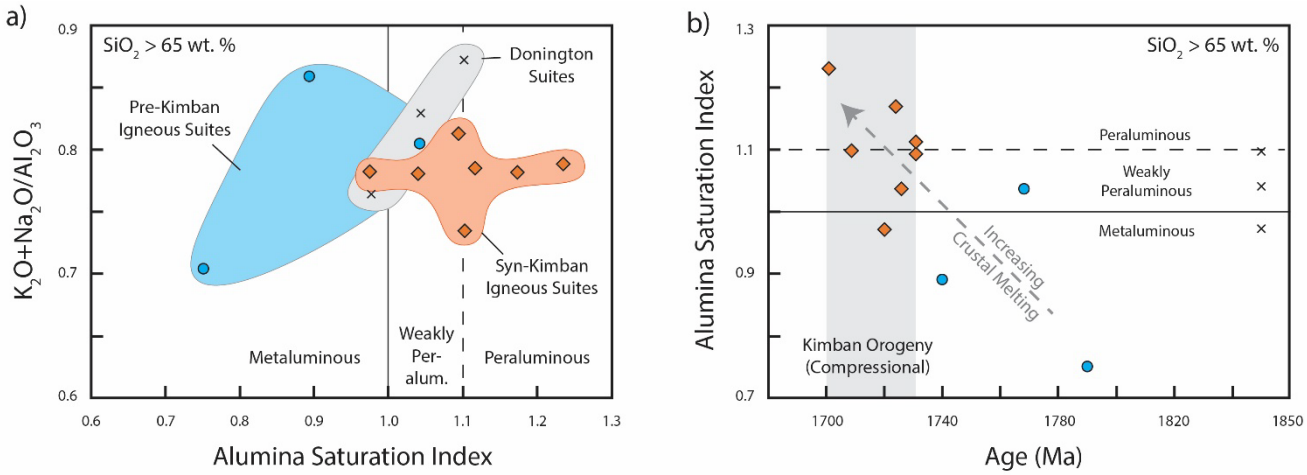

Figure 1.4: Alumina saturation index compared with the abundance of a) alkalis and b) through time (1850 – 1700 Ma). Syn-tectonic granitoids are generally much more peraluminious than pre-tectonic igneous suites. Data compiled from Schaefer (1998), Szpunar and Fraser (2010), McAvaney et al., (2016), Fraser and Neumann (2010), Wade and McAvaney (2016) and Budd (2006).

The magmatism during the post-peak stage (1720 – 1700 Ma) of the Kimban Orogeny is characterised by a renewed phase of anatectic crustal melting and granite formation. Strongly-peraluminous, garnet-bearing leucogranites (Fraser et al., 2010), and two-mica monzogranites (Wade and McAvaney, 2016), are widespread in the Eyre Peninsula during this time, though low-SiO_2 (55 wt. %) monzonites (i.e. 1701 Ma Chinmina Monzonite; Fanning et al. (2007)) are also known. All granitoids, including the low-SiO_2 Chinmina Monzonite, have strongly-evolved εNdt signatures (~-5 to -10; Fig. 1.5), consistent with predominantly crustal melt sources. Post-peak metamorphic assemblages indicate a clockwise P-T-t path (Tong et al., 2004), with rapid exhumation (Dutch, 2009) and decompressive anatexis in a thrust-sheet structural setting (Tong et al., 2004) similar to the Himalayan Leucogranites (Harris et al., 1986).

1.3.5 Crustal Reworking versus Crustal Renewal in the Late Paleoproterozoic

Overall, the mineralogical, geochemical and Sm-Nd isotopic signatures of igneous suites related to the Pre-, Syn-, and Late Kimban orogenic periods are consistent with the increasing contribution of crustal-melting to magmatism. εNd_t and εHf_t signatures of felsic rocks show a steady descent toward strongly-evolved signatures from the Pre-Kimban (~0 to -5), to the Syn- and Late-Kimban Periods (-5 to <-10), suggestive of a progressive increase in crustal melt generation (Fig. 1.5). However, the nature of crustal evolution in the Gawler Craton appears to change dramatically immediately following the Kimban Orogeny. A sudden increase in mantle-driven magmatism is suggested by an increase in the juvenile εNd_t signatures related to the 1690 - 1670 Ma Tunkillia Suite which were emplaced along the ~1690 Ma continental margin of the Gawler Craton (Fig. 1.5). The influence of mantle-driven magmatism appears to have continued for the remaining tectonic history of the Gawler Craton (Fig. 1.5), culminating in the widespread ~1590 Ma Hiltaba/ Gawler Range magmatic event. The exact tectonic mechanism which triggered the switch from 1765 - 1700 Ma crustal

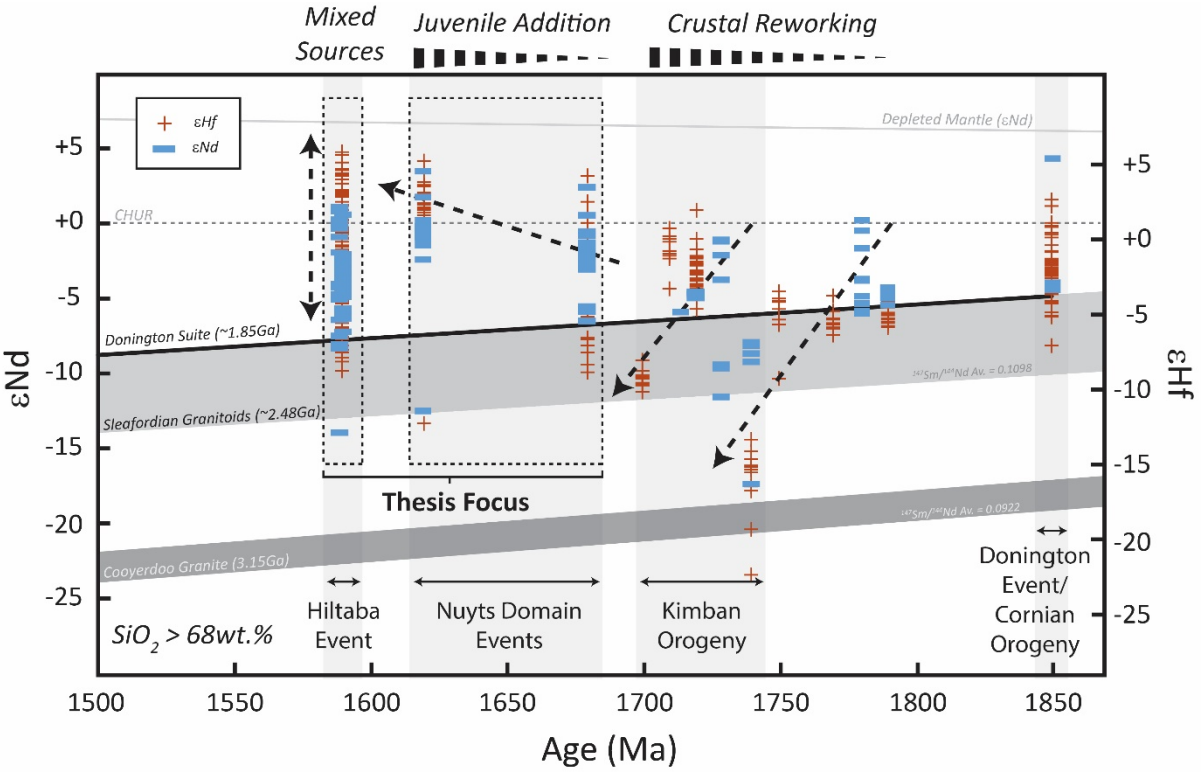

Figure 1.5: εNd_t and εHf_t for felsic igneous suites (SiO_2 >68 wt. %) of the Gawler Craton. Data compiled from Budd (2006), Fraser et al. (2010), Hopper (2001), McAvaney et al. (2016), Payne et al. (2010), Reid and Payne (2017), Stewart (1994), Stewart and Foden (2003), Swain et al. (2008), Szpunar and Fraser (2010), Wade and McAvaney (2016), Wurst (1994).

reworking, to rejuvenated mantle input during the 1690 – 1590 Ma period remains an outstanding question in the evolution of the Gawler Craton. Importantly, the period of renewed mantle-input responsible for 1690 – 1590 Ma magmatism is also associated with much of the economic mineralisation within the Gawler Craton, including the Central Gawler Au belt (e.g. Tunkillia and Tarcoola Au Fields Budd and Skirrow (2007); Ferris (2001)), Pb-Zn mineralisation of Menninnie Dam (Roache, 1996), and of course, the world-class IOCG province (Olympic Dam, Prominent Hill, Carrapateena, Oak Dam, Acropolis and Wirrda Well; Belperio et al. (2007); Davidson et al. (2007); Skirrow et al. (2007)). It is for these important reasons, that the crustal evolution and metallogenesis of the Gawler Craton during the period of 1690 – 1590 Ma will be the focus of this thesis.

1.4 The Pb-isotopic System in the Context of Crustal Evolution and Alkali Feldspars

1.4.1 Introduction

There are four main Pb-isotopes (^{204}Pb, ^{206}Pb, ^{207}Pb and ^{208}Pb) with three of these (^{206}Pb, ^{207}Pb and ^{208}Pb) generated as the end result of radioactive decay of ^{238}U, ^{235}U and ^{232}Th, respectively. ^{204}Pb is a non-radiogenic Pb-isotope which was largely generated during nucleosynthesis in the early universe, and whose concentration in the Earth has remained relatively unchanged since the Late Heavy Bombardment during the Hadean (4.1 – 3.8 Ga). A component of the radiogenic Pb-isotopes (^{206}Pb, ^{207}Pb and ^{208}Pb) were also generated during nucleosynthesis as well as produced from radioactivity between the beginning of the universe (13.8 Ga), and the formation of the Earth (4.54 Ga). The best estimate of the 'primordial Pb' - which represents bulk Earth at the time of formation - is derived from the Pb-isotopic composition of troilite (a high-temperature polymorph of pyrrhotite) within the Canyon Diablo iron meteorite (Patterson, 1956; Tatsumoto et al., 1973).

The value, in real terms, of the Pb-isotopic system (such as Pb-Pb), which contains both non-radiogenic and radiogenic isotopic constituents, is that the effects of time *OR* U-Th-Pb concentration to be normalised by ratioing (i.e. ^{206}Pb/^{204}Pb). Variations in Pb-isotopic ratios (i.e. ^{206}Pb/^{204}Pb, ^{207}Pb/^{204}Pb, ^{208}Pb/^{204}Pb) produced at any one time in geological history indicate variations in the relative concentrations of U-Th-Pb (i.e. U/Pb, Th/Pb, Th/U) throughout the Earth. Conversely, in any reservoir with a constant U/Pb, Th/Pb and Th/U, the variations in Pb-isotopic ratio must be the result of time-dependant decay of ^{235}U, ^{238}U and ^{232}Th. The difference between the Pb-Pb isotopic system (studied here) and the U-Pb isotopic system commonly used in geochronology, is that the daughter radiogenic Pb-isotopes (^{206}Pb, ^{207}Pb, ^{208}Pb) have *generally* not remained in a closed system with, parental ^{235}U, ^{238}U, ^{232}Th. Therefore, geological ages cannot be unequivocally obtained from using the Pb-Pb isotopic system alone.

The implicit open system behaviour of the Pb-Pb system is also a key advantage for its use in studying crustal evolution. Since the geochemical behaviour of U, Th and Pb is radically different in

all magmatic, metamorphic and hydrothermal conditions, secular isotopic reservoirs can develop depending on U-Th-Pb concentrations as well as residency of these elements within the isotopic reservoir. These discrete Pb-isotopic signatures can then be used to trace the sources of magmatic Pb (Allègre et al., 1988; Dupre and Allegre, 1983; Zartman and Doe, 1981; Zartman and Haines, 1988) or the sources of ore Pb (i.e. Cannon and Pierce (1969); Russell and Farquhar (1960); Russell et al. (1961); Stanton and Russell (1959)), in order to better understand how the crust evolved, an igneous suite developed, or an ore deposit formed. Therefore, Pb-isotopes represent an ideal way to investigate the ancient behaviours of U, Th and Pb within the crust, and assess the range of melt-sources contributing to a magmatic event.

The approach of crustal evolution studies using Pb-isotopes tend to follow one of two-themes (Fig. 1.6);

1) Studies targeting Pb hosted in Pb-rich minerals (i.e. galena),

2) Studies targeting Pb hosted in Pb-poor, but U-Th deficient minerals (i.e. alkali feldspar).

Studies that focus on Pb-rich minerals such as galena rely on the high-concentration of Pb to preserve the original Pb-isotopic signature against post-formational modification by radiogenic Pb, however can be strongly by influenced how mineralization formed and therefore may not indicate crustal evolution, *sensu stricto*. For example, convective hydrothermalism associated with syngenetic deposits (i.e VHMS and SEDEX) tends to result in homogenous average isotopic compositions of the crust in which they form (Russell, 1972), whereas orthomagmatic deposits (i.e. Cu-Au-Mo porphyries) mostly reflect the Pb-isotopic composition of very localised sources (magmatic and crustal sources; Carr et al. (1995); Sillitoe and Hart (1984)). In contrast, studies that use Pb-poor minerals such as K-feldspar rely on the absence of U and Th within the crystal to preserve the original Pb-isotopic signatures, and exclusively host igneous or metamorphic Pb-

isotopic signatures related to crustal and mantle variation. The work in this thesis uses both approaches.

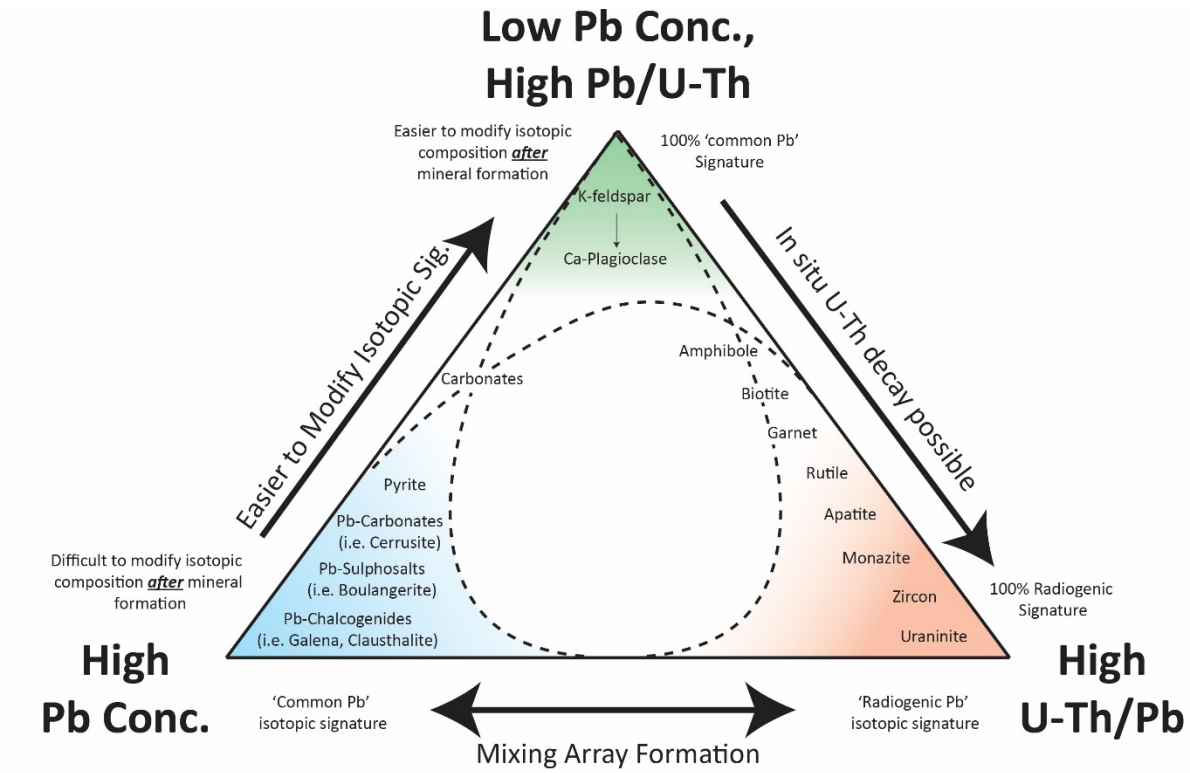

Figure 1.6: Summary of the different approaches to the U-Th-Pb system. The Pb-Pb system specifically relates to the top and left vertices (High Pb/(U-Th)), while U-Pb and Th-Pb (High (U-Th)/Pb) relates to the right vertex.

1.4.2 Crustal Growth Curves

Crustal growth curves, and the concepts behind them form an important framework for this thesis. The literature regarding growth curves is vast, and the evolution in thinking which has led to their development is complicated. As such, only a short overview of the two most commonly used growth curves will be discussed below. However, curious readers are referred to the works of Alpher and Herman (1951); Holmes (1946); Oversby (1974); Russell (1972); Stanton and Russell (1959).

Many Pb-rich SEDEX and VHMS deposits ('Conformable Pb') from around the world and from different geological periods contain homogeneous Pb-isotopic signatures that appear to indicate they formed from a single, isotopic reservoir within the Earth (Fig. 1.7). This fact was recognised early on (i.e. Holmes (1946); Nier et al. (1941)) and seems to suggest that the addition of radiogenic

Pb to a common Pb component (i.e. "growth") occurred at a relatively steady rate, and thus could be numerically-modelled to investigate the development of the Earth's crust. However, the disparity between the Pb-isotopic signatures of conformable Pb deposits (crust) and meteoritic Pb-isotopic compositions (primitive earth) suggested that the formation of crust either; a) did not occur *linearly*, or b) did not occur *continuously* (Oversby, 1974; Tatsumoto et al., 1973*)*. In 1975, two growth curve models were independently published by Stacey and Kramers (1975) and Cumming and Richards (1975) which provided very different resolutions to this conundrum, and are still used widely in modern Pb-isotopic research. The Stacey and Kramers (1975) model assumes *linear* crustal growth which occurred sometime considerably after formation of the primitive Earth. In contrast, the Cumming and Richards (1975) approach assumes continuous formation of the crust, with a linear acceleration in the U/Pb ratio of the crust. The various nuances and advantages/ disadvantages of the two models will be discussed further below, with the aim of determining which model is the most appropriate to use for the Late Proterozoic rocks of the Gawler Craton.

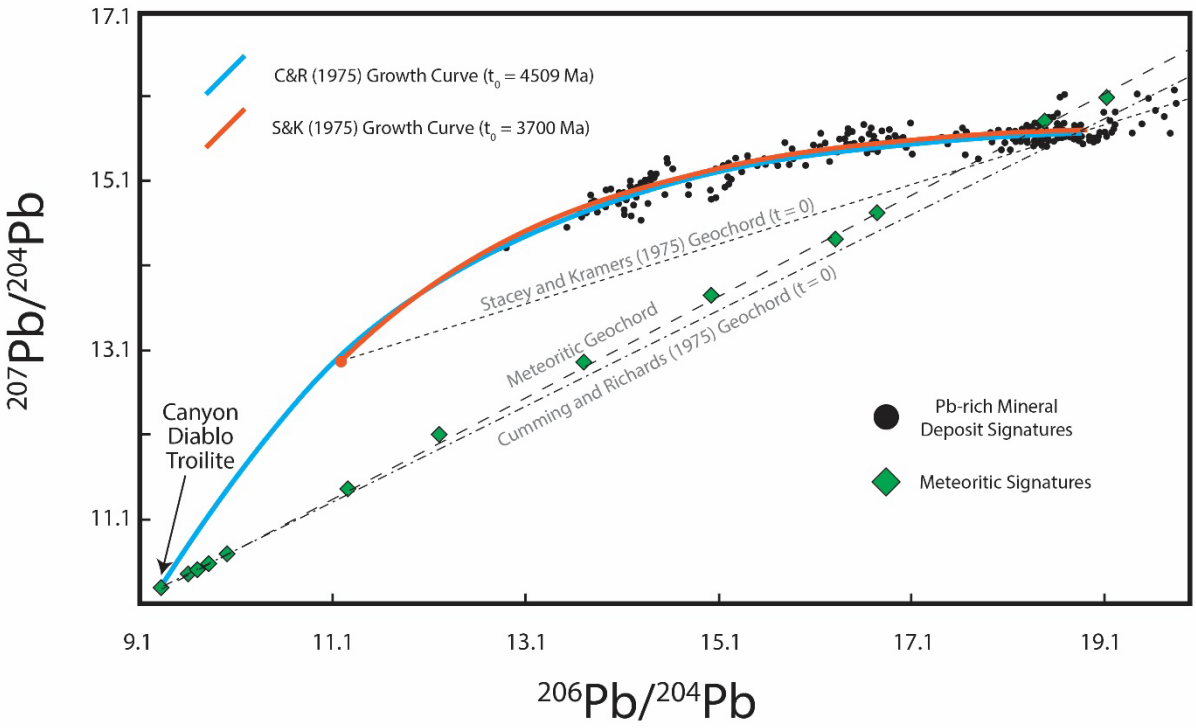

Figure 1.7: Summary of the Stacey and Kramers (1975) and Cumming and Richards (1975) Pb-isotopic growth curves in relation to the meteoritic compositions (Gopel et al. (1985); Tatsumoto et al. (1973) and Tatsumoto et al. (1976)) and major Pb-rich mineral deposits (Stanton and Russell (1959)).

Table 1.1: Growth Curve Parameters

	Stacey and Kramers (1975)	Cumming and Richards (1975)
$^{238}U/^{204}Pb$ (μ)	9.74	10.75
$^{238}U/^{235}U$	137.8	137.8
$^{232}Th/^{238}U$ (κ)	3.78	3.84
ε $^{238}U/^{204}Pb$	-	0.00005
ε $^{235}U/^{204}Pb$	-	0.00005
ε $^{232}Th/^{238}U$	-	$3.73x10^{-05}$
λ_{238}	0.000155	0.000155
λ_{235}	0.000985	0.000985
λ_{232}	$4.95x10^{-5}$	$4.95x10^{-5}$
t_0 (Ga)	3.7	4.509
$^{206}Pb/^{204}Pb$ (t_0)	11.152	9.307
$^{207}Pb/^{204}Pb$ (t_0)	12.998	10.294
$^{208}Pb/^{204}Pb$ (t_0)	31.23	29.476
$^{206}Pb/^{204}Pb$ ($t = 0$)	18.703	18.824
$^{207}Pb/^{204}Pb$ ($t = 0$)	15.631	15.671
$^{208}Pb/^{204}Pb$ ($t = 0$)	38.626	38.886
Modifiable μ?	Yes	Yes
Modifiable κ?	Yes	Yes
Modifiable t_0?	Yes	No
Modifiable ε?	No	Yes

- The Cumming and Richards (1975) Model

In essence, the Cumming and Richards (1975) growth curve is a single-stage model which starts from the Canyon Diablo Troilite Pb-isotopic signature of Tatsumoto et al. (1973), passing through the major 'conformable' Pb-isotopic signatures, before being forced through the Pb-isotopic signature of the Captains Flat VHMS, located in the central Lachlan Orogen, Australia. Being forced through the Captains Flat signature means that the Cumming and Richards (1975) model is the most accurate for the Lachlan Orogen (Carr et al., 1995), and this is presumably why it is the favoured model by Australian researchers (Carr et al., 1996; Huston et al., 2016; Sun et al., 1994). The unique feature of the Cumming and Richards (1975) growth curve, is that it incorporates a steady-increase, or acceleration, of the μ and κ parameters ('ε' parameter; Table 1.1) that would be consistent with the preferential concentration of U and Th over Pb. There is strong geological support for a steadily increasing μ in some reservoirs (i.e. carbonates; Babinski et al. (1999)) and following certain geological events (i.e. greisen development; Dostal et al. (2004)). However, there is even greater

evidence that the Pb-isotopic evolution of the crust and mantle has not evolved as a single, closed system (Allègre et al., 1986; Dupre and Allegre, 1983; Elliott et al., 1999; Sun et al., 1975; Tatsumoto, 1978).

The real utility of the Cumming and Richards (1975) growth curve when applied to modelling crustal evolution, is the ability to modify the acceleration factor ('ε'). Modification of ε, allows a curve to be regionally-calibrated to a single, homogeneous signature, usually from a Pb-rich deposit with a well constrained geological age (i.e. HYC; Sun et al., 1994, Captains Flat, Carr et al., 1995). Unfortunately, however, the Gawler Craton lacks the conformable, Pb-rich mineralisation of the temporally-similar Curnamona Province (Broken Hill) and Mt Isa Inlier (HYC), and therefore this major advantage is largely lost. The closest example from the Gawler Craton relates to the Menninnie Dam Zn-Pb-Ag deposit, which yield ~1590 Ma model ages, yet is hosted in Paleoproterozoic sediments of the Hutchison Group and has been variably interpreted as both syngenetic and epigenetic (Roache, 1996). Furthermore, the efficacy for invoking accelerated growth is questionable in the absence of evidence for it (i.e. accelerated μ-variation), and may be misleading if the geological age is not well-constrained (i.e. Rb-Sr dating is prone to thermal resetting) or there is any uncertainty as to whether a Pb-isotopic signature has been affected by post-formational modification by radiogenic Pb (such is common with K-feldspar studies).

- The Stacey and Kramers (1975) Model

In contrast to the single-stage model of Cumming and Richards (1975) which extrapolated forwards from the known isotopic composition of the Canyon Diablo Troilite, the Stacey and Kramers (1975) model is a two-stage growth curve, which works backwards from an average crustal Pb-isotopic value represented by a mixture of pelagic sediments and deep-sea manganese nodules. The Stacey and Kramers (1975) model supposes that the beginning of a second growth stage (t_0) may have some geologically-significant meaning, and therefore μ and κ parameters were derived such that the growth curve best fits the 'conformable' Pb-isotopic signatures. The start-time (t_0) was calculated to

be 3.7 Ga, which is consistent with many previous studies which show that major mantle-crustal differentiation event had largely concluded around this time (Hawkesworth and Kemp, 2006; Moorbath et al., 1978).

In terms of modelling crustal evolution, the Stacey and Kramers (1975) growth curve is less flexible than the Cumming and Richards (1975) growth curve. While μ and κ can be varied to fit a known Pb-isotopic signature, the absence of an acceleration factor (i.e. 'ε') means that the only option is to change the start time (t_0), finishing Pb-isotopic composition ($t = 0$) or addition of a growth stage (μ_3, κ_3). The significance of a modified t_0 is difficult to ascertain, and geological validation requires recognition of a crustal reservoir with an age and Pb-isotopic composition consistent with the invoked t_0 (i.e. Kramers and Tolstikhin (1997)) or calculated μ_3 (i.e. Godwin and Sinclair (1982)).

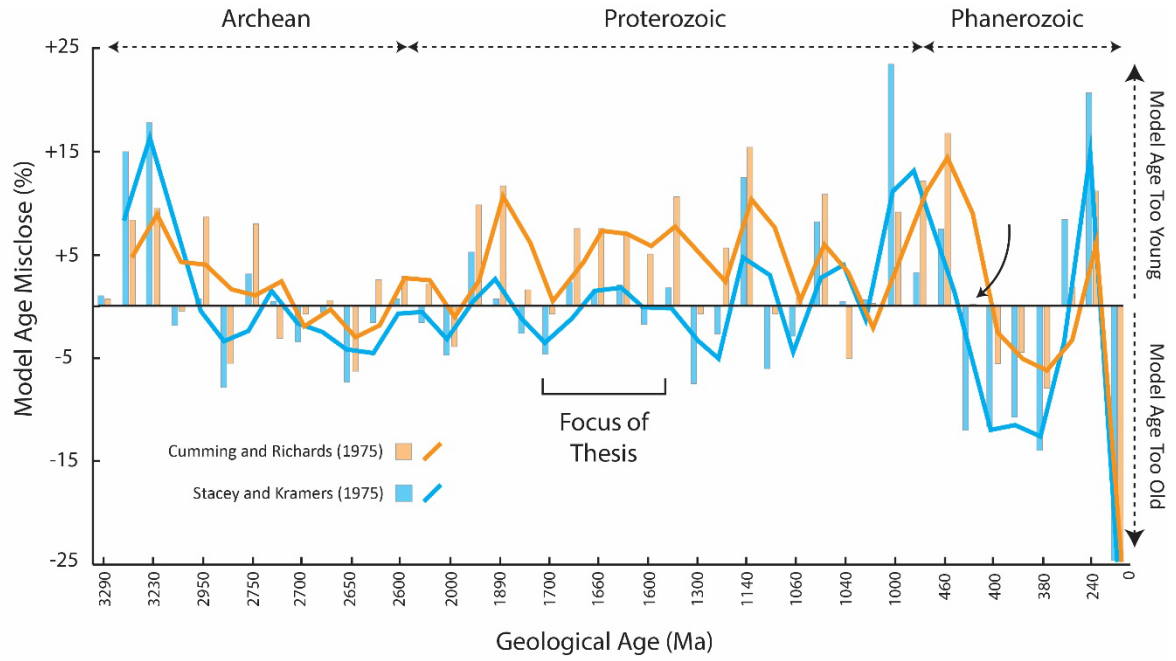

Figure 1.8: A diagram outlining the performance of model ages produced by the Stacey and Kramers (1975) and Cumming and Richards (1975) growth curves relative to geological ages ("Model Age Misclose"). For the period of geological time which this thesis focusses on (1690 – 1590 Ma), the Stacey and Kramers (1975) is the most accurate.

- Which Growth Curve to Use?

The true test of the accuracy of crustal growth curves, relates to how closely a model age derived from the curves reflects the geological age (U-Pb). Figure 1.8 shows this, by comparing the misclose between model age and geological age of various deposits used by both Cumming and Richards (1975) and Stacey and Kramers (1975). Neither model is particularly effective during the Eoarchean-Mesoarchean or Phanerozoic, generally producing model ages which are younger than geological ages. The Cumming and Richards (1975) appears to be best suited during the Neoarchean and Mid Phanerozoic, although part of this is related to the fact that its calibrated to an Ordovician-ages Pb-isotopic signature. In contrast, the Stacey and Kramers (1975) growth curve is the most accurate model during the Proterozoic. Therefore, since this thesis focusses on igneous suites from the late Paleoproterozoic to Mesoproterozoic, the Stacey and Kramers (1975) model will be used.

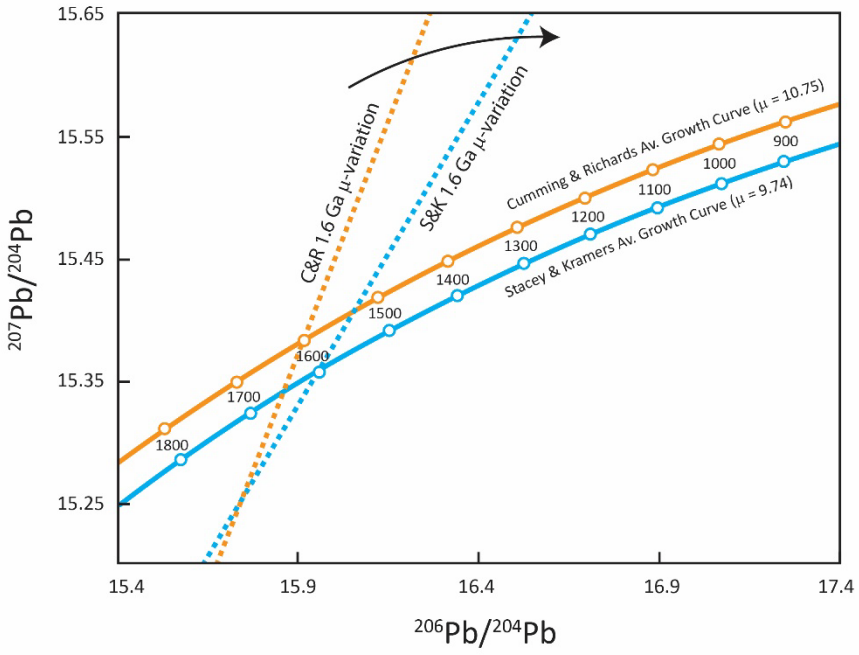

Figure 1.9: The difference between the slope of the 1.6 Ga isochron linking μ-variation for the Stacey and Kramers (1975) and Cumming and Richards (1975) growth curves.

The slope of the isochrons is an additional aspect of the growth curves that should be considered, although it is difficult to consider in the absence of previous regional Pb-isotopic studies, and will be continuously tested through this research. Isochrons (or geochords) are lines which start

from the t_0 signature, and link all μ-variations (and κ) belonging to the same model age. As Figure 1.9 shows, the 1.6 Ga isochron for the Cumming and Richards (1975) model is significantly steeper than the same isochron for the Stacey and Kramers (1975). Theoretically, low-μ igneous rocks (i.e. mantle-derived) should sit on the same isochron as a coeval and comagmatic higher-μ igneous rock that has achieved a higher-μ signature by incorporating, say, an upper crustal Pb-isotopic signature.

1.4.3 Alkali Feldspar (K-rich) as a medium for initial Pb-isotopes

The importance of K-feldspar as a medium for Pb-isotopic studies in both economic geology and petrology was recognised early on. A 1956 abstract presented at the 20th International Geological Congress by Patterson et al. detailed how the Pb-isotopic compositions in K-feldspar may retain evidence of the crustal sources of a granite body. Murthy and Patterson (1961) then took this idea further, supposing that if a mineral deposit was related to a granite, then the Pb-isotopic composition of galena related to mineralisation should match the signature of granitic K-feldspars. Ironically, the study by Murthy and Patterson (1960) is also one of the earliest records to point out that interpreting the Pb-isotopic compositions retained in K-feldspar is not necessarily a straight forward procedure, and can be strongly affected by alteration/ metamorphism.

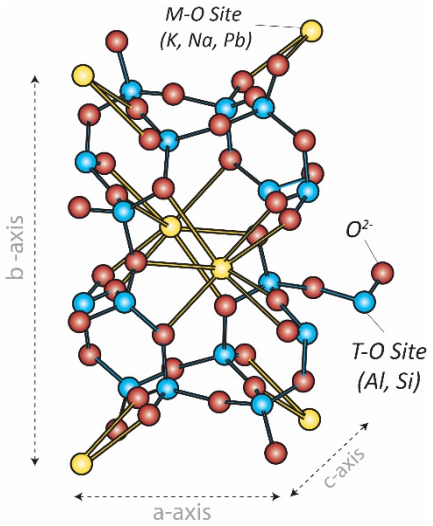

Figure 1.10: 3D C2/m centred crystal lattice structure of alkali feldspar, showing the M- (metal), T- (tetrahedral) and O-sites (oxygen). This particular lattice was measured for the 1590 Ma Roxby Downs Granite during the course of this research.

The use of K-feldspars for Pb-isotopic studies is built on the premise that a Pb-retained within the crystal lattice of a mineral which does not contain U or Th will retain the unmodified Pb-isotopic signature of the magmatic sources (mantle, upper crust and lower crust), irrespective of closed-system magmatic processes such as differentiation and crystal fractionation (Doe, 1967). Since Pb-isotopic analyses of K-feldspar comprises a large portion of the work presented in this thesis, it is important to consolidate information regarding where Pb sits within the feldspar lattice, and understand the thermodynamic processes which can lead to the modification of Pb within an alkali feldspar.

- Pb in Alkali (K-Na) Feldspars

Feldspars, both plagioclases and K-rich alkali feldspars, form crystals with the general chemical formula $M_1T_4O_8$, where; M = metal site (K^+, Na^+, Ca^{2+}), T = tetrahedral site (Al^{3+}, Si^{4+}) and, O = oxygen site (Fig. 1.10). As a metal with a low valency ($<^{3+}$), Pb within the feldspars is situated within the M-site. Despite the similar valencies of Pb^{2+} and Ca^{2+}, Pb is more compatible in K-bearing feldspar. This is due to the ionic radius of Pb^{2+} (119 pm) which is too large to fit into the M-site of Ca-plagioclases (Ca^{2+} = 100 pm) or Na-plagioclases (Na^+ = 102 pm), but is compatible with the lattice site of K^+ (138 pm). The net ionic deficit caused by substituting Pb^{2+} for K^+ is mitigated either through direct substitution ($2K^+ \rightarrow Pb^{2+}$) leaving a lattice defect, or through a coupled-substitution ($K^+ + Si^{4+} \rightarrow Pb^{2+} + Al^{3+}$) where Al-Si remain disordered in the T_1 and T_2-sites (Fig. 1.10). At the higher temperatures (and higher entropy) consistent with the magmatic conditions of granite formation (>600°C), tetrahedral (Al-Si) disorder is thermodynamically-favoured over vacancy defects ($-K^+$) in a crystal lattice (Brown and Parsons, 1989; Hovis, 1997), and therefore coupled-substitution is the more likely process to account for the Pb in granitic K-feldspars which retain an unmodified initial Pb-isotopic composition. At lower temperatures, crystal lattices are more rigid and therefore vacancy defects (i.e. Schottky defects) are more likely (Brown and Parsons, 1989).

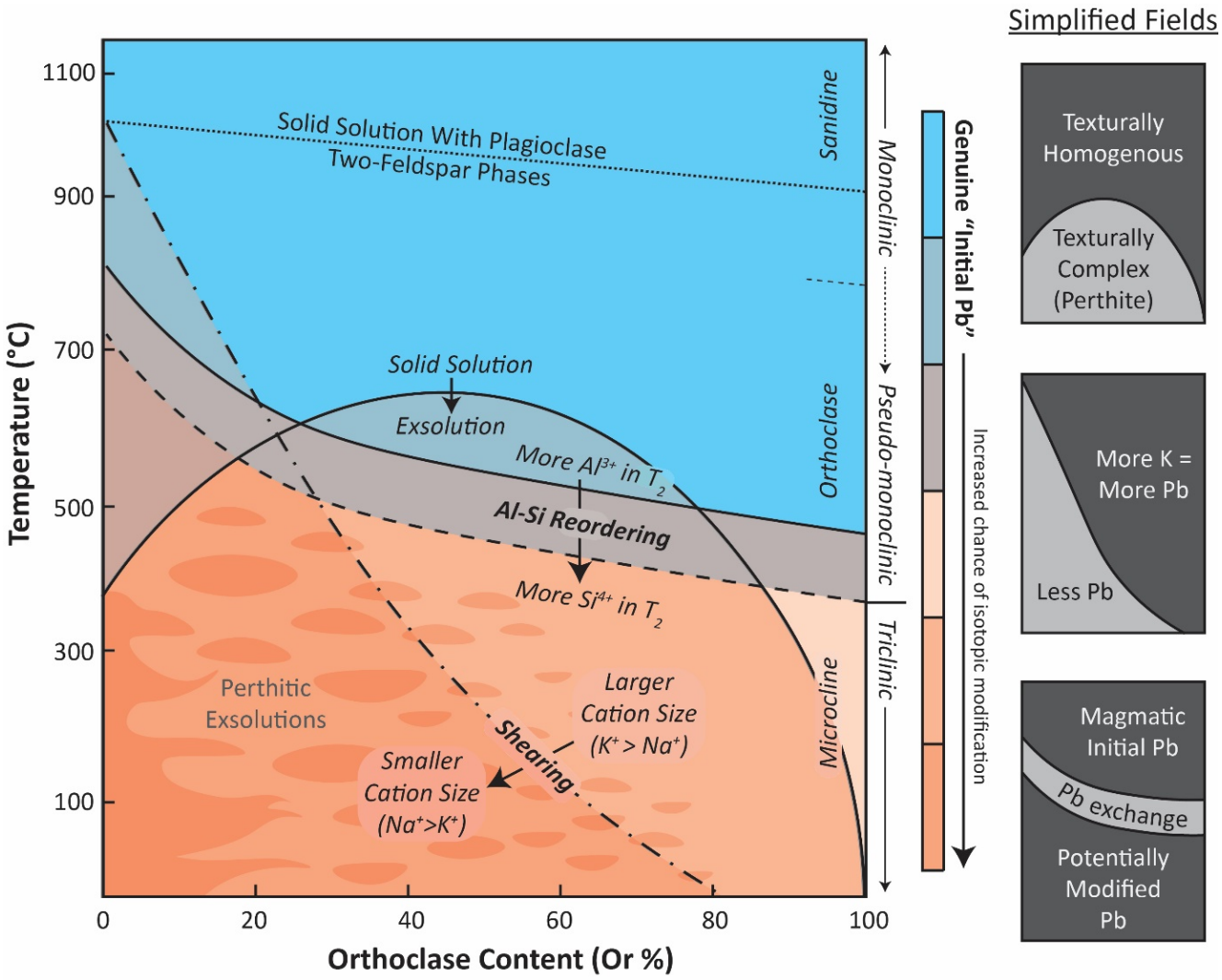

Figure 1.11: Thermodynamic affects to alkali feldspar crystallinity and their inferred effects to retention of initial (magmatic) Pb-isotopic compositions. Colour spectrum related to likelihood of initial Pb-isotopic signatures (blue = likely, orange = unlikely). Simplified fields on right. Left diagram modified from Parsons and Brown (1991).

- Translating alkali feldspar crystallinity to retention of initial Pb-isotopic signature

The phase diagram in Figure 1.11 attempts to synthesise the range of thermodynamic process acting on an alkali feldspar which may lead to modification of a genuine, initial Pb-isotopic composition. During slow cooling from magmatic temperatures, monoclinic orthoclase may undergo a transition to triclinic microcline which is more stable at low temperatures (Benisek et al., 2010; Brown and Parsons, 1989). This conversion process requires the redistribution of Al^{3+} from the T_2 to the T_1 site, thus potentially recreating the charge-imbalance caused by Pb^{2+}. If the monoclinic-triclinic transition occurs in the presence of late-stage hypersolvus fluids interacting with wallrock lithologies, Pb in the

K-feldspar may be theoretically exchanged thus modifying the initial Pb-isotopic signature (Parsons, 1978). Alternatively, if the conversion is driven by relatively high-grade metamorphism which has occurred a geologically-significant period of time after granite emplacement, then the initial Pb-isotopic signature may also be affected. The best example in the literature which highlights the link between K-feldspar crystallography and Pb-isotopic composition is presented by Doe and Hart (1963) and Hart (1964). In these studies, contact metamorphism from a Laramide-aged intrusion (80-70 Ma) has caused microclines in the Grevillian-age (1400 Ma) gneissic basement to convert to orthoclase (Fig. 1.12). Orthoclase related to the thermal aureole records Pb-isotopic signatures which have been increasingly reset with proximity to the intrusion. The conversion of microcline to orthoclase is noted to a distance of ~300m from the intrusion, where the Pb-isotopic signatures in microcline return to compositions akin to the ~1400 Ma age of the basement (Fig. 1.12).

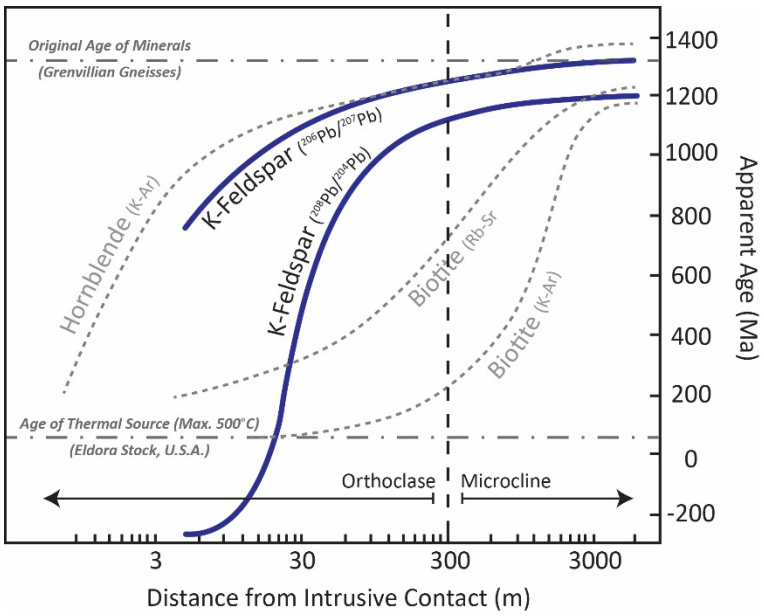

Figure 1.12: The effects of contact metamorphism (thermal perturbation) on the retention of primary Pb-isotopic compositions in alkali feldspar. Pb-isotopic signatures return to primary compositions approximately 100-200m from the heat source (Eldora Stock), while K-Ar and Rb-Sr in biotite remains affected for more than 2 km. Uranogenic Pb-isotopic compositions ($^{206}Pb/^{207}Pb$) appears to behave similarly to K-Ar system of hornblende. Diagram modified from Hart (1964).

While high-grade regional metamorphism is also well documented to affect the Pb-isotopic signatures in K-feldspar (i.e. Dostal and Capedri (1978); Gray and Oversby (1972); Moorbath et al.

(1969); Whitehouse (1989)) few studies outline the specific mechanism for Pb exchange. It is reasonable to suspect that Pb exchange in K-feldspars exposed to relatively high-grade metamorphism (>500°C; Middle Amphibolite Facies) would be controlled by crystallographic changes such as strain induced plastic recrystallisation via sub grain rotation (Benisek et al., 2010). At lower temperatures, however, any modification to the initial Pb-isotopic signature is more likely to be driven by a combination of passive diffusion (Cherniak, 1995; Parsons and Brown, 1991), fluid-assisted alteration focussed along lattice defects, such as albitisation (Lee et al., 1995; Norberg et al., 2011; Putnis et al., 2007) or retrogressive recrystallisation related to strain and deformation (Parsons and Brown, 1991), though for the most-part, all of these features can be identified using macro- and microscopic observations.

- Pb-diffusion and Closure Temperature in K-feldspar

Compared to many other minerals containing Pb, K-feldspar is a comparatively robust Pb-reservoir which is resistant to diffusivity process alone. Low-temperature Pb-diffusivity in K-feldspar is comparable to that seen in rutile and is orders of magnitude more resistant to Pb diffusion than sphene (titanite), apatite and uraninite (Fig. 1.13a) which are commonly used as U-Pb geochronometers (Mezger et al., 1989; Willigers et al., 2002). To put the Pb-diffusivity rate of K-feldspar into perspective, since the stabilisation of the Gawler Craton, Pb atoms within feldspar of the ~1590 Ma Hiltaba Suite have moved less than $2x10^{-17}$ mm through diffusion. In the scale of 10 – 20 mm phenocrystic alkali feldspar, this distance is very little. The concept of ‘closure temperature’ was first raised by Dodson (1973) and attempts to quantify the temperature when the diffusivity of isotopic elements (i.e. Rb, Sr, Pb, U, etc.) in a minerals effectively reaches zero. The ‘closure temperature’ equation of Dodson (1973) is a derivative of the Arrhenius Equation, which in addition to element diffusivity also accounts for the size and shape of a mineral. In minerals such as K-feldspar, where the diffusivity of an element (i.e. Pb) does not vary significantly between the crystallographic axis (Cherniak, 1995), it is common to assume an isotropic model (i.e. sphere) in the

calculation of closure temperature (Bellucci et al., 2011; Dodson, 1973). The relationship between closure temperature and crystal size is shown in Figure 1.13b for K-feldspars and other Pb-bearing minerals. At the typical crystal size ranges for alkali feldspar used in this study (~1.5 cm to 5cm), and indeed most feldspar in nature, it can be shown that alkali feldspar is effectively closed to the effects of Pb diffusion below temperatures 680 – 720°C, which significantly outperforms the Pb retention ability of apatite and sphene. Since this temperature exceeds the orthoclase-microcline transition, it should be expected that regional metamorphism at a lower grade than middle amphibolite facies will have minimal effect on the Pb-isotopic signatures in igneous alkali feldspars. Such conditions in the Gawler Craton were only established during the 2480 – 2420 Ma Sleafordian Orogeny and 1730 – 1700 Ma Kimban Orogeny, and thus widespread thermal effects are not likely to have affected the initial Pb-isotopic composition of igneous alkali feldspars analysed in this study (1690 – 1590 Ma).

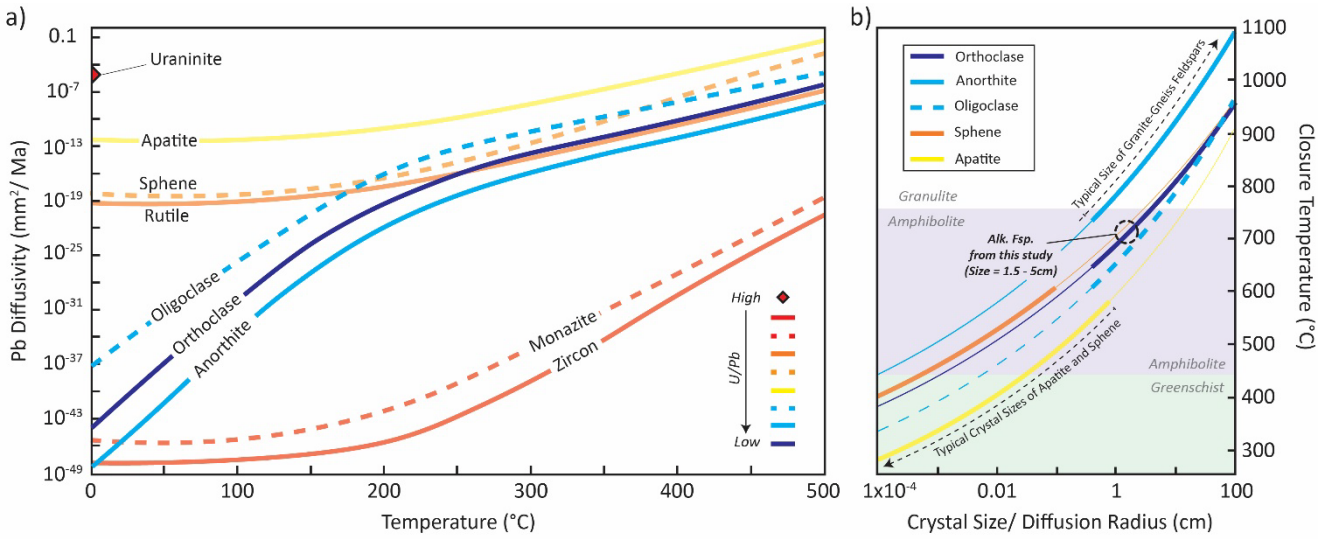

Figure 1.13: Pb-diffusivity data for the alkali feldspar and other important minerals containing Pb. a) At temperatures less than 200°C, alkali feldspars are effectively closed to Pb-diffusion. Above 200°C, the Pb-diffusivity rate of alkali feldspar is similar to slightly better than typically-resistate sphene and rutile. b) At crystal sizes typical of alkali feldspar phenocrysts studied in this research (1.5 – 5 cm), alkali feldspars remain effectively closed to Pb diffusion below ~700°C. Diffusivity parameters obtained from Cherniak (1995); Cherniak (2010); Cherniak and Watson (2001); Cherniak et al. (2000).

1.5 Summary

The crustal evolution of the Mesoarchean – Mesoproterozoic Gawler Craton is marked by cycles of crustal renewal and crustal reworking. Mesoarchean granites of the eastern Eyre Peninsula have an enigmatic origin, and are believed to be genetically similar to TTG suites of the Yilgarn and Pilbara Cratons. Neoarchean magmatism thought to be associated with a long-lived arc and hot-spot activity, terminated in 2480 Ma with the onset of high-grade metamorphism of the Sleafordian Orogeny, which formed supracrustal magmas and paragneisses throughout the northern, central and southern Gawler Craton. A period of relative tectono-thermal quiescence during the Early and Middle Paleoproterozoic ended with the intrusion of the widespread, bimodal ~1850 Ma Donington Suite into the eastern Gawler Craton, which may have formed within an extensional environment related to the far-field effects of convergent margin tectonics in the Halls Creek and Capricorn Orogens. Magmatism (volcanics and granitoids) between 1790 - 1730 Ma is associated with the development of volcano-sedimentary basins throughout the eastern and northern Gawler Craton, indicating an extensional tectonic regime at this time. By 1730 Ma, extension gave way to compression marking the onset of the 1730 - 1700 Ma Kimban Orogeny, which peaked at granulite facies in the southern Eyre Peninsula and upper amphibolite facies throughout the north, forming peraluminious supracrustal granitoids. Existing geochemical and isotopic data for the igneous suites emplaced between 1790 and 1700 Ma show that magmatism was increasingly dominated by high-volumes of crustal melting. In contrast, Sm-Nd isotopic evidence for the 1690 – 1670 Ma Tunkillia Suite, 1630 - 1608 Ma St Peters Suite and ~1590 Ma Hiltaba Suite/ Gawler Range Volcanics suggest that magmatism was driven by the addition of juvenile, mantle-derived melts into the crust. The exact tectono-thermal mechanisms associated with mantle-driven magmatism and crustal evolution during this period remain unclear, with definitive geological context prohibited by thick Neoproterozoic – Paleozoic cover sequences. With much of the Gawler Craton's economic mineral endowment temporally- and spatially-associated associated with the emplacement of relatively-juvenile magmas during this period, understanding the 1690-1590 Ma crustal evolution of the

Gawler Craton is of immense interest.

Pb-isotopic studies of alkali feldspars present an ideal way to investigate 1690 – 1590 Ma crustal evolution of the Gawler Craton. Pb-retained within the crystal lattice of magmatic alkali feldspars is not affected by magmatic processes such as crystal fractionation, with variation in initial (magmatic) Pb-isotopic signatures the result of U-Th-Pb residency, concentration and age of the melt source components. Transformations to the crystal structure of magmatic alkali feldspars (monoclinic) to low-temperature lattice geometries (triclinic) can potentially cause re-equilibration of Pb-isotopic signatures if exposed to open-system behaviour (I.e. assimilation, hydrothermalism). Once magmatic crystallisation is complete, Alkali feldspars are thermally robust reservoirs of Pb, requiring temperatures in excess of 700°C (Upper Amphibolite or Hornfels facies) for diffusional resetting processes to take place. However, initial Pb-isotopic compositions of alkali feldspars are not immune from the modifying effects of alteration and retrogressive recrystallisation, which require textural and geochemical observations to ensure that initial Pb-isotopic compositions have been retained.

Chapter 2: Determination of Pb-isotopic Ratios in Alkali Feldspar by LA-ICP-MS

2.1 Introduction

Most of the Pb-isotopic analyses comprising this thesis, were undertaken using in situ, laser ablation inductively coupled quadrupole mass spectrometry (LA-ICP-Q-MS, hereafter referred to as LA-ICP-MS). Only the results of Chapter 5 were analysed using higher-precision techniques such as laser ablation inductively coupled plasma multi-collector mass spectrometry (LA-ICP-MC-MS). LA-ICP-MS presents a number of benefits over conventional dissolution solution-based multi-collector ICP-MS, and thermal ionisation mass spectrometry (TIMS) despite the lower precision results. This chapter aims to demonstrate the effectiveness of Pb-isotopic analyses of alkali feldspars by LA-ICP-MS. This will be achieved by first highlighting the benefits of single-collector LA-ICP-MS, discussing the level of precision required for Pb-isotopic studies of crustal evolution, optimisation of analytical parameters for LA-ICP-MS and testing the optimised method on a K-feldspar standard.

2.2 Benefits of Laser Ablation Microsampling

The high-spatial resolution offered by LA-ICP-MS allows for the precise targeting of specific mineral phases. This is particularly important in the context of Pb-isotopic analyses of alkali feldspar, since alkali feldspars can be quite heterogeneous at microscopic scales. Moreover, the commonly complex intergrowth and inclusions of minerals containing radiogenic Pb (i.e. zircon, apatite, biotite etc), coupled with the low-Pb concentrations of alkali feldspar (5 – 100 ppm), make Pb-isotopic analyses using dissolution-based methods susceptible to problems related to mixing of Pb from different parts of the sample.

Laser ablation, integrated with other analytical techniques such as laser raman spectroscopy, hyperspectral cathodoluminescence and single-crystal x-ray diffraction allows for the targeting of

well-characterised sample domains. As discussed previously in Chapter 1, determining the crystallinity of alkali feldspars can provide additional confidence that magmatic, initial Pb-isotopic signatures have been preserved.

Laser ablation sampling also requires only minimal sample preparation, compared with conventional dissolution methods used for Pb-isotopic analyses of alkali feldspar (i.e. Ludwig and Silver (1977); Maas et al. (2015)). Sample preparation for LA-ICP-MS analyses typically involves fabricating an epoxy resin mount, polishing the ablation surface flat and cleaning the surface with relatively safe solvents (i.e. methanol etc). In contrast, the typical dissolution techniques for alkali feldspar (i.e. Ludwig and Silver (1977); Maas et al. (2015)) require time-consuming digestions (i.e. >15 hours; Maas et al. (2015)) involving the use of hazardous substances (i.e. HF).

2.3 Benefits of coupling Laser Ablation with Quadrupole ICP-MS

Coupling the laser ablation microsampling with ICP-MS analyses (single-collector or multi-collector) provides a Pb-isotopic method which is unrivalled in terms of sample throughput and analytical turn-around. While the simultaneous-detection of Pb-isotopes offered by multicollector ICP-MS undoubtably yields higher-precision results, single-collector (quadrupole) ICP-MS offers a number of benefits over MC-ICP-MS at a level of precision which remains fit for most petrological purposes (at least 0.2% uncertainty; Crowe et al. (2003)). Aside from being the most cost-effective of the two instruments, the key benefits of single-collector analyses versus multi-collector analyses are 1) dynamic range, and 2) ability to measure a large number of masses.

The ability to measure tens of masses through peak hopping modes, represents a major advantage of single-collector instruments over multi-collector instruments (Vanhaecke et al., 2009) through better characterisation of the ablated mineral. While many faraday detectors can feasibly be incorporated into a multi-collector's detector array (i.e. 9; Zhang et al. (2018), the additional cost and added difficulty in calibration has restricted availability of these instruments. The ability to

detect a large number of masses is useful in Pb-isotopic analyses of alkali feldspars for number of reasons. Firstly, it can quantitatively show that no U or Th is present in the alkali feldspar. Secondly, the geochemical composition of the alkali feldspars can be quantified (i.e. K, Na, Ca, Al, Si, Rb, Sr, La, Ce, Nd, Eu, Gd), and used to validate that only alkali feldspar was ablated during the Pb-isotopic analysis. Thirdly, the abundances of certain masses can be monitored to ensure no mineral inclusions were inadvertently ablated which may have affected the Pb-isotopic signature (i.e. Zr, P, Fe, Mg). The time-resolved nature of LA-ICP-MS provides an additional dimension to the combined Pb-isotopic/ multielement geochemistry of alkali feldspars, by providing a means to assess the relative homogeneity of the mineral, and quantify the causes of variations in Pb-isotopic ratios.

The flexible, dynamic range of modern single-collector instruments (Beauchemin, 2017) is also an important benefit in Pb-isotopic analyses of alkali feldspars. Pb concentrations of alkali feldspars vary over a wide range from as little as 2 ppm (Bellucci et al., 2011), to in excess of 2.5 wt. % (Stevenson and Martin, 1986). This range in Pb concentrations can be problematic for multi-collector instruments, where sudden increases in Pb-signal intensities can cause overloading (and destruction) of ion counters and faraday arrays (Vanhaecke et al., 2009). In contrast, modern single-collector instruments such as the Agilent 7900 mostly used in this study, can easy handle signal variations from 10 - 10^9 counts per second, by switching from pulse to analogue detection modes in the middle of the range.

2.4 How much analytical precision do we need?

The fundamental difference between single-collector and multi-collector instruments relates to precision – but how much precision do we *really* need for Pb-isotopic determinations of alkali feldspars? Typical 2σ uncertainties obtained by LA-ICP-MS from glass standard reference materials (SRM's) for the $^{206}Pb/^{204}Pb$ ratio during this study range between 0.25% for NIST610 and 0.58% for BCR-2G (Fig. 2.1).

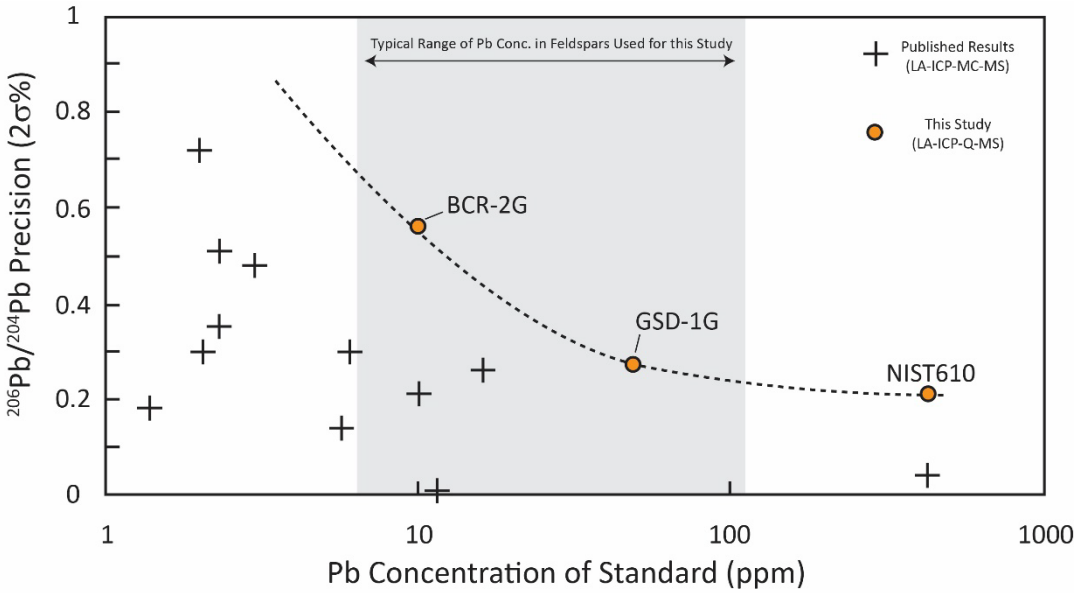

Figure 2.1: Comparison between LA-ICP-MS (this study) and LA-MC-ICP-MS $^{206}Pb/^{204}Pb$ Pb-isotope results obtained from glass standard reference materials (SRM's). LA-MC-ICP-MS SRM data after Paul et al. (2005), Souders and Sylvester (2008) and Zhang et al. (2014).

To put these uncertainties into a geological context, absolute uncertainties of 0.2% and 0.5% have been plotted on the Stacey and Kramers (1975) growth curve (Fig. 2.2). At a 0.5% absolute uncertainty, or the median uncertain based on typical feldspar Pb concentrations, the model age determination for a Hiltaba Suite-aged granite (~1.6 Ga Ma) will be ± 50 Ma, with μ = ± 0.8 and κ = ± 0.15. At the highest level of uncertainty expected of our LA-ICP-MS analyses in alkali feldspars (~0.2%), Figure 2.2 shows that ^{204}Pb-based Pb-isotopic ratios will provide a model age resolution of ± 25 Ma, with μ = ± 0.16 and κ = ± 0.07. This precision is sufficient to differentiate between mantle (μ =

9.2 – 9.5, κ = 3.6), upper crust (μ = 10.75, κ = 3.72) and lower crust (μ = 8.4, κ = 4.4) reservoirs (Zartman and Doe, 1981) and provide temporal constraints.

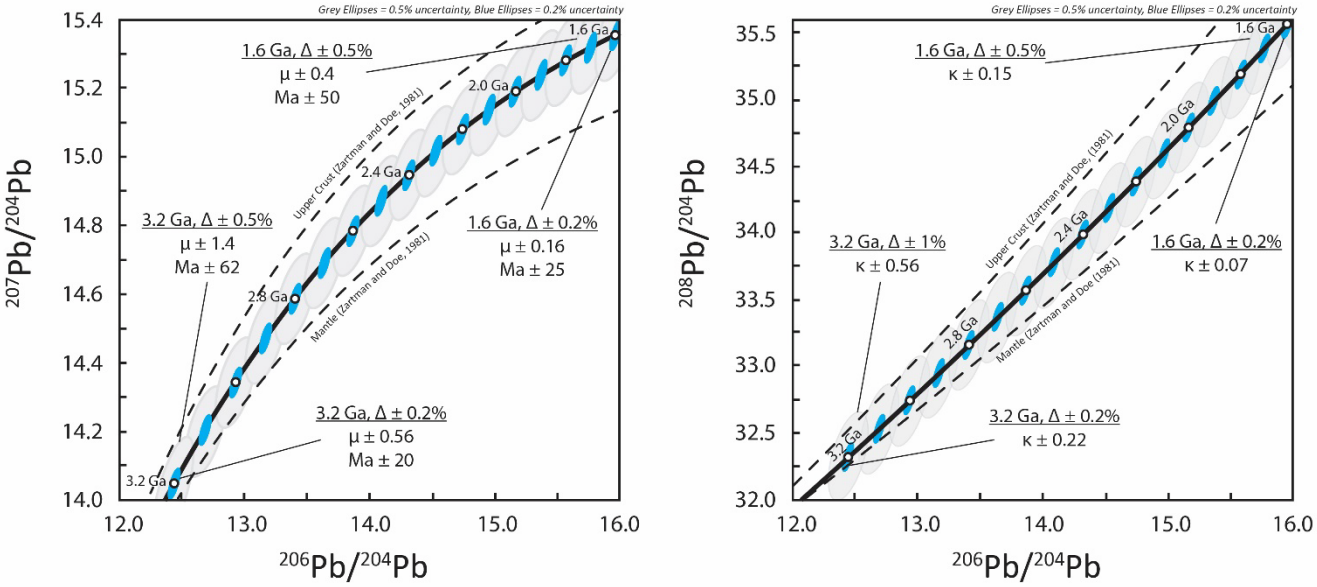

Figure 2.2: Analytical uncertainty (0.2% and 0.5%) in the context of average crustal reservoir of Stacey and Kramers (1975) and the Upper Crustal, Lower Crustal and Mantle Reservoirs modelled by Zartman and Doe, (1981). Blue ellipses represent 0.2% uncertainty. Grey ellipses represent ±0.5% uncertainty.

2.5 LA-ICP-MS Modelling and Optimisation

This section aims to optimise and validate the laser ablation-related analyses used throughout this thesis. Optimum analytical parameters for LA-ICP-MS were investigated using a computer-based model. The value of the model-driven approach taken here, is that the effect of individual variables on Pb-isotopic precision can be viewed in isolation, and thus allows us to view the impact on precision imparted by these variables.

2.5.1 Model Design and Apparatus

A computation based model was developed in collaboration with Prof. Leonid Danyushevsky, which accounts for a range of modifiable variables, including signal washout time, signal washout

geometry, dwell-time, dead-time, sweep-time, signal strength, signal-stacking, spot-size (Pb-concentration), Pb-isotopic composition, noise and counting statistics.

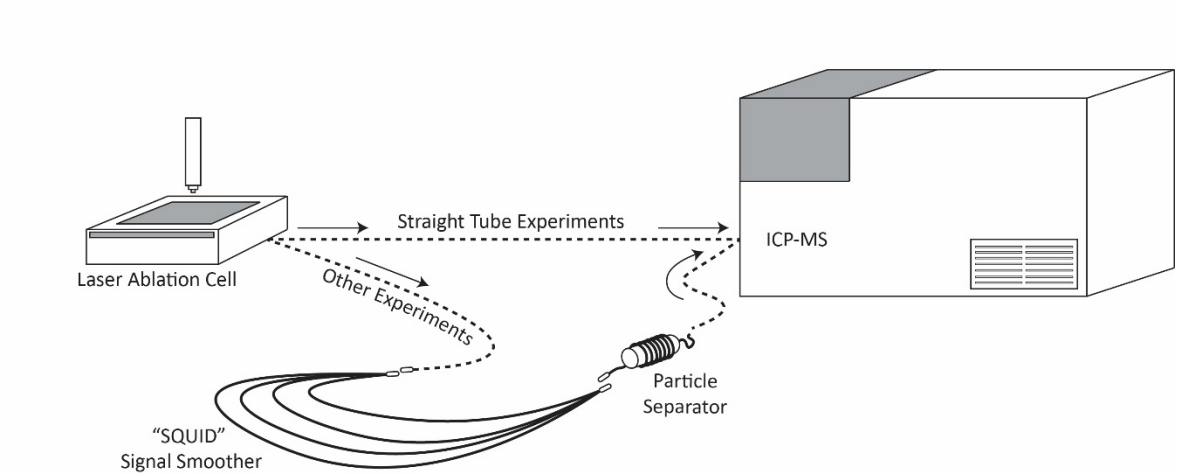

Figure 2.3: Apparatus design for the signal washout experiment, which the computer-based LA-ICP-MS model is derived from before.

The computer-based model is built around empirically-derived spectral curves, whose geometry is strongly affected by signal washout (i.e. time it takes for the ablated sample to completely pass from the ablation cell through the ICP-MS). The effect of signal washout was measured by single-firing the laser at NIST 610 glass and recording the spectral shape of a single mass (^{208}Pb) as the signal washed out. This was repeated with a straight-line tube between the ablation cell and ICP-MS which varied in length from 64cm, 74cm, 84cm and 400cm (Fig. 2.3). The effect of adding an inline signal smoothing device and particle separator (total tube length 1731 cm) were also calculated, and will henceforth be referred to as the SQUID experiment. The influence of concentration on signal intensity was nullified by normalising the area under each of the washout curves, so that the only variable was signal throughput. No significant differences were observed between the shorter tube lengths (i.e. 64 cm, 74cm, 84cm), and therefore they were combined to form the "70cm straight tube" curve (Fig. 2.4).

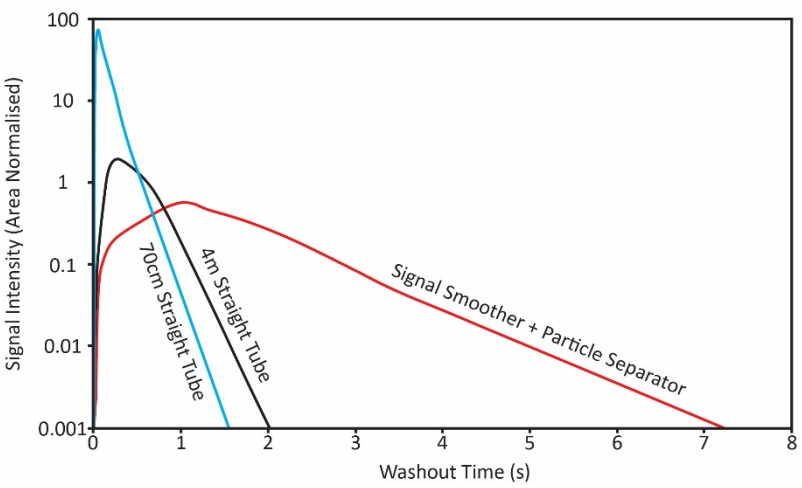

Figure 2.4: Area normalised (Pb concentration normalised) signal washout curves for ^{208}Pb derived from the single-shot ablation of NIST610 glass. Each curve represents the average of 10 individual experiments.

The washout curves (Fig. 2.4) were then integrated into a final computerised model which incorporates the effect of counting statistics on ICP-MS measurements. The model allows users to modify most of the major parameters that are crucial in LA-ICP-MS analysis (spot size, repetition-rate, dwell-time, sweep-time, dead-time, peak-stacking). For use in modelling the effect of these parameters on Pb-isotopic analysis, it was also important to be able to customise the signal intensities of the Pb-masses (204, 206, 207, 208). Signal intensities for the four masses were derived by using a typical ^{204}Pb signal intensity encountered in a K-feldspars with known Pb concentration, and back-calculating the intensities for ^{206,207,208}Pb at a given Pb-isotopic signature (i.e. 1590 Ma on the Stacey and Kramers (1975) Growth Curve).

Optimisation of the various LA-ICP-MS parameters was achieved by comparing the Relative Standard Error (RSE%; Eq. 2.1) for Pb-isotopic ratios yielded from the various experiments. Each experiment was repeated 10 times for any one variable (i.e. spot size = 110 µm). In order to reduce the number of data yielded from each experiment, RSE% was only calculated on the ratio

$^{208}Pb/^{204}Pb$, which should have the highest uncertainty of any Pb-isotopic ratios due to the sequential measurement of masses on single detector ICP-MS.

$$2RSE_{analysis}(\%) = \frac{(\sigma/\bar{x}_{208/204}).100}{\sqrt{n}} \quad (2.1)$$

2.5.2 Modelled signal variation/ Effect of signal washout

Shorter tube lengths were determined to have the largest signal variance (~1% RSE), compared to the 4m (0.003% RSE) and SQUID (0.008% RSE) experiments when the only variable is tube length (Fig. 2.5). The improvement seen between the 4m and SQUID experiments is not considered significant enough to negate the benefits of using the inline signal smoothing and particle separation devices, the effect of which could not be incorporated into the model. Inline particle separators (Fig. 2.5) minimise the effects of signal variance caused by larger ablated particles, by employing centrifugal force to separate heavier particles as the ablated particulates passes through a tight coil (Guillong et al., 2003). Signal smoothing devices (Müller et al., 2009) homogenise the delivery rate of ablated material to the ICP-MS plasma, by forcing the gasses through a parallel array of tubes, each with differing lengths.

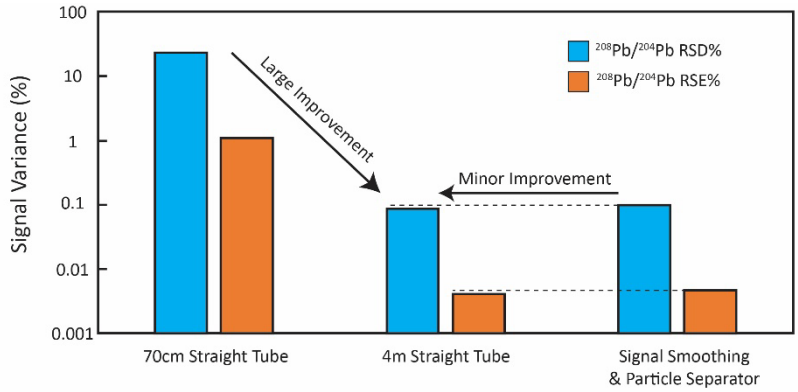

Figure 2.5: The modelled effect of tube length between laser ablation cell and ICP-MS.

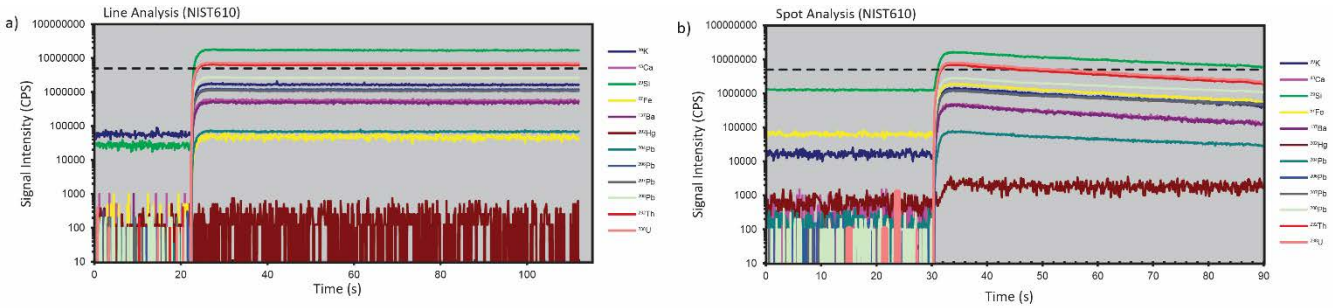

Figure 2.6: Typical LA-ICP-MS time-resolved spectra for NIST610 glass showing the downhole signal loss of spot analyses vs line analyses.

2.5.3 Spot vs Line Analysis

One of the key differences between spot and line (raster) analysis is the amount of downhole signal dropoff encountered (Fig. 2.6). The effect of downhole signal dropoff was modelled by varying the gradient of the signal from 0 (simulating line analysis) to -300 cps/s (simulating spot analysis). The data show that signal dropoff does contribute additional uncertainty (+0.06 RSE%) to spot analysis and therefore line analyses are optimal for Pb-isotopic analyses in K-feldspar (Fig. 2.7). Positive signal variance represents the effects of a gradually increasing Pb signal (mineral zonation or broad inclusion).

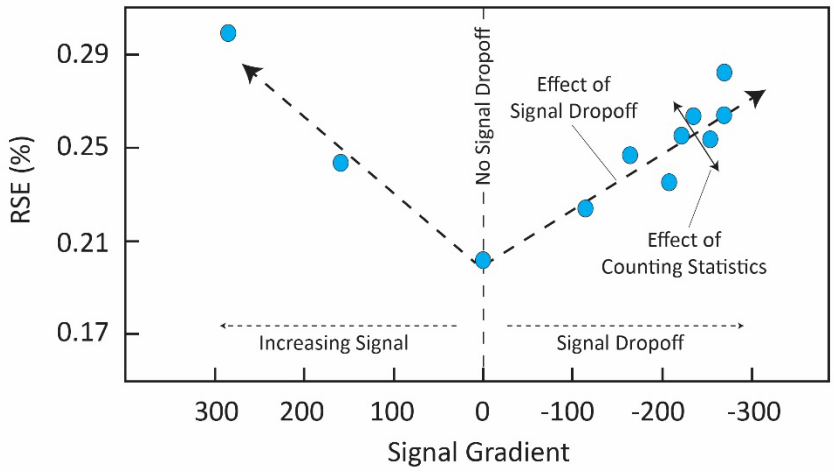

Figure 2.7: The modelled effect of downhole signal dropoff related on RSE% of Pb-isotopic analysis.

An argument can also be made for the implimentation of line analyses on a mineral textural basis. Firstly, if SEM/ BSE are integrated into the sample reconaissance workflow, the indentification of mineral inclusions which are deleterious to Pb-isotopic analysis is limited by the interaction volume of the SEM which is typically in the order of µm. Through the course of this study, perthitic exsolution lamellae were found to contain slightly higher concentrations of U than K-rich feldspars, leading to more radiogenic Pb-isotopic signatures. For example, an ablation transect across a pethitic lamination from the 1590 Ma Pinding Rocks Granite (Hiltaba Suite) (Fig. 2.8), shows that the K-feldspar contains $^{207}Pb/^{206}Pb$ signatures of 0.967, while the perthite contains $^{207}Pb/^{206}Pb$ signatures

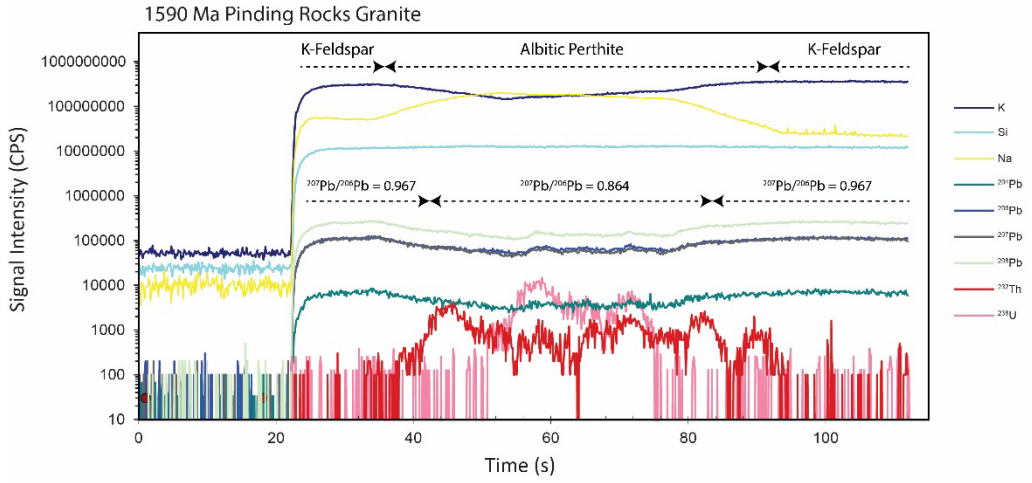

Figure 2.8: LA-ICP-MS line analysis showing the relationship between perthite lamellae (centre) and U-, Th-concentration as well as Pb-isotopic signature.

of 0.864. Furthermore, rastering across an feldspar provides an insight into the reletive homogeneity of Pb-isotopic signatures within these minerals, providing an additional method by which to validate the authenticity of initial Pb-isotopic signatures.

2.5.4 Beam Diameter (spot size)

With the overall low concentrations of Pb (<100 ppm) encountered in K-feldspar, it is generally best to operate with the largest spot size possible. From the results of the model (Fig. 2.9) it can be seen that at higher Pb concentration (100 ppm), little improvement is yielded in RSE% by using spot sizes

above 79 µm. However, at lower concentrations (5 ppm), uncertainty (RSE%) is improved considerably by increasing the laser beam diameter.

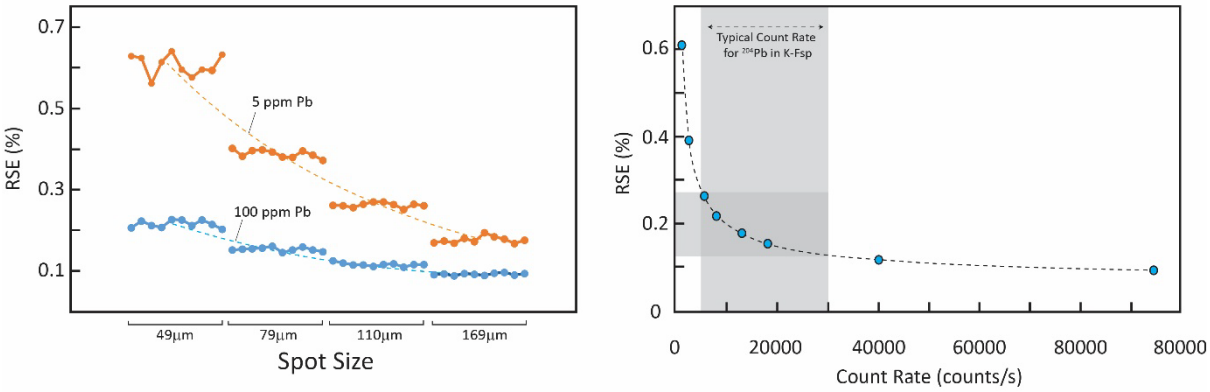

Figure 2.9: The modelled effect of beam diameter (related to signal intensity) on RSE%

In K-feldspar analyses, larger spot sizes (i.e. 169 µm) run an increased risk of ablating perthitic exsolutions, fractures, or zones of porosity which may contain radiogenic Pb (Fig. 2.8). From reconnaissance back-scattered electron (BSE) imaging undertaken during the course of this research, it was found that textural features of K-rich feldspars such as zonation and patch-perthites, favoured the use of spots sizes between 79 µm and 110 µm. For example, Figure 2.10 shows that 169 µm spot sizes constantly overlap with fractures and other microscopic variations, while 110 µm, and to a greater degree 79 µm, often avoids such heterogeneities. Therefore, as a general guide, a 110 µm spot offers the best compromise between the spatial targeting requirements inherent in K-feldspar

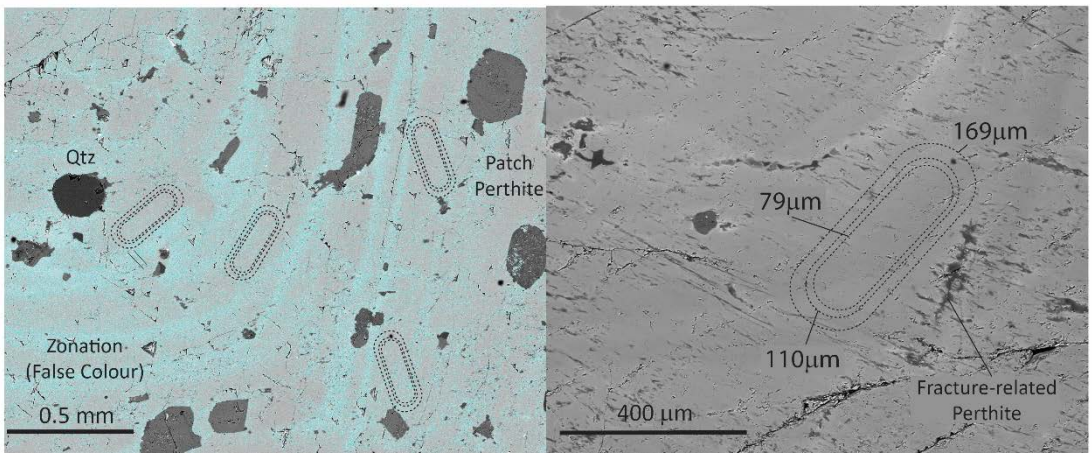

Figure 2.10: Comparison between typical beam sizes (line analyses) and common textures in feldspar such as oscillatory zonation, patch-perthite, fractures and mineral inclusions. False colour shows higher K in alkali feldspar.

analyses, with the requirement to maximise Pb-signal intensities (±0.12 to 0.23 RSE% at 100 – 20 ppm Pb).

2.5.5 Repetition-rate

Repetition rate relates to the number of laser pulses per second which is ablating the target mineral. Increasing the repetition rate can sometimes increase the signal intensity by contributing more measurable material, however this is largely considered to be dependent on the mineral matrix in question (Souders and Sylvester, 2010). Using signal increases obtains from real K-feldspar analyses, increasing the repetition rate at higher frequencies (10 - 30 Hz) resulted in no systematic improvement in uncertainty (Fig. 2.11). Variation in uncertainty is tentatively ascribed to the effects of counting statistics.

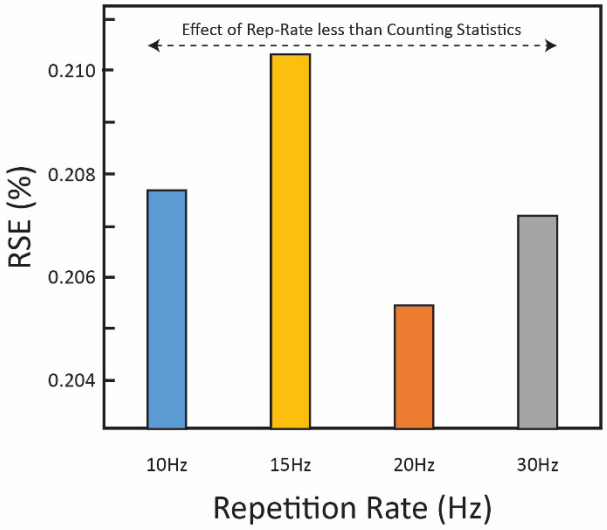

Figure 2.11: The modelled effect of laser pulse repetition rate on RSE%

Some minor effects were observed in the physical ablation characteristics of K-feldspars with various, naturally-occurring textural attributes. In pristine K-feldspars (Fig. 2.12) with weak to absent perthitic exsolutions, the drill rate through the feldspar remained consistently at 0.1 ± 0.01 µm/Hz from 5 to 20 Hz (Table 2.1). In porous, mesoperthitic feldspars which had undergone coupled dissolution-reprecipitation (Fig. 2.12), the drill rate appeared to vary considerably from 0.064 µm/Hz

to 0.08 µm/Hz (Table 2.1). Catastrophic ablation, which can result in an uneven particle size distribution and heterogeneous plasma loading (Perkins et al., 1997), was particularly evident in the porous K-feldspar at lower repetition rates but stabilised at higher rep-rates (20 Hz). Therefore, while no improvement is seen for repetition rates above 10 Hz in homogenous K-feldspars, increasing the repetition rate to 20 Hz may assist in the ablation of heterogenous K-feldspars.

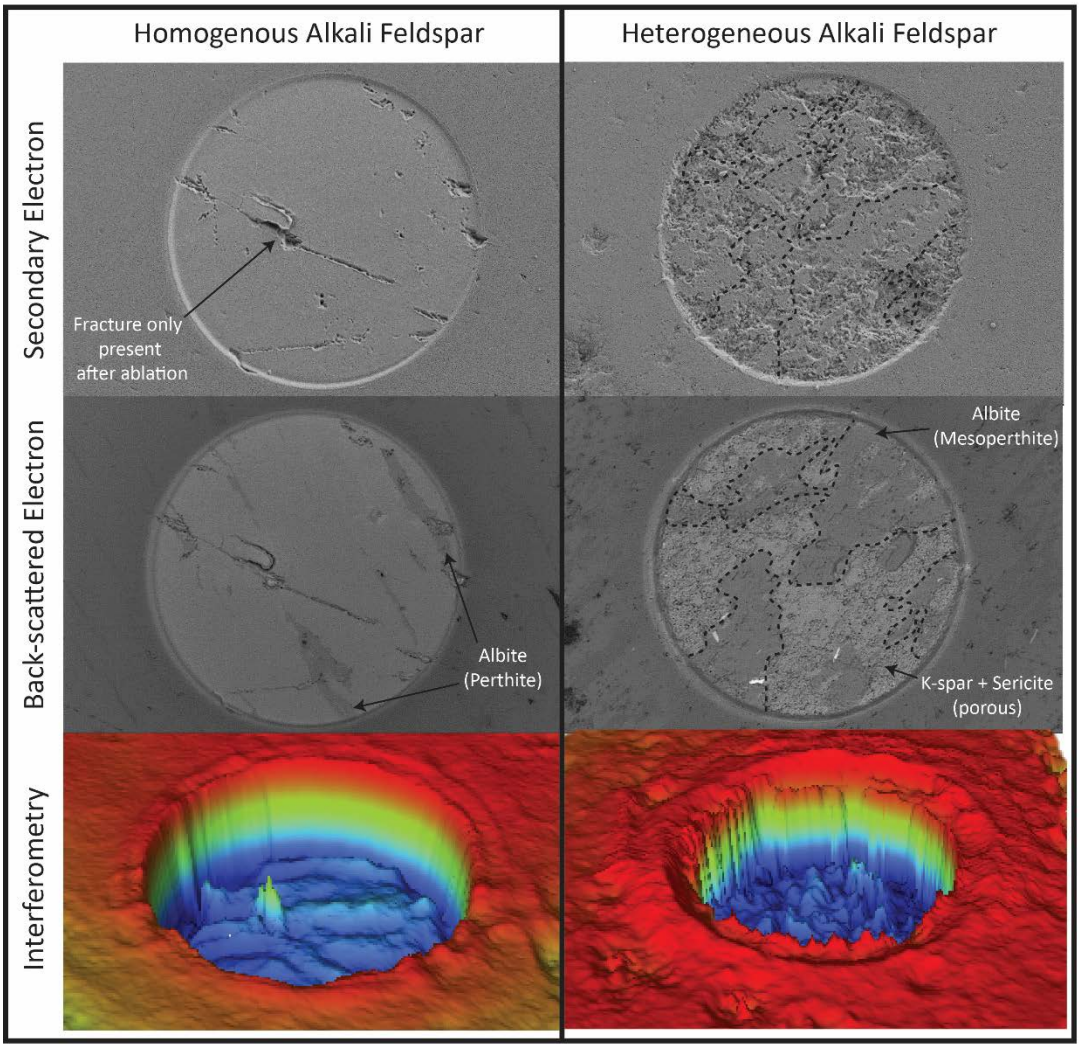

Figure 2.12: Physical effects of laser ablation (5 Hz) on homogenous alkali feldspar (left column) and heterogeneous, perthitic feldspars (right column).

Table 2.1: Physical Ablation Characteristics of K-feldspars based on a single laser pulse

Sample	Textural Characteristics	Colour	Pit depth @ 5hz (µm)	Pit depth @10Hz (µm)	Pit depth @20Hz (µm)	Ablation Rate (µm/Hz)
Pristine (Paxton Granite)	Weakly perthitic. Minor cleavage-related fractures	Clear	0.35 µm	0.8 µm	1.8 µm	0.09-0.1
Hetero-geneous (Burkitt Granite)	Porous, mesoperthitic. Extensive dissolution-reprecipitation.	Pale Pink	0.48 µm	0.8 µm	1.6 µm	0.064-0.08

2.5.6 Dwell-time

Increasing the measurement time, or dwell-time, on a specific mass generally improves uncertainties. However, increasing the dwell-time for one, or all of the Pb-masses increases the sweep-time thus reducing the number of Pb-isotopic measurements per analysis.

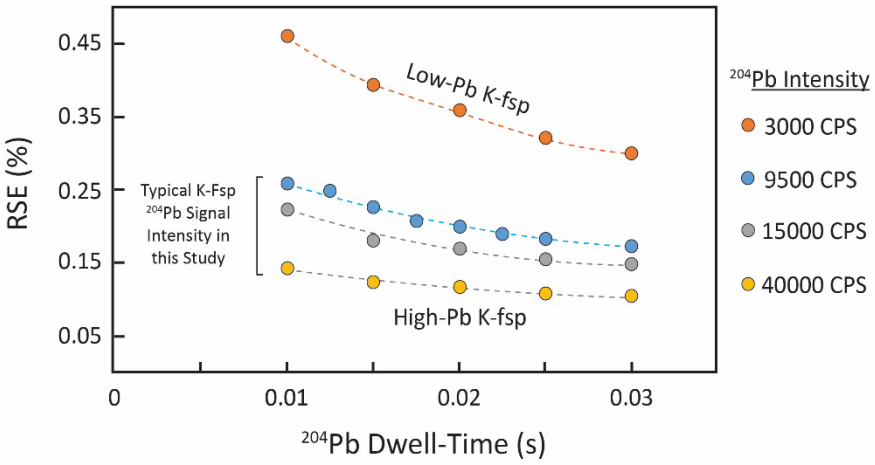

Figure 2.13: The effect of ^{204}Pb dwell-time on RSE% at Pb-concentrations typical for alkali feldspars.

Increasing the dwell-time on ^{204}Pb, the isotope that contributes the most uncertainty to Pb-isotopic ratios, is beneficial at very low Pb concentrations (Fig. 2.13). At ^{204}Pb count rate of 3000 CPS (~5ppm Pb), increasing the ^{204}Pb dwell-time from 0.01 s to 0.03 s results in an RSE% improvement from ~0.45% to 0.3%. At higher count-rates, which are more typical of natural K-feldspar samples (15000 – 30000 cps), little improvement is seen beyond dwell-times of 0.02 to 0.025 s (RSE% = 0.12).

Measuring ^{202}Hg is important for calculating and correcting for the interference caused by

^{204}Hg on ^{204}Pb. Analytical uncertainty on ^{202}Hg measurements for background signals can be significantly improved by implementing a dwell-time of 0.02 s or above, thereby reducing the contribution of uncertainties to isobaric interference corrections (Fig. 2.14).

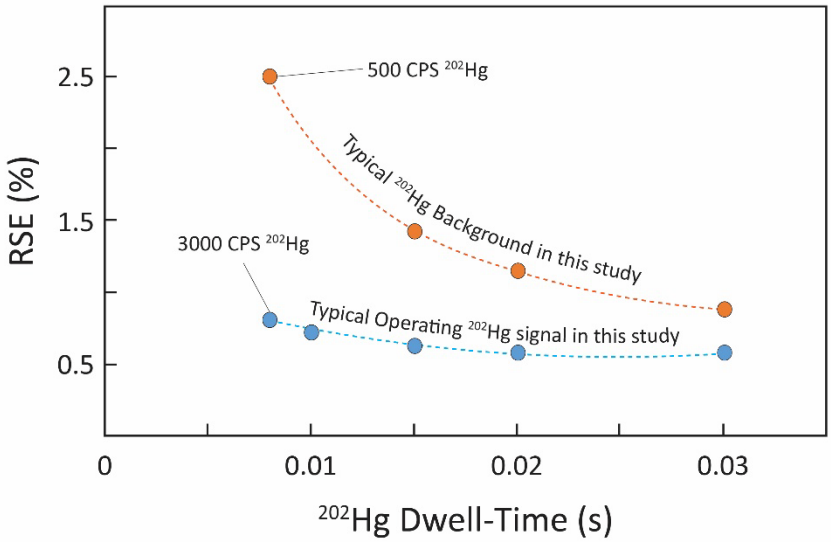

Figure 2.14: The effect of dwell-time on RSE% for ^{202}Hg used to correct isobaric interference between ^{204}Hg and ^{204}Pb.

2.5.7 Optimum Laser Ablation Conditions and Parameters

A summary of the experimental results is shown in Table 2.2. Based on the results of the LA-ICP-MS model just discussed, Pb-isotopic analyses of alkali feldspar should be able to produce Pb-isotopic ratios with a 2σ-uncertainty (2RSE%) approaching ~0.2%. This is in good agreement with the findings of Crowe et al. (2003) who suggested that uncertainty of Pb-isotopic ratios in low-Pb minerals was limited by the effects of counting statistics.

Table 2.2: Optimal Conditions and Parameters

Parameter	Optimal Conditions
Signal Washout	No deleterious effect of running in-line signal smoothing and particle separator devices
Spot or Line	Line analysis (rastering) – up to 0.1% improvement on RSE% over spot analyses
Spot size	Above 79µm – >0.4% improvement on RSE% at low Pb conc between 49µm and 169µm
Repetition-Rate	No systematic variation above 10 Hz – increased mechanical pounding in perthitic feldspars
^{204}Pb Dwell-time	At least 0.02 s – little improvement at longer times in typical feldspar Pb concentrations
^{202}Hg Dwell-time	At least 0.02 s – ~0.5% improvement on RSE% for background measurements

2.6 Isobaric Corrections

In ICP-MS, the ^{204}Pb isotope (At. Mass = 204.976 652 Da) suffers a mass-overlap (isobaric interference) with ^{204}Hg (At. Mass = 203.973494 Da). Since the ^{202}Hg:^{204}Hg ratio is relatively invariant in nature (^{204}Hg/^{202}Hg = 0.2299; Rosman and Taylor (1998)), the effect of ^{204}Hg on ^{204}Pb can be calculated indirectly by measuring the abundance of ^{202}Hg, and subtracting the resulting signal intensity from the ^{204}Pb signal. At higher K-feldspar Pb-concentrations (i.e. 78 ppm), ^{204}Hg does not pose a considerable issue (<0.5%). However, at low concentrations (i.e. 5 ppm), the signal intensity of ^{202}Hg (and therefore ^{204}Hg) can be a large contribution to the uncorrected ^{204}Pb signal (~18%; Fig. 2.15).

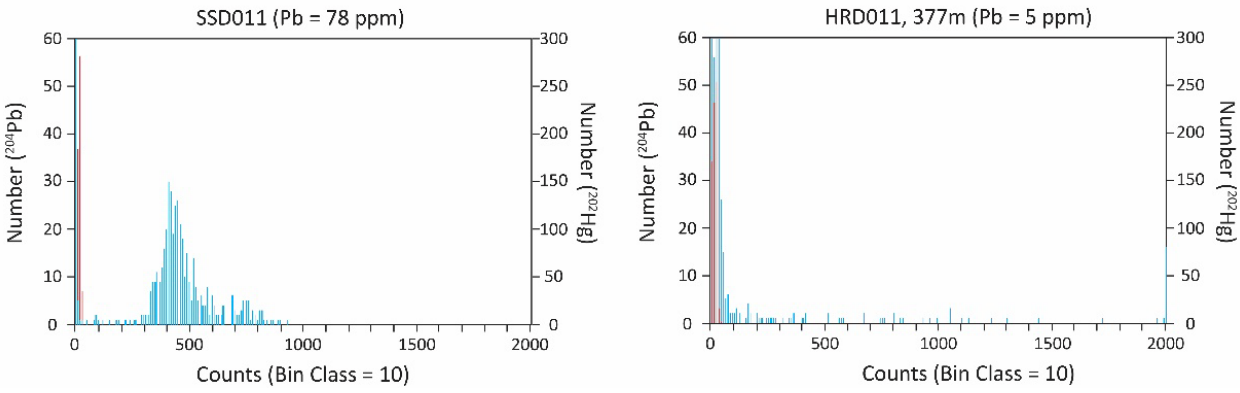

Figure 2.15: Samples of alkali feldspar with very low Pb concentrations (i.e. 5 ppm), will have their ^{204}Pb signal affected much more than typical alkali feldspar with Pb-concentration between 100 – 20 ppm. Orange represent ^{202}Hg. Blue represents ^{204}Pb

The exact source of the background Hg signal remains unclear. The potential contribution of Hg from laser ablations carrier gasses (He and Ar) is mitigated on instruments used in this study by employing inline Hg filters (Au-coated filters which sequester volatile Hg by forming an amalgam), but background Hg does vary both between laboratories and between sessions. Some of this Hg is present as a residual build-up in the ablation cell from Hg-contaminants from previous analytical sessions, since periodic measurements of blank silica glass throughout a single analytical session (every 30 analyses), appears to shows that the concentration of ^{202}Hg decreases during a single analytical session (Fig. 2.16).

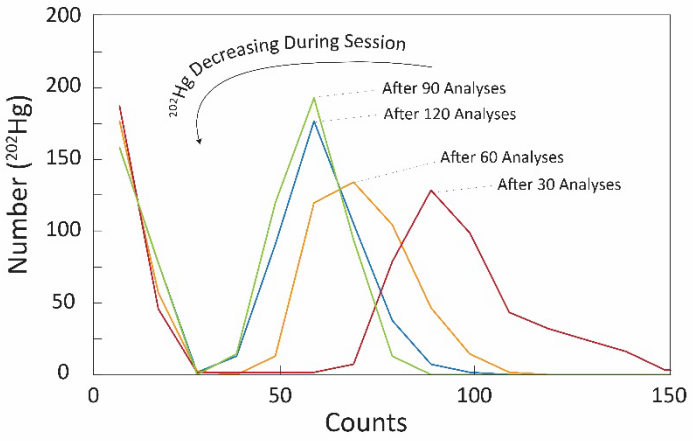

Figure 2.16: Periodic measurements (every 30 unknowns) of background ^{202}Hg achieved by ablating blank SiO_2, shows that ^{202}Hg background concentration decreases during the course of a single analytical session.

2.7 Error Correlation

Error correlation refers to the tendency of measurement uncertainties in one variable to systematically vary in a single trend. In Pb-isotopic analyses of low-Pb samples (such as alkali feldspar), much of the analytical uncertainty resides in the measurement of ^{204}Pb, and since most Pb-isotopic diagrams involve the use of bivariant ^{204}Pb-based isotopic ratios, ^{206}Pb/^{204}Pb, ^{207}Pb/^{204}Pb and ^{208}Pb/^{204}Pb can be affected. This can be shown by observing systematic variations in measurements

of the low-Pb (9 ppm), glass-matrix standard BCR-2G (Fig. 2.17). It can also be calculated using Equation 2.2. Error correlation for the analytical apparatus used in this thesis was determined to be 0.798.

$$\rho_{x,y} = \frac{\Sigma(x_i - \bar{x}).(y_i - \bar{y})}{\sqrt{\Sigma(x_i - \bar{x})^2.\Sigma(y_i - \bar{y})^2}} \quad (2.2)$$

Where;

x_i = $^{206}Pb/^{204}Pb$ of every analysis

$\bar{x}$ = mean of all $^{206}Pb/^{204}Pb$

y_i = $^{207}Pb/^{204}Pb$ of every analysis

$\bar{y}$ = mean of all $^{207}Pb/^{204}Pb$

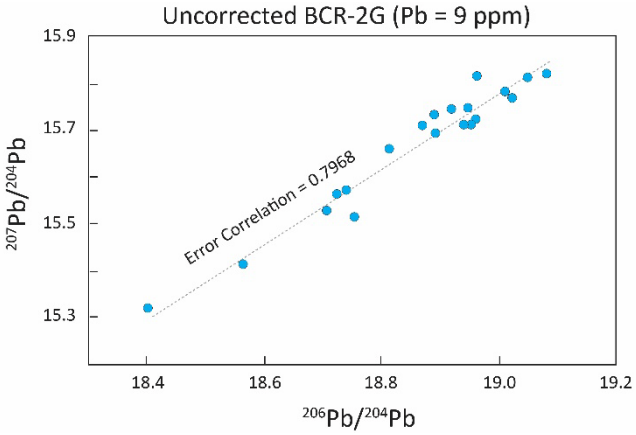

Figure 2.17: Error correlation (0.7968) in uncorrected ^{204}Pb-based Pb-isotopic ratios in the low-Pb (9 ppm) SRM BCR-2G.

The effect of error correlation is an important consideration when calculating Pb-Pb isochron ages, and when interpreting the variation of μ ($^{238}U/^{204}Pb$). For the Stacey and Kramers (1975) growth curve, error correlation (~0.8) coincides with the μ-variation between 3200 Ma (gradient = 0.814) and 3100 Ga (gradient = 0.784). Error correlation is therefore unlikely to affect the interpretation of μ-variation for the time-period which this thesis focusses on (1690 – 1590 Ma).

2.8 Proof of Method - Development of the Matrix-Matched Broken Hill Amazonite Standard

In order to demonstrate the accuracy and precision of the LA-ICP-MS method employed throughout this thesis, the optimum parameters derived from the computer model will be applied to natural K-feldspar sample with a known isotopic composition was analysed using the optimised parameters derived from the computer model.

Amazonites (Pb-rich K-feldspar) from the Broken Hill orebody were used in this study as a matrix-matched Pb-isotope standard. The high-Pb concentrations (Table 2.3) which can cause a green hue in amazonite, reduces the effects of analytical uncertainty and mitigates deleterious effects on primary Pb-isotopic signatures caused by the ingress of radiogenic Pb into low-Pb feldspars (i.e. Ludwig and Silver (1977)). Furthermore, because the amazonites hosted within the Broken Hill orezones likely formed during 1630 – 1600 Ma granulite-facies metamorphism of the deposits, the Pb-isotopic signature retained within the crystal structure is identical to the homogenous, well-characterised Pb-isotopic signature of the galena ores (Stevenson and Martin, 1986). The Broken Hill amazonite used here (Sample No. 16282 from the University of Tasmania collection), was originally sourced from Level 17 of the Zinc Corp Main Lode (Fig. 2.18). It is optically-pure (transparent), containing few inclusions with no evidence of microcline retrogression (cloudiness).

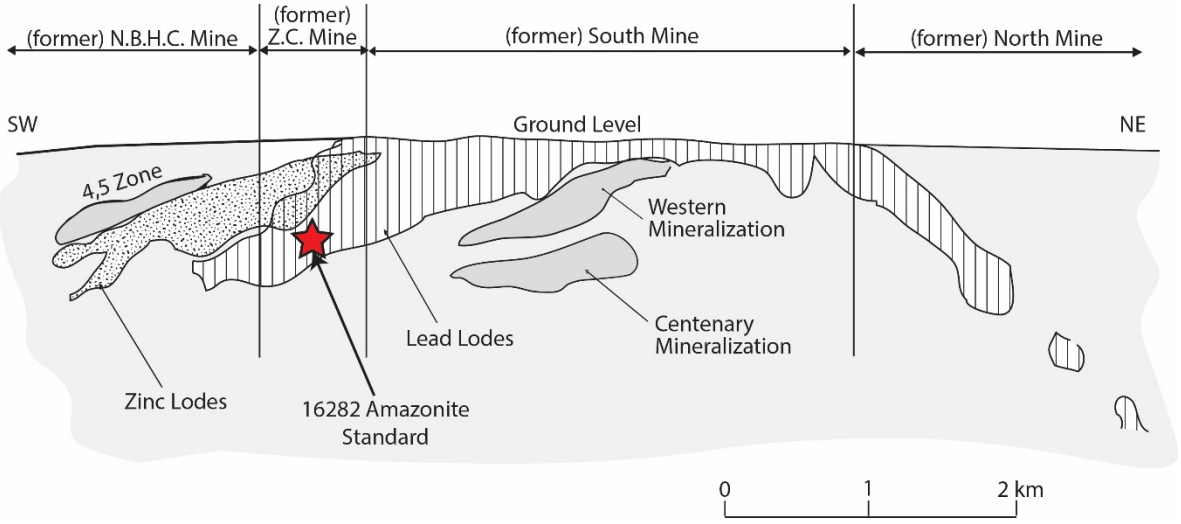

Figure 2.18: Schematic cross-section of the Broken Hill Pb-Zn deposit, showing the location of the 16282 sample relative to the ore zones. Diagram modified after Spry et al. (2007).

2.8.1 Method

15 LA-ICP-MS Pb-isotopic analyses were conducted using the same methodology outlined in Chapters 3 and 4. Single-collector LA-ICP-MS results (n = 15) were compared to LA-MC-ICP-MS (n = 4), which were obtaining using the same analytical parameters outlined in Chapter 5. Trace-element abundances were also obtained using the LA-ICP-MS method described in Chapter 5.

Table 2.3: Average Geochemical Composition of 16282 Broken Hill Amazonite Standard (n = 5)

Major Oxides	Wt. %	S.D.
SiO_2	62.88	0.09
Al_2O_3	19.22	0.07
K_2O	15.03	0.06
CaO	0.06	0.01
Na_2O	0.79	0.01
BaO	0.14	0.01
PbO	5.09	0.19

Mol. Prop.	Mol. %	S.D.
An	0.28	0.03
Ab	7.40	0.06
Or	92.31	0.08

Trace Elements	ppm	S.D.
Rb	601	12
Sr	311	17
P	302	8.
Fe	44	3
Ti	16.7	2.1
Cs	10.29	1.39
Li	4.08	0.49
Mn	2.60	0.24
Zn	1.52	0.35
Mg	1.29	0.18
La	0.29	0.15
Ce	0.07	0.04
Nd	0.02	0.01
Sm	0.02	0.00
Eu	3.04	0.28
Gd	0.01	0.00
Eu/Eu*	541	

2.8.2 Geochemistry

Trace element analysis (LA-ICP-MS) reveals the sample is geochemically homogenous. Molar orthoclase content (Or%) is particularly homogenous showing a standard deviation of 0.8. Chondrite-normalised REE patterns are typical of feldspar (Fig. 2.19), with enrichment in LREE and strong Eu-anomaly (Eu_N/Eu_N^* = 541). Molar PbO content was calculated to be 5.09 wt. % (st. dev. = 0.19). Based on the molar geochemical composition of the Broken Hill amazonite sample studied here, the mineral formula was determined to be; $K_{3.57}Na_{0.29}Pb_{0.24}Ca_{0.01}Ba_{0.01}Al_{4.22}Si_{11.73}O_{32}$

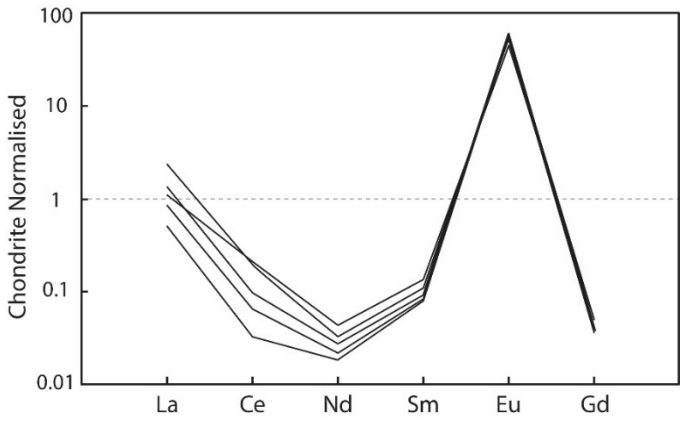

Figure 2.19: Chondrite-normalised REE pattern for 16282 Broken Hill amazonite specimen.

Table 2.4: Pb-isotopic signatures of amazonite and galena from Broken Hill using different Pb-isotopic methods.

Pb-rich Mineral	Method	$^{206}Pb/^{204}Pb$	± (2σ)	$^{207}Pb/^{204}Pb$	± (2σ)	$^{208}Pb/^{204}Pb$	± (2σ)	Reference
Amazonite (Wt. Av.) n = 23	LA-ICP-MS	15.977	0.018	15.361	0.019	35.622	0.041	This Study
Amazonite (Wt. Av.) n = 4	LA-MC-ICP-MS	16.017	0.005	15.401	0.005	35.711	0.011	This Study
Amazonite	TIMS	16.002	0.021	15.387	0.022	35.667	0.050	Stevenson and Martin (1986)
Galena	TIMS	16.003	0.011	15.390	0.013	35.66	0.036	Cooper et al. (1969)

2.8.3 Pb-isotopic Results and Discussion

The Pb-isotopic results of both LA-ICP-MS and LA-MC-ICP-MS methods are provided in Table 2.4 and Figure 2.20. Existing data high-precision TIMS and sector-field ICP-MS (SF-ICP-MS) results for Broken Hill galena and amazonite are also shown in Table 2.4 and Figure 2.20.

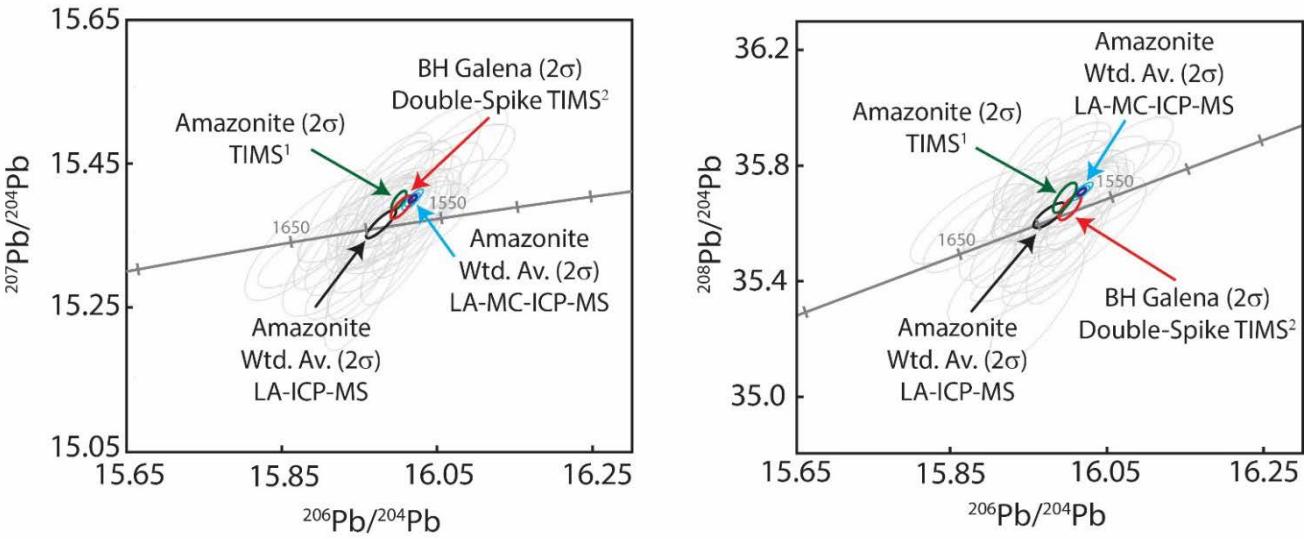

Figure 2.20: Pb-isotopic results of LA-ICP-MS and LA-MC-ICP-MS for the 16282 Broken Hill amazonite obtained here. [1] Stevenson and Martin (1986). [2] Cooper et al. (1969). Grey ellipses represent 2σ uncertainty from 23 individual LA-ICP-MS analyses.

Analytical uncertainties (2σ) for individual LA-ICP-MS analyses range from 0.36% to 0.55%, which is slightly higher than the 0.26% (2RSE%) predicated by the optimisation model. Some of the discrepancy may be due to subtle differences between the Agilent 7900 (used in the model) and Agilent 7500 (used here). A weighted average of the 15 analyses yields 2σ uncertainties between 0.112% and 0.124%. The low mean square weighted deviation (MSWD) for the 15 Pb-isotopic results obtained from LA-ICP-MS highlight the relative Pb-isotopic homogeneity of the Broken Hill sample analysed here. MSWD's range from ^{204}Pb-based ratios range from 0.3 ($^{206}Pb/^{204}Pb$) to 1.5 ($^{208}Pb/^{204}Pb$) (Fig. 2.21). The weighted average for the 15 LA-ICP-MS analyses overlaps with the Pb-isotopic signature for the Broken Hill ores presented by Cooper et al. (1969) and Broken Hill amazonite of Stevenson and Martin (1986). The weighted average of 4 LA-MC-ICP-MS Pb-isotopic show a slight discrepancy with the quadrupole data just outside the 2 sigma uncertainties with the multi-collector data systematically higher (av 0.15%) in all three ^{204}Pb based ratios on the TIMS and

quadrupole data. Although the small discrepancy has not been resolved during the course of this study the consistency of the quadrupole results with previous Pb-isotopic studies from Broken Hill demonstrates the accuracy of the LA-ICP-MS at precisions of 0.15%. However, further analytical development is required to take the uncertainty below this level.

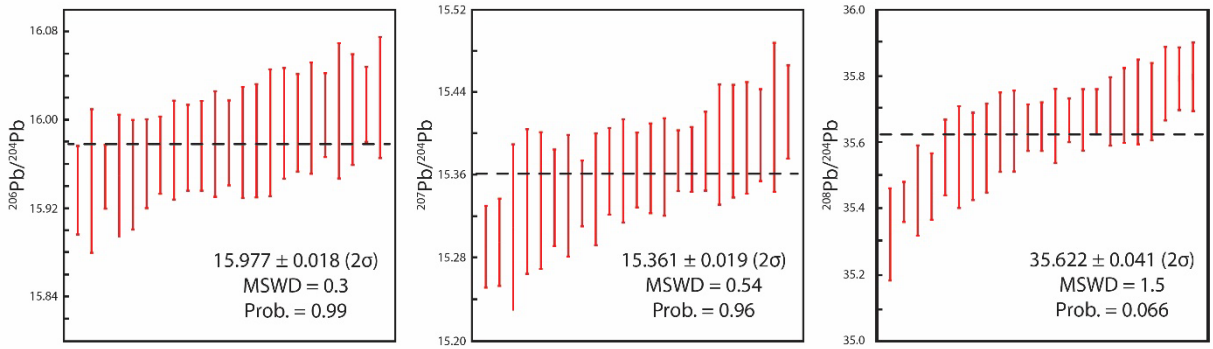

Figure 2.21: Weighted average diagram highlighting the reproducibility of the Pb-isotopic signature the 16282 Broken Hill amazonite sample over 23 individual analyses.

2.9 Summary

Microsampling by laser ablation offers a number of advantages for Pb-isotopic analyses of alkali feldspar over conventional dissolution-based techniques. When coupled with the cost-effectiveness and ability to measure a large suite of elements of single-collector ICP-MS, LA-ICP-MS presents an ideal method by which to conduct regional-scale, Pb-isotopic studies of crustal evolution.

Optimisation of LA-ICP-MS analytical parameters allows for the acquisition of Pb-isotopic ratios with a level of uncertainty which is fit-for-purpose. Modelling suggests that LA-ICP-MS is capable of producing analytical uncertainties for ^{204}Pb-based Pb-isotopic ratios at typical K-feldspar Pb concentration (25 – 100 ppm) in the order of ~0.2% (2σ). In the context of the Stacey and Kramers (1975) growth curve at 1600 Ma, this equates to a 2σ-uncertainty of ± 0.2 (μ), ± 0.08 (κ) and ± 26 Ma (model age).

Application of the optimised analytical parameters to Pb-rich amazonites from Broken Hill reveals 2σ-uncertainties for individual LA-ICP-MS analyses are around 0.3%, which are slightly higher

than those predicted by the model. For isotopically-homogeneous alkali feldspars, applying a weighted average can reduce 2σ-uncertainties to ~0.12%. Accuracy of this statistical method is demonstrated by the consistency of LA-ICP-MS Pb-isotopic signatures with the results of previous studies.

Chapter 3: The Bearing Of Pb-Isotopic Compositions On The Petrogenesis Of The Tunkillia Suite, Gawler Craton

Chapman, N. D.[1‡], Meffre, S. J.[1], Mass, R.[2] Ehrig, K.[3]

[1] School of Physical Sciences, University of Tasmania, Hobart, TAS, Australia

[2] School of Earth Sciences, University of Melbourne, Melbourne, VIC, Australia

[3] BHP Olympic Dam Operations, Adelaide, SA, Australia

[‡] Corresponding Author: Ph: +61 421772135

Email: nathan.chapman@utas.edu.au

Declaration of Interests: None

3.1 Abstract

In situ Pb-isotopic compositions of alkali feldspars from laser ablation ICP-MS (LA-ICP-MS) were used to constrain melt-sources of the ~1690-1670 Ma Tunkillia Suite, an important suite of intrusive rocks located in the Archean-Mesoproterozoic Gawler Craton, South Australia. Tunkillia Suite magmatism has been variously attributed to either a supra-subduction, or post-collisional setting. A robust interpretation of the Tunkillia Suite's tectonic setting is important for models of the Proterozoic evolution of the Gawler Craton and Australian Continent.

The Pb-isotopic results indicate a systematic, regional variation of at least two crustal Pb components corresponding to an ancient, U-depleted isotopic reservoir in the western Tunkillia Suite, and another which reflects mantle-crustal hybridisation. Unradiogenic Pb-isotopic compositions observed in the western Tunkillia Suite ($^{206}Pb/^{204}Pb$ = 15.060-15.785, $^{207}Pb/^{204}Pb$ = 15.154-15.426, $^{208}Pb/^{204}Pb$ = 34.963-35.766) are a globally-rare phenomenon which are inextricably-linked to inheritance from U/Pb-depleted granulites. Pb-isotopic reservoirs containing unradiogenic Pb are among the least melt-fertile sources and are inconsistent with granites generated during continent-continent collision which are typically derived by partial-melting of fertile metasedimentary protoliths.

In contrast, the eastern Tunkillia Suite displays Pb-isotopic compositions indicative of crust-mantle mixing, with a volumetrically-dominant mantle component ($^{206}Pb/^{204}Pb$ = 15.945-16.143, $^{207}Pb/^{204}Pb$ = 15.325-15.414, $^{208}Pb/^{204}Pb$ = 35.330-35.757). These values are consistent with published $\varepsilon Nd_{(1680Ma)}$ (+2.6 to -2.1) and $\varepsilon Hf_{(1680Ma)}$ (+5.9 to +0.7) signatures which confirm the role of juvenile, mantle-melts in the petrogenesis of the Tunkillia Suite, yet, contrast with the Sm-Nd composition of the 1730 - 1700 Ma Kimban Orogeny granitoids which clearly demonstrate crustal reworking ($\varepsilon Nd_{(t)}$ -11.7 to -0.7) consistent with a syn-collisional tectonic petrogenesis. Conversely, Pb- and Nd-isotopes highlight the similarities between the Tunkillia Suite and arc-related ~1630 Ma St Peters Suite granitoids ($\varepsilon Nd_{(t)}$ +2.31 to -3.46).

Isotopic arrays for the Tunkillia Suite implicate the same mixing phenomena involved in the extensive mantle-lower crustal hybridisation occurring beneath the Andean Cordillera. The diverse range of crustal-signatures demonstrated by both Pb-isotopic and geochemical constraints highlights that the crustal component is less important in the genesis of the Tunkillia, but rather the addition of mantle-magmas is the unifying characteristic, and thus favour a continental arc-like setting.

Keywords: Pb-isotopes; Sm-Nd isotopes; Gawler Craton; Paleoproterozoic tectonics; Tunkillia Suite

3.2 Introduction

The diorites, granodiorite and granites of the c.1690 - 1670 Tunkillia Suite, emplaced along the periphery of the Nuyts Terrane in the western Gawler Craton (Fig. 3.1), represent an important window into the tectono-thermal evolution of the Gawler Craton, and wider geodynamic setting of the Paleoproterozoic Australian continent. Emplacement of the Tunkillia Suite coincides with a major deviation in the Australian apparent polar wander path (Idnurm, 2000) and aligns with a shift away from the transpressional tectonics of the Kimban and Strangways Orogeny (1740-1690 Ma) associated with continental amalgamation (Betts & Giles, 2006), and towards subduction-dominated convergent margins represented by the 1633 – 1608 Ma St Peters Suite (Swain et al. 2008) and penecontemporaneous juvenile magmatic rocks within the Warumpi Province of the Arunta Inlier

(Scrimgeour et al., 2005).

Contrasting scenarios have been proposed for the genesis of the Tunkillia Suite. Early assignment of the Tunkillia Suite to a convergent margin like setting (i.e. Teasdale (1997), Karlstrom et al. (2001), Giles et al. (2004), Betts & Giles (2006), Betts et al. (2008)) was largely based on trace-element-reliant tectonic discrimination diagrams of Pearce (1976) and Harris et al. (1986). Tectonic discrimination diagrams used in this manner are not without issues (i.e. Förster et al., 1997), and a reinvestigation by Payne et al. (2010) based on geochemical modelling of source rocks argues against a supra-subduction setting for the magmatism. In favour of a continent-continent collisional setting. Major-, trace- and rare-earth element geochemistry are subject to fractional crystallisation, which partially obscure source chemistry and may give misleading estimates of magmatic components. In contrast, isotopic systems such as Pb-Pb and Sm-Nd remain unaffected by closed-system magmatic processes such as crystal fractionation, and are useful for investigating magmatic sources and thus constraining the tectonic setting of the rocks. Regional variation in both geochemical characteristics and Sm-Nd isotopic signatures within the Tunkillia Suite (Payne et al., 2010) provides significant scope to consider diverse intrasuite sources and/or process which may be related to geodynamic setting. Thus, the supra-subduction setting envisioned by Teasdale (1997), Ferris (2001) and Betts & Giles (2006) should not be unequivocally-rejected, based on inconclusive trace-element variations. Here, we present the results of a Pb-isotopic investigation in alkali feldspar to determine the likely sources for the Tunkillia Suite, and provide constraints for the tectonic setting of Tunkillia magmatism.

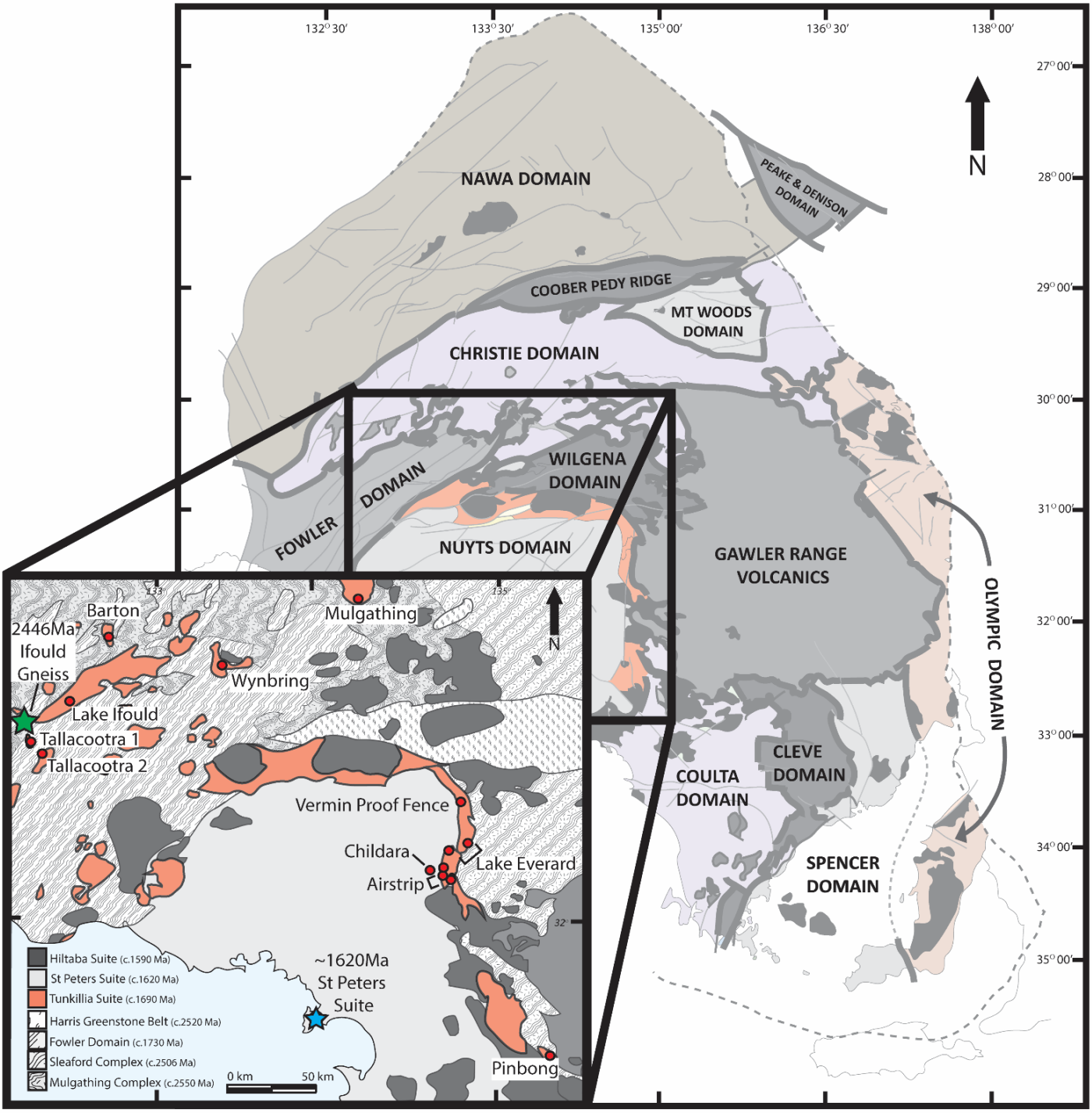

Figure 3.1: Regional and local (inset) context for the Tunkillia Suite. Thick-lines demarcate regional domains (after Ferris et al. (2002)). Inset shows regional distribution of Tunkillia Suite (orange) in relation to Neoarchean Mulgathing and Sleaford complexes and Harris Greenstone Belt, as well as Paleoproterozoic Fowler Domain. Cover by Gawler Range Volcanics removed in inset to show probable stratigraphy intruded by Tunkillia Suite. Red circles indicate sample site with informal plutonic names after Ferris (2001); Payne et al. (2010). Extent of the Tunkillia Suite is heavily obscured by cover and thus inferred from geophysics (after Ferris (2001); Ferris and Schwarz (2004); Payne et al. (2010); Teasdale (1997)). Blue star represents sample of St Peters Suite analysed in this study.

3.3 Geological Setting

The Gawler Craton is a Mesoarchean to earliest Mesoproterozoic (Flint, 1993) terrane overlain by Neoproterozoic and Phanerozoic sedimentary sequences (Gravestock, 1995). The Neoproterozoic and younger cover has greatly impeded knowledge of field-relationships for the crystalline basement of the Gawler Craton, with good outcrop exposure largely limited to segments of the coastline. With the regional distribution of the Tunkillia Suite restricted to inland areas of South Australia, outcrop is poor and much of the regional extent of the Tunkillia Suite is interpreted from geophysics (Ferris, 2001; Payne et al., 2010; Teasdale, 1997).

Mesoarchean granitic gneisses (3.15 Ga; Fraser et al. (2010)) located along north-eastern margin of Eyre Peninsula comprise the oldest crust of the Gawler Craton, albeit with limited spatial extent. The Sleaford and Mulgathing Complexes (Daly and Fanning, 1993) located within the Nawa, Christie and Coulta Domains (Fig. 3.1) were emplaced c.600 Mya later. They are believed to represent volcano-sedimentary basins which terminated during, and were deformed by the 2480 – 2420 Ma Sleafordian Orogeny (Reid et al., 2007). These gneisses form the dominant lower to upper crustal component in the north-western Gawler Craton where they are intruded by the Tunkillia Suite. A comparatively-smaller wedge of similarly-aged Archean ultramafic rocks (Hoatson et al., 2005) is located in the Harris Greenstone Belt (lower inset, Fig. 3.1), adjacent to the Wilgena Domain. The next major tectonic event to affect the Gawler Craton occurred during the 1850 – 1830 Ma Cornian Orogeny (Reid et al., 2008), during which the voluminous Donington Suite was emplaced along the eastern margin of the Gawler Craton (Spencer and Olympic Domains; Fig. 3.1). Crustal extension during 1810 – 1740 Ma (Reid et al., 2008) led to the widespread formation of volcano-sedimentary depocentres and the emplacement and deposition of the 1790 Ma Myola Volcanics (Fanning et al., 1988), 1774 Ma Tidnamurkuna Volcanics (Fanning et al., 2007) and 1760 – 1740 Ma Wallaroo Group (Cowley et al., 2003). The regionally-significant Kimban Orogeny (1730 – 1690 Ma; Hand et al. (2007); Hoek and Schaefer (1998); Payne et al. (2008)) led to high-grade metamorphism (amphibolite-granulite facies; Teasdale (1997)), partial melting and structural deformation over

much of the presently-exposed craton. Penecontemporaneous metamorphism (1780 – 1710 Ma; Collins and Shaw, 1995) in the Strangways Complex of the Arunta Inlier (Bagas, 2004; Maidment et al., 2005) has been suggested by some authors to be the far-field tectonic equivalents of the Kimban Orogeny, thus invoking a long-lived collisional setting for the south of Australia at this time (Betts and Giles, 2006; Payne et al., 2009). Emplacement of the Tunkillia Suite at ~1690 - 1670 Ma following the Kimban Orogeny, was followed by the intrusion of the bimodal c.1633 Ma (Reid et al., 2016) to 1608 Ma (Swain et al., 2008) St Peters Suite (Nuyts Domain; Fig. 3.1), whose calc-alkaline affinities and juvenile $\varepsilon Nd_{(t)}$ isotopic character suggest a subduction-related genesis (Swain et al., 2008).

3.4 Samples Analysed

Samples used in this study were obtained from extant collections (see Fig. 1 for locations). Samples prefixed with "879-", "WGC" and "444…" are derived from the collections of Ferris (2001); Taylor (1987); Teasdale (1997), respectively. Samples from the collections of Taylor (1987); and Teasdale (1997) were whole-rock samples, while those of Ferris (2001) were light-fraction Wilfley Table mineral separates. These same samples form the basis for Sm-Nd isotope, U-Pb geochronology, as

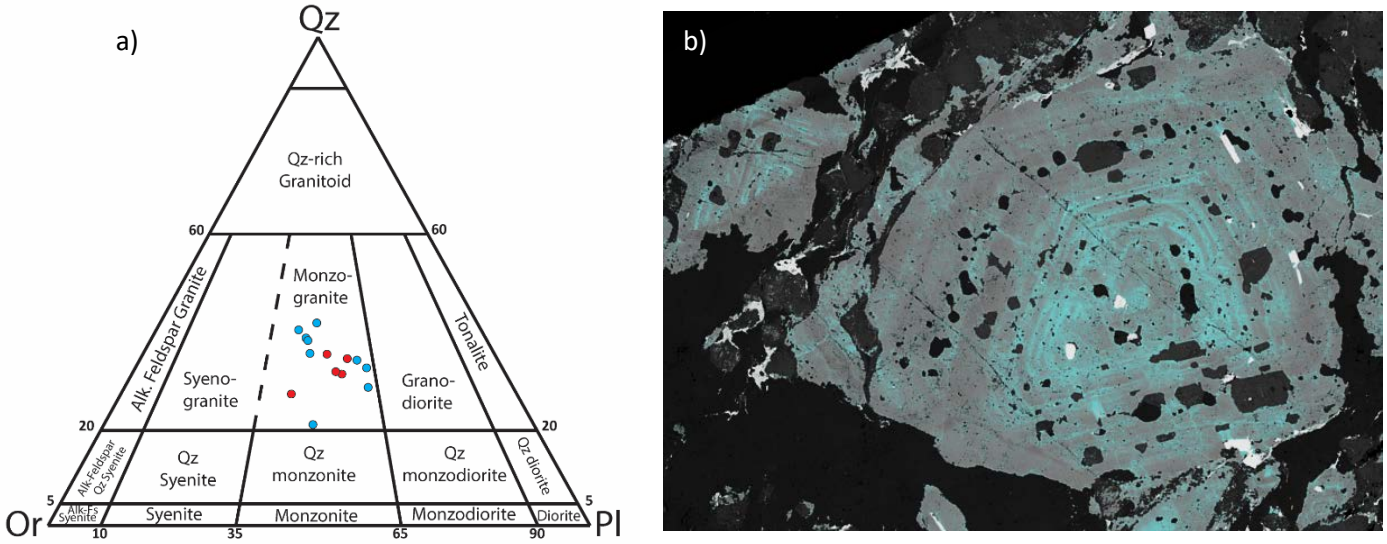

Figure 3.2: Mineralogical constraints on the Tunkillia Suite. a) Eastern (blue) and western (red) Tunkillia Suite samples analysed here plot mostly as monzogranite on the QAP diagram. b) Complex oscillatory zoning in alkali feldspar of the Vermin Proof Fence pluton containing abundant plagioclase, quartz and biotite inclusions suggesting an evolving magmatic system. Higher-K given false colour to highlight zonation.

well as whole-rock and trace-element concentrations (see Appendix A) previously published in Payne et al. (2010).

The Tunkillia suite samples analysed here are medium- to coarse-grained, seriate- to porphyritic plutonic granitoids with weak to strong metamorphic fabric. Alkali feldspar, plagioclase, quartz and biotite are the major rock-forming minerals, and classify mostly as quartz monzonite on the QAP diagram (Fig. 3.2) while in the R1-R2 scheme of De la Roche et al. (1980) equate to granodiorite to alkali granite mineralogy. Alteration is weak to absent, with only minor sericitisation of plagioclase and weak retrogression of biotite to chlorite. For more detailed petrographic descriptions of the Tunkillia Suite samples used here, the reader is directed to previous published works on these samples (References in Table 3.2). One sample of a c.2446 Ma gneiss representative of the regional isotopic signature of the Western Gawler Craton, and younger granite samples of the ~1630 - 1608 Ma St Peter Suite were also examined and analysed to provide additional context for the Tunkillia Suite Pb-isotopic results. The 2466 Ma gneissic sample is indistinguishable in hand-specimen from the Tunkillia Suite, with significantly-less foliation than is typical of an Archean-Early Paleoproterozoic rock in the Gawler Craton. This similarity likely led to the initial misclassification of this sample as Tunkillia Suite. The St Peters Suite granitic samples are equigranular, and contain little-to-no foliation.

All K-feldspar crystals targeted for LA-ICP-MS are translucent to transparent indicating that recrystallisation of orthoclase to microcline, which may have modified Pb-isotopic compositions, has not taken place. Primary oscillatory zonation is commonly preserved, further indicating that the K-feldspars analysed here are largely pristine. Most K-feldspar crystals have undergone weak to moderate perthitic exsolution (patch- to microperthite; Lee and Parsons, 1997), however retain a substantial amount of perthite-absent domains which were targeted for in situ Pb-isotopic analyses (Fig. 3.2).

3.5 Analytical Procedures

Samples preparation involved fabricating 25 mm round, epoxy resin mounts of either saw-cut samples, or light-fraction mineral separates of alkali feldspar. Samples were then polished to 0.1µm-diamond grade, cleaned using ethanol, washed in an ultrasonic bath of de-ionised water for 20 minutes, air-dried and then carbon-coated. Mineral purity was confirmed (Fig. 3.3) using back-scattered electron imaging (BSE) acquired on the Hitachi SU-70 field-emission SEM housed at the Central Science Laboratory, University of Tasmania, using a 15kV accelerating voltage. Careful sample reconnaissance using BSE maps is crucial to the successful application of microsampling techniques such as LA-ICP-MS. Physical attributes such as microfractures can deleteriously effect signal stability (Fig. 3.3) while mineral intergrowths associated with perthite grain-boundaries can effect Pb-isotopic results. Time-integrated LA-ICP-MS analyses are very sensitive to even subtle variations in feldspar composition (e.g. Gagnevin et al. (2005)) and is a valuable utility for distinguishing post-crystallisation effects which may have altered Pb-isotopic compositions. Figure 3.3 demonstrates the effectiveness of distinguishing both major-, trace- and Pb-isotopic variations in feldspar.

In situ Pb-isotopes and trace-elements were determined using a quadrupole LA-ICP-MS. The Agilent 7900 ICP-MS was coupled to a Coherent COMPex Pro 193nm ArF Excimer laser system equipped with a Laurin Technic RESOlution (now ASI) S155 cell. Ablation was carried out in a He atmosphere, with nitrogen added at 3.5 mL/s to improve sensitivity (i.e. Crowe et al. (2003); Hu et al. (2008)). An inline smoothing device ("SQUID"; Müller et al. (2009)) and Tygon particle-separator (Guillong et al., 2003) were added to improve signal-stability and remove spikes. A spot-size of 110µm with a repetition rate of 10 Hz (fluence at sample = 3.5 J/cm^2) was used to obtain relatively-precise ^{204}Pb measurement, yet provided enough spatial resolution to target clean K-feldspar and avoid most mineral intergrowths and inclusions. A transect line geometry was selected to mitigate down-hole signal loss, with a raster rate of 5 µm/s. Data collection was conducted over 110 seconds per sample with 22 seconds of background measurements and 90 seconds of laser-on

measurements. Short dwell-times and a short element list were used to offset the effects of the non-simultaneous detection of the Pb isotopes on the quadrupole mass spectrometer. ^{39}K, ^{43}Ca, ^{23}Na and ^{137}Ba were counted for 5 ms each to confirm alkali feldspar was being ablated. In some samples where inclusions were numerous ^{24}Mg, ^{27}Al, ^{29}Si, ^{31}P, ^{47}Ti, ^{56}Fe were also analysed to 5 ms to help with rejection of spurious data caused by other mineral phases, and assist in rejecting spurious data. ^{206}Pb, ^{207}Pb, ^{208}Pb, ^{232}Th and ^{238}U were counted for 10 ms while ^{202}Hg and ^{204}Pb for 20 ms giving a total quadrupole cycle time of 180 ms and 600 - 1000 measurements of each isotopes during the 90 s ablation.

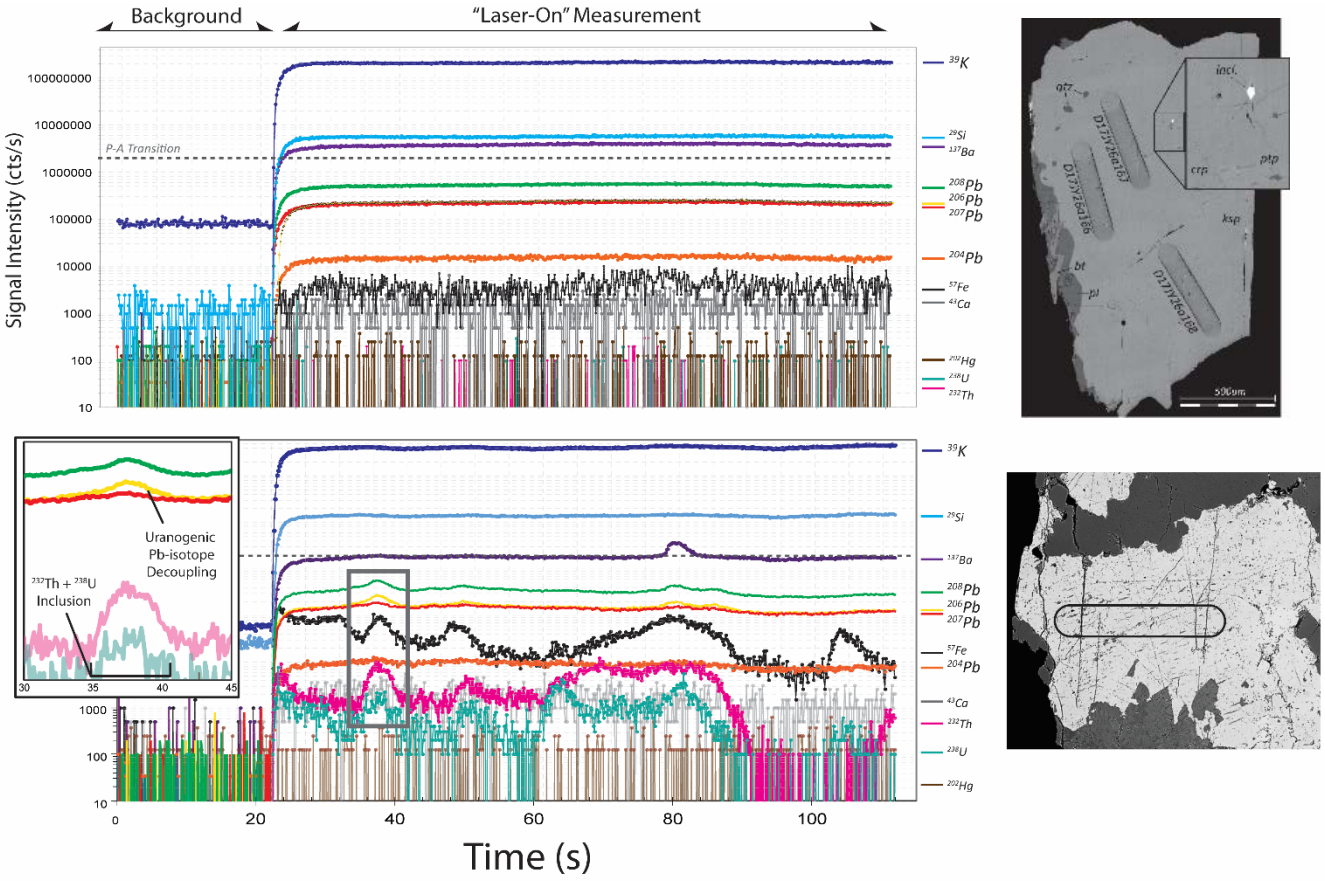

Figure 3.3: (Top left) A representative mass-spectra of analysis "D17JY26a168" from the Barton Pluton demonstrating the stable signal obtained from a homogenous alkali feldspar. Note high-stability of the signal, that all Pb-isotopes remain below the pulse to analogue transition (P-A) and ^{238}U, ^{232}Th, ^{202}Hg are equivalent in intensity to background. (Top right) BSE image of alkali feldspar mount from sample 444825 (Barton Pluton) showing the heterogeneities inherent in feldspars and laser ablation lines (with data reference). Targeted LA-ICP-MS allows for avoidance of radiogenic inclusions ("incl."), mineral intergrowths (plagioclase = "plag", biotite = "bt", quartz = "qtz") and exsolutions (patch-perthite = "ptp", cryptoperthite = "crp"). (Bottom left) LA-ICP-MS spectra from a heterogenous, perthitic feldspar. Fractures in feldspar (best shown by ^{57}Fe spectrum) also contains trace amounts of Ba, Th and U which has accumulated excess radiogenic Pb demonstrated by decoupled $^{206}Pb/^{207}Pb$ (inset, bottom left).

Reproducibility and instrument drift corrections were achieved using standard bracketing procedures. NIST610 glass (Pb = 426 ppm) was selected as the primary SRM, with the flux-free glass SRM's GSD-1G (Pb = 50 ppm) and BCR-2G (Pb = 11 ppm) used as low-Pb check standards. SRM's were analysed every 30 analyses using the same analytical conditions as the samples however with 50 - 110 µm spots instead of lines, since there is no downhole fractionation of the Pb-isotopes. Average single-analysis uncertainties (2σ) on NIST610 were 0.23% for ^{206}Pb-based ratios and 0.59% for ^{204}Pb-based ratios. Typical precision on the weighted average of 10 lines on alkali-feldspar taking into account uncertainty on the samples and standards is 0.2-0.6% (2σ) depending on the Pb concentrations in the feldspars, with analytical precision to three decimal places.

Data reduction was conducted offline using in-house spreadsheets. ^{204}Hg isobaric interference corrections were employed using a ^{204}Hg:^{202}Hg ratio of 4.32 and the background/ peak-stripping method of Willigers et al. (2002). ^{204}Pb/^{204}Hg corrections were generally less than 0.4% for samples but less than 0.14% for NIST610. The data for each sample were calculated to a single weighted average with respect to internal uncertainties using Isoplot v.4.15 (Ludwig, 2012). Average mean square weighted deviations (MSWD) were 1.10 (0.33 - 1.78). Rejection of data from averages was based on occurrence of detectable ^{238}U (as mineral inclusions) where ^{206}Pb/^{204}Pb was evidently affected (Fig. 3.3), and/ or where sub-surface mineral intergrowth/ inclusions (i.e. Fig. 3.3) were inadvertently ablated. Overall <5% of analyses were rejected.

In order to demonstrate the accuracy of the LA-ICP-MS method used here, a single-sample from this study was analysed both using the quadrupole LA-ICP-MS method and solution-based multi-collector ICP-MS (MC-ICP-MS) method outlined in Maas et al. (2015) (Appendix B). External reproducibility is further demonstrated using a plumbian microcline ('amazonite') sample from the Broken Hill Main Load (Level 17, Zinc Corporation Mine), which is used as a matrix-matched secondary standard for the Tunkillia Suite analyses. Although no matrix-effects have been observed when correcting LA-ICP-MS Pb-isotopic results from feldspar (Souders and Sylvester, 2010) or pyrite (Woodhead et al., 2009) to glass SRM's, this additional step provides further validation for the

method outlined here. Pb-isotopic analyses from the Broken Hill amazonite were performed using both LA-ICP-MS and LA-ICP-MC-MS and compared to the Double-Spike TIMS results of Broken Hill ores presented in (Cooper et al., 1969).

Model ages and time-integrated $^{238}U/^{204}Pb$ (μ_2) and $^{232}Th/^{238}U$ (κ_2) source reservoirs were calculated using the average two-stage crustal growth curve model of Stacey and Kramers (1975) by minimising the sum of the square differences for μ, κ and model age to best fit the data. Where mentioned, Pb-isotopic data adapted from the literature was re-calculated to the two-stage Stacey and Kramers (1975) model to be directly comparable to the new Pb-isotopic results presented here.

Table 3.1: Results of SRMs (Recommended values after Jochum et al. (2007))

	NIST610		**GSD-1G**		**BCR-2G**	
	GeoREM Recommended Value	Our Av. (n=22)	GeoREM Recommended Value	Our Av. (n= 14)	GeoREM Recommended Value	Our Av. (n=14)
$^{207}Pb/^{206}Pb$	0.910	0.910	0.804	0.805	0.833	0.832
+/- (2σ)	0.0002	0.0004	0.0001	0.0009	0.001	0.001
MSWD	-	1.024	-	0.335	-	0.782
$^{208}Pb/^{206}Pb$	2.169	2.169	1.987	1.986	2.066	2.063
+/- (2σ)	0.0004	0.0011	0.0005	0.0018	0.001	0.003
MSWD	-	1.147	-	1.621	-	2.068
$^{206}Pb/^{204}Pb$	17.052	17.052	19.579	19.566	18.765	18.781
+/- (2σ)	0.004	0.014	0.004	0.041	0.007	0.056
MSWD	-	0.601	-	0.310	-	0.893
$^{207}Pb/^{204}Pb$	15.515	15.528	15.745	15.742	15.626	15.606
+/- (2σ)	0.004	0.015	0.002	0.031	0.006	0.046
MSWD	-	0.393	-	0.262	-	1.045
$^{208}Pb/^{204}Pb$	36.991	36.996	38.908	38.865	38.730	38.748
+/- (2σ)	0.009	0.033	0.009	0.075	0.020	0.116
MSWD	-	0.323	-	0.207	-	0.784

Table 3.2: Collated geochronology, relevant geochemistry and isotopic data from the literature, together with Pb isotopic data from this study (absolute uncertainty at 2σ)

Suite	Sample No.	Pluton Name	Easting (UTM Zone 53)	Northing (UTM Zone 53)	Age (Ma)	$\varepsilon Nd_{(1680Ma)}$	Ce/Lu	U/Pb (WR)	Th/Pb (WR)	μ_2 ($^{238}U/^{204}Pb$)	κ_2 ($^{232}Th/^{238}U$)	Model Age (Myr)	ΔModel Age$_{(Pb\text{-}Pb)}$	$^{206}Pb/^{204}Pb$	$^{207}Pb/^{204}Pb$	$^{208}Pb/^{204}Pb$
Gneissic Basement	879-29b	'Archean Gneiss'	226746	6583029	2446 ±12[1]	-10.4[1] (t = +2.7)	1720[1]	0.03[1]	0.96[1]	9.72 (0.22)	4.05 (0.06)	1991 (29)	-	15.170 (0.030)	15.193 (0.035)	35.061 (0.078)
Western Tunkillia Suite (Informal)	879-47	Lake Ifould[1]	224020	6580364	1672 ±17[7]	-5.3[1]	800[1]	0.04[1]	0.68[1]	9.46 (0.15)	4.13 (0.03)	1886 (2)	-214	15.273 (0.060)	15.183 (0.033)	35.262 (0.084)
	879-47	Lake Ifould (MC-ICP-MS)	224020	6580364	1672 ±17[7]	-5.3[1]	800[1]	0.04[1]	0.68[1]	9.37 (0.01)	4.10 (0.04)	1890 (5)	-218	15.223 (0.008)	15.159 (0.008)	35.178 (0.018)
	444825	Barton	283614	6619257	1675 ±25[7]	-5.5[1]	556[1]	0.13[6]	0.72[6]	10.43 (0.15)	4.13 (0.04)	1844 (19)	-169	15.785 (0.023)	15.426 (0.025)	35.766 (0.057)
	444833	Tallacootra 1[5]	232451	6567700	1680*	-5.6[1]	190[1]	0.07[6]	0.17[6]	9.71 (0.21)	4.21 (0.17)	1967 (24)	-287	15.215 (0.038)	15.202 (0.036)	35.267 (0.200)
	444834	Tallacootra 2[5]	231647	6564845	1680*	-5.6[1]	583[1]	0.03[6]	0.23[6]	9.62 (0.21)	4.06 (0.13)	2026 (25)	-346	15.060 (0.035)	15.154 (0.035)	34.957 (0.145)
	WGC81	Wynbring[7]	357085	6618513	1669 ±10[7]	-6.3[1]	325[1]	0.10[1]	1.02[1]	9.52 (0.21)	3.93 (0.05)	1948 (29)	-279	15.176 (0.030)	15.169 (0.034)	34.963 (0.066)
Eastern Tunkillia Suite (Informal)	444835	Mulgathing[1] (Symons Granite[5])	399000	6653600	1684 ±10[5]	-2.1[1]	206[1]	0.25[6]	3.00[6]	9.74 (0.42)	3.78 (0.12)	1619 (66)	+64	15.923 (0.073)	15.352 (0.078)	35.560 (0.191)
	444824	Pinbong[1] (Little Pinbong Rockhole[5])	544165	6367104	1670 ±17[5]	-2.1[1]	229[1]	0.20[6]	1.10[6]	9.55 (0.15)	3.56 (0.03)	1557 (10)	+113	15.945 (0.058)	15.325 (0.034)	35.330 (0.080)
	350424	Airstrip 1[6]	466840	6500257	1680 ± 9[5]	+2.6[1]	133[1]	0.15[1]	0.59[1]	9.66 (0.11)	3.75 (0.03)	1547 (16)	+133	16.020 (0.023)	15.355 (0.021)	35.627 (0.052)
	350428	Airstrip 2[6]	477797	6490815	1680 ± 9[5]	-1.3[1]	233[1]	0.16[1]	0.90[1]	9.89 (0.08)	3.77 (0.01)	1545 (5)	+135	16.143 (0.030)	15.414 (0.018)	35.757 (0.041)
	350435	Airstrip 3[6]	480718	6490622	1680 ± 9[5]	-2.0[1]	240[1]	1.50[1]	4.50[1]	9.86 (0.08)	3.76 (0.03)	1618 (15)	+62	15.985 (0.067)	15.382 (0.024)	35.587 (0.100)
	370936	Lake Everard 1[6]	489674	6512791	1680*	-1.0[1]	153[1]	0.25[1]	1.39[1]	9.68 (0.11)	3.74 (0.08)	1523 (9)	+157	16.078 (0.072)	15.368 (0.029)	35.668 (0.164)
	370932	Lake Everard 2[6]	478400	6503092	1680*	-1.7[1]	311[1]	0.12[1]	0.88[1]	9.74 (0.11)	3.73 (0.01)	1515 (11)	+165	16.124 (0.078)	15.386 (0.031)	35.699 (0.058)
	378924	Vermin Proof Fence[6]	484352	6536030	1686 ± 5[5]	-0.3[1]	360[1]	0.03[1]	0.38[1]	9.73 (0.08)	3.77 (0.04)	1546 (10)	+140	16.057 (0.023)	15.372 (0.017)	35.683 (0.062)
	370938	Childara[6]	474771	6494106	1680*	-0.6[1]	122[1]	0.19[1]	1.39[1]	9.77 (0.13)	3.73 (0.04)	1540 (20)	+140	16.089 (0.028)	15.385 (0.026)	35.666 (0.069)
St Peters Suite	7563	St Peters 1	393591	6399421	1608 ±8[2]	-2.1 to +3.1[3,4]	146 - 291[3]	0.10[6]	0.66[6]	10.06 (0.28)	3.86 (0.07)	1636 (41)	-	16.046 (0.049)	15.423 (0.051)	35.753 (0.113)
	7580	St Peters 2	392332	6399176	1608 ±8[2]	-2.1 to +3.1[3,4]	146 - 291[3]	0.10[6]	0.48[6]	10.20 (0.20)	3.93 (0.04)	1662 (27)	-	16.062 (0.040)	15.448 (0.038)	35.847 (0.082)

[1] Payne et al. 2010; [2] Reid et al. 2016; [3] Swain et al. 2008; [4] Chalmers 2009; [5] Fanning et al. 2007 ; [6] Ferris, 2001; [7] Teasdale, 1997. *Assigned to Tunkillia Suite by Ferris & Schwarz, 2004. ‡Age of pluton, not specific sample. Age is mean Tunkillia Suite age.

3.6 Results

The results of all 168 LA-ICP-MS single analyses on 17 samples and a single MC-ICP-MS analysis are provided in Supplementary Appendix C, with weighted averages shown in Table 3.2. All secondary standards (GSD-1G and BCR-2G) are within uncertainty of recommended values (table 3.1, Fig. 3.4). Both the in situ LA-ICP-MS results and replicate solution-based MC-ICP-MS results for the 'Ifould Pluton' sample (Table 2) are also within uncertainty, demonstrating the accuracy of this method. External reproducibility (matrix-matched) is further demonstrated by the Broken Hill amazonites (Fig. 3.5), which are within 2σ uncertainty of previously established values. A collation of geochronology, Sm-Nd isotopic and whole-rock geochemical data on samples analysed here are provided in Table 3.2.

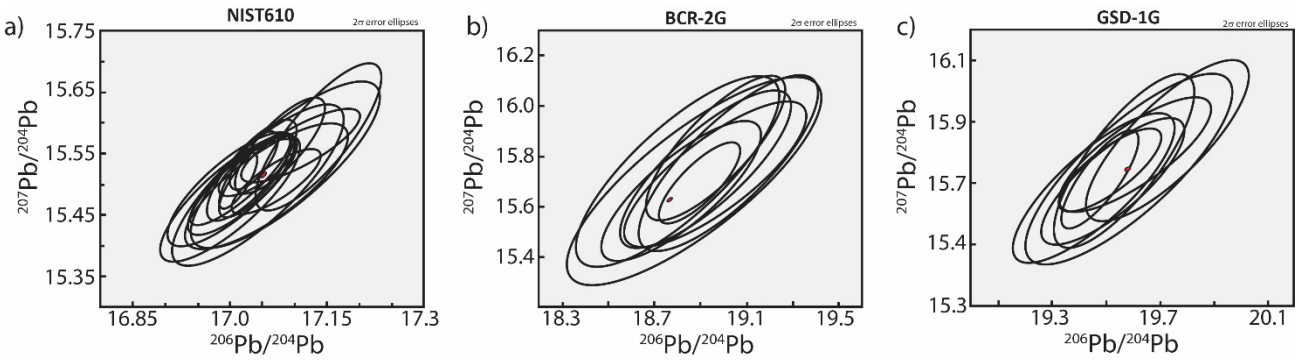

Figure 3.4: Results of Pb-isotope LA-ICP-MS analyses on SRM's (black), and preferred values (red)

The Tunkillia Suite alkali feldspar vary widely in their initial Pb-isotope values, forming two discrete data-clusters. The least-radiogenic cluster is found in plutons of the western Tunkillia Suite and range from 15.060 – 15.273, 15.154 – 15.202 and 34.957 – 35.267 for $^{206}Pb/^{204}Pb$, $^{207}Pb/^{204}Pb$ and $^{208}Pb/^{204}Pb$, respectively. The Pb-isotopic signature of the nearby 2446 Ma gneiss which was analysed to test for isotopic inheritance, yields a Pb-isotopic signature ($^{206}Pb/^{204}Pb$ = 15.170 ± 0.030, $^{207}Pb/^{204}Pb$ = 15.193 ± 0.035 and $^{208}Pb/^{204}Pb$ = 35.061 ± 0.078) indistinguishable from the uranogenic ratios of the western Tunkillia Suite members, the Wynbring Pluton ($^{206}Pb/^{204}Pb$ = 15.176 ± 0.030, $^{207}Pb/^{204}Pb$ = 15.169 ± 0.034) and Tallacootra 1 Pluton ($^{206}Pb/^{204}Pb$ = 15.215 ± 0.038, $^{207}Pb/^{204}Pb$ =

15.202 ± 0.036) (Table 3.2).

In contrast, values for the eastern Tunkillia Suite are considerably more radiogenic and range from 15.923 – 16.143, 15.325 – 15.414 and 35.330 – 35.757 for $^{206}Pb/^{204}Pb$, $^{207}Pb/^{204}Pb$ and $^{208}Pb/^{204}Pb$, respectively. In terms of Pb-isotopic values, the eastern Tunkillia is more similar to the 1633 – 1608 Ma St Peters Suite samples ($^{206}Pb/^{204}Pb$ = 16.046 -16.062, $^{207}Pb/^{204}Pb$ = 15.423 – 15.448, $^{208}Pb/^{204}Pb$ = 35.753 – 35.847), than the western Tunkillia Suite. The grouping of the data, stability of the integrated LA-ICP-MS signals (Fig. 3.3), coupled-variation in the $^{206}Pb/^{204}Pb$, $^{207}Pb/^{204}Pb$ and $^{208}Pb/^{204}Pb$ systems (Fig. 3.7) and mineralogical homogeneity suggest that the results are reflecting magmatic source variation rather than the post-crystallisation ingress of radiogenic Pb.

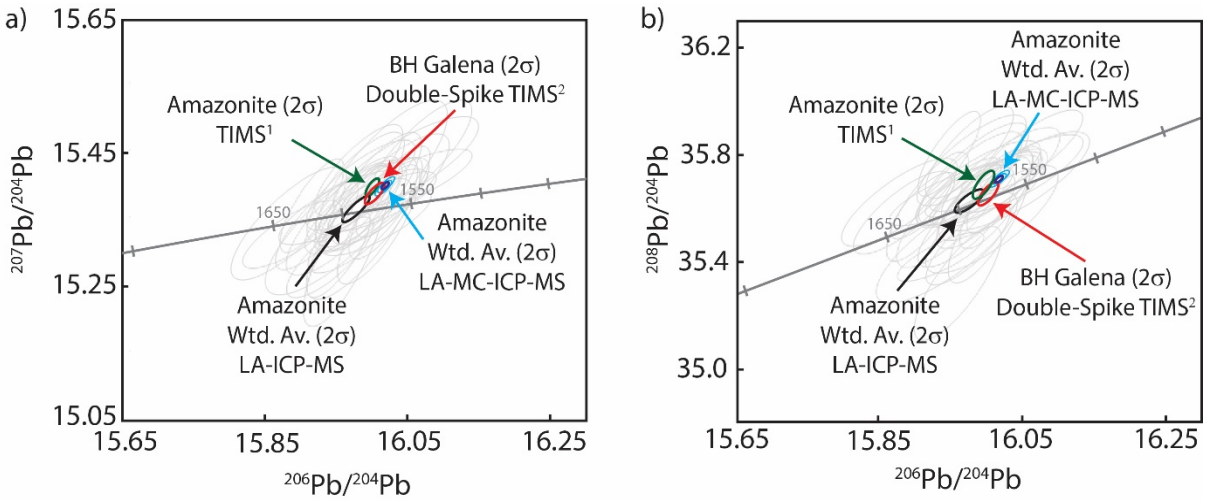

Figure 3.5: Results of LA-ICP-MS and LA-MC-ICP-MS Pb-isotopic analyses on Broken Hill amazonite which is used as a matrix-matched secondary standard. Grey ellipses represent individual LA-ICP-MS analyses [2]Cooper et al., (1969).

The data are generally consistent with the Stacey & Kramers (1975) model growth (μ = 9.74). While model ages for the St Peters Suite samples provided by this growth curve are consistent with the U-Pb geochronology (Fanning et al., 2007; Swain et al., 2008), the model ages of the alkali feldspar for the Tunkillia Suite are more difficult to explain. Eastern Tunkillia samples yield $^{207}Pb/^{206}Pb$ ratios (0.960 – 0.963) indicating model ages slightly more radiogenic than their U-Pb zircon ages suggest. Conversely, the Pb-isotopic ratios (1.006 > $^{207}Pb/^{206}Pb$ > 0.977) of the western

Tunkillia Suite suggest model ages which are significantly older than their U-Pb ages (-214 to 346 Ma) (Fig. 3.7).

3.7 Discussion

The new isotopic data from the alkali feldspars from intrusive rocks of the Tunkillia Suite suggest that the Tunkillia Suite can be divided into two, geographically-distinct populations (Fig 3.6): One sub-suite which was dominantly generated from a source with relatively ordinary, crustal-like Pb-isotopic systematics (eastern Tunkillia Suite) and another that contains distinctly unradiogenic Pb (western Tunkillia Suite). The Unradiogenic Pb-isotopic signatures of the type found in the western Tunkillia Suite plutons area relatively rare phenomenon and fundamentally invoke isotopic inheritance from an ancient crustal reservoir. Although the Pb-isotopic disparity seen between the eastern and western Tunkillia Suite superficially mirrors the variation previously seen in the Sm-Nd isotopic system, the rarity of the phenomenon and unique circumstances involved in the formation of unradiogenic Pb-isotopic reservoirs provides temporal and geochemical constraints on the crustal-

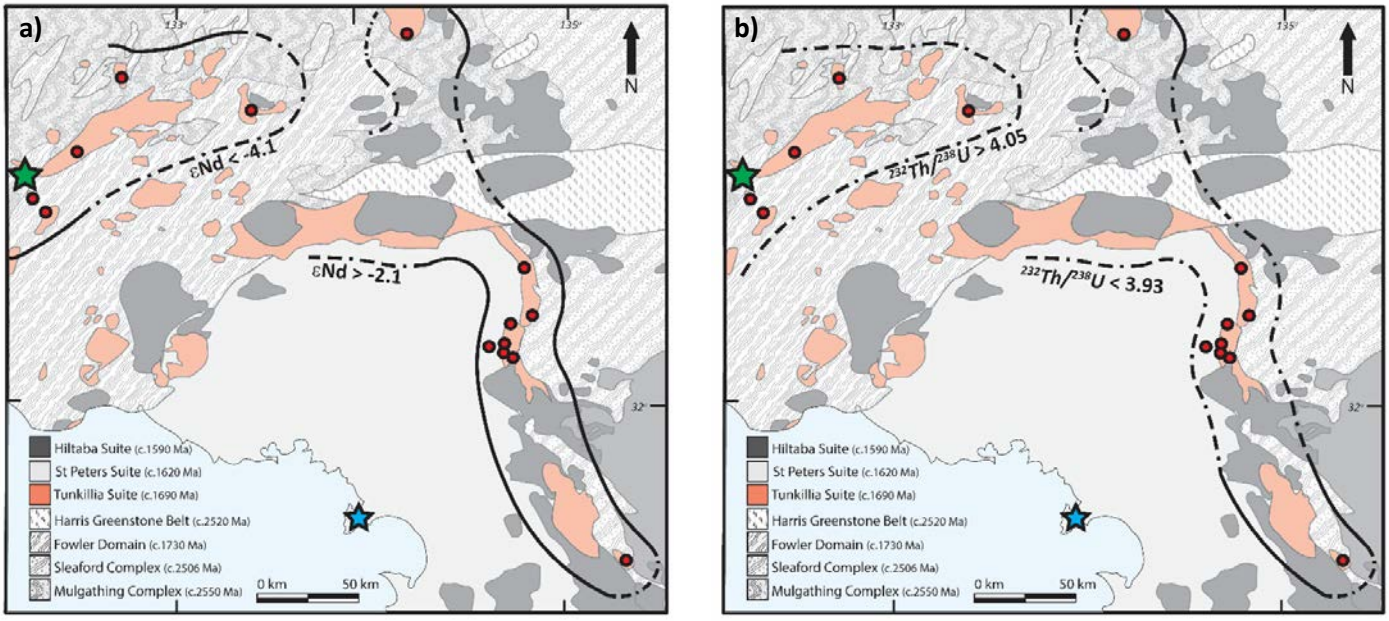

Figure 3.6: Isotopic domains of the Tunkillia Suite. Red circles indicate samples analysed here. a) $\varepsilon Nd_{(t)}$ values show a clear geometrical distribution between more evolved values (-6.3 < $\varepsilon Nd_{(t)}$ < -4.1) in the west and more juvenile values in the east (-2.1 < $\varepsilon Nd_{(t)}$ < +2.6). Blue star indicate location of St Peters Suite Pb-Pb results. Sm-Nd analyses after Payne et al. (2010). b) The coincident distribution of unradiogenic Tunkillia Suite (west) and Pb-normal Tunkillia Suite (east) with equivalent Sm-Nd isotope results shows the variation in melt-source chemistry between a dominantly old, crustal source in the west, yet a more juvenile, U-Th-Pb ordinary source in the east.

melt component involved in the mobility of U and Th, and generation of the western Tunkillia Suite Pb-isotopic composition.

Feldspar textures (fig. 3.2) and chemical compositions indicate that limited post-crystallisation modification has taken place within the samples analysed here, and therefore Pb-isotopic compositions represent initial values. K-feldspars are compositionally-varied (Fig. 3.2; mol% $Or_{65\text{-}95}$), however display neither intrasuite variation, nor high-$Or_{\%}$ which may indicate recrystallisation of K-feldspar and resetting of the Pb-isotopic signature. Likewise, the preservation of primary textures (i.e. oscillatory zonation) in K-feldspar phenocrysts of both eastern and western Tunkillia Suite implies that post-crystallisation P-T conditions were insufficiently high to cause recrystallisation of K-feldspar. Furthermore, closure temperatures calculated for the K-feldspars (1 mm to 1 cm; T_c = ~680 to 820°C) from the equations of Dodson (1973) and diffusivity coefficients of Cherniak (1995) indicate that Pb-diffusion is not likely to have occurred. Thus, neither Pb-diffusion nor K-feldspar recrystallisation (resetting) can explain the differences in Pb-isotopic signature of the eastern and western Tunkillia Suite, and therefore variation must be due to innate variations in the Pb-isotopic signature of melt-sources.

3.7.1 Formation of Unradiogenic Pb-isotopic Signatures and its bearing on the Petrogenesis of the western Tunkillia Suite

In order to generate unradiogenic Pb-isotopic compositions, the first requirement is a crustal reservoir which initially conformed to ordinary crustal growth models, however subsequently became significantly depleted in U. U-depletion effectively limits the amount of radiogenic Pb which can be produced by decay of ^{238}U and ^{235}U, thus slowing Pb-isotopic 'growth'. A convenient comparison is that of a clock whose mechanisms have slowed. Due to the long respective half-lives of $^{238, 235}U$ and ^{232}Th, the Pb-isotopic reservoir which was depleted of U must also have been and isolated for a geologically-significant period of time prior to the Tunkillia Suite event, such that the

addition of radiogenic Pb to the common Pb system is slower than that occurring in average crustal rocks and the inferred temporal differences can be observed (Fig. 3.8). To further the clock-analogy, this is the equivalent of enough real-time passing such that the slowed-rate of the clock may be noticed.

U/Th-Pb depletion and the development of unradiogenic Pb-isotopic signatures has long-been associated with granulite-facies metamorphism (Gray and Oversby, 1972; Hildreth and Moorbath, 1988; James, 1982; Whitehouse, 1989). A prolonged history of partial melting of a crustal reservoir resulting in a melt-depleted restite could also theoretically lead to the formation of unradiogenic Pb-isotopic reservoirs, since labile U and Pb not bound within the crystalline lattice of resistate minerals, will preferentially partition strongly into melt relative to residual crust (Bea, 1996; Peiffert et al., 1994). The P-T conditions in either of these situations, but especially in the case of granulite facies metamorphism, are above biotite-metastability. Unradiogenic Pb-isotopic reservoirs such as that which is involved in forming the Pb-isotopic compositions of the western Tunkillia Suite are therefore fundamentally less-capable at contributing to a biotite-dehydration-fluxed crustal melt as espoused for the Tunkillia Suite by Payne et al. (2010) and theoretically melt-infertile (Clemens and Vielzeuf, 1987; Patiño Douce and Johnston, 1991). Such a mechanism is seemingly-paradoxical with regard to the syn-collisional tectonic model for magmatism which typically invokes anatexis of melt-fertile, undepleted crust, such as quartzofeldspathic or pelitic crust (Clemens and Vielzeuf, 1987; Patiño Douce and Johnston, 1991). The rarity of the unradiogenic Pb-isotopic occurrences despite the theoretically-common conditions required to form unradiogenic reservoirs is probably an indication to the sparingly melt-fertile nature of these isotopic reservoirs. It therefore seems prudent to compare the tectonic settings where unradiogenic Pb-isotopic signatures are inherited by a younger magmatism elsewhere in the world, as a clue to the tectonic environment of the Tunkillia Suite.

3.7.2 Isotopic Constraints on Crustal Component of the Western Tunkillia Suite

Although Pb-Pb model ages are typically an unreliable indicator of age when reservoir-mixing is involved, the range of model ages inferred from the Pb-istopic composition of the western Tunkillia Suite (2026 – 1844 Ma) suggests that the crustal reservoir containing the unradiogenic Pb-isotopic signature is at least this old. Complex-zoned zircon cores in the Wynbring Pluton provide evidence for inheritance from a ~2500 Ma protolith (Fanning et al. 2007), which broadly coincides with the Sleafordian Orogeny at 2480 – 2420 Ma. A Sleafordian-aged protolith which became U/ Th-Pb depleted during the later stages of the Sleafordian Orogeny or sometime before ~2000 Ma would thus satisfy the temporal requirements of the unradiogenic Pb-isotopic signature of the western Tunkillia Suite (Fig. 3.8).

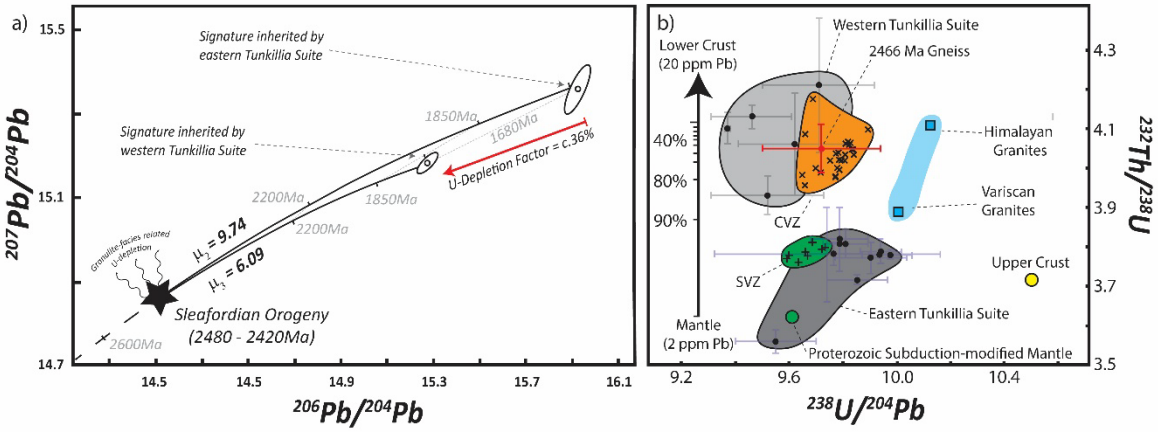

Figure 3.8: (a) Uranogenic Pb-isotope systematics invoked for the differences between the Pb-isotopic composition of the eastern and western Tunkillia Suite. U/Th-depletion caused by granulite-facies metamorphism during the 2480 – 2420 Ma Sleafordian Orogeny in the western Gawler Craton creates a low-$^{238}U/^{204}Pb$ reservoir which retards Pb-isotopic evolution of the crustal component hybridised with the western Tunkillia Suite. In contrast, the eastern Tunkillia Suite evolved from mixing between two relatively-normal Pb-reservoirs. (b) Time-integrated $^{232}Th/^{238}U$ and $^{238}U/^{204}Pb$ arrays outline the disparity between the Pb-isotopic signatures of the western and eastern Tunkillia Suite (2σ error crosses), which is a comparable isotopic phenomenon to that seen in the Southern Volcanic Zone (SVZ) and Central Volcanic Zone (CVZ) of the Andean Cordillera. The isotopic characteristics of the eastern Tunkillia Suite (and SVZ) reflects mixing between a mantle and normal-crustal component, while the western Tunkillia Suite (and CVZ) reflects mixing between U-depleted, melt-infertile lower crustal granulites and mantle. SVZ data from (Hildreth and Moorbath, (1988), CVZ data from (Tilton and Barreiro, (1980); Davidson et al., (1991)). 'Upper crust' signature after Zartman and Doe, (1981). 'Proterozoic Subduction-modified mantle' signature after Ellam et al., (1990). Variscan data after Bernard-Griffiths et al., (1985), Himalaya data after Gariepy et al., (1985).

Payne et al. (2010) demonstrated that assimilation of some component of early Paleoproterozoic basement rock, such as the 2446 Ma gneissic sample '879-29b', could broadly

explain the anomalously-evolved Sm-Nd isotopic composition of the western Gawler Craton ($\varepsilon Nd_{(1680Ma)}$ = -5.31 to -6.31). The alkali feldspar Pb-isotopic signature of the 2446 Ma gneiss is within analytical uncertainty of many of the western Tunkillia Suite data and thus, this signature is interpreted to represent the Pb-isotopic composition of the gneiss at the time of feldspar recrystallisation which coincided with the Tunkillia Suite event. Time-integrated $^{238}U/^{204}Pb_{(t)}$ calculated for the 2466 Ma gneiss (μ_2 = 9.72) indicates it initially conformed to global growth models (μ_2 = 9.74), however must have been reduced to μ_3 = 6.09 by 1690 – 1670 Ma in order to generate the Pb-isotopic signature sampled by the western Tunkillia Suite (Fig. 3.8). Present day $^{238}U/^{204}Pb$ for the 2466 Ma gneiss (2.33) calculated from whole-rock geochemical data (U/Pb = 0.03: Table 3.2) indicates this gneiss satisfies the requirements of the theoretical U-depleted crustal reservoir. The preferential depletion of U over Th and Pb in the gneiss is observed in the high time-integrated $^{232}Th/^{238}U$ (κ_2 = 4.05), which is consistent with values expected in the lower crust (Zartman and Doe, 1981). Such a uranium depletion factor (~36%) is within the range encountered in the granulites of Mt. Aloysius, Western Australia (5 to 40%; Gray and Oversby (1972)) and Lewisian complex of Scotland (39 to 90%; Whitehouse (1998)).

The Pb-isotopic composition of the 2446 Ma gneiss presented here cannot, however, explain all variation seen in the western Tunkillia Suite. Both the Lake Ifould Pluton (μ_2 = 9.37, κ_2 = 4.1) and Barton Pluton (μ_2 = 10.43, κ_2 = 4.13) remain outside of 2σ uncertainty, and suggest an Archean to Early Paleoproterozoic lower crust with strong temporal and compositional variability. In addition to probable lower crustal compositional variation through the central-western Gawler Craton, the lower μ_2 and higher $\varepsilon Nd_{(1680Ma)}$ of the western Tunkillia Suite relative to the 2466 Ma gneiss allows for the melt-hybridisation between crustal- and mantle-derived melts. The crustal-melt was of similar isotopic composition to the 2466 Ma gneiss, and the juvenile-mafic magma was characterised by higher $^{147}Sm/^{144}Nd$ and lower $^{238}U/^{204}Pb_{(t)}$ with a Pb-concentration significantly lower than the crustal component represented by the 2466 Ma Gneiss (13.5 ppm Pb). Hybridisation of juvenile mafic magma with some portion of Archean-Early Paleoproterozoic lower crust fulfils the

isotopic requirements of the western Tunkillia Suite, and also explains how a melt volume equivalent to the western Tunkillia Suite can be generated from typically melt-infertile granulitic lower crust. Moreover, a scenario involving a variable percentage of crustal-assimilant with a mantle-derived melt provides petrological consistency linking the evolved isotopic signature of the western Tunkillia with the relatively-juvenile isotopic signatures of the eastern Tunkillia Suite.

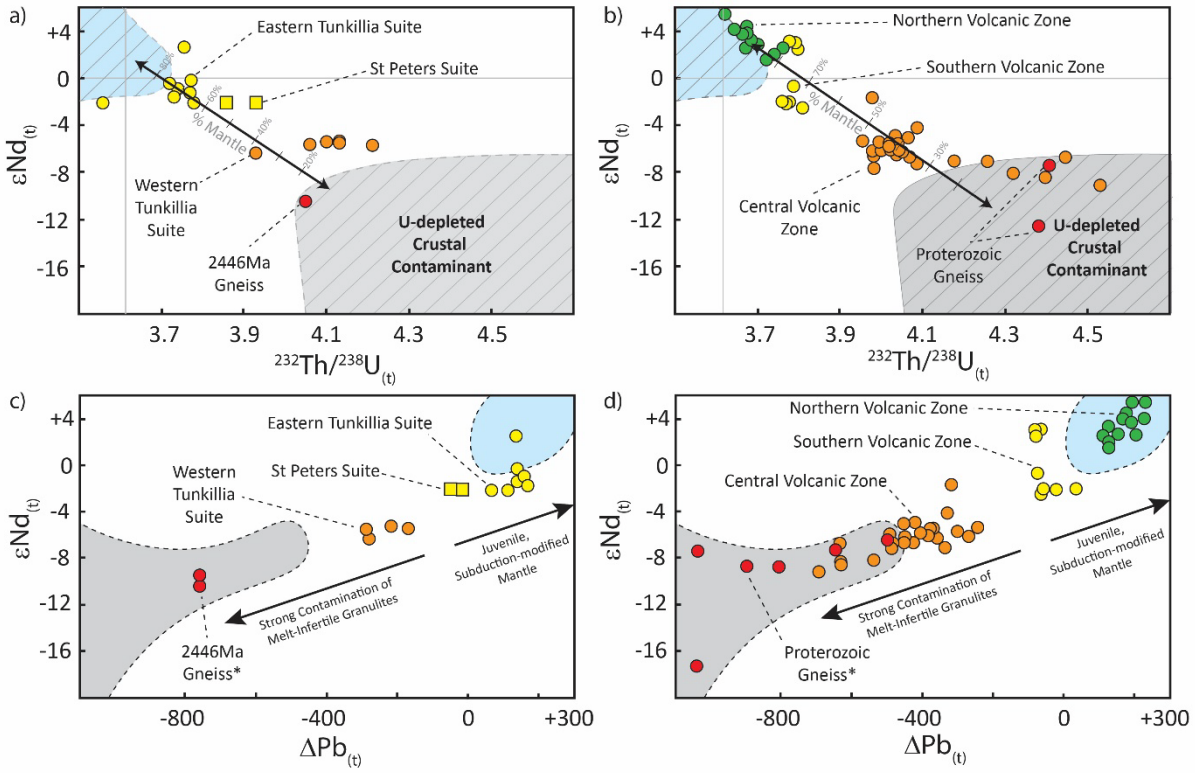

Figure 3.9: Combined Pb-Pb vs. Sm-Nd isotopic mixing arrays for the Tunkillia Suite, St Peters Suite and 2446 Ma gneiss (left) and the Andean Cordillera (right). Mixing arrays join the same basic end-member isotopic reservoirs of a subduction-modified mantle (vertical grey line; Ellam et al., 1990), and a U-depleted, granulitic lower crust characterised by evolved $\varepsilon Nd_{(t)}$ and unradiogenic, high-$^{232}Th/^{238}U$ (>4.0) Pb-isotopic signatures. Hybridisation or assimilation of mantle-like magmas with a crustal component of melt-infertile granulitic lower crust is suggestive of a dynamic, continental arc-like tectonic environment. ΔModel $Age_{(Pb\text{-}Pb)}$ represents the U-Pb zircon age subtracted by the Pb-Pb model age (Stacey and Kramers, 1975), and is intended to reduce two-dimensional $^{206}Pb/^{204}Pb$ vs/ $^{207}Pb/^{204}Pb$ data into a single-dimension for comparison against $\varepsilon Nd_{(t)}$, as well as igneous suites of different ages. Pb-Pb model ages are notoriously inaccurate at indicating geologically-relevant 'ages', however do effectively demonstrate the differences between the Pb-isotope data, and a modelled average crust (Stacey and Kramers, 1975).Note: ΔModel $Age_{(Pb\text{-}Pb)}$ for the gneisses represents the age of intrusion (i.e. Tunkillia Suite, or Andean volcanics) minus the theoretical model age at the time of formation of the gneiss. 'Proterozoic Gneiss' data after Tilton and Barreiro, (1980) and Wörner et al., (2000)). 'Central Volcanic Zone', 'Southern Volcanic Zone' and 'Northern Volcanic Zone' data after Davidson et al., (1991), Hildreth and Moorbath, (1988) and Bryant et al., (2006), respectively.

3.7.3 Isotopic Mixing as an Indicator of Tectonic Environment: The Andean Cordillera

Of the few localities globally which record unradiogenic Pb-isotopic signatures inherited by a younger magmatic event (i.e. Neymark et al., 1994), the most studied example is located in the Central Volcanic Zone (CVZ) of the Andean Cordillera (Davidson et al., 1991; James, 1982; Mamani et al., 2010; Tilton and Barreiro, 1980). Here, subduction of the Nazca Plate occurs beneath a thickened lithosphere (~70km; Beck et al. (1996)) comprised of a Mesoproterozoic to Ordovician (~1500 to 440 Ma) allochthon (Loewy et al., 2004) with peak metamorphic grades of granulite facies sustained during the Grenvillian Orogeny (Wasteneys et al., 1995). The temporal difference between peak-metamorphic grade and the onset of the inheriting magmatic event (~1000 Myr) is convenient since it provides a potential granulitic crustal component directly comparable to that of the western Tunkillia Suite and Archean – Early Paleoproterozoic Gawler Craton nucleus (~820 Myr difference).

Assimilation during melt-ascent (Harmon et al., 1984) and MASH-zone hybridisation (Hildreth and Moorbath, 1988) between the granulitic crust and intruding subduction-related melts have led to the inheritance of strongly evolved, crustal isotopic compositions. The incorporation of the granulitic isotopic composition is distinguished by the range of radiogenic isotopic compositions revealed from volcanics of the Arequipa and Antofalla regions of the CVZ (Fig. 3.9). The $\varepsilon Nd_{(t)}$ composition of the volcanics range from -15.2 in the Arequipa Domain (Mamani et al., 2008) to +5.2 in the Antofalla Region (Kay et al., 1994). For the Pb-Pb isotopic system, time-integrated μ_2 ranges from 9.97 in the Arequipa Domain to 9.65 in the Barroso Volcanics, while κ_2 ranges from 4.53 in the Arequipa Domain to 3.96 in the Barroso Volcanics (Davidson et al., 1991; James, 1982; Tilton and Barreiro, 1980). This isotopic distribution overlaps with those values recorded in the western Tunkillia Suite (Fig. 3.9), and form a crustally-dominated mixing array when compared with other arc-segments of the Andean Cordillera (Fig. 3.9). Taken in isolation however, and without the benefit of modern-day geological exposures (such is the case for the Tunkillia Suite), the majority of data from the CVZ are indicative of simple crustal reworking. However, the end-members involved in the formation of this array illustrate a unique mixing paradigm which is indicative of the mode of

tectonic formation. The required amount of U-depleted, melt-infertile, granulitic lower crust in order to form the dominantly crustal-isotopic composition of the mafic, subduction-related melts is a key consideration. Mamani et al. (2008) suggested mixing between subduction-modified mantle and as little as 15 to 18% of mafic granulite (low-degree partial-melt) is capable of producing the more-crustal isotopic and geochemical composition of the intermediate volcanics of the El Misti Volcano. These values would be expected to decrease significantly with increasing SiO_2 of the proposed crustal contaminant, (due to increasing Pb-concentration) and thus should be viewed as an upper estimate. Freymuth et al. (2015) calculated that the felsic Lauca Ignimbrites required a greater crustal contribution (22 - 68%), facilitated by a slow magma ascent-rate through the thickened lithosphere. Both these ranges are in accordance with mantle-crust mixing proportion estimates provides by the $\varepsilon Nd_{(t)}$ vs. $^{232}Th/^{238}U_{(t)}$ array (Fig. 3.9). The western Tunkillia Suite, ranges from ~30 to 40% subduction-modified mantle material which is most similar to the estimates of the Lauca Ignimbrite of Freymuth et al. (2015). Mantle-component estimates increase substantially for the eastern Tunkillia Suite (70 – 90%) (Fig. 3.9). Both these ranges are largely insensitive to Pb-related assumptions of the crustal component and demonstrate the requirement of a mantle-like Pb component (low-κ_2, μ_2) in both the eastern and western Tunkillia Suite.

The isotopic composition of the Andean CVZ contrasts strongly with the more-typical continental arc magmatism of the Northern and Southern Volcanic Zones (NVZ and SVZ), which displays Nd-Pb systematics more analogous to those in the eastern Tunkillia Suite. The relatively modest crustal assimilation ($\varepsilon Nd_{(t)}$ = -2.5 to +3.08; Hildreth and Moorbath (1988)) seen in the SVZ, is further limited in the NVZ as shown by $\varepsilon Nd_{(t)}$ values in the range of +1.46 (Chacana Volcano) to +5.5 (Pululagua Volcano) (Bryant et al., 2006). The decreasing evolved, crustal component is argued to be the result of decreasing lithospheric thickness (~40km; Bohm et al. (2002)), which is a potential explanation for the dichotomy of $\varepsilon Nd_{(t)}$ values seen between the eastern (-2.11 to +2.6) and western Tunkillia Suite (-6.31 to -5.31) (Fig. 3.10). Pb-isotopic signatures in both the NVZ and SVZ (μ_2 = 9.59 to 9.93, κ_2 = 3.62 to 3.81; Bryant et al. (2006); Hildreth and Moorbath (1988)) are equivalent to those of

the eastern Tunkillia Suite (μ_2 = 9.55 to 9.89, κ_2 = 3.56 to 3.78) and illustrate crustally-biased mantle-crust hybridisation vis-à-vis the 'orogene' model of Zartman and Doe (1981).

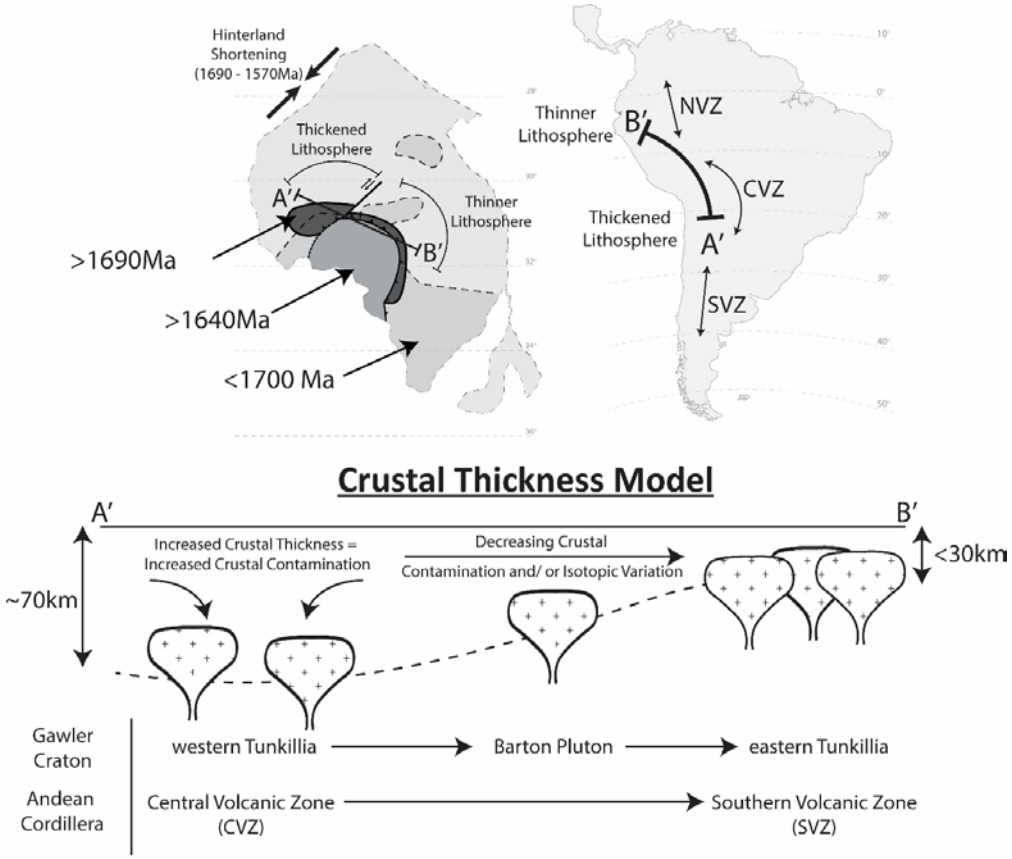

Figure 3.10: A model involving the interplay of crustal thickness variation and subduction based on analogous isotopic systematics observed in the Andean Cordillera. In the Andean Cordillera, increased crustal thickness exerts a strong influence over the amount of crustal inheritance, however at least some age and geochemical variation exists between the crustal components of the western and eastern Tunkillia Suite which led to the development of the unique isotopic phenomenon of unradiogenic inheritance. The single unifying feature driving the Tunkillia Suite is the mantle-like magmatic component suggesting supra-subduction tectonic setting.

While overall time-integrated μ_2, κ_2 for both the eastern Tunkillia Suite and the Andean SVZ-NVZ are broadly conformable with global growth evolution, the model ages yielded from the Pb-isotopic compositions are not (Table 3.2). Pb-isotopic model ages are notoriously inadequate at providing geologically-reconcilable ages, however do provide a means of normalising two-dimensional Pb-isotopic data (i.e. $^{207}Pb/^{204}Pb$ vs $^{206}Pb/^{204}Pb$) to a single-dimension (Fig. 3.9). This allows for the discrepancies between Pb-isotopic growth models and Pb-isotopic data to be illustrated on a bivariant diagram. ΔModel $Age_{(Pb\text{-}Pb)}$ (Fig. 3.9), which is the U-Pb zircon age minus the Pb-Pb model age, goes one step further highlighting Pb-isotopic inheritance from ancient crustal

reservoirs (negative values), or accelerated crustal reservoirs (positive values). The identification of accelerated Pb-isotopic signatures and model ages indicates excess radiogenic $^{206}Pb/^{204}Pb$ in the magmatic source. This is a common phenomenon in modern island arcs systems such as the Banda Arc (i.e. Vroon et al. (1993); Elburg et al. (2004)) and Lesser Antilles (i.e. Thirlwall et al. (1996); Carpentier et al. (2008)), where excess radiogenic $^{206}Pb/^{204}Pb$ (ΔModel $Age_{(Pb\text{-}Pb)}$ > +200 Myr) is demonstrated to reflect increased melt-contribution of subducted sediment-load (Vroon et al. (1993); Elburg et al. (2004); Thirlwall et al. (1996); Carpentier et al. (2008)). In the context of Nd-Pb mass-balance, this cannot occur from mixing between two volumes of crustal melt with roughly-equal Pb-concentrations and requires large additions (~70 - 95%) of Pb-poor mantle magma (Fig. 3.9). Thus, while the unique unradiogenic Pb-isotopic compositions of the western Tunkillia Suite (and CVZ) demonstrate magmatic hybridisation between ancient, U-depleted crustal reservoirs, the slightly accelerated phenomenon in the east (and NVZ-SVZ) could be explained by the inheritance Pb from subducting sediments.

In contrast, the Pb-isotopic signatures of magmas produced by continent-continent collision such as the Hercynian Variscides and Himalayas are not similar to those of either the eastern or western Tunkillia Suite. In the leucogranites of the Armorican Massif, Bernard-Griffiths et al. (1985) report Pb-isotopic results from alkali feldspars which yield average Pb-isotopic compositions corresponding to time-integrated (Stacey and Kramers, 1975) $^{238}U/^{204}Pb_{(t)}$ and $^{232}Th/^{238}U_{(t)}$ of 10.1 and 3.88, respectively. Likewise, Himalayan alkali feldspar Pb-isotopic compositions reported by Gariepy et al. (1985) reveal average $^{238}U/^{204}Pb_{(t)}$ of 10.13 and $^{232}Th/^{238}U_{(t)}$ of 4.1. The higher-$^{238}U/^{204}Pb_{(t)}$ and $^{232}Th/^{238}U_{(t)}$ of both collisional granite suite examples suggest a dominant magmatic Pb source from a reservoir originally generated in the upper crust, and are consistent with a typical syn-collisional granite petrogenesis involving anatectic melting of fertile metasedimetary rock. While a degree of mantle involvement is inferred for some parts of the Variscan Orogen (Altherr et al., 2000), the isotopic constraints do not indicate the mafic magmas to be as significant to overall petrogenesis as is implied by the isotopic data in the Tunkillia Suite.

3.7.4 Trace-element Geochemistry

Petrological insights from geochemistry alone is complicated in continental arc settings by open-system mantle-crust mixing in addition to the effects of closed-system magmatic processes such as fractional crystallisation. For example, volcanics of the Andean CVZ, which have undergone extensive crust-mantle hybridisation, display higher average SiO_2 compared with other arc segments (due to addition of silicate-rich crustal melt; Davidson et al. 1991) as well as low MgO (developed through crystal fractionation; Mamani et al., 2009). Further, innate geochemical variations of the crustal-melt component can vary strongly, both within a single continental arc segment as well as globally,

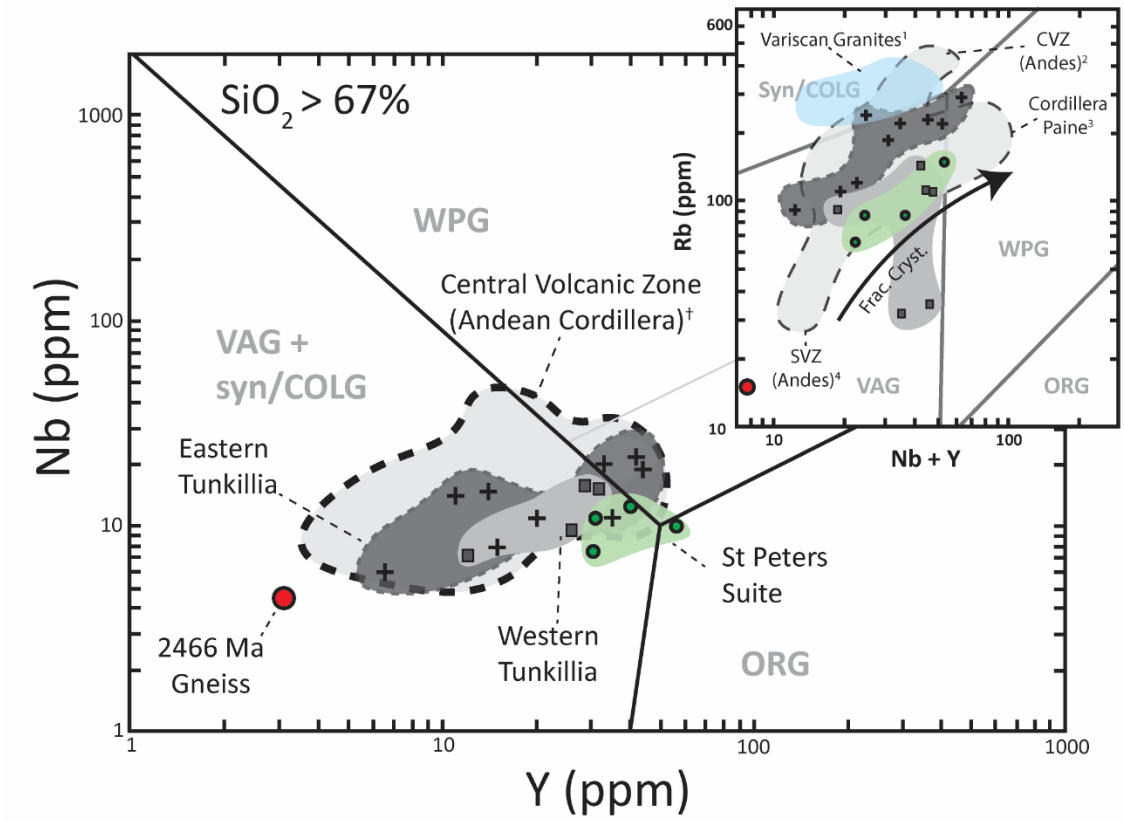

Figure 3.11: The Nb-Y and Rb/Nb+Y tectonic discrimination diagrams of Pearce et al. (1984), based on whole-rock geochemistry. While the Tunkillia Suite falls within the volcanic arc field (VAG) of Nb-based discriminant diagrams Payne et al. (2010) showed Ta-based diagrams suggest Syn-Collisional tectonic environment. Unlike Island Arc magmas, continental arcs magmas may display transitional affinities with both syn-collisional and volcanic arc geochemical trends. This is readily shown by the fractionated Cordillera Paine intrusions (Michael, 1991) plotting as within-plate granites ('WPG'), and crustally-contaminated CVZ (i.e. Huavlillas and Barroso Volcanics) plotting as syn-collisional granites ('syn-COL'). Tunkillia Suite and St Peters Suite geochemistry from Payne et al. (2010) and Swain et al. (2008), respectively. CVZ, SVZ and Cordillera Paine data after Mamani et al., (2008), Hildreth and Moorbath, (1988) and Michael (1991), respectively.

inhibiting simple tectonic discrimination based solely on geochemistry. In this regard, continental arc magmas share many geochemical characteristics transitional to those displayed by magmas generated within continent-continent collisional settings, which can be shown through the overlap of the two fields (Förster et al., 1997) on various tectonic discrimination diagrams (e.g. Pearce et al. (1984)). Both the eastern and western Tunkillia Suite plot dominantly within the volcanic arc field ('VAG'), with some samples plotting marginally within the syn-collisional ('Syn/COL') and within-plate fields ('WPG') of the Rb-Nb-Y diagrams (Fig. 3.11). The Tunkillia Suite data distribution is entirely consistent with the distribution of Andean Cordilleran volcanics and intrusives of the same SiO_2-range (Fig. 3.11). The control exerted by fractionation of biotite and plagioclase (Pearce et al., 1984) can explain the majority of these trends in the eastern Tunkillia Suite. Feldspar crystal fractionation is supported by the range of Eu/Eu_N* in the eastern Tunkillia Suite (2.04 – 0.22; Fig. 3.12) and the common presence of zoned plagioclases and alkali feldspars (Fig. 3.2b). The similarities of Nb and Ta allow for Ta-variants on the tectonic discrimination diagrams. Elevated Ta is observed in the eastern Tunkillia Suite ($\overline{x}$ = 4 ppm) relative to the western Tunkillia Suite ($\overline{x}$ = 0.8 ppm) which is linked to partial melting of biotite-rich crust (Stepanov and Hermann, 2013). High-Ta forces data to plot in the Within-Plate/ Collisional fields of the tectonic discrimination diagrams of Pearce et al. (1984) and Harris et al. (1986). The elevated-Ta character of the eastern Tunkillia Suite is not present in the western Tunkillia Suite (Ta $\overline{x}$ = 0.8 ppm), and therefore this is considered to be the result of a variable crustal component rather than a critical petrological constraint. Furthermore, a number of examples from the Lower Miocene Huaylillas Arc and Upper Barroso arc segment of the Andean CVZ display even greater-Ta concentrations (3.5 – 16.2 ppm Ta; Mamani et al. (2008)) than is seen in the eastern Tunkillia Suite, which places these continental arc volcanics well into the syn-collisional/ within plate fields. This illustrates the limitations inherent in use of Ta-dependent tectonic discrimination diagrams which in the majority of cases will only be reflecting the geochemical characteristics of the crustal component, rather than any contribution from a mantle-derived melt which may be driving the magmatic event. Similarly, the very high Ce/Lu ($\overline{x}$ = 443) and Y/Yb ($\overline{x}$ = 11;

Fig. 3.12) expressed by the western Tunkillia Suite and suggesting the presence of garnet in the melt source, are inconsistent with the lower values for Ce/Lu ($\bar{x}$ = 240) and Y/Yb ($\bar{x}$ = 8) of the eastern Tunkillia Suite. Since the exceedingly-long half-lives of radiogenic isotopes (Pb-Pb, Sm-Nd etc) preclude the time-effects of closed-system magmatic processes such as differentiation, coupled isotopic-geochemical covariation is interpreted to reflect the innate geochemical differences of the crustal component. Thus this variation between the Ce/Lu and Y/Yb (Fig. 3.12) reflects the presence of garnetiferous crustal component of the western Tunkillia Suite which is not present in the eastern Tunkillia Suite, while the range in Y/Yb in the eastern Tunkillia Suite is likely due to closed-system magmatic processes (Fig. 3.12). These geochemical variations are therefore not indicative of the driver for Tunkillia Suite magmatism, which is at the heart of the tectonic argument, but instead reflecting the diversity of lower to mid-crustal material to which the mantle component was added.

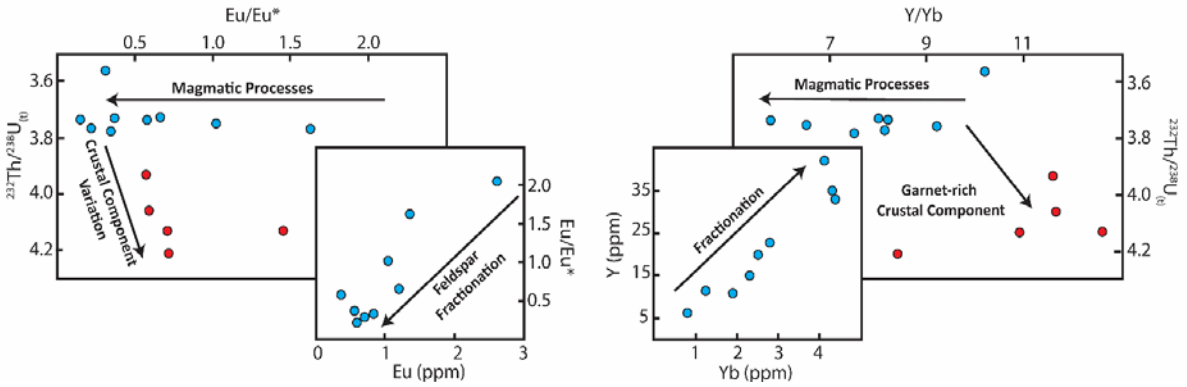

Figure 3.12: Since Pb-isotopes do not fractionate with magmatic processes they can be used to differentiate the geochemical effects of crustal hybridisation from magma processes such as fractionation. Much of the geochemical variability of the eastern Tunkillia Suite can be explained by fractionation, while differences between the eastern and western Tunkillia Suite are mostly related to innate variation in the composition of the crustal-melt component.

Strong depletions in Nb, Sr and Ti which are often considered hallmarks of arc magmatism (Hollings and Kerrich (2000); Polat and Kerrich (2001); Sajona et al. (1993); Smithies et al. (2005)) which appear insensitive to crustal assimilation (Davidson et al., 1991) and are thus present a good geochemical indication of primary magma source. However, the same trace-element patterns can also theoretically be generated by partial-melting with Ti-oxide and feldspar-rich restite as is the case for the S- and I-type Variscan granites (Altherr et al., 2000; Neiva et al., 2009). The post-

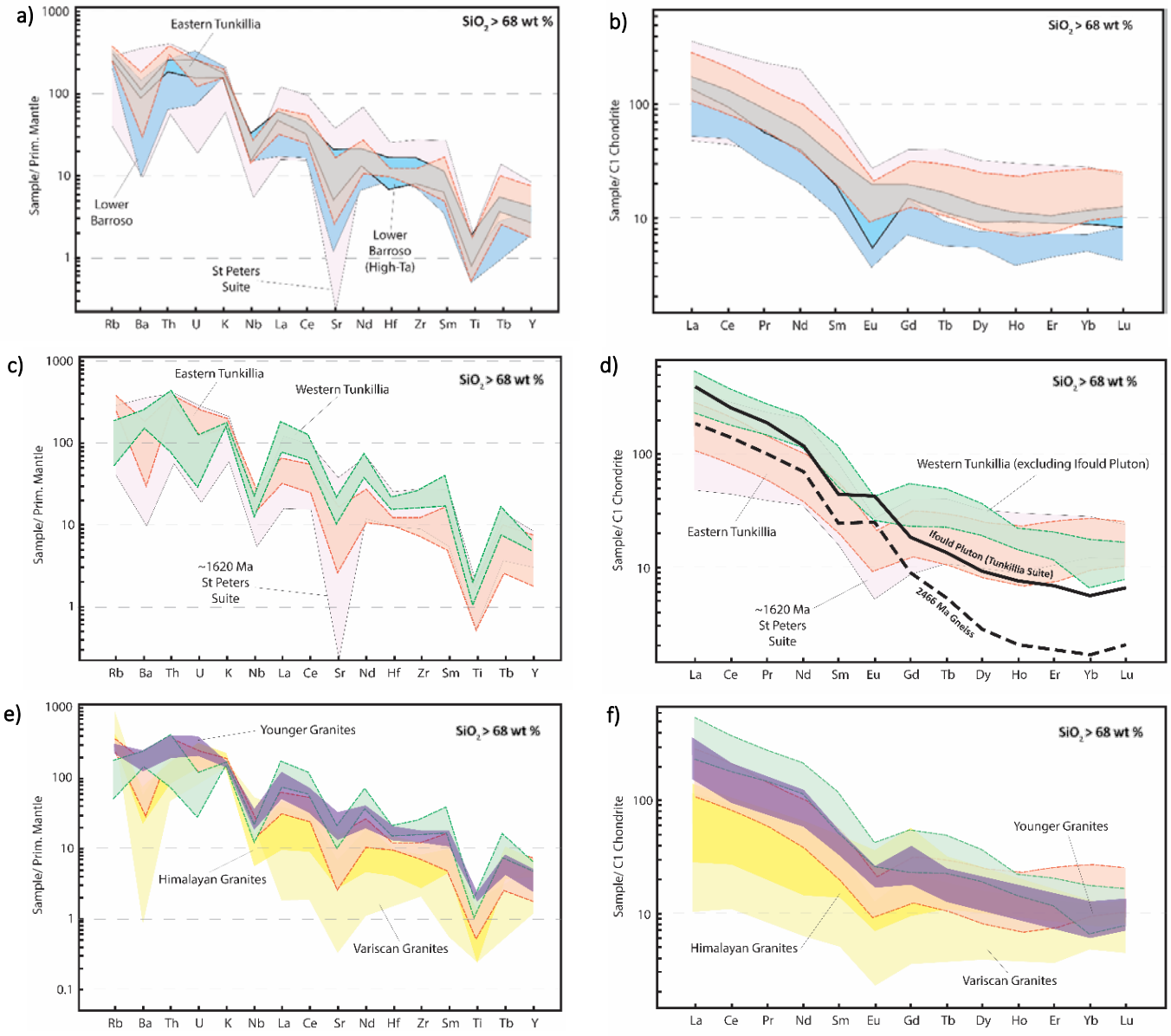

Figure 3.13: (left) Primitive mantle (McDonough et al., 1992) and (right) chondrite-normalised (McDonough and Sun, 1995) trace-element plots. a) 75th- and 25th-percentile trace-element similarities between the eastern Tunkillia Suite (red), c.1620 Ma St Peters Suite (pink) and Lower Barroso Volcanics of the Andean Cordillera. Nb-, Sr- and Ti-depletions typical of arc-related magmas are preserved through crustal hybridisation. b) Moderately-steep LREE, Eu-depletion and Ba-depletion (in a)) are largely the result of fractionation. Differences in HREE-enrichment and Th-U in a) point to the effects of variable geochemistry of lower-crustal components, between the Pliocene volcanics and Paleoproterozoic Tunkillia Suite and St Peters Suite. c) 75th- and 25th-percentile trace-element differences of the eastern and western Tunkillia Suite. The granulitic crustal component in the western Tunkillia Suite has caused LILE and Th-U variation. d) Higher-LREE and relatively-depleted HREE in the western Tunkillia, illustrated more effectively by comparing the Lake Ifould pluton with the 2466 Ma gneiss, and support the isotopic evidence for a garnetiferious crustal component in the western Tunkillia Suite. e) The Tunkillia Suite has been previously compared to the collisional 'Younger Granites' (purple), however the weaker Sr-, Ti- and Ba-depletion suggest a different melt source. Geochemical differences between the Tunkillia Suite and more typical collisional granites (i.e. Variscan and Himalayan leucogranites) further suggest a collisional-setting is inappropriate for the Tunkillia Suite. Whole-rock geochemical data after Payne et al., (2010) (Tunkillia Suite), Swain et al., (2008) (St Peters Suite), Mamami et al., (2008) (Lower Barroso Volcanics), Altherr et al., (2000) (Younger Granites), Williamson et al., (1996) (Variscan Granites), and Inger and Harris, (1993) (Himalayan Granites).

collisional I-type (At SiO_2 > 68%, ASI = 1.04 – 1.140) Younger Granites of the Northern Vosges (Altherr et al., 2000), were suggested by Payne et al., (2010) to be similar to the I-type (ASI = 0.99 – 1.09) Tunkillia Suite, and thus imply a continent-continent collisional setting. However, at SiO_2 > 68% (Altherr et al., 2000), the Younger Granites have higher Sr/Sr_N (Av. 26.29) and Ti/Ti_N (Av. 6.38) than the eastern Tunkillia Suite (Sr/Sr_N = 9.83, Ti/Ti_N = 3.85). Sr-anomalies ($Sr/Sr_N^* = Sr_N/ \sqrt{(Ce_N \times Nd_N)}$) for the Tunkillia Suite (~0.37) are more pronounced than is present in the Younger Granites (0.64), which implies a melt-source different from the one responsible for the significant Nb-Sr-Ti depletions in Tunkillia Suite. These differences are orders of magnitude different again, when comparing the Tunkillia Suite to the strongly-peraluminious granitoids which are more-typical of a collisional tectonic setting (Fig. 3.13e, f), such as the Variscan two-mica granitoids (i.e. Williamson et al., (1996)) or Himalayan leucogranite examples (e.g. Inger and Harris (1993); Zhang et al. (2004)). Instead, the closer geochemical (and isotopic) similarities between the Tunkillia Suite and felsic magmatism represented by the Barroso Volcanics of the Andean Cordillera (Fig. 3.13) suggest the Tunkillia Suite may have been generated within a continental arc-like setting. At SiO_2 > 68%, the Barroso Volcanics display the same LILE, HFSE and LREE enrichment/ depletion patterns as the eastern Tunkillia Suite (Fig. 3.13e), and when combined with isotopic constraints, indicates a comparable baseline mafic melt with similar levels of crustal hybridisation and fractionation.

3.7.5 Similarities to the 1630 – 1608 Ma St Peters Suite

A closer geochemical, temporal and isotopic correlative of the Tunkillia Suite is the 1630 – 1608 Ma St Peters Suite which has island arc-like isotopic and geochemical characteristics (Swain et al., 2008). The felsic granitoids of the St Peters Suite (SiO_2 > 68%) display trace-element characteristics equivalent to the eastern Tunkillia Suite (Fig. 3.13), including similar degrees of Ba-Nb-Sr-Ti depletions relative to primitive mantle, Eu/Eu_N^* depletions (0.25 to 0.57) and flat chondrite-normalised HREE trends (Tb_N/Yb_N = 1.22 – 1.52) all of which suggest derivation and fractionation

from a similar range of sources. These sources were interpreted by Swain et al. (2008) to be a subduction-modified mantle mixed with Archean-Early Paleoproterozoic crust of the Gawler Craton.

A compilation of Sm-Nd isotopic results from the Gawler Craton demonstrate that the magmatic sources involved in generating the 1686 – 1670 Ma eastern Tunkillia Suite are more similar to the arc-related 1630 – 1608 Ma St Peters Suite granitoids than the collisional-related granitoids of the ~1730 – 1700 Ma Kimban Orogeny (Fig. 3.14). The isotopic compositions of the Kimban-aged granites illustrate magmatic petrogenesis which primarily reworks and are dominantly-derived from, crustal isotopic reservoirs ($\varepsilon Nd_{(t)}$ = -11.7 to -0.7). In contrast, both the St Peters Suite ($\varepsilon Nd_{(t)}$ = -3.56 to +2.31) and eastern Tunkillia Suite ($\varepsilon Nd_{(t)}$ = -2.8 to +2.6) require significantly-greater contributions of mantle-derived melt to form the relatively-juvenile $\varepsilon Nd_{(t)}$ distributions. More recent Lu-Hf results reported in Reid and Payne (2017) confirm that the eastern Tunkillia Suite ($\varepsilon Hf_{(t)}$ = +0.7 to +5.9) required significant juvenile input, which contrasts against the more-evolved signatures of the Kimban-aged granitoids ($\varepsilon Hf_{(t)}$ = -20.7 to +3.6). The initial Pb-isotopic results for the eastern Tunkillia Suite presented here (i.e. Pinbong Pluton $^{238}U/^{204}Pb_{(t)}$ = 9.55, $^{232}Th/^{238}U_{(t)}$ = 3.56), yield signatures which are more in line with Proterozoic subduction-modified mantle ($^{238}U/^{204}Pb_{(t)}$ = 9.55, $^{232}Th/^{238}U_{(t)}$ = 3.56; after Ellam et al. (1990)), or mantle-crustal mixing Zartman and Haines (1988).

The Sm-Nd, Lu-Hf and geochemical phenomena observed in the eastern Tunkillia Suite are equivalent to those which were argued to represent a subduction-related setting for the St Peters Suite. This point, at the very least, suggests inconsistencies in the current collisional-tectonic classification of the Tunkillia Suite. Thus, on the basis of the isotopic and geochemical similarities between the ~1630 – 1608 Ma St Peters Suite and ~1690 – 1670 Ma Tunkillia Suite, in addition to the similarities between the Tunkillia Suite and Andean Cordillera it remains conceivable for a continental arc-like setting for the Tunkillia Suite as originally suggested by Betts and Giles (2006); Ferris (2001); Teasdale (1997).

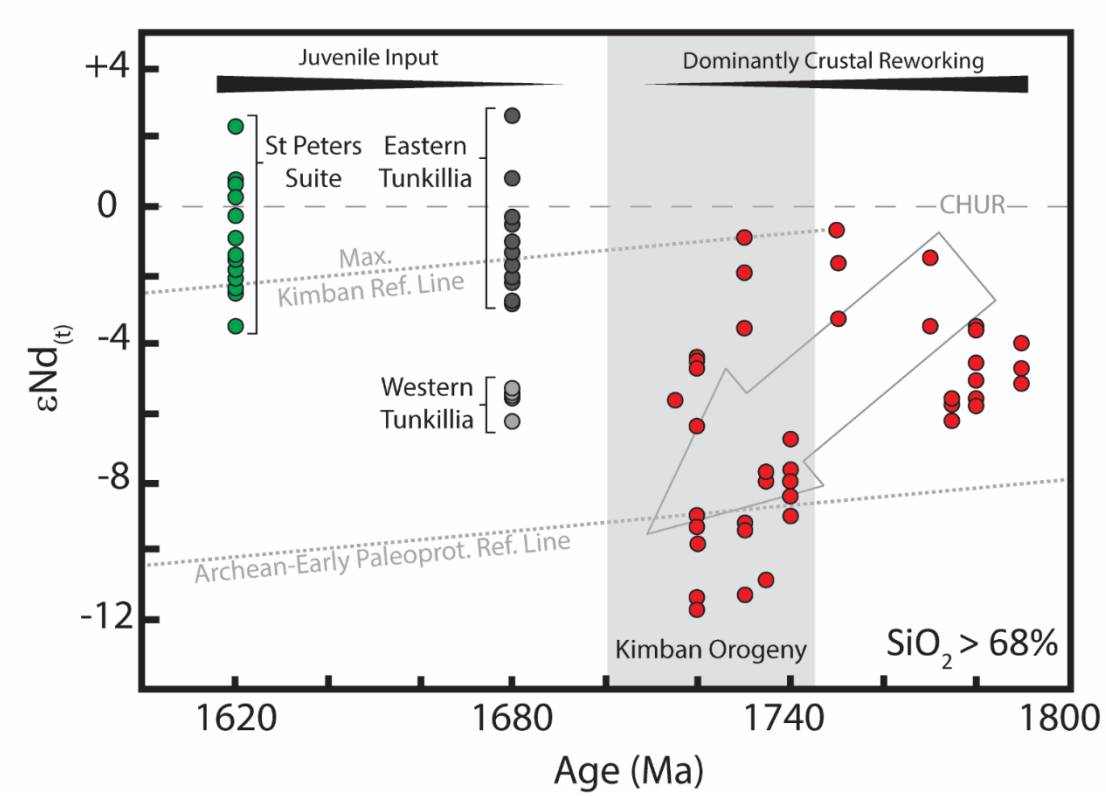

Figure 3.14: Contextual $\varepsilon Nd_{(t)}$ time-plot illustrating the isotopic dissimilarity between the granitoids related to the Kimban Orogeny, yet similarities between the eastern Tunkillia Suite and arc-related granites of the c.1620 Ma St Peters Suite. The Kimban Orogen granitoids reflect a significant period of crustal reworking, which transitions abruptly to more-juvenile signatures coinciding with emplacement of the Tunkillia Suite. 'Archean-Early Paleoproterozoic Reference Line' based on $^{147}Sm/^{144}Nd$ of 0.0652 for the 2446 Ma gneiss representative of the western Gawler Craton country rock (Payne et al., 2008). 'Maximum Kimban Reference Line' based on $^{147}Sm/^{144}Nd$ of the Middlecamp granite (0.0931; Stewart, (1994)), which is the most isotopically-juvenile example of the granitoids related to the Kimban Orogeny. Compilation of data from Budd and Skirrow, (2007), Budd, (2006), Chalmers, (2009), Dove, (1997), Fraser et al., (2010), Goodwin, (2010), Hopper, (2001), Howard et al., (2011), Knight, (1997), McAvaney et al., (2016), Neumann, (2001), Payne et al., (2010), Stewart, (1994), Swain et al., (2008), Szpunar and Fraser, (2010), Szpunar et al., (2011), Turner et al. (1993).

3.8 Conclusion

LA-ICP-MS Pb-isotopic analyses of alkali feldspars have clearly defined two, spatially-distinct Pb-isotopic signatures in the ~1690 - 1670 Ma Tunkillia Suite. These range from unradiogenic in the western Tunkillia Suite, to relatively-normal and accelerated in the eastern Tunkillia Suite. While these values may superficially mirror the previously published Sm-Nd isotopic results, they also provide a crucial constraint on the nature of the crustal component, particularly within the western Tunkillia Suite. Unradiogenic Pb-isotopic signatures, such as those inherited by the western Tunkillia Suite, are a globally-rare phenomenon which invoke a long-term, U-depleted granulitic crustal

component. High Y/Yb and depleted-HREE indicating the presence of garnet in the crustal source support the inference from Pb-isotopic evidence for a significant granulitic crustal component. Such anhydrous, U-depleted granulitic reservoirs are among the least melt-fertile crustal reservoirs from which to derive a biotite-fluxed partial melt, as is the typical petrogenesis of continent-continent collisional granitoids. Comparison with occurrences elsewhere in the world, such as the Central Volcanic Zone of the Andean Cordillera, suggest that inheritance of the anhydrous-granulitic Pb-isotopic signature requires addition of mantle-derived melt (low-Pb concentration, juvenile Nd-isotopic signature) as is the dominant thermal and chemical driver for magmatism within a supra-subduction setting.

By contrast, the eastern Tunkillia suite contains Pb-isotopic source signatures characterised by lower-$^{232}Th/^{238}U_{(t)}$, and $^{238}U/^{204}Pb_{(t)}$ consistent with magmas generated by extensive crust-mantle hybridisation. This is supported by relatively-juvenile $\varepsilon Nd_{(t)}$ which indicate some mantle contribution to a crustal component significantly different to that of the western Tunkillia Suite. These isotopic signatures are consistent with characteristics of the Southern Volcanic Zone of the Andean Cordillera, yet contrast with signatures typical of collisional granites such as those of the Variscan Orogeny or Himalayas which display higher $^{232}Th/^{238}U_{(t)}$, $^{238}U/^{204}Pb_{(t)}$ and more-radiogenic Nd-isotopic signatures. A collisional setting was suggested for the Tunkillia based on elevated Ta, presumed to be derived from biotite-dehydration melting, but such a mechanism is inconsistent with the western Tunkillia Suite where only low-Ta is observed, and isotopic evidence which suggests a biotite-poor

(granulitic) crustal component. In addition, higher-Ta values are observed in felsic members of the Lower Barroso Volcanics of the Andean Cordillera which demonstrates the geochemical diversity of magmas generated at a continental arc. The range of geochemical compositional between the eastern and western Tunkillia Suite are therefore taken to reflect innate variations in the crustal component, rather than an indicative of a crustal-dominant petrogenesis. Both the eastern and western Tunkillia Suite show strong depletions is Nb, Sr and Ti relative to primitive mantle, which is

a common feature of arc-related magmatism. These geochemical characteristics are also shared with granitoids of the 1630 – 1608 Ma St Peters Suite from the Gawler Craton which have been previously characterised as arc-related. Furthermore, the isotopic similarity of the eastern Tunkillia Suite with the St Peters Suite, contrasted against the isotopically-distinct ~1730 – 1700 Ma Kimban Orogeny granitoids, argue for a closer genetic link to the St Peters Suite.

Given the geochemical and isotopic similarities of the Tunkillia Suite with continental arc-related magmas of the Andean Cordillera and St Peters Suite, it is argued that the characterisation of the Tunkillia Suite as a collisional granite suite be reconsidered in favour of an continental arc-derived or supra-subduction-related setting.

Acknowledgements

BHP Olympic Dam are thanked for financial support. Sandrin Feig and Karsten Gormann from the Central Science Laboratory, University of Tasmania, and Paul Olin and Jay Thompson from the CODES LA-ICP-MS laboratory are gratefully thanked for their technical assistance. Alexander Cherry, Mathew Ferguson and Sasha Stepanov are thanked for critical discussions. Martin Hand (U.Adel.) and the staff of the GSSA Core Library are thanked for access to samples. Tony Hill and Michael Anderson from Euro Exploration Services are thanked for their assistance with sample acquisition.

Chapter 4: Pb-isotopic constraints on the source of A-type Suites: Insights from the Hiltaba Suite - Gawler Range Volcanics Magmatic Event, Gawler Craton, South Australia

Chapman, N. D.[1], Ferguson, M.[1], Meffre, S. J.[1], Stepanov, A.[1], Maas, R.[2], Ehrig, K. J.[3]

[1]Department of Earth Sciences, University of Tasmania, Hobart, TAS, Australia
[2]School of Earth Sciences, University of Melbourne, Melbourne, VIC, Australia
[3]BHP Olympic Dam Operations, Adelaide, SA, Australia

Keywords: Pb-isotopes; A-type; petrology; Gawler Craton; Hiltaba

4.1 Abstract

The 1595-1575 Ma Hiltaba Suite intrusives and coeval Gawler Range Volcanics (GRV) represent a significant crustal component of the Mesoarchean-Mesoproterozoic Gawler Craton, South Australia, and one of the largest silicic igneous provinces in the world. They are also spatially and temporally-affiliated with world-class IOCG mineral deposits (i.e. Olympic Dam) thus making an understanding of these rocks important both economically, and petrologically. Here, we present the results of 177 in situ Pb-isotopic analyses of alkali feldspar in the Hiltaba Suite/ GRV, which when integrated with existing Sm-Nd isotopic and geochemical data, reveal a craton-wide isotopic zoning. Pb-isotopic zonation is controlled by the varying interaction of a parental melt derived from a sub-continental lithospheric mantle (SCLM)-like enriched mantle reservoir ($^{238}U/^{204}Pb \leq 9.4$, $^{232}Th/^{238}U \leq 3.66$) and twocrustal end-member reservoirs: an unradiogenic reservoir ($^{207}Pb/^{206}Pb \geq 0.97$, $^{208}Pb/^{204}Pb \geq 35.7$) and a radiogenic reservoir ($^{238}U/^{204}Pb \geq 10$, $^{232}Th/^{238}U \geq 3.95$). The SCLM-like reservoir exerts a strong control on Pb-isotopic compositions around the central-western Gawler Craton (Nuyts Terrane), while the unradiogenic reservoir which represents granulitic lower crust, appears to be spatially limited to the northwest of the Gawler Craton. The radiogenic reservoir, coincident with the IOCG province and probably represented by monazite-rich metasediments, is more prevalent in the eastern Gawler Craton. Correlation between melt-source $^{238}U/^{204}Pb_{(t)}$ and $^{232}Th/^{238}U_{(t)}$, with LREE (i.e.

La, Ce etc) and HFSE (Zr, Nb etc) which are characteristically enriched in A-type magmas, suggest the importance of hybridisation between a crustal melt component and enriched-mantle melt component in the formation of A-type magmas.

The isotopic and geochemical compositions of the ~1592 Ma Lower GRV and ~1588 Ma Upper GRV effectively bracket the Hiltaba Suite intrusive rocks, and thus provide an avenue for investigating the temporal Pb-isotopic development of a representative part of the Hiltaba Suite/ GRV magmatic systems. The Pb-isotopic characteristics imply that either Lower and Upper GRV magma systems developed independently, or reflect a magmatic system evolving substantially over a ~2 Ma period, dominated by mafic input at first (3 to 8% crustal melt; Lower GRV) and moving towards homogeneous, crustal, isotopic compositions with increased crustal melt proportions (15 to 20%) in the Upper GRV.

The consistency of these melt source constraints - isotopically, geochemically and proportionally - with other A-type suites around the world favours a unified petrogenetic model for A-types involving dominantly mantle-derived melts, with varying proportions of crustal material which impart characteristically LREE-HFSE enriched geochemical signatures.

4.2 Introduction

The melt sources involved in the petrogenesis of A-type, or ferroan (Frost et al., 2001) granitoids, are among the least-understood of all igneous rocks. They contain a number of geochemical and isotopic characteristics which suggests both mantle-derived and crustal-derived melts are important in magmagenesis. The relative enrichment of large-ion-lithophile (i.e. K, Rb, Sr), high-field-strength (i.e. Nb, Ta, Zr) and light rare-earth elements (i.e. La, Ce) in A-type granites all advocate for the importance of crustal-melt contributions. However the prevalence of high-temperature, anhydrous mineral assemblages (i.e. fayalite + pyroxene) in many A-type felsic volcanics (Allen and McPhie, 2002; Stewart, 1994) and granitoids (Anderson et al., 2003), coupled with the common-association

with tholeiitic anorthosite-gabbros strongly implicates a comagmatic role for mantle-derived melts in A-type petrogenesis.

Radiogenic isotopic compositions provide the clearest evidence for the diverse role and proportions of both crustal- and mantle-derived melts in forming A-type granites. Unlike major- and trace-element compositions, radiogenic isotopic signatures are not affected by magmatic processes (such as crystal fractionation) and thus only reflect the melt sources involved in magmagenesis. The relatively-juvenile isotopic signatures of 1.43 Ga A-type granitoids from the North American Grenvillian Terrane which indicate the major influence of mantle-derived melts, contrasts with the more-evolved, crustal, isotopic signatures present in the 1.54-1.56 Ga A-type granitoids of the Karelian and Fennoscandian Province of Finland and surrounds. Crustal contamination/ hybridisation is a significant feature of mantle-derived rocks associated with A-type granites, and can obscure the isotopic signature of the parental melt. For example, mantle-derived anorthosites emplaced contemporaneously with A-type granites of both the Grenvillian and Fennoscandian terranes yield isotopic compositions indistinguishable from the A-type granites, yet more-radiogenic than depleted mantle models would suggest (Anderson et al., 2003; Heinonen et al., 2010). A further layer of complexity is added by innate variations in the age and geochemistry of the crustal-melt component, which can modify isotopic signatures to varying degrees. Regional-scale variations are seen in the isotopic signatures of the A-type rapakivi granites from across the Fennoscandian terrane (Andersson et al., 2002; Heinonen et al., 2010; Rämö, 1991) and into the Karelian terrane (Neymark et al., 1994) which demonstrate a clear change in the crustal signature. It is therefore crucial that regional isotopic context be considered before defining the relative importance of crustal- and mantle-derived melt proportions.

The 1595 – 1575 Ma Hiltaba Suite granites and coeval Gawler Range Volcanics (GRV) provide an ideal case through which to investigate the various melt-sources involved in the generation of A-type magmas. The regionally-extensive coverage of the Hiltaba Suite granites means that a range of possible crustal isotopic reservoirs can be identified, while the well-constrained stratigraphy of the

GRV provides an insight into the isotopic evolution of parental melts which produce A-type magmas. Early authors (Creaser, 1996; Giles, 1988; Kilpatrick and Ellis, 1992) suggested a dominantly crustal-derived melt contribution from high-grade metamorphic rocks which argued against significant proportions of mafic magma contribution on the basis of absent hornblende and geochemical similarities with charnockites. In contrast, more recent work (Budd, 2006; Stewart, 1994; Stewart and Foden, 2003) indicates significant contributions of mafic magma (up to 70 vol. %; Stewart and Foden (2003)), with relatively-unevolved $\varepsilon Nd_{(1585Ma)}$ suggesting majority-proportions of Archean-Early Paleoproterozoic crustal-melt contributions are not possible. Clearly, the melt-sources and proportions involved in forming the Hiltaba Suite/ GRV are unresolved.

Here, we have investigated the regional variations in the Pb-isotopic composition of K-feldspars from the Hiltaba Suite and coeval GRV using in situ laser ablation inductively-coupled mass spectrometry (LA-ICP-MS). In K-feldspar, Pb is incorporated into the crystal structure while U and Th are excluded, therefore retaining the Pb-isotopic signature of the magma sources. In situ techniques such are laser ablation provide a high-level of spatial resolution, which is critical in targeting only the most pristine domains of K-feldspar, thus ensuring the integrity of Pb-isotopic results. Existing isotopic and geochemical results for the Hiltaba/ GRV are collated with Pb-isotopic results presented here which provides a more comprehensive insight into the melt-sources involved in the formation the Hiltaba Suite/ GRV and A-type petrogenesis more broadly.

4.3 Geological background

The Hiltaba Suite and Gawler Range Volcanics (GRV) represent one of the most voluminous silicic large igneous provinces in the world, with an estimated volume in excess of 100 000 km^3 (Jagodzinski et al., 2016). The Gawler Range Volcanics (GRV) are divided into two sub-suites, with the basaltic to rhyolitic Lower Gawler Range Volcanics (LGRV), significantly less-voluminous (<530 km^3; Agangi, 2011) than the homogeneous, dacitic Upper Gawler Range Volcanic (UGRV) which comprises

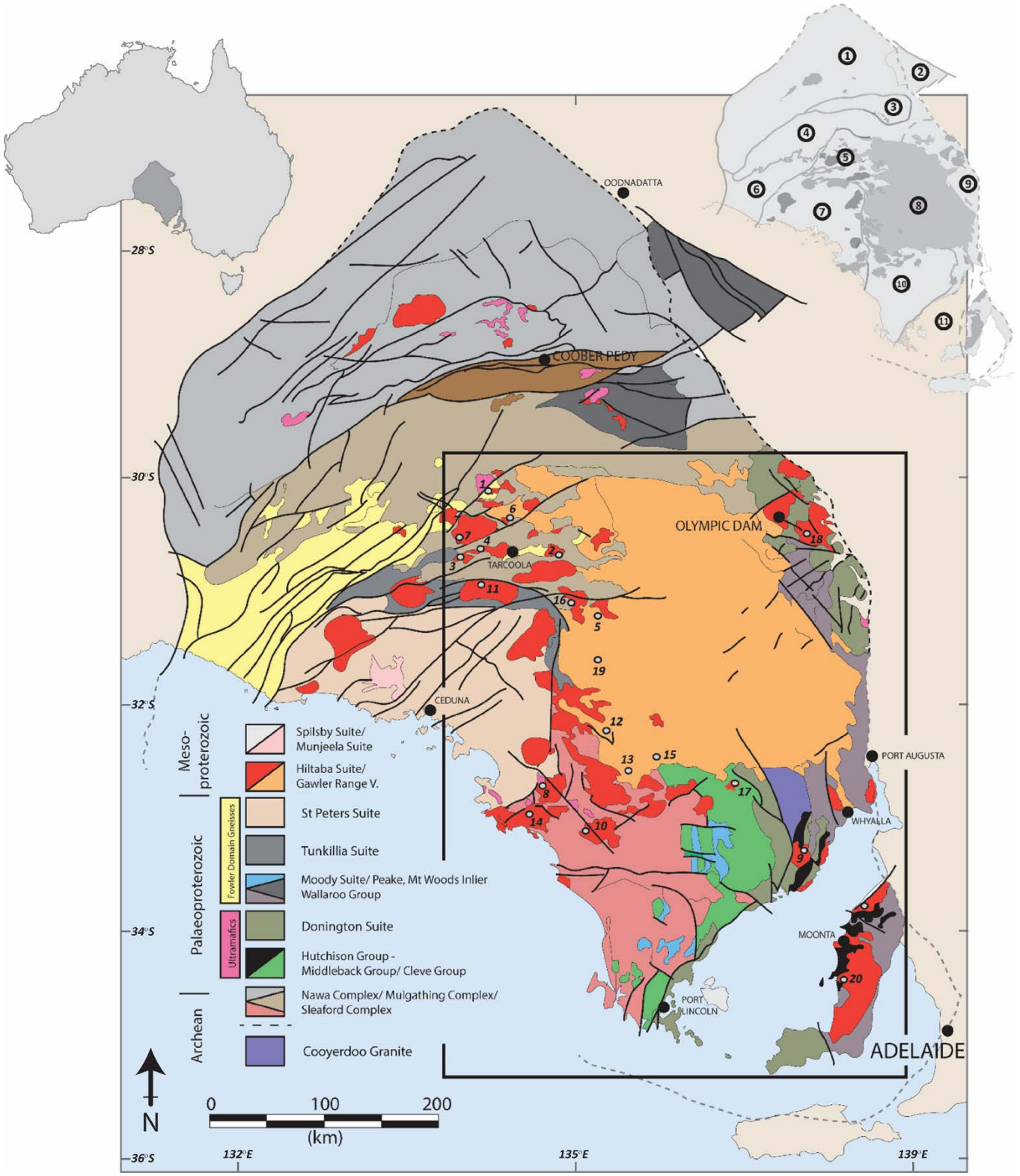

Figure 4.1: Regional geology of the Gawler Craton, with major igneous suites shown in bottom left. Large box outlines the region of focus. Samples of Hiltaba Suite (red) and Gawler Range Volcanics (orange) are shown, and numbered according to display in Table 4.2. Inset (top right) shows the major litho-tectonic terranes comprising the Gawler Craton (nomenclature after Ferris et al., (2002)); 1) Nawa Domain, 2) Peake and Denison Inlier, 3) Mount Woods Inlier/ Coober Pedy Ridge, 4) Christie Domain, 5) Wilgena Domain/ Harris Greenstone Belt, 6) Fowler Domain, 7) Nuyts Domain, 8) Gawler Range Volcanics, 9) Olympic Domain, 10) Spencer Domain, 11) Coulta + Cleve Domain. Sample numbers link with data in Table 4.2, and are extended to all following diagrams.

4200 km^3 (Allen et al., 2003). Recent high-precision CA-TIMS U-Pb zircon geochronology suggests the Upper (1587.5 – 1587.2 Ma) and Lower GRV (1591.2 – 1587.7 Ma) are separated by less than ~2 Ma age difference (Jagodzinski et al., 2016). The Hiltaba Suite granitoids have a broader distribution of crystallisation ages ranging from 1593 ± 0.21 Ma for the Roxby Downs Granite (Cherry et al., 2018) in the north-eastern Gawler Craton (Fig. 4.1), to 1577 ± 7 Ma for the Tickera Granite in the south-east of the Gawler Craton (Fig. 4.1) (Fanning et al., 2007). The Hiltaba Suite granites intrude all major lithotectonic domains of the Gawler Craton (Fig. 4.1), however are most prevalent through the central and eastern Gawler Craton (Fig. 4.1). Geochemically, all are high-K, ferroan granites (Frost et al., 2001), oxidised (magnetite-bearing) to strongly oxidised (hematite-bearing), A-type in character (Creaser et al., 1991), and anomalous in F, LILE, REE and the HFSE-group ((Budd, 2006; Giles, 1988; Stewart, 1994; Stewart and Foden, 2003). Two-pyroxene geothermometry presented by Creaser (1991) and zircon saturation temperatures by Agangi et al. (2011) coupled with the aforementioned geochemical characteristics suggest a genesis involving high-temperature partial melting of dry (<2 wt. % H_2O), lower crustal material (Creaser, 1996; Giles, 1988; Kilpatrick and Ellis, 1992; Stewart, 1994).

The age of the Gawler Craton basement, through which the Hiltaba Suite plutons have intruded, range from Mesoarchean to late Paleoproterozoic (Fig. 4.1). Isostatic equilibrium was reached at high-levels in the crust as suggested by common rapakivi textures in the Hiltaba Suite granites and emplacement of Hiltaba pluton within their extrusive equivalents, the Gawler Range Volcanics. In the western two-thirds of the Gawler Craton, Hiltaba Suite plutons intrude through felsic orthogneisses and ultramafics of the Archean-Early Paleoproterozoic Mulgathing and Sleaford Complexes (Fig. 4.1) which were metamorphosed to amphibolite-granulite facies during the ~2480 Ma Sleafordian Orogeny and ~1730 Ma Kimban Orogeny. In the eastern Gawler Craton, Hiltaba Suite granites are predominantly emplaced within c.1850 Donington Suite granitoids, and c.1740 Ma volcano-sedimentary sequences of the Wallaroo Group in the Eastern Gawler 'Olympic Domain' (Fig. 4.1).

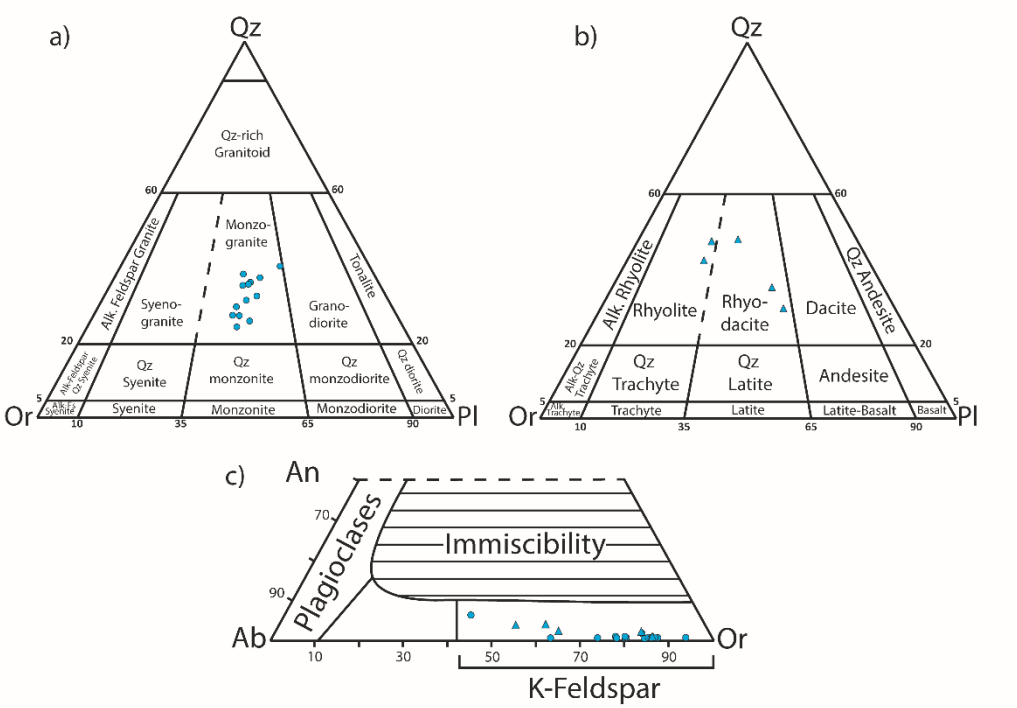

Figure 4.2: Quartz-Alkali Feldspar-Plagioclase (QAP) diagram showing the normative mineral composition of the (a) Hiltaba Suite granitoids and (b) Gawler Range Volcanics samples referred to henceforth. SiO2 is in the range 65-77 wt.%. (c) The feldspar ternary diagram showing a range of alkali-feldspars analysed in this study. Most alkali-feldspar from intrusive Hiltaba Suite samples (circles) fall in the range Or_{75-85} while many GRV samples (triangles) extend further towards the peristeritic gap (Or_{55-85}).

Temporally, the Hiltaba Suite/ GRV event follows the emplacement of the c.1690 – 1670 Ma Tunkillia Suite and 1630 – 1608 Ma St Peter Suite. A subduction-related setting of these igneous suites (Swain et al., 2008) places the formation of the Hiltaba Suite/ GRV within an intra-continental back-arc type setting, with NE/SW compression and oblique transpression (Hand et al., 2007). Further afield, the Hiltaba Suite/ GRV has been linked with similar-aged intrusives and extrusives of the Curnamona Province (1588.2 – 1587.3 Ma Benagerie Volcanics; Wade et al. (2012)), and volcanics from the Terre Adélie Craton of Antarctica (Peucat et al., 2002).Minimal, low-PT, epi-orogenic deformation has affected the Hiltaba Suite/ GRV, indicates that stabilisation of the Gawler Craton occurred soon after Hiltaba granite emplacement . The absence of deformation in the Hiltaba Suite largely precludes Pb-isotopic resetting via recrystallisation.

4.4 Sample sources, description and preparation

Samples used in this study (Fig. 4.1) were obtained from existing collections which have previous geochronological, geochemical and Sm-Nd isotopic data already available (see Table 4.1). Sample locations cover a wide area of the Gawler Craton, and represent Hiltaba Suite granites from most of the major lithostratigraphic domains of the Gawler Craton (inset, Fig. 4.1). In the absence of formal names for the individual plutons of the Hiltaba Suite, nomenclature has been adopted after Stewart and Foden (2003) and Budd (2006) which use the names of the localities from which they were obtained (Table 4.1). Whole-rock major- and trace-element geochemistry, U-Pb geochronology and Sm-Nd isotopic data used in this study are collated from their respective authors (Appendix D). Where used, $\varepsilon_{Nd(t)}$ data is calculated at t = 1590 Ma using the C1 chondrite isotopic composition of Bouvier et al. (2008) ($^{143}Nd/^{144}Nd = 0.512630$).

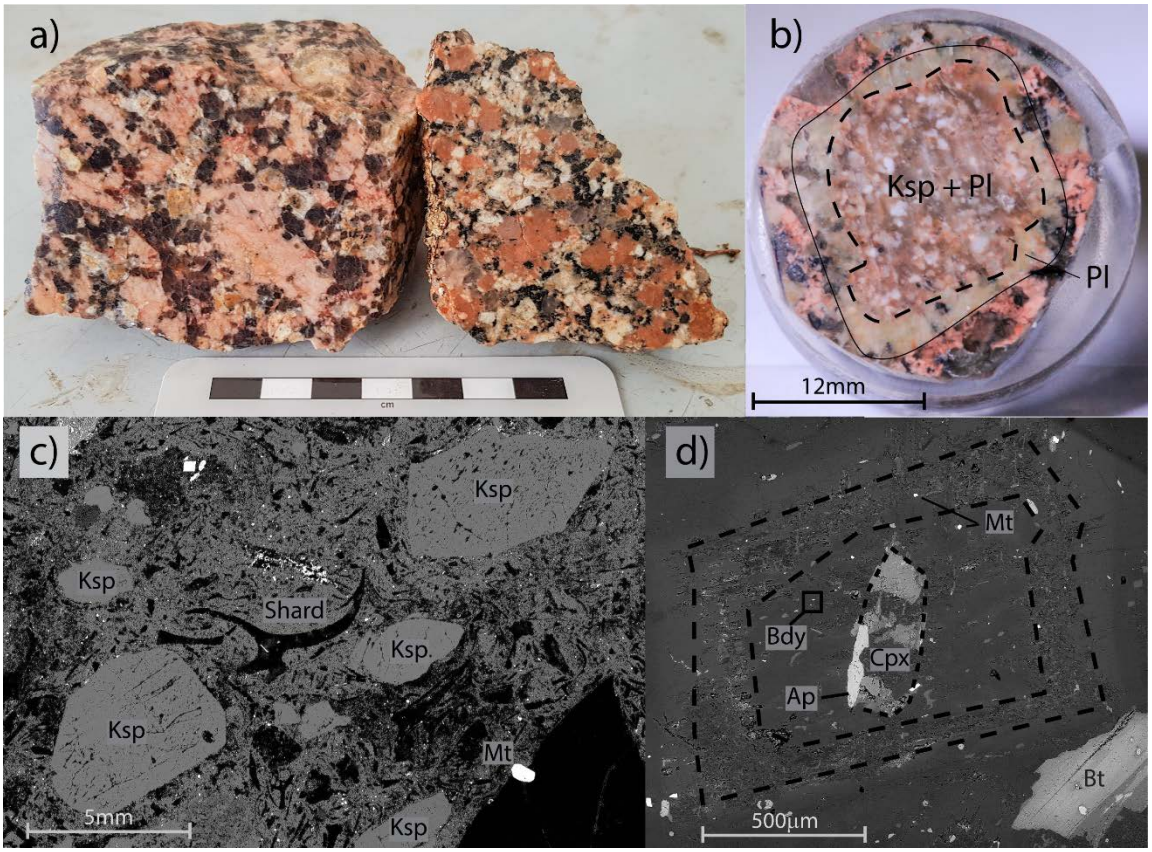

Figure 4.3: Macro- and microscopic characteristics of the Hiltaba Suite. (a) Hiltaba Suite granitoid samples (left: 'Pinbong', right: 'Parla') (b) Plagioclase-mantled K-feldspar (rapakivi texture) of the Charleston Granite (Hiltaba Suite) (c) Backscattered electron microscope (BSE) image of tuffaceous quartz-feldspar-phyric Lake Gairdner Rhyolite (Lower GRV) containing abundant glass shards. (d) Zoned plagioclases from the Pegler Granite containing cumulate-like cores of clinopyroxene (cpx), apatite (Ap), magnetite (Mt) and baddeleyite (Bdy).

Based on normative mineralogy, all intrusive samples fall within the monzogranite field on the Streckeisen diagram (Fig. 4.2), with only the volcanics showing strongly K-feldspar (Or) – quartz (Qz)/ plagioclase (Pl) deviations (rhyodacite to rhyolite). Samples of the Gawler Range Volcanics analysed here are variably hypocrystalline, feldspar-(quartz)-phyric lavas with microlitic feldspar (Eucarro Rhyolite, Yardea Dacite and Yantea Rhyolite). One sample of quartz-feldspar-phyric Lake Gairdner Rhyolite is more tuffaceous in nature, containing abundant glass shards (Fig. 4.3). The Hiltaba Suite granite samples are all coarse-grained with commonly large (~4 cm) porphyritic K-feldspar crystals present in addition to smaller, K-feldspar phenocrysts (~1 cm). The Hiltaba Suite commonly display rapakivi textures (plagioclase mantles surrounding K-feldspar crystals) including wyborgitic textures (ovoid to sub-rounded K-feldspars phenocrysts mantled by plagioclase: Fig. 4.3)). Both plagioclase and K-feldspar crystals are often zoned, indicating growth in an evolving magma system. Rare examples exist of zoned plagioclase phenocrysts containing cumulate-like clusters of clinopyroxene-apatite-magnetite-baddelyite (Fig. 4.3) at the core, which has been suggested to indicate the involvement of a mafic magma component in other A-type granitoids (Scoates and Chamberlain, 1995). Colour in hand specimen suggests variable oxidation states with red, high-Fe_2O_3 K-feldspars contrasting with pink, low-Fe_2O_3 K-feldspars (Fig. 4.3). Non-perthitic domains within the K-feldspar samples were targeted for LA-ICP-MS, so as to avoid any possibility of isotopic resetting which may occur during perthitic-unmixing which may post-date granite crystallisation (Fig. 4.4). K-feldspars analysed in this study form a compositional range from Or_{46} to Or_{94} (Fig. 4.2c). Plagioclases are slightly turbid, exhibiting only weak, patchy sericite-dusting, and were not analysed in this study.

Biotite and magnetite are the two most common, primary ferromagnesian minerals present in Hiltaba Suite granites. Hornblende (± biotite) is rare and only observed in one sample of the Hiltaba Suite (Pegler Granite), which also has a relatively-low SiO_2 content (67.9 wt. %). Clinopyroxene is present in all Upper GRV samples. Biotite is only scarcely chloritised and together with the preservation of plagioclase indicate that the samples analysed here are minimally-altered.

Twenty-five mm epoxy mounts were prepared for rock samples and hand-separated alkali

feldspar crystals. Mount surfaces were then polished to 0.01 µm-diamond grade, cleaned using ethanol, washed in an ultrasonic bath of de-ionised water for 20 minutes, oven-dried at 60°C for 30 mins and then carbon-coated. Mineral purity and textural relationships were investigated on both a FEI MLA 650 ESEM and Hitachi SU-70 field-emission SEM housed at the Central Science Laboratory, University of Tasmania, using a 15 kV accelerating voltage, beam current of 5 nA and imaging parameters optimised for the mean-atomic weight of alkali feldspar.

4.5 Analytical Procedures

In situ Pb-isotope and trace-element compositions were determined using LA-ICP-MS. The Agilent 7900 ICP-MS was coupled to a Coherent COMPex Pro 193 nm ArF Excimer laser system equipped with a Laurin Technic RESOlution S155 cell. Ablation was carried out in a He-Ar (3:1) atmosphere, with nitrogen added at 3.5 mL/s to improve sensitivity (i.e. Crowe et al. (2003)). An inline smoothing device ("SQUID"; Müller et al. (2009)) and particle-separator (Guillong et al., 2003) were added to improve signal-stability and mitigate signal spikes. A spot-size of 110 µm provided a high-^{204}Pb count-rate and a sufficiently-high spatial resolution which allowed for the avoidance of mineral intergrowths (i.e. perthitic exsolution), fractures in the feldspar and mineral inclusions. A linear transect geometry was selected to mitigate down-hole signal drop-off, with a raster rate of 5 µm/s. Transect lines were pre-ablated to remove any potential surface contamination. Data collection was conducted over 110 seconds per sample with 20 seconds of background measurements and 90 seconds of laser-on measurements (Fig. 4.4). Short dwell-times and a short element list were used to offset the effects of the non-simultaneous detection of the Pb isotopes on the quadrupole mass spectrometer. ^{39}K, ^{43}Ca, ^{23}Na and ^{137}Ba were counted for 5 ms each to confirm alkali feldspar was being ablated. In some samples where inclusions were numerous ^{24}Mg, ^{27}Al, ^{29}Si, ^{31}P, ^{47}Ti, ^{56}Fe were also analysed for 5 ms to help with rejection of spurious data caused by inadvertent ablation of other mineral phases which may compromise Pb-isotopic data. ^{206}Pb, ^{207}Pb, ^{208}Pb, ^{232}Th and ^{238}U

were counted for 10 ms while ^{202}Hg and ^{204}Pb for 20 ms giving a total quadrupole cycle time of 180 ms and 600-1000 measurements of each isotope during the 90 second ablation period.

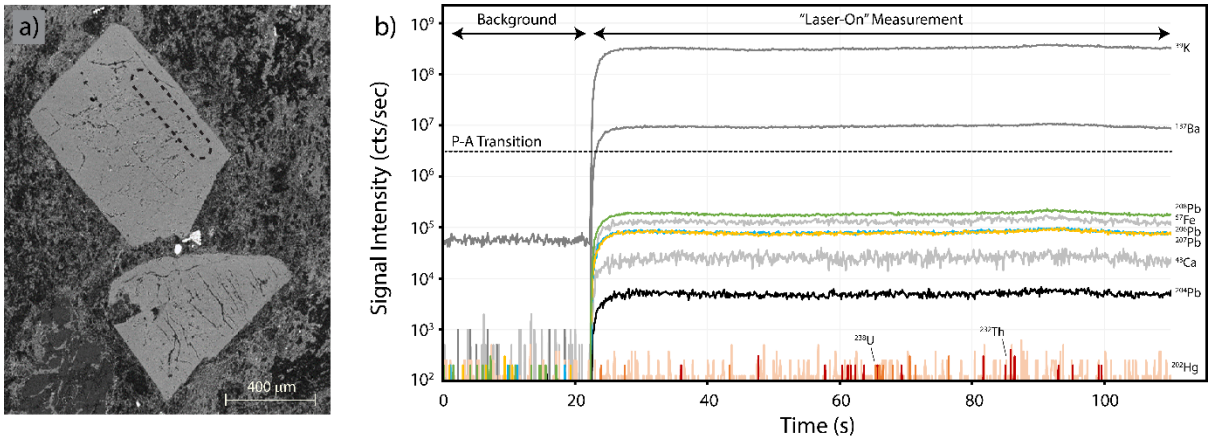

Figure 4.4: (a) BSE image of typical alkali feldspar phenocryst within the Lake Gairdner Rhyolite (Lower Gawler Range Volcanics) and (b) the LA-ICP-MS time-resolved spectra obtained from alkali feldspar shown, with some typical feldspar related masses being measured (note low-^{202}Hg).

Reproducibility and instrument drift corrections were achieved using standard bracketing procedures. NIST610 was the primary standard, with GSD-1G and BCR-2G flux-free glasses used as secondary standards. Analytical uncertainty on NIST610 (n = 24) over a typical session was less than 0.12% for all ratios (range: 0.116%-0.068%). Data reduction was conducted offline using in-house spreadsheets. ^{204}Hg isobaric interference corrections were employed using a ^{204}Hg:^{202}Hg ratio of 4.32 and the background/ peak-stripping method of Willigers et al. (2002). The total interference caused by ^{204}Hg/^{204}Pb amounted to an average correction of 0.025%. Data for each sample were calculated to a single weighted mean with respect to internal uncertainties using Isoplot v.4.15 (Ludwig, 2012). Average mean square weighted deviations for alkali feldspar from Hiltaba Suite samples were 2.21 (0.18 – 6.55). Where Pb-isotopic analyses were demonstrably affected by ^{238}U, ^{232}Th-bearing inclusions, or variation in Na-Fe-Ca-Ba indicated non-representativeness of alkali-feldspar samples, analyses were rejected. This amounted to a rejection rate of less than 9%. Error correlation between ^{206}Pb/^{204}Pb, ^{207}Pb/^{204}Pb and ^{208}Pb/^{204}Pb was calculated to be 0.8 based on repeat analyses of the NIST 610 standard.

Time-integrated, melt-source reservoir parameters (^{238}U/^{204}Pb$_{(t)}$ (μ) and ^{232}Th/^{238}U$_{(t)}$ (κ)), are

calculated using the second-stage model of Stacey and Kramers (1975), following the equation; $\mu = \frac{t_1}{t_0+(e^{\lambda.t_0}-e^{\lambda.t_1})}$, where t_1 is the Pb-isotopic ratio at crust-mantle differentiation (3700 Ma), t_0 is the Pb-isotopic ratio determined from alkali feldspar fixed at the most accurate U-Pb geochronological age, and λ is the decay constant of the U, or Th parental isotope. Unlike Pb-isotopic ratios, these growth parameters are not affected by age and allow for comparison of the data generated here, with A-type igneous suites of different ages, from around the world.

4.5.1 U-Pb geochronology

While geochronology data (U-Pb, Sm-Nd, Rb-Sr) already exists for most Hiltaba Suite samples studied here (see Table 4.1 for references), zircon U-Pb was re-evaluated to confirm the ~1590 Ma age of the Bulpara Granite which yielded anomalously 'old' model Pb-Pb ages. Samples were ring-milled to sand-sized particles and panned to produce a heavy mineral concentrate, from which the magnetic fraction was removed and the remaining zircon grains hand-picked under microscope. Zircon grains were mounted as 25 mm epoxy resin disks and polished to 0.1 µm diamond grade. U-Pb analysis was conducted using LA-ICP-MS at the University of Tasmania on the same apparatus described above for initial Pb-isotopes using a spot size of 29 µm, with a 5 Hz repetition rate and 2 mJ/cm^2 fluence. An inline smoothing device ('SQUID'; Mueller et al, 2009) was employed to reduced signal spikes and N_2 added to the carrier gas to improve sensitivity. The 91500 zircon (Wiedenbeck et al., 1995) used as a primary standard to correct for U-Pb downhole fractionation, while NIST610 (Baker et al., 2004) was used for Pb-isotopic U-Pb mass bias and instrument drift corrections. Temora (Black et al., 2003) and Plesovice zircons (Sláma et al., 2008) were selected as secondary standards. Corrections and data reduction were performed offline using in-house spreadsheet macros. No analyses were rejected.

Potential for inheritance and zonation was investigated post-analysis using a Gatan ChromaCL2 polychromatic cathodoluminence detector attached to a Hitachi SU-70 field-emission SEM using an acceleration voltage of 20 kV and beam current of 22 uA to compensate for decreased

resolution. No indications of potential inheritance (i.e. resorbed xenocrystic cores) were encountered (see Appendix G).

4.6 Results

The results of LA-ICP-MS Pb-isotopic analyses on SRMs are shown in Table 4.2 as well as Appendix E. All results are within 2σ uncertainty of recommended values for SRM's (Table 4.2) and demonstrate the accuracy of the method utilised here. Although no matrix-related effects have been observed in LA-ICP-MS Pb-isotopic analysis between glass SRM's and feldspars (i.e. Souders and Sylvester (2010)), external reproducibility is confirmed in the Charleston Granite (southern Gawler Craton) alkali feldspar samples (Fig. 4.5), which for all three samples, are within 2σ uncertainty of the solution-based ID-ICP-MS results of Neumann (2001). The potential for differences in Pb-isotopic signature between rapakivi-textured, porphyritic and phenocrystic K-feldspars was also tested using the three Charleston Granite samples which had difference K-feldspar size and texture distributions (Fig. 4.5). All three results are within 2σ analytical uncertainty of each other (Fig. 4.5) indicating no difference between porphyritic,

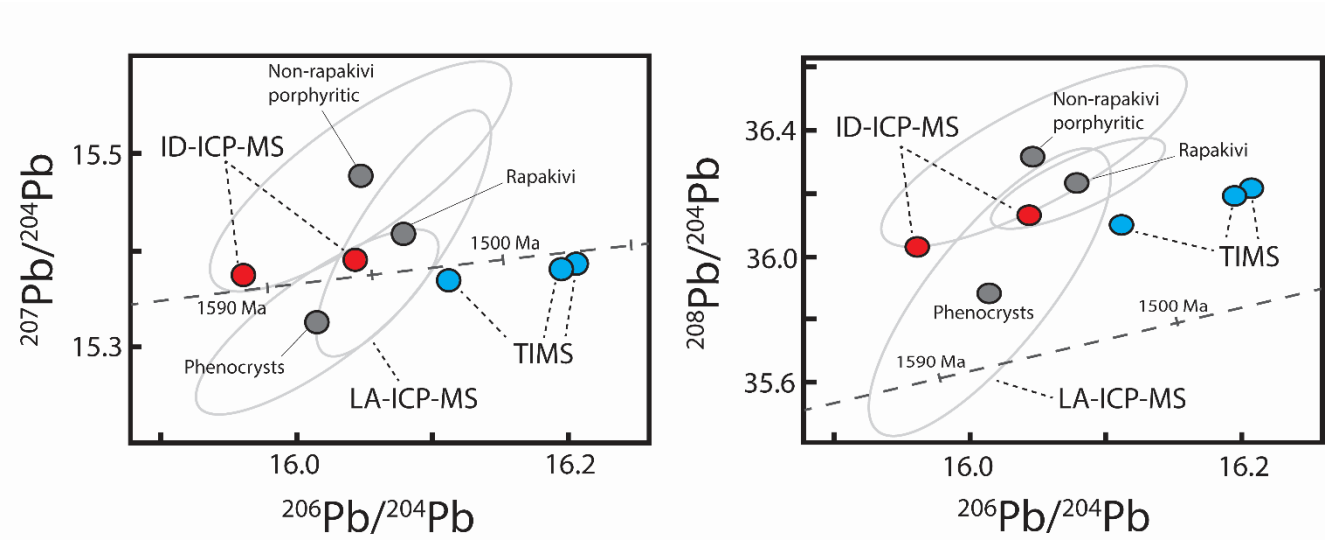

Figure 4.5: Pb-isotope plots showing the comparable results of the Charleston Granite using both in situ LA-ICP-MS (grey: presented here), and dissolution-based techniques such as isotope dilution on both a high-resolution ICP-MS (red: "ID-ICPMS") and thermal ionisation mass spectrometer (blue: "TIMS"). Error ellipses represent 2σ uncertainty of three different samples approximately 7 km apart, with different feldspar sizes and textures. ID-ICP-MS results from Neumann, (2001). TIMS results from Dean, (1994, unpublished) presented in Roache, (1996).

Table 4.1: LA-ICP-MS Pb-isotopic results of Hiltaba Suite and Gawler Range Volcanics alkali-feldspar, with U-Th-Pb and $\varepsilon Nd_{(1590Ma)}$ from previous workers.

Number	Pluton/ Strat. Name (informal)	Age (Ma)	UTM Zone	UTM mE	UTM mN	U (ppm)	Th (ppm)	Pb (ppm)	$\varepsilon Nd_{(1590Ma)}$	$^{238}U/^{204}Pb$	±2σ	$^{232}Th/^{238}U$	±2σ	$^{207}Pb/^{206}Pb$	±2σ	$^{208}Pb/^{206}Pb$	±2σ	$^{206}Pb/^{204}Pb$	±2σ	$^{207}Pb/^{204}Pb$	±2σ	$^{208}Pb/^{204}Pb$	±2σ
1	Pegler	1591.7 ± 5.8 [1]	53J	428366	6659598	3.95 [1]	22.2 [1]	22.4 [1]	-3.05 [1]	10.10	0.27	4.17	0.055	0.980	0.002	2.278	0.002	15.698	0.034	15.362	0.044	35.736	0.084
2	Bulpara	1590	53J	490198	6591582	9 [5]	54 [5]	35 [5]	-3.32 [5]	10.33	0.27	4.12	0.013	0.971	0.003	2.259	0.008	15.918	0.082	15.440	0.056	35.911	0.091
3	Kychering	1574.4 ± 4.3 [1]	53J	411149	6600069	5.55 [1]	37.8 [1]	32.6 [1]	-1.64 [1]	9.93	0.08	4.01	0.018	0.966	0.001	2.251	0.001	15.901	0.015	15.377	0.015	35.788	0.033
4	Pinding Rocks	1590	53J	423169	6603850	10 [6]	40 [6]	15 [6]	-2 [13]	9.26	0.05	3.70	0.002	0.965	0.001	2.236	0.003	15.831	0.030	15.261	0.013	35.399	0.029
5	Lake Gairdner Rhyolite	1591-1587 [2]	53J	524029	6542642	3.84 [7]	19.3 [7]	42 [7]	-	9.52	0.10	3.65	0.073	0.964	0.001	2.228	0.005	15.869	0.021	15.308	0.019	35.364	0.098
6	Konkaby West	1590	53J	449307	6631560	15.8 [1]	50.5 [1]	47.2 [1]	-	9.22	0.31	3.71	0.032	0.960	0.003	2.229	0.002	15.971	0.020	15.276	0.054	35.556	0.039
7	Lyons	1590	53J	406785	6612505	3.39 [1]	24.5 [1]	43.6 [1]	-	8.92	0.30	3.48	0.083	0.959	0.002	2.218	0.005	15.934	0.028	15.220	0.056	35.273	0.105
8	Parla	1590	53H	472425	6372266	3 [5]	17 [5]	40 [5]	1.5 [12]	9.59	0.11	3.67	0.066	0.959	0.003	2.221	0.008	16.028	0.046	15.345	0.025	35.543	0.118
9	Charleston	1585 ± 5 [3]	53H	693396	6303645	15 [6]	70 [6]	39 [6]	-7.5 [13]	9.76	0.15	4.10	0.069	0.958	0.001	2.245	0.004	16.039	0.021	15.374	0.027	36.050	0.095
10	Pordia	1590	53H	512705	6325631	4 [5]	33 [5]	40 [5]	-	9.36	0.30	3.67	0.105	0.958	0.004	2.224	0.008	15.959	0.038	15.297	0.055	35.493	0.143
11	Frogs Eyes	1575 ± 13 [5]	53J	424855	6566593	8 [8]	27 [8]	12 [8]	-4.4 [13]	9.69	0.72	3.84	0.052	0.957	0.001	2.228	0.003	16.074	0.024	15.369	0.117	35.788	0.047
12	Yardea Dacite 1	1587.2 ± 0.5 [2]	53H	530404	6423855	-	29 [9]	-	-4.1 [10]	10.04	0.25	3.96	0.058	0.956	0.002	2.229	0.004	16.190	0.037	15.444	0.046	36.028	0.095
13	Eucarro Rhyolite	1590	53H	542251	6385723	7.3 [9]	33 [9]	31 [9]	-4.38 [10]	9.68	0.38	4.10	0.097	0.952	0.003	2.221	0.003	16.205	0.055	15.408	0.067	36.019	0.133
14	Tyringa	1583 ± 11 [1]	53H	465556	6341837	5 [5]	30 [5]	4.3 [5]	1.16 [1]	10.22	0.06	3.99	0.090	0.952	0.004	2.223	0.002	16.229	0.065	15.481	0.020	36.100	0.178
15	Yardea Dacite 2	1587.2 ± 0.5 [2]	53H	571350	6396800	7 [10]	33 [10]	30 [10]	-3.27 [10]	10.08	0.16	3.92	0.031	0.951	0.006	2.219	0.006	16.223	0.030	15.457	0.030	36.020	0.060
16	Kokatha	1590	53J	500868	6549341	8.45 [1]	36.8 [1]	38.9 [1]	-4.21 [1]	9.45	0.09	3.66	0.000	0.950	0.003	2.210	0.006	16.172	0.060	15.346	0.025	35.681	0.054
17	Buckleboo	1590	53H	638429	6372470	4 [5]	28 [5]	25 [5]	-6 [13]	9.90	0.09	3.80	0.020	0.946	0.001	2.202	0.003	16.326	0.025	15.443	0.019	35.989	0.046
18	Opal Fields	1590 ± 4 [4]	53J	698872	6616261	7 [11]	19 [11]	24 [11]	-	10.01	0.25	3.90	0.059	0.941	0.002	2.200	0.015	16.404	0.061	15.474	0.051	36.182	0.124
19	Yantea Rhyolite	1591-1587 [2]	53J	523013	6493194	2.74 [7]	8.9 [7]	14 [7]	-2.3 [10]	9.15	0.23	3.64	0.067	0.939	0.009	2.209	0.030	16.281	0.066	15.308	0.050	35.789	0.136
20	Arthurton	1582 ± 7 [4]	53H	722695	6185982	26 [5]	50 [5]	9 [5]	-3.5 [12]	10.57	7.54	3.89	2.671	0.855	0.157	2.121	0.014	18.524	6.330	15.806	2.068	38.496	15.900
Nueman n	Arthurton	1582 ± 7 [4]	53H	758400	6267300	12 [12]	33 [12]	3.7 [12]	-4.47 [12]	10.10	-	3.70	-	0.854	0.02% [*]	2.070	0.02% [*]	18.380	0.02% [*]	15.693	0.000	38.043	0.000
Roache	Cunyarie	1590	53H	603460	6353143	4 [5]	28 [5]	25 [5]	-5.7 [13]	9.62	- [*]	1.47	- [*]	0.937	0.02% [**]	2.015	0.02% [*]	16.441	0.03% [*]	15.413	0.000	33.124	0.000

Sources: [1] Budd (2006); [2] Jagodzinski et al. (2016); [3] Creaser & Fanning (1993); [4] Creaser & Cooper (1993); [5] Stewart & Foden (2003); [6] Webb et al. (1986); [7] Agangi (2011); [8] Ferris (2001); [9] Allen et al. (2002); [10] Stewart (1994); [11] BHP unpublished report; [12] Wurst (1994); [13] Stewart & Foden (2003), [14] Jagodzinski et al. (2016)

phenocrystic and rapakivi-textured K-feldspars can be asserted in this case. Furthermore, the triplicate analyses of the Charleston Granite, as well as replicate analyse of the Yardea Dacite (Table 4.1), demonstrate the reproducibility of our initial Pb-isotopic values in unknowns.

The ^{204}Pb-based results (weighted average) of Pb-isotopic LA-ICP-MS of Hiltaba Suite and Gawler Range Volcanics are shown in Figures 4.6 and 4.7, as well as Table 4.1. The results of individual analyses are provided in Appendix F. Analytical uncertainties (2σ) for alkali feldspar analyses averaged 0.28% for ^{206}Pb-based ratios, and 0.26% for ^{204}Pb-based ratios. Interpretations of $^{238}U/^{204}Pb_{(t)}$ (μ) based on a Stacey and Kramers (1975) two-stage Pb model, have 95% confidence within 0.25 – 0.75 μ-deviations. These uncertainties are comparable to those encountered in other studies involving laser ablation of feldspar for Pb-isotopes (i.e. 0.043 – 0.558%; Tyrrell et al. (2006), , Souders and Sylvester (2010)), and galena using quadrupole mass-spectrometers (i.e. 0.09 – 0.24%; McFarlane et al. (2016)).

Table 4.2: Results of SRMs (Recommended values after Jochum et al., (2007)

	NIST610*			**GSD-1G**			**BCR-2G**	
	GeoREM Preferred Value	Our Av. (n=24)		GeoREM Preferred Value	Our Av. (n= 12)		GeoREM Preferred Value	Our Av. (n=12)
^{207}Pb/^{206}Pb	0.910	0.910		0.804	0.804		0.833	0.833
+/- (2σ)	0.0002	0.0004		0.0001	0.001		0.001	0.001
MSWD	-	1.442		-	0.680		-	0.787
^{208}Pb/^{206}Pb	2.169	2.170		1.987	1.985		2.066	2.061
+/- (2σ)	0.0004	0.001		0.0005	0.002		0.001	0.007
MSWD	-	1.322		-	0.666		-	3.756
^{206}Pb/^{204}Pb	17.052	17.047		19.579	19.577		18.765	18.773
+/- (2σ)	0.004	0.010		0.004	0.049		0.007	0.074
MSWD	-	0.179		-	0.255		-	0.344
^{207}Pb/^{204}Pb	15.515	15.516		15.745	15.745		15.626	15.649
+/- (2σ)	0.004	0.010		0.002	0.038		0.006	0.062
MSWD	-	0.432		-	0.501		-	0.415
^{208}Pb/^{204}Pb	36.991	36.977		38.908	38.854		38.730	38.751
+/- (2σ)	0.009	0.023		0.009	0.098		0.020	0.137
MSWD	-	0.587		-	0.168		-	0.321

*Denotes primary standard

A median feldspar $^{207}Pb/^{206}Pb$ value of 0.958, which is within 2σ analytical uncertainty of the 1590 Ma isochord of the Stacey and Kramers (1975) growth model, shows that the feldspars have experienced little radiogenic Pb ingress post-crystallisation (Housh and Bowring, 1991; Ludwig and Silver, 1977). Most results can be reconciled by simple variation in $^{238}U/^{204}Pb$ (μ) from 10.33 to 9.15. Application of the Cumming and Richards (1975) model-III curve requires modification of μ to 11.76 and the acceleration factor (Є) by c.40% to 7.048x10^{-5} and 7.11x10^{-5} for $Є_{t=1580}^{235/204}$ and $Є_{t=1580}^{238/204}$, respectively, however satisfies 2% less of the sample distributions including analytical uncertainties. A single sample (Yantea Rhyolite) did determinatively show the effects of radiogenic Pb ingress, dominated by anomalous $^{206}Pb/^{204}Pb$ relative to $^{207}Pb/^{204}Pb$, since this ingress occurred at some point after the c.1600 Ma $^{207}Pb/^{206}Pb$ growth inflexion. Therefore the regression models of Russell et al. (1954) may be applied to offset this with little effect on $^{207}Pb/^{204}Pb$ signature, albeit with a high degree of caution. For all other samples, variations outside of analytical uncertainty in ^{204}Pb-based ratios are taken to represent genuine variation in source signature. Population variance for $^{207}Pb/^{204}Pb$ (0.0053) and is lower than other A-type suites in the literature (i.e. 0.13 and 0.18 for Almeida et al. (2016) and Andersson et al. (2002), respectively) while standard deviation (0.0741) is greater than that of Andersson et al. 2002 (0.0327). Attempts to determine initial Pb isotopic ratios

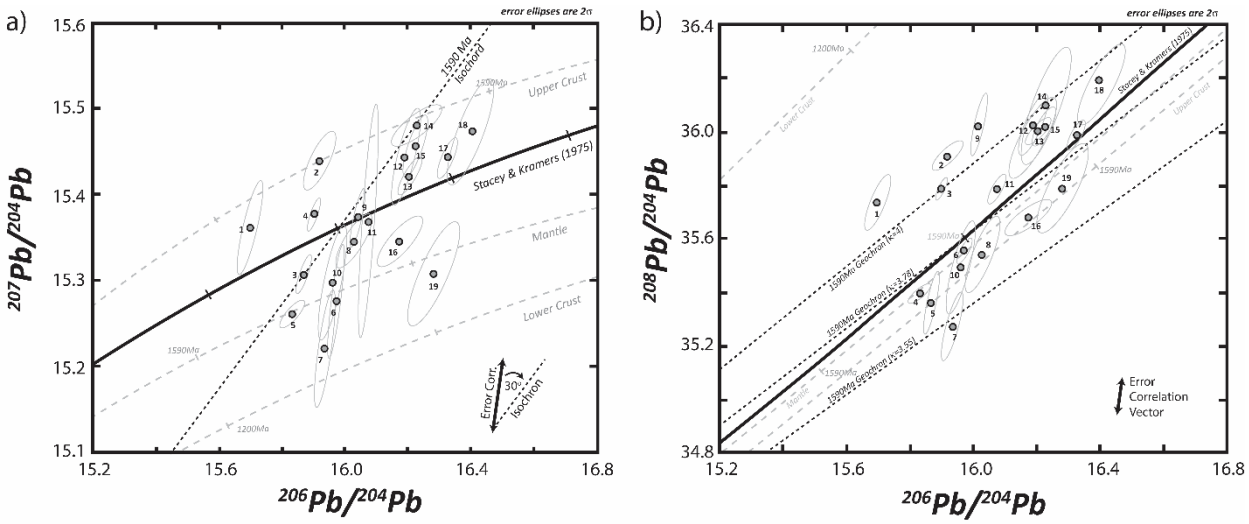

Figure 4.6: Pb-isotopic results from alkali feldspar of the Hiltaba Suite granitoids and Gawler Range Volcanics. Error ellipses are 2σ (weighted average). a) Uranogenic Pb-isotopic diagram. b) Thoro-uranogenic Pb-isotopic diagram. Growth curves representing 'Lower Crust', 'Mantle' and 'Upper Crust' reservoirs are adapted after the parameters of Zartman & Doe, (1981) and Zartman & Haines, (1988).

of Yorke Peninsula Hiltaba Suite granites failed, yielding similarly excessively radiogenic ($^{207}Pb/^{206}Pb$ = ~0.85) results of Neumann (2001). These feldspars are both heterogeneous, low in Pb (<5 ppm) and contain abundant macro- and microscopic evidence of post-crystallisation disturbance.

The results of U-Pb geochronology which confirm the Hiltaba Suite-age of the Bulpara Granite which displays unradiogenic Pb-isotope behaviour (i.e. initial Pb-Pb model ages older than 1590 Ma) are presented in Appendix G. A compilation of existing geochronology for all other Hiltaba Suite/ GRV samples analysed here is presented in table 4.1. A high degree of metamictisation was encountered, with 50% of zircon grains separated from the Bulpara Pluton sample unsuitable for LA-ICP-MS geochronology. Of the 14 zircon grains suitable, only 6 grains were less than 90% concordant with zero-time Pb-loss and common Pb-gain. The most concordant analyses (n = 8) with greater than 98% concordance yield a weighted average age of 1578 ± 24 Ma.

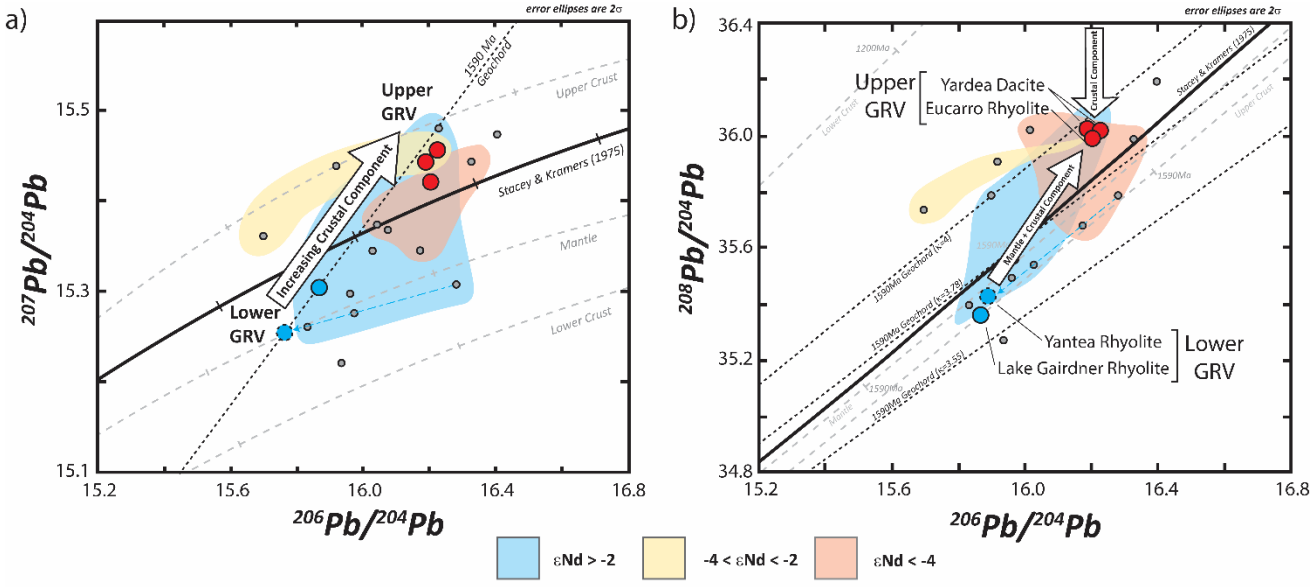

Figure 4.7: Pb-isotopic results compared with εNd(1590Ma) fields (coloured) for the Hiltaba Suite (grey points), Upper GRV (red circles) and Lower GRV (blue circles).

4.7 Discussion

Initial Pb-isotopic ratios obtained from alkali feldspars of the Hiltaba Suite and Gawler Range Volcanics (GRV) reveal a near-linear distribution which parallels the Stacey and Kramers (1975) 1590

Ma isochord (Fig. 4.7). Variation of Pb-isotopic data along the isochord (Fig. 4.7) implies mixing between low- and high-U/Pb Pb-isotopic reservoirs. Low time-integrated $^{238}U/^{204}Pb_{(t)}$ (8.92 – 9.60) values coupled with low $^{232}Th/^{238}U_{(t)}$ (3.48 – 3.67) suggests that one mixing end-member is a mantle-like reservoir. High-$^{232}Th/^{238}U_{(t)}$ (3.89 – 4.17) associated with more uranogenic crustal signatures ($^{238}U/^{204}Pb_{(t)}$ = 9.89 – 10.22) indicates that the dominant crustal reservoir resides in the lower crust. Variation outside of uncertainty, to the left of the 1590 Ma isochord ($^{207}Pb/^{206}Pb$ = 0.98 to 0.966) indicates at least partial source derivation from a reservoir depleted in U/Th and U/Pb for a geologically-significant time, thereby retarding the growth of radiogenic Pb. In contrast, Pb-isotopic signatures to the right of the ~1590 Ma isochord on the $^{207}Pb/^{204}Pb$ vs $^{206}Pb/^{204}Pb$ indicates a melt-source enriched in U and Th relative to Pb. Together, these data indicate complex mixing between several, discrete, Pb-isotopic reservoirs located throughout the Gawler Craton crust, and 1590 Ma mantle-derived melt were involved in the petrogenesis of the Hiltaba Suite and GRV.

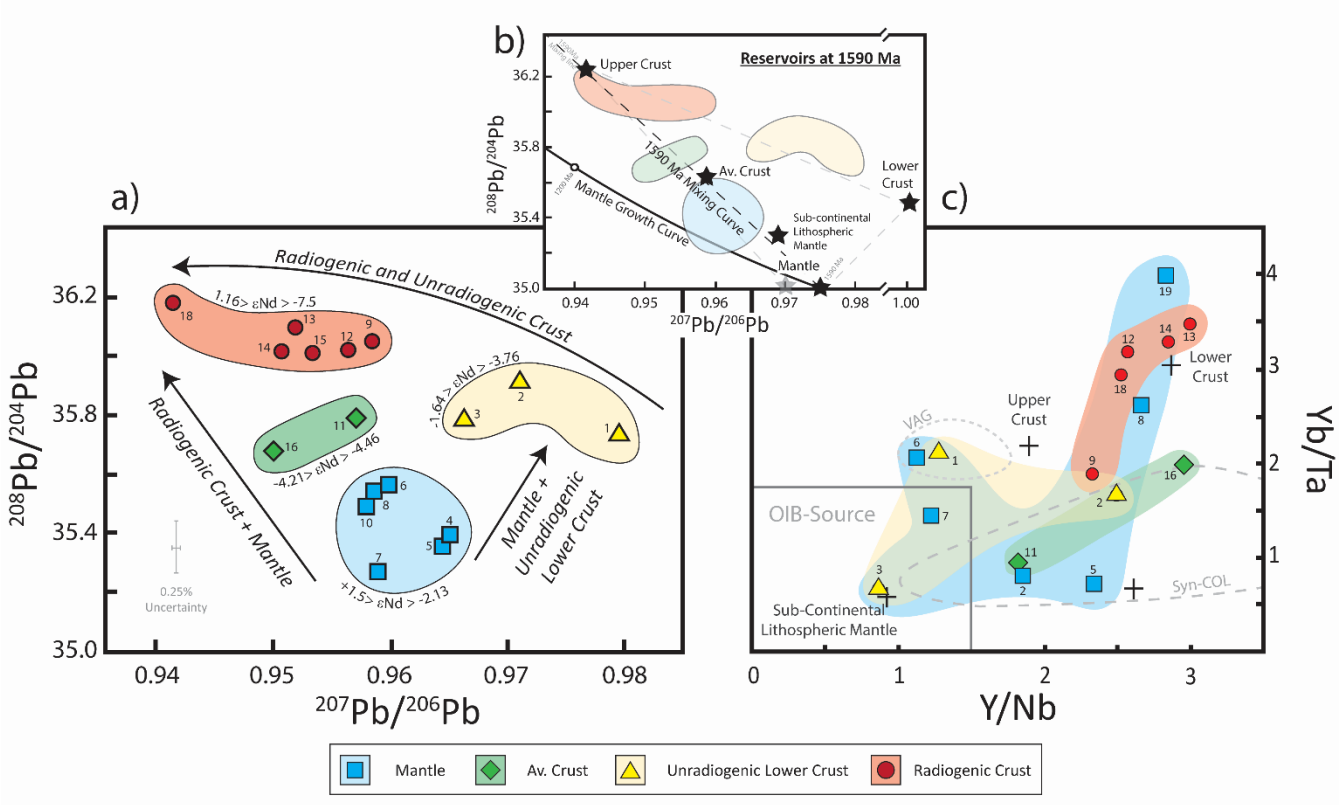

Figure 4.8: An outline of the Pb-isotopic (a, b) and geochemical (c) mixing relationships for the Hiltaba Suite and Gawler Range Volcanics. (a) Thorogenic vs uranogenic Pb-isotope diagram. (b) A comparison between Pb-isotopic signatures of the Hiltaba Suite/ GRV with the plumbotectonic reservoirs of Zartman & Haines, (1988) (solid stars) and mantle-parameters (pale star) of Allegre et al., (1986). (c) A-type source diagram with fields from Eby, (1990). "Sub-continental lithospheric mantle" location from McDonough, (1990). "Upper Crust" and "Lower Crust" averages from McLennan, (2001).

The complex mixing relationship between a number of Pb-isotopic reservoirs involved in the Hiltaba Suite and GRV signatures is effectively illustrated through the $^{208}Pb/^{204}Pb$ vs $^{207}Pb/^{206}Pb$ diagram (Fig. 4.8). Contrasting Th/Pb values for the mantle (i.e. N-MORB = 0.4; Sun and McDonough (1989)) and lower crust (3.8; Taylor and McLennan (1995)) provide distinct variations in $^{208}Pb/^{204}Pb$ between these reservoirs. Isolation of lower crustal reservoirs from isotopic exchange decouples the uranogenic Pb-isotopic system (Zartman and Haines, 1988) leading to secular variation in the $^{207}Pb/^{206}Pb$ signatures of the individual crustal reservoirs. Thus at least three end-member isotopic reservoirs can be identified: one residing in the mantle and two-distinct reservoirs within the crust.

The melt-sources involved in the formation of the A-type magmas are a point of considerable debate in the literature. The common association of mafic, anorthositic massifs with A-type granitoids has led some authors to favour a dominantly mantle-derived origin (i.e. Anderson et al. (2003); Frost et al. (1999). However, the unique REE-HFSE-F-enriched geochemical compositions of A-type granites is often argued as evidence for a crustal origin, either as a dominant-melt contribution (i.e. Collins et al. (1982)) or relatively minor partial-melt contribution (i.e. Andersson et al. (2002); Kosunen (2004)). Uncertainty also remains as to whether the nature of the crustal component is an important factor in generating the geochemical characteristics of A-types, with tonalite-trondhjemite-granodiorite-series (i.e. Creaser et al. (1991); Kosunen (2004) and high-grade metamorphic charnockites (i.e. Collins et al. (1982); Kilpatrick and Ellis (1992)) being the preferred crustal protoliths in generating A-type melts. The range of Pb-isotopic reservoirs for the Hiltaba Suite/ GRV presents an ideal case by which to explore the relative role of mantle- and crustal-derived melts in generating A-type rocks. Each of the three-dominant reservoirs implicated in the formation of the Hiltaba Suite/ GRV will be discussed independently so as to outline their unique features and similarity with those melt-sources invoked for A-types elsewhere in the world.

4.7.1 Mantle source reservoir

The role of a mantle-component in A-type magmas, whether as a hybridising contribution or merely a heat source, has long been a point of conjecture among previous authors (Anderson et al., 2003; Clemens et al., 1986; Collins et al., 1982; Creaser et al., 1991; Eby, 1990; Frost and Frost, 1997; Haapala and Rämö, 1990; Haapala and Rämö, 1992; Whalen et al., 1987). Since Pb-isotopes do not fractionate via magmatic processes they may preserve mantle-like signatures even in geochemically-evolved, high-SiO_2 (65 to 77 wt. %) granitoids. Melt-sources with low time-integrated $^{238}U/^{204}Pb_{(t)}$ (8.92 to 9.58) coupled with low-$^{232}Th/^{238}U_{(t)}$ (3.48 to 3.71) are recorded for approximately a third of the Hiltaba Suite and GRV samples, which imply a dominantly mantle-like source was important in the overall generation of these A-type magmas. Sm-Nd isotopic studies indicating relatively juvenile sources ($\varepsilon_{Nd(1590Ma)}$ = -2.13 to +1.5; Table 4.1) support this interpretation for Hiltaba Suite members with mantle-like Pb-isotopic signatures. The range of these Pb-isotopic values, in particular the average $^{232}Th/^{238}U_{(t)}$ = 3.64, is slightly higher than those expected for asthenospheric mantle sources such as MORB, where $^{238}U/^{204}Pb_{(t)}$ and $^{232}Th/^{238}U_{(t)}$ are typically in the order of ~9.2 and ~3.5 respectively (i.e. Ito et al. 1987). Instead, the source signatures are more consistent with a weakly-radiogenic, enriched mantle source (Fig. 4.9) such as sub-continental lithospheric mantle ($^{232}Th/^{238}U_{(t)}$ = 3.4 – 3.76; Jung et al. (2011); Zartman and Haines (1988)) or subduction-modified back-arc mantle ($^{238}U/^{204}Pb_{(t)}$ = 9.1 to 9.5, $^{232}Th/^{238}U_{(t)}$ = 3.62 to 3.77; Cohen and O'Nions (1982); Ikeda et al. (2000)). While these isotopic signatures may also be seen as evidence for some degree of crustal-assimilation, the anomalously-radiogenic $\varepsilon_{Nd(1590Ma)}$ compositions of coeval basalts (<+2.5; Fricke (2005); Stewart (1994)) advocates for an enriched mantle-source of parental melt-contribution.

Hiltaba Suite/ GRV which yield Pb-isotopic compositions indicating derivation from an enriched mantle source most closely resemble the Pb-isotopic signature displayed by the A-type granitoids (Fig. 4.9) of the Mesoproterozoic Anorthosite-Mangerite-Charnockite-Granite (AMCG) suites of the U.S. Grenvillian Terrane (Frost et al., 1999; Zartman, 1965). Pb-isotopic compositions of

the Red Mountain Complex and Sherman Batholith as well as the Long Grove Pluton suggest a derivation from a melt-source with second-stage $^{238}U/^{204}Pb_{(t)}$ values ranging from 9.27 to 9.56 and $^{232}Th/^{238}U_{(t)}$ values ranging from 3.26 to 3.82 (Frost et al., 1999; Zartman, 1965). These low values were argued by Anderson et al. (2003) to result from minimal crustal contamination of a parental tholeiitic melt. The range of $\varepsilon_{Nd(1431Ma)}$ (+0.74 to -2.32; Anderson et al. (2003); Frost et al. (1999)) is more radiogenic than the depleted mantle at that time (+6.9; Workman and Hart (2005)) and thus is more consistent with reworking of an older mantle Sm-Nd reservoir such as rocks derived from previously underplated basalts (Frost et al., 1999) or SCLM. Given the similarities in the Pb-Nd isotopic compositions between the Hiltaba Suite/ GRV and the Mesoproterozoic AMCG suites of the Grenville Terrane, it seems probable that similar mantle-reservoirs were involved in their genesis.

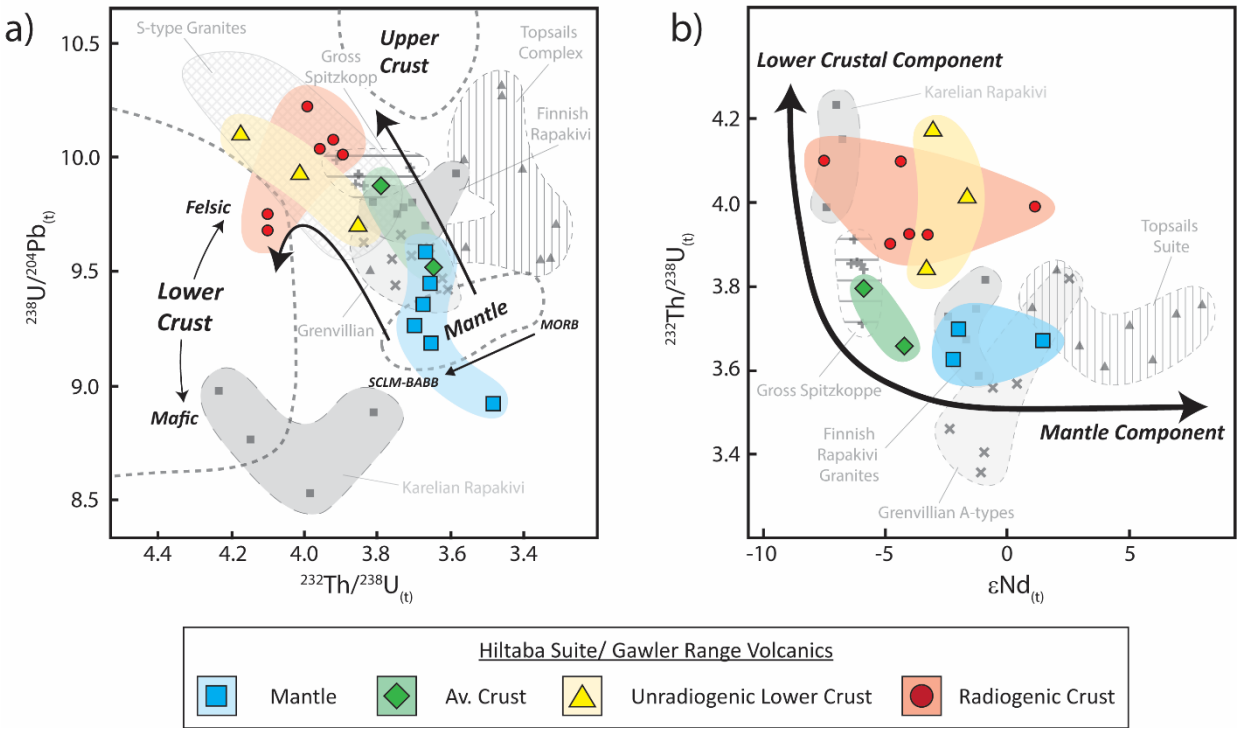

Figure 4.9: A compilation (a) Pb-Pb and (b) Pb-Nd isotopic data from Paleozoic and Proterozoic A-type igneous suites. Topsails Complex data from Whalen et al., (1996). "Finnish Rapakivi" data compiled from Ramo, (1991), Ramo et al., (2001), Heinonen et al., (2010). "Karelian Rapakivi" after Neymark et al., (1994). "Grenvillian A-type" data compiled from Zartman et al., (1965), Frost et al., (1999), Kolker et al., (1991). "Gross Spitzkoppe" data after Frindt et al., (2004) and Jung, (1998). "S-type Granite" field compiled from Bernard-Griffiths et al., (1985), Gariépy et al., (1985) and Jung (2005).

The relationship between coeval anorthositic complexes and the Paleoproterozoic rapakivi granites of Finland and Sweden has also been used as evidence of the importance of mantle-derived

tholeiitic melts in generating A-type igneous suites. Although there is some disagreement regarding whether the Finnish anorthosites represent parental A-type magmas or simply reflect a mantle-derived heat source (Haapala and Rämö, 1990), the indistinguishable range of Nd-signatures from anorthosites and rapakivi granites of the Ahvenisto Complex, Finland (-0.9 to -1.1; Heinonen et al. (2010)) and the Salmi Batholith (Neymark et al., 1994) is strong evidence that they are comagmatic. The range of Pb-isotopic signatures of the rapakivi granites provided in Heinonen et al. (2010); Rämö (1991), and Andersson et al. (2002) are more crustal ($^{238}U/^{204}Pb_{(t)}$ = 9.57 to 9.97; Fig. 4.9) than the mantle-component present in the Hiltaba Suite/ GRV or AMCG suite of the Midwestern U.S. implying that an additional contribution of a higher-$^{238}U/^{204}Pb$, crustal material was important in the overall isotopic characteristics of the rapakivi suite. A variable crustal component is supported by the range of $\varepsilon_{Nd(t)}$ in the Swedish rapakivi (-6.7 to -7.1; Andersson et al. (2002)) indicating significant contribution of crustal derived melt (Fig. 4.9). The isotopic contrasts between A-type granitoid suites associated with mantle-derived anorthosites and Hiltaba Suite/ GRV with mantle-like Pb-isotopic compositions implies that varying proportions of crustal and mantle derived melts are important in overall geochemical differences between A-type granites, worldwide. However, the most important petrogenetic control which is common to all these A-type suites is partial derivation from a tholeiitic reservoir with radiogenic Nd-isotopic signatures, yet mantle-like Pb-isotopic ratios, most consistent with the SCLM.

Hiltaba Suite granitoids (and GRV) which retain Pb-isotopic evidence for dominant proportions of a mantle-derived melt, also show geochemical characteristics which are distinct from other Hiltaba Suite/ GRV. These samples display a range of Nb (11.2 – 22 ppm) and Y (21.1 – 48 ppm) concentrations which are generally the lowest of the Hiltaba Suite/ GRV and plot in the volcanic arc/ syn-collisional field of (Pearce et al., 1984), suggesting they are the least crustal-like of the Hiltaba Suite/ GRV. Likewise, in the A-type discriminant scheme of Whalen et al. (1987) these samples have the lowest Ga*10000/Al ratios and Zr+Nb+Ce+Y (Fig. 4.10), and are therefore the least-enriched in incompatible elements. Together, co-variations between Pb-isotopic and geochemical signatures

suggest that the most mantle-like Hiltaba Suite/ GRV are the least-enriched in incompatible-elements and thus are likely to most closely represent the least-hybridised examples of the mantle-derived parental melt responsible for the Hiltaba Suite/ GRV. Modified alkali-lime index (Na_2O+K_2O-CaO) values range from 7.71 to 9.59 implying an alkali to alkali-calcic source (Frost et al. 1999). They also display high $FeO_{(tot)}$/ $FeO_{(tot)}$+MgO (0.789 – 0.892) which suggests they are derived from the same ferroan melt source as most of the other Hiltaba Suite/ GRV, which is a typical characteristic of tholeiitic parental melt (Frost and Frost, 1997).

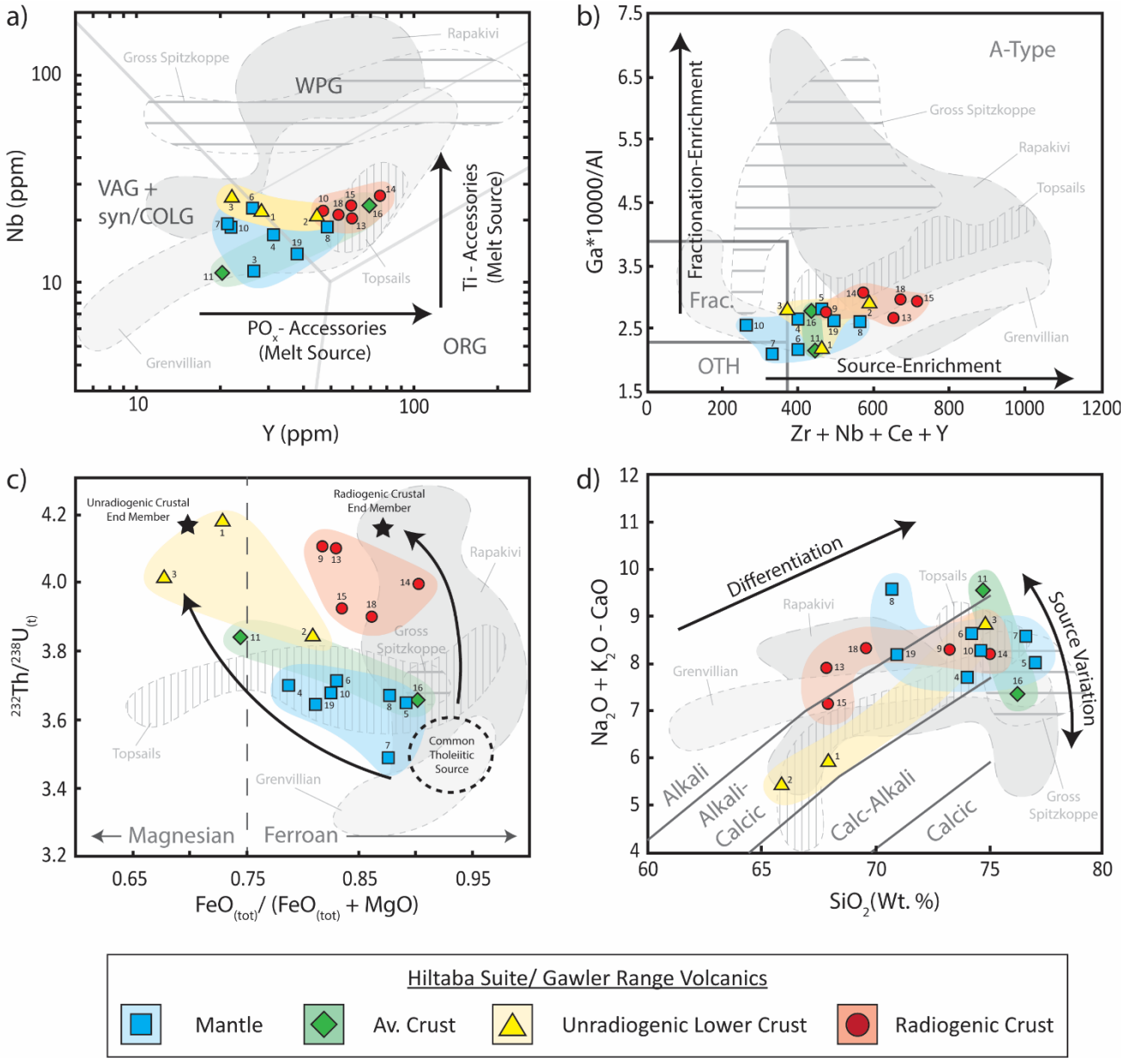

Figure 4.10: Petrogenetic diagrams of (a) Pearce et al., (1984) and (b) Whalen et al., (1987) and (c, d) Frost et al., (2001).

4.7.2 Unradiogenic source reservoir

Unradiogenic lower crust is interpreted to represent a second end-member of the Pb-isotopic mixing array and is characterised by high $^{207}Pb/^{206}Pb$ (>0.97) and high $^{208}Pb/^{204}Pb$ (>35.7) and $^{232}Th/^{238}U$ (>4) consistent with some melt-contribution from a crustal reservoir residing in the lower crust. In order to generate these unradiogenic Pb-isotopic compositions, a second-stage crustal reservoir which initially conformed to high $^{238}U/^{204}Pb_{(t)}$ (>9.93) growth, became significantly depleted in U relative to Th and Pb. Hiltaba Suite granites interacting with the unradiogenic reservoir show second-stage (Stacey and Kramers, 1975) Pb-isotopic model ages which are significantly older than ~1590 Ma (1812 to 1673 Ma) (Table 4.1, Fig. 4.7). These older model ages suggest the U-depletion event which generated the unradiogenic reservoir occurred at least during the mid-Paleoproterozoic (~1800 Ma), but more likely during the early Paleoproterozoic (>2200 Ma). U-depletion is commonly observed in granulite-facies metamorphics (Bea, 2012; Gray and Oversby, 1972)) and typically attributed to mineralogical changes and fluid-loss during the transition from amphibolite to granulite facies (Whitehouse, 1989). Previous workers have also argued for the involvement of a lower crustal granulitic component in the genesis of the Hiltaba Suite/ GRV (Giles, 1988; Kilpatrick and Ellis, 1992).

The high-$^{238}U/^{204}Pb_{(t)}$ (9.93 to 10.1) indicate that the protolith which underwent a U-depletion event, was likely Neoarchean to Early Paleoproterozoic in age (>~2500 Ma). Considering that the $\varepsilon_{Nd(1590Ma)}$ compositions (-3.32 to -1.64) of these granitoids are less evolved than those expected of Archean crust, the unradiogenic reservoir must have been either a relatively minor-melt component in the formation of these Hiltaba Suite intrusives, or the unradiogenic reservoir represents juvenile basalts/ gabbros generated from a depleted mantle at ~2230 Ma. While the latter of these scenarios is largely precluded by the strongly-crustal Pb-isotopic signatures (i.e. $^{238}U/^{204}Pb_{(t)}$ >9.98, $^{232}Th/^{238}U_{(t)}$ > 4.01), a role for silica-undersaturated, mantle-derived melts is supported by the preservation of baddeleyite within the cores zoned-plagioclase crystals (Fig. 4.3), similar to those described in mafic rocks associated with A-type granitoids elsewhere (Scoates and Chamberlain, 1995).

Unique, whole-rock geochemical characteristics of Hiltaba Suite granites with unradiogenic initial Pb-isotopic signatures support a derivation of these intrusives from melt-sources which are distinct from the other Hiltaba Suite granites. Na_2O+K_2O-CaO (0.809 – 0.678) and $FeO_{(tot)}/FeO_{(tot)}$+MgO (8.85 – 5.44) are lower than most Hiltaba Suite granitoids, reflecting a more magnesian and less alkali-enriched source (Frost et al., 2001), as opposed to a Fe- and alkali-rich sources implied for Hiltaba Suite granites which do not exhibit unradiogenic Pb-isotopic signatures (Fig. 4.10c, d). The Pegler and Bulpara plutons (Table 4.1) are anomalously metaluminous (A/CNK = 0.953 and 0.956) for the Hiltaba Suite which are typically weakly-metaluminous to peraluminous (A/CNK = 1.010 – 1.175). These geochemical characteristics suggest that the lower crustal melt-source representing the unradiogenic Pb-isotopic reservoir is akin to I-type igneous rocks, similar to that inferred from the Topsails Suite of Newfoundland (Fig. 4.10) which were interpreted to be subduction-modified subcontinental lithospheric mantle (Whalen et al., 1996). The rock type representing the unradiogenic reservoir in the Gawler Craton, however, displays much more crustal Pb-Nd-isotope compositions (Fig. 4.9) and while geochemically-similar to those involved in the Topsails Suite (i.e. alkali-calcic and magnesian; Fig. 4.10), are unlikely to be geodynamically linked to a recently-modified crustal source. Instead the high-$^{232}Th/^{238}U_{(t)}$ (3.98 to 4.23) and older second-stage model ages (+~300 Ma older than U-Pb zircon age) Pb-isotopic signatures are more consistent with hybridisation between an enriched-mantle component, such as SCLM, and an Archean lower crust, as has been suggested for the isotopically similar Salmi Batholith of the Russian Karelian Terrane (Neymark et al., 1994). This combination of protoliths would be consistent with unradiogenic Pb-isotopic signatures which are biased towards crustal compositions, combined with only weakly-evolved Nd-isotopic signatures shown by some members of the Hiltaba Suite. Additionally, it is an instance where granulitic lower crust may be important in the petrogenesis of the Hiltaba Suite/ GRV, as has been suggested for A-types rocks elsewhere in the world (Clemens et al., 1986); Collins et al. (1982); (Eby, 1990; Frindt et al., 2004)

4.7.3 Radiogenic source reservoir

Hiltaba Suite granitoids and GRV characterised by high uranogenic initial Pb-isotopic compositions ($^{206}Pb/^{204}Pb$ = 16.039 – 16.404, $^{207}Pb/^{204}Pb$ = 15.374 – 15.481) imply a melt-component sourced from a crustal reservoir enriched in U relative to Pb. Consequently, time-integrated, second-stage $^{238}U/^{204}Pb_{(t)}$ derived from these Pb-isotopic ratios yield the highest values for the Hiltaba Suite/ GRV (9.83 – 10.52), implying that this isotopic reservoir contained ~11% more ^{238}U relative to ^{204}Pb at 1590 Ma than that required by Pb-isotopic signatures of the mantle-like Hiltaba Suite intrusives. Thorogenic Pb-isotope ratios are also high ($^{208}Pb/^{204}Pb$ = 36.019 – 36.182), yielding elevated time-integrated $^{232}Th/^{238}U_{(t)}$ ranging from 3.93 to 4.11 which are indistinguishable from those Hiltaba Suite granites partially derived from the unradiogenic reservoir. However in contrast to the unradiogenic reservoir inferred from Hiltaba Suite granites with retarded Pb-growth the crustal reservoir responsible for these Pb-isotopic compositions yields $^{207}Pb/^{206}Pb$ ratios which are comparatively more-radiogenic (0.959 – 0.943; Fig. 4.8). This suggests that the 'radiogenic reservoir' responsible for the radiogenic Pb-isotopic compositions in some Hiltaba Suite granites did not undergo U-depletion experienced by the unradiogenic crustal reservoir, but instead continued to evolve uranogenic Pb until melt extraction during the Hiltaba event at ~1590 Ma. Furthermore, it also suggests that the high-$^{232}Th/^{238}U_{(t)}$ signatures of the radiogenic reservoir is related to a high abundances of Th in the reservoir, as opposed to U-depletion as is invoked for the unradiogenic reservoir. These results indicate that while U concentration was high in this reservoir (relative to Pb), the concentration of Th was even greater.

The combination of elevated-$^{232}Th/^{238}U_{(t)}$ (>4) and $^{238}U/^{204}Pb_{(t)}$ (>10.1) inferred for the radiogenic reservoir most closely resembles the Pb-isotopic signatures of granites with a metasedimentary protolith component, such as S-type leucogranites (Fig. 4.9). For example, feldspar Pb-isotopic ratios for Variscan S-type granites (Bernard-Griffiths et al., 1985) and Himalayan leucogranites (Gariépy et al., 1985) yield $^{238}U/^{204}Pb_{(t)}$ ranging from ~9.8 to 10.4, and $^{232}Th/^{238}U_{(t)}$ values which range from ~3.8 to 4.3 (Fig. 4.9). The most similar Pb-isotopic signatures of A-type

granitoids are those of the Namibian Damara Belt, such as Gross Spitzkoppe ($^{238}U/^{204}Pb_{(t)}$ = 9.88 – 9.99 and $^{232}Th/^{238}U_{(t)}$ = 3.56 – 3.91). Jung (2005) and Frindt et al. (2004) argued these Pb-isotopic signatures reflected a metasedimentary crustal melt component, on the basis of the similarity of these Pb-isotopic compositions with Proterozoic metasediments and S-type granites of the Damara Belt. Given the Pb-isotopic similarity of S-type granites and Hiltaba Suite granites derived from the radiogenic reservoir (Fig. 4.9), it is likely that the lithology of the crustal reservoir involved in generating the radiogenic Pb-isotopic compositions of the Hiltaba Suite/ GRV is metasedimentary in origin. This is also geochemically-supported by the more peraluminous (A/CNK = 0.998 – 1.171) and alkali-rich (K_2O+Na_2O-CaO/SiO_2 = 0.105 to 0.119; Fig. 4.10) nature of these Hiltaba Suite/ GRV.

$\varepsilon Nd_{(1590Ma)}$ signatures are mostly evolved (-3.27 to -7.5: Table 4.1) relative to the other reservoirs, indicating some relationship between radiogenic Pb and Nd. Co-variation between Pb-isotopic signatures and chondrite-normalised Nd (Fig. 4.11) suggests the relationship between radiogenic Pb and Nd is related to the relative proportion of crustal melt contribution. This is despite the lack of obvious relationship between $\varepsilon Nd_{(1590Ma)}$ and Nd-concentration in the Hiltaba Suite (Budd, 2006), and simple correlation between Pb-isotopic compositions and Pb-concentration for the data presented here. Instead the relationship between radiogenic Pb-isotopic compositions and Nd may be explained by a crustal melt contribution from a reservoir with more general, systematic enrichment in both radiogenic Pb and REE (Fig. 4.11). High concentrations of Nd and Pb within the radiogenic reservoir would allow even small proportions of crustal melt to mask the subdued Nd-Pb-isotopic signatures of a parental, mantle-derived melt.

Radiogenic Pb-isotopic signatures co-vary with a number of HFSE-based petrogenetic indices. Nb (20 – 26 ppm) and Y (49 – 74 ppm) concentrations increase systematically with radiogenic Pb-isotopic compositions (Fig. 11), plotting as within-plate granitoids (Pearce et al., 1984), in contrast to Hiltaba Suite with mantle-like Pb-isotopic signatures which plot mostly within the syn-collisional field. Similarly, Zr+Nb+Ce+Y vs Ga*10000/Al, which Whalen et al. (1987) demonstrated to be an effective discriminant of A-type granites, also shows a systematic increase with radiogenic Pb

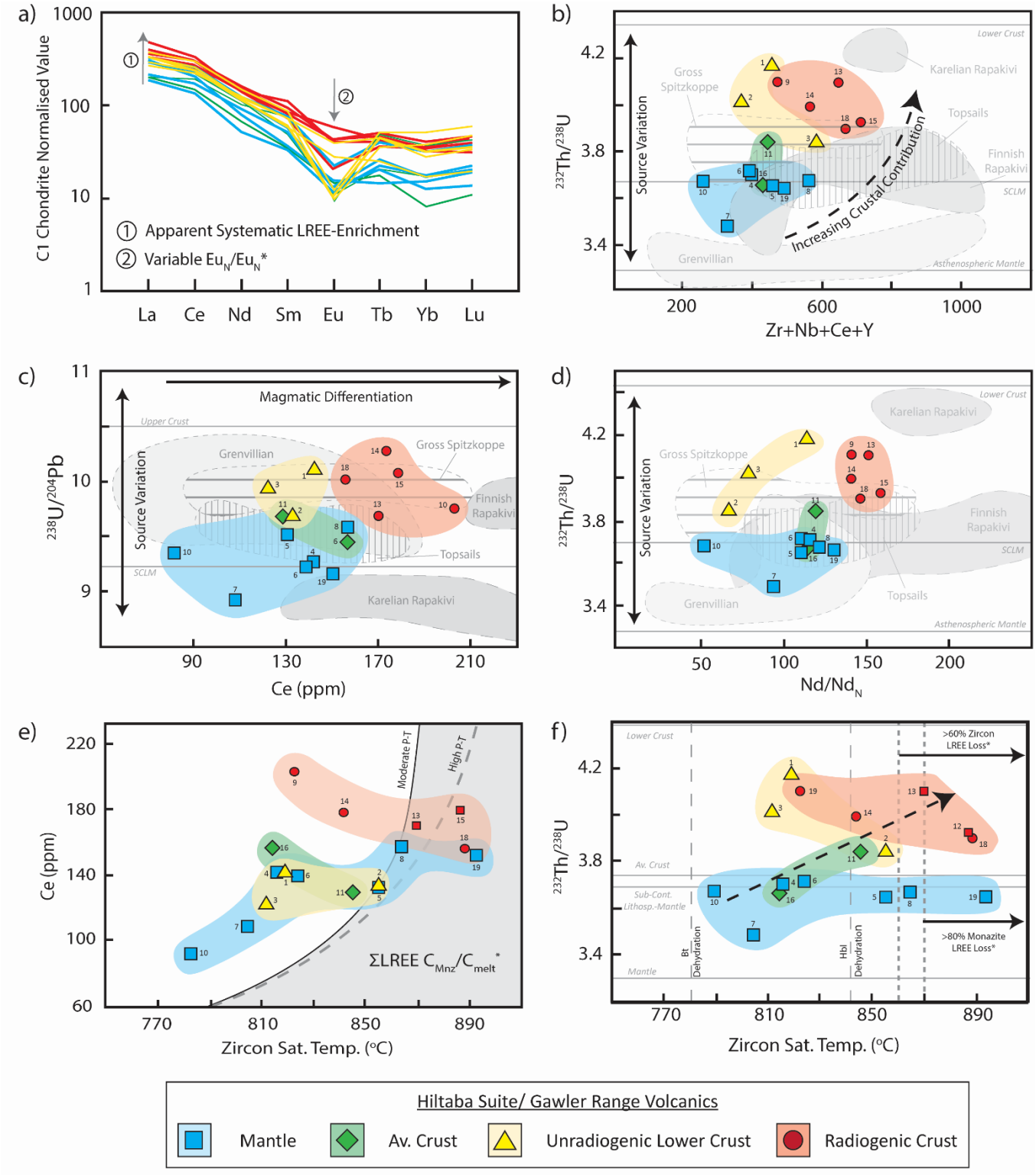

Figure 4.11: (a) C1 chondrite-normalised (McDonough and Sun, 1995) REE plot for Hiltaba Suite and Gawler Range Volcanics samples analysed here. (b) Plot of 232Th/238U vs. Nb+Y+Ce for the HSGRV melt sources (modified from Whalen et al., 1987). Major crustal reservoir isotopic signatures after Zartman and Haines, (1988). (c) Plot of 238U/204Pb vs. Ce (ppm) for the HSGRV melt source. 238U/204Pb reservoir signatures after Zartman and Haines, (1988), modified to Stacey and Kramers, (1975) 2-stage growth model. (d) Plot of 232Th/238U vs. chondrite-normalised Nd. (e) Plot of Ce (ppm) vs. zircon saturation temperature. Grey area and curves inferred from data in Yakymchuk and Brown, (2014), and based on the U-Th-LREE monazite partition coefficients of Stepanov et al., (2012). (f) Plot of 232Th/238U vs. zircon saturation temperature compared with anatectic mineral stability (<5 wt. % H2O, 10kbar).

(Fig. 4.11). These relationships suggest that the high-HFSE abundances of some Hiltaba Suite/ GRV which are characteristic of A-type granite geochemistry are linked with an increased melt-contribution from the radiogenic crustal reservoir.

Radiogenic Pb-isotopic compositions of the Hiltaba Suite/ GRV broadly correlate with increasing REE abundance (Fig. 4.11), and in particular LREE (Fig. 4.11). Systematic co-enrichment of these elements with radiogenic Pb-isotopic compositions implies that LREE variation in the Hiltaba Suite/ GRV is dominantly controlled by crustal melt contributions and melting conditions, rather than enrichment by closed-system magmatic processes such as crystal fractionation. This is at odds with the work of previous authors who considered that the enrichment of LREE in the Hiltaba Suite/ GRV was controlled by the late-stage crystallisation of apatite (Giles (1988); Stewart and Foden (2003)). The lack of obvious correlation between radiogenic Pb-isotopic signatures and LREE abundances in other A-type suites elsewhere (Fig. 4.11) largely limits the definitive role of a radiogenic reservoir in contributing to the high LREE abundances to the Hiltaba Suite/ GRV. A-type suites that include mineralogically evolved granites, such as the topaz-bearing Suomenniemi batholith of the Finnish rapakivi granites (Rämö, 1991) and Gross Spitzkoppe, of the Namibian Damara Belt (Frindt et al., 2004) do not display a correlation between Pb-isotopic signatures and LREE-HFSE, despite elevated LREE concentrations (Fig. 4.11). This, in conjunction with the commonly strong Eu-depletions observed in most A-type granites highlights that magmatic processes in addition to melt-source controls are likely both crucial in the overall LREE-HFSE enrichment characteristic of the Hiltaba Suite/ GRV and A-type magmas in general.

4.7.4 An accessory mineral mechanism for Pb-isotopic variation in A-types

Both Zr and Ce vary systematically with high-$^{238}U/^{204}Pb_{(t)}$ Pb-isotope compositions. Higher Zr concentrations (128-451 ppm) show a positive relationship with increasing Th/U and U/Pb of the melt source, inferred from high $^{232}Th/^{238}U_{(t)}$ Pb-isotopic signatures (Fig. 4.11). The high LREE

concentrations and high-Th/U inferred from the elevated $^{232}Th/^{238}U_{(t)}$ signature of the radiogenic Hiltaba Suite/ GRV indicates that U-Th-REE-rich mineral phases (e.g. monazite, allanite, zircon) are important constituents in the radiogenic reservoir. If the radiogenic reservoir does indeed represent metasedimentary rocks as suggest by this work, monazite is likely the accessory mineral key in hosting radiogenic Pb with high Th/U signatures. This suggests that increased melting of a monazite-rich metasediment might explain the high Th/U Pb-isotopic characteristics of the radiogenic reservoir, as well as elevated LREE-abundances, governed by equilibrium mineral-melt partitioning behaviour.

Zircon saturation temperature (T_{Zirc}) is highest in the most-radiogenic Hiltaba Suite/ GRV (T_{Zirc} = 822-891°C; Fig. 4.11) suggesting that the highest temperatures of zircon saturation were experienced by melt derived from the radiogenic reservoir. The lack of evidence for xenocrystic zircons, use of pluton-averaged concentrations of Zr and high-SiO_2 range of the Hiltaba Suite indicate that the differences between T_{Zirc} of the radiogenic Hiltaba and other reservoirs are likely real (Siégel et al., 2018). While the lower end of this temperature spectrum broadly conforms to the biotite-dehydration window (Le Breton and Thompson, 1988) important in the generation of some S-type granites, the upper end of this temperature range (~900°C) are likely to promote higher degrees of partial-melting (>40%) even at low H_2O (<1 wt. %) conditions ((Clemens and Vielzeuf, 1987; Patiño Douce and Johnston, 1991). At temperatures above 870°C, as implied by T_{Zirc} of the radiogenic Upper GRV, REE melt-partition coefficients indicate that around 80% of monazite LREE and radiogenic Pb with high ratios of $^{208}Pb/^{206}Pb$ will be lost to a prevailing partial melt (Stepanov et al., 2012; Yakymchuk and Brown, 2014). Likewise, at around 860°C, approximately 60% of the LREE held in zircon could be expected to be lost (Yakymchuk and Brown, 2014). Therefore, a mafic melt, hybridising with even a small volume of melt derived from a monazite(-zircon)-rich, low-grade metasediment will likely be rich in both LREE, as well as thorogenic (and uranogenic) Pb.

Similar mineralogical controls may also explain the preservation of mantle-like Pb-isotopic signature in the Hiltaba Suite/ GRV, and other high-temperature, A-type igneous suites. K-feldspar

and plagioclase are the major mineral-reservoirs for non-radiogenic ('common') Pb within the crystalline crust, and in the case of K-feldspar, can remain unmelted at temperatures in-excess of ~850°C (Carrington and Watt, 1995; Le Breton and Thompson, 1988). Thus, any parental mafic melt with the potential to hybridise with a crystalline lower-crust where the dominant host of common Pb is K-feldspar could feasibly avoid contamination by much of the crustal-Pb-isotopic signature while still acquiring some the crustal geochemical characteristics (i.e. high-K, -HFSE) from melting of other silicates such as biotite.

4.7.5 Insights of magmagenesis from the GRV lavas

The Gawler Range Volcanics (GRV) are the coeval extrusive equivalents of the Hiltaba granitoids and effectively isotopically-bracket the Hiltaba Suite intrusives (Fig. 4.7). Thus, the two subdivisions - the Upper and Lower GRV - represent an ideal analogue to observe the effects of hybridisation and isotopic reservoir interaction on Pb-isotopic evolution of the Hiltaba Event magmatic system as a whole. Figure 4.12 shows that the earlier phase of volcanism, the LGRV, has mantle-like Pb-isotopic signatures ($^{238}U/^{204}Pb$ = 9.15 – 9.45, $^{232}Th/^{238}U$ = 3.64 – 3.65) most similar to the Pleistocene Bandelier Tuff from the Valles Caldera (Wolff and Ramos, 2003), and volcanics of the Central San Juan caldera cluster (Riciputi et al., 1995). The Pb-isotopic data from Valles and the Central San Juan was interpreted by Wolff and Ramos (2003) and Riciputi et al. (1995) to implicate a major magma component derived from the mantle, with only minor but important, crustal hybridisation. Similar, very minor open-system isotopic behaviour may explain the range of Pb-isotopic signatures in the Lower GRV, however the consistently-low $^{232}Th/^{238}U_{(t)}$ suggest that the non-mantle Pb was likely not from the lower crust. Further, since mantle-like Pb-isotopic signatures are still preserved in the high-SiO_2 (>75 wt. %) Lower GRV samples analysed here, it can be implied that the mafic to felsic compositional range seen in the Lower GRV was dominantly the result of closed-system magmatic processes such as crystal fractionation. This is geochemically supported by the pronounced Eu-

depletion compared with the Upper GRV, which in light of the Pb-isotopic data, indicates extensive fractionation of feldspar was experienced by the Lower GRV as it evolved from mafic to felsic compositions.

The mantle-like Pb-isotopic results of the Lower GRV contrast with the consistently more-crustal Pb-isotopic signature of the slightly-younger Upper GRV ($^{238}U/^{204}Pb$ = 9.68 – 10.08, $^{232}Th/^{204}Pb$ = 3.92 – 4.10). The Pb-isotopic composition of the Upper GRV is most comparable to the high-$^{232}Th/^{238}U_{(t)}$, -$^{238}U/^{204}Pb_{(t)}$ signature of volcanics from the Snake River Plain (Wright et al., 2002) and Yellowstone (Doe et al., 1982; Rivera et al., 2016) (Fig. 4.12). Overall, this signature in the Upper GRV

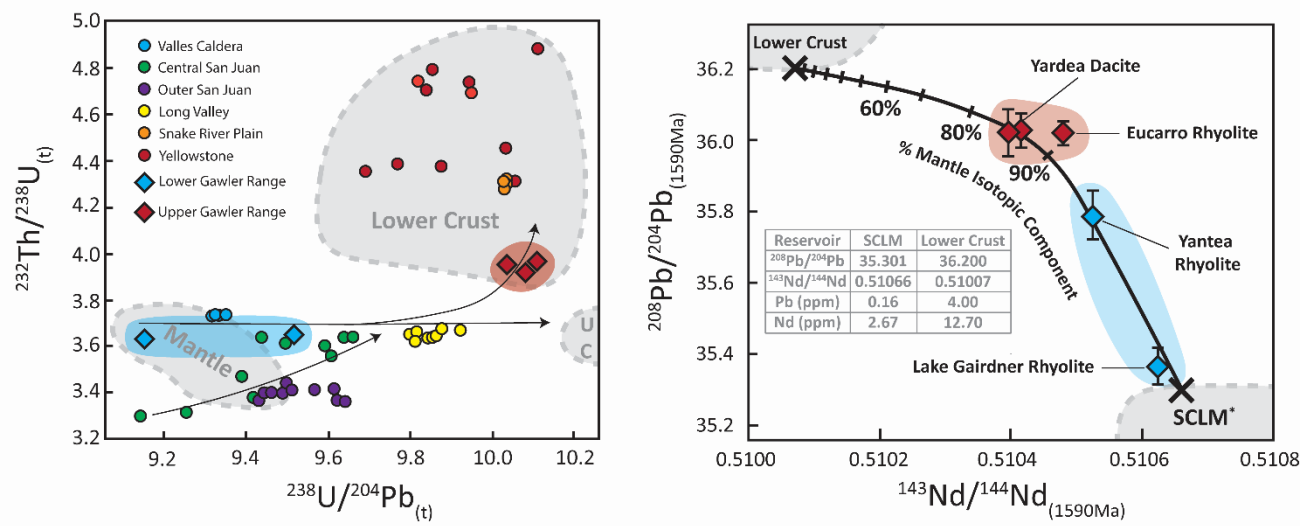

Figure 4.12: (a) A comparison between initial Pb-isotopic characteristics of recent (<Miocene), felsic (SiO_2 > 65 wt.%) A-type volcanic centres with the c.1590 Ma volcanics of the GRV. (b) Binary Pb-Pb vs. Nd-Nd isotopic mixing models suggest the Lower GRV reflects less than 10% (max.) crustal addition to a SCLM-like melt (Pb (ppm) = 0.16, Nd (ppm) = 2.67; based on McDonough (1990)), while the Upper GRV requires approximately 15 to 20% (min.) lower crustal contribution (Pb (ppm) = 4, Nd (ppm) = 12.7; based on Taylor and McLennan, 1995). Pb-isotopic data from Wolff and Ramos, (2003) (Valles); Riciputi et al., (1995) (Central San Juan), Lipman et al., (1978) (Outer San Juan); Davies et al., (1994) (Long Valley); Heumann et al., (2002) (Long Valley); Wright et al., (2002) (Snake River Plain); Doe et al., (1982) (Yellowstone); Rivera et al., (2016) (Yellowstone).

implies a lower crustal source-component. Homogeneous Pb-isotopic compositions in the Upper GRV both between units (i.e. Eucarro Rhyolite and Yardea Dacite) strongly suggests that thorough mixing of the mantle- and crustal melt signatures occurred prior to eruption of the Upper GRV lavas. Crucially, the difference between the Upper and Lower GRV Pb-isotopic signatures implies one of two scenarios; either the Upper and Lower GRV are not co-magmatic (i.e. the lavas were derived from two or more magma chambers), or the role of a crustal melt component became increasingly important with time. High, contemporaneous, regional geothermal gradients including ultrahigh

temperature metamorphism identified in the northern Gawler Craton (Cutts et al., 2011), may have contributed to an increase in the crustal melt component through time, as seen in the Upper GRV. The evolution of the GRV magmatic system from primarily mantle-derived magmas, towards increasingly-crustal compositions is particularly significant due to the relatively short time constraints (<2 Ma; Jagodzinski et al. (2016)) on generating such large volumes of crustal melt, and then mixing them with a mantle-derived melt to the degree of homogeneity observed in the Upper GRV lavas.

Mass-balance modelling provides an insight into the fundamental mantle-crustal melt proportions required to form the Lower and Upper GRV isotopic signatures, and also the development of large magmatic systems in general. While simplistic (i.e. two end-members), utilising both Nd- and Pb-isotopic systems ensures that the model is not biased towards either the age of the components (due to variations in the concentration of parent isotopes as well as their respective decay constants) nor the crustal end-member(due to contrasting concentrations of daughter isotopes between mantle and crust). The modelling parameters for both the lower crustal and SCLM end-members are detailed in Figure 4.12, while modelling was achieved using the FC-AFC-FCA-Mixing modeller of Ersoy and Helvacı (2010). Nd-isotope and geochemical data for the SCLM end-member were adapted after the least-radiogenic LGRV Nuckulla basalts reported in Stewart (1994), while Pb-isotopic compositions were adapted after SCLM modelling of Zartman and Haines (1988). The Pb-isotopic parameters for the lower crustal end-member are also based on the modelling of Zartman and Haines (1988) assuming a $^{232}Th/^{238}U_{(t)}$ = 4.009, with $^{143}Nd/^{144}Nd_{(1590Ma)}$ calculated based a Sleafordian-aged (2440 Ma) protolith with $\varepsilon_{Nd(2440\ Ma)}$ = 0, and average lower-crustal whole-rock concentrations of Nd-Pb suggested by Taylor and McLennan (1995).

The results of binary-mixing modelling (Fig. 4.12) suggest that the isotopic signature of the Lower GRV could be accounted for by as little as 3 – 8% of lower crustal melt component. In order to account for the more radiogenic Nd-Pb signature in the Upper GRV, however, the contribution of crustal melt would need to increase to 3 to 4-fold, to 15 – 20%. These values are in accordance with

the <30 vol. % crustal melt proportion suggested for the Upper GRV by Stewart and Foden (2003), on the lower side of the ~15 – 40 vol. % range suggested by Creaser and White (1991), but far smaller than the >90 vol. % crustal melt contribution suggested by Giles (1988) and Kilpatrick and Ellis (1992). The estimates of crustal melt proportion in the GRV lavas presented here are consistent with other estimates of A-type magmas elsewhere in the world. For example, Haapala and Rämö (1992) suggested a ~20 vol. % crustal melt component was involved in the genesis of the Fennoscandian rapakivi granites, while both Anderson (1983) and Kerr and Fryer (1993) estimated 10 – 30 vol. % crustal component was required to form the anorogenic granites of the midcontinental U.S.A. and Canada. Together, these demonstrate that the Hiltaba Suite/ GRV, and A-type magmas in general, most likely represent volumetrically-dominant mantle-derived material with minor contributions of lower crustal material conveying the characteristic enrichments of HFSE and LREE.

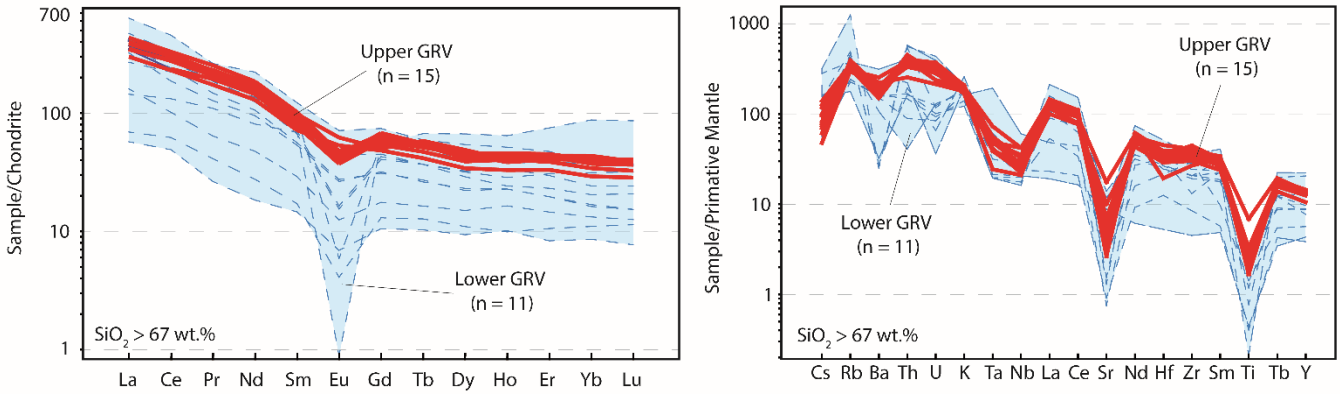

Figure 4.13: (a) Chondrite-normalised (McDonough and Sun, 1995) and (b) Primitive mantle normalised diagrams of the felsic (SiO_2 > 67 wt.%) Lower (LGRV) and Upper Gawler Range Volcanics (UGRV). Primitive-mantle normalising values after McDonough et al., (1992). Geochemical data for the LGRV from Agangi et al., (2011) and Fricke, (2005). Upper GRV geochemical data from Stewart, (1994) and Curtis, (not published; OZCHEM database accessed through: https://d28rz98at9flks.cloudfront.net/65464/65464_sa.zip*).*

Maximum crustal melt contributions of less than 20% are also in line with theoretical and experimental constraints on partial melting of water-poor crustal lithologies (Clemens et al., 1986; Clemens and Vielzeuf, 1987; Patiño Douce and Johnston, 1991). The large contrast in lava volume between the LGRV (<530 km^3; Agangi et al. (2012)) and UGRV (>4000km^3; Allen and McPhie (2002)), combined with the limited range in isotopic (Fig. 4.7) and geochemical compositions (Fig. 4.13) of

the Upper GRV indicates that batch melting higher than 20 – 30% would exceed the fertility limit of an anhydrous crustal source ((Clemens et al., 1986; Clemens and Vielzeuf, 1987; Patiño Douce and Johnston, 1991). For low water contents (e.g. <2%; Creaser and White (1991)) and high minimum temperatures of the Upper GRV melt indicated by zircon saturation temperatures (890-895°C), experimental work (Clemens and Vielzeuf, 1987; Patiño Douce and Johnston, 1991) suggests maximum melt productivity in the order of ~40% to ~85%, and ~45% at 5 and 7 kbar, respectively. Therefore, even at anhydrous conditions likely experienced in the lower crust of the Gawler Craton at the time of mantle-melting, crustal melt contributions in the order of 20% was achievable.

4.7.6 Spatial controls on Pb-isotopic signature as an indicator for tectonic setting of the Hiltaba Suite/ GRV

Initial Pb-isotopic results of Hiltaba Suite intrusives (and GRV) reveal a craton-wide zonation (Fig. 4.14). In general, $^{238}U/^{204}Pb_{(t)}$, $^{235}U/^{204}Pb_{(t)}$ and $^{232}Th/^{204}Pb_{(t)}$ all increase away from the edge of the Nuyts Terrane in the southwest, towards the Olympic Domain in the east (Fig. 4.14). Both unradiogenic and radiogenic Pb-isotopic reservoir signatures are intrinsically related to isotopic variations in the crust rather than a geodynamic constraint. The mantle-like Pb-isotopic signatures, however, are more-difficult to preserve even with relatively modest crustal melt contributions (i.e. ~10%) and are likely to indicate proximity to the parental mantle-derived melt source. Thus, the craton-wide zonation with mantle-like Pb-isotopic signatures closest to the Nuyts Terrane (central-west), and more crustal-like signatures further afield (east and north) may provide a clue to the geodynamic mechanisms for formation of the Hiltaba Suite/ GRV magmatic event.

Three intensive parameters for the mantle-derived melt source are seemingly at odds with one another, and require consideration before discussing the potential tectonic setting of the Hiltaba Suite/ GRV. Firstly, from our reported Pb-isotopic values, as well as constraints provides by Nd-isotopic ($\varepsilon Nd_{(1590Ma)}$ = +2.5 to -0.9; Fricke (2005); Stewart (1994)) and Hf isotopic ($\varepsilon Hf_{(1590Ma)}$ =

+2.73 to + 4.95; Pankhurst et al. (2013)) compositions of the most primitive known GRV basalts, an enriched mantle source (such as SCLM) is required. This is consistent with pressure estimates of 1 – 1.5 GPa for the generation of these primitive basalts (Tregeagle, 2014), placing them in the upper SCLM beneath the Gawler Craton. However, previous studies suggest a temperature range of 1000 – 1300°C for these basalts (Agangi et al., 2012; Tregeagle, 2014), which is consistent with asthenospheric mantle rather than those predicted for SCLM (~850°C). Thus a mechanism is required which allows for the increasing enriched-mantle-melt component toward the west, at asthenospheric-temperatures and SCLM- pressures. This seeming paradox is usually accounted for either by invoking models related to plume-driven extensional tectonics (Anderson et al., 2003; Haapala and Rämö, 1992; Kerr and Fryer, 1993) or post-orogenic SCLM delamination (Whalen et al., 1996).

An alternative explanation for the Pb-isotope variability of the Hiltaba Suite/ GRV magmatic systems incorporates penecontemporaneous subduction-related processes related to the St Peters Suite (1630 – 1608 Ma) in the western Gawler Craton. The subduction zone related to the formation of the St Peters Suite was active just 13 Ma prior to initiation of the earliest GRV volcanism at ~1595 Ma (Jagodzinski et al., 2016), placing the Hiltaba Suite/ GRV within a continental back-arc setting (Swain et al., 2008). The direction of this subduction zone is unclear, with both north- (Betts and Giles, 2006) and south-directed (Swain et al., 2008) subduction considered plausible. If north-dipping subduction were the case (Fig. 4.14), underplating of mafic melts beneath the Gawler Craton nucleus was likely to have taken place close to the subduction front. Asthenospheric mantle upwelling was driven by the down-going slab and sufficiently increased temperatures within the SCLM to instigate melting at SCLM-like pressures. This scenario provides an explanation for mantle-like Pb-isotopic compositions in Hiltaba Suite intrusive rocks closest to the Nuyts Terrane (Fig. 4.14). A similar mechanism has been proposed for the volcanics of the Basin and Range Province (i.e. Dixon et al. (2000)), which have comparable Pb-isotopic constraints on parental melt source (Fig. 4.12). Further away from the Nuyts Terrane, Pb- and Nd-isotopic signatures are controlled by an increase in crustal

melt contribution, which varies based on the innate U-Th-Pb characteristics of that particular crust. While the zonation from mantle-like Pb-isotopic compositions in Hiltaba Suite intrusive rocks in the west, to more crustal signatures in the east and north does not require a hot spot-based model, our work does not rule out such a model for the transition from mantle-dominated Lower GRV Pb isotope compositions towards a more-crustal Pb isotope compositions in the Upper GRV.

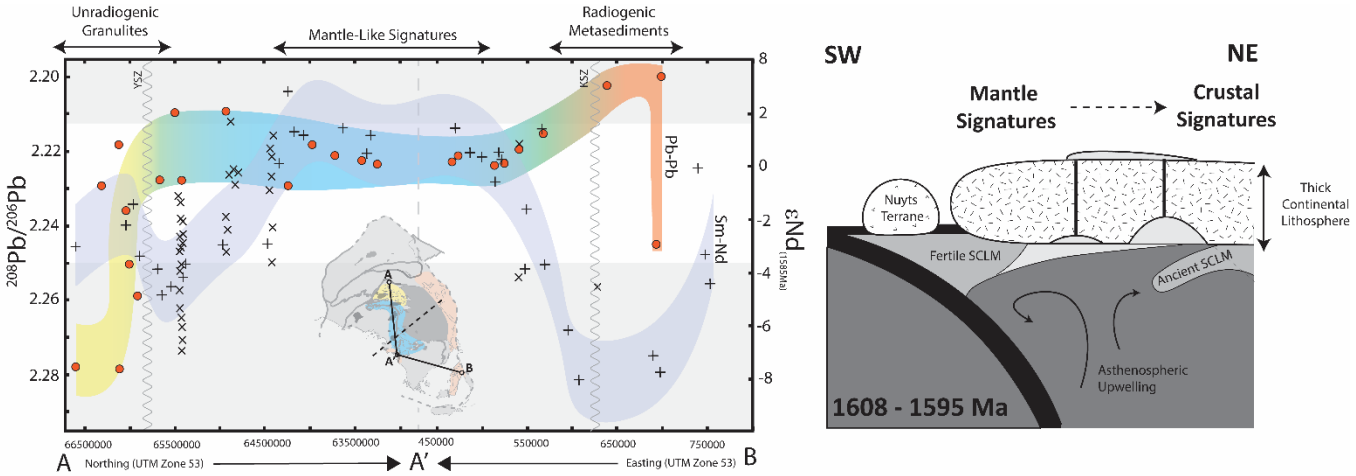

Figure 4.14: An outline of the spatial-control on isotopic composition (Pb-Pb and Sm-Nd) of the Hiltaba Suite and GRV, and possible geodynamic setting. (a) N-S, then E-W transect across the Gawler Craton highlighting the major isotopic variation revealed in the Hiltaba Suite/ GRV. Nd-isotopic data after Stewart and Foden, (2003). YSZ = Yarlbrinda Shear Zone, KSZ = Kalinjala Shear Zone (b) A schematic interpretation for the geodynamic setting of the HSGRV within a continental back-arc.

4.8 Conclusions

The Pb-isotopic results and discussion presented here, reveal a craton-wide zonation in the isotopic and geochemical composition of the Hiltaba Suite, which is the result of complex mixing between three end-member Pb-isotopic reservoirs; sub-continental lithospheric mantle (SCLM), unradiogenic lower crust, and radiogenic lower crust.

Mantle-like Pb-isotopic signatures in the Lower GRV imply that the earliest phase of magmatism associated with the Hiltaba Suite/ GRV event was driven by the addition of mantle-derived melts to the crust with little contribution from crustal melting (>8%). Similar Pb-isotopic

compositions are preserved in the Hiltaba Suite granitoids nearest to the Nuyts Terrane, whose mantle-like signature may be associated with an increased prevalence of fertile SCLM related to the north-east trending subduction zone which terminated <15 Ma prior.

Higher-$^{238}U/^{204}Pb_{(t)}$ and $^{232}Th/^{238}U_{(t)}$ Pb-isotopic signatures in the Upper GRV require that either the Upper and Lower GRV are not co-magmatic (i.e. represent discrete magma systems), or reflect almost a three-fold increase in crustal melt contribution over the space of 2 Ma coinciding with a more-than four-fold increase in lava volume. The radiogenic crustal reservoir responsible for these Pb-isotopic compositions is similar to the one involved in the generation of Hiltaba Suite granites in the eastern Gawler Craton, which advocates for discrete magma systems.

Correlation between trace-elements abundances which are characteristically-high in A-type rocks (i.e. LREE and HFSE) and crustal Pb-isotopic signatures implies that these geochemical features are provided to some extent by the crustal melt component, rather than solely enriched by closed-system processes such as crystal fractionation. The highest LREE-HFSE abundances coupled with a high-U/Pb and Th/U source signature for the most radiogenic Hiltaba Suite/ GRV suggests that the crustal reservoir responsible for these Pb-isotopic compositions is a monazite-rich metasediment.

The occurrence of unradiogenic Pb-isotopic signatures in the Hiltaba Suite – that is, Pb-isotopic compositions yielding model ages in the past – is spatially-restricted to the central-northern Gawler Craton, and implies that the crustal melt source for these rocks was U-depleted granulitic lower crust. Such dry, lower crustal rocks are commonly invoked in the literature as important in the generation of A-type geochemical characteristics. However, the non-specific nature to which crustal signatures are inherited in the Hiltaba Suite/ GRV and A-types worldwide would suggest that the underpinning mechanism for forming A-type magmas is the voluminous addition of an enriched mantle-derived melt into the crust. While the crustal melt component of A-types may be small (<20%), correlation of Pb-isotopic signatures with LREE and HFSE in the Hiltaba Suite/ GRV implies that the crust plays an important role in providing the enrichment of these elements characteristic of A-types.

Acknowledgements

This research was funded by BHP Olympic Dam Operations, which we gratefully thank. We also thank Jay Thompson from the CODES LA-ICP-MS laboratory as well as Karsten Gormann and Sandrin Feig from the Central Science Laboratory for their technical assistance. The editorial handling by Andrew Kerr and input from three anonymous reviewers is greatly appreciated and improved the manuscript significantly.

Chapter 5: Integrating Pb-Isotopic And Crystallographic Analyses On Alkali Feldspar Of The Roxby Downs Granite – Constraints On The Melt-Source And Cooling History Of The Host To Olympic Dam

Chapman, N. D.[1], Meffre, S. J.[1], Gardiner, M. G.[2], Maas, R.[3], Ehrig, K.[4]

[1]Transforming the Mining Value Chain (TMVC) ARC Industrial Transformation Research Hub, University of Tasmania, Hobart, Australia

[2]School of Chemistry, University of Tasmania, Hobart, Australia

[3]School of Earth Sciences, University of Melbourne, Melbourne, Australia

[4]BHP Olympic Dam Operations, Adelaide, Australia

5.1 Abstract

Despite hosting the world's largest polymetallic accumulation - Olympic Dam - little is understood about how the 1593 Ma Roxby Downs Granite (RDG) may have participated in the ore-forming process. Even less is known about the petrogenetic origins of the RDG, or whether melt-sources enriched in ore-metals such as U, played a role in forming the unique metal inventory and endowment of Olympic Dam.

To answer these questions, integrated in situ crystallographic (synchrotron and single-crystal x-ray diffraction (SCXRD)) and Pb-isotopic analyses (laser ablation multicollector inductively coupled plasma mass spectrometry (LA-MC-ICPMS) were undertaken on K-bearing feldspars. Pb is incorporated into the crystal lattice of K-feldspars while U and Th are excluded thus preserving the initial U-Th-Pb signature of the melt sources involved. Furthermore, crystal-lattice parameters of these K-bearing feldspars provide a means by which to trace the cooling evolution of the RDG from orthomagmatic conditions, through to late-stage and deuteric re-equilibration.

Initial Pb-isotopic compositions ($^{206}Pb/^{204}Pb$ = 16.465 ± 0.052, $^{207}Pb/^{204}Pb$ = 15.524 ± 0.050, $^{208}Pb/^{204}Pb$ = 36.310 ± 0.1159) yielded from rare, pristine alkali feldspar (Or_{56}) reveals that the RDG

was partially-derived from an Archean crustal melt (~20%) which was anomalous in both U ($^{238}U/^{204}Pb$ = 11.084) and Th ($^{232}Th/^{204}Pb$ = 4.032) with regard to typical crustal abundances. Therefore, part of the reason for the anomalous tenor of U-mineralisation at Olympic Dam may be due to innate enrichment of the host granite. Crystal-lattice parameters determined using both synchrotron and SCXRD confirm that the alkali feldspar formed under orthomagmatic conditions (830 – 870°C), and thus preserves the Pb-isotopic signature of the melt-sources involved in generating the RDG.

By contrast, the common brick-red K-feldspar (Or_{80-99}) of the RDG which replaces the primary alkali feldspar display a wide-range of Pb-isotopic signatures ($^{207}Pb/^{206}Pb$ = 0.927 – 0.608, $^{208}Pb/^{206}Pb$ = 2.172 – 1.433). Pb-isotopic disequilibrium between the two feldspar phases indicates that replacement did not occur through topochemical processes (i.e. Al-Si reordering) and instead suggests that feldspar replacement occurred either some-time after granite emplacement, or during open-system exchange with an external Pb-reservoir, such as the surrounding country rocks. Unit-cell parameters indicate that K-feldspar formation occurred at temperatures consistent with the earliest stages of hydrothermal ore-genesis at Olympic Dam (400 - 300°C). This is reconcilable with the fluid-mixing model invoked for the formation of Olympic Dam, and highlights the potential importance of open-system process in ore genesis.

5.2 Introduction

The 1593 Ma Roxby Downs Granite (RDG) plays host to the world's largest mineral accumulation yet discovered – the Olympic Dam iron oxide-copper-gold-uranium (IOCG-U) deposit. The RDG, part of the larger Burgoyne Batholith, is generally considered to be more than a passive host to mineralisation; it is thought to have provided some metal contribution to ore-formation of this supergiant deposit. However it remains poorly understood just how the RDG may have participated in the ore-forming process, or even the importance of its contribution to ore-formation. Was the

RDG generated from a melt-source anomalous in ore-forming metals, such as U? Was the RDG the sole metal contributor to ore-formation at Olympic Dam? How might the evolution from orthomagmatic to magmatic-hydrothermal conditions have influenced metallogenesis at Olympic Dam?

Understanding the melt-sources involved in generating the RDG is fundamental to understanding the contribution of the RDG to ore-genesis of Olympic Dam and reasons why the RDG should be prospective for IOCG-style mineralisation. If the RDG was partially-derived from a crustal reservoir enriched in U-LREE, then the reason for the anomalous endowment of these elements within the ores of Olympic Dam can be simply explained. Pb-isotopic studies of K-rich feldspars provide a means to test whether the ancient melt-sources involved in generating the RDG were, in fact, enriched in U. This is possible for two reasons. Firstly, the time-scales involved in the radioactive decay of U (and Th) to Pb are orders of magnitude greater than the time-scales involved in melt-generation through to crystallisation, and thus the Pb within even a late-stage melt preserves the U/Pb, Th/Pb and U/Th characteristics of its melt source(s). Secondly, while Pb is incorporated into the crystal structure of K-rich feldspars, U (and Th) is not, and therefore the Pb within a K-feldspar preserves the initial Pb-isotopic signature of the melt source(s).

How the RDG may have contributed to ore-formation remains one of the least-well understood aspects of ore genesis. Previous authors have concluded through geochemical- and mineralogical constraints of the ore assemblage, that formation of Olympic Dam probably required mixing between a higher-temperature granite-derived fluid component, and a lower-temperature fluid sourced externally from the RDG (Bastrakov et al., 2007; Haynes et al., 1995; Oreskes and Einaudi, 1992). K-feldspar is a ubiquitous mineral in the RDG, and is also part of the high-temperature alteration assemblage of Olympic Dam, and thus records the cryptic cooling history of the RDG, from orthomagmatic stages through to ore-formation. In our contribution to understanding how the RDG may have contributed to ore-genesis, we integrate in situ

crystallographic and Pb-isotopic analyses of alkali feldspars (K+Na) and K-feldspars in an attempt to unravel the final stages of the magmatic to post-magmatic history of the RDG. Previous attempts to ascertain the initial, magmatic Pb-isotopic signature of the RDG have failed (Nuemann, 2001), yielding spuriously-radiogenic results indicative of modification after granite crystallisation. It is hypothesised that if formation of paragenetically-later K-feldspar formed as a result of open-system fluid-mixing and alteration, Pb-isotopic exchange should also be recorded in these feldspars, providing constraints on the timing and/or source of the externally-derived fluids.

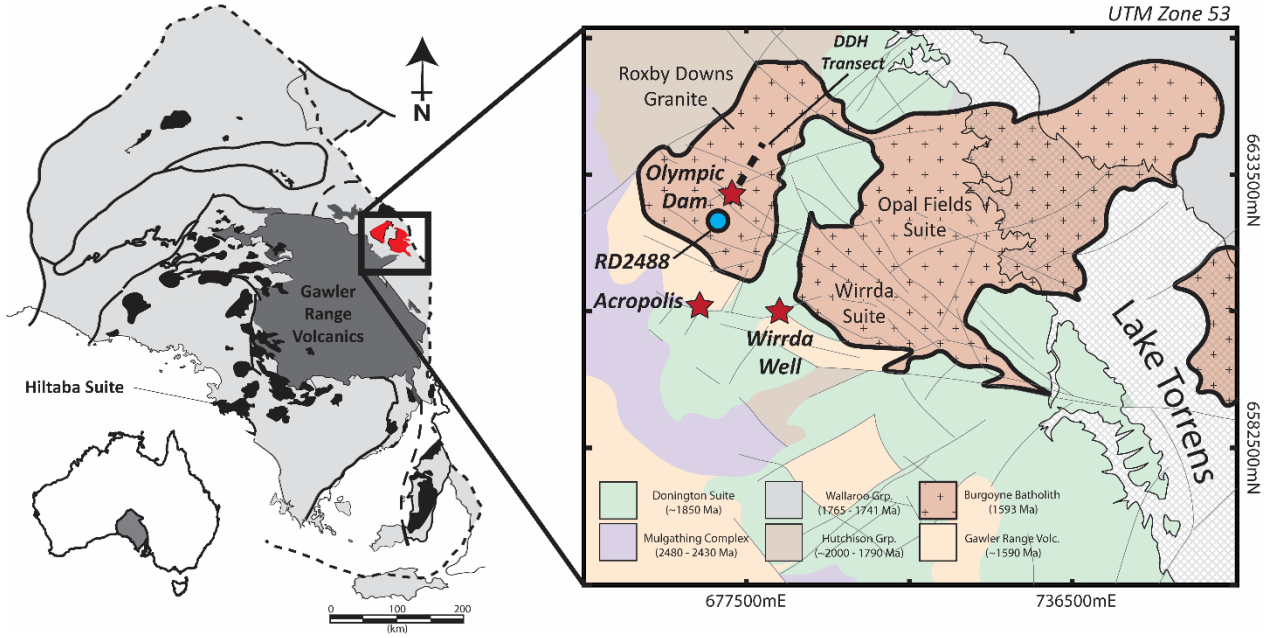

Figure 5.1: Regional-, and district-scale geological context of the 1593 Ma Roxby Downs Granite (red, left). The Roxby Downs Granite (RDG) belongs to the regionally-extensive Hiltaba Suite intrusives (black, left) and coeval Gawler Range Volcanics (mid grey, left). The RDG is a member of the Burgoyne Batholith, which also comprises the informal Wirrda and Opal Fields subsuites (Creaser, 1996). The RDG (and Burgoyne Batholith) mostly intrudes megacrystic granitoids of the ~1850 Ma Donington Suite and volcaniclastic metasedimentary sequences of the ~1765 Ma Wallaroo Group.

5.3 Geological Context

The 1593 Ma Roxby Downs Granite is a sub-divided unit of the much larger Burgoyne Batholith, which is located in the north-east of the Gawler Craton, South Australia (Fig. 5.1). The Burgoyne Batholith is informally divided into the Wirrda Sub-suite (east) and Opal Fields Sub-suite (White Dam; Creaser (1996)), which range in composition from low-SiO_2 (~56 wt. %) quartz monzodiorites, to

high-SiO_2 (75 wt. %) granites and syenites. Complementary trace-element signatures in the high- and low-SiO_2 granitoids indicates that geochemical and mineralogical variation developed principally through cumulate-like differentiation (Creaser, 1996).

The Burgoyne Batholith, like the RDG,is a member of the voluminous Hiltaba Suite granitoids which are distributed across much of the Gawler Craton (Fig. 5.1). The A-type Hiltaba Suite intrusives are coeval with the extensive felsic volcanism of the Gawler Range Volcanics, and developed over a period from ~1595 to 1575 Ma. Significant disagreement exists in the literature regarding the petrogenetic processes which led to the formation of the Hiltaba Suite/ GRV magmatic rocks. The prevalence of pyroxene-bearing, high-temperature assemblages indicates that these felsic rocks developed from a relatively hot, dry, melt (<2 wt. % H_2O; T > 1000°C). Geochemical evidence for the origin and contribution of a mafic-component is obscured by dominant geochemical characteristics (i.e. high-K, F-, LILE-, REE- and HFSE-enriched) which are more akin to crustal-derived melts. Nd-isotopic compositions of picritic basalts associated with the GRV suggest the mafic component is derived from an enriched sub-continental lithosphere, which inhibits simple delineation of crustal-mantle contributions from the Sm-Nd isotopic system alone. Work by Creaser and Fanning (1993) clearly demonstrates that crustal partial-melts are an integral part of the isotopic and geochemical characteristics of the Hiltaba Suite, with the most-evolved signatures (Creaser and Fanning, 1993; Fraser et al., 2010) observed in the Charleston Granite, which intrudes a Mesoarchean granite. Similarly, strongly evolved εNd_t signatures of the RDG and other granitoids of the Burgoyne Batholith hint at the role of Archean- to Paleoproterozoic crust as a melt source. Crucially, the Hiltaba Suite/ GRV represents the last major tectonothermal event to affect the Gawler Craton, and as such have been largely unaffected by deformation which may have reset the Pb-isotopic signature of the feldspars.

The Burgoyne Batholith and surrounding crystalline-basement is largely hidden beneath more than 200 m of Mesoproterozoic to Cambrian marine sediments. Deformed granitoids of the

1850 Ma Donington Suite comprise much of the known basement intruded by the Burgoyne Batholith. The spatial extent of other lithologies is largely interpreted from geophysics (Fig. 5.1). Proposed basement lithologiesrange from Archean-Early Paleoproterozoic high-grade metamorphics of the Mulgathing Complex, mid-grade metasediments of the Hutchison Group, and low-grade schists of the Mid Paleoproterozoic Wallaroo Group (Fig. 5.1).

5.4 Methodology

5.4.1 Samples and Sample Location

Feldspar samples from least-altered Roxby Downs Granite (RDG) were obtained from quartered HQ drillcore of RD2488 at 767 and 770m depth, which is the furthest drillhole south of Olympic Dam (~6.5 km; Fig. 5.1). All drillholes to the north of Olympic Dam intercept RDG which is moderately- to strongly-altered, containing chloritised biotite, and turbid, brick-red K-feldspar and plagioclase.

The RDG sampled from RD2488 (Fig. 5.2a) is medium- to coarse-grained monzogranite, with K-feldspar (35%), plagioclase (30%), quartz (30%), biotite (5%) and magnetite (<1%) comprising the major rock-forming minerals. Equant, K-feldspar crystals are approximately 1 cm in size, and display complex colour zonation, from clear/ translucent to cloudy and red (Fig. 5.2b). Larger phenocrystic plagioclases (1 cm) are mostly-turbid in hand specimen, however also preserve domains of unaltered, translucent plagioclase (Fig. 5.2b). Biotite is often well-preserved, with only minor alteration to chlorite. Quartz is coarse-crystalline (0.5 – 1 cm) at 770 m, becoming more-granophyric towards 400 – 450m.

5.4.2 Sample Preparation

K-feldspar crystals retaining pristine domains were cut out of drillcore into 2 cm round pucks, using a diamond-bladed rock saw. Samples were then prepared into standard 25 mm epoxy resin mounts and polished to 0.01 µm-diamond-grade. Samples then underwent a cleaning protocol involving an ethanol rub followed by an ultrasonic bath in de-ionised H_2O for 20 min, oven-drying at 60°C for 30

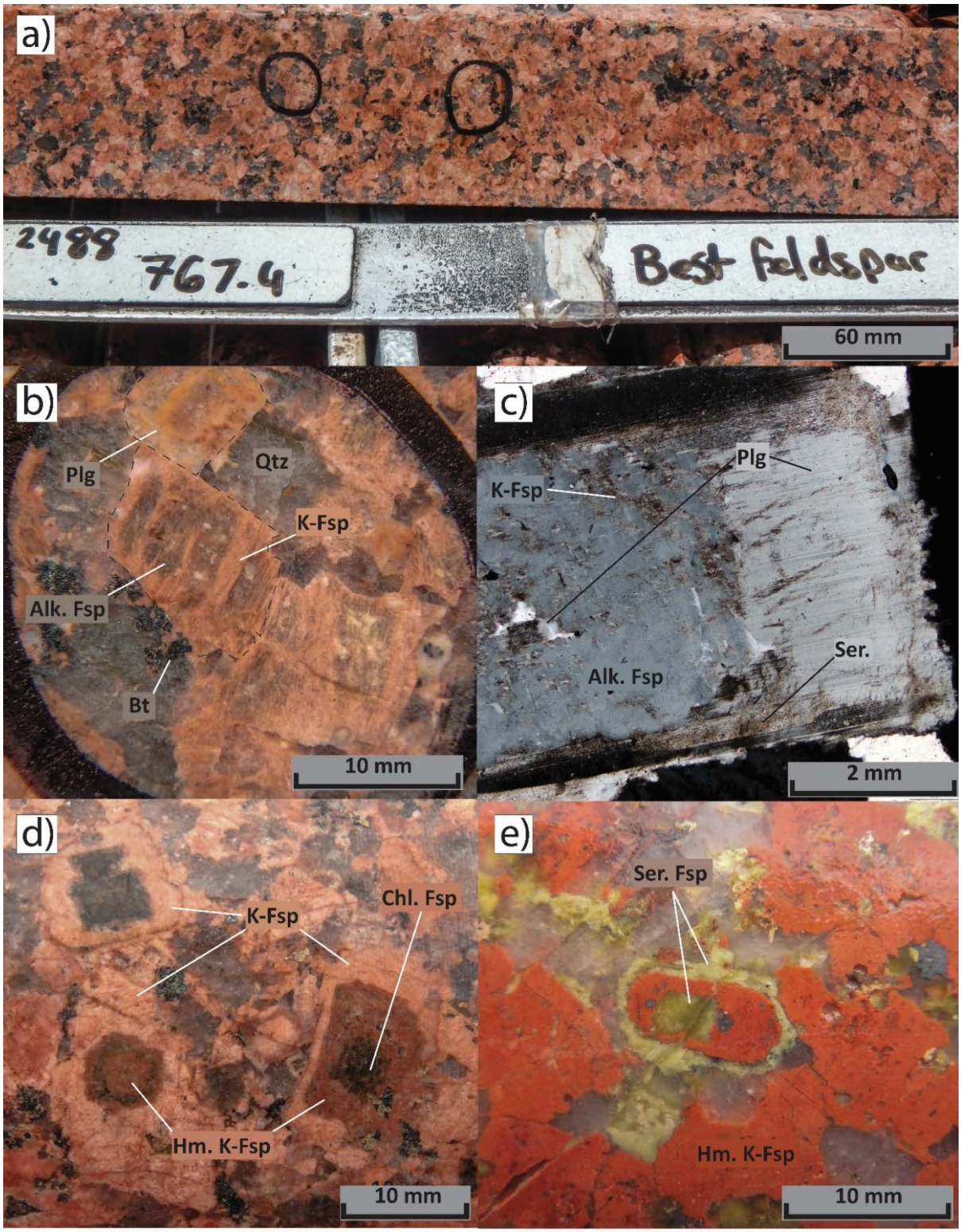

Figure 5.2: (a) An example of the least-altered Roxby Downs Granite (RDG) from drillcore located approximately 6.5 km from the Olympic Dam deposit (DDH RD2488 770m). (b) A close up of the left-area circled in (a) showing the rare, preserved orthomagmatic alkali feldspar (Or_{55}; 'Alk. Fsp') being partially-converted to a pink, near-endmember K-feldspar (Or_{80-99}; 'K-Fsp'). (c) Thin-section view (xpl) of the feldspars of the RDG. Here, oligoclase ('Plg'; $Ab_{\sim 83}$) is mantling euhedral alkali feldspar ('Alk. Fsp') which is undergoing partial-conversion to microcline ('K-Fsp'). Note that plagioclase contains only very minor sericite-dusting ('Ser.') around the crystal margins. (d, e) Examples of the alteration-styles of the feldspars with increasing proximity to the Olympic Dam deposit. In general, the Fe-content of the K-feldspars increases towards Olympic Dam (indicated by the red colouration from Fe_2O_3). Alteration of individual feldspars often displays complex domaining, related to innate zonation of the original feldspar crystal. For example, note the similarity between the location of vibrant-green sericite areas in (e) and the domains of plagioclase – both on the rim and centre – in (c).

mins and finally carbon-coating. A series of reconnaissance SEM mapping techniques (described below) were then carried out on samples in order to characterise mineral purity, geochemistry and to assist with laser targeting.

5.4.3 SEM and Hyperspectral CL

Wavelength dispersive spectroscopy (WDS) and hyperspectral cathodoluminescence (CL) spectra and images were obtained on a JEOL JXA-8530F Plus field emission electron microprobe, fitted with a JEOL xCLent IV hyperspectral system housed at the Central Science Laborartory, University of Tasmania. A 20 kV acceleration voltage and a 20 nA emission current were used during measurements. For WDS and hyperspectral CL mapping, a step-size of 4 µm with a dwell-time of 40 ms led to the development of images comprising a total of 250 000 individual pixels of data.

5.4.4 Crystallography

Crystal fragments (300 - 500 um) of pristine alkali feldspar sited using SEM techniques detailed above, were hand-microdrilled, washed in acetone, rinsed in distilled water and allowed to evaporate dry in an oven at 60°C for 5 hours. Feldspar samples prepared for synchrotron analysis were obtained from fragments of thick-section which were microdrilled under petrographic microscope. Feldspar samples for both SCXRD and synchrotron were oil-mounted onto Hampton Scientific cryoloop filaments.

Transparent fragments of the most pristine alkali feldspar yielding the least-radiogenic Pb-isotopic compositions were examined on a Bruker AXS D8 Quest, Single-Crystal XRD (SCXRD) (150 µm microfocus) using Cu-Kα (λ = 1.54178 Å) housed at the University of Tasmania. Measurements were collected at 295 K (21.9°C) to a resolution of 0.84 Å using the strategies suggested by the SCXRD control software set to a redundancy of 3.

Twinning inference in microcline samples ($Or_{>80}$) were mitigated and refined using the high-spatial resolution (5 μm) of the MX2 micro-collimated beamline at the Australian Synchrotron. Data was collected at 20°C using a wavelength of (0.71069 Å) with a fixed-point detector. Rotation of the single-axis goniometer was limited to 60° of total rotation (1° frame slices) in order to prevent adjacent twin-phases from encroaching into the beamline.

Crystal structure solutions and refinements for both Synchrotron and SCXRD data were achieved by direct methods using SHELXT (Sheldrick, 2015b) and full-matrix least squares routines against F^2 using SHELXL (Sheldrick, 2015a), respectively. Visualisation was achieved using the OLEX2 program of (Dolomanov et al., 2009). All non-hydrogen atoms were refined anisotropically without restraints. Refinement of Al/ Si disorder was guided by observed T-O distances and combined with major elemental analyses gained from WDS (described above).

5.4.5 In situ LA-MC-ICP-MS

In situ, laser ablation multicollector ICP-MS (LA-MC-ICP-MS) Pb-isotopic analyses of feldspar were conducted at the University of Melbourne. A Coherent COMPex Pro 193 nm Excimer laser system, containing a Laurin Technic RESOlution S155 ablation cell were coupled to a Nu Plasma MC-ICP-MS, which was stabilised pre-session on a desolvator (due to He sensitivity of plasma), before additional stabilisation under gas-only conditions. Carrier gases were introduced to the plasma at a flow-rate of 210 mL/sec and 900 mL/sec for He and Ar, respectively. Instrument tuning was undertaken using laser-traverses of NIST610 glass.

Ablation sequencing and measurement acquisition were conducted on full-manual mode to ensure complete signal wash out. Background measurements we conducted over a 30 sec period, prior to laser-on measurement which lasted from 30 – 45 secs depending on the quality of data. Large spot sizes (200 μm), low fluence (3 J/cm^2), coupled with a slow laser repetition-rate (5 Hz) negated downhole-signal loss and compensated for low-Pb signal (<30 mV) in the alkali feldspar

sample (Fig. 5.3).

Data reduction was achieved offline using the iolite program (Paton et al., 2011). Isobaric interference caused by ^{204}Hg on ^{204}Pb was corrected independently using the peak-stripping method outlined in Willigers et al. (2002), and a ^{204}Hg:^{202}Hg ratio of 4.32.

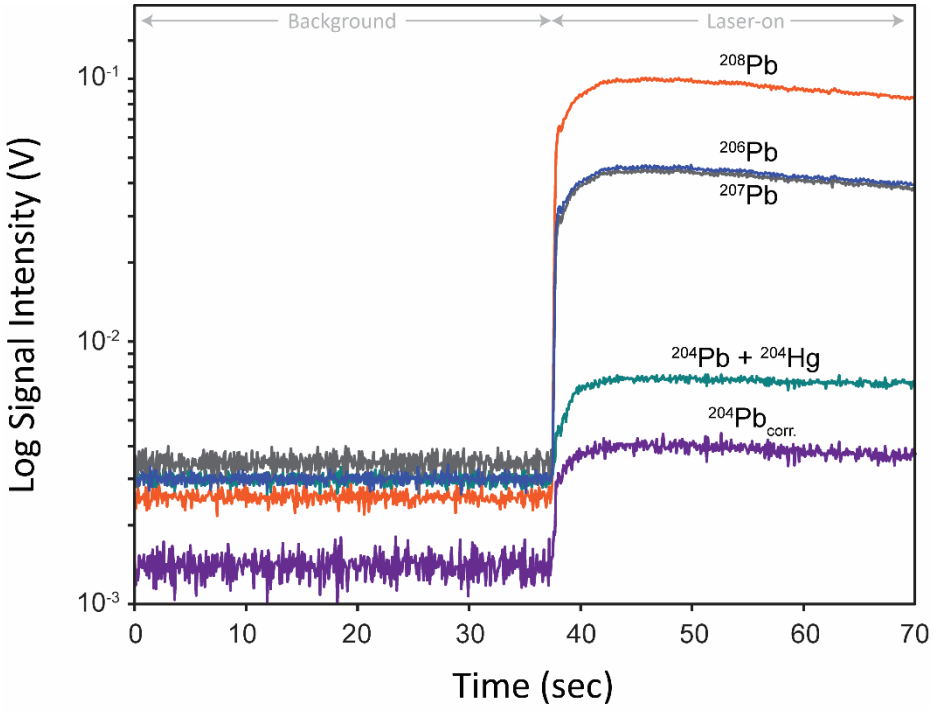

Figure 5.3: A typical Pb-isotopic signal obtained using multicollector LA-ICP-MS, highlighting signal-stability and thus Pb-isotopic homogeneity of the alkali feldspar (Or_{55}) being analysed.

5.4.6 Solution-based (Step leach) MC-ICP-MS

Alkali-feldspar step-leach dissolution were performed at the School of Earth Sciences, University of Melbourne, following procedures adapted from (Maas et al., 2015; Woodhead, 2002). Pristine alkali feldspar grains were micro-drilled then lightly ground in an agate mortar & pestle to an approximate grainsize of less than 0.5 mm, before being weighed into a teflon beaker (sample weight 120.9 mg) and subjected to a four-stage acid leach protocol:

1) 6M HCl, 20°C, 3 hrs
2) 6M HNO_3, 20°C, 3hrs

3) 5M (ca. 20%) HF, 60°C, 3 hrs

4) 6M HNO_3, 60°C, 3 hrs

The leach solutions from each step (plus rinse water) were transferred into separate beakers. Where required, settling of the residual material was accelerated by centrifuging within the original beaker. The residue after the fourth-stage of leeching was then completely dissolved in 3:1 HF-HNO3 and pure HNO3 (120°C, 12 hrs each). Each solution was split to provide a small (~ 10%) aliquot for trace element analysis by quadrupole ICP-MS. The remainder of each solution was dried, picked up in 1 ml of 0.6M HBr and loaded onto a 0.1 ml bed of AG1-X8 (100 - 200 mesh) anion exchange resin. The loading HBr and subsequent HBr fractions were collected within the original beakers and stored. Pb was eluted from the resin using 6M HCl. This procedure was repeated on a smaller bed of anion resin. Several procedural blanks indicate Pb contributions from the combined step leach and extraction protocols of 0.1 ng or less. By comparison, samples sizes for Pb are 147 - 820 in the leachates but 2.2 ng in the residue.

Pb-isotope ratios were measured on a Nu Plasma multi-collector ICP-MS, with sample aspiration via a Glass Expansion OpalMist PFA nebuliser (~0.07 ml/min uptake) and a CETAC Aridus desolvator. Pb fractions were re-dissolved in 2% nitric acid doped with 10 ppb of thallium, to allow correction of instrumental mass bias using the Tl doping method (Woodhead, 2002). For samples large enough to produce sustained signals near 10 V of total Pb (for a typical 5-minute mass spectrometer run this consumes ca. 20 ng of Pb), this correction protocol produces external precisions of ±0.05 - 0.09% (2σ). The long-term average for a Broken Hill galena solution is 16.004 ± 0.038% ($^{206}Pb/^{204}Pb$), 15.388 ± 0.057% ($^{207}Pb/^{204}Pb$) and 35.659 ± 0.076% ($^{208}Pb/^{204}Pb$) (n = 73, 2σ), consistent with TIMS reference values ($^{206}Pb/^{204}Pb$ = 16.004, $^{207}Pb/^{204}Pb$ = 15.389, $^{208}Pb/^{204}Pb$ = 35.651; Richards (1986)).

5.4.7 Feldspar Trace-Elements

Trace-elements in both alkali feldspar (K+Na) and K-feldspars from the Roxby Downs Granite were analysed using a Resonetics Resolution s155 laser ablation system linked to Coherent COMPex Pro 110 ArF excimer laser, operating at 193 nm with a 20 ns pulse width. The laser apparatus were coupled to Agilent 7900 quadrupole ICP-MS housed at the CODES analytical laboratories, University of Tasmania, Hobart. All samples were ablated for 60 secs (excluding 30 sec background) using a 43 µm spot-size with a repetition rate of 5 Hz, equating to a fluence of 5.9 J/cm^2. The elemental masses measured were; ^{7}Li, ^{23}Na, ^{24}Mg, ^{27}Al, ^{29}Si, ^{31}P, ^{39}K, ^{43}Ca, ^{49}Ti, ^{55}Mn, ^{57}Fe, ^{66}Zn, ^{85}Rb, ^{88}Sr, ^{89}Y, ^{90}Zr, ^{133}Cs, ^{137}Ba, ^{139}La, ^{140}Ce, ^{141}Pr, ^{146}Nd, ^{147}Sm, ^{153}Eu, ^{157}Gd, ^{159}Tb, ^{163}Dy, ^{165}Ho, ^{166}Er, ^{169}Tm, ^{172}Yb, ^{175}Lu, ^{206}Pb, ^{207}Pb, ^{208}Pb, ^{232}Th, ^{238}U.

Table 5.1: Pb-isotopic results from primary SRM's

	NIST 981[1,2]	Our Value (MC-ICP-MS)	NIST 610[3]	Our Value (LA-MC-ICP-MS)
Pb Conc.	40 ppb	-	426 ppm	-
^{207}Pb/^{206}Pb	0.9146	0.9144	0.9090	0.9096
± (2σ)	-	-	0.0001	0.0001
MSWD	-	-	-	0.111
^{208}Pb/^{206}Pb	2.1672	2.1664	2.1694	2.1680
± (2σ)	-	-	0.0002	0.0001
MSWD	-	-	-	0.269
^{206}Pb/^{204}Pb	16.935	16.930	17.0520	17.0472
± (2σ)	-	0.004	0.0020	0.007
MSWD	-	-	-	0.0065
^{207}Pb/^{204}Pb	15.489	15.481	15.5150	15.5091
± (2σ)	-	0.005	0.0018	0.0063
MSWD	-	-	-	0.016
^{208}Pb/^{204}Pb	36.701	36.678	36.9910	36.9756
± (2σ)	-	0.013	0.0043	0.0149
MSWD	-	-	-	0.019

[1] Richards (1986), [2] Woodhead and Hergt (2000), [3] Jochum et al. (2011a), [4] Jochum et al. (2011b)

A laser spot-size of 74 µm and 43 µm was employed on primary (NIST612) and secondary standards (GSD-1G, BCR-2G), respectively. Duplicates of each standard were routinely analysed every 30 analyses to correct for instrument drift. Data reduction was achieved offline using the LADR program. Oxygen (~46 wt. %) was assigned by stoichiometry (Fe = FeO_{total}) and the total normalised to 100%.

Table 5.2: Pb-isotopic results of secondary (matrix-matched) standards

	Alder Creek Sanidine[1]	Our Value (LA-MC-ICP-MS)	Broken Hill Amazonite[2]	Our Value (LA-MC-ICP-MS)
Pb Conc.	40 ppm	-	2.5 wt. %	-
$^{207}Pb/^{206}Pb$	0.8178	0.8177	0.9616	0.9613
± (2σ)	0.0003	0.0001	0.0003	0.0000
MSWD	-	1.7827	-	0.55
$^{208}Pb/^{206}Pb$	2.0312	2.0311	2.2283	2.2276
± (2σ)	0.0002	0.0007	0.0011	0.0001
MSWD	-	16.4217	-	0.87
$^{206}Pb/^{204}Pb$	19.124	19.1376	16.003	16.0193
± (2σ)	0.017	0.0122	0.011	0.0110
MSWD	-	0.4101	-	6.07
$^{207}Pb/^{204}Pb$	15.640	15.6482	15.390	15.4012
± (2σ)	0.009	0.0104	0.013	0.0120
MSWD	-	0.5842	-	6.41
$^{208}Pb/^{204}Pb$	38.846	38.8692	35.660	35.7006
± (2σ)	0.037746	0.0250	0.036	0.0252
MSWD	-	0.9597	-	5.69

[1] Maas (pers. comms.), [2] Cooper et al. (1969),

5.5 Results

The results of LA-MC-ICP-MS Pb-isotopic analyses on primary and secondary (matrix-matched) standards are shown in Table 5.1 and 5.2, respectively. All results are within 2σ uncertainty of recommended values. In situ Pb-isotopic results from alkali feldspar in the Roxby Downs Granite are shown in Table 5.3. While signal intensities during the session were low, owing to low Pb-concentrations contained in the feldspar (10 ppm), the stability of the time-resolved spectra (Fig. 5.3

and 5.4) and internal-reproducibility of individual analyses (MSWD = 0.403 – 0.929 (n = 13)) demonstrate the accuracy of these results.

Table 5.3: In situ Initial Pb-isotopic results for the Roxby Downs Granite (LA-MC-ICP-MS; n = 13)

	$^{238}U/^{204}Pb_{(t)}$	$^{232}Th/^{238}U_{(t)}$	$^{206}Pb/^{204}Pb$	$^{207}Pb/^{204}Pb$	$^{208}Pb/^{204}Pb$
Results	11.084	4.032	16.465	15.524	36.310
(± 2σ)	0.173	0.054	0.052	0.050	0.1159
MSWD	-	-	0.929	0.486	0.403

The unit-cell parameters of K-bearing feldspars analysed for their Pb-isotopic compositions are shown in Table 5.5. All parameters show an increasing axial-length for the K-feldspar with higher $Or_{mol.\%}$. Unit cell volume increases by more than 1% (owing to an increase of K^+), while Al-occupancy within the second-tetrahedral site ($Al_{(T2)}$) shows a decrease of nearly 80% indicative of Si-Al reordering.

The results of high-precision, dissolution-based MC-ICP-MS are shown in Table 5.6. Despite considerable analytical effort, all ^{204}Pb-based ratios far-exceed Pb-isotopic compositions predicted by global growth models of Stacey and Kramers (1975) and Cumming and Richards (1975) and are therefore not considered to represent the initial Pb-isotopic composition of the melt-sources involved in generating the RDG. The first four digestion-steps yield an internally-consistent linear array of Pb-isotopic compositions, with the least radiogenic compositions obtained from the penultimate-step of the dissolution method (6M HNO_3 at 60°C). The final residue, leached by HF-HNO_3 at 120°C, yields the most-radiogenic Pb-isotopic compositions of all.

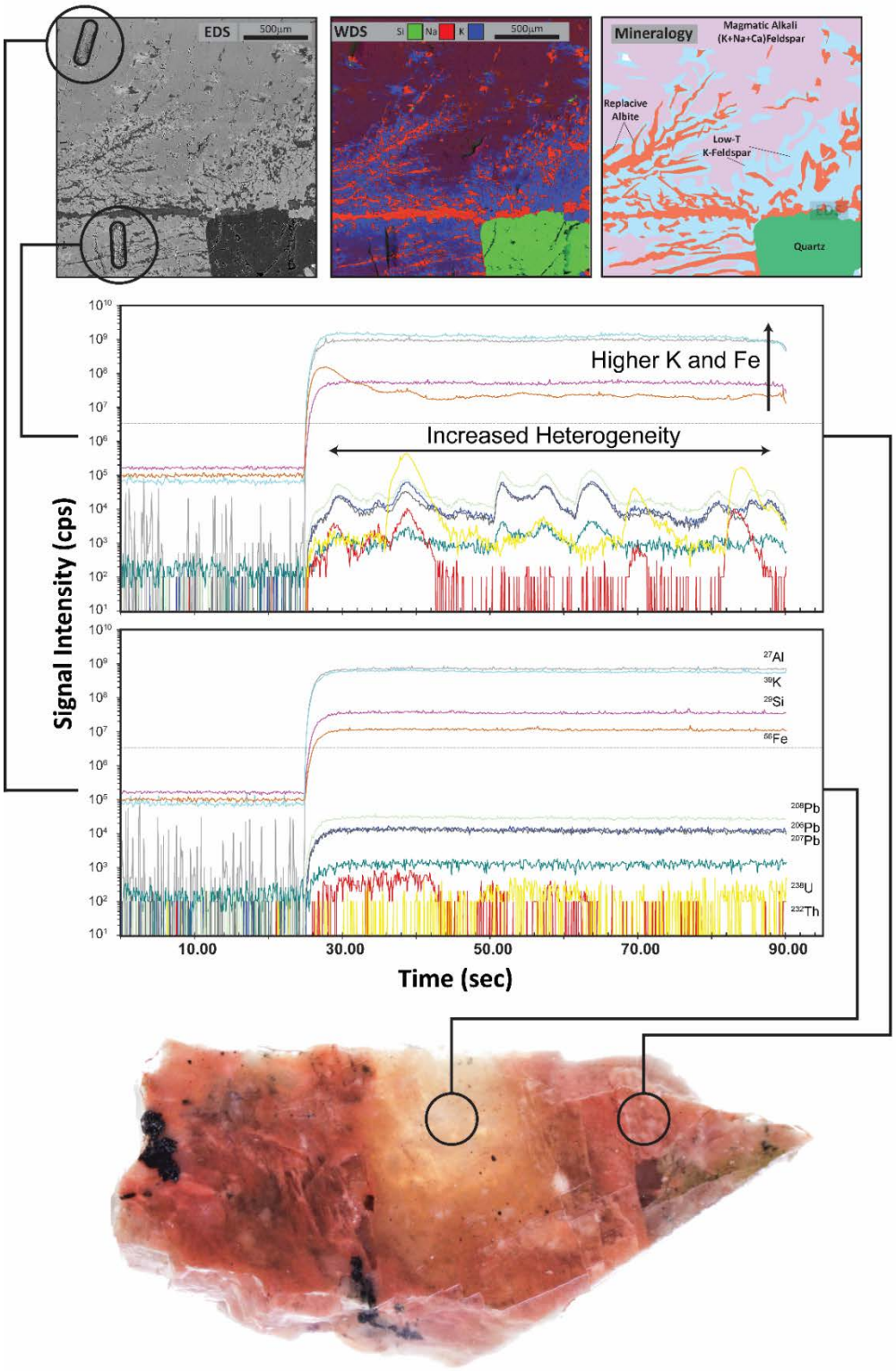

Figure 5.4: A schematic diagram relating micrometre-sized textural features identified by EDS/WDS (left) with geochemical spectra from LA-ICP-MS (centre) and macroscopic observations (right). The pristine alkali feldspar ($Or_{\sim 55}$) is translucent to transparent, and being replaced by a brick-red, hematite-inclusion-rich K-feldspar ($Or_{>80}$) phase. (left) Replacement of the alkali feldspar is often transgressive to crystallographic features (i.e. cleavage), and appears to be the result of fluid-assisted, coupled dissolution-reprecipitation (i.e. Putnis et al., 2007). Note the LA-ICP-MS ablation pit-lines circled in black. (Centre) The geochemical changes associated with this alteration are evident in the time-resolved LA-ICP-MS spectra which are homogeneous in the alkali feldspar, however extremely heterogeneous in the red K-feldspar owing to nano- and micron-scale mineral inclusions (i.e. albite) exsolved during alkali feldspar unmixing and replacement. Importantly in the context of this study, is the homogeneity of the Pb-isotopic signals ($^{204, 206, 207, 208}Pb$) in the alkali feldspar relative to those of the more-prevalent red K-feldspar.

5.6 Discussion

5.6.1 Feldspar Paragenesis

At least two phases of K-bearing feldspar are present within the least-altered Roxby Downs Granite (Fig. 5.4 and 5.5). The paragenetically earliest form is a translucent, cryptoperthitic alkali feldspar (Or_{56}) which is scarcely preserved (Fig. 5.4). The paragenetically later, near-endmember microcline K-feldspar (Or_{80-99}) replaces the earliest form of alkali feldspar (Fig. 5.4), in an unmixing reaction (Fig. 5.4) following the equation;

$$2.(K_{0.53}Na_{0.43}Al_{1.03}Si_{2.98}O_8) <-> KAlSi_3O_8 + NaAlSi_3O_8$$

While some unmixing appears to follow perthitic processes, many of the interpenetrating textures which transect lamellae and cleavage indicate the interaction and facilitation of fluids (Fig. 5.4) following the processes involved in coupled dissolution-reprecipitation (Norberg et al., 2011; Putnis et al., 2007). The end result of umixing and fluid-assisted dissolution-reprecipitation is the formation of the typical hematite-bearing, porous, 'brick-red' K-feldspars which comprise the majority of

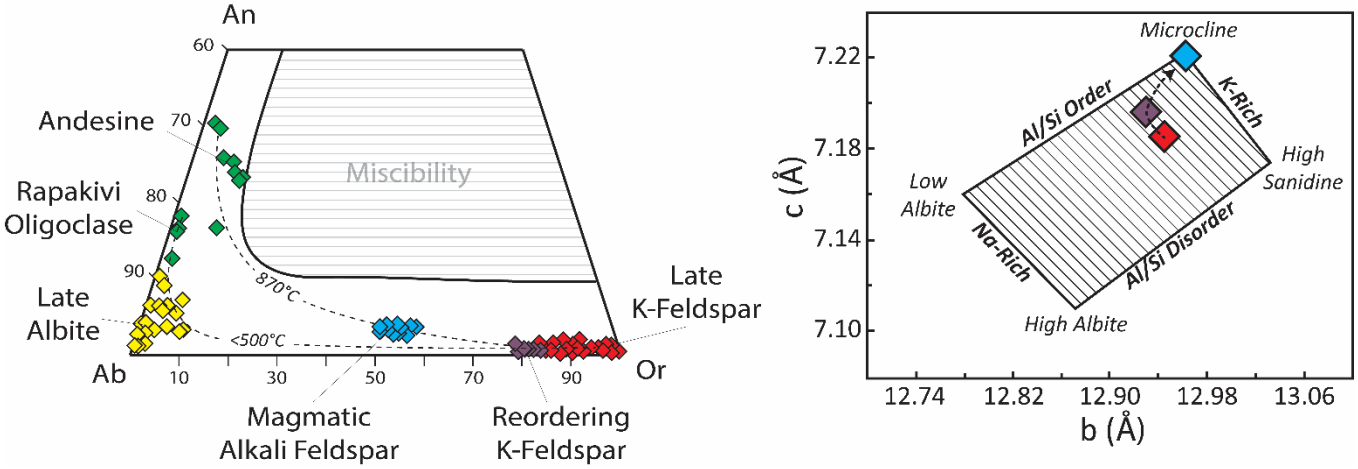

Figure 5.5: An overview of the chemical (left) and crystallographic (right) systematics associated with the conversion of alkali feldspar (Or55) to end-member K-feldspar. (left) A feldspar ternary diagram truncated at An60, demonstrating that geochemical relationships between the feldspar phases from data obtained by SEM/EDS. Dashed curves represent tie-lines between feldspar couplets interpreted to be in equilibrium (calculated after Benisek et al., 2010, at 2.2 kbar). The first of these is an average using couplets of phenocrystic andesine-alkali feldspar. The latter is based on couplets of paragenetically-later K-feldspar and oligoclase mantles around alkali feldspar (rapakivi). The lowest of these temperatures approaches the limit of the model and is only considered a relative estimate. (Right) Schematic diagram showing the changes in both 'b' and 'c' lengths of the unit cell for both alkali feldspar (blue) and K-feldspar (red). The associated increase in 'b' and 'c' parameters is related to increasing K-content, and increased Al, Si ordering. Modified after Wright and Stewart, 1968.

observable feldspar in the RDG (Fig. 5.2e). The presence of relict orthomagmatic alkali feldspars (cryptoperthites) decreases significantly with proximity to Olympic Dam, becoming absent within 3 km of the deposit to the south, and completely absent to the north. Hematite-content of the secondary K-feldspars increases significantly with proximity to Olympic Dam (Fig. 5.2e). Alteration of the primary alkali feldspar (cryptoperthite/ orthoclase) to secondary K-feldspar (microcline) results in a decrease in most-major elements (excluding K and Fe) from the K-feldspar (Table 5.6), as well as the marked loss of LREE (Fig. 5.6).

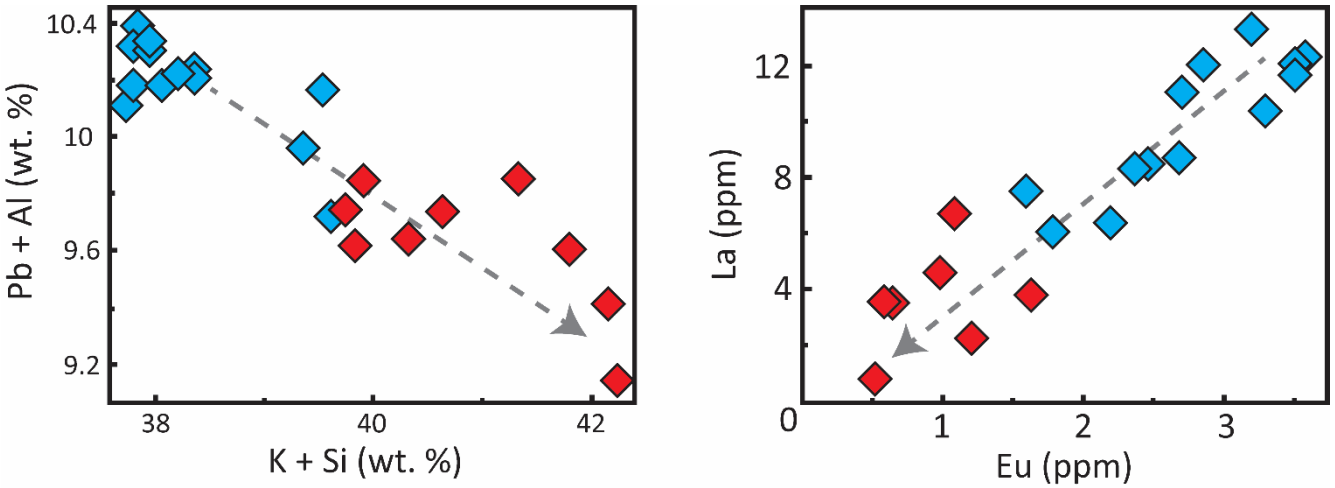

Figure 5.6: Geochemical correlations associated with the conversion of alkali feldspar (blue) to K-feldspar (red). (left) The negative correlation between Pb + Al (wt. %) vs. K + Si (wt. %) confirms that Pb incorporation in the alkali feldspar lattice follows the coupled-reaction $Pb^{2+} + Al^{3+} \rightleftharpoons K^{+} + Si^{4+}$. (right) Correlation between La- and Eu-concentration highlights that a potentially significant loss of LREE is associated with the alteration of alkali feldspar to K-feldspar.

5.6.2 Crystallographic Validation of Complex Feldspar Samples

In K-bearing feldspar, Pb^{2+} is spatially-accommodated in the M1 site left by substitution of K^{+}. In monoclinic K-bearing feldspars, such as the pristine alkali feldspar (cryptoperthite) encountered in this study, net ionic charge may be balanced by the concomitant substitution of K^{+} and Si^{4+}, following the equation outlined by Cherniak (1995);

$$Pb^{2+} + Al^{3+} \rightarrow K^{+} + Si^{4+}$$

This substitution mechanism is supported by the negative correlation between Pb + Al and K + Si associated with the alteration of alkali feldspar to K-feldspar (Fig. 5.6) and implies that lattice-bound Pb whose isotopic composition genuinely reflects the granitic melt-sources, should follow an increase in Al-Si disorder (increasing Al). The degree of Al-Si disorder is a readily quantifiable phenomenon which can be detected using in situ crystallographic techniques such as synchrotron and single-crystal x-ray diffraction (SCXRD). These techniques were employed to validate or dismiss our initial Pb-isotopic results which are slightly-accelerated (time-integrated U-rich) compared to current Pb-growth models.

Table 5.4: Representative geochemical analyses (LA-ICP-MS) of K-bearing feldspar phases. Note: U and Th concentrations were below detection in all feldspars.

(Wt. %)	Alkali Feldspar (n = 11)	Reordering K-Feldspar (n = 9)	K-Feldspar (n=5)
SiO_2	65.17	65.00	64.64
Al_2O_3	19.23	18.04	18.47
K_2O	9.75	13.54	15.39
Na_2O	4.91	2.35	0.95
CaO	0.38	0.26	0.13
BaO	0.29	0.20	0.04
FeO_{total}	0.19	0.49	0.5
(mol. %)			
Or	54.73	78.26	90.83
Ab	43.19	20.54	8.52
An	2.09	1.20	0.64
(ppm)			
Pb	9.15	7.32	3.58
Sr	184.80	82.37	68.95
Rb	251.86	554.86	587.51
Ti	173.36	67.49	51.07
U	<0.01	<0.01	<0.01
Th	<0.01	0.02	0.06
(ppb)			
La	9594	4373	2813
Ce	7633	2686	1683
Pr	387	129	70
Nd	775	249	123
Sm	42	23	17
Eu	2682	1167	1085
Gd	20	26	27
Eu/Eu_N*	283	146	51

Refined unit-cell parameters obtained from the synchrotron and SCXRD is shown in Table 5.4, including T-O lengths (Å). Levels of Al and Si occupancy in tetrahedral sites t_1 and t_2, in addition to the overall order-disorder parameter (Z) are calculated following the procedures outlined in Hovis (1997). The results show that the alkali feldspar hosts significantly-greater Al within the t_2-site ($Al_{(T2)}$ = 0.1962) compared with K-feldspar ($Al_{(T2)}$ = 0.0243). The alkali feldspar is therefore significantly more disordered (Z = 0.2151) with respect to Al-Si than the K-feldspar (Z = 0.9026) (Fig. 5.7), and is more likely to host a lattice-bound Pb whose Pb-isotopic composition will genuinely reflect the melt-sources for the RDG. This differs with the results for the K-feldspar, which suggest equilibration occurred at temperatures more-consistent with post-magmatic conditions, and therefore may yield Pb-isotopic signatures which do not reflect the U-Th-Pb chemistry of the melt-sources involved in generating the RDG magma.

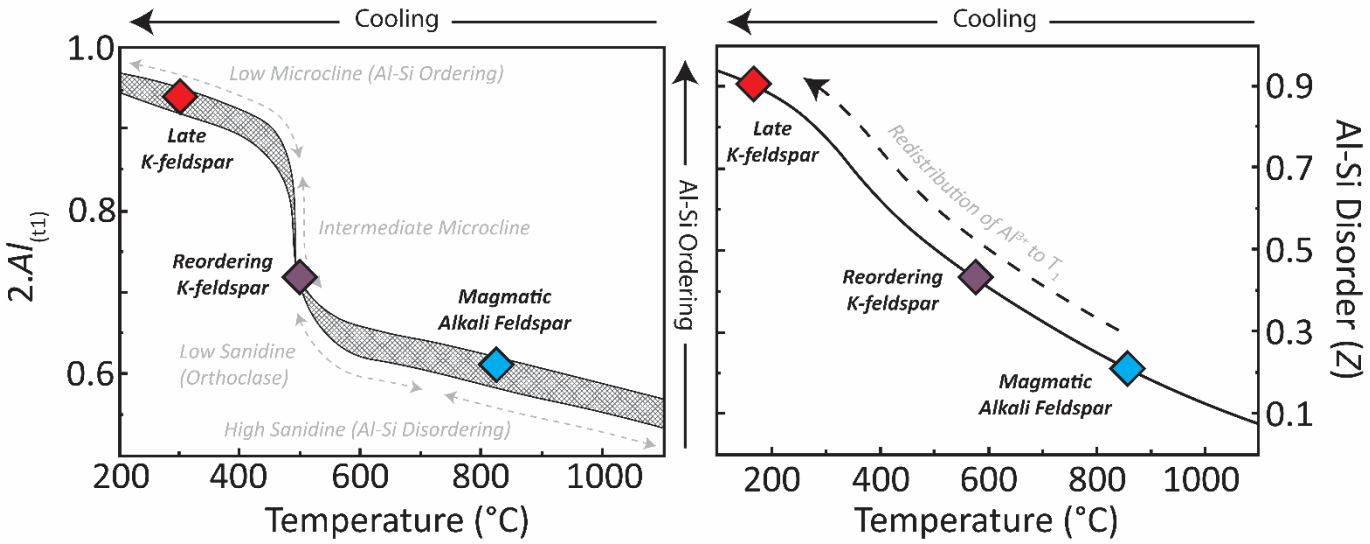

Figure 5.7: Temperature constraints on K-bearing feldspar phases, based on the level of Al/Si disorder obtained from crystallographic measurements. Both the models of Brown and Parsons, 1989 (left) and Hovis, 1997 (right) are in broad agreement and demonstrate that the alkali feldspar crystallised under orthomagmatic conditions (830 - 850°C) however re-equilibrated under deuteric or post-magmatic temperatures (200 – 300°C).

5.6.3 Thermodynamic constraints on Feldspar Paragenesis

An additional benefit of integrating crystallographic studies into the feldspar Pb-isotope workflow is that the unit-cell parameters yielded provide thermodynamic constraints on the paragenesis of the

analysed feldspars. Temperature estimates based on the Al-occupancy for t_1 models of Brown and Parsons (1989) (Fig. 5.7), imply temperatures for the alkali feldspar in excess of ~830°C. This is in good agreement with the Al-Si tetrahedral distribution model of Hovis (1997) which suggests the alkali feldspar formed at ~850°C (Fig. 5.7). Similarly, two-feldspar geothermometry based on the calorimetric model of Benisek et al. (2010), also indicate that phenocrystic plagioclase (An_{25-30}) - alkali feldspar (Or_{56}) couplets (Fig. 5.5) formed at high-magmatic temperatures around ~870°C (P = 2.2 kbar). The range of temperatures indicated here (830 – 870°C) are significantly-higher than the ~765°C suggested by previous feldspar studies (Kontonikas-Charos et al., 2017), and more in-line with the 850°C zircon-saturation temperature suggested by Creaser (1989) as well as the 840°C indicated by Ti content in zircon (Ferguson pers. comms.).

Table 5.5: Unit-cell parameters (C*2/m*) for end-member K-bearing Feldspars. $Al_{(Tx)}$ and Z calculated after Hovis (1997)

	Alkali Feldspar (Or_{52-59})	Reordering K-Feldspar (Or_{78-85})	K-Feldspar (Or_{84-99})
a (Å)	8.612	8.631	8.656
b (Å)	12.954	12.930	12.981
c (Å)	7.186	7.196	7.220
β (°)	116.11	116.19	116.20
Vol. ($Å^3$)	719.82	720.62	727.91
$Al_{(T1)}$	0.3038	0.3666	0.4757
$Al_{(T2)}$	0.1962	0.1334	0.0243
Z	0.2151	0.4662	0.9026

In contrast, temperatures indicated by the paragenetically-later, K-feldspar are significantly lower than those of the alkali feldspar. Temperatures of ~270°C to ~300°C are suggested by the models of Hovis (1997) and Brown and Parsons (1989), respectively. These thermodynamic constraints on the temperature of formation for the well-ordered K-feldspar are below a theoretical magmatic-hydrothermal transition (~500°C), and imply equilibrium was obtained well after the completion of granite crystallisation. By comparison, textural development of patch-perthites which are seen to replace the alkali feldspar were interpreted by Kontonikas-Charos et al. (2017) to

represent the beginning of deuteric coarsening at around 430°C. The range of temperatures shown by the paragenetically-late K-feldspar are broadly consistent with data from fluid inclusion and stable isotope studies for the earliest ore-forming stage at Olympic Dam (~400°C; Oreskes and Einaudi (1992)), and suggest that ore-formation occurred at similar conditions and timing relative to granite emplacement.

5.6.4 Pb-isotopic Disequilibrium in K-bearing Feldspar

Due to the extreme difference between the time-scales of magmatic processes (i.e. $<10^3$ years) and radioactive decay of U-Th to Pb (i.e. $>10^6$ years), Pb-isotopic signatures preserved within feldspar should remain unchanged through a closed-system cooling-evolution of a granite. Therefore, if re-equilibration of the disordered alkali feldspar to a more ordered K-feldspar occurred as a topochemical-process in response to cooling of the granite (i.e. ~850°C → ~300°C), then the Pb-isotopic signature of the alkali feldspar should be preserved within the K-feldspar. This is not the case. The Pb-isotopic signature observed in the K-feldspar ($^{207}Pb/^{206}Pb$ = 0.927 – 0.608, $^{208}Pb/^{206}Pb$ = 2.172 – 1.433) is significantly more radiogenic than is present in primary alkali feldspar ($^{207}Pb/^{206}Pb$ = 0.942 ± 0.003, $^{208}Pb/^{206}Pb$ = 2.204 ± 0.006). The concentration of U (< 0.1 ppm) and Th (0.06 ppm) within the K-feldspar (Table 5.4) are insufficient to account for the radiogenic Pb-isotopic compositions as a result of in situ decay alone, and therefore requires either diffusion of Pb into the K-feldspar sometime after formation, or incorporation of Pb with a more radiogenic isotopic composition during feldspar recrystallisation. Thus, we suggest two scenarios which may be considered to explain the Pb-isotopic disequilibrium (Fig. 5.8);

1) Alteration of alkali feldspar to K-feldspar occurred sometime significantly after crystallisation of the granite (>+200 myr), such that the Pb-isotopic system of the granite had evolved sufficiently to produce the radiogenic compositions observed.

2) Conversion of the alkali feldspar to K-feldspar occurred contemporaneously with late-

stage, deuteric processes. Fluid-assisted, open-system behaviour during this late-stage allowed for Pb-isotopic exchange between the cooling granite and surrounding country rock.

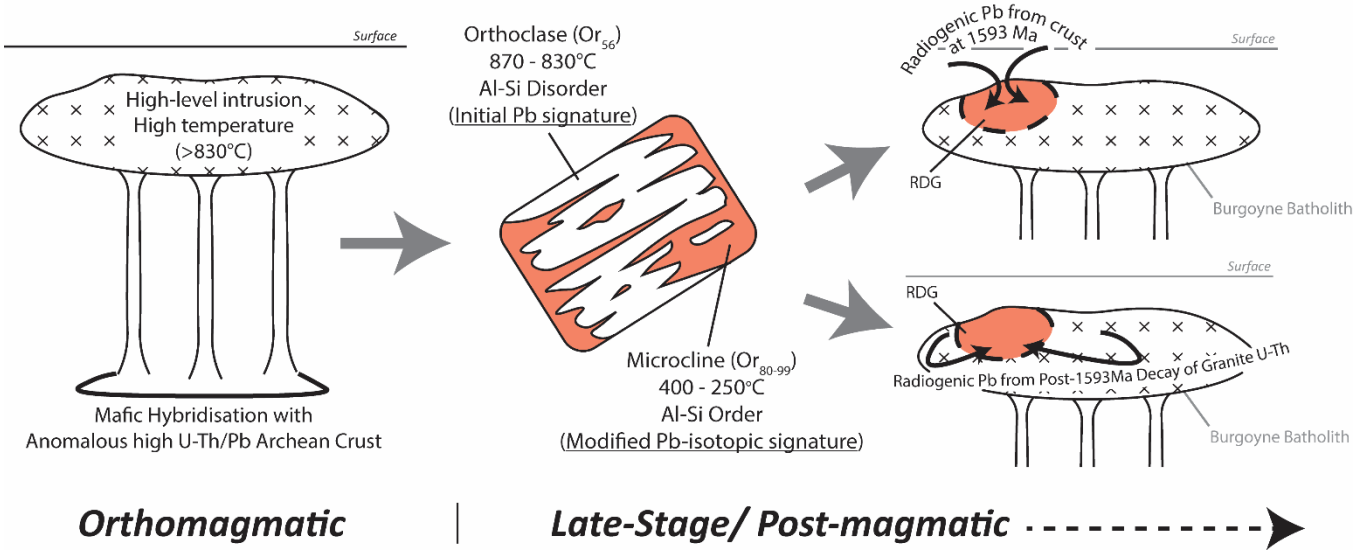

Figure 5.8: Schematic diagram summarising the orthomagmatic and late-stage/ post-magmatic constraints provided by integrated crystallographic and Pb-isotopic studies of K-bearing feldspar. Pb-isotopic signatures in the orthomagmatic alkali feldspar indicate the U-Th-Pb chemistry of the melt-source(s) of the Roxby Downs Granite. Modification of this initial Pb-isotopic signature has occurred with alteration of the alkali feldspar to the end-member K-feldspar, suggesting either significant open-system exchange between the RDG and surrounding country rocks (if the reaction occurred at ~1593 Ma), or the reaction occurred significantly after 1593 Ma (if radiogenic Pb sourced from U-Th decay in RDG).

In the first of these scenarios, radiogenic Pb is sourced from the granite itself. Strongly radiogenic Pb-isotopic compositions are produced over time as a result of the high-U/Pb ratios common in granites which have undergone late-stage magmatic processes (i.e. Dostal et al. (2004)). The meta-stability of the alkali feldspar means that re-crystallisation to an ordered K-feldspar (i.e. microcline) requires little energy added to the system, and occurs passively in response to lowering temperatures. Modification of the initial Pb-isotopic signature is assisted by an overall-low Pb concentration in the feldspars (10 ppm), while the exchange of Pb bound in the feldspar lattice is facilitated by re-crystallisation. Diffusivity calculations based on Arrhenius equations, such as those associated with the concept of 'closure temperature' (i.e. Dodson (1973)) suggest diffusivity rates for Pb in K-feldspar are in the order of $1x10^{-14}$ mm^2/Ma at 300°C (Cherniak, 1995). This value is similar to the diffusivity rate for Pb in rutile (Cherniak, 2000) and implies that a ~1 cm K-feldspar, such as those

present in the RDG, is effectively closed to Pb-diffusion at temperatures at and below 300°C. Since the RDG (and Hiltaba Suite in general) have not been affected by regional metamorphism of this tenor, passive isotopic diffusion is not considered an adequate explanation for the modification of initial Pb-isotopic signatures preserved in the paragenetically-later K-feldspar.

The second explanation for the Pb-isotopic disequilibrium in feldspars from the RDG involves open-system behaviour during the late-stages of granite cooling. Upon cooling below orthomagmatic temperatures, Pb is exchanged between the RDG and country rock, and the modified Pb-isotopic signature preserved within the low-T K-feldspar. Textures preserved in the alkali feldspar (Figs. 5.2 and 5.3) indicate fluid may have assisted in the conversion, which would have also facilitated Pb-isotopic exchange between the RDG and country rock. This scenario is comparable to the fluid-mixing model which has been invoked for the genesis of Olympic Dam (Bastrakov et al., 2007; Haynes et al., 1995; Oreskes and Einaudi, 1992). K-feldspar associated with 400 - 500°C mineralisation at the nearby Acropolis IOA deposit (Fig. 5.1) contains heavy oxygen isotopic signatures ($\delta^{18}O_{VSMOW}$ = 9.0 – 11.5 ‰; Oreskes and Einaudi (1992)) suggesting a significant contribution of oxygen in the K-feldspar is derived from the surrounding country rock. It is therefore likely that formation of the Al-Si ordered K-feldspar with radiogenic Pb-isotopic signatures occurred penecontemporaneously with ore-formation, in response to post-magmatic (deuteric), hydrothermal convection/ circulation.

Variability of the Pb-isotopic compositions in the K-bearing feldspar form an secondary mixing array, intercepting the initial Pb-isotopic signature of the alkali feldspar and extending outwards through the in situ results of paragenetically-late K-feldspar, solution-mode results of (Neumann, 2001) and those dissolution-based results presented here (Fig. 5.9). Though imprecise and therefore unable to resolve the exact age of the high U/Pb radiogenic Pb-reservoir (i.e. 1609 ± 48 Ma), uncertainty on the result would suggest that alteration of the alkali feldspar to K-feldspar occurred before 1561 Ma, most likely temporally-coinciding with extended cooling of the RDG after

1593 Ma (Cherry et al., 2018). Such a result is also in accordance with recent Sm-Nd isochrons yielded from calcites (1537 ± 42 Ma) which are part of the earliest-phase of mineralisation in Olympic Dam (Apukhtina et al., 2017), and provide a temporal link between cooling of the RDG, subsequent feldspar alteration and ore-formation.

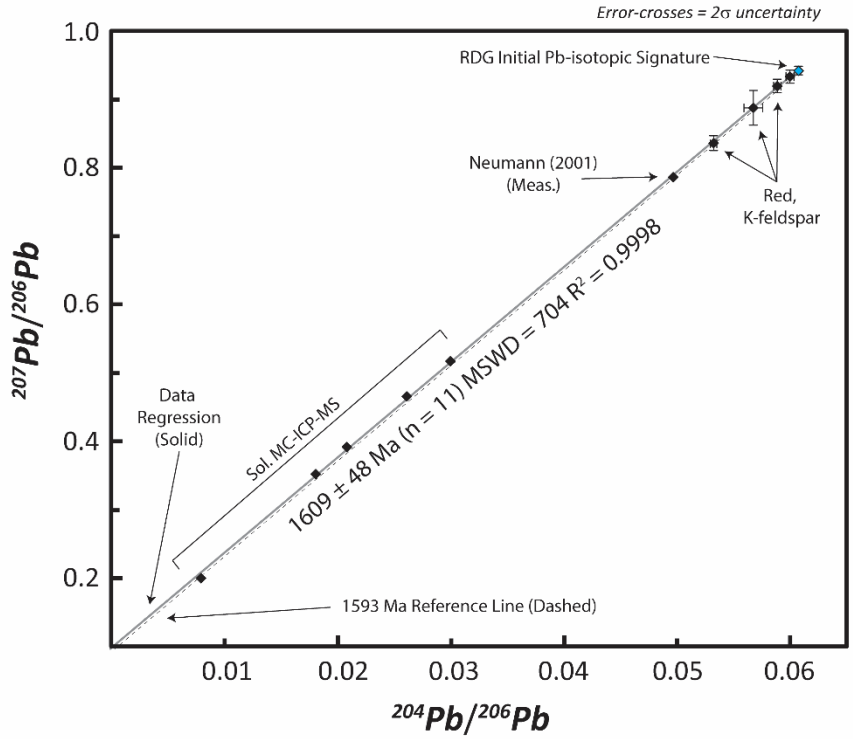

Figure 5.9: Inverse uranogenic Pb-isotope plot ($^{207}Pb/^{206}Pb$ vs $^{204}Pb/^{206}Pb$) showing the isochron yielded from all feldspar analyses (in situ and dissolution-based). The benefit of this diagram over conventional ^{204}Pb-based plots, is that it mitigates error correlation associated with ^{204}Pb measurement, which are particularly deleterious to age-calculations. While imprecise, the result is within uncertainty of the known crystallisation age of the RDG (1593 Ma) and suggests that radiogenic Pb in the paragenetically-later K-feldspar was heterogeneously sourced from a high-U/Pb reservoir at around the time of granite crystallisation.

5.6.5 Possible Implications for the Sequential Leach Technique in Complex Feldspar Samples

Previous attempts to determine initial Pb-isotopic compositions from feldspars of the Roxby Downs Granite via dissolution-based methods (Neumann, 2001) have all yielded spuriously-radiogenic results ($^{206}Pb/^{204}Pb$ = 18.2363 ± 0.0023, $^{207}Pb/^{204}Pb$ = 15.6576 ± 0.0019, $^{208}Pb/^{204}Pb$ = 37.4438 ± 0.0047). High-precision, dissolution-based techniques employed here (MC-ICP-MS), also yielded similarly-radiogenic results (Table 5.5), despite quantitatively-containing initial Pb-isotopic compositions within the same sample (LA-MC-ICP-MS). The inability of the sequential leach method

to yield true initial Pb-isotopic values from the alkali feldspar samples of the Roxby Downs Granite suggests that the solution-based method is less-effective than in situ techniques at yielding geologically-meaningful results when applied to complex feldspars samples.

Table 5.6: Step-leach Least Radiogenic Pb-isotopic results (MC-ICP-MS)

	1st Leach (6M HCl)	2nd Leach (6M HCl, repeat)	3rd Leach (6M HNO_3)	4th Leach (5M HF, 60°C)	5th Leach (6M HNO_3, 60°C)	Final Residue (HF + HNO_3, 120°C)
$^{206}Pb/^{204}Pb$ (± 2σ)	48.014 (0.005)	48.017 (0.003)	55.251 (0.005)	38.324 (0.002)	33.387 (0.002)	126.128 (0.220)
$^{207}Pb/^{204}Pb$ (± 2σ)	18.822 (0.002)	18.824 (0.002)	19.486 (0.002)	17.862 (0.001)	17.281 (0.001)	25.305 (0.044)
$^{208}Pb/^{204}Pb$ (± 2σ)	75.166 (0.008)	75.171 (0.005)	83.756 (0.008)	60.316 (0.004)	54.733 (0.003)	73.014 (0.126)

The findings presented here support the assertion of Lee and Parsons (1997), that under certain circumstances, original isotopic (and geochemical) compositions may only be preserved within metastable cryptoperthitic alkali feldspars. This presents a problem for dissolution-based Pb-isotopic methods where only the final residue is considered to contain initial Pb-isotopic values and thus routinely analysed (DeWolf and Mezger, 1994; Ludwig and Silver, 1977). The high-interfacial strain present in the cryptoperthitic alkali feldspar make it more-susceptible to dissolution in the weak acids of earlier digestion steps, and therefore fundamentally less-capable at retaining Pb until the final digestion stage, compared to the low-strain K-feldspar (microcline). However, it should be noted that modification of a Pb-isotopic signature does not necessarily accompany all conversion of a cryptoperthite to a microcline, and where conversion occurs topochemically within a closed-system, initial Pb-isotopic values may be retained. It is therefore argued that in instances where K-bearing feldspar do not yield Pb-isotopic compositions resembling genuine initial values, in situ Pb-isotopic analyses should be combined with in situ crystallography to validate the authenticity of the results.

5.6.6 Pb-isotopic constraints on the melt-sources of the Roxby Downs Granite

Initial Pb-isotopic compositions retained in pristine alkali feldspars (Table 3) demonstrate that the crustal melt-component of the Roxby Downs Granite (RDG) is anomalous with respect to U/Pb, Th/Pb and Th/U. Pb-isotopic source modelling implies that the crustal-melt component of the RDG had a time-integrated $^{238}U/^{204}Pb_{(t)}$ of 11.08 and a $^{232}Th/^{238}U_{(t)}$ of 4.03. This is 13.8% and 6.7% higher, respectively, than average crust (Stacey and Kramers, 1975). The crustal melt-component for the RDG is also anomalous for the Gawler Craton. Pb-isotopic data from other Hiltaba Suite intrusives coeval with the RDG (Fig. 5.10), suggest melt-derivation from distinctly mantle-related sources ($^{238}U/^{204}Pb_{(t)} < 9.58$, $^{232}Th/^{238}U_{(t)} < 3.7$) increasing in crustal-melt contributions nearer to Olympic Dam (Chapman et al., 2019).

The high $^{207}Pb/^{204}Pb$ initial Pb-isotopic signature, in addition to the apparent acceleration in $^{206}Pb/^{204}Pb$ signature, indicates that some melt-component which formed the Roxby Downs Granite was likely sourced from an Archean-aged (2.9 to 3.2 Ga) crustal protolith (Fig. 5.10a). More specifically, modelling of Pb-isotopic reservoirs indicates a best-fit for a reservoir which separated from a Stacey and Kramers (1975)-like average crustal reservoir at approximately 3.1 Ga. Within the Gawler Craton, this model age would suggest the occurrence of the ~3.15 Ga Cooyerdoo Granite, or equivalent, in the mid-to-lower crust of the Olympic Province. This was suggested by Fraser et al. (2010) who also showed that the Cooyerdoo Granite contained sufficient radiogenic heat-producing elements (i.e. U = 5 - 16 ppm, Th = 17 – 51 ppm) to explain the South Australian Heat Flow Anomaly (Neumann, 2001), and would therefore theoretically satisfy the Pb-isotopic requirements for a ~3.1 Ga-aged, high U-Th reservoir.

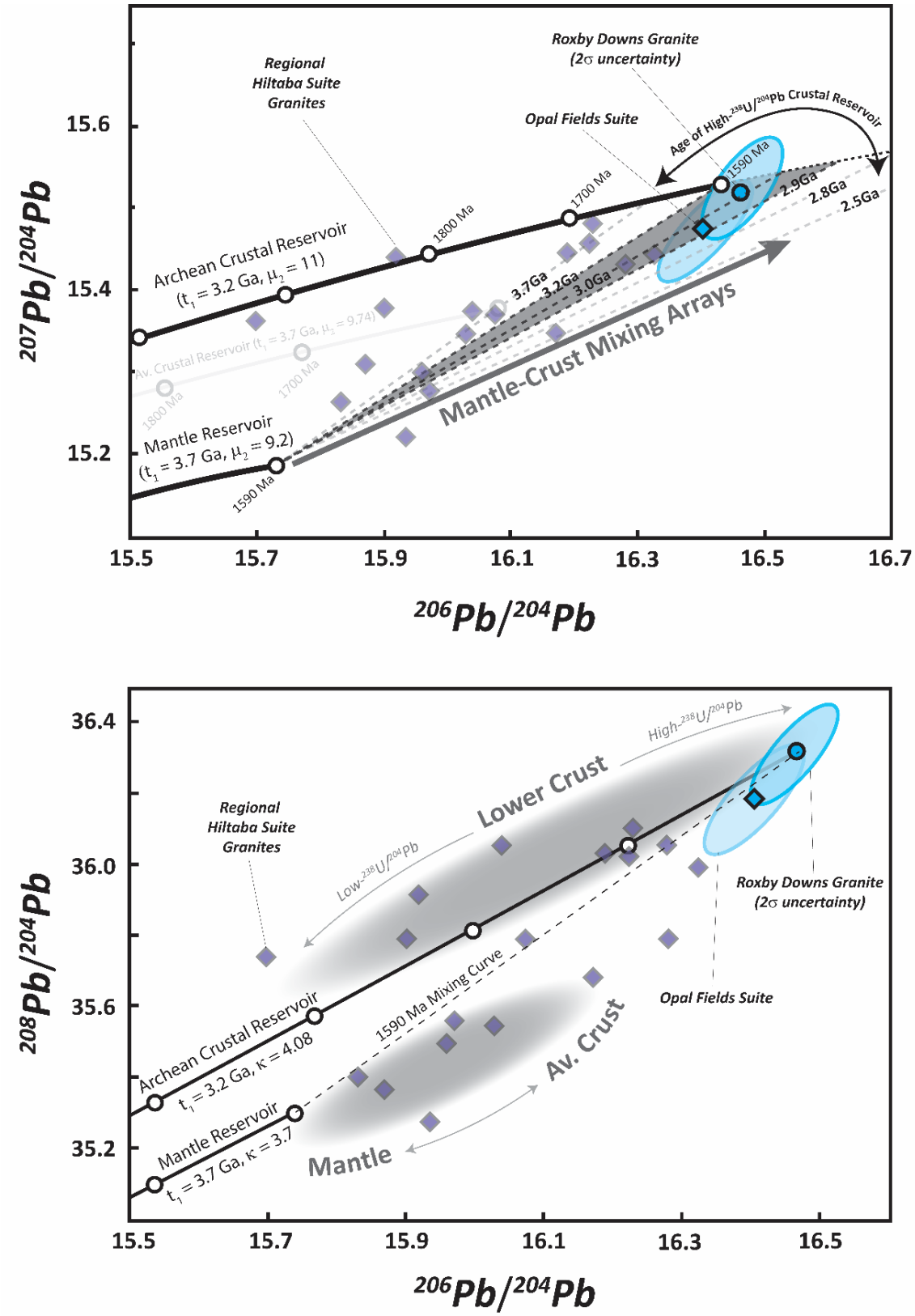

Figure 5.10: ^{204}Pb-based diagrams contextualising the initial Pb-isotopic signature of the RDG against the coeval Hiltaba Suite. a) The uranogenic Pb-isotopic signature of the RDG overlaps with that obtained for the Opal Fields subsuite (Chapman et al., 2019), confirming a co-magmatic origin. The signature is both a higher-$^{238}U/^{204}Pb$ and slightly-accelerated with respect to the Stacey and Kramers, 1975. This suggests the crustal reservoir from which the melt was sourced from was Archean, and enriched in U. b) Thoro-uranogenic diagram highlighting that the crustal reservoir was also high-Th/U.

Partial-melting of a tonalite-trondjhemite-granodiorite (TTG) protolith, such as the Cooyerdoo Granite, was suggested by Creaser (1996) to be important in the petrogenesis of the co-magmatic Wirrda- and Opal Fields ('White Dam') suite granitoids of the Burgoyne Batholith (Fig. 5.1). The similarity between the Pb-isotopic signatures of the RDG and Opal Fields Suite supports a co-magmatic origin, albeit suggesting the possibility of a greater mantle-contribution to the Opal Fields Suite relative to the RDG, given the lower $^{238}U/^{204}Pb_{(t)}$. Given the incompatibility of U and Th, relative to Pb in the lower crust compared to bulk crust ($D_{U/Pb}^{Lower\ Crust/Bulk\ Crust}$ = 42%; Rudnick and Gao, 2003), partial melting of any source would be expected to further decouple the U-Th-Pb system resulting in much higher U/Pb than those predicted by the Pb-isotopic signature of the source. Incipient, low-degrees of partial melting of a TTG gneissic source such as the Cooyerdoo Granite, would be expected to enrich U, relative to Pb, by a factor of as much as 30%, depending on refractivity of the mineralogical host for U and Pb (Bea, 2012; Dostal and Capedri, 1978). Therefore, even though the $^{238}U/^{204}Pb_{(t)}$ ratio of the crustal melt-component which is predicted by Pb-isotopic compositions is only ~14% higher than average global crust, the U/Pb and U-concentration in the resulting melt is likely to be significantly-higher. Magmatic processes such as crystal fractionation, especially in a halide-rich (i.e. fluorine-bearing) magma such as the RDG (McPhie et al., 2011) are likely to increase the U/Pb even further due to the extreme incompatibility and solubility of U in such magmatic systems (Peiffert et al., 1994). Thus, a crustal-melt component from an anomalous source identified by initial Pb-isotopic composition could ostensibly be capable of providing enough U to a late-stage or post-magmatic hydrothermal system, and contribute to forming the world's largest U-resource in Olympic Dam.

A key requirement often discussed in genetic models for late-stage, magmatic-related Cu-deposits such as porphyries, is the presence of a large reservoir of mafic melt at depth, which ultimately provides sulphur and chalcophile elements to the magmatic-hydrothermal system (i.e. (Hattori and Keith, 2001). The Pb-isotopic results provided here suggest that the majority of melt for

the RDG was provided by a crustal reservoir, and therefore may not be capable of producing the Cu-resource present at Olympic Dam. However, the Pb-isotopic signature of coeval Hiltaba Suite granitoids and Gawler Range Volcanics (Fig. 5.10) represents complex mixing between crustal and mantle signatures, which is biased towards crustal signatures due to differences in Pb concentration between mantle- and crustal-derived melts. This is best demonstrated through a Pb-Nd isotopic mass-balance for the RDG (Fig. 5.11) which shows that contributions of crustal-derived melt above ~10-15 vol. % yield almost entirely crustal Pb-isotopic signatures. Therefore, although the Pb-isotopic signatures for the RDG represent crustally-dominant Pb-isotopic signatures which imply anomalous U-Th-Pb, it is likely that the actual crustal-melt proportion of the overall magma was as low as 20%. This helps to reconcile the potential Cu-contributed from a mantle-derived melt (75 – 80 vol. %), as well as the high-prevalence of co-magmatic, low-SiO_2 intrusives (55 – 60 wt. %) which are part of the Burgoyne Batholith, such as the Opal Fields and Wirrda Suites.

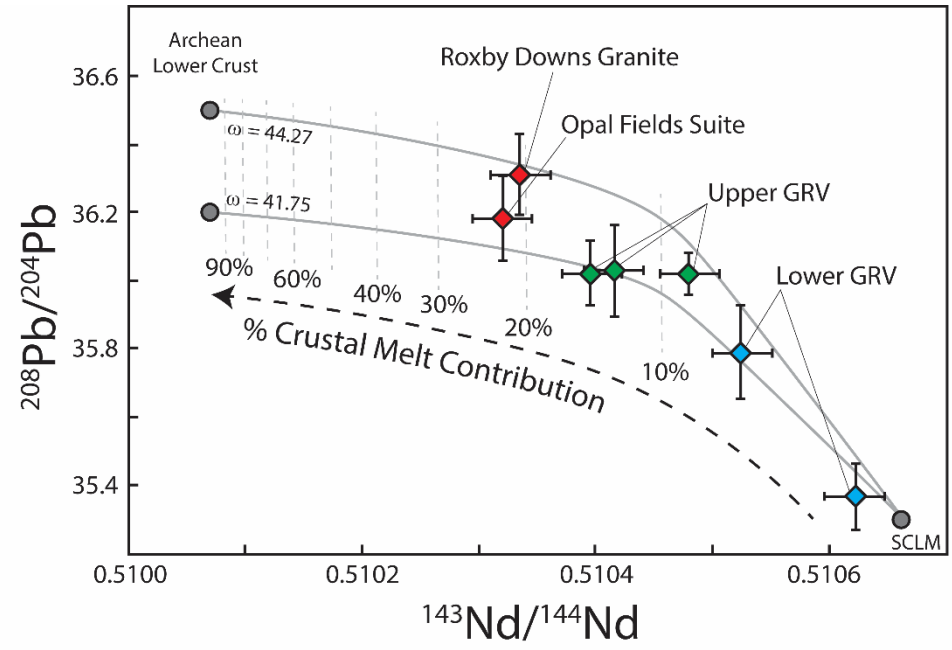

*Figure 5.11: Crust-mantle melt contribution modelling based on both Nd- and Pb-isotopic data. Combining both isotopic systems ensures that there is no bias towards either mantle, or crustal reservoir due to differences in concentration. The results for the RDG (22% crustal melt contribution) forms the end-member of an array which includes the coeval Gawler Range Volcanics, and highlights the importance of crust-mantle hybridisation in forming the RDG. SCLM = sub continental lithospheric mantle, ω = $^{232}Th/^{204}Pb$. Diagram modified after Chapman et al. (**2019**). End-member SCLM Pb-isotopic compositions adapted after Zartman and Haines, 1988; and Stewart, 1994, and Nd, Pb concentrations from McDonough, 1990.*

5.7 Conclusion

An integrated approach using in situ crystallographic and Pb-isotopic techniques has provided an insight into the magmatic origins, and post-magmatic modifications of the Roxby Downs Granite, which hosts the supergiant Olympic Dam Cu-Au-Ag-U deposit. The complex feldspar-phase relationships revealed here, highlight the advantages of in situ techniques over sequential-leach methods for investigating ancient initial Pb-isotopic compositions.

High-temperature (830 – 870°C) cryptoperthitic alkali feldspars (Or_{55}) retain initial Pb-isotopic signatures which indicate that the crustal-melt component of the Roxby Downs Granite was partially melted from an Archean lower crustal reservoir, that had a long term enrichment in U and Th, producing anomalous Pb. Olympic Dam is unique among the IOCG-class of ore-deposits in that it contains appreciable-quantities of U-mineralisation. Our finding that the Roxby Downs Granite was partially-sourced (~20% crustal melt) from a crustal reservoir anomalous in U provides a previously unrecognised link between granite petrogenesis and metal-inventory of the Olympic Dam ore deposit.

During the late-stage cooling-evolution of the Roxby Downs Granite, high-interfacial strain of the cryptoperthitic alkali feldspar has facilitated unmixing into albite and microcline components, which appears to be fluid-assisted. High-degrees of Al-Si ordering, and larger unit-cell parameters indicate the formation of microcline K-feldspar occurred at temperature conditions consistent with those involved in the earliest phase of ore-formation at Olympic Dam. Pb-isotopic disequilibrium between the primary-orthomagmatic alkali feldspar and post-magmatic microcline K-feldspar indicates that the replacement process did not occur topochemically, instead suggesting the prevalence of open-system behaviour between the granite and a country-rock from which radiogenic Pb was sourced. Open-system, Pb-isotopic exchange observed in the K-feldspars accompanied deuteric conditions in the Roxby Downs Granite and is consistent with the fluid-mixing model invoked for ore-genesis at Olympic Dam.

Acknowledgements

Funding for this research was primarily funded by BHP Olympic Dam Operations. Funding was also obtained as part of the Transforming the Mining Value Chain (TMVC) ARC Industrial Transformation Research Hub. The assistance of Dr. Sandrin Feig and Dr. Karsten Goemann from the Central Science Laboratory, University of Tasmania was invaluable during WDS and Hyperspectral CL work.

Chapter 6: Pb-Isotope Systematics Of The Olympic Dam IOCG-U: Evidence For A Protracted History Of Modification

N. D. Chapman[1] and S. J. Meffre[1]

[1] Transforming the Mining Value Chain (TMVC) ARC Industrial Transformation Research Hub/ Department of Earth Sciences, University of Tasmania, Hobart, Tasmania, Australia

6.1 Abstract

The Olympic Dam Cu-Au-Ag-U deposit, South Australia, represents one the largest polymetallic occurrences known, and yet, despite many years of concerted effort, there is still much to learn. The tenor of U mineralisation within Olympic Dam is considered particularly anomalous compared to other iron oxide-copper-gold (IOCG) deposits, where U concentrations are typically low, or sub-economic. Previous textural and isotopic (U-Pb and U-U) studies of U-mineralisation in Olympic Dam shows that most U has undergone some form of reworking, and it remains possible that the present grade and distribution of U within the deposit does not reflect primary mineralisation at ~1593 Ma. Since U radioactively decays to Pb, the Pb-isotopic system can present a unique insight into the ancient behaviour and concentrations of U, Th and Pb within Olympic Dam. This study reports the results of 397 individual Pb-isotopic analyses by laser ablation inductively coupled plasma mass spectrometry (LA-ICP MS) of Pb-chalcogenides (i.e. galena and clausthalite), pyrite and carbonate minerals (i.e. calcite and siderite) related to economic Cu-mineralisation at Olympic Dam. The textural, mineralogical and spatial constraints offered by this in situ isotopic technique, has been supplemented MLA and whole-rock geochemical datasets to provide the greatest possible context to the Pb-isotopic data presented here.

The least-radiogenic Pb-isotopic compositions of gangue carbonates and Pb-rich mineralisation provides constraints on the source and primary makeup of the U-Th-Pb system within Olympic Dam. Calcite crystals comprising some of the deepest and paragenetically-earliest magnetite-pyrite-chalcopyrite-apatite mineralisation known at Olympic Dam, contain some of the

most homogeneous and least-radiogenic Pb-isotopic isotopic signatures within the deposit ($^{206}Pb/^{204}Pb$ = 16.758 ± 0.098, $^{207}Pb/^{204}Pb$ = 15.476 ± 0.096, $^{208}Pb/^{204}Pb$ = 36.018 ± 0.116). Pb-isotopic arrays yielded from galena within areas of the deposit with the greatest Pb concentration, intersect the initial Pb-isotopic signature of the 1593 Ma Roxby Downs Granite, inferring that much of the Pb and possibly other metals were indeed derived from the host A-type granite. The Pb-Pb isochron age obtained from this low-$^{232}Th/^{238}U$ array suggest that high-U mineralisation was present before 1527 ± 147 Ma (MSWD = 2.6), confirming that U was part of the earliest-formed mineral assemblage.

The wide-range and systematic variations seen in the Pb-isotopic ratios of orezone Pb-chalcogenides, demonstrates a protracted history of mixing and U-disturbance at Olympic Dam. $^{232}Th/^{238}U$ and $^{238}U/^{204}Pb$ ratios inferred from Pb-isotopic signatures show a generally-poor correspondence to whole-rock geochemistry, suggesting that present-day concentrations of U, Th and Pb in parts of the deposit do not necessarily reflect the U/Th or U/Pb characteristics of the orezones in the past. Variations in peak $^{208}Pb/^{206}Pb$ and $^{207}Pb/^{206}Pb$ signature populations of the main Cu-ore types, suggest that highest-U concentrations should be associated with the bornite and chalcocite ores. Uranogenic Pb signatures correlate inversely with bornite (positive) and chalcopyrite (negative) inferring that highest U/Th and U/Pb conditions developed in association with bornite, at the expense of chalcopyrite.

A number of samples, most of which are from bornite and chalcocite zones of the deposit, show two-stage Pb-isotopic development, mixing first along a least-uranogenic trend ($^{232}Th/^{238}U \approx 1$) before departing towards strongly uranogenic Pb-isotopic compositions ($^{232}Th/^{238}U \approx 0$), consistent with recording a major U-disturbance event. The range of Pb-Pb isochron ages yielded from these uranogenic arrays (770 ± 140 Ma to 608 ± 71 Ma) are consistent with ~676 Ma marine transgression and deposition of clastic sediments directly above the Olympic Dam unconformity. We therefore contest that the incursion of oxidised marine fluids during the Cryogenean – Ediacaran into the breccia complex was responsible for redox-driven modification of U mineralisation which led to some redistribution and upgrading of the U-resource at Olympic Dam. Furthermore, the relationship

between uranogenic Pb-isotopic signatures and bornite-chalcocite dominant assemblages, leads us to believe that Cu-ores were also affected during the Late Neoproterozoic, contributing to the deposit-wide and economically-important vertical zonation between chalcopyrite and bornite-chalcocite observed at Olympic Dam.

6.2 Introduction

Decades of research on the Olympic Dam Cu-Au-Ag-U deposit has seen continued advancements in our understanding of this world-class resource, and yet many more questions still remain. As one of the world's largest polymetallic resources (Total Resource 10892 Mt @ 0.73% Cu, 0.24 kg/t U3O8, 0.31 g/t Au, 1 g/t Ag (BHP Annual Report, 2019)), understanding how a deposit of this size is formed remains crucial to driving future exploration discoveries. Deposit models for Olympic Dam have cycled from the early syngenetic, sediment-hosted model of Roberts and Hudson (1983), to the volcanogenic maar-diatreme model (Cross et al., 1993; Reeve et al., 1990) and has more recently returned to focus on the potential influence of syngenetic, sedimentation (McPhie et al., 2011b) and magmatic-related scenarios (Verdugo-Ihl et al., 2019). The absence of concrete geochronological evidence for a ~1.59 Ga primary mineralisation event during the earliest studies, led some authors to introduce the idea of epigenetic, structurally-controlled mineralisation which post-dates and is unrelated to magmatism (Oreskes and Einaudi, 1990). More-recently, however, 1593.5 Ma U-Pb ages have been found in rare, euhedral uraninites (Apukhtina et al., 2017), 1590-1577 Ma U-Pb ages obtained from hematite (Ciobanu et al., 2013; Courtney-Davies et al., 2018), and ~1590-1537 Sm-Nd isochrons yielded from the work of Johnson and McCulloch (1995) and Apukhtina et al. (2017) all demonstrate that at least some mineralisation must have occurred penecontemporaneous with the emplacement of the Roxby Downs Granite.

A growing body of isotopic evidence, however, has returned to the concept of an epigenetic overprint of the deposit and potential for post-1593 Ma introduction of metals as an explanation for

the enormous size of the resource. Early U-Pb analyses of uraninites by Trueman (1986) yielded distinct age populations at ~1400 Ma and ~550 Ma which confirm textural observations suggesting periodic recrystallisation of earlier-formed uraninites (Ehrig et al., 2012; Macmillan et al., 2016; Reeve et al., 1990). Whole-rock Sm-Nd isochrons from step-leached ores yield ~1300-1100 Ma apparent ages (Maas et al., 2011), while ~500 Ma Sm-Nd ages are obtained from paragenetically-late fluorite-rich veins (Warwyk, 1989). A similar range of ages is also reflected in the Rb-Sr system which reveal ~1315 Ma (Gustafson and Compston, 1979) and 550-450 Ma (Maas et al., 2011) ages obtained from sericite which forms part of the alteration assemblage of Olympic Dam. Recent studies have identified the incorporation of large blocks of ~1440 Ma Pandurra Formation within the ODBC (Cherry et al., 2017), providing a geological basis for some of these isotopic ages. The correlation of these ages with the amalgamation of Rodinia (1.2-1.1 Ga) and the ~500 Ma Delamerian Orogeny has led some authors to speculate that the exceptional size of Olympic Dam may be due to the confluence of several stages of metal deposition in response to renewed crustal-scale fluid flow (Cherry et al., 2017; Maas et al., 2011; Oreskes and Einaudi, 1992). At the very least, the convergence of multiple isotopic systems indicates some disturbance event/s has affected Olympic Dam post crystallisation of the major magmatic units.

Recent U-U isotopic studies at Olympic Dam have found little evidence for a ~1590 Ma formation of high-grade U ore (Kirchenbaur et al., 2016), and together with the aforementioned U-Pb age populations, infer that the ancient distribution of U within Olympic Dam does not correlate with what is observable today. The Pb-isotopic system (^{204}Pb, ^{206}Pb, ^{207}Pb, ^{208}Pb) can be used to investigate the history of U enrichment within the deposit. ^{206}Pb, ^{207}Pb and ^{208}Pb are produced from the radioactive decay of ^{238}U, ^{235}U and ^{232}Th, respectively, while ^{204}Pb is non-radiogenic. Since the geochemical behaviours of U, Th, and Pb are all radically different, Pb-isotopic compositions can be used to reveal the ancient relationships, disturbances and sources of U, Th and Pb. Variations in uranogenic ^{206}Pb and ^{207}Pb relative to non-radiogenic ^{204}Pb also provide a way of investigating the age of U enrichment and remobilisation. The major aim of this study is to investigate the potential

for modification and enrichment of U within Olympic Dam.

6.3 Geological Context

Olympic Dam is located in the northeast of the Mesoarchean to Mesoproterozoic-aged Gawler Craton, of southern Australia (fig. 6.1). Mineralisation at Olympic Dam is hosted within the Olympic Dam Breccia Complex (ODBC), which is approximately 7 km long at its widest, and extends to a known depth of at least 2.3 km. The ODBC is entirely enclosed with the 1593 Ma (Cherry et al., 2018) Roxby Downs Granite (RDG) – a medium-grained monzogranite belonging to the Hiltaba Suite which is widespread throughout the Gawler Craton. The ODBC and RDG are disconformably overlain by approximately 300 m of Late Proterozoic and Early Cambrian, shallow-marine carbonates, sandstones and shales.

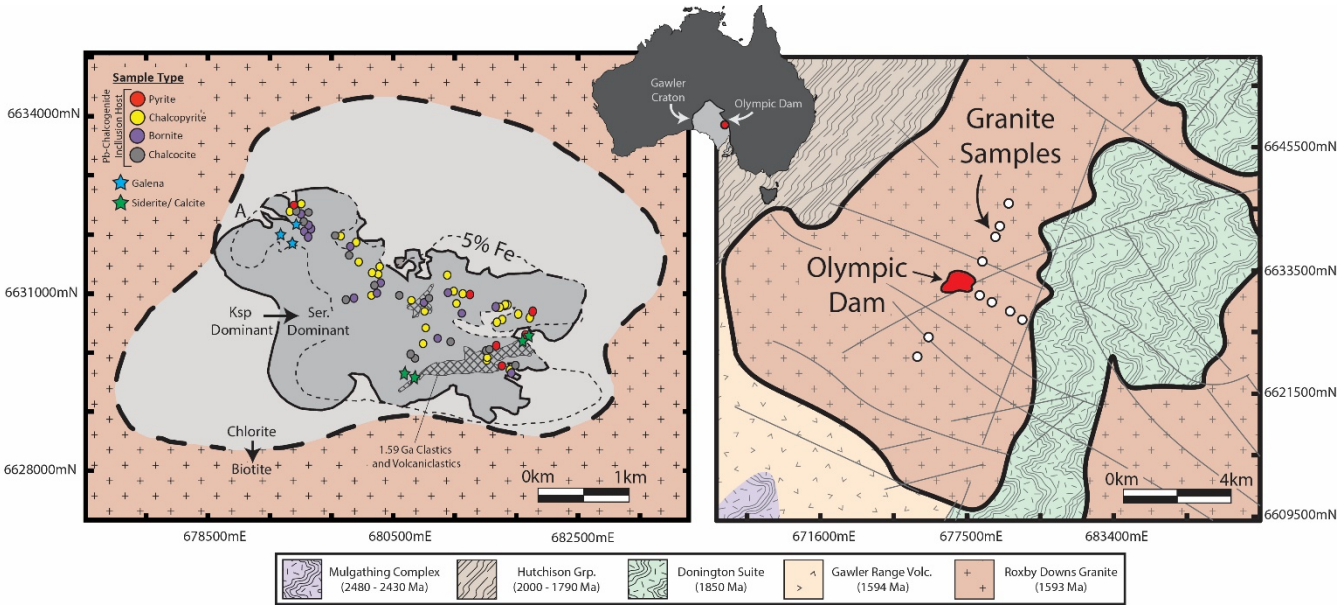

Figure 6.1: Overview of the sample locations used in this study. Ore zone sample locations (left) are shown within the context of major alteration facies and Fe-concentration. Whole-rock drillcore samples of the Roxby Downs Granite (right) are shown in a regional context (excluding two additional samples from the same drillhole).

Most breccia clasts within the ODBC are dominantly derived from the RDG. The clasts show a spectrum of size and shape distributions indicative of both mechanical brecciation and chemical abrasion (McPhie et al., 2011a). Large blocks of ~1590 Ma bedded, clastic sediments as well as clasts

of both felsic and mafic equivalents of the ~1590 Ma Gawler Range Volcanics are also incorporated in the breccia (Cherry et al., 2018). All clast lithologies are strongly sericite-hematite- siderite altered with a dominantly hematite-quartz-siderite-sericite-chlorite matrix. Cu-sulphides, U-mineralisation and Au (as electrum) occur as fine-grained disseminations and blebs within the hematitic breccia matrix.

Chalcopyrite ($CuFeS_2$) constitutes approximately 67% of the Cu-sulphide ore at Olympic Dam, with important but subordinate contributions from bornite (~24%; Cu_5FeS_4) and chalcocite-digenite (9%; Cu_2S – Cu_9S_5) (Ehrig et al., 2012). The deposit-wide zonation of Cu-sulphide ore is well-established (Cross et al., 1993; Ehrig et al., 2012; Reeve et al., 1990), forming a broad yet irregular horizontal interface between bornite and chalcocite zones overlying chalcopyrite-pyrite zones. Cu-sulphide textures in proximity to the chalcopyrite-bornite/ chalcocite interface are complex and often show conflicting paragenetic relationships. Away from the interface, chalcocite and bornite form complex intergrowths which are interpreted to be exsolution textures from primary solid solutions initially formed at temperatures in-excess of 300°C (Ciobanu et al., 2017). Importantly, the limited abundance of 'sooty' chalcocite has been considered evidence that chalcocite is part of the primary, hypogene assemblage (Reeve et al., 1990). Pyrite is most commonly associated and in textural equilibrium with chalcopyrite, although chalcopyrite is also commonly observed replacing pyrite in an apparent sulphur-scavenging reaction (Ehrig et al., 2012).

The textural and paragenetic relationships between U-ore minerals are also complex, suggesting repeated episodes of dissolution and reprecipitation (Ehrig et al., 2012; Macmillan et al., 2016; Reeve et al., 1990). Unlike the Cu-sulphide minerals, there is no apparent deposit-scale zonation observed in the U-ore minerals (Ehrig et al., 2012), though concentrations vary, with higher-grades of nearly 1% U_3O_8 reported near to the chalcopyrite-bornite transition in some parts of the deposit (Cross et al., 1993; Reeve et al., 1990). Approximately 56% of U-ore mineral hosts at Olympic Dam is represented by coffinite ($U(SiO_4)_{1-x}(OH)_{4x}$), with a further 31% as brannerite (UTi_2O_6)

and 13% as uraninite (UO_2). Uraninite becomes an increasingly important U-host in ore with Fe-concentrations greater than 20 wt. % (Ehrig et al., 2012).

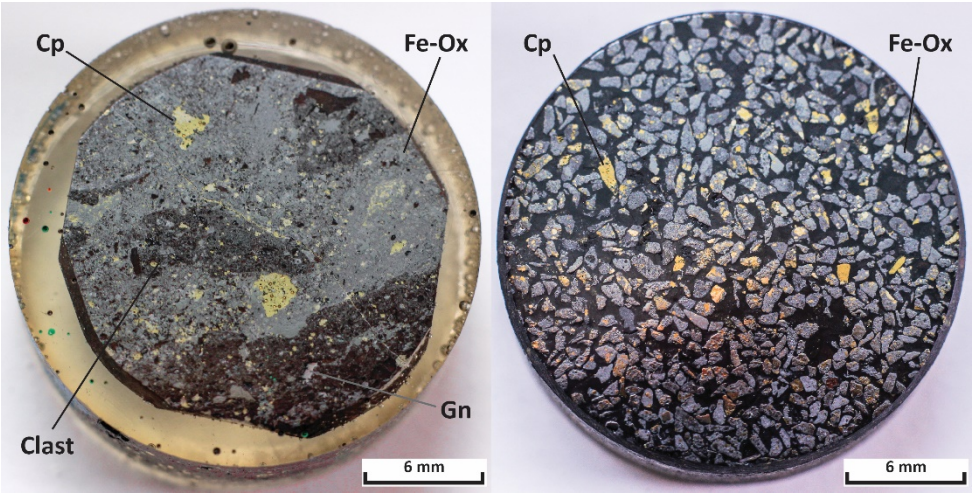

Figure 6.2: a) A 1-inch round epoxy resin mount, typical of non-crushed ore samples analysed here. Samples such as this were prepared to provide additional macroscopic textural context for Pb-isotopic host mineralogy. b) A 1-inch round epoxy resin mount typical of crushed ore samples. The splits from these samples also underwent XRD and whole-rock geochemical analysis. Cp = chalcopyrite, Gn = galena, Fe-Ox = iron oxides.

6.4 Sampling Strategy

6.4.1 Sampling strategy and preparation

High-Pb sulphide minerals (i.e. galena) and low-Pb, U-Th absent minerals (i.e. calcite) were obtained from a wide range of locations throughout the Olympic Dam deposit. 66 samples in total, yielded 409 individual Pb-isotopic analyses. Of the 409 analyses, 352 were obtained exclusively from Pb-associated with Cu-sulphides (as inclusions and intergrowths), while 44 analyses were obtained from carbonates (i.e. siderite and calcite) genetically-associated with ore. Carbonate samples were obtained from diamond-drill core, while sulphide samples were yielded from a combination of diamond-drill core and mineral separates (fig. 6.2). Sulphide samples with the prefix "FCO-" are 20 m composite-intervals of half-cut diamond drill core, representative of Olympic Dam head-grade ore types. Rock was crushed to 1 - 5 mm size fraction, which preserves assemblage textures and geological context for high-Pb sulphides targeted in this study (fig. 6.2). FCO-samples are categorised

by their dominant Cu-Fe sulphide species (i.e. chalcopyrite, bornite, chalcocite), which along with a suite of 85 silicate, carbonate, sulphate and sulphide minerals, were quantified using a combination of powder-XRD (see Ehrig et al., 2012) and Mineral Liberation Analysis (MLA; Gu (2003)).

13 whole-rock samples of weakly-altered, unmineralized Roxby Downs Granite were acquired from around the Olympic Dam deposit with the purpose of creating a baseline to compare with Pb-isotopic signatures from the deposit itself. Specimens were all half-core, HQ-size diamond drill hole samples, obtained from at least 100 m below the Early Mesoproterozoic – Late Neoproterozoic unconformity to minimise potential near-surface effects on U-Pb fractionation (Rosholt et al., 1973). 5 samples were collected from 2.8 to 5.3 kms south of the deposit, with 4 samples from between 4.4 and 7.2 km to the north and a further 4 samples between 1 to 2 kms to the east of the deposit (fig. 6.1).

6.4.2 Analytical targets, and targeting criteria

The dominant Pb-chalcogenide species associated with the ores of Olympic Dam are galena (PbS), clausthalite (PbSe) and altaite (PbTe). Pb is also incorporated within the crystal structures of common gangue minerals such as calcite ($CaCO_3$), siderite ($FeCO_3$) and pyrite (FeS_2).

Galena is by far the most prevalent Pb-rich mineral present at Olympic Dam, and represents approximately 70% of the Pb-chalcogenides in samples used for this study. It is observed as interstitial-growths between minerals such as pyrite and hematite, as intergrowths with Cu-sulphides (such as chalcopyrite; fig. 6.3d, e) and as inclusions within other minerals (such as bornite). It is generally fine-grained (<300 μm), however forms coarser-blebs (<2 mm; fig. 6.3e) in parts of the deposit with the highest Pb (>1 wt. %). Fine-grained galena is very commonly developed as poikilitic inclusions within, and rimming U-rich minerals such as coffinite, brannerite and uraninite (fig. 6.3f). A large portion of the Pb with such textured galena is almost certainly derived from the nearby U-rich minerals through diffusion or during recrystallisation (i.e. Macmillan et al. (2016)). Since we are

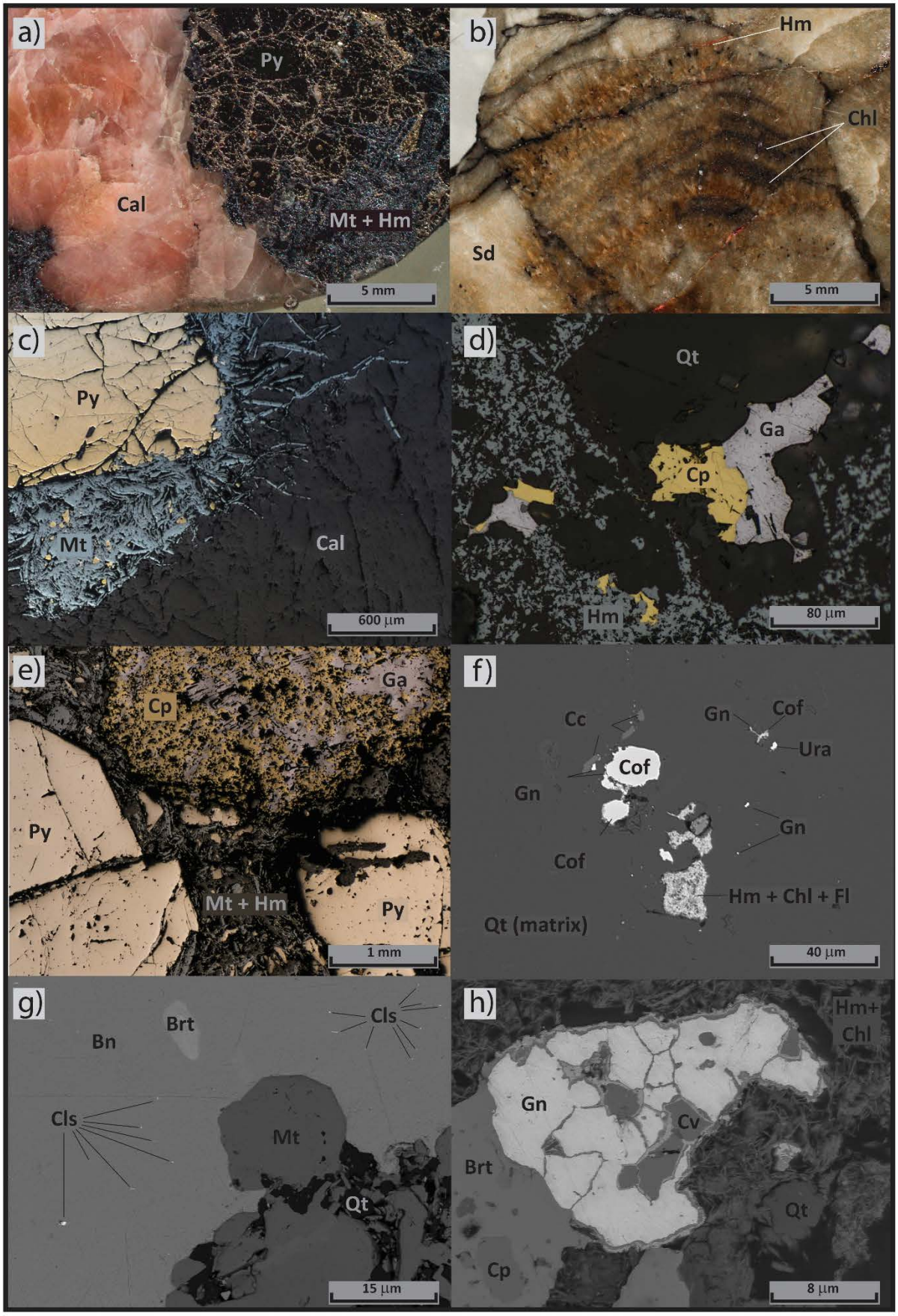

Figure 6.3: Macro- and microscopic mineralogical context for the Pb-chalcogenides (galena and clausthalite), pyrite and carbonates (calcite and siderite) analysed in this study. Abbreviations: Cal = calcite, Py = pyrite, Mt = magnetite, Hm = hematite, Chl = chlorite, Sd = siderite, Qt = quartz, Cp = chalcopyrite, Ga = galena, Cof = coffinite, Urn = uraninite, Fl = fluorite, Cc = chalcocite, Bn = bornite, Brt = barite, Cls = clausthalite, Cv = covellite.

targeting common Pb and unsupported Pb isotopic signatures within Olympic Dam, galena within ~10 µm of observable U-rich minerals was not chosen for analysis.

Clausthalite is the second most-common Pb-chalcogenide mineral at Olympic Dam, representing ~22% of the Pb-chalcogenides in samples used in this study. It was only observed as fine-inclusions (<10 µm; fig. 6.3g) and symplectites within bornite and chalcocite. Altaite is far rarer (<5% of Pb-chalcogenides), and was only observed as microinclusions (<2 µm) within chalcocite which were too small to directly target using the in situ Pb-isotopic technique applied here.

Siderite was analysed in samples with cream- to brown-beige breccia clasts (fig. 6.3b) in a dominantly hematite matrix. Siderite is coarse-crystalline (1 – 3 mm) and has developed epitaxially to the prominent millimetre- to centimetre-sized laminations. Siderite crystals are variably intergrown with hematite and chlorite. Chalcopyrite, galena, sphalerite, hematite and fluorite form abundant inclusions along laminations and clast boundaries. Clasts and laminations are cross-cut by paragenetically-late barite (± chalcopyrite) filled fractures and veinlets.

The calcite samples analysed here are from the deepest (2182 mRL) and paragenetically-earliest mineral assemblage present at Olympic Dam (Apukhtina et al., 2017). Calcite is developed as centimetre-sized, pink crystals (fig. 6.3a) within a cockscomb-textured breccia matrix. The pink, calcite matrix hosts breccia clasts (1 – 10 cm) comprised of pyrite-chalcopyrite-magnetite (1 – 10 cm; fig. 6.3c) and strongly sericitised quartz-phyric rhyolite dyke. Calcite crystals are optically translucent to transparent, containing almost no inclusions.

6.5 Analytical Procedures

6.5.1 Electron Microscopy and Mineral Liberation Analysis (MLA)

Sample reconnaissance mapping and textural characterisation was achieved through a combination of reflected-light optical microscopy, and scanning electron microscopy (SEM). Electron dispersive spectroscopy (EDS) and back-scatter electron images (BSE) was undertaken using an FEI MLA 650

ESEM and a Hitachi SU-70 field-emission SEM housed at the Central Science Laboratory, University of Tasmania, using a 15 kV accelerating voltage, and 5 nA beam current. Imaging parameters were optimised to identify galena and other Pb-rich minerals. Mineral liberation analysis (MLA) was carried out on all ore-samples with the prefix 'FCO-' using the FEI MLA 650 ESEM with inbuilt, automated MLA (v3.1) software (Gu, 2003) at the University of Tasmania.

6.5.2 Whole-rock Geochemistry

A suite of 55 elements was obtained from 43 of the whole-rock ore samples to inform the interpretation of the Pb-isotopic results. All analyses were undertaken at Intertek Laboratory in Adelaide, Australia. A summary of the sample preparation and analytical techniques used to acquire the geochemical dataset are summarised below;

- Lithium metaborate fusion, inductively coupled plasma – mass spectroscopy (ICP-MS):
  La, Ce, Pr, Nd, Sm, Eu, Gd, Tb, Dy, Ho, Er, Tm, Yb, Lu, Ba, Be, Cs, Ga, Hf, Mo, Nb, Rb, Sb, Sn, Ta, Th, U, W, Y, Zr.
- Lithium metaborate fusion, inductively coupled plasma – optical emission spectroscopy (ICP-OES):
  (Al, Ca, Cr, Fe, K, Mg, Mn, Na, P, Sc, Si, Sr, Ti, V)
- Four-acid digest ($HClO_4$, HF, HNO_3, HCL) with inductively coupled plasma – mass spectroscopy (ICP-MS);
  (Ag, As, Bi, Cd, Co, In, Re, Se, Te, Tl)
- Four-acid digest ($HClO_4$, HF, HNO_3, HCL) with inductively coupled plasma – optical emission spectroscopy (ICP-OES):
  (Li, Ni, Pb, Zn, Cu)

6.5.3 Laser ablation inductively coupled mass spectrometry (LA-ICP-MS)

In situ Pb-isotope and trace-elements in sulphide ore samples were determined using LA-ICP-MS. LA-ICP-MS provides three-major advantages over high-precision solution-based MC-ICP-MS; low-cost, fast analytical throughput, and a flexible, dynamic signal range which can tolerate transient, high-Pb signals. Pb-isotopic analyses were obtained over several sessions from 05/2015 to 12/2015 at the University of Tasmania Laser Ablation Analytical Facility.

An Agilent 7500 ICP-MS was coupled to a Coherent COMPex Pro 193 nm ArF Excimer laser system equipped with a Laurin Technic RESOlution S155 cell. Laser frequencies of 5 Hz with a high-energy fluence (13 J/cm^2) ensured that downhole signal loss was minimal in sulphide analyses (fig. 6.4). For carbonate analyses (siderite and calcite), laser pulse frequencies of 10 Hz and energy density of 3.5 J/cm^2 were used. Ablation was carried out in a He-Ar (3:1) atmosphere, with nitrogen added at 3.5 mL/s to improve sensitivity (i.e. Crowe et al. (2003); Hu et al. (2008)), with an overall carrier gas flow-rate of 350 mL/min. An inline smoothing device ("SQUID"; Müller et al. (2009)) were added to improve signal-stability. For the carbonate analyses, an inline particle separator (Guillong et al., 2003) was employed to smooth the signal and improve analytical uncertainty.

A spot-size of 25 µm was used to provide spatial resolution necessary for analysis of the fine-grained sulphides ores. Measurement took place over 60 seconds, with 20 seconds of background and 40 s of ablation (fig. 6.4b). A total of 38 masses were analysed during sulphide analyses, in an attempt to effectively characterise the mineral host of the Pb. A short dwell-time (5 ms) was used for non-Pb masses to minimise the effects of the non-simultaneous detection of the Pb isotopes on the quadrupole mass spectrometer (^{27}Al, ^{34}S, ^{47}Ti, ^{55}Mn, ^{57}Fe, ^{59}Co, ^{60}Ni, ^{65}Cu, ^{66}Zn, ^{75}As, ^{77}Se, ^{82}Se, ^{89}Y, ^{90}Zr, ^{95}Mo, ^{109}Ag, ^{111}Cd, ^{118}Sn, ^{121}Sb, ^{126}Te, ^{140}Ce, ^{157}Gd, ^{172}Yb, ^{178}Hf, ^{181}Ta, ^{182}W, ^{185}Re, ^{197}Au, ^{205}Tl, ^{209}Bi). A longer dwell-time (20 ms) was used for ^{202}Hg, ^{204}Pb, ^{206}Pb, ^{207}Pb, ^{208}Pb, ^{232}Th, ^{235}U, ^{238}U.

For carbonates, larger spot-sizes (110 – 165 µm) were used due to the lower-Pb concentrations, while the 60 second analysis comprised of 10 seconds of background and 50 seconds of ablation (fig. 6.4a). ^{23}Na, ^{24}Mg, ^{27}Al, ^{29}Si, ^{31}P, ^{39}K, ^{43}Ca, ^{47}Ti, ^{56}Fe, and ^{137}Ba were counted for 5 ms

each, while ^{202}Hg, ^{204}Pb, ^{206}Pb, ^{207}Pb, ^{208}Pb, ^{232}Th, and ^{238}U, ^{208}Pb were counted for 20 ms each.

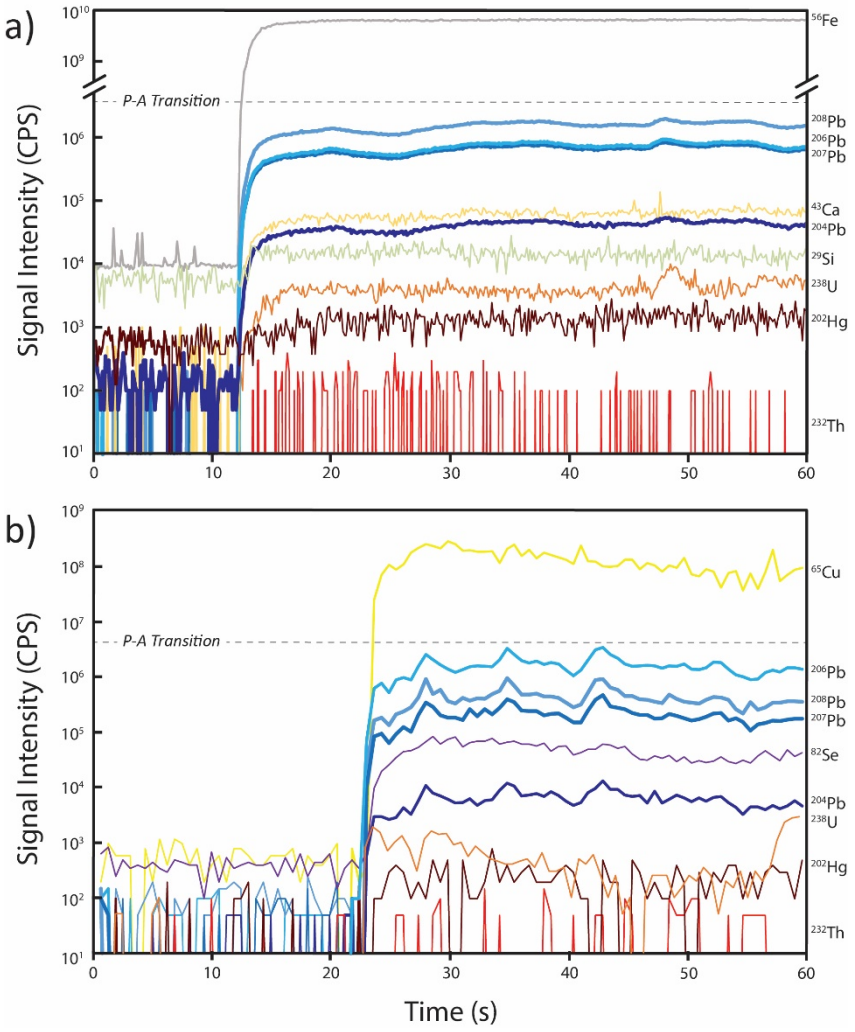

Figure 6.4: Typical examples of time-resolved LA-ICP MS spectra obtained from analysing a) carbonates and b) sulphides. Analytical conditions were optimised to ensure high signal intensities that also remained below the pulse-analogue transition. Note the difference in signal intensity maintained between ^{202}Hg and ^{204}Pb, which minimises the effects of ^{204}Hg/^{204}Pb isobaric interference.

Isobaric interferences caused by ^{204}Hg on ^{204}Pb, were corrected using the peak-stripping method outlined in Willigers et al. (2002), using a ^{202}Hg:^{204}Hg ratio of 4.32. Data reduction was carried out using in-house software. Analyses were rejected if stable Pb signals could not be maintained for more than 5 secs, in order to mitigate the potentially deleterious effects caused by single-detector measurements on transient signals (Crowe et al., 2003). Additionally, analyses were also rejected if ^{204}Pb count-rate was less than 10-times ^{202}Hg count-rate, in order to reduce the effects of isobaric interference corrections (^{204}Hg/^{204}Pb) at lower signal count rates. This introduces some bias towards relatively unradiogenic Pb-isotopic results, but removes problems associated

with $^{204}Hg/^{204}Pb$ uncertainty.

Unless otherwise stated, all regression used for isochrons utilise the method of York (1968) from data plotted on $^{207}Pb/^{206}Pb$ vs $^{204}Pb/^{206}Pb$ diagrams. Inverse Pb diagrams, coupled with York Regressions mitigate the effects of ^{204}Pb-based error-correlation, and better account for individual uncertainty within the data (Ludwig, 2012).

6.5.4 Whole-rock Pb-isotopic analyses (Four-acid digest, ICP-MS)

13 whole-rock samples of Roxby Downs Granite were analysed for Pb-isotopes in the ALS laboratory, Vancouver, Canada. Samples were crushed to a maximum particle size of 75 µm before riffle splitting. Each aliquot (0.5 g) then under went four-acid digestion ($HClO_4$, HF, HNO_3, HCL), followed by an additional round of heat-leaching by HCl at 100°C. The cooled solution was then diluted to a volume of 25 mL with 10% HCl and analysed by ICP-MS. Internal standards were run at the beginning and end of the 13-sample session. External standards (megacrystic feldspar) and blanks (pure SiO_2) were also run every 8 analyses to further monitor QA/QC performance.

Table 6.1: Results of LA-ICP-MS Pb-isotopic analyses on standard reference materials

	Pb Conc.	**$^{206}Pb/^{204}Pb$ [MSWD]**	**$^{207}Pb/^{204}Pb$ [MSWD]**	**$^{208}Pb/^{204}Pb$ [MSWD]**
GSD-1G (Rec. Values[1])	50 ppm	19.5790 ± 0.0408	15.7450 ± 0.0254	38.9080 ± 0.0462
Our Values (Wt. Av.)	-	19.5779 ± 0.0472 [1.01]	15.7381 ± 0.0428 [0.75]	38.8935 ± 0.0940 [0.49]
STDGL2B2 (Rec. Values[2])	0.12 wt. %	16.383	15.327	35.578
Our Value (Wt. Av.)	-	16.3738 ± 0.0167 [0.92]	15.3165 ± 0.0147 [0.64]	35.5221.0377 [0.39]

[1] Jochum et al. 2007, [2] Danyushevsky et al. pers. comms.

6.6 Results

The LA-ICP-MS Pb-isotopic results of standard reference materials are presented in Table 6.1 and summarised in Figure 6.5. Data were reduced to GSD-1G (primary calibration standard). External reproducibility was confirmed using the sulphide-matrix STDGL2b2 (secondary check standard). All

results are within 2σ uncertainty of reference values and yield mean square weighted deviations (MSWD) for ^{204}Pb-based ratios of between 1.01 and 0.39. Average uncertainties for ^{206}Pb-based and ^{204}Pb-based ratios of yielded from GSD-1G (50 ppm Pb) are 1.22% and 2.38%, respectively. Average uncertainties or ^{206}Pb-based and ^{204}Pb-based ratios of yielded from STDGL2b2 (1200 ppm Pb) are 0.86% and 0.72%, respectively.

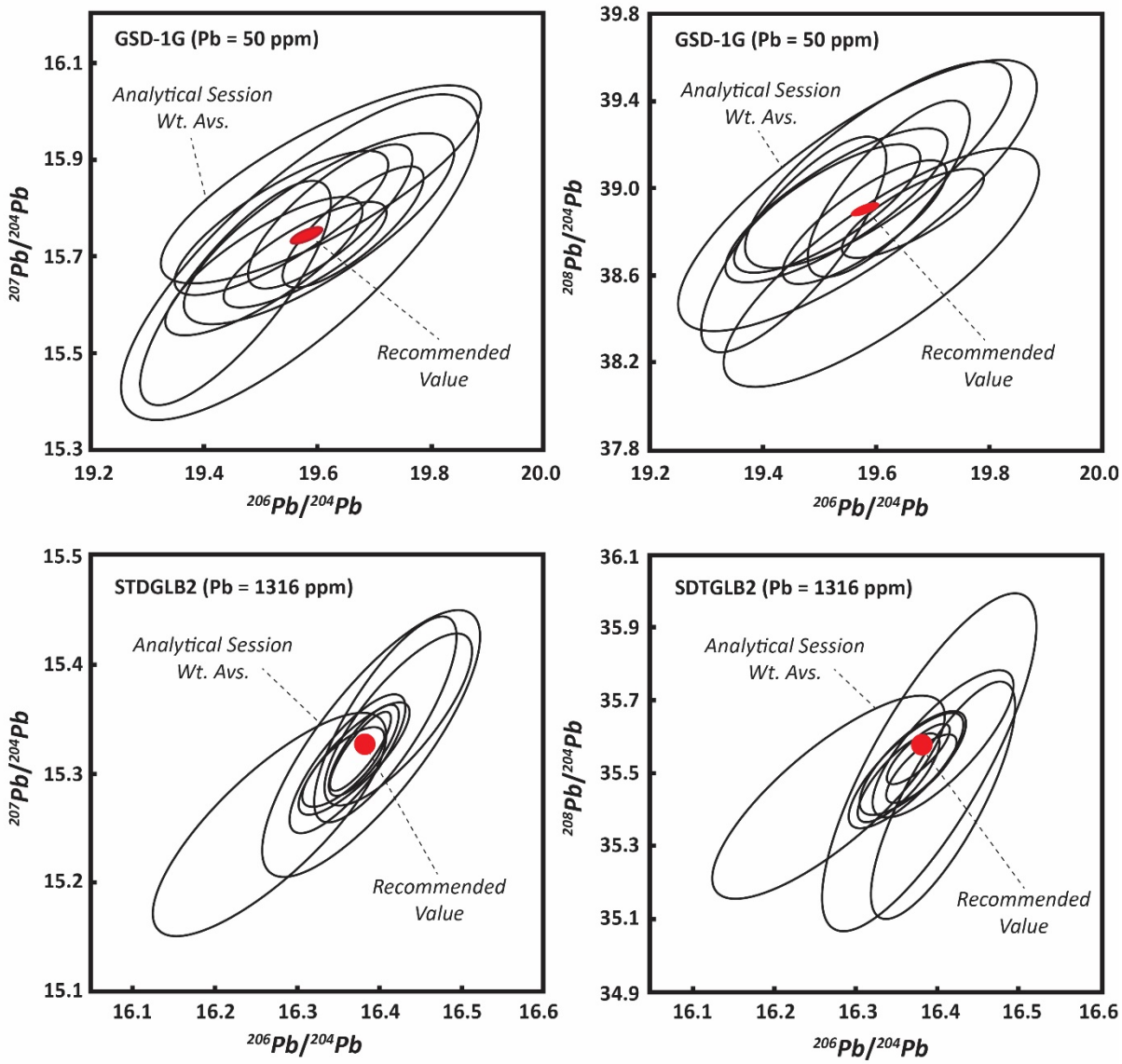

Figure 6.5: ^{204}Pb-based Pb-isotopic plots demonstrating the accuracy an of LA-ICP MS analyses on glass-matrix (primary standard) and sulphide-matrix (secondary standards) reference materials. Individual ellipses represent the 2σ weighted average of each analytical session.

All 397 in situ Pb-isotopic results for the Olympic Dam ore-assemblage are presented in Appendix H and figures/ tables herein. Analytical uncertainties vary depending on Pb signal intensity

and size of spectral integration of the Pb-rich mineral (i.e. longer integration times yielded smaller uncertainties). Average uncertainties (2σ) on ^{204}Pb-based ratios of galena were 0.66%, 0.65% for pyrite, 0.71% for carbonates (siderite and calcite), and 2.9% for Pb-chalcogenide inclusions in Cu-Fe sulphides.

For whole-rock granite Pb-isotopic results, a nominal analytical uncertainty of 2% (2σ) is assigned for ^{204}Pb-based ratios. However, Pb-isotopic results for megacrystic K-feldspar analysed as an external standard suggest analytical reproducibility may in fact be slightly better, approaching 0.82% (2σ) for ^{204}Pb-based ratios, and 0.52% (2σ) for ^{206}Pb-based ratios. Nonetheless, all calculations related to whole-rock Pb-isotopic compositions of the RDG apply the nominal 2% (2σ) uncertainty.

6.7 Discussion

Pb-isotopic compositions obtained from both carbonate and sulphide minerals at Olympic Dam cover a wide range of values, from least-radiogenic compositions in paragenetically-early calcites (^{206}Pb/^{204}Pb = 16.758, ^{207}Pb/^{204}Pb = 15.476, ^{208}Pb/^{204}Pb = 36.018) to extremely radiogenic compositions of clausthalite inclusions hosted by chalcocite (^{206}Pb/^{204}Pb = 834.05, ^{207}Pb/^{204}Pb = 69.03, ^{208}Pb/^{204}Pb = 78.68). Since all ore-zone Pb-isotopic results presented here were obtained in situ from Pb-chalcogenides, with very little U-Th (orders of magnitude less than the Pb), and not immediately adjacent to minerals rich in U or Th, all radiogenic Pb-isotopic compositions are considered unsupported by direct or nearby contribution from parental ^{238}U, ^{235}U, or ^{232}Th. Fundamentally, unsupported radiogenic compositions indicate that the Pb system has been fractionated from U and Th to some extent.

The overall lack of correlation between Pb-isotopic compositions and whole-rock U, Th, Pb concentrations suggests disturbance of the isotopic system has taken place (fig. 6.6). In fact, few samples analysed here show whole-rock U/Pb or Th/U ratios indicative of direct radiogenic Pb contribution from U-rich minerals within the samples (fig. 6.6). It is therefore considered highly-

probable that Pb and probably U has been redistributed and remobilised at some time after the initial mineralising event.

The discussion of the potential significance of U, Th and Pb redistribution at Olympic Dam will be structured to first look at the least-radiogenic signatures measured, before considering the more-radiogenic compositions associated with the Cu-ores. Emphasis will be placed on understanding the isotopic composition of both common Pb and radiogenic Pb end-members to differentiate early U-Th-Pb variations at Olympic Dam from potentially later modification, before placing temporal and geochemical constraints on the modification events.

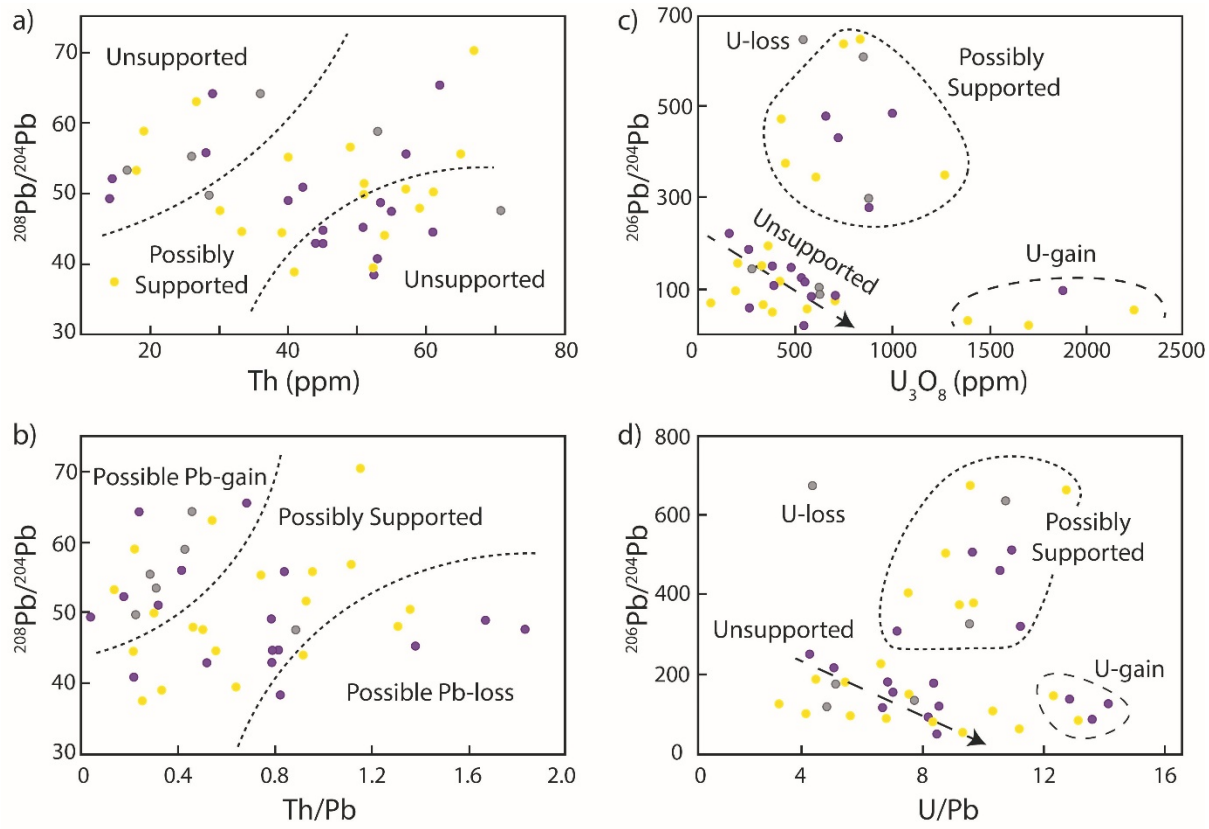

Figure 6.6: Whole-rock geochemical relationship of U, Th, Pb against Pb-isotopic compositions. Yellow points represent chalcopyrite-dominant samples, purple points represent bornite-dominant samples, grey points represent chalcocite-dominant samples.

6.7.1 Roxby Downs Granite Whole-Rock System

13 whole-rock Pb-isotopic analyses of weakly-altered but unmineralized Roxby Downs Granite (RDG) were analysed to provide an insight into the Pb-isotopic behaviour of the granite for comparison.

These samples return Pb-isotopic values in the following ranges $^{206}Pb/^{204}Pb$ = 21.3 - 61.0, $^{207}Pb/^{204}Pb$ = 15.9 – 19.1, $^{208}Pb/^{204}Pb$ = 39.3 – 89.9 (Table 6.2). The data forming an array on Pb-isotopic plots indicating the coupled behaviour of U/Pb and Th/Pb systems. The least radiogenic end of the array intercepts the initial Pb-isotopic signature of the RDG. The slope of the $^{206}Pb/^{204}Pb$ vs $^{208}Pb/^{204}Pb$ array implies a $^{232}Th/^{238}U$ ratio of ~4 similar to that modelled for the $^{232}Th/^{238}U_t$ of the RDG initial Pb-isotopic signature (4.032; Chapter 5). This implies a relatively simple behaviour of U, Th and Pb systems within the granite, in contrast to the very complex Pb-isotopic systematics of the ODBC.

Table 6.2: Whole Rock Pb-isotopic analyses for the Roxby Downs Granite

Drillhole	Depth (m)	Pb (ppm)	$^{206}Pb/^{204}Pb$	±(2σ)	$^{207}Pb/^{204}Pb$	±(2σ)	$^{208}Pb/^{204}Pb$	±(2σ)
RD2488	576.0	2.6	21.38	0.43	15.95	0.32	39.33	0.79
HRD002	438.0	17.5	22.90	0.46	16.11	0.32	42.08	0.84
HRD001	382.0	13.1	26.67	0.53	16.40	0.33	44.72	0.89
RD2488	491.0	13.7	27.53	0.55	16.50	0.33	48.91	0.98
RD2274	342.0	4.8	29.74	0.59	16.66	0.33	52.47	1.05
RD2488	513.7	10.9	31.44	0.63	16.70	0.33	54.42	1.09
RD2323	446.1	15.7	41.41	0.83	17.74	0.35	62.51	1.25
RD2488	369.3	6.5	43.71	0.87	17.90	0.36	65.68	1.31
RD2326	444.6	5.5	45.18	0.90	17.82	0.36	66.75	1.34
RD2336	428.8	6.9	50.21	1.00	18.38	0.37	73.61	1.47
RD2499	499.3	10.1	50.30	1.01	18.22	0.36	69.74	1.39
RD2280	452.2	5.4	51.14	1.02	18.36	0.37	69.54	1.39
RD2347	533.6	6.9	61.01	1.22	19.08	0.38	83.88	1.68

Regression through the Pb-isotopic data array on the $^{206}Pb/^{204}Pb$ vs $^{207}Pb/^{204}Pb$ diagram (fig. 6.7a) yields a gradient of 0.0823, corresponding to an apparent age of 1252 ± 86 Ma (MSWD = 0.32) using the equation of Nier et al. (1941). This age is interpreted to reflect the last time the Pb-isotopic system was reset to a single common value (Rosholt et al., 1973). While inconsistent with the 1593 Ma age of emplacement for the RDG, it is consistent with the 1315 Ma Rb-Sr age obtained for altered RDG by Gustafson and Compston (1979), and ~1300 Ma Rb-Sr ages obtained from ores by (Maas et al., 2011). The coincidence of these ages suggests isotopic disturbance of the RDG during the Mid to Late Mesoproterozoic. This may coincide with initial unroofing of the RDG or the regional-

scale tectonic events which have faulted blocks of 1440 Ma Pandurra Formation with the ODBC (Cherry et al., 2017).

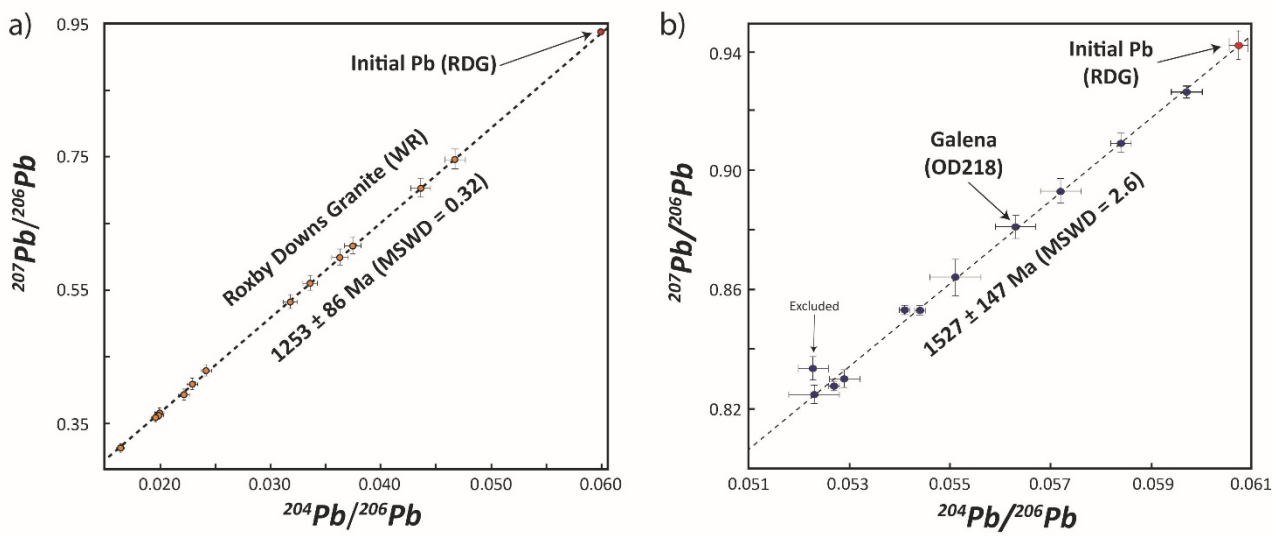

Figure 6.7: Isochron diagrams for a) the Roxby Downs Granite, and b) galena from the greatest Pb concentration area of the deposit (Pb > 1 %).

Pb-isotopic compositions of the RDG appear to show a systematic variation around the ODBC. Samples obtained from east of the deposit, and to some extent south of the deposit, show a very clear decrease in radiogenic Pb signature away from the edge of the deposit (fig. 6.8). This trend is consistent with Pb-isotopic haloes surrounding other Proterozoic, high-U/Pb deposits (Holk et al., 2003), as radiogenic Pb produced in the deposit is diluted outward by an increasing common Pb contribution from the surrounding country rock and ambient fluid. However, the reverse of this phenomenon can be seen in samples located north of the deposit (fig. 6.8), where Pb-isotopic ratios increase away from high-U mineralisation. Inconclusive relationships between Pb-isotopic values and U-Th-Pb concentrations prohibit a simple explanation. Further work is clearly required since definition of an isotopic halo may be used to detect Olympic Dam style deposits up to ~7.5 km from the edge of known mineralisation – an improvement of +5 km compared to observations based on mineral alteration alone (i.e. alteration of biotite: Ehrig et al., 2012).

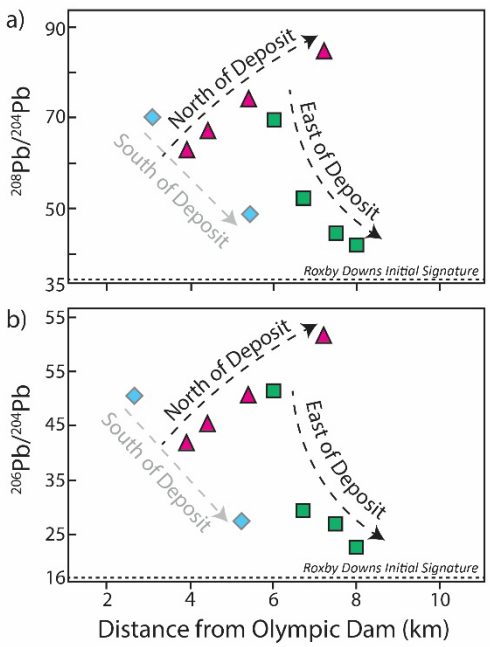

Figure 6.8: Pb-isotopic increase with increasing proximity to Olympic Dam and suggest the Pb-isotopic footprint of Olympic Dam may be detectable nearly 8km away. However, the opposite Pb-isotopic behaviour in granite to the north of the deposit suggests another explanation may be required.

6.7.2 Least Radiogenic Ore Assemblages

The least radiogenic Pb-isotopic signatures observed at Olympic Dam are preserved in pink calcite ($^{206}Pb/^{204}Pb$ = 16.758, $^{207}Pb/^{204}Pb$ = 15.476, $^{208}Pb/^{204}Pb$ = 36.018; Table 6.3) veins associated with the deepest chalcopyrite-pyrite-magnetite-hematite-calcite-apatite mineralisation (RL = 2182 m). The pink calcites have higher-$^{206}Pb/^{204}Pb$ (16.757 ± 0.097) and lower-$^{207}Pb/^{206}Pb$ (0.921 ± 0.002) signatures compared with the initial Pb-isotopic signature of the RDG ($^{206}Pb/^{204}Pb$ = 16.464 ± 0.052, $^{207}Pb/^{206}Pb$ = 0.943 ± 0.006) (fig. 6.9). The Pb-isotopic compositions of pink calcite are also among the most homogeneous of any Pb-isotopic compositions seen within the ODBC, with the $^{208}Pb/^{204}Pb$ ratios (36.018) showing particular consistency (± 0.217). Given the Sm-Nd and U-Pb isotopic evidence provided by Apukhtina et al. (2017), the relatively unradiogenic and homogeneous Pb-isotopic signatures of the pink calcites indicates the deep mineralisation preserves rare domains of early Olympic Dam-style mineralisation.

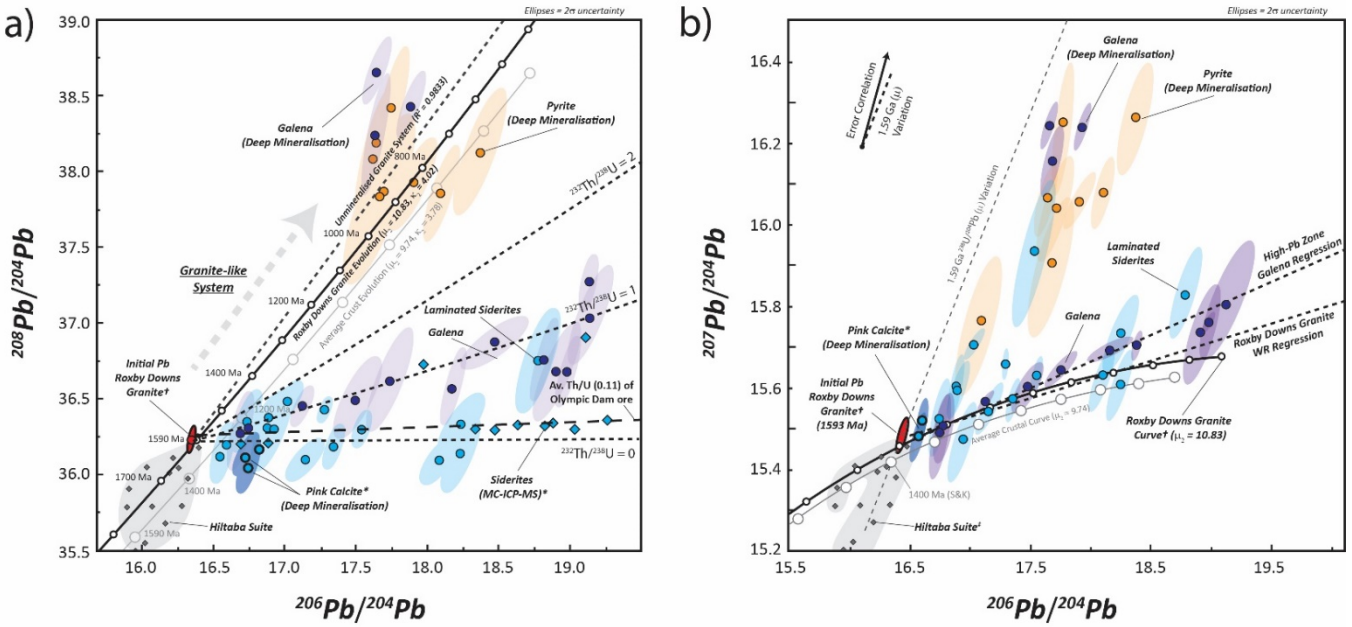

Figure 6.9: Least-radiogenic Pb-isotopic composition of Olympic Dam in a) Thoro-uranogenic and b) Uranogenic space. The arrays formed from the signatures of galena ($^{232}Th/^{238}U \approx 1$) and siderites ($^{232}Th/^{238}U \approx 0.11$) intercept the initial Pb-isotopic signature of the Roxby Downs Granite (RDG), indicating the primary source of Pb, and probably other metals, was the RDG. Blue diamonds represent siderite data from Apukhtina, (2016). ‡Hiltaba Suite data from Chapman et al., (2019). †Initial Pb-isotopic composition of the RDG after Chapter 5.

At higher levels in the deposit, least-radiogenic compositions comparable to the pink calcite are encountered in siderite breccia clasts near the south-eastern extent of the ODBC ($^{206}Pb/^{204}Pb$ = 16.600, $^{207}Pb/^{204}Pb$ = 15.526, $^{208}Pb/^{204}Pb$ = 36.197; Table 6.3), and galena from the Pb-rich (whole-rock assays >1 wt. %), north-western arm of the deposit ($^{206}Pb/^{204}Pb$ = 16.743, $^{207}Pb/^{204}Pb$ = 15.514, $^{208}Pb/^{204}Pb$ = 35.987; Table 6.4). Unlike the pink calcites however, Pb-isotopic values in siderites and galena show significant, systematic variations (fig. 6.9). The $^{207}Pb/^{206}Pb$ ratios of siderite vary from 0.94 to 0.84, with a commensurate change also seen in galena (0.926 to 0.825) from the high-Pb area of the ODBC. Pb-rich minerals such as galena, which are hosted within Pb-rich, low-U mineralisation is typically the least susceptible to isotopic modification, and serves to demonstrate the scale and significance of Pb-isotopic disturbance in Olympic Dam.

The relative change in $^{206}Pb/^{204}Pb$ ratios (16.743 to 19.143) from galena in the high-Pb zone is significantly greater than the variation seen in $^{208}Pb/^{204}Pb$ ratios (35.919 to 37.205). The relatively-flat slope of the Pb-isotope array on the thoro-uranogenic diagram (fig. 6.9), indicates a dominantly

uranogenic Pb source with a $^{232}Th/^{238}U$ ratio of 0.9. The siderite-data presented here, combined with data sourced from Apukhtina (2016), shows an even greater uranogenic Pb contribution ($^{232}Th/^{238}U$ = 0.011). Both of these uranogenic arrays contrast strongly with the trend seen in unmineralized RDG ($^{232}Th/^{238}U$ = 4.01) and show that fractionation of U from Th was a key geochemical feature of mineralisation. The low-Th/U signature indicated by the galena and siderite Pb-isotopic arrays is similar to the average Th/U of high-grade Cu ores in Olympic Dam (0.11; Ehrig et al., 2012). Therefore, a uranium-rich reservoir similar to that represented by the Olympic Dam ore must have been present within the ODBC at, or before the time in which radiogenic Pb was mixing with common Pb.

The consistency of the array yielded from galena in the Pb-rich domain of the ODBC presents an opportunity to constrain the age at which the high $^{232}Th/^{238}U$ reservoir (0.9) began mixing with the least-radiogenic Pb. Error-weighted regression through the data (fig. 6.7b) yields a radiogenic $^{207}Pb/^{206}Pb$ ratio of 0.0956, equating to an age of 1527 ± 147 Ma (MSWD = 2.6) using the equation of Nier et al. (1941). This age is within uncertainty of U-Pb ages determined from rare, euhedral uraninites at Olympic Dam and Sm-Nd isochrons yielded from deep, primary mineralisation (Apukhtina et al., 2017). While imprecise it presents additional evidence seeming to confirm that high-U mineralisation was present at Olympic Dam from the earliest stages of its history. The introduction of significant quantities of U during the Mid to Late Mesoproterozoic as suggested by previous studies (Cherry et al., 2017; Kamenetsky et al., 2015), is not required.

The common Pb signature, or unradiogenic Pb component of a mineral deposit provides constraints on the types of rocks and metal sources involved in metallogenesis. It is often either inferred from the point at which a regression through a radiogenic Pb array intercepts a crustal growth curve, or indicated by passing through any other common Pb reservoir with a known composition (Doe and Stacey, 1974; Russell and Farquhar, 1960; Stacey et al., 1968). Least-radiogenic Pb arrays of both siderite (which also intersects the composition of pink calcite) and galena from the high-Pb area of Olympic Dam pass through the ~1.59 Ga initial Pb signature of the

RDG (fig. 6.9). Therefore, while none of the least-radiogenic compositions presented here match perfectly with the initial-Pb signature of the RDG, it can be shown that a major contributor of early Pb and perhaps other metals, was similar in composition to the host-granite.

Table 6.3: LA-ICP-MS Pb-isotopic analyses of least-radiogenic gangue carbonate minerals

Sample No.	Mineral	$^{207}Pb/^{206}Pb$	±(2σ)	$^{208}Pb/^{206}Pb$	±(2σ)	$^{206}Pb/^{204}Pb$	±(2σ)	$^{207}Pb/^{204}Pb$	±(2σ)	$^{208}Pb/^{204}Pb$	±(2σ)
OD827	Calcite	0.921	0.003	2.148	0.008	16.758	0.097	15.476	0.096	36.018	0.217
RD2775	Calcite	0.923	0.002	2.152	0.005	16.775	0.065	15.472	0.051	36.122	0.135
OD1050	Siderite	0.935	0.004	2.181	0.008	16.600	0.074	15.523	0.090	36.197	0.202
OD1050	Siderite	0.934	0.004	2.181	0.010	16.568	0.116	15.480	0.106	36.142	0.306
OD1050	Siderite	0.925	0.008	2.150	0.014	16.874	0.108	15.600	0.136	36.278	0.242
OD1050	Siderite	0.914	0.006	2.146	0.020	16.915	0.206	15.455	0.184	36.293	0.408
OD1050	Siderite	0.909	0.008	2.109	0.012	17.518	0.306	15.931	0.304	36.942	0.550
OD1050	Siderite	0.907	0.008	2.105	0.024	17.152	0.188	15.550	0.104	36.101	0.194
OD1050	Siderite	0.897	0.002	2.086	0.004	17.350	0.092	15.571	0.088	36.188	0.206
OD1047	Siderite	0.927	0.004	2.171	0.008	16.742	0.142	15.526	0.164	36.353	0.302
OD1047	Siderite	0.923	0.004	2.153	0.016	16.894	0.162	15.600	0.116	36.372	0.264
OD1047	Siderite	0.922	0.006	2.143	0.016	17.026	0.146	15.707	0.064	36.486	0.188
OD1047	Siderite	0.906	0.004	2.107	0.008	17.287	0.050	15.659	0.066	36.428	0.116
OD1047	Siderite	0.890	0.004	2.069	0.008	17.547	0.084	15.625	0.084	36.300	0.168
OD1047	Siderite	0.863	0.004	1.995	0.012	18.092	0.182	15.622	0.130	36.091	0.216
OD1047	Siderite	0.862	0.008	1.991	0.018	18.250	0.248	15.734	0.160	36.337	0.290
OD1047	Siderite	0.856	0.006	1.981	0.014	18.239	0.188	15.606	0.142	36.135	0.376
OD1047	Siderite	0.843	0.002	1.957	0.012	18.783	0.222	15.834	0.192	36.751	0.530

Table 6.4: LA-ICP-MS Pb-isotopic analyses of least-radiogenic galena and pyrite

Name	Mineral	$^{207}Pb/^{206}Pb$	±(2σ)	$^{208}Pb/^{206}Pb$	±(2σ)	$^{206}Pb/^{204}Pb$	±(2σ)	$^{207}Pb/^{204}Pb$	±(2σ)	$^{208}Pb/^{204}Pb$	±(2σ)
OD218	Galena	0.825	0.006	1.932	0.028	19.134	0.392	15.816	0.246	36.962	0.424
OD218	Galena	0.830	0.006	1.934	0.026	18.915	0.240	15.730	0.204	36.576	0.468
OD218	Galena	0.853	0.002	1.982	0.012	18.383	0.062	15.705	0.070	36.431	0.304
OD218	Galena	0.926	0.004	2.151	0.016	16.743	0.146	15.514	0.124	35.987	0.288
OD218	Galena	0.893	0.008	2.079	0.022	17.469	0.216	15.601	0.106	36.291	0.236
OD218	Galena	0.864	0.012	2.010	0.030	18.161	0.322	15.695	0.052	36.479	0.162
OD218	Galena	0.909	0.006	2.119	0.014	17.127	0.106	15.570	0.036	36.270	0.156
OD218	Galena	0.881	0.008	2.057	0.026	17.754	0.242	15.648	0.076	36.505	0.344
OD218	Galena	0.828	0.004	1.929	0.018	18.970	0.084	15.715	0.044	36.576	0.234
RD2775	Pyrite	0.909	0.014	2.165	0.022	17.750	0.172	16.233	0.280	38.402	0.546
RD2775	Pyrite	0.900	0.010	2.141	0.028	17.665	0.336	15.897	0.286	37.814	0.742
OD827	Pyrite	0.901	0.010	2.144	0.026	17.931	0.380	16.241	0.240	38.439	0.692
OD827	Pyrite	0.909	0.008	2.168	0.020	17.643	0.136	16.127	0.190	38.241	0.530
OD827	Pyrite	0.915	0.004	2.191	0.014	17.651	0.136	16.244	0.100	38.658	0.296
OD211	Pyrite	0.895	0.008	2.118	0.024	17.902	0.226	16.060	0.118	37.912	0.406
OD211	Pyrite	0.920	0.006	2.201	0.016	17.069	0.318	15.752	0.284	37.568	0.748
OD211	Pyrite	0.882	0.010	2.075	0.022	18.373	0.248	16.261	0.226	38.125	0.552
OD211	Pyrite	0.908	0.008	2.162	0.018	17.628	0.178	16.061	0.144	38.111	0.562
OD211	Pyrite	0.903	0.006	2.140	0.026	17.705	0.248	16.038	0.214	37.891	0.554
OD211	Pyrite	0.885	0.004	2.091	0.014	18.104	0.170	16.081	0.148	37.853	0.420

6.7.3 Pb-isotopic Signatures Of Cu-Ores In The Olympic Dam Breccia Complex

The results of 397 in situ analyses of Pb-rich chalcogenide (galena and clausthalite) inclusions hosted in Cu-sulphide minerals from Olympic Dam ores show dominantly radiogenic Pb-isotopic compositions (fig. 6.10), extending from the least-radiogenic signatures of galena in chalcocite ($^{206}Pb/^{204}Pb$ = 18.104, $^{207}Pb/^{204}Pb$ = 15.781, $^{208}Pb/^{204}Pb$ = 36.845), to extremely radiogenic clausthalite hosted in chalcocite ($^{206}Pb/^{204}Pb$ = 834.050, $^{207}Pb/^{204}Pb$ = 69.028, $^{208}Pb/^{204}Pb$ = 78.685). The relative

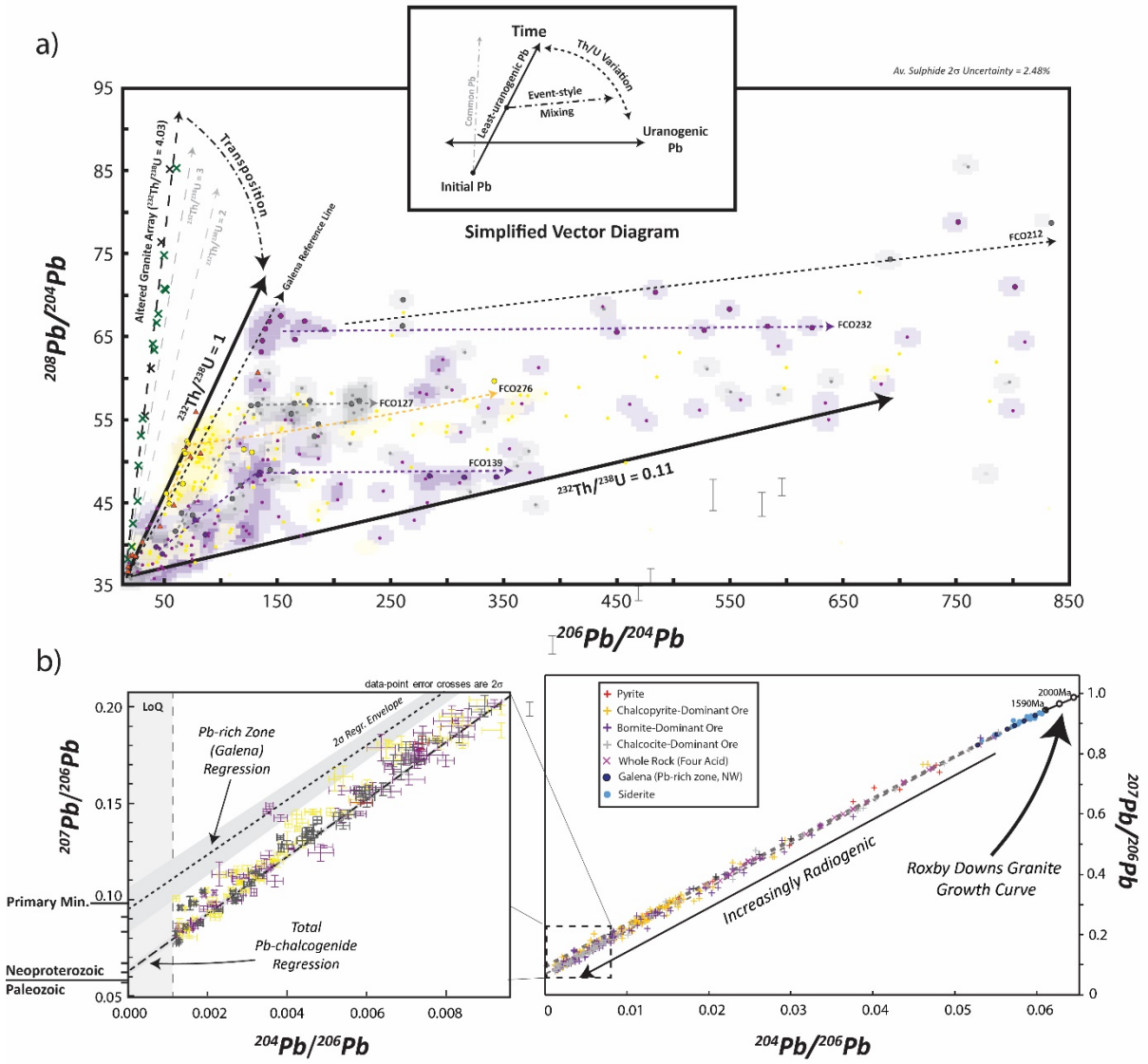

Figure 6.10: Pb-isotopic variation in Pb-chalcogenides associated with Chalcopyrite (yellow), bornite (purple) and chalcocite (grey) ore zones. a) The thoro-uranogenic diagram shows that most Pb-isotopic signatures are constrained between $^{232}Th/^{238}U$ = 1 and 0.11, while the Roxby Downs Granite conforms to $^{232}Th/^{238}U$ = 4. The individual uranogenic departures seen in some samples are shown as arrow. The simplified vector diagram (top inset), explains the isotopic variation seen in the thoro-uranogenic diagram. b) Inverse uranogenic diagram, which shows that much of the uranogenic variation is the result of mixing between a ~1590 Ma common Pb component sourced from the Roxby Downs Granite ($^{204}Pb/^{206}Pb$ = 0.061), and a radiogenic component ($^{204}Pb/^{206}Pb$ = 0) generated during the Late Neoproterozoic.

contributions of radiogenic Pb to the Pb-isotopic signatures of orezone Pb-chalcogenides can be seen in Figure 6.10b, where the common Pb component (high-$^{204}Pb/^{206}Pb$) has been strongly diluted by a dominant radiogenic component (low-$^{204}Pb/^{206}Pb$). This figure also indicates that some contribution of radiogenic Pb which is much younger than 1.59 Ga is required to form the wide range of uranogenic compositions seen in the orezone Pb-chalcogenides.

As a whole, Pb-isotopic compositions for orezone Pb-chalcogenides are considerably more uranogenic than thorogenic with most data yielding $^{208}Pb/^{206}Pb$ ratios much smaller than 1.0. The differences between the $^{232}Th/^{238}U$ signatures of Olympic Dam mineralisation and the unmineralized RDG become increasingly evident at more-radiogenic isotopic compositions, where the linear arrays constraining Pb-isotopic signatures of orezone Pb-chalcogenides to $^{232}Th/^{238}U$ signatures between ~1 and ~0.1 are much flatter than the RDG whole-rock data ($^{232}Th/^{238}U$ = ~4) (fig. 6.10a). This highlights that the fractionation of Th from U was a key geochemical feature of the hydrothermal fluids which formed Olympic Dam within the RDG.

- Pb-Isotopic Differences Between Dominant Olympic Dam Cu-Ore Assemblages

Most of the Pb-isotopic signatures found in association with chalcopyrite-dominant assemblages appear to be largely restricted to $^{232}Th/^{238}U \approx 1$ (fig. 6.10a). In contrast, many of the Pb-isotopic signatures associated with bornite- and chalcocite-dominant assemblages have developed from systems where $^{232}Th/^{238}U < 1$ and consequently plot to the right of the galena reference line (fig. 6.10a).

There are large differences in the Pb-isotopic signatures associated with the three main Cu-sulphide assemblages (fig. 6.11). Pb-associated with chalcopyrite-dominant assemblages have bimodal $^{208}Pb/^{206}Pb$ peaks (0.6 and 0.24), with two peaks also reproduced in $^{207}Pb/^{206}Pb$ ratios (0.24 and 0.1). Notably, the first, or least-radiogenic of these populations is not as prevalent in the Pb-associated with bornite- or chalcocite-dominated assemblages. Such systematic variations between

Cu-ores, with less-radiogenic signatures associated with chalcopyrite-dominant ores can be principally explained one of three ways;

- The concentrations of U, Th and Pb are different between the Cu-ore types,
- The modern-day concentrations of U, Th and Pb do not reflect the ancient, or primary abundances of these elements,
- Differences in the isotopic signatures are the result of a disturbance event which has affect some of the Cu-ores, but not the others.

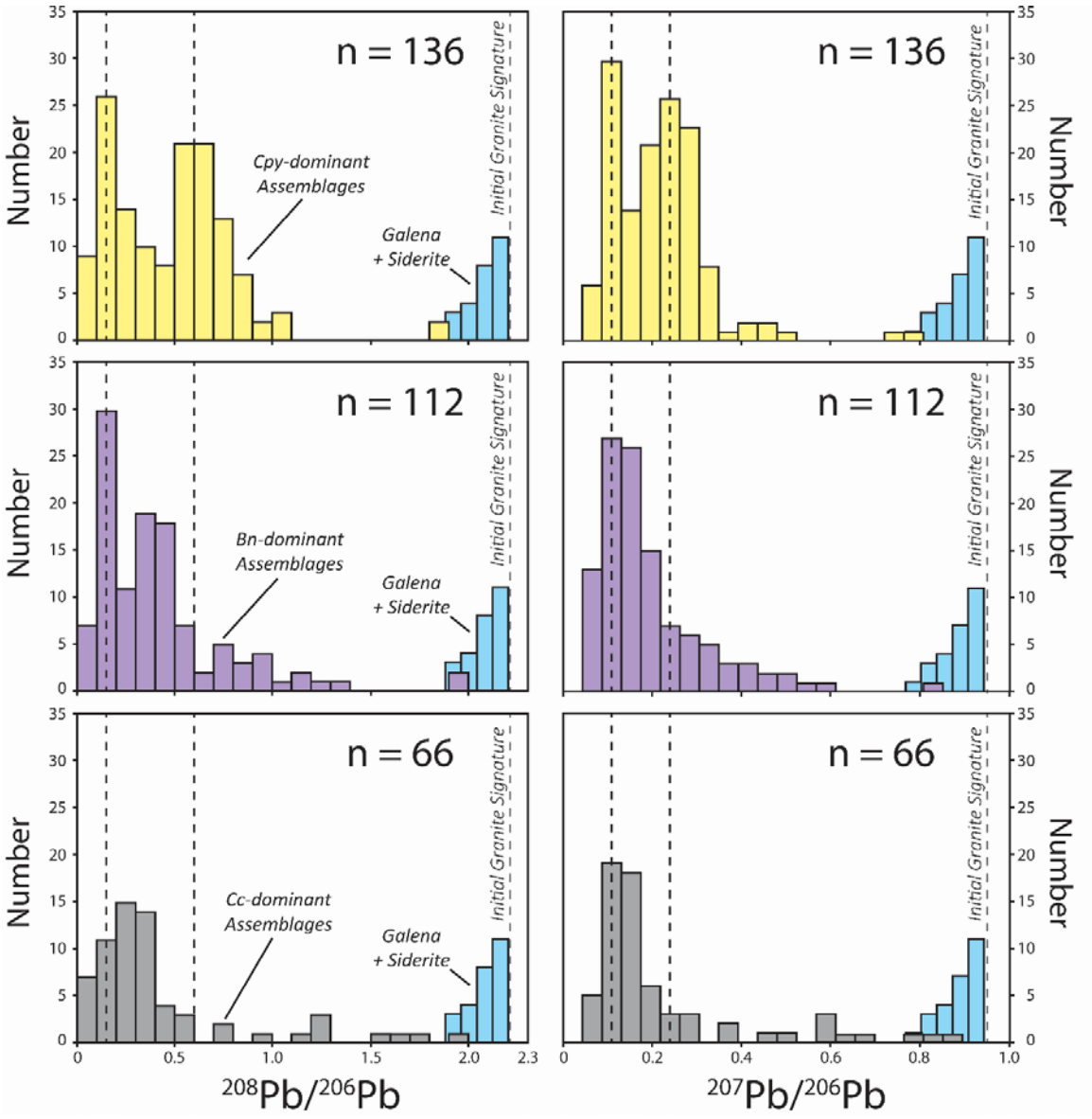

Figure 6.11: Population diagrams for the Pb-isotopic signatures obtained from Pb-chalcogenides associated with the three main Cu-sulphide ores. The pronounced first peak in chalcopyrite-dominant assemblages ($^{208}Pb/^{206}Pb$ = 0.6, $^{207}Pb/^{206}Pb$ = 0.24) is absent from bornite and chalcocite Pb-isotopic signatures. Cpy = chalcopyrite, Bn = bornite, Cc = chalcocite.

The first of these scenarios can be discounted as a valid explanation, since the whole-rock values for U/Pb, Th/Pb and, Th/U are similar among the three Cu-ore types (Fig. 6.6). The second possibility, on the other hand, is considered possible considering the large disparity between some whole-rock U/Pb, Th/Pb and U/Th ratios, and Pb-isotopic compositions. For example, some degree of ancient U-loss is suggested in the chalcocite zone in the western arm of the deposit (fig. 6.12) due to the disparity between high-$^{206}Pb/^{204}Pb$ signatures and high-U concentrations with low-U/Pb ratios (i.e. FCO243, FCO374, FCO138). Conversely, ancient U-gain is suggested in some bornite-dominant zones (i.e. FCO162, FCO380) within the deposit where high, modern-day, U concentrations contrast with relatively unradiogenic Pb-isotopic compositions (Fig. 6.6). However, neither U-loss or U-gain is consistent enough between the Cu-ore types to completely explain the differences in Pb-isotopic

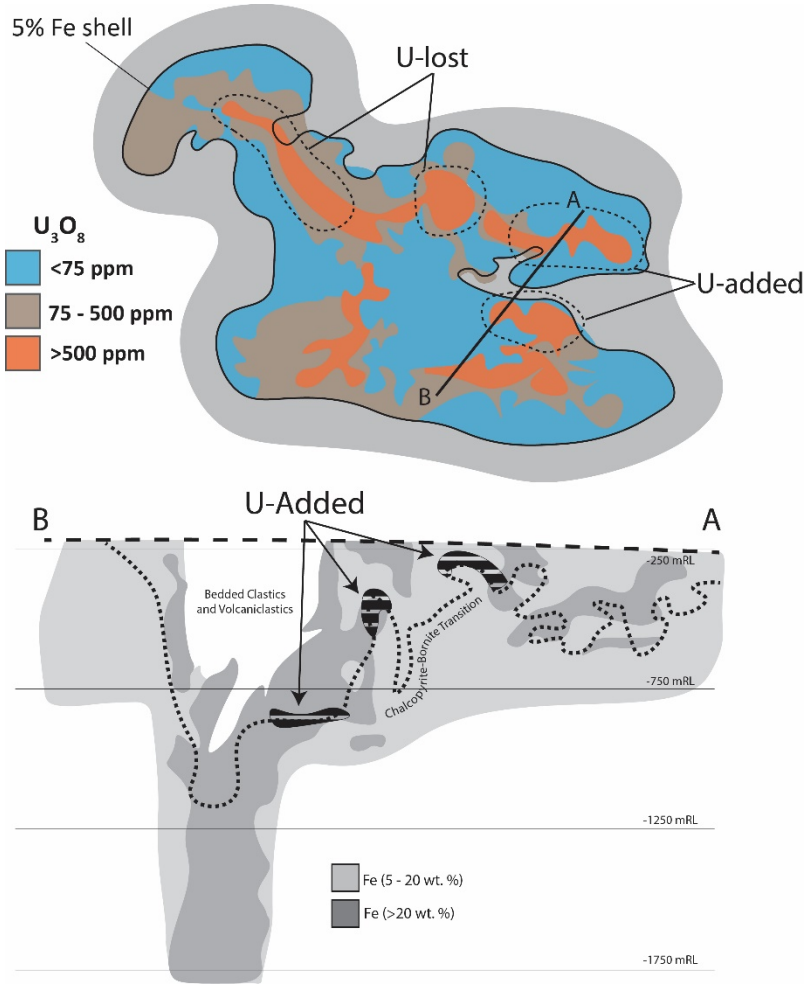

Figure 6.12: Schematic diagram of Olympic Dam showing the location of areas of the deposit where discrepancies between Pb-isotopic compositions and whole-rock abundances of U, Th and Pb indicate the loss, or gain of U after 1590 Ma. Modified after Ehrig et al. (2012).

signatures (Fig. 6.11), and therefore requires additional explanation.

The third scenario is supported by the correlation between the amount of radiogenic Pb ($^{204}Pb/^{206}Pb$) and the abundance of bornite and chalcopyrite determined by XRD (fig. 6.13). Since variations in U and Pb concentration between bornite and chalcopyrite are unlikely to explain this isotopic difference (fig. 6.6), the overall positive relationship between bornite and radiogenic Pb suggests that the U-rich minerals in the bornite zones have released more radiogenic Pb ($^{207, 206}Pb$), perhaps through recrystallisation, than U-rich minerals in the chalcopyrite zones. The inverse

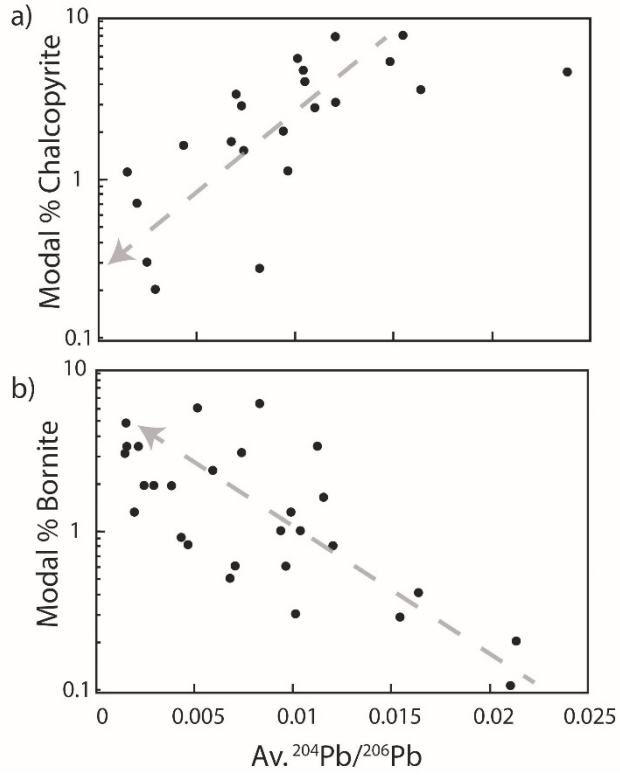

Figure 6.13: Inverse covariation between modal percent chalcopyrite and bornite (MLA), and the Av. proportion of radiogenic Pb ($^{204}Pb/^{206}Pb$).

relationship between chalcopyrite, bornite and radiogenic Pb implies that the conditions which caused U-rich minerals to release uranogenic Pb also facilitated the formation of bornite at the expense of chalcopyrite. It therefore seems possible that the late disturbance of U-minerals may have led to the development of some Cu-ore zonation. If formation of the chalcopyrite-bornite interface formed considerably after primary mineralisation, the resulting low-$^{206}Pb/^{204}Pb$ signature of the uranogenic Pb would contribute to the consistently low-$^{208}Pb/^{206}Pb$ (and $^{207}Pb/^{206}Pb$) isotopic

composition seen in the bornite- and chalcocite dominant assemblages (fig. 6.11), as well as explain textural observations in bornite by previous authors which were interpreted to indicate that some bornite formed after primary mineralisation (Oreskes and Einaudi, 1990).

- Uranogenic Departures In Orezone Pb-Isotopic Signatures

The effects of mixing between a common Pb component and radiogenic Pb contributed from minerals rich in U and Th can be seen clearly in the thoro-uranogenic diagram (fig. 6.10a). In this diagram, the highest density of data has developed near the $^{232}Th/^{238}U = 1$ curve and represents the least-uranogenic signatures present within the ores of Olympic Dam. Pb-isotopic compositions of pyrite associated with chalcopyrite-dominant assemblages commonly fall along this trend, which is also coincident with the extrapolation of the least-radiogenic array of galena from the highest Pb zone of the deposit (fig. 6.10a). The consistent delineation of least-uranogenic isotopic compositions by minerals which are typically the most resistant to Pb-isotopic modification - either through a high-Pb concentration (i.e. galena in Pb-rich samples) or relatively-refractory mineral habit (i.e. pyrite) - highlights that this isotopic pattern ("Least-uranogenic Pb"; inset, fig. 6.10a) reflects the *minimum mixing* possible between a purely uranogenic Pb component and a radiogenic, 'common Pb' component.

A number of individual samples yield Pb-isotopic arrays which start and continue along the least-uranogenic trend, before departing towards strongly-uranogenic compositions (fig. 6.10a). Most samples recording this apparent two-stage Pb-isotopic behaviour characterised by strong departures in uranogenic Pb are from bornite- and chalcocite-dominant orezones. The recurrent expression of this characteristic trend within Pb-isotopic signatures of Olympic Dam ores (~1/4 of all samples analysed here) is interpreted to reflect a widespread, two-stage mixing history between three principle constituents; a common-Pb component and two radiogenic Pb end-members, each derived from discrete isotopic reservoirs (inset, fig. 6.10a).

The first stage of development involves the mixing between a common Pb component and a radiogenic Pb component which is generated in an isotopic reservoir with $^{232}Th/^{238}U$ no greater than ~1 (~1 to 0.4). Lower Th/U values such as are seen in FCO139 (~0.4; Fig. 6.10a) forces the first-stage of mixing along a lower thoro-uranogenic trajectory. Heterogeneous mixing between these two components causes variable Pb-isotopic compositions to plot along the least-uranogenic trend on Figure 6.10a. The greater the distance a Pb-isotopic signature lies from least-radiogenic compositions of calcite-siderite-galena, the greater the abundance of radiogenic Pb relative to common Pb. In essence, the mixing system just described is equivalent to the mechanism which led to the formation of the least-radiogenic galena-siderite arrays, as well as the RDG whole-rock array.

The second stage of Pb-isotopic development requires a least-uranogenic Pb formed during the first-stage, mixing with another radiogenic Pb generated in an isotopic reservoir with a $^{232}Th/^{238}U$ 0.1. The strongly-uranogenic characteristic of the second-stage radiogenic Pb is indicated by the flat-trajectory of these arrays on the thoro-uranogenic diagram (fig. 6.10a) and caused by the relatively-small changes in $^{208}Pb/^{204}Pb$ ratios compared to the large variations seen in $^{206}Pb/^{204}Pb$. The locus at which the second-stage of mixing departs from the least-uranogenic array is determined by the (U+Th)/Pb ratio of the first-stage system, such that higher values will force second-stage arrays to depart at higher points along the least-uranogenic array, and vice versa. Similarly, the distance the Pb-isotopic signature plots from the least-uranogenic curve is proportional to the relative concentrations of uranogenic Pb, and first-stage radiogenic Pb.

Fundamentally, second-stage Pb-isotopic arrays show that the amount of uranogenic Pb in sulphide ores increased dramatically at a paragenetically-late stage in the history of Olympic Dam. This is significant since it either records a large increase in the U-concentration across parts of the deposit, or reflects a disturbance event which has mostly-affected U-bearing minerals. A drastic increase in the amount of U throughout parts of the deposit related to redistribution, would cause a sudden increase in the proportion of $^{206,207}Pb$ relative to ^{208}Pb. However, as previously discussed, such a scenario can neither be ruled in nor out since the ancient changes in the U-Th-Pb system

recorded by Pb-isotopic ratios are largely inconsistent with the modern-day concentrations of U, Th and Pb. The alternative, though not mutually-exclusive explanation for the second-stage arrays reflects an isotopic disturbance event which has affected U-rich minerals (Th/U ≈ 0) such as uraninite, coffinite and brannerite. The expulsion and diffusion of uranogenic Pb from high-U minerals following a disturbance event such as recrystallisation, could explain the large changes in $^{206}Pb/^{204}Pb$ compared with $^{208}Pb/^{204}Pb$ required by the uranogenic departures in second-stage Pb. This is supported by textural studies which suggest that most U-rich minerals have undergone at least one-cycle of recrystallisation through coupled dissolution-reprecipitation processes since their primary formation (Cross et al., 1993; Ehrig et al., 2012; Macmillan et al., 2016; Reeve et al., 1990).

The disturbance of U-minerals (low-Th/U), compared to Th(U)-bearing mineral phases (moderate to high-Th/U) places some physicochemical constraints on the nature of the isotopic disturbance event. Within the ores of Olympic Dam, the dominant U-hosts (low-Th/U), in order of prevalence, are coffinite, brannerite and uraninite which comprise a combined 0.0327 wt. % of ore (Ehrig et al., 2012). These minerals have very high Pb diffusivity rates (i.e. $1x10^{-5}$ to $1x10^{-1}$ mm^2/Ma for uraninite; Rosenqvist (1949)) at almost ambient temperatures (<50°C) and are therefore capable at continually contributing relatively high volumes of uranogenic Pb. Apatite is abundant within the ores of Olympic Dam (0.1029 wt. %; Ehrig et al. 2012), and is the only other U-bearing mineral realistically capable of producing the volume a radiogenic Pb required for the uranogenic departure. The Pb diffusivity rates of apatite, however, are more than 6-orders of magnitude slower than uraninite ($1x10^{-11}$ mm^2/Ma at <150°C; Cherniak (2010)), effectively limiting radiogenic Pb contributions Pb-chalcogenides outside of the apatite crystal to zero at temperatures below 500°C. With much of the radiogenic Pb with Th/U ratios similar to the first-stage mixing system ($^{232}Th/^{238}U$ ≈ 1) effectively locked-up in resistate mineral reservoirs, it is likely that the paragenetically-later uranogenic Pb departure is related to a low-temperature, possibly chemically-controlled, disturbance event.

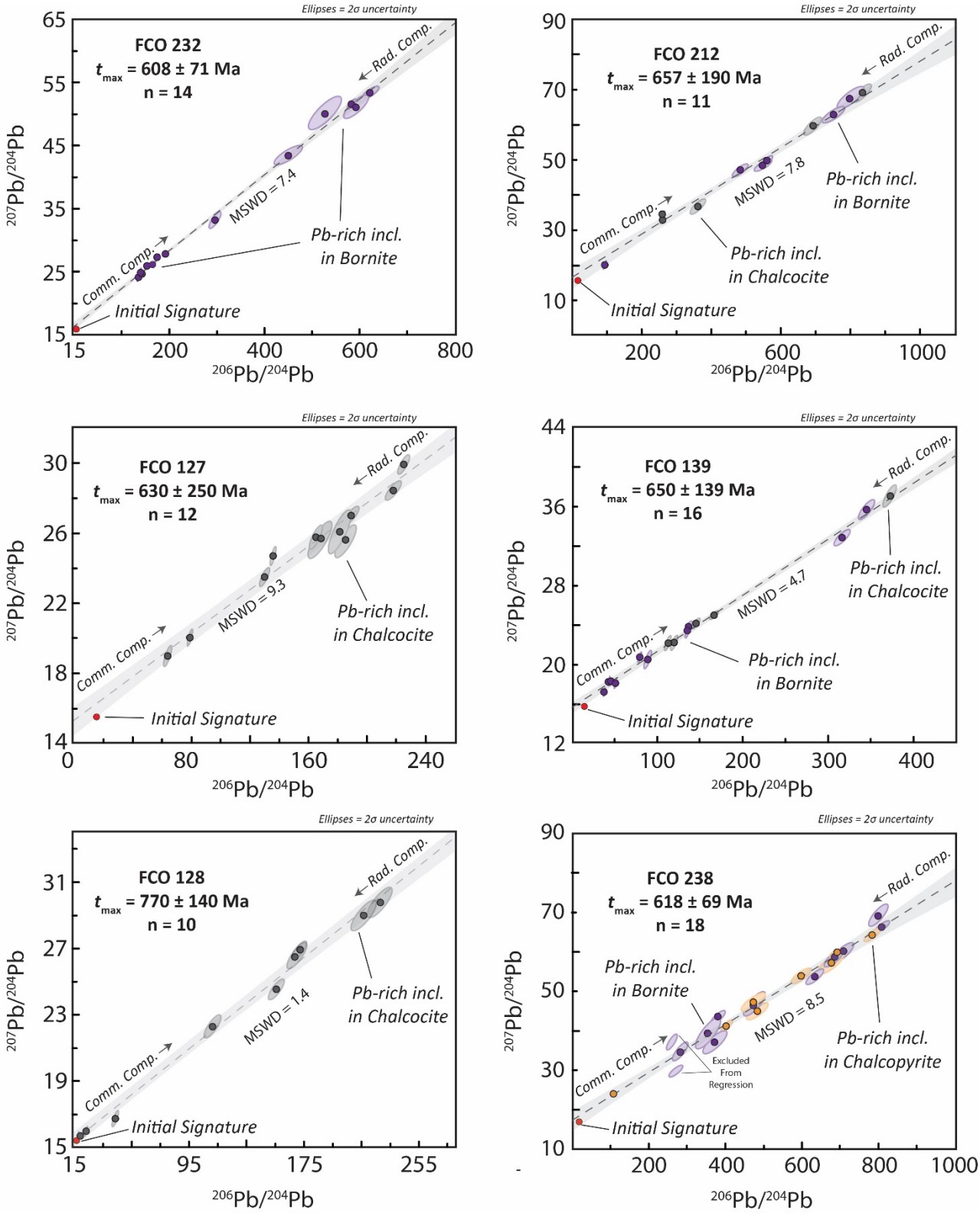

Figure 6.14: Pb-Pb isochrons yielded from individual samples which show significant departures in their Pb-isotopic signatures towards uranogenic compositions. The intersection of these regressions through the RDG initial signature (within uncertainty) satisfies the criteria for non-transposed isochrons (Russell and Farquhar, 1960). Light grey envelopes represent 2σ uncertainty on the regressions. The range of ages calculated most closely correspond to sedimentation above the unconformity at Olympic Dam during the Cryogenian (676 – 635 Ma).

- Temporal Constraints On U-Disturbance Events

11 samples in total (FCO118, -127, -128, -[232], -276, -138, -139, -192, -212, -[238] and -400) all show uranogenic departures in their thoro-uranogenic Pb-isotopic compositions. 7 of these samples (FCO118, -127, -128, -[232], -276, -139, -192, -212 and -[238]) show isochron-like Pb-isotopic arrays, with Pb-isotopic signatures distributed along a regression on $^{207}Pb/^{204}Pb$ vs $^{206}Pb/^{204}Pb$ diagrams (fig. 6.14). All error-weighted regressions (York, 1968) through the data, within uncertainty, intercept a known common Pb composition (RDG initial Pb), which is crucial in ensuring that no isochron transposition ('pseudoisochron') has occurred (Kanasewich, 1962; Russell and Farquhar, 1960). Isochrons incorporate between 10 and 18 individual data points. Samples yielding Pb-Pb isochrons contain between 471 and 4962 ppm U, with U/Pb ratios between 5.4 and 17.4), and thus could theoretically generate and contribute uranogenic Pb in semi-continuous manner since the time when U-Pb equilibrium was last achieved (Nier et al., 1941; Russell and Farquhar, 1960). A full list of the $^{207}Pb/^{206}Pb$ ratios derived for the end-member radiogenic component ($^{207}Pb_r/^{206}Pb_r$), is shown in Table 6.5.

$$\frac{^{207}_{t2}Pb - {}^{207}_{t1}Pb}{^{206}_{t2}Pb - {}^{206}_{t1}Pb} = \frac{^{207}_{r}Pb}{^{206}_{r}Pb} = \frac{(e^{\lambda_{235}.t} - 1)}{137.88.(e^{\lambda_{238}.t} - 1)} \qquad (Eq.1)$$

Application of the Nier et al. (1941) equation reveals that U-Pb system last reached equilibrium, following the departure towards strongly-uranogenic Pb-isotopic signatures, sometime between 770 ± 140 Ma and 608 ± 71 Ma. The Pb-Pb ages derived from these samples (Wt. Av. = 664 ± 66 Ma, MSWD = 2.27) correspond locally with the 676 Ma (Webb et al., 1983) Rb-Sr age of the Tregolana Shale which was deposited directly above the disconformity at Olympic Dam, providing a geological basis for the ages obtained from the radiogenic Pb arrays of Olympic Dam. The range of Pb-Pb ages obtained are also broadly conformable with the 600 – 480 Ma range of U-Pb ages determined from recrystallised uraninites at Olympic Dam (Trueman, 1986), which confirm the authenticity of a major

U-disturbance event occurring during the Mid to Late Neoproterozoic. Similar ages obtained from Sm-Nd and Rb-Sr (~550 Ma) in paragenetically-late fluorite-barite-siderite-chalcopyrite veins at Olympic Dam (Maas et al., 2011), suggest that REE (and Sr) were also affected during the Late Neoproterozoic U-disturbance event. The convergence of multiple isotopic systems (Pb-Pb, U-Pb, Sm-Nd, Rb-Sr) towards a Late Neoproterozoic-aged isotopic disturbance event which correspond to a known geological event occurring directly above mineralised breccias provides strong support for the Pb-isotopic ages seen at Olympic Dam.

Table 6.5: Results of Pb-Pb isochron regressions

Sample	n	$^{207}Pb_r/^{206}Pb_r$	MSWD	Age (Ma)[1]	Age (Ma)[2]	Ore Mineralogy	Gangue Minerals (in order of abundance)
High-Pb Zone (OD218)	9	0.0957	2.6	1527 ± 147	881 ± 85	Cp-Ur-Cf-Br-El	Qz-Hm-Chl-Ser-Py-Gn
RDG (WR)	14	0.0823	0.32	1253 ± 86	-	-	Kf-Pl-Qz-Bt-Chl-Ser-Zr-Ap
Pb-chalcogenide Isochrons							
FCO127	11	0.0626	9.3	630 ± 250	369 ± 146	Cc-Bn-Cf-Br-Ur	Qz-Hm-Ser-Chl
FCO128	10	0.0649	1.4	770 ± 140	413 ± 75	Cc-Bn-Cf-Br-Ur	Qz-Hm-Ser-Chl
FCO138	8	0.0645	9	758 ± 72	406 ± 39	Bn-Cc-Br-Cf-Ur-El	Hm-Qz-Ser-Chl-Fl-Ba
FCO139	15	0.0613	4.7	650 ± 139	344 ± 74	Bn-Cc-Ur-Cf-El	Hm-Qz-Ser-Chl
FCO212	11	0.0615	7.8	657 ± 190	348 ± 101	Bn-Cc-Cv-Cf-Br-El	Qz-Ser-Hm-Rt-Fl
FCO232	14	0.0601	8.5	608 ± 69	320 ± 36	Bn-Cp-Ur-Cf-Br-El	Hm-Qz-Ser-Rt-Chl-Ba-Fl
FCO238	21	0.0605	8.5	618 ± 69	328 ± 37	Bn-Ur-El	Hm-Ap
		Wt. Av.	2.3	664 ± 66	353 ± 38		

Mineral abbreviations: Cp (chalcopyrite), Bn (bornite), Cc (chalcocite), Ur (uraninite), Cf (coffinite), Br (brannerite), El (electrum), Cv (covellite), Qz (quartz), Hm (hematite), Chl (chlorite), Ser (sericite), Py (pyrite), Gn (galena), Kf (K-feldspar), Pl (plagioclase), Bt (biotite), Zr (zircon), Ap (apatite), Fl (fluorite), Ba (barite), Rt (rutile). [1] Nier et al. (1941); [2] Russell et al. (1954).

An alternative radiogenic Pb age equation (Eq. 2), first proposed by Russell et al. (1954), works on the supposition that radiogenic Pb may be extracted from a U-Th-rich mineral and subsequently incorporated into a high-Pb mineral where it has remained *instantaneously* isolated from any further input of radiogenic Pb (e.g. Sudbury, Canada and Thackaringa, Australia; (Russell and Farquhar, 1960; Russell et al., 1961). Application of this equation to Pb-chalcogenide isochrons yields a range of Paleozoic ages between 320 ± 36 and 413 ± 75 Ma. We consider the validity of these ages questionable for a number of reasons. Firstly, the data forming the isochrons here cover

a much greater range of radiogenic compositions than either the Sudbury Deposits (Darling et al., 2012; Dickin et al., 1996; Russell and Farquhar, 1960) or the Thackaringa Deposits (Bierlein et al., 1996; Reynolds, 1971; Russell et al., 1961), and are therefore considered more likely to represent semi-continuous mixing. Secondly, the U concentration within the ores of Olympic Dam are significantly higher than either Sudbury (1 ppm U; Darling et al. (2012)) or the Thackaringa ores (<9.4 ppm U; Bierlein et al. (1996)), and are therefore considered more likely to be semi-continuously contributing uranogenic Pb. Thirdly, the ages yielded from Eq. 2 (wt. av. = 353 ± 38 Ma) are not supported by any geological observations or previous isotopic studies. In contrast, the ages yielded from Eq. 1 (wt. av. = 664 ± 64 Ma) coincide with both a known geological event (i.e. Cryogenian sedimentation), results from multiple isotopic systems (Sm-Nd, Rb-Sr) and a known radiogenic Pb-loss event at Olympic Dam (Trueman, 1986).

$$t\,(Ma) = \frac{1}{\lambda_{235} - \lambda_{238}} . \ln \frac{137.88. \left[\frac{^{207}Pb}{^{206}Pb}_{r}\right] . \lambda_{238}}{\lambda_{235}} \qquad (Eq. 2)$$

The major contribution of the Pb-Pb ages presented here, in addition to validating previously established U-Pb Pb-loss ages, is the temporal link it makes between the reworking of U-mineralisation and the potential for upgrading of Cu-species. Bornite and chalcocite zones, display Pb-isotopic signatures that cannot be explained through modern-day concentrations of U, Th and Pb alone, which infer that these areas of Olympic Dam have been the most affected by a ~664 Ma U-disturbance event. In addition, the positive relationship between uranogenic Pb and bornite abundance is inverse to the negative relationship between uranogenic Pb and chalcopyrite abundance, strongly suggesting that the reworking of U-mineralisation occurred at the same time (~664 Ma) as chalcopyrite was converted to bornite (and chalcocite). It is therefore possible that the well-known and economically-important bornite-chalcopyrite zonation developed at Olympic Dam,

was formed at ~664 Ma in response to the same event which caused widespread dissolution, remobilisation and reprecipitation of U-ore minerals.

6.7.4 A Model for Post-formational Modification of U-Cu ores at Olympic Dam

Post-1590 Ma modification of mineralisation at Olympic Dam has been a point considered by many previous workers (Cherry et al., 2017; Maas et al., 2011; Oreskes and Einaudi, 1992; Reeve et al., 1990). Recent studies have pointed to the fault-related incorporation of 1440 Ma Pandurra Formation sediments into the Olympic Dam Breccia Complex some time between ~1200 Ma and 820 Ma as one potential event which has led to modification of the deposit (Cherry et al., 2017). Pb-isotopic arrays yielded from weakly-altered Roxby Downs Granite (1252 ± 86 Ma) appear to support the occurrence of such an event (fig. 6.15a). The consistency of 1300 – 1100 Ma results from three isotopic systems (Pb-Pb, Rb-Sr and Sm-Nd) lends credibility to this claim, the limited Pb-isotopic evidence for a 1300 – 1100 Ma event obtained from this study prohibits a more considered discussion of the topic. It remains possible that if a 1300 – 1100 Ma event had affected the U-Th-Pb system of mineralisation at Olympic Dam, much of the Pb-isotopic evidence could have been overprinted by successive Pb-isotopic mixing processes/ events.

The most significant, post-1590 Ma modification event suggested by Pb-isotopic arrays appears to have taken place during deposition of calcareous sediments belonging to the the c.635 Ma Nuccaleena Formation (Rose and Maloof, 2010) and 676 Ma Tregolana Shale which are located directly above the erosional unconformity subjugating the ODBC. The transgressive nature of these sediments has been interpreted to represent rising global sea levels following global, Cryogenian glaciation (Rose and Maloof, 2010). Considering that the top of the ODBC was exposed at the paleosurface during this time (fig. 6.15b), it seems more than likely that marine transgression would have led to the incursion of seawater into the ODBC through the unconformity. The porous and permeable nature of the ODBC would have facilitated downward percolation of the surficially-

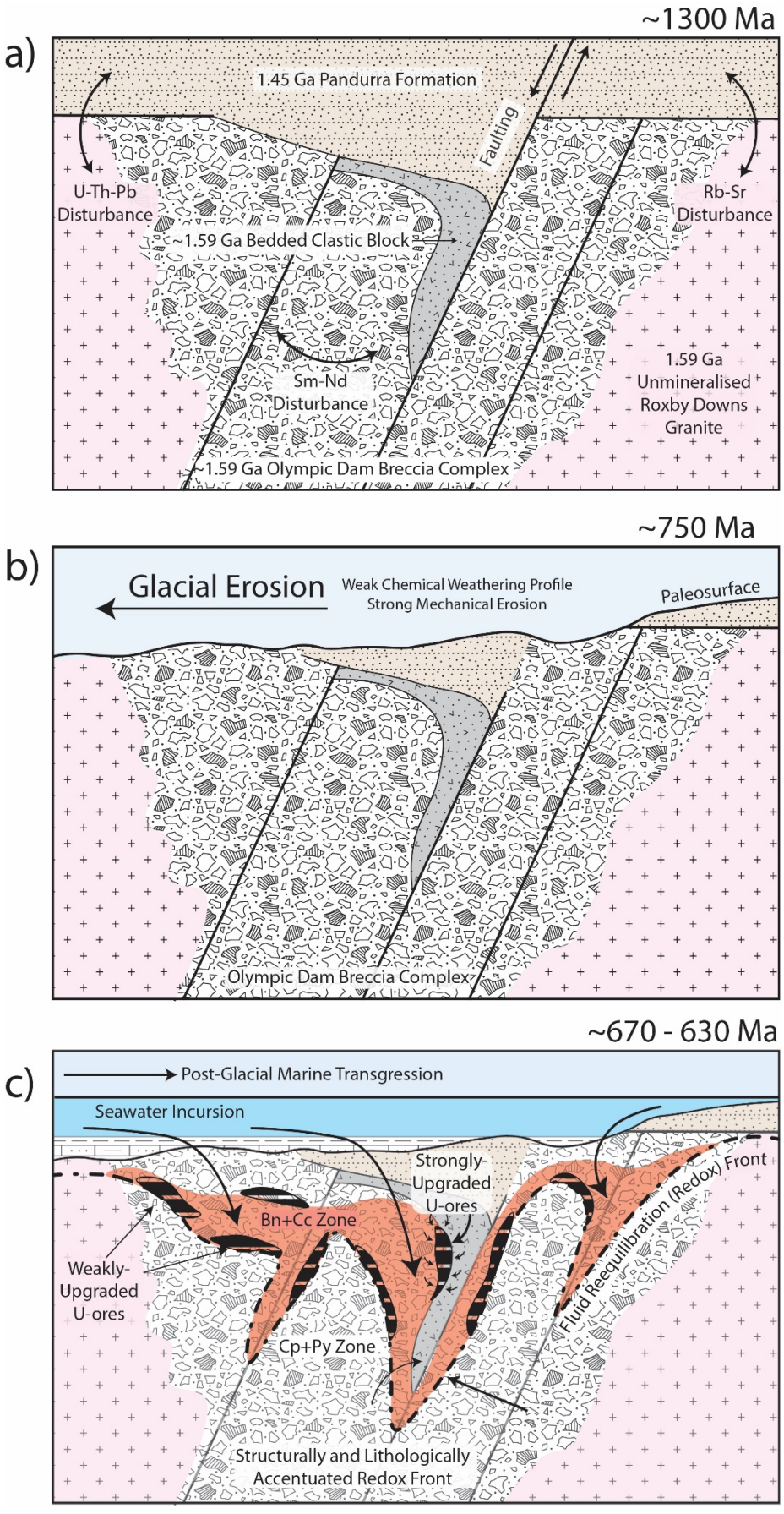

Figure 6.15: Schematic reconstruction of the post-1593 Ma geological processes which are interpreted to have led to the Pb-isotopic phenomena (and potentially U-Cu upgrading) observed at Olympic Dam.

derived fluids, while the saline, oxidised and carbonate-bearing chemistry would have caused disequilibrium in much of the ore-assemblages (i.e. sulphides, magnetite, uraninite etc). Physicochemical modelling of the mineral assemblages and fluid inclusions of Olympic Dam repeatedly indicate the necessary involvement of a low-temperature, oxidised fluids in forming Olympic Dam (Bastrakov et al., 2007; Haynes et al., 1995; Oreskes and Einaudi, 1992) similar to the surficial-marine waters which we have constrained to the Late Neoproterozoic. Despite the pertinence of these observation, the potential importance of a Late Neoproterozoic marine fluid overprint has received only scant consideration in the current literature (Oreskes and Einaudi, 1990). The incursion of oxidised marine fluids into the Olympic Dam Breccia Complex during the Late Neoproterozoic provides a temporally-constrained, geologically-founded mechanism to link Pb-isotopic phenomenon described in this study, with the complex paragenetic/ redox relationships in Cu- and U-ores observed at Olympic Dam.

The incursion of the relatively oxidised and carbonate-rich marine waters accompanying Cryogenian-Ediacaran sedimentation would have had a great effect on both the stability and solubility of U-mineralisation at Olympic Dam. U solubility is extremely redox-sensitive, becoming increasingly mobile in oxidised, carbonate-rich waters as uranyl (U^{6+}) bi- and tri-carbonate complexes (Langmuir, 1978). Strongly uranogenic Pb-isotopic compositions which do correspond to either high-U concentrations, high-U/Pb ratios nor generation within a low-$^{232}Th/^{238}U$ reservoir (≈ 0) require the remobilisation of U over a distance in excess of 20 m (i.e. the size of the sample composites used here). Smaller-scale redistribution and potential upgrading of U (< 20 m) is considered highly-likely. All other departures in Pb-isotopic signatures towards uranogenic compositions that are not supported by variations in whole-rock Th/U or U/Pb ratios reflect the addition of radiogenic Pb expelled from U-minerals during recrystallisation/ dissolution-reprecipitation at ~664 Ma.

Textural and isotopic evidence from the U-minerals themselves also indicate that the Cryogenian-Ediacaran event significantly modified U mineralisation at Olympic Dam. Early work on the U-Pb isotopic dating of texturally-constrained uraninites reveals that most recrystallised

uraninite yield ages on concordia between 600 and 400 Ma (Trueman, 1986). Fissionogenic ^{149}Sm values yielded from high-grade U orezones (>5 wt. % U) at Olympic Dam are lower than expected if the high-grade ores were present from ~1590 Ma (Kirchenbaur et al., 2016), and may be explained by the formation/ remobilisation of the highest-grade U zones during Late Neoproterozoic fluid incursion. Textural and chemical analysis by Macmillan et al. (2016), show that only very few uraninites preserve primary characteristics. High-grade U ores are dominated by massive, amorphous uraninite (pitchblende) related to low-temperature dissolution-reprecipitation such as occurred during Cryogenian event. Crucially, the low U/Pb ratios of the later-uraninites (Macmillan et al., 2016) indicate extensive radiogenic Pb loss, and provides a direct link to uranogenic Pb departures recorded by the Pb-isotopic compositions of Pb-chalcogenides.

The ingress of surface waters into Olympic Dam during Cryogenian-Ediacaran sedimentation, and exacerbated by porosity and permeability of the faulted ODBC, is also inferred from Pb-isotopic signatures to have had an effect on Cu-sulphide mineralisation. Inverse correlations between modal percent bornite and chalcopyrite with uranogenic Pb suggests U-disturbance and mobility was related to the development of bornite at the expense of chalcopyrite. The relatively-oxidised fluids accompanying marine transgression would force the Cu-sulphide stability field from relatively reduced Cu-species (i.e. chalcopyrite) to those Cu-species stable at higher electron potentials such as bornite, chalcocite and covellite. Some of the highest uranium grades present at Olympic Dam have been noted to occur with bornite-chalcocite mineralisation (Cross et al. 1993) and in proximity to the chalcopyrite-bornite transition (Reeve et al., 1990). It is therefore conceivable that the positive relationship between U and bornite indicated by Pb-isotopic compositions but which is not present today, was the result of the same redox processes which remobilised U. The downward percolation of a relatively-oxidised, surficial fluid would also be consistent with the vertical zonation of chalcopyrite (lower) and bornite (higher) at Olympic Dam (Fig. 6.15c). The complex geometry of the chalcopyrite-bornite interface (Ehrig et al., 2012; Reeve et al., 1990) could be explained by a mixture of structural and lithological control, which affected the local porosity/ permeability and thus

equilibration of the descending fluid with the surrounding rock. Cu-grade is noted by Reeve et al. (1990) to show a marked increase across the chalcopyrite-bornite interface, moving from ~3% on the chalcopyrite side, to 4-6% on the bornite/ chalcocite side. High-^{34}S enrichment seen in chalcocite mineralisation at higher levels in Olympic Dam (Bastrakov et al., 2007) is entirely consistent with the influx of a surficial fluid. Curiously, such high ^{34}S-enrichments are not observed in any of the sub-economic IOCG deposits of the Gawler Craton (Bastrakov et al., 2007). It is therefore possible, that the incursion of surficial, marine fluids during the Cryogenian-Ediacaran which is indicated by Pb-isotopic arrays has led to the upgrading of Cu-sulphide ores at Olympic Dam.

It is important to note that the modification processes described here to explain Pb-isotopic behaviour during the ~664 Ma disturbance event and redox zonation does not require the post-1590 Ma addition of metals, in contrast to the additions of U and/ or Cu suggested by other authors (Cherry et al., 2017; Kamenetsky et al., 2015). The upgrading of chalcopyrite to bornite is envisioned to be a largely topochemical process, where Cu-mobility is not required. Cu/Fe and Cu/S mineral ratios are increased stepwise from chalcopyrite (Fe/Cu = 1, Cu/S = 2) to bornite (Fe/Cu = 5, Cu/S = 1.25) and eventually to chalcocite (Fe = 0, Cu/S = 2). Similarly, U is considered to have been already present at Olympic Dam in significant quantities with only local redistribution. In addition to the confirmed presence of 1593 Ma uraninite, the high-^{238}U/^{232}Th ratios of radiogenic Pb mixing with least-radiogenic galenas from at least 1527 ± 147 Ma indicates that some U-rich mineralisation was already present from relatively early stages of primary mineralisation. Surficial, oxidised fluids migrating downwards would be in greater disequilibrium with U-mineralisation proximal to the unconformity, leading to variable, mostly local-scale (<10 m) U redistribution and recrystallisation (fig. 6.15c). Isolated, high-grade U mineralisation above the chalcopyrite-bornite interface is most likely to reflect Cryogenian upgrading, although some contribution to some of the higher-U zones near the chalcopyrite-bornite interface (Reeve et al., 1990) is also possible. We consider that any hexavalent uranyl complexes mobilised from pre-existing U-mineralisation during the ~664 Ma fluid incursion, would be easily reduced to immobile, uranous minerals (i.e. uraninite, coffinite,

brannerite) by electron-donors already present within the iron oxide (i.e. magnetite) and sulphide mineralisation itself. The high-prevalence of potential reductants in Olympic Dam is thus likely to have also limited the distance of U-redistribution. Therefore, modification of primary U and Cu need not be considered any more than redox-driven, local-scale U-redistribution with a concomitant increase in the Cu/Fe ratios of Cu-sulphide minerals (chalcopyrite -> bornite -> bornite/chalcocite).

The economic implications of modification may, nonetheless, be significant especially for U. Despite highly-anomalous U-concentrations encountered in most iron oxide-copper-gold deposits of the Gawler Craton, U is still considered sub-economic in many deposits and worse still, a metallurgical penalty (Li et al., 2015). A two- to three-fold increase in U-grade resulting from redistribution on a scale of 10's of metres, would modify a deposit with a U-grade of ~150 ppm, similar to that encountered at Prominent Hill (Belperio et al., 2007), to the ~400 ppm average resource grade at Olympic Dam (Ehrig et al., 2012). Pb-isotopic signatures of Olympic Dam suggest that the $^{232}Th/^{238}U$ ratio of the deposit have seen a three-fold decrease, from ~4 in the early mineralisation and altered RDG, to ≤1 following the Late Neoproterozoic event. A two- to three-fold increase in U-grade is noted by Cross et al. (1993) to occur across the chalcopyrite-bornite interface. It therefore seems plausible that the well-noted, anomalous, economic tenor of U-mineralisation at Olympic Dam (Haynes et al., 1995; Hitzman and Valenta, 2005) at least partially the result of post-formational modification related to Late Neoproterozoic fluid incursion during deposition of marine sediments above the ODBC unconformity.

6.8 Summary and Conclusion

In situ Pb-isotopic analyses of Pb-rich chalcogenides, pyrites and carbonates associated with chalcopyrite, bornite and chalcocite-dominant ore assemblages of Olympic Dam reveal a difference in the ancient U-Th-Pb systematics of the various Cu-ore zones, and a protracted history of isotopic disturbance.

High-$^{232}Th/^{238}U$ Pb-isotopic signatures in galena from the highest Pb zone of Olympic Dam indicate that primary U-rich mineralisation was present in appreciable quantities during the earliest stages of the deposits history (1527 ± 147 Ma). Least-radiogenic Pb-isotopic compositions form arrays which intercept the initial Pb-isotopic signature of the RDG, indicating that much of the early Pb, and probably other metals, were contributed by the RDG itself. The origin and significant of whole-rock granite Pb-isotopic arrays which yield apparent ages of 1252 ± 86 Ma remains unresolved, though it may be related to a similar isotopic disturbance event also recorded by the Rb-Sr and Sm-Nd isotopic systems. Systematic geometric variations in the Pb-isotopic signatures of the RDG suggest that the high-U footprint of the Olympic Dam resource may be detectable in excess of 7 km from the edge of known mineralisation.

Significant Pb-isotopic mixing has affected much of the Pb-rich chalcogenides of the Olympic Dam orebody. Thoro-uranogenic arrays show both single and two-stage radiogenic mixing has occurred in the orezones of Olympic Dam. Uranogenic departures are recorded in the Pb-isotopic compositions of ore-zone Pb-chalcogenides associated with bornite and chalcocite-assemblages indicate that a significant isotopic disturbance event has affected the U-rich mineralisation of Olympic Dam during the Cryogenian-Ediacaran (664 + 66 Ma), coincident with 676-635 Ma clastic sedimentation directly above the unconformity at Olympic Dam.

The lack of correlation between uranogenic Pb-isotopic ratios and the present-day abundances of U- Th- or Pb indicates that some U has been remobilised during the Late Neoproterozoic isotopic disturbance event. Positive correlation between increasingly radiogenic compositions and modal percent bornite contrasts with the negative correlation of radiogenic compositions with modal percent chalcopyrite suggests that some component of the economically-important chalcopyrite-bornite zonation at Olympic Dam may have also been established during the Late Neoproterozoic.

We contend that post-glacial, marine transgression which led to sedimentation directly above the disconformity at Olympic Dam during the Cryogenian was also accompanied by the

ingress of oxidised, marine fluids which modified the U and Cu resource at Olympic Dam. Late Neoproterozoic fluid incursion would explain uranogenic Pb-isotopic departures at ~664 Ma which indicate major affects to the Th/U characteristics of the ore zone, as well as systematic relationships between the Pb-isotopic signatures and the various Cu-ore species. The electrochemical requirements of U dissolution-reprecipitation during Cryogenian fluid incursion are somewhat complimentary to the redox requirements of the Cu-ore species, and therefore we consider that Late Neoproterozoic reworking of mineralisation contributed to the world-class tenor of the U-Cu resource at Olympic Dam.

Future studies should build on the Pb-isotopic framework developed here and utilise higher-precision techniques to refine Pb-Pb isochron ages. Smaller-scale studies of specific areas within the deposit (i.e. NW area) would help to refine the distance of U (and Pb) remobilisation, since U-movement is likely to be pronounce over distances less than the 4m resolution provided by this study. Further studies should also focus on the U-Th-Pb systematics of the RDG, since current Pb-isotopic data suggests that the Olympic Dam footprint may be detectable undercover up to 7.5 km away from known mineralisation.

Acknowledgements

Funding for this study was obtained primarily from BHP Olympic Dam Operations. Partial funding was also obtained through the Transforming the Mining Value Chain (TMVC) ARC Industrial Transformation Research Hub. Dr. Kathy Ehrig, Dr. Roland Maas, Dr. Maya Kamanetsky and Dr. Vadim Kamanetsky are thanked for discussions related to the formulation of this research. Dr. Sandrin Feig and Dr. Karsten Göemann of the Central Science Laboratory, University of Tasmania are gratefully acknowledged for their contributions to SEM-related research. Jay Thompson and Dr. Paul Olin of the CODES Laser Ablation Laboratory and Dr. Maya Kamenetsky were indispensable in the

acquisition of LA-ICP-MS data. Dr. Alexander Cherry, Dr. Brian McNulty and Dr. Matthew Ferguson are thanked for their advice on earlier version of this manuscript.

REFERENCES

Apukhtina, O., 2016, Distribution, petrology, geochemistry and geochronology of carbonate assemblages at the Olympic Dam deposit, University of Tasmania.

Apukhtina, O. B., Kamenetsky, V. S., Ehrig, K., Kamenetsky, M. B., Maas, R., Thompson, J., McPhie, J., Ciobanu, C. L., and Cook, N. J., 2017, Early, deep magnetite-fluorapatite mineralization at the Olympic Dam Cu-U-Au-Ag deposit, South Australia: Economic Geology, v. 112, p. 1531-1542.

Bastrakov, E. N., Skirrow, R. G., and Davidson, G. J., 2007, Fluid evolution and origins of iron oxide Cu-Au prospects in the Olympic Dam district, Gawler Craton, south Australia: Economic Geology, v. 102, p. 1415-1440.

Belperio, A., Flint, R., and Freeman, H., 2007, Prominent Hill: A hematite-dominated, iron oxide copper-gold system: Economic Geology, v. 102, p. 1499-1510.

Bierlein, F. P., Haack, U., Förster, B., and Plimer, I. R., 1996, Lead isotope study on hydrothermal sulfide mineralisation in the Willyama Supergroup, Olary Block, South Australia: Australian Journal of Earth Sciences, v. 43, p. 177-187.

Chapman, N. D., Ferguson, M., Meffre, S. J., Stepanov, A., Maas, R., and Ehrig, K. J., 2019, Pb-isotopic constraints on the source of A-type Suites: Insights from the Hiltaba Suite - Gawler Range Volcanics Magmatic Event, Gawler Craton, South Australia: Lithos, v. 346-347, p. 105156.

Cherniak, D. J., 2010, Diffusion in Accessory Minerals: Zircon, Titanite, Apatite, Monazite and Xenotime: Reviews in Mineralogy and Geochemistry, v. 72, p. 827-869.

Cherry, A. R., Ehrig, K., Kamenetsky, V. S., McPhie, J., Crowley, J. L., and Kamenetsky, M. B., 2018, Precise geochronological constraints on the origin, setting and incorporation of ca. 1.59 Ga surficial facies into the Olympic Dam Breccia Complex, South Australia: Precambrian Research, v. 315, p. 162-178.

Cherry, A. R., McPhie, J., Kamenetsky, V. S., Ehrig, K., Keeling, J. L., Kamenetsky, M. B., Meffre, S., and Apukhtina, O. B., 2017, Linking Olympic Dam and the Cariewerloo Basin: Was a sedimentary basin involved in formation of the world's largest uranium deposit?: Precambrian Research, v. 300, p. 168-180.

Ciobanu, C. L., Cook, N. J., and Ehrig, K., 2017, Ore minerals down to the nanoscale: Cu-(Fe)-sulphides from the iron oxide copper gold deposit at Olympic Dam, South Australia: Ore Geology Reviews, v. 81, p. 1218-1235.

Ciobanu, C. L., Wade, B. P., Cook, N. J., Mumm, A. S., and Giles, D., 2013, Uranium-bearing hematite from the Olympic Dam Cu-U-Au deposit, South Australia: A geochemical tracer and reconnaissance Pb-Pb geochronometer: Precambrian Research, v. 238, p. 129-147.

Courtney-Davies, L., Ciobanu, C. L., Tapster, S. R., Cook, N. J., Ehrig, K. J., Kennedy, A. K., Condon, A. J., Verdugo-Ihl, M. R., Wade, B. P., and Gilbert, S. E., 2018, The U-Pb systematics of hydrothermal hematite: insights from the IOCG system at Olympic Dam, South Australia: 15th Quadrennial International Association on the Genesis of Ore Deposits Symposium, Salta, Argentina, 28-31 August, 2018, p. 171-172.

Cross, K. C., Daly, S. J., and Flint, R. B., 1993, The Olympic Dam Deposit, *in* Drexel, J. F., Preiss, W. V., and Parker, A. J., eds., The Geology of South Australia, The Precambrian, 1, Department of Mines and Energy, p. 132-137.

Crowe, S. A., Fryer, B. J., Samson, I. M., and Gagnon, J. E., 2003, Precise isotope ratio determination of common Pb using quadrupole LA-ICP-MS with optimized laser sampling conditions and a robust mixed-gas plasma: Journal of Analytical Atomic Spectrometry, v. 18, p. 1331-1338.

Darling, J. R., Storey, C. D., Hawkesworth, C. J., and Lightfoot, P. C., 2012, In-situ Pb isotope analysis of Fe–Ni–Cu sulphides by laser ablation multi-collector ICPMS: New insights into ore

formation in the Sudbury impact melt sheet: Geochimica et Cosmochimica Acta, v. 99, p. 1-17.

Dickin, A. P., Artan, M. A., and Crocket, J. H., 1996, Isotopic evidence for distinct crustal sources of North and South Range ores, Sudbury Igneous Complex: Geochimica et Cosmochimica Acta, v. 60, p. 1605-1613.

Doe, B. R., and Stacey, J. S., 1974, The Application of Lead Isotopes to the Problems of Ore Genesis and Ore Prospect Evaluation: A Review: Economic Geology, v. 69, p. 757-776.

Ehrig, K., McPhie, J., and Kamenetsky, V. S., 2012, Geology and mineralogical zonation of the Olympic Dam Iron Oxide Cu-U-Au-Ag Deposit, South Australia, *in* Hedenquist, J. W., Harris, M., and Camus, F., eds., Economic Geology Special Publication 16, p. 237-267.

Gu, Y., 2003, Automated scanning electron microscope based mineral liberation analysis an introduction to JKMRC/FEI mineral liberation analyser: Journal of Minerals and Materials Characterization and Engineering, v. 2, p. 33.

Guillong, M., Kuhn, H. R., and Günther, D., 2003, Application of a particle separation device to reduce inductively coupled plasma-enhanced elemental fractionation in laser ablation-inductively coupled plasma-mass spectrometry: Spectrochimica Acta - Part B Atomic Spectroscopy, v. 58, p. 211-220.

Gustafson, L., and Compston, W., 1979, Rb-Sr dating of Olympic Dam core samples: Australian National University, Research School of Earth Sciences January, v. 18, p. 1979.

Haynes, D. W., Cross, K. C., Bills, R. T., and Reed, M. H., 1995, Olympic Dam Ore Genesis - a Fluid-Mixing Model: Economic Geology & the Bulletin of the Society of Economic Geologists, v. 90, p. 281-307.

Hitzman, M. W., and Valenta, R. K., 2005, Uranium in iron oxide-copper-gold (IOCG) systems: Economic Geology, v. 100, p. 1657-1661.

Holk, G. J., Kyser, T. K., Chipley, D., Hiatt, E. E., and Marlatt, J., 2003, Mobile Pb-isotopes in Proterozoic sedimentary basins as guides for exploration of uranium deposits: Journal of Geochemical Exploration, v. 80, p. 297-320.

Hu, Z., Gao, S., Liu, Y., Hu, S., Chen, H., and Yuan, H., 2008, Signal enhancement in laser ablation ICP-MS by addition of nitrogen in the central channel gas: Journal of Analytical Atomic Spectrometry, v. 23, p. 1093-1101.

Johnson, J. P., and McCulloch, M. T., 1995, Sources of mineralising fluids for the Olympic Dam Deposit (South Australia) - Sm-Nd isotopic constraints: Chemical Geology, v. 121, p. 177-199.

Kamenetsky, V., K., E., Maas, R., Meffre, S., Kamenetsky, M., McPhie, J., Apukhtina, O., Huang, Q., Thompson, J., Ciobanu, C., and Cook, N., 2015, The supergiant Olympic Dam Cu-U-Au-Ag ore deposit: towards a new genetic model: Society of Economic Geologists, Hobart, Tasmania, 2015.

Kanasewich, E. R., 1962, Approximate Age of Tectonic Activity Using Anomalous Lead Isotopes: Geophysical Journal of the Royal Astronomical Society, v. 7, p. 158-168.

Kirchenbaur, M., Maas, R., Ehrig, K., Kamenetsky, V. S., Strub, E., Ballhaus, C., and Münker, C., 2016, Uranium and Sm isotope studies of the supergiant Olympic Dam Cu–Au–U–Ag deposit, South Australia: Geochimica et Cosmochimica Acta, v. 180, p. 15-32.

Langmuir, D., 1978, Uranium solution-mineral equilibria at low temperatures with applications to sedimentary ore deposits: Geochimica et Cosmochimica Acta, v. 42, p. 547-569.

Li, K., Pring, A., Etschmann, B., Macmillan, E., Ngothai, Y., O'Neill, B., Hooker, A., Mosselmans, F., and Brugger, J., 2015, Uranium scavenging during mineral replacement reactions†: American Mineralogist, v. 100, p. 1728-1735.

Ludwig, K., 2012, User's manual for Isoplot version 3.75–4.15: a geochronological toolkit for Microsoft: Excel Berkley Geochronological Center Special Publication.

Maas, R., Kamenetsky, V., Ehrig, K., Meffre, S., McPhie, J., and Diemar, G., 2011, Olympic Dam U-Cu-Au deposit, Australia: New Age Constraints: Mineralogical Magazine, v. 75, p. 1375.

Macmillan, E., Cook, N. J., Ehrig, K., Ciobanu, C. L., and Pring, A., 2016, Uraninite from the Olympic Dam IOCG-U-Ag deposit: Linking textural and compositional variation to temporal evolution: American Mineralogist, v. 101, p. 1295-1320.

McPhie, J., Kamenetsky, V. S., Allen, S., Ehrig, K., Agangi, A., and Bath, A., 2011a, The fluorine link between a supergiant ore deposit and a silicic large igneous province Geology, v. 39, p. 1003-1006.

McPhie, J., Kamenetsky, V. S., Chambefort, I., Ehrig, K., and Green, N., 2011b, Origin of the supergiant Olympic Dam Cu-U-Au-Ag deposit, South Australia: Was a sedimentary basin involved?: Geology, v. 39, p. 795-798.

Müller, W., Shelley, M., Miller, P., and Broude, S., 2009, Initial performance metrics of a new custom-designed ArF excimer LA-ICPMS system coupled to a two-volume laser-ablation cell: Journal of Analytical Atomic Spectrometry, v. 24, p. 209-214.

Nier, A. O., Thompson, R. W., and Murphey, B. F., 1941, The Isotopic Constitution of Lead and the Measurement of Geological Time. III: Physical Review, v. 60, p. 112-116.

Oreskes, N., and Einaudi, M. T., 1990, Origin of rare-earth element-enriched hematite breccias at the Olympic-Dam Cu-U-Au-Ag Deposit, Roxby Downs, south Australia: Economic Geology, v. 85, p. 1-28.

Oreskes, N., and Einaudi, M. T., 1992, Origin of Hydrothermal Fluids at Olympic Dam: Preliminary Results from Fluid Inclusions and Stable Isotopes: Economic Geology and the Bulletin of the Society of Economic Geologists, v. 87, p. 64-90.

Reeve, J. S., Cross, K. C., Smith, R. N., and Oreskes, N., 1990, Olympic Dam copper-uranium-gold-silver deposit, *in* Hughes, F. E., ed., Geology of the mineral deposits of Australia and Papua New Guinea, Monograph 14: Melbourne, Australasian Institute of Mining and Metallurgy, p. 1009-1035.

Reynolds, P. H., 1971, A UThPb lead isotope study of rocks and ores from Broken Hill, Australia: Earth and Planetary Science Letters, v. 12, p. 215-223.

Roberts, D. E., and Hudson, G. R. T., 1983, The Olympic Dam copper-uranium-gold deposit, Roxby Downs, south Australia: Economic Geology, v. 78, p. 799-822.

Rosenqvist, I. T., 1949, Diffusjonskoeffisienten for bly i noen radioaktive mineraler: GFF, v. 71, p. 57-70.

Rosholt, J. N., Zartman, R. E., and Nkomo, I. T., 1973, Lead Isotope Systematics and Uranium Depletion in the Granite Mountains, Wyoming: Geological Society of America Bulletin, v. 84, p. 989-1002.

Russell, R. D., and Farquhar, R. M., 1960, Dating galenas by means of their isotopic constitutions-II: Geochimica et Cosmochimica Acta, v. 19, p. 41-52.

Russell, R. D., Farquhar, R. M., Cumming, G. L., and Wilson, J. T., 1954, Dating galenas by means of their isotopic constitutions: Eos, Transactions American Geophysical Union, v. 35, p. 301-309.

Russell, R. D., Ulrych, T. J., and Kollar, F., 1961, Anomalous leads from Broken Hill, Australia: Journal of Geophysical Research, v. 66, p. 1495-1498.

Stacey, J. S., Zartman, R. E., and NKomo, I. T., 1968, A lead isotope study of galenas and selected feldspars from mining districts in Utah: Economic Geology, v. 63, p. 796-814.

Trueman, N. A., 1986, Lead-uranium systematics of the Olympic Dam deposit and Stuart shelf mineralization: Summary report of U-REE mineralization, Adelaide, Australia, XPSA86/1, 13 January 1986, 7 p: unpublished group memo, Western Mining Corporation.

Verdugo-Ihl, M. R., Ciobanu, C. L., Cook, N. J., Ehrig, K. J., and Courtney-Davies, L., 2019, Defining early stages of IOCG systems: evidence from iron oxides in the outer shell of the Olympic Dam deposit, South Australia: Mineralium Deposita.

Warwyk, C., 1989, Strontium and rare earth geochemistry of barite-fluorite mineralisation at Olympic Dam, South Australia, University of Adelaide.

Webb, A. W., Coats, R. P., Fanning, C. M., and Flint, R. B., 1983, Geochronological Framework of the Adelade Geosyncline 1983.

Willigers, B. J. A., Baker, J. A., Krogstad, E. J., and Peate, D. W., 2002, Precise and accurate in situ Pb-Pb dating of apatite, monazite, and sphene by laser ablation multiple-collector ICP-MS: Geochimica et Cosmochimica Acta, v. 66, p. 1051-1066.

York, D., 1968, Least squares fitting of a straight line with correlated errors: Earth and planetary science letters, v. 5, p. 320-324.

Chapter 7: Synthesis and Summary

7.1 Introduction

The work outlined in this thesis had four main aims;

1) Demonstrate the value and effectiveness of LA-ICP-MS Pb-isotopic analyses at both regional and deposit-scale studies.
2) Contribute to the understanding of Late Paleoproterozoic – Early Mesoproterozoic crustal evolution in the Gawler Craton.
3) Provide a link between the crustal evolution of the Gawler Craton and IOCG metallogenesis.
4) Investigate the potential for post-formational modification of the world-class Olympic Dam ore deposit.

This chapter will summarise the findings of each of the studies presented in this thesis, linking them chronologically from the complex crustal evolution observed during the Late Paleoproterozoic – Early Mesoproterozoic in the Gawler Craton, and finally to the possible effects of Cryogenian marine transgression on mineralisation at Olympic Dam.

7.2 Late Paleoproterozoic – Early Mesoproterozoic Crustal Evolution of the Gawler Craton

7.2.1 The Tunkillia Suite and St Peters Suite (1690 – 1608 Ma)

The 1690 – 1670 Ma Tunkillia Suite represents a pivotal point in the crustal evolution of the Gawler Craton, between dominantly continental-continental collisional regime of the 1730 – 1700 Ma Kimban Orogeny, and island arc like characteristics of the 1630 – 1608 Ma St Peters Suite. Previous interpretations of the geological setting of the Tunkillia Suite has changed from the arc-like setting suggested by (Betts and Giles, 2006; Ferris, 2001; Teasdale, 1997), to a syn-collisional/ post-tectonic origin suggested by Payne et al. (2010). Previous Sm-Nd and Lu-Hf studies shows that the syn-

collisional granites of the Kimban Orogeny which precede the Tunkillia Suite, reflect dominantly crustal melt sources. In contrast, the Tunkillia suite requires the contribution of a significantly more juvenile melt component similar to the arc-like St Peters Suite (Fig. 7.1). However, the bimodal Nd and Hf signatures of the Tunkillia Suite presents an additional complication, requiring some melt component generated from an isotopically evolved source rock in the crust.

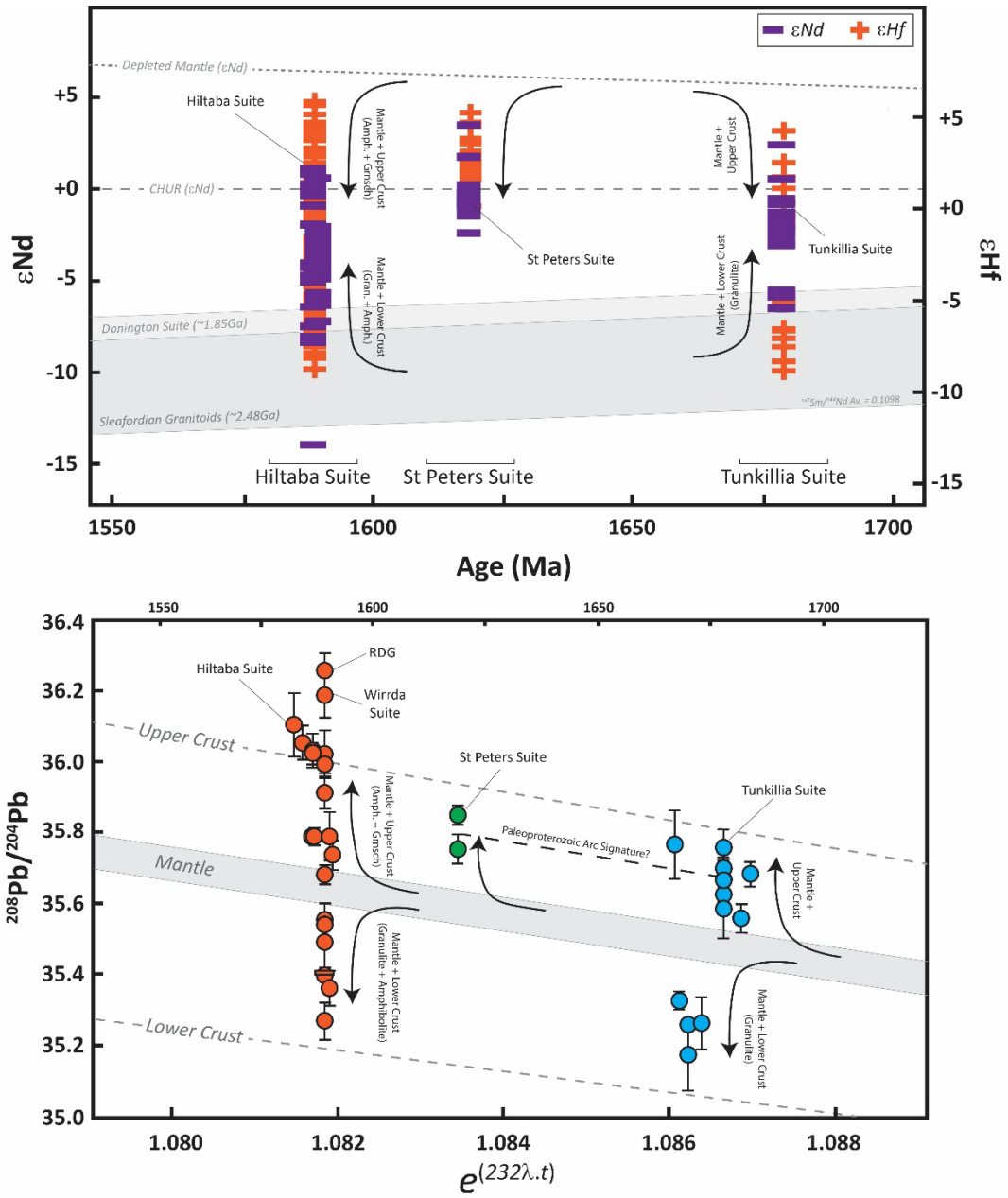

Figure 7.1: Isotope vs time plots for the 1690 – 1590 Ma igneous suites of the Gawler Craton. a) εNd_t and εHf_t vs time. b) $^{208}Pb/^{204}Pb$ vs $e^{232\lambda t}$ *(non-linear time) showing similar source requirements. 'Upper Crust' and 'Lower Crust' adapted after Zartman and Haines (1988). 'Mantle' field adapted after Allegre et al. (1986), Dupre and Allegre (1983), Tatsumoto (1978) and Zartman and Haines (1988). εHf_t data compiled from Pankhurst et al. (2013) and Reid and Payne (2017). εNd_t* data compiled from Payne et al. (2010), Swain et al. (2008), Budd and Skirrow (2007), Stewart and Foden (2003), Stewart and Foden (2001), Wurst (1994), Stewart (1994).

Initial Pb-isotopic signatures from alkali feldspars of the Tunkillia Suite effectively mirror the isotopic duplicity recorded in the εNd_t and εHf_t system. Strongly unradiogenic Pb-isotopic signatures recorded in the western Tunkillia Suite contrast with the ordinary Pb-isotopic signatures in the eastern Tunkillia Suite. The strongly-unradiogenic Pb-isotopic signatures of the westernmost Tunkillia Suite plutons record ancient Pb- model ages indicative of a crustal reservoir which has undergone significant U-depletion, similar to rocks affected by granulite-facies metamorphism. A sample of 2440 Ma felsic granulite located near the western Tunkillia Suite matches well with the unradiogenic Pb isotopic signature of the western Tunkillia Suite, and therefore represents a likely source for the unradiogenic Pb-component. Paradoxically however, granulites represent one of the most-refractory and least-fertile crustal melt sources and are therefore considered by this research to be incapable of producing voluminous granitoids in a syn-collisional/ post-tectonic setting with the mineralogical and chemical compositions of the western Tunkillia Suite. Alternatively, it is suggested that the western Tunkillia Suite may have been derived from limited hybridisation between a primarily mantle-derived melt and a limited component of lower crustal granulites, where Pb-isotopic mixing was biased towards crustal signatures through a high Pb-concentration gradient between the two melt source types.

The relatively ordinary Pb-isotopic signatures of the eastern Tunkillia Suite range from mantle-like and orogene-like compositions. In particular, the low $^{232}Th/^{238}U$ of the eastern Tunkillia Suite is markedly different to the granitoids of the syn-collisional/ post-tectonic Himalayas or Variscan Orogeny. Instead, the Pb-isotopic and geochemical compositions of the eastern Tunkillia Suite are far more similar to the St Peters Suite granites, which are considered to be generated in an island arc-like setting (Swain et al., 2008). The isotopic and geochemical similarity of the eastern Tunkillia Suite to the St Peters Suite suggest that Tunkillia Suite may well have been generated in a supra-subduction setting, and at the very least, highlights an inconsistent approach to previous

interpretations of some granite suites within in the Gawler Craton.

The Pb-isotopic behaviour shown by the Tunkillia Suite is a globally-rare phenomenon, and the geological setting for other examples of it may provide an insight into the true tectonic regime for the Tunkillia Suite. The closest Pb-isotopic and geochemical analogue was found to be the Central Volcanic Zone of the Andean Cordillera. Here, subduction-related melts are forced through a thickened, Paleoproterozoic lithosphere, where they inherit both the Pb and Nd-isotopic signature of the surrounding granulitic crust, with only limited effects to the overall geochemical characteristics of the magma. It is therefore suggested that the collisional tectonics of the Kimban Orogeny terminated with the failure of oceanic crust outboard from the Paleoproterozoic Gawler Craton nucleus. Collision then resumed as continental arc subduction (Fig. 7.2), with the possibility of slab-roll back leading to the formation of the St Peters Suite island arc some 30-40 Ma later.

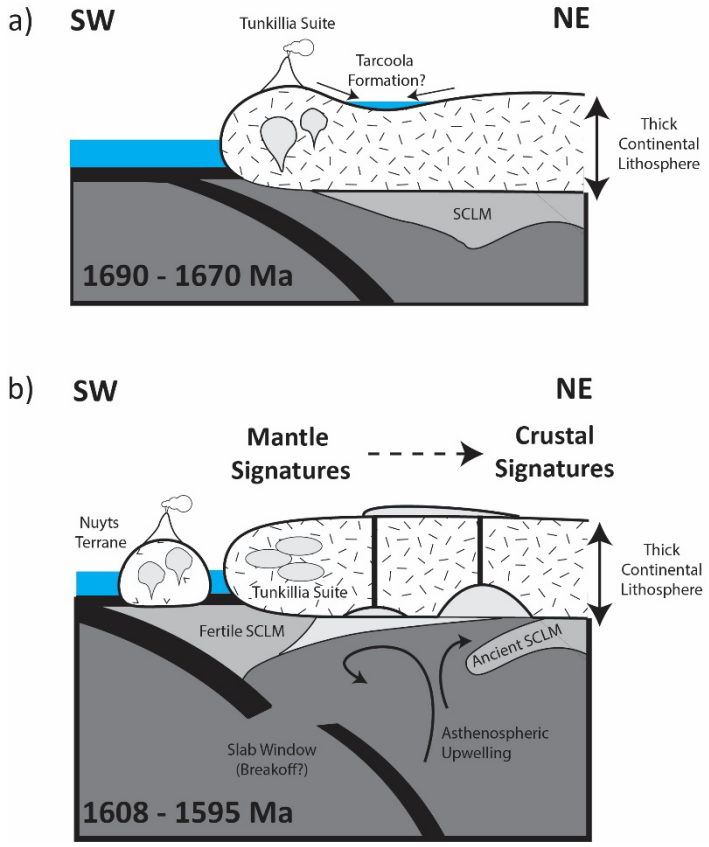

Figure 7.2: Schematic diagram for the proposed tectonic setting of the a) Tunkillia Suite, b) St Peters Suite and Hiltaba Suite.

7.2.2 The Hiltaba Suite and Gawler Range Volcanics (1595 – 1575 Ma)

Following 1608 Ma, the subduction-related paradigm which appears to have driven much of the crustal evolution in the Gawler Craton during the latest Paleoproterozoic, made a dramatic switch to the hot, anhydrous and anorogenic magmatism of the Hiltaba Suite/ Gawler Range Volcanics (GRV). Between 1595 and 1575 Ma, the Hiltaba/ GRV magmatic event added huge volumes of largely felsic magmas to the crust (100 000 km^3), which culminated in the final tectonic stabilisation of the Gawler Craton.

Magmatism with A-type affinities (anhydrous, anorogenic, HFSE/REE rich) such as the Hiltaba / GRV event, were widespread throughout the world during the Proterozoic. Previous studies of A-type suites have largely focused on mineralogical and geochemical studies to ascertain the origin of A-type magmas with varying degrees of success. The wide spatial-distribution of the Hiltaba Suite granitoids, coupled with the time-constraints applied by the coeval extrusive GRV, make the Hiltaba/ GRV event the ideal way to isotopically investigate the possible drivers and melt sources involved in A-type genesis.

Hiltaba Suite granitoids show a range of Pb-isotopic compositions, indicative of a number of dominant melt-sources. Systematic variation in the $^{238}U/^{204}Pb$ signature of Hiltaba Suite granitoids demonstrate the importance of hybridisation between tholeiitic mantle and crustal sources. At least two crustal end-, granulitic, members are apparent; a U-depleted crustal source similar to that encountered in the Tunkillia Suite, and a U-enriched upper crustal reservoir. Increasing HFSE/ REE enrichment (considered a feature of A-types granites), and Pb-isotopic signatures with crustal compositions suggest that at least part of the A-type geochemical characteristics are due to crustal hybridisation. However, the diversity in crustal sources, coupled with the innate HFSE/ REE enrichment observed in Hiltaba Suite granites with dominantly mantle-like signatures indicates that primary A-type geochemical characteristics are likely inherited from an enriched reservoir such as subcontinental lithospheric mantle. Similar relationships between Pb-isotopic compositions and Nd-isotopic composition, as well as Pb-isotopic compositions and HFSE/ REE enrichment in A-type

granitoids around the world advocates for the addition of an enriched tholeiitic melt to the crust as the primary driver for magmatism.

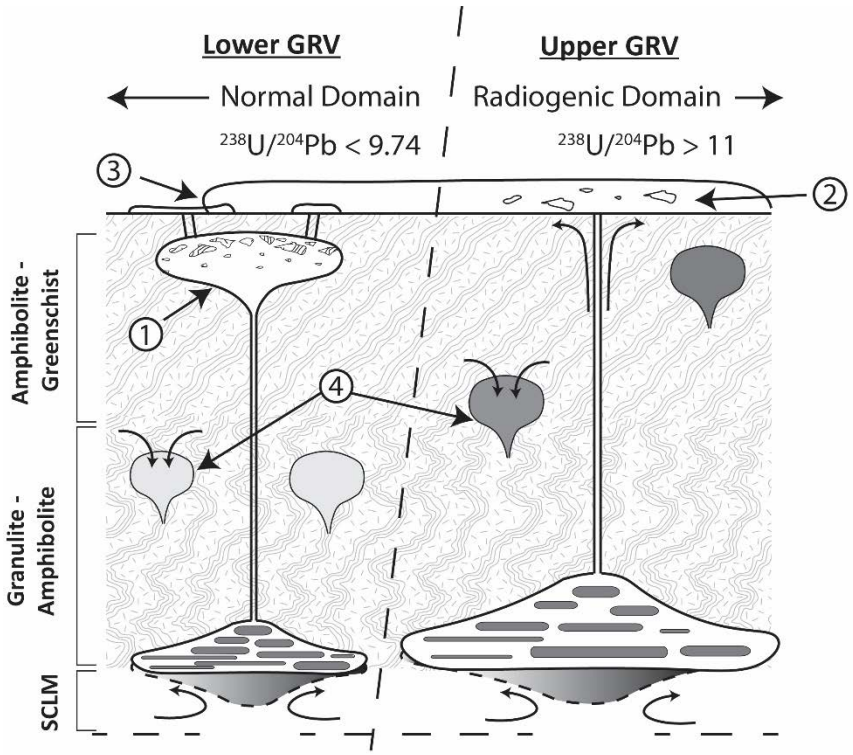

Figure 7.3: Schematic diagram explaining the Pb-isotopic differences between Lower GRV and Upper GRV. 1) Pb-isotopic heterogeneity and bimodalism of the Lower GRV compared with homogenous, dacitic Upper GRV suggest upper crustal residency and fractionation of the Lower GRV magmas. 2) Abundant boulder-sized xenoliths within flows for the Upper GRV have been interpreted to represent wallrock fragments incorporated during eruption (Garner and McPhie, 1999). 3) Recent CA-TIMS dating reveals the Lower and Upper GRV may have erupted contemporaneously (Jagodzinski et al., 2016). 4) Hiltaba Suite intrusives show a similar range of Pb-isotopic signatures as the GRV (crustal variation + melt proportion).

Vast differences between the Pb-isotopic signatures of the older Lower GRV (1594 Ma) and younger Upper GRV (1592 Ma) provide an insight into the evolution of A-type magmatic systems. The mantle-like Pb-isotopic signatures of rhyolites from the bimodal Lower GRV highlights that fractionation plays an important role in forming felsic A-type suites. In contrast, the homogenous and strongly-crustal Pb-isotopic signatures of the mostly-felsic Upper GRV demonstrates that large-scale crustal melting is also associated with A-type magmatic systems. The difference between the Upper and Lower GRV strongly suggests the two magmas are not co-magmatic, and developed as two separate and discrete magma systems (Fig. 7.3). If the Upper and Lower GRV were to be considered genuinely co-magmatic, then a mechanism is required which accounts for the huge

volumes of crustal melt to be generated (4200 km^3; Allen et al. (2003)) over a short period of time (<2 Ma; Jagodzinski et al. (2016)), without the presence of a hydrous flux (<2 wt. % H_2O; Creaser (1996); Stewart (1994)), which then thoroughly homogenised before extrusion. The significance of this last point cannot be understated as the GRV event would represent one of the most dynamic magmatic systems thus far recognised.

Large volumes of hot, dry, felsic magmas, enriched in HFSE and REE are currently produced within continental backarc settings (such as the Basin and Range Province) and present a possible geodynamic allegory for the GRV. Differences in the Pb-isotopic signatures of the Upper and Lower GRV closely match the Pb-isotopic signatures of some Cenozoic continental back-arc volcanics of the North American Cordillera. The Lower GRV Pb-isotopic signatures are most similar to volcanics from the Valles and Central San Juan Volcanic Fields, while the Upper GRV most closely resembles the crustal source in volcanics from Yellowstone and Snake River Plain. Spatial distributions in the Pb-isotopic signatures of the Hiltaba Suite granites support a possible backarc setting for the GRV. Mantle-like signatures are mostly encountered around the periphery of the Nuyts Terrane which hosts the arc-like St Peters Suite, while crustal Pb-isotopic compositions increase with distance from this terrane.

It is suggested that a NE-plunging continental margin subduction system which initiated with the 1690 – 1670 Ma Tunkillia Suite and concluded with the 1630 – 1608 Ma St Peters Suite could have led to mechanical erosion of the Gawler Craton sub-continental lithospheric mantle combined with the underplating of large volumes of enriched mantle-derived melt within the continental backarc of the Gawler Craton. Some HFSE and REE enrichments were inherited as the ascending primitive melts interacted with the SCLM. Crustal hybridisation when the ascending melt ponds, would be feature which accentuates the HFSE/ REE enrichment of A-type magmas. Therefore, the marked increase in relatively juvenile, mantle-like Nd- and Pb-isotopic signatures in magmatic rocks emplaced in the Gawler Craton between 1690 - 1590 Ma are geodynamically-related to onset of subduction and supra-subduction processes (Fig. 7.2).

7.3 Linking Crustal Evolution to Metallogenesis – The RDG and Olympic Dam

7.3.1 The 1594 Ma Roxby Downs Granite

The Roxby Downs Granite (RDG), a member of the A-type Hiltaba Suite, hosts the world's single largest polymetallic resource – Olympic Dam. However, the direct role played by the RDG in the genesis of Olympic Dam remains unresolved, with opinions of its importance varying between a passive host, to a direct contributor of most metals. Part of the reason for the speculation relates to the fact that the RDG is fairly unremarkable in terms of its mineralogy and geochemistry compared with other Hiltaba Suite A-type granites. In particular, little geochemical evidence can be found that directly links the RDG with large volumes of uranium within Olympic Dam.

The initial Pb-isotopic signatures from alkali feldspars of the RDG indicates that it was partially-derived from the most U-Th enriched crust of all the Hiltaba Suite. Both the $^{238}U/^{204}Pb$ and $^{232}Th/^{238}U$ signatures indicate that the RDG and Wirrda Suites represents the most radiogenic end-members of the Hiltaba Suite granites. Moreover, the high $^{207}Pb/^{204}Pb$ ratios of the RDG initial Pb signature indicate that the U-Th-enriched crustal reservoir which contributed melt to the RDG magma was Mesoarchean in age (~3200 Ma). The Mesoarchean Cooyerdoo Granite (3157 Ma), located to the south of Olympic Dam in the eastern Eyre Peninsula represents a likely melt-source analogue, matching the age requirements as well as U-Th-enriched criteria. While the RDG initial Pb-isotopic signature suggests the Mesoarchean crustal melt source which is only 14% higher than average crust, low-degrees of partial melting of the U-Th-enriched lower crust would have accentuated the U/Pb ratio of the resulting melt owning to the extreme incompatibility and solubility of U compared with Pb in a granitic melt (Peiffert et al. 1994). Low-degrees of partial melting are supported by Pb-Nd isotopic modelling which suggests that crustal-derived melts comprised less than 30% of the overall magma composition. The high mantle-derived melt component suggested by the mixing model is supported by the prevalence of Hiltaba-aged mafic-intermediate intrusive rocks within the Olympic Dam area (Fig. 7.4).

Complex textural features of the alkali feldspars hosting the initial Pb-isotopic signature of the RDG provide an insight into the transition of the RDG from orthomagmatic conditions, to magmatic-hydrothermal conditions. Initial Pb-isotopic signatures are exclusively hosted within preserved domains of orthomagmatic alkali feldspars (cryptoperthites/ orthoclase), whose large crystal lattice size and disordered arrangement of Al and Si imply high temperatures of formation (~870°C). In contrast, lower-temperature (400 – 250°C), ordered K-feldspar (microcline) which has largely replaced orthomagmatic alkali feldspar in the RDG, hosts highly-radiogenic Pb-isotopic compositions. The lower-temperature, replacive K-feldspar displays textures indicative of formation through fluid-assisted dissolution-reprecipitation (Fig. 7.4). Pb-isotopic isochrons derived from step-leached feldspars yield radiogenic Pb ages of 1609 ± 48 Ma suggesting that fluid-assisted alteration of the primary alkali feldspars occurred more-or-less at the same time as granite emplacement (1594 Ma). However, for this to be the case, some of the radiogenic Pb associated with the hydrothermal fluid must have also been sourced from outside of the RDG, perhaps from the surrounding country rock during open-system fluid convection in a mechanism akin to the fluid-mixing model of Haynes et al. (1995) (Fig. 7.4).

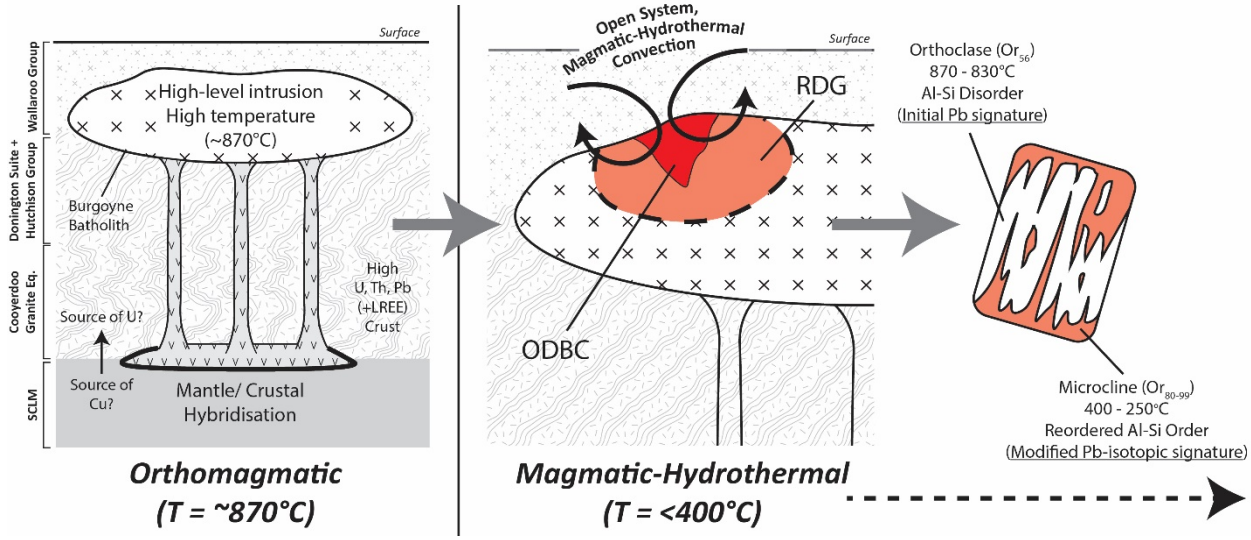

Figure 7.4: Schematic diagram outlining how the RDG may have contributed to the formation of the Olympic Dam deposit, as constrained by Pb-isotopic and crystallographic variations of alkali feldspar in the RDG.

Pb-isotopic and crystallographic changes recorded in alkali feldspars suggest two possible mechanism for linking the RDG to the formation of Olympic Dam. Firstly, the anomalous U in Olympic Dam compared to other IOCG deposits around the world may be partially the result of melt-derivation from a Mesoarchean crust enriched in U. Secondly, hydrothermal fluids at temperatures consistent with the earliest phase of ore formation at Olympic Dam were present around the time of granite emplacement, causing alteration of primary alkali feldspars throughout the RDG.

7.3.2 Pb-isotope systematics of the Olympic Dam Cu-Au-Ag-U Deposit

The Pb-isotopic and crystallographic changes seen in the alkali feldspars of the RDG provides a link between Mesoproterozoic granitic-melt derivation from a U-enriched crustal source, post-magmatic hydrothermal activity, and U-mineralisation at Olympic Dam. However, numerous isotopic systems applied to the ores of Olympic Dam by previous workers, imply that ore formation may have either occurred significantly after emplacement of the RDG, or the suffered extensive reworking at a time which significantly post-dates primary mineralisation. To investigate the veracity of these scenarios, the Pb-isotopic signatures of Pb-chalcogenides (galena and clausthalite), pyrite and gangue carbonates associated with Cu-ores were analysed.

The least-radiogenic Pb-isotopic compositions form arrays that intercept the initial Pb-isotopic signature of the RDG, indicating that the primary source of Pb, and possibly other metals was the RDG itself. The high $^{238}U/^{204}Pb$ and low $^{232}Th/^{238}U$ signature of radiogenic Pb component forming these isotopic arrays, implies that high-U/Pb, U/Th mineralisation was present by at least the time when the array formed (*minimum age* = 1527 ± 147 Ma)

The strongly-radiogenic Pb-isotopic signatures of the Olympic Dam ore zone indicates that the deposit evolved within a $^{232}Th/^{238}U$ system which was three to four-times more uranogenic than the RDG and average crust. Pb-isotopic signatures of the orezone show poor-correspondence with U,

Th and Pb abundances, suggesting that some degree of U-Th-Pb redistribution may have been experienced by the ores.

Variations in the Pb-isotopic signatures between the chalcopyrite-, bornite- and chalcocite dominant assemblages suggest that higher U/Pb, Th/Pb and U/Th ratios should be associated with the bornite and chalcocite ores compared to chalcopyrite. This is not the case, however and implies that some of the differences between the Pb-isotopic compositions of the Cu-ore types may be related to the preferential disturbance/ recrystallisation of U-rich minerals in the bornite and chalcocite zones. Positive correlation between modal % bornite and radiogenic Pb suggest that recrystallisation of U-minerals may be related bornite formation. Moreover, the negative correlation between modal % chalcopyrite and radiogenic Pb suggests that that bornite may have formed at the expense of chalcopyrite in response to the event which cause recrystallisation of U-minerals. Strongly uranogenic departures in the Pb-isotopic compositions of some samples associated with the bornite and chalcocite zones support the theory that uranogenic Pb was mixed over a short period of time.

Linear isochrons formed by these data, yield consistent radiogenic Pb ages around 664 ± 66 Ma. This age is comparable to apparent ages indicated by the Rb-Sr, Sm-Nd and U-Pb systems of previous authors. Critically, the ages indicated by Pb-Pb isochrons are wholly-consistent with the age of sedimentation above the Olympic Dam unconformity in response to marine transgression following the Marinoan Glaciation event (Fig. 7.5). It is suggested that the incursion of oxidised marine fluids during the Cryogenian affected U-mineralisation at higher levels in the deposit. The stability of U-rich minerals is strongly diminished in the presence of oxidised fluids, leading to remobilisation and redeposition of U (Fig. 7.5). Increasing oxidation related to the incursion of surficial fluids is thought to have forced the Cu-sulphide stability field from chalcopyrite-stability, to bornite- and chalcocite-stability, explaining the inverse correlations between radiogenic Pb, bornite and chalcopyrite. It is therefore inferred that the ingress of surficial, relatively-oxidised marine fluids

during the Late Neoproterozoic led to some U and Cu-upgrading at Olympic Dam, thus contributing to the economic tenor of this giant deposit (Fig. 7.5).

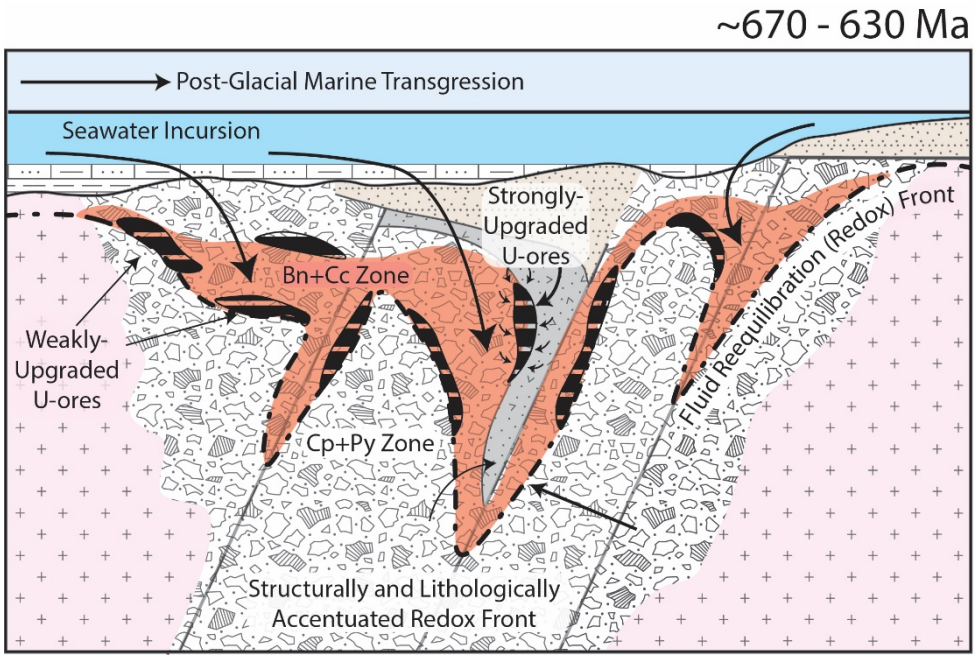

Figure 7.5: Neoproterozoic (Cryogenian) effects on the Olympic Dam mineralisation as suggested by variations in Pb-isotopic variations.

7.4 Future Work

A number of aspects of work have been identified during the course of this research which remain either unknown, or under investigated.

1) It is noted that a definitive resolution for the geological setting of the Tunkillia Suite, may only be possible through studies of mafic-equivalents of the Tunkillia Suite. Ultimately, this remains the sole difference between the accepted arc-setting for the St Peters Suite and the enigmatic setting of the Tunkillia Suite. Few examples of Tunkillia-aged mafic rocks are known from the Gawler Craton, however in this regard, the evidence of absence should not be regarded and the absence of evidence since there have been few attempts to date mafic rocks from the Tunkillia region. Furthermore, it should be pointed out that the identification of mafic equivalents of the St Peters Suite are only known due to good exposure of Gawler

Craton geology along the South Australian coastline, while the Tunkillia Suite (and probable mafic equivalents) remains inland and obscured by cover/ poor outcrop.

2) The varied Pb-isotopic signatures between the Lower and Upper Gawler Range Volcanics (GRV), as well as the Hiltaba Suite in general, may be of use in tectonic reconstructions. Temporal equivalents of the Gawler Range Volcanics are known from the Curnamona Formation (i.e. Benagerie Volcanics) and comparing the Pb-isotopic signature may help in constraining their magmatic sources as either Upper or Lower GRV-like. Similarly, Early Mesoproterozoic A-type granitoids are known in the Peake and Denison Inliers, as well as the Mt Isa Inlier and comparing the signatures of these granites with the varied signatures of the Hiltaba Suite may assist in aligning crustal domains of the Gawler Craton with crustal blocks of the Northern Australian Component.
3) Considering its role in the formation of Olympic Dam, the unique Pb-isotopic signature of the Roxby Downs Granite (RDG) provides a possible means of identifying prospectivity in the Hiltaba Suite granitoids in underexplored areas of the Gawler Craton.
4) The success of an integrated approach to crystallographic and Pb-isotopic studies of complex alkali feldspars provides a means of validating initial Pb's which do not conform to global crustal growth models. The increasing recognition of retarded and accelerated Pb-isotopic evolution is likely to yield a fascinating insight into the true evolution of the Earth's crustal Pb-isotopic reservoirs.
5) The identification of rare, preserved, orthomagmatic alkali feldspars of the RDG, open a plethora of avenues to study the range of melt-sources of this granite. In particular, $\delta^{18}O$ would provide a direct and reliable comparison between the $\delta^{18}O$ signatures of the earliest-formed calcites from deep within Olympic Dam, and magmatic quartz of the RDG. High-precision, high-spatial resolution results may be obtained for $\delta^{18}O$ through use of the SHRIMP microprobe. Further attempts at Sr-isotopic studies of the pristine alkali feldspars is

likely to shed further light on the role of mantle- and crustal-derived melts in forming the RDG, though will face difficulties when using dissolution-based methods.

6) Limited studies on the whole-rock Pb-isotopic signatures of the RDG suggests that a cryptic isotopic halo may exist which is related to Olympic Dam. Present data indicates that the detectable Pb-isotopic footprint may extend at least 7km from known mineralisation. The exploration implications of this are obvious and profound.
7) Higher precision Pb-isotopic studies, such as LA-MC-ICP-MS will refine the ages yielded from ores at Olympic Dam, and more-conclusively differentiate between Cryogenian surficial fluids related to sedimentation (676 – 635 Ma), and thermal-tectonic effects of the 514 Ma Delamerian Orogeny espoused by some previous workers.
8) Further Pb-isotopic studies of the Olympic Dam ore deposit will shed more light on the degree of U remobilisation which has affected the Olympic Dam ores. Systematic sampling throughout the ore deposit will narrow down the areas which been most affected, and the spatial relationship/ geometry of the most affected areas will help confirm the effects of a surficially-derived fluid. Further Pb-isotopic studies of Olympic Dam should also place an increased emphasis in constraining isotopic vs concentration mixing (i.e. 1/Pb (ppm) vs Pb-isotopic signature). Early attempts (not presented here) suggest there may be as many as three mixing events, with the last (i.e. ~664 Ma) the most volumetric contributor of radiogenic (uranogenic) Pb.

References

Agangi, A., Kamenetsky, V. S., and McPhie, J., 2012, Evolution and emplacement of high fluorine rhyolites in the Mesoproterozoic Gawler silicic large igneous province, South Australia: Precambrian Research, v. 208-211, p. 124-144.

Agangi, A., 2011, Magmatic and volcanic evolution of a silicic large igneous province (SLIP): the Gawler Range Volcanics and Hiltaba Suite, South Australia, University of Tasmania.

Allègre, C. J., Dupré, B., and Lewin, E., 1986, Thorium/uranium ratio of the Earth: Chemical Geology, v. 56, p. 219-227.

Allègre, C. J., Lewin, E., and Dupré, B., 1988, A coherent crust-mantle model for the uranium-thorium-lead isotopic system: Chemical Geology, v. 70, p. 211-234.

Allen, S. R., and McPhie, J., 2002, The Eucarro Rhyolite, Gawler Range Volcanics, South Australia: A >675 km3, compositionally zoned lava of Mesoproterozoic age: Geological Society of America Bulletin, v. 114, p. 1592-1609.

Allen, S. R., Simpson, C. J., McPhie, J., and Daly, S. J., 2003, Stratigraphy, distribution and geochemistry of widespread felsic volcanic units in the Mesoproterozoic Gawler Range Volcanics, South Australia: Australian Journal of Earth Sciences, v. 50, p. 97-112.

Almeida, R. V., Cai, Y., Hemming, S. R., Christie-Blick, N., and Neiswanger, L. S., 2016, Reexamination of the Crustal Boundary Context of Mesoproterozoic Granites in Southern Nevada Using U-Pb Zircon Chronology and Nd and Pb Isotopic Compositions: The Journal of Geology, v. 124, p. 313-329.

Alpher, R. A., and Herman, R. C., 1951, The Primeval Lead Isotopic Abundances and the Age of the Earth's Crust: Physical Review, v. 84, p. 1111-1114.

Altherr, R., Holl, A., Hegner, E., Langer, C., and Kreuzer, H., 2000, High-potassium, calc-alkaline I-type plutonism in the European Variscides: Northern Vosges (France) and northern Schwarzwald (Germany): Lithos, v. 50, p. 51-73.

Anderson, I. C., Frost, C. D., and Frost, B. R., 2003, Petrogenesis of the Red Mountain pluton, Laramie anorthosite complex, Wyoming: implications for the origin of A-type granite: Precambrian Research, v. 124, p. 243-267.

Anderson, J. L., 1983, Proterozoic anorogenic granite plutonism of North America, *in* Medaris, J. L. G., Byers, C. W., Mickelson, D. M., and Shanks, W. C., eds., Proterozoic Geology: Selected Papers from an International Proterozoic Symposium, Geological Society of America.

Andersson, U. B., Neymark, L. A., and Billström, K., 2002, Petrogenesis of Mesoproterozoic (Subjotnian) rapakivi complexes of central Sweden: implications from U–Pb zircon ages, Nd, Sr and Pb isotopes: Transactions of the Royal Society of Edinburgh: Earth Sciences, v. 92, p. 201-228.

Apukhtina, O. B., Kamenetsky, V. S., Ehrig, K., Kamenetsky, M. B., Maas, R., Thompson, J., McPhie, J., Ciobanu, C. L., and Cook, N. J., 2017, Early, deep magnetite-fluorapatite mineralization at the Olympic Dam Cu-U-Au-Ag deposit, South Australia: Economic Geology, v. 112, p. 1531-1542.

Apukhtina, O., 2016, Distribution, petrology, geochemistry and geochronology of carbonate assemblages at the Olympic Dam deposit, University of Tasmania.

Babinski, M., Van Schmus, W. R., and Chemale, F., 1999, Pb–Pb dating and Pb isotope geochemistry of Neoproterozoic carbonate rocks from the São Francisco basin, Brazil: implications for the mobility of Pb isotopes during tectonism and metamorphism: Chemical Geology, v. 160, p. 175-199.

Bagas, L., 2004, Proterozoic evolution and tectonic setting of the northwest Paterson Orogen, Western Australia: Precambrian Research, v. 128, p. 475-496.

Baker, J., Peate, D., Waight, T., and Meyzen, C., 2004, Pb isotopic analysis of standards and samples using a 207Pb–204Pb double spike and thallium to correct for mass bias with a double-focusing MC-ICP-MS: Chemical Geology, v. 211, p. 275-303.

Bastrakov, E. N., Skirrow, R. G., and Davidson, G. J., 2007, Fluid evolution and origins of iron oxide Cu-Au prospects in the Olympic Dam district, Gawler Craton, south Australia: Economic Geology, v. 102, p. 1415-1440.

Bea, F., 1996, Residence of REE, Y, Th and U in granites and crustal protoliths; implications for the chemistry of crustal melts: Journal of Petrology, v. 37, p. 521-552.

Bea, F., 2012, The sources of energy for crustal melting and the geochemistry of heat-producing elements: Lithos, v. 153, p. 278-291.

Beauchemin, D., 2017, Inductively Coupled Plasma Mass Spectrometry Methods, *in* Lindon, J. C., Tranter, G. E., and Koppenaal, D. W., eds., Encyclopedia of Spectroscopy and Spectrometry (Third Edition): Oxford, Academic Press, p. 236-245.

Beck, S. L., Zandt, G., Myers, S. C., Wallace, T. C., Silver, P. G., and Drake, L., 1996, Crustal-thickness variations in the central Andes: Geology, v. 24, p. 407-410.

Bellucci, J. J., McDonough, W. F., and Rudnick, R. L., 2011, Thermal history and origin of the Tanzanian Craton from Pb isotope thermochronology of feldspars from lower crustal xenoliths: Earth and Planetary Science Letters, v. 301, p. 493-501.

Belperio, A., Flint, R., and Freeman, H., 2007, Prominent Hill: A hematite-dominated, iron oxide copper-gold system: Economic Geology, v. 102, p. 1499-1510.

Benisek, A., Dachs, E., and Kroll, H., 2010, A ternary feldspar-mixing model based on calorimetric data: development and application: Contributions to Mineralogy and Petrology, v. 160, p. 327-337.

Bernard-Griffiths, J., Peucat, J. J., Sheppard, S., and Vidal, P., 1985, Petrogenesis of Hercynian leucogranites from the southern Armorican Massif: contribution of REE and isotopic (Sr, Nd, Pb and O) geochemical data to the study of source rock characteristics and ages: Earth and Planetary Science Letters, v. 74, p. 235-250.

Betts, P. G., and Giles, D., 2006, The 1800–1100Ma tectonic evolution of Australia: Precambrian Research, v. 144, p. 92-125.

Bierlein, F. P., Haack, U., Förster, B., and Plimer, I. R., 1996, Lead isotope study on hydrothermal sulfide mineralisation in the Willyama Supergroup, Olary Block, South Australia: Australian Journal of Earth Sciences, v. 43, p. 177-187.

Black, L. P., Kamo, S. L., Allen, C. M., Aleinikoff, J. N., Davis, D. W., Korsch, R. J., and Foudoulis, C., 2003, TEMORA 1: A new zircon standard for Phanerozoic U-Pb geochronology: Chemical Geology, v. 200, p. 155-170.

Bohm, M., Lüth, S., Echtler, H., Asch, G., Bataille, K., Bruhn, C., Rietbrock, A., and Wigger, P., 2002, The Southern Andes between 36° and 40°S latitude: Seismicity and average seismic velocities: Tectonophysics, v. 356, p. 275-289.

Bouvier, A., Vervoort, J. D., and Patchett, P. J., 2008, The Lu–Hf and Sm–Nd isotopic composition of CHUR: Constraints from unequilibrated chondrites and implications for the bulk composition of terrestrial planets: Earth and Planetary Science Letters, v. 273, p. 48-57.

Brown, W. L., and Parsons, I., 1989, Alkali feldspars: ordering rates, phase transformations and behaviour diagrams for igneous rocks: Mineralogical Magazine, v. 53, p. 25-42.

Bryant, J. A., Yogodzinski, G. M., Hall, M. L., Lewicki, J. L., and Bailey, D. G., 2006, Geochemical constraints on the origin of volcanic rocks from the Andean Northern volcanic zone, Ecuador: Journal of Petrology, v. 47, p. 1147-1175.

Budd, A. R., 2006, The Tarcoola Goldfield of the Central Gawler Gold Province, and the Hiltaba Association Granites, Gawler Craton, South Australia, Australian National University.

Budd, A. R., and Skirrow, R. G., 2007, The nature and origin of gold deposits of the Tarcoola Goldfield and implications for the central Gawler Gold Province, South Australia: Economic Geology, v. 102, p. 1541-1563.

Cannon, R. S., and Pierce, A. P., 1969, Lead isotope guides for Mississippi Valley lead-zinc exploration, US Government Printing Office.

Carpentier, M., Chauvel, C., and Mattielli, N., 2008, Pb-Nd isotopic constraints on sedimentary input into the Lesser Antilles arc system: Earth and Planetary Science Letters, v. 272, p. 199-211.

Carr, G. R., Dean, J. A., Suppel, D. W., and Heithersay, P. S., 1995, Precise lead isotope fingerprinting of hydrothermal activity associated with Ordovician to Carboniferous metallogenic events in the Lachlan fold belt of New South Wales: Economic Geology, v. 90, p. 1467-1505.

Carr, G. R., Sun, S.-S., Page, R. W., and Hinman, M., 1996, Recent Developments in the use of lead isotope model ages in Proterozoic terrains: New Developments in Metallogenic Research - The McArthur-Mt Isa-Cloncurry Province, Townsville, 1996.

Carrington, D. P., and Watt, G. R., 1995, A geochemical and experimental study of the role of K-feldspar during water-undersaturated melting of metapelites: Chemical Geology, v. 122, p. 59-76.

Chalmers, N. C., 2009, Geodynamic evolution of the St Peter Suite, Gawler Craton, South Australia : stratigraphic geochemical and isotopic investigation, Monash University.

Chapman, N. D., Ferguson, M., Meffre, S. J., Stepanov, A., Maas, R., and Ehrig, K. J., 2019, Pb-isotopic constraints on the source of A-type Suites: Insights from the Hiltaba Suite - Gawler Range Volcanics Magmatic Event, Gawler Craton, South Australia: Lithos, v. 346-347, p. 105156.

Cherniak, D. J., 1995, Diffusion of lead in plagioclase and K-feldspar: an investigation using Rutherford Backscattering and Resonant Nuclear Reaction Analysis: Contributions to Mineralogy and Petrology, v. 120, p. 358-371.

Cherniak, D. J., 2000, Pb diffusion in rutile: Contributions to Mineralogy and Petrology, v. 139, p. 198-207.

Cherniak, D. J., 2010, Diffusion in Accessory Minerals: Zircon, Titanite, Apatite, Monazite and Xenotime: Reviews in Mineralogy and Geochemistry, v. 72, p. 827-869.

Cherniak, D. J., and Watson, E. B., 2001, Pb diffusion in zircon: Chemical Geology, v. 172, p. 5-24.
Cherniak, D. J., Watson, E. B., Grove, M., and Harrison, T. M., 2004, Pb diffusion in monazite: a combined RBS/SIMS study1: Geochimica et Cosmochimica Acta, v. 68, p. 829-840.

Cherry, A. R., Ehrig, K., Kamenetsky, V. S., McPhie, J., Crowley, J. L., and Kamenetsky, M. B., 2018, Precise geochronological constraints on the origin, setting and incorporation of ca. 1.59 Ga surficial facies into the Olympic Dam Breccia Complex, South Australia: Precambrian Research, v. 315, p. 162-178.

Cherry, A. R., McPhie, J., Kamenetsky, V. S., Ehrig, K., Keeling, J. L., Kamenetsky, M. B., Meffre, S., and Apukhtina, O. B., 2017, Linking Olympic Dam and the Cariewerloo Basin: Was a sedimentary basin involved in formation of the world's largest uranium deposit?: Precambrian Research, v. 300, p. 168-180.

Ciobanu, C. L., Wade, B. P., Cook, N. J., Mumm, A. S., and Giles, D., 2013, Uranium-bearing hematite from the Olympic Dam Cu-U-Au deposit, South Australia: A geochemical tracer and reconnaissance Pb-Pb geochronometer: Precambrian Research, v. 238, p. 129-147.

Ciobanu, C. L., Cook, N. J., and Ehrig, K., 2017, Ore minerals down to the nanoscale: Cu-(Fe)-sulphides from the iron oxide copper gold deposit at Olympic Dam, South Australia: Ore Geology Reviews, v. 81, p. 1218-1235.

Clemens, J. D., and Vielzeuf, D., 1987, Constraints on melting and magma production in the crust: Earth and Planetary Science Letters, v. 86, p. 287-306.

Clemens, J. D., Holloway, J. R., and White, A. J. R., 1986, Origin of an A-type granite: experimental constraints: American Mineralogist, v. 71, p. 317-324.

Cohen, R. S., and O'Nions, R. K., 1982, Identification of recycled continental material in the mantle from Sr, Nd and Pb isotope investigations: Earth and Planetary Science Letters, v. 61, p. 73-84.
Collins, W. J., and Shaw, R. D., 1995, Geochronological constraints on orogenic events in the Arunta Inlier: a review: Precambrian Research, v. 71, p. 315-346.

Collins, W. J., Beams, S. D., White, A. J. R., and Chappell, B. W., 1982, Nature and origin of A-type granites with particular reference to southeastern Australia: Contributions to Mineralogy and Petrology, v. 80, p. 189-200.

Cooper, J. A., Reynolds, P. H., and Richards, J. R., 1969, Double-spike calibration of the broken hill standard lead: Earth and Planetary Science Letters, v. 6, p. 467-478.

Cowley, W. M., and Fanning, C. M., 1991, Low grade Archaean metavolcanics in the northern Gawler Craton: Quarterly Geological Notes, v. 119, p. 2-16.

Cowley, W. M., Conor, C. H. H., and Zang, W., 2003, New and revised Proterozoic stratigraphic units on the northern Yorke Peninsula: Minerals and Energy South Australia Journal, v. 29, p. 46-58.

Creaser, R. A., 1989, The geology and petrology of Middle Proterozoic felsic magmatism of the Stuart Shelf, South Australia, La Trobe University.

Creaser, R. A., 1996, Petrogenesis of a Mesoproterozoic quartz latite-granitoid suite from the Roxby Downs area, South Australia: Precambrian Research, v. 79, p. 371-394.

Creaser, R. A., and Cooper, J. A., 1993, U-Pb geochronology of middle Proterozoic felsic magmatism surrounding the Olympic Dam Cu-U-Au-Ag and Moonta Cu-Au-Ag deposits, South Australia: Economic Geology, v. 88, p. 186-197.

Creaser, R. A., and Fanning, C. M., 1993, A U‐Pb zircon study of the Mesoproterozoic Charleston Granite, Gawler Craton, South Australia: Australian Journal of Earth Sciences, v. 40, p. 519-526.

Creaser, R. A., and White, A. J. R., 1991, Yardea Dacite—Large-volume, high-temperature felsic volcanism from the Middle Proterozoic of South Australia: Geology, v. 19, p. 48-51.

Creaser, R. A., Price, R. C., and Wormald, R. J., 1991, A-type granites revisited: assessment of a residual-source model: Geology, v. 19, p. 163-166.

Cross, K. C., Daly, S. J., and Flint, R. B., 1993, The Olympic Dam Deposit, *in* Drexel, J. F., and Preiss, W. V. P., A.J., eds., The Geology of South Australia, The Precambrian, 1, Department of Mines and Energy, p. 132-137.

Crowe, S. A., Fryer, B. J., Samson, I. M., and Gagnon, J. E., 2003, Precise isotope ratio determination of common Pb using quadrupole LA-ICP-MS with optimized laser sampling conditions and a robust mixed-gas plasma: Journal of Analytical Atomic Spectrometry, v. 18, p. 1331-1338.

Cumming, G. L., and Richards, J. R., 1975, Ore lead isotope ratios in a continuously changing earth: Earth and Planetary Science Letters, v. 28, p. 155-171.

Cutts, K., Hand, M., and Kelsey, D. E., 2011, Evidence for early Mesoproterozoic (ca. 1590Ma) ultrahigh-temperature metamorphism in southern Australia: Lithos, v. 124, p. 1-16.

Daly, S. J., and Fanning, C. M., 1993, Archaean, *in* Drexel, J. F., Preiss, W. V. and Parker, A. J., ed., The Geology of South Australia, Volume 1, The Precambrian, 1: Adelaide, South Australia Geological Survey.

Daly, S. J., Fanning, C. M., and Fairclough, M. C., 1998, Tectonic evolution and exploration potential of the Gawler Craton, South Australia: AGSO Journal of Australia Geology and Geophysics, v. 17, p. 145-168.

Darling, J. R., Storey, C. D., Hawkesworth, C. J., and Lightfoot, P. C., 2012, In-situ Pb isotope analysis of Fe–Ni–Cu sulphides by laser ablation multi-collector ICPMS: New insights into ore formation in the Sudbury impact melt sheet: Geochimica et Cosmochimica Acta, v. 99, p. 1-17.

Davidson, G. J., Paterson, H., Meffre, S., and Berry, R. F., 2007, Characteristics and origin of the Oak Dam East breccia-hosted, iron oxide Cu-U-(Au) deposit: Olympic Dam region, Gawler craton, South Australia: Economic Geology, v. 102, p. 1471-1498.

Davidson, J. P., Harmon, R. S., and Wörner, G., 1991, The source of central Andean magmas; Some considerations, Special Paper of the Geological Society of America, 265, p. 233-243.

Davies, G. R., Halliday, A. N., Mahood, G. A., and Hall, C. M., 1994, Isotopic constraints on the production rates, crystallisation histories and residence times of pre-caldera silicic magmas, Long Valley, California: Earth and Planetary Science Letters, v. 125, p. 17-37.

De la Roche, H., Leterrier, J., Grandclaude, P., and Marchal, M., 1980, A classification of volcanic and plutonic rocks using R1R2-diagram and major-element analyses - Its relationships with current nomenclature: Chemical Geology, v. 29, p. 183-210.

DeWolf, C. P., and Mezger, K., 1994, Lead isotope analyses of leached feldspars: Constraints on the early crustal history of the Grenville Orogen: Geochimica et Cosmochimica Acta, v. 58, p. 5537-5550.

Dickin, A. P., Artan, M. A., and Crocket, J. H., 1996, Isotopic evidence for distinct crustal sources of North and South Range ores, Sudbury Igneous Complex: Geochimica et Cosmochimica Acta, v. 60, p. 1605-1613.

Dixon, T. H., Miller, M., Farina, F., Wang, H., and Johnson, D., 2000, Present-day motion of the Sierra Nevada block and some tectonic implications for the Basin and Range province, North American Cordillera: Tectonics, v. 19, p. 1-24.

Dodson, M. H., 1973, Closure temperature in cooling geochronological and petrological systems: Contributions to Mineralogy and Petrology, v. 40, p. 259-274.

Doe, B. R., 1967, The bearing of lead isotopes on the source of Granitic Magma: Journal of Petrology, v. 8, p. 51-83.

Doe, B. R., and Hart, S. R., 1963, The effect of contact metamorphism on lead in potassium feldspars near the Eldora stock, Colorado: Journal of Geophysical Research, v. 68, p. 3521-3530.

Doe, B. R., and Stacey, J. S., 1974, The Application of Lead Isotopes to the Problems of Ore Genesis and Ore Prospect Evaluation: A Review: Economic Geology, v. 69, p. 757-776.

Doe, B. R., Leeman, W. P., Christiansen, R. L., and Hedge, C. E., 1982, Lead and strontium isotopes and related trace elements as genetic tracers in the Upper Cenozoic rhyolite-basalt association of the Yellowstone Plateau Volcanic Field: Journal of Geophysical Research: Solid Earth, v. 87, p. 4785-4806.

Dolomanov, O. V., Bourhis, L. J., Gildea, R. J., Howard, J. A. K., and Puschmann, H., 2009, OLEX2: a complete structure solution, refinement and analysis program: Journal of Applied Crystallography, v. 42, p. 339-341.

Dostal, J., and Capedri, S., 1978, Uranium in metamorphic rocks: Contributions to Mineralogy and Petrology, v. 66, p. 409-414.

Dostal, J., Chatterjee, A., and Kontak, D., 2004, Chemical and isotopic (Pb, Sr) zonation in a peraluminous granite pluton: role of fluid fractionation: Contributions to Mineralogy and Petrology, v. 147, p. 74-90.

Dove, M. B., 1997, The geology, petrology, geochemistry and isotope geology of the eastern St Peter Suite western Gawler Graton, South Australia, University of Adelaide.

Dupre, B., and Allegre, C. J., 1983, Pb-Sr isotope variation in Indian Ocean basalts and mixing phenomena: Nature, v. 303, p. 142-146.

Dutch, R. A., 2009, Reworking the Gawler Craton: metamorphic and geochronologic constraints on palaeoproterozoic reactivation of the southern Gawler Craton, Australia.

Eby, G. N., 1990, The A-type granitoids: A review of their occurrence and chemical characteristics and speculations on their petrogenesis: LITHOS, v. 26, p. 115-134.

Ehrig, K., McPhie, J., and Kamenetsky, V. S., 2012, Geology and mineralogical zonation of the Olympic Dam Iron Oxide Cu-U-Au-Ag Deposit, South Australia, *in* Hedenquist, J. W., Harris, M., and Camus, F., eds., Economic Geology Special Publication 16, p. 237-267.

Elburg, M. A., van Bergen, M. J., and Foden, J. D., 2004, Subducted upper and lower continental crust contributes to magmatism in the collision sector of the Sunda-Banda arc, Indonesia: Geology, v. 32, p. 41-44.

Ellam, R. M., Hawkesworth, C. J., and McDermott, F., 1990, Pb isotope data from late Proterozoic subduction-related rocks: Implications for crust-mantle evolution: Chemical Geology, v. 83, p. 165-181.

Elliott, T., Zindler, A., and Bourdon, B., 1999, Exploring the kappa conundrum: the role of recycling in the lead isotope evolution of the mantle: Earth and Planetary Science Letters, v. 169, p. 129-145.

Ersoy, Y., and Helvacı, C., 2010, FC–AFC–FCA and mixing modeler: A Microsoft® Excel© spreadsheet program for modeling geochemical differentiation of magma by crystal fractionation, crustal assimilation and mixing: Computers & Geosciences, v. 36, p. 383-390.

Fanning, C. M., Flint, R. B., Parker, A. J., Ludwig, K. R., and Blissett, A. H., 1988, Refined Proterozoic evolution of the Gawler Craton, South Australia, through U-Pb zircon geochronology: Precambrian Research, v. 40-41, p. 363-386.

Fanning, M., Reid, A. J., Teale, G. S., Teale, G. S., and SA, P. I. a. R., 2007, A geochronological framework for the Gawler Craton, South Australia: Adelaide: Primary Industries and Resources SA, 2007.

Ferris, G. M., 2001, The geology and geochemistry of granitoids in the CHILDARA region, western Gawler Craton, South Australia: Implications for the Proterozoic tectonic history of the western Gawler Craton and development of lode-style gold mineralisation at Tunkillia, University of Tasmania, 160 p.

Ferris, G. M., and Schwarz, M., 2004, Definition of the Tunkillia Suite, western Gawler Craton: Minerals and Energy South Australia Journal, v. 34, p. 32 - 41.

Ferris, G. M., Schwarz, M. P., and Heithersay, P., 2002, The geological framework, distribution and controls of Fe-oxide Cu-Au mineralisation in the Gawler Craton, South Australia. Part 1: Geological and tectonic framework, *in* Porter, T. M., ed., Hydrothermal iron oxide copper-gold and related deposits: a global perspective, 2: Adelaide, PCG Publishing, p. 9-31.

Ferris, G., Schwarz, M., and Heithersay, P., 2002, The Geological Framework, Distribution and Controls of Fe-Oxide and Related Alteration, and Cu-Au Mineralisation in the Gawler Craton, South Australia - Part 1: Geological and Tectonic Framework, *in* Porter, T., ed., Hydrothermal Iron Oxide Copper Gold & Related Deposits: A Global Perspective, 2: Adelaide, PGC Publishing.

Flint, R. B., 1993, Mesoproterozoic, *in* Drexel, J. F., Preiss, W. V. and Parker, A. J., ed., The Geology of South Australia, Volume 1, The Precambrian, 1: Adelaide, South Australia Geological Survey.

Förster, H. J., Tischendorf, G., and Trumbull, R. B., 1997, An evaluation of the Rb vs. (Y + Nb) discrimination diagram to infer tectonic setting of silicic igneous rocks: Lithos, v. 40, p. 261-293.

Fraser, G. L., and Neumann, N. L., 2010, New SHRIMP U-Pb zircon ages from the Gawler Craton and Curnamona Province, South Australia, 2008 - 2010, Geoscience Australia.

Fraser, G., McAvaney, S., Neumann, N., Szpunar, M., and Reid, A., 2010, Discovery of early Mesoarchean crust in the eastern Gawler Craton, South Australia: Precambrian Research, v. 179, p. 1-21.

Freymuth, H., Brandmeier, M., and Wörner, G., 2015, The origin and crust/mantle mass balance of Central Andean ignimbrite magmatism constrained by oxygen and strontium isotopes and erupted volumes: Contributions to Mineralogy and Petrology, v. 169.

Fricke, C., 2005, Source and origin of the Lower Gawler Range Volcanics (GRV), South Australia: geochemical constraints from mafic magmas, Monash University.

Frindt, S., Trumbull, R. B., and Romer, R. L., 2004, Petrogenesis of the Gross Spitzkoppe topaz granite, central western Namibia: a geochemical and Nd–Sr–Pb isotope study: Chemical Geology, v. 206, p. 43-71.

Frost, B. R., Barnes, C. G., Collins, W. J., Arculus, R. J., Ellis, D. J., and Frost, C. D., 2001, A geochemical classification for granitic rocks: Journal of Petrology, v. 42, p. 2033-2048.

Frost, C. D., and Frost, R. B., 1997, Reduced rapakivi-type granites: the tholeiite connection: Geology, v. 25, p. 647-650.

Frost, C. D., Frost, B. R., Chamberlain, K. R., and Edwards, B. R., 1999, Petrogenesis of the 1.43 Ga Sherman Batholith, SE Wyoming, USA: a Reduced, Rapakivi-type Anorogenic Granite: Journal of Petrology, v. 40, p. 1771-1802.

Gagnevin, D., Daly, J. S., Waight, T. E., Morgan, D., and Poli, G., 2005, Pb isotopic zoning of K-feldspar megacrysts determined by Laser Ablation Multi-Collector ICP-MS: Insights into granite petrogenesis: Geochimica et Cosmochimica Acta, v. 69, p. 1899-1915.

Gariépy, C., Allègre, C. J., and Rong Hua, X., 1985, The Pb-isotope geochemistry of granitoids from the Himalaya-Tibet collision zone: implications for crustal evolution: Earth and Planetary Science Letters, v. 74, p. 220-234.

Giles, C. W., 1988, Petrogenesis of the Proterozoic Gawler Range Volcanics, South Australia: Precambrian Research, v. 40–41, p. 407-427.

Godwin, C. I., and Sinclair, A. J., 1982, Average lead isotope growth curves for shale-hosted zinc-lead deposits, Canadian Cordillera: Economic Geology, v. 77, p. 675-690.

Goodwin, S., 2010, Geochemical and Isotopic Investigation into the Tectonic Setting of Mesoarchean and Paleoproterozoic Granitoid Suites within the Eastern Gawler Craton, South Australia, University of Adelaide.

Göpel, C., Manhès, G., and Allègre, C. J., 1985, U-Pb systematics in iron meteorites: Uniformity of primordial lead: Geochimica et Cosmochimica Acta, v. 49, p. 1681-1695.

Gravestock, D. I., 1995, The geology of South Australia, Volume 2, The Phanerozoic: Adelaide, South Australia Geological Survey, 357 p.

Gray, C. M., and Oversby, V. M., 1972, The behaviour of lead isotopes during granulite facies metamorphism: Geochimica et Cosmochimica Acta, v. 36, p. 939-952.

Gu, Y., 2003, Automated scanning electron microscope based mineral liberation analysis an introduction to JKMRC/FEI mineral liberation analyser: Journal of Minerals and Materials Characterization and Engineering, v. 2, p. 33.

Guillong, M., Kuhn, H. R., and Günther, D., 2003, Application of a particle separation device to reduce inductively coupled plasma-enhanced elemental fractionation in laser ablation-inductively coupled plasma-mass spectrometry: Spectrochimica Acta - Part B Atomic Spectroscopy, v. 58, p. 211-220.

Gustafson, L., and Compston, W., 1979, Rb-Sr dating of Olympic Dam core samples: Australian National University, Research School of Earth Sciences January, v. 18, p. 1979.

Haapala, I., and Ramo, O. T., 1990, Petrogenesis of the Proterozoic rapakivi granites of Finland, Special Paper of the Geological Society of America, 246, p. 275-286.

Haapala, I., and Rämö, O. T., 1992, Tectonic setting and origin of the Proterozoic rapakivi granites of southeastern Fennoscandia: Earth and Environmental Science Transactions of the Royal Society of Edinburgh, v. 83, p. 165-171.

Hand, M., Reid, A., and Jagodzinski, L., 2007, Tectonic framework and evolution of the Gawler craton, Southern Australia: Economic Geology, v. 102, p. 1377-1395.

Harmon, R. S., Barreiro, B. A., Moorbath, S., Hoefs, J., Francis, P. W., Thorpe, R. S., Déruelle, B., McHugh, J., and Viglino, J. A., 1984, Regional O-, Sr-, and Pb-isotope relationships in late Cenozoic calc-alkaline lavas of the Andean Cordillera: Journal of the Geological Society, v. 141, p. 803-822.

Harris, N. B. W., Pearce, J. A., and Tindle, A. G., 1986, Geochemical characteristics of collision-zone magmatism: Collision tectonics, p. 67-81.

Hart, S. R., 1964, The Petrology and Isotopic-Mineral Age Relations of a Contact Zone in the Front Range, Colorado: The Journal of Geology, v. 72, p. 493-525.

Hattori, K. H., and Keith, J. D., 2001, Contribution of mafic melt to porphyry copper mineralization: evidence from Mount Pinatubo, Philippines, and Bingham Canyon, Utah, USA: Mineralium Deposita, v. 36, p. 799-806.

Hawkesworth, C. J., and Kemp, A. I. S., 2006, Evolution of the continental crust: Nature, v. 443, p. 811-817.

Haynes, D. W., Cross, K. C., Bills, R. T., and Reed, M. H., 1995, Olympic Dam Ore Genesis - a Fluid-Mixing Model: Economic Geology & the Bulletin of the Society of Economic Geologists, v. 90, p. 281-307.

Heinonen, A. P., Rämö, O. T., Johanson, B., Mänttäri, I., and Alviola, R., 2010, Formation and fractionation of high-Al tholeiitic magmas in the Ahvenisto rapakivi granite - massif-type anorthosite complex, southeastern Finland: The Canadian Mineralogist, v. 48, p. 969-990.

Heumann, A., Davies, G. R., and Elliott, T., 2002, Crystallization history of rhyolites at Long Valley, California, inferred from combined U-series and Rb-Sr isotope systematics: Geochimica et Cosmochimica Acta, v. 66, p. 1821-1837.

Hildreth, W., and Moorbath, S., 1988, Crustal contributions to arc magmatism in the Andes of Central Chile: Contributions to Mineralogy and Petrology, v. 98, p. 455-489.

Hitzman, M. W., and Valenta, R. K., 2005, Uranium in iron oxide-copper-gold (IOCG) systems: Economic Geology, v. 100, p. 1657-1661.

Hoatson, D. M., Sun, S.-S., Duggan, M. B., Davies, M. B., Daly, S. J., and Purvis, A. C., 2005, Late Archean Lake Harris Komatiite, Central Gawler Craton, South Australia: Geologic Setting and Geochemistry: Economic Geology, v. 100, p. 349-374.

Hoek, J. D., and Schaefer, B. F., 1998, Palaeoproterozoic Kimban mobile belt, Eyre Peninsula: Timing and significance of felsic and mafic magmatism and deformation: Australian Journal of Earth Sciences, v. 45, p. 305-313.

Holk, G. J., Kyser, T. K., Chipley, D., Hiatt, E. E., and Marlatt, J., 2003, Mobile Pb-isotopes in Proterozoic sedimentary basins as guides for exploration of uranium deposits: Journal of Geochemical Exploration, v. 80, p. 297-320.

Hollings, P., and Kerrich, R., 2000, An Archean arc basalt-Nb-enriched basalt-adakite association: The 2.7 Ga Confederation assemblage of the Birch-Uchi greenstone belt, Superior Province: Contributions to Mineralogy and Petrology, v. 139, p. 208-226.

Holmes, A., 1946, An estimate of the age of the earth: Nature, v. 157, p. 680.

Hopper, D. J., 2001, Crustal evolution of paleo- to mesoproterozoic rocks in the Peake and Denison Ranges, South Australia, University of Queensland.

Housh, T., and Bowring, S. A., 1991, Lead isotopic heterogeneities within alkali feldspars: Implications for the determination of initial lead isotopic compositions: Geochimica et Cosmochimica Acta, v. 55, p. 2309-2316.

Hovis, G. L., 1997, Determination of Chemical Composition, State of Order, Molar Volume, and Density of a Monoclinic Alkali Feldspar using X-ray Diffraction In Teaching Mineralogy: JB Brady, DW Mogk, y DI Perkins, Eds, p. 107-118.

Howard, K. E., Hand, M., Barovich, K. M., Payne, J. L., and Belousova, E. A., 2011, U–Pb, Lu–Hf and Sm–Nd isotopic constraints on provenance and depositional timing of metasedimentary rocks in the western Gawler Craton: Implications for Proterozoic reconstruction models: Precambrian Research, v. 184, p. 43-62.

Hu, Z., Gao, S., Liu, Y., Hu, S., Chen, H., and Yuan, H., 2008, Signal enhancement in laser ablation ICP-MS by addition of nitrogen in the central channel gas: Journal of Analytical Atomic Spectrometry, v. 23, p. 1093-1101.

Huston, D. L., Champion, D. C., Mernagh, T. P., Downes, P. M., Jones, P., Carr, G., Forster, D., and David, V., 2016, Metallogenesis and geodynamics of the Lachlan Orogen: New (and old) insights from spatial and temporal variations in lead isotopes: Ore Geology Reviews, v. 76, p. 257-267.

Ikeda, Y., Stern, R. J., Kagami, H., and Sun, C.-H., 2000, Pb, Nd, and Sr isotopic constraints on the origin of Miocene basaltic rocks from northeast Hokkaido, Japan: Implications for opening of the Kurile back-arc basin: Island Arc, v. 9, p. 161-172.

Inger, S., and Harris, N., 1993, Geochemical constraints on leucogranite magmatism in the Langtang Valley, Nepal Himalaya: Journal of Petrology, v. 34, p. 345-368.

Jagodzinski, E. A., Reid, A., Crowley, J. L., McAvaney, S., and Wade, C. E., 2016, New CA-TIMS dates for the Gawler Range Volcanics: stratigraphic issues arising from results and future directions: Geological Survey of South Australia Discovery Day, 2016.

James, D. E., 1982, A combined O, Sr, Nd, and Pb isotopic and trace element study of crustal contamination in central Andean lavas, I. Local geochemical variations: Earth and Planetary Science Letters, v. 57, p. 47-62.

Jochum, P., Nohl, U., Herwig, K., Lammel, E., Stoll, B., and Hofmann Albrecht, W., 2007, GeoReM: A New Geochemical Database for Reference Materials and Isotopic Standards: Geostandards and Geoanalytical Research, v. 29, p. 333-338.

Johnson, J. P., and McCulloch, M. T., 1995, Sources of mineralising fluids for the Olympic Dam Deposit (South Australia) - Sm-Nd isotopic constraints: Chemical Geology, v. 121, p. 177-199.

Jung, S., 2005, Isotopic equilibrium/disequilibrium in granites, metasedimentary rocks and migmatites (Damara orogen, Namibia)—a consequence of polymetamorphism and melting: Lithos, v. 84, p. 168-184.

Jung, S., Pfänder, J. A., Brauns, M., and Maas, R., 2011, Crustal contamination and mantle source characteristics in continental intra-plate volcanic rocks: Pb, Hf and Os isotopes from central European volcanic province basalts: Geochimica et Cosmochimica Acta, v. 75, p. 2664-2683.

Kamenetsky, V., K., E., Maas, R., Meffre, S., Kamenetsky, M., McPhie, J., Apukhtina, O., Huang, Q., Thompson, J., Ciobanu, C., and Cook, N., 2015, The supergiant Olympic Dam Cu-U-Au-Ag ore deposit: towards a new genetic model: Society of Economic Geologists, Hobart, Tasmania, 2015.

Kanasewich, E. R., 1962, Approximate Age of Tectonic Activity Using Anomalous Lead Isotopes: Geophysical Journal of the Royal Astronomical Society, v. 7, p. 158-168.

Kay, S. M., Coira, B., and Viramonte, J., 1994, Young mafic back arc volcanic rocks as indicators of continental lithospheric delamination beneath the Argentine Puna Plateau, central Andes: Journal of Geophysical Research, v. 99, p. 24,323-24,339.

Kerr, A., and Fryer, B. J., 1993, Nd isotope evidence for crust-mantle interaction in the generation of A-type granitoid suites in Labrador, Canada: Chemical Geology, v. 104, p. 39-60.

Kilpatrick, J. A., and Ellis, D. J., 1992, C-type magmas: igneous charnockites and their extrusive equivalents: Earth and Environmental Science Transactions of the Royal Society of Edinburgh, v. 83, p. 155-164.

Kirchenbaur, M., Maas, R., Ehrig, K., Kamenetsky, V. S., Strub, E., Ballhaus, C., and Münker, C., 2016, Uranium and Sm isotope studies of the supergiant Olympic Dam Cu–Au–U–Ag deposit, South Australia: Geochimica et Cosmochimica Acta, v. 180, p. 15-32.

Knight, J., 1997, Geochemistry and Geochronology of the St Peters Suite west of Ceduna, University of Adelaide.

Kolker, A., Frost, C. D., Hansom, G. N., and Geist, D. J., 1991, Neodymium, strontium, and lead isotopes in the Maloin Ranch Pluton, Wyoming: Implications for the origin of evolved rocks at anorthosite margins: Geochimica et Cosmochimica Acta, v. 55, p. 2285-2297.

Kontonikas-Charos, A., Ciobanu, C. L., Cook, N. J., Ehrig, K., Krneta, S., and Kamenetsky, V. S., 2017, Feldspar evolution in the Roxby Downs Granite, host to Fe-oxide Cu-Au-(U) mineralisation at Olympic Dam, South Australia: Ore Geology Reviews, v. 80, p. 838-859.

Kosunen, P. J., 2004, Petrogenesis of mid-Proterozoic A-type granites: Case studies from Fennoscandia (Finland) and Laurentia (New Mexico), University of Helsinki.

Kramers, J. D., and Tolstikhin, I. N., 1997, Two terrestrial lead isotope paradoxes, forward transport modelling, core formation and the history of the continental crust: Chemical Geology, v. 139, p. 75-110.

Langmuir, D., 1978, Uranium solution-mineral equilibria at low temperatures with applications to sedimentary ore deposits: Geochimica et Cosmochimica Acta, v. 42, p. 547-569.

Le Breton, N., and Thompson, A. B., 1988, Fluid-absent (dehydration) melting of biotite in metapelites in the early stages of crustal anatexis: Contributions to Mineralogy and Petrology, v. 99, p. 226-237.

Lee, M. R., Waldron, K. A., and Parsons, I., 1995, Exsolution and alteration microtextures in alkali feldspar phenocrysts from the Shap granite, Mineralogical Magazine, 59, p. 63.

Li, K., Pring, A., Etschmann, B., Macmillan, E., Ngothai, Y., O'Neill, B., Hooker, A., Mosselmans, F., and Brugger, J., 2015, Uranium scavenging during mineral replacement reactions†: American Mineralogist, v. 100, p. 1728-1735.

Lipman, P. W., Doe, B. R., Hedge, C. E., and Steven, T. A., 1978, Petrologic evolution of the San Juan volcanic field, southwestern Colorado: Pb and Sr isotope evidence: Geological Society of America Bulletin, v. 89, p. 59-82.

Loewy, S. L., Connelly, J. N., and Dalziel, I. W. D., 2004, An orphaned basement block: The Arequipa-Antofalla Basement of the central Andean margin of South America: Bulletin of the Geological Society of America, v. 116, p. 171-187.

Ludwig, K. R., and Silver, L. T., 1977, Lead-isotope inhomogeneity in Precambrian igneous K-feldspars: Geochimica et Cosmochimica Acta, v. 41, p. 1457-1471.

Ludwig, K., 2012, User's manual for Isoplot version 3.75–4.15: a geochronological toolkit for Microsoft: Excel Berkley Geochronological Center Special Publication.

Maas, R., Grew, E. S., and Carson, C. J., 2015, Isotopic constraints (Pb, Rb-Sr, Sm-Nd) on the sources of early Cambrian Pegmatites with boron and beryllium minerals in the Larsemann hills, Prydz Bay, Antarctica: Canadian Mineralogist, v. 53, p. 249-272.

Maas, R., Kamenetsky, V., Ehrig, K., Meffre, S., McPhie, J., and Diemar, G., 2011, Olympic Dam U-Cu-Au deposit, Australia: New Age Constraints: Mineralogical Magazine, v. 75, p. 1375.

Macmillan, E., Cook, N. J., Ehrig, K., Ciobanu, C. L., and Pring, A., 2016, Uraninite from the Olympic Dam IOCG-U-Ag deposit: Linking textural and compositional variation to temporal evolution: American Mineralogist, v. 101, p. 1295-1320.

Maidment, D. W., Hand, M., and Williams, I. S., 2005, Tectonic cycles in the Strangways Metamorphic Complex, Arunta Inlier, central Australia: Geochronological evidence for exhumation and basin formation between two high-grade metamorphic events: Australian Journal of Earth Sciences, v. 52, p. 205-215.

Mamani, M., Tassara, A., and Wörner, G., 2008, Composition and structural control of crustal domains in the central Andes: Geochemistry, Geophysics, Geosystems, v. 9.

Mamani, M., Wörner, G., and Sempere, T., 2010, Geochemical variations in igneous rocks of the Central Andean orocline (13°S to 18°S): Tracing crustal thickening and magma generation through time and space: Bulletin of the Geological Society of America, v. 122, p. 162-182.

McAvaney, S., 2012, The Cooyerdoo Granite: Paleo- and Mesoarchean basement of the Gawler Craton: MESA Journal, v. 65, p. 31-40.

McAvaney, S., Wade, C. E., and Jagodzinski, E., 2016, Tip Top and Wertigo granites, c.1775 Ma magmatism on northeastern Eyre Peninsula: MESA Journal, v. 80, p. 63-76.

McDonough, W. F., 1990, Constraints on the composition of the continental lithospheric mantle: Earth and Planetary Science Letters, v. 101, p. 1-18.

McDonough, W. F., and Sun, S. s., 1995, The composition of the Earth: Chemical Geology, v. 120, p. 223-253.

McDonough, W. F., Sun, S. S., Ringwood, A. E., Jagoutz, E., and Hofmann, A. W., 1992, Potassium, rubidium, and cesium in the Earth and Moon and the evolution of the mantle of the Earth: Geochimica et Cosmochimica Acta, v. 56, p. 1001-1012.

McFarlane, C. R. M., Dehnavi, A. S., and Lentz, D. R., 2016, Pb-isotopic study of galena by LA-Q-ICP-MS: Testing a new methodology with applications to base-metal sulphide deposits: Minerals, v. 6.

McLennan, S. M., 2001, Relationships between the trace element composition of sedimentary rocks and upper continental crust: Geochemistry, Geophysics, Geosystems, v. 2.

McPhie, J., Kamenetsky, V. S., Allen, S., Ehrig, K., Agangi, A., and Bath, A., 2011, The fluorine link between a supergiant ore deposit and a silicic large igneous province Geology, v. 39, p. 1003-1006.

McPhie, J., Kamenetsky, V. S., Chambefort, I., Ehrig, K., and Green, N., 2011b, Origin of the supergiant Olympic Dam Cu-U-Au-Ag deposit, South Australia: Was a sedimentary basin involved?: Geology, v. 39, p. 795-798.

Mezger, K., Hanson, G. N., and Bohlen, S. R., 1989, High-precision UPb ages of metamorphic rutile: application to the cooling history of high-grade terranes: Earth and Planetary Science Letters, v. 96, p. 106-118.

Michael, P. J., 1991, Intrusion of basaltic magma into a crystallizing granitic magma chamber: The Cordillera del Paine pluton in southern Chile: Contributions to Mineralogy and Petrology, v. 108, p. 396-418.

Moorbath, S. E., McConnell, R. B., Brown, G. C., Brown, G. M., O, M. J., apos, Hara, and Oxburgh, E. R., 1978, Age and isotope evidence for the evolution of continental crust: Philosophical Transactions of the Royal Society of London. Series A, Mathematical and Physical Sciences, v. 288, p. 401-413.

Moorbath, S., Welke, H., and Gale, N. H., 1969, The significance of lead isotope studies in ancient, high-grade metamorphic basement complexes, as exemplified by the Lewisian rocks of Northwest Scotland: Earth and Planetary Science Letters, v. 6, p. 245-256.

Mortimer, G. E., Cooper, J. A., Paterson, H. L., Cross, K., Hudson, G. R. T., and Uppill, R. K., 1988, Zircon U-Pb Dating in the Vicinity of the Olympic Dam Cu-U-Au Deposit, Roxby Downs, South-Australia: Economic Geology, v. 83, p. 694-709.

Müller, W., Shelley, M., Miller, P., and Broude, S., 2009, Initial performance metrics of a new custom-designed ArF excimer LA-ICPMS system coupled to a two-volume laser-ablation cell: Journal of Analytical Atomic Spectrometry, v. 24, p. 209-214.

Murthy, V. R., and Patterson, C., 1961, Lead isotopes in ores and rocks of Butte, Montana: Economic Geology, v. 56, p. 59-67.

Neiva, A. M. R., Williams, I. S., Ramos, J. M. F., Gomes, M. E. P., Silva, M. M. V. G., and Antunes, I. M. H. R., 2009, Geochemical and isotopic constraints on the petrogenesis of Early Ordovician granodiorite and Variscan two-mica granites from the Gouveia area, central Portugal: Lithos, v. 111, p. 186-202.

Neumann, N. L., 2001, Geochemical and isotopic characteristics of South Australian Proterozoic granites: implications for the origin and evolution of high heat-producing terrains, University of Adelaide.

Neumann, N., Sandiford, M., and Foden, J., 2000, Regional geochemistry and continental heat flow: implications for the origin of the South Australian heat flow anomaly: Earth and Planetary Science Letters, v. 183, p. 107-120.

Neymark, L. A., Yu. Amelin, V., and Larin, A. M., 1994, Pb-Nd-Sr isotopic and geochemical constraints on the origin of the 1.54-1.56 Ga Salmi rapakivi granite-Anorthosite batholith (Karelia, Russia): Mineralogy and Petrology, v. 50, p. 173-193.

Nier, A. O., Thompson, R. W., and Murphey, B. F., 1941, The Isotopic Constitution of Lead and the Measurement of Geological Time. III: Physical Review, v. 60, p. 112-116.

Norberg, N., Neusser, G., Wirth, R., and Harlov, D., 2011, Microstructural evolution during experimental albitization of K-rich alkali feldspar: Contributions to Mineralogy and Petrology, v. 162, p. 531-546.

Norman, A. R., and Clarke, G. L., 1990, A barometric response to late compression in the Strangways Metamorphic Complex, Arunta Block, central Australia: Journal of Structural Geology, v. 12, p. 667-684.

Oreskes, N., and Einaudi, M. T., 1990, Origin of rare-earth element-enriched hematite breccias at the Olympic-Dam Cu-U-Au-Ag Deposit, Roxby Downs, south Australia: Economic Geology, v. 85, p. 1-28.

Oreskes, N., and Einaudi, M. T., 1992, Origin of Hydrothermal Fluids at Olympic Dam: Preliminary Results from Fluid Inclusions and Stable Isotopes: Economic Geology and the Bulletin of the Society of Economic Geologists, v. 87, p. 64-90.

Oversby, V. M., 1974, New look at the lead isotope growth curve: Nature, v. 248, p. 132-133.

Pankhurst, M. J., Schaefer, B. F., Turner, S. P., Argles, T., and Wade, C. E., 2013, The source of A-type magmas in two contrasting settings: U–Pb, Lu–Hf and Re–Os isotopic constraints: Chemical Geology, v. 351, p. 175-194.

Parker, A. J., 1993, Palaeaoproterozoic, *in* Drexel, J. F., Preiss, W. V., and Parker, A. J., eds., The Geology of South Australia, Vol. 1. The Precambrian, 1. Bulletin 54: Adelaide, South Australia, Geological Survey of South Australia.

Parsons, I., 1978, Feldspars and fluids in cooling plutons: Mineralogical Magazine, v. 42, p. 1-17.

Parsons, I., and Brown, W. L., 1991, Mechanisms and Kinetics of Exsolution—Structural Control of Diffusion and Phase Behavior in Alkali Feldspars Alkali Feldspars, *in* Ganguly, J., ed., Diffusion, Atomic Ordering, and Mass Transport: Selected Topics in Geochemistry: New York, NY, Springer US, p. 304-344.

Patiño Douce, A. E., and Johnston, A. D., 1991, Phase equilibria and melt productivity in the pelitic system: implications for the origin of peraluminous granitoids and aluminous granulites: Contributions to Mineralogy and Petrology, v. 107, p. 202-218.

Paton, C., Hellstrom, J., Paul, B., Woodhead, J., and Hergt, J., 2011, Iolite: Freeware for the visualisation and processing of mass spectrometric data: Journal of Analytical Atomic Spectrometry, v. 26, p. 2508-2518.

Patterson, C., 1956, Age of meteorites and the earth: Geochimica et Cosmochimica Acta, v. 10, p. 230-237.

Paul, B., Woodhead, J. D., and Hergt, J., 2005, Improved in situ isotope analysis of low-Pb materials using LA-MC-ICP-MS with parallel ion counter and Faraday detection: Journal of Analytical Atomic Spectrometry, v. 20, p. 1350-1357.

Payne, J. L., Ferris, G., Barovich, K. M., and Hand, M., 2010, Pitfalls of classifying ancient magmatic suites with tectonic discrimination diagrams: An example from the Paleoproterozoic Tunkillia Suite, southern Australia: Precambrian Research, v. 177, p. 227-240.

Payne, J. L., Hand, M., Barovich, K. M., and Wade, B. P., 2008, Temporal constraints on the timing of high-grade metamorphism in the northern Gawler Craton: implications for assembly of the Australian Proterozoic: Australian Journal of Earth Sciences, v. 55, p. 623-640.

Payne, J. L., Hand, M., Barovich, K. M., Reid, A., and Evans, D. A. D., 2009, Correlations and reconstruction models for the 2500-1500 Ma evolution of the Mawson Continent: Geological Society, London, Special Publications, v. 323, p. 319-355.

Pearce, J. A., Harris, N. B. W., and Tindle, A. G., 1984, Trace element discrimination diagrams for the tectonic interpretation of granitic rocks: Journal of Petrology, v. 25, p. 956-983.

Peiffert, C., Cuney, M., and Nguyen-Trung, C., 1994, Uranium in granitic magmas: Part 1. Experimental determination of uranium solubility and fluid-melt partition coefficients in the uranium oxide-haplogranite-H2O-Na2CO3 system at 720-770°C, 2 kbar: Geochimica et Cosmochimica Acta, v. 58, p. 2495-2507.

Perkins, W. T., Pearce, N. J. G., and Westgate, J. A., 1997, The Development of Laser Ablation ICP-MS and Calibration Strategies: Examples from the Analysis of Trace Elements in Volcanic Glass Shards and Sulfide Minerals: Geostandards Newsletter, v. 21, p. 175-190.

Peucat, J. J., Capdevila, R., Fanning, C. M., Ménot, R. P., Pécora, L., and Testut, L., 2002, 1.60 Ga felsic volcanic blocks in the moraines of the Terre Adélie Craton, Antarctica: Comparisons with the Gawler Range Volcanics, South Australia: Australian Journal of Earth Sciences, v. 49, p. 831-845.

Polat, A., and Kerrich, R., 2001, Magnesian andesites, Nb-enriched basalt-andesites, and adakites from late-Archean 2.7 Ga Wawa greenstone belts, Superior Province, Canada: Implications for late Archean subduction zone petrologenetic processes: Contributions to Mineralogy and Petrology, v. 141, p. 36-52.

Putnis, A., Hinrichs, R., Putnis, C. V., Golla-Schindler, U., and Collins, L. G., 2007, Hematite in porous red-clouded feldspars: Evidence of large-scale crustal fluid–rock interaction: Lithos, v. 95, p. 10-18.

Ramo, O. T., 1991, Petrogenesis of the Proterozoic rapakivi granites and related basic rocks of southeastern Fennoscandia: Nd and Pb isotopic and general geochemical constraints.: Bulletin Geological Survey of Finland, p. 161.

Rämö, O. T., 2001, Isotopic composition of pyterlite in Vyborg (Viipuri), Wyborg batholith, Russia: Bulletin of the Geological Society of Finland, v. 73, p. 111-115.

Reeve, J. S., Cross, K. C., Smith, R. N., and Oreskes, N., 1990, Olympic Dam copper-uranium-gold-silver deposit, *in* Hughes, F. E., ed., Geology of the mineral deposits of Australia and Papua New Guinea, Monograph 14: Melbourne, Australasian Institute of Mining and Metallurgy, p. 1009-1035.

Reid, A. J., and Hand, M., 2012, Mesoarchean to Mesoproterozoic evolution of the southern Gawler Craton, South Australia: Episodes-Newsmagazine of the InternationalUnion of Geological Sciences, v. 35, p. 216.

Reid, A. J., and Payne, J. L., 2017, Magmatic zircon Lu–Hf isotopic record of juvenile addition and crustal reworking in the Gawler Craton, Australia: Lithos, v. 292-293, p. 294-306.

Reid, A. J., Jagodzinski, E. A., Fraser, G. L., and Pawley, M. J., 2014, SHRIMP U–Pb zircon age constraints on the tectonics of the Neoarchean to early Paleoproterozoic transition within the Mulgathing Complex, Gawler Craton, South Australia: Precambrian Research, v. 250, p. 27-49.

Reid, A. J., Jagodzinski, E. A., Wade, C. E., Payne, J. L., and Jourdan, F., 2017, Recognition of c. 1780Ma magmatism and metamorphism in the buried northeastern Gawler Craton: Correlations with events of the Aileron Province: Precambrian Research, v. 302, p. 198-220.

Reid, A. J., Pawley, M. J., Jagodzinski, E. A., and Dutch, R. A., 2016, Magmatic processes of the St Peters Suite, Gawler Craton: New U-Pb geochronological data and field observations: Adelaide, South Australia, Department of State Development, p. 103.

Reid, A., Hand, M., Jagodzinski, E., Kelsey, D., and Pearson, N., 2008, Paleoproterozoic orogenesis in the southeastern Gawler Craton, South Australia: Australian Journal of Earth Sciences, v. 55, p. 449-471.

Reid, A., Vassallo, J. J., Wilson, C. J. L., and Fanning, C. M., 2007, Timing of the Kimban Orogeny on southern Eyre Peninsula: Adelaide, South Australia, Department of Primary Industries and Resources.

Reynolds, P. H., 1971, A UThPb lead isotope study of rocks and ores from Broken Hill, Australia: Earth and Planetary Science Letters, v. 12, p. 215-223.

Richards, J. R., 1986, Lead isotopic signatures: further examination of comparisons between South Africa and Western Australia: Transactions of the Geological Society of South Africa, v. 89, p. 285-304.

Riciputi, L. R., Johnson, C. M., Sawyer, D. A., and Lipman, P. W., 1995, Crustal and magmatic evolution in a large multicyclic caldera complex: isotopic evidence from the central San Juan volcanic field: Journal of Volcanology and Geothermal Research, v. 67, p. 1-28.

Rivera, T. A., Schmitz, M. D., Jicha, B. R., and Crowley, J. L., 2016, Zircon Petrochronology and 40Ar/39Ar Sanidine Dates for the Mesa Falls Tuff: Crystal-scale Records of Magmatic Evolution and the Short Lifespan of a Large Yellowstone Magma Chamber: Journal of Petrology, v. 57, p. 1677-1704.

Roache, M. W., 1996, The Geology, Timing of Mineralisation, and Genesis of the Menninnie Dam Zn-Pb-Ag Deposit, Eyre Peninsula, South Australia, University of Tasmania.

Roberts, D. E., and Hudson, G. R. T., 1983, The Olympic Dam copper-uranium-gold deposit, Roxby Downs, south Australia: Economic Geology, v. 78, p. 799-822.

Rosenqvist, I. T., 1949, Diffusjonskoeffisienten for bly i noen radioaktive mineraler: GFF, v. 71, p. 57-70.

Rosholt, J. N., Zartman, R. E., and Nkomo, I. T., 1973, Lead Isotope Systematics and Uranium Depletion in the Granite Mountains, Wyoming: Geological Society of America Bulletin, v. 84, p. 989-1002.

Rosman, K., and Taylor, P., 1998, Isotopic compositions of the elements 1997 (Technical Report): Pure and Applied Chemistry, v. 70, p. 217-235.

Russell, R. D., and Farquhar, R. M., 1960, Dating galenas by means of their isotopic constitutions-II: Geochimica et Cosmochimica Acta, v. 19, p. 41-52.

Russell, R. D., Farquhar, R. M., Cumming, G. L., and Wilson, J. T., 1954, Dating galenas by means of their isotopic constitutions: Eos, Transactions American Geophysical Union, v. 35, p. 301-309.

Russell, R. D., Ulrych, T. J., and Kollar, F., 1961, Anomalous leads from Broken Hill, Australia: Journal of Geophysical Research, v. 66, p. 1495-1498.

Russell, R., 1972, Evolutionary model for lead isotopes in conformable ores and in ocean volcanics: Reviews of Geophysics, v. 10, p. 529-549.

Spry, P. G., Heimann, A., Messerly, J. D., and Houk, R. S., 2007, Discrimination of Metamorphic and Metasomatic Processes at the Broken Hill Pb-Zn-Ag Deposit, Australia: Rare Earth Element Signatures of Garnet-Rich Rocks*: Economic Geology, v. 102, p. 471-494.

Sajona, F. G., Maury, R. C., Bellon, H., Cotten, J., Defant, M. J., and Pubellier, M., 1993, Initiation of subduction and the generation of slab melts in western and eastern Mindanao, Philippines: Geology, v. 21, p. 1007-1010.

Schaefer, B. F., 1998, Insights into Proterozoic tectonics from the southern Eyre Peninsula, South Australia, University of Adelaide.

Scoates, J. S., and Chamberlain, K. R., 1995, Baddeleyite (ZrO2) and zircon (ZrSiO4) from anorthositic rocks of the Laramie anorthosite complex, Wyoming: petrologic consequences and U-Pb ages: American Mineralogist, v. 80, p. 1317-1327.

Scrimgeour, I. R., Kinny, P. D., Close, D. F., and Edgoose, C. J., 2005, High-T granulites and polymetamorphism in the southern Arunta Region, central Australia: Evidence for a 1.64Ga accretional event: Precambrian Research, v. 142, p. 1-27.

Sedgmen, A., Hazell, M. S., Budd, A. R., and Champion, D. C., 2007, OZCHEM National Whole Rock Geochemistry Dataset, Commonwealth of Australia (Geoscience Australia).

Sheldrick, G., 2015a, Crystal structure refinement with SHELXL: Acta Crystallographica Section C, v. 71, p. 3-8.

Sheldrick, G., 2015b, SHELXT - Integrated space-group and crystal-structure determination: Acta Crystallographica Section A, v. 71, p. 3-8.

Siégel, C., Bryan, S. E., Allen, C. M., and Gust, D. A., 2018, Use and abuse of zircon-based thermometers: A critical review and a recommended approach to identify antecrystic zircons: Earth-Science Reviews, v. 176, p. 87-116.

Sillitoe, R. H., and Hart, S. R., 1984, Lead-isotopic signatures of porphyry copper deposits in oceanic and continental settings, Colombian Andes: Geochimica et Cosmochimica Acta, v. 48, p. 2135-2142.

Skirrow, R. G., Bastrakov, E. N., Baroncii, K., Fraser, G. L., Creaser, R. A., Fanning, C. M., Raymond, O. L., and Davidson, G. J., 2007, Timing of iron oxide Cu-Au-(U) hydrothermal activity and Nd isotope constraints on metal sources in the Gawler craton, south Australia: Economic Geology, v. 102, p. 1441-1470.

Sláma, J., Košler, J., Condon, D. J., Crowley, J. L., Gerdes, A., Hanchar, J. M., Horstwood, M. S. A., Morris, G. A., Nasdala, L., Norberg, N., Schaltegger, U., Schoene, B., Tubrett, M. N., and Whitehouse, M. J., 2008, Plešovice zircon - A new natural reference material for U-Pb and Hf isotopic microanalysis: Chemical Geology, v. 249, p. 1-35.

Smithies, R. H., Champion, D. C., Van Kranendonk, M. J., Howard, H. M., and Hickman, A. H., 2005, Modern-style subduction processes in the Mesoarchaean: Geochemical evidence from the 3.12 Ga Whundo intra-oceanic arc: Earth and Planetary Science Letters, v. 231, p. 221-237.

Souders, A. K., and Sylvester, P. J., 2010, Accuracy and precision of non-matrix-matched calibration for lead isotope ratio measurements of lead-poor minerals by LA-MC-ICPMS: Journal of Analytical Atomic Spectrometry, v. 25, p. 975-988.

Souders, K. A., and Sylvester, P. J., 2008, Improved in situ measurements of lead isotopes in silicate glasses by LA-MC-ICPMS using multiple ion counters: Journal of Analytical Atomic Spectrometry, v. 23, p. 535-543.

Stacey, J. S., and Kramers, J. D., 1975, Approximation of terrestrial lead isotope evolution by a two-stage model: Earth and Planetary Science Letters, v. 26, p. 207-221.

Stacey, J. S., Zartman, R. E., and NKomo, I. T., 1968, A lead isotope study of galenas and selected feldspars from mining districts in Utah: Economic Geology, v. 63, p. 796-814.

Stanton, R. L., and Russell, R. D., 1959, Anomalous leads and the emplacement of lead sulfide ores: Economic Geology, v. 54, p. 588-607.

Stepanov, A. S., and Hermann, J., 2013, Fractionation of Nb and Ta by biotite and phengite: Implications for the "missing Nb paradox": Geology, v. 41, p. 303-306.

Stepanov, A. S., Hermann, J., Rubatto, D., and Rapp, R. P., 2012, Experimental study of monazite/melt partitioning with implications for the REE, Th and U geochemistry of crustal rocks: Chemical Geology, v. 300-301, p. 200-220.

Stevenson, R. K., and Martin, R. F., 1986, Implications of the presence of amazonite in the Broken Hill and Geco metamorphosed sulfide deposits: The Canadian Mineralogist, v. 24, p. 729-745.

Stewart, K., 1994, High temperature felsic volcanism and the role of mantle magmas in Proterozoic crustal growth: the Gawler Range Volcanic Province, University of Adelaide, Department of Geology and Geophysics.

Stewart, K., and Foden, J., 2003, Mesoproterozoic granites of South Australia, *in* Resources, D. o. P. I. a., ed.: Adelaide, South Australia.

Sun, S.-s., and McDonough, W. F., 1989, Chemical and isotopic systematics of oceanic basalts: implications for mantle composition and processes: Geological Society, London, Special Publications, v. 42, p. 313-345.

Sun, S.-S., Page, R. W., and Carr, G. R., 1994, Lead isotope-based stratigraphic correlations and ages of Proterozoic sediment-hosted Pb-Zn deposits in the Mount Isa Inlier: Australian Geological Survey Organisation Research Newsletter, v. 20.

Sun, S.-S., Tatsumoto, M., and Schilling, J.-G., 1975, Mantle Plume Mixing Along the Reykjanes Ridge Axis: Lead Isotopic Evidence: Science, v. 190, p. 143-147.

Swain, G., Barovich, K., Hand, M., Ferris, G., and Schwarz, M., 2008, Petrogenesis of the St Peter Suite, southern Australia: Arc magmatism and Proterozoic crustal growth of the South Australian Craton: Precambrian Research, v. 166, p. 283-296.

Swain, G., Woodhouse, A., Hand, M., Barovich, K., Schwarz, M., and Fanning, C. M., 2005, Provenance and tectonic development of the late Archaean Gawler Craton, Australia; U–Pb zircon, geochemical and Sm–Nd isotopic implications: Precambrian Research, v. 141, p. 106-136.

Szpunar, M., and Fraser, G., 2010, Age of Deposition and Provenance of Paleoproterozoic Basins on North-Eastern Eyre Peninsula: Adelaide, South Australia, Department of Primary Industries and Resources.

Szpunar, M., Hand, M., Barovich, K., Jagodzinski, E., and Belousova, E., 2011, Isotopic and geochemical constraints on the Paleoproterozoic Hutchison Group, southern Australia: Implications for Paleoproterozoic continental reconstructions: Precambrian Research, v. 187, p. 99-126.

Tatsumoto, M., 1978, Isotopic composition of lead in oceanic basalt and its implication to mantle evolution: Earth and Planetary Science Letters, v. 38, p. 63-87.

Tatsumoto, M., Knight, R. J., and Allegre, C. J., 1973, Time Differences in the Formation of Meteorites as Determined from the Ratio of Lead-207 to Lead-206: Science, v. 180, p. 1279-1283.

Tatsumoto, M., Unruh, D. M., and Desborough, G. A., 1976, U-Th-Pb and Rb-Sr systematics of Allende and U-Th-Pb systematics of Orgueil: Geochimica et Cosmochimica Acta, v. 40, p. 617-634.

Taylor, M. J., 1987, The metamorphism, petrology and geochemistry of the Ooldea 2 drillcore and the Lake Ifould area., University of Adelaide.

Taylor, S. R., and McLennan, S. M., 1995, The geochemical evolution of the continental crust: Reviews of Geophysics, v. 33, p. 241-265.

Teasdale, J., 1997, Methods for understanding poorly exposed terranes: The interpretive geology and tectonothermal evolution of the western Gawler Craton., University of Adelaide, 179 p.

Thirlwall, M. F., Graham, A. M., Arculus, R. J., Harmon, R. S., and Macpherson, C. G., 1996, Resolution of the effects of crustal assimilation, sediment subduction, and fluid transport in island arc magmas: Pb-Sr-Nd-O isotope geochemistry of Grenada, Lesser Antilles: Geochimica et Cosmochimica Acta, v. 60, p. 4785-4810.

Tilton, G. R., and Barreiro, B. A., 1980, Origin of Lead in Andean Calc-Alkaline Lavas, Southern Peru: Science, v. 210, p. 1245-1247.

Tong, L., Wilson, C. J. L., and Vassallo, J. J., 2004, Metamorphic evolution and reworking of the Sleaford Complex metapelites in the southern Eyre Peninsula, South Australia: Australian Journal of Earth Sciences, v. 51, p. 571-589.

Tregeagle, J., 2014, Petrogenesis of magma chamber evolution of the Gawler Range Volcanics, University of Adelaide.

Trueman, N. A., 1986, Lead-uranium systematics of the Olympic Dam deposit and Stuart shelf mineralization: Summary report of U-REE mineralization, Adelaide, Australia, XPSA86/1, 13 January 1986, 7 p: unpublished group memo, Western Mining Corporation.

Turner, S., Foden, J., Sandiford, M., and Bruce, D., 1993, Sm-Nd isotopic evidence for the provenance of sediments from the Adelaide Fold Belt and southeastern Australia with implications for episodic crustal addition: Geochimica et Cosmochimica Acta, v. 57, p. 1837-1856.

Tyrrell, S., Haughton, P. D. W., Daly, J. S., Kokfelt, T. F., and Gagnevin, D., 2006, The use of the common Pb isotope composition of detrital K-feldspar grains as a provenance tool and its application to Upper Carboniferous paleodrainage, northern England: Journal of Sedimentary Research, v. 76, p. 324-345.

van Hunen, J., and Moyen, J., 2012, Archean Subduction: Fact or Fiction?: Annual Review of Earth and Planetary Sciences, v. 40, p. 195-219.

Vanhaecke, F., Balcaen, L., and Malinovsky, D., 2009, Use of single-collector and multi-collector ICP-mass spectrometry for isotopic analysis: Journal of Analytical Atomic Spectrometry, v. 24, p. 863-886.

Vassallo, J. J., and Wilson, C. J. L., 2002, Palaeoproterozoic regional-scale non-coaxial deformation: an example from eastern Eyre Peninsula, South Australia: Journal of Structural Geology, v. 24, p. 1-24.

Verdugo-Ihl, M. R., Ciobanu, C. L., Cook, N. J., Ehrig, K. J., and Courtney-Davies, L., 2019, Defining early stages of IOCG systems: evidence from iron oxides in the outer shell of the Olympic Dam deposit, South Australia: Mineralium Deposita.

Vroon, P. Z., Van Bergen, M. J., White, W. M., and Varekamp, J. C., 1993, Sr-Nd-Pb isotope systematics of the Banda Arc, Indonesia: combined subduction and assimilation of continental material: Journal of Geophysical Research, v. 98, p. 22,349-22,366.

Wade, C. E., and McAvaney, S., 2016, Stratigraphy and geochemistry of the 1745 - 1700 Ma Peter Pan Supersuite: Adelaide, South Australia, Department of State Development.

Wade, C. E., and McAvaney, S., 2017, Neoarchean to earliest Palaeoproterozoic magmatism in the southern Gawler Craton; petrogenesis of the Minbrie Gneiss and Carpa Granite: Adelaide, South Australia, Department of State Development.

Wade, C. E., Reid, A. J., Wingate, M. T. D., Jagodzinski, E. A., and Barovich, K., 2012, Geochemistry and geochronology of the c. 1585Ma Benagerie Volcanic Suite, southern Australia: Relationship to the Gawler Range Volcanics and implications for the petrogenesis of a Mesoproterozoic silicic large igneous province: Precambrian Research, v. 206-207, p. 17-35.

Warwyk, C., 1989, Strontium and rare earth geochemistry of barite-fluorite mineralisation at Olympic Dam, South Australia, University of Adelaide.

Wasteneys, H. A., Clark, A. H., Farrar, E., and Langridge, R. J., 1995, Grenvillian granulite-facies metamorphism in the Arequipa Massif, Peru: a Laurentia-Gondwana link: Earth and Planetary Science Letters, v. 132, p. 63-73.

Webb, A. W., Thomson, B. P., Blissett, A. H., Daly, S. J., Flint, R. B., and Parker, A. J., 1986, Geochronology of the Gawler Craton, South Australia: Australian Journal of Earth Sciences, v. 33, p. 119-143.

Whalen, J. B., Currie, K. L., and Chappell, B. W., 1987, A-type granites: geochemical characteristics, discrimination and petrogenesis: Contributions to Mineralogy and Petrology, v. 95, p. 407-419.

Whalen, J. B., Jenner, G. A., Longstaffe, F. J., Robert, F., and GariÉPy, C., 1996, Geochemical and Isotopic (O, Nd, Pb and Sr) Constraints on A-type Granite Petrogenesis Based on the Topsails Igneous Suite, Newfoundland Appalachians: Journal of Petrology, v. 37, p. 1463-1489.

Whitehouse, M. J., 1989, Pb-isotopic evidence for U-Th-Pb behaviour in a prograde amphibolite to granulite fades transition from the Lewisian complex of north-west Scotland: Implications for Pb-Pb dating: Geochimica et Cosmochimica Acta, v. 53, p. 717-724.

Wiedenbeck, M., AllÉ, P., Corfu, F., Griffin, W. L., Meier, M., Oberli, F., Quadt, A. V., Roddick, J. C., and Spiegel, W., 1995, Three Natural Zircon Standards For U - Th - Pb, Lu - Hf, Trace Element And Ree Analyses: Geostandards Newsletter, v. 19, p. 1-23.

Williamson, B. J., Shaw, A., Downes, H., and Thirlwall, M. F., 1996, Geochemical constraints on the genesis of Hercynian two-mica leucogranites from the Massif Central, France: Chemical Geology, v. 127, p. 25-42.

Willigers, B. J. A., Baker, J. A., Krogstad, E. J., and Peate, D. W., 2002, Precise and accurate in situ Pb-Pb dating of apatite, monazite, and sphene by laser ablation multiple-collector ICP-MS: Geochimica et Cosmochimica Acta, v. 66, p. 1051-1066.

Wolff, J., and Ramos, F., 2003, Pb isotope variations among Bandelier Tuff feldspars: no evidence for a long-lived silicic magma chamber: Geology, v. 31, p. 533-536.

Woodhead, J., 2002, A simple method for obtaining highly accurate Pb isotope data by MC-ICP-MS: Journal of Analytical Atomic Spectrometry, v. 17, p. 1381-1385.

Woodhead, J., Hergt, J., Meffre, S., Large, R. R., Danyushevsky, L., and Gilbert, S., 2009, In situ Pb-isotope analysis of pyrite by laser ablation (multi-collector and quadrupole) ICPMS: Chemical Geology, v. 262, p. 380-390.

Workman, R. K., and Hart, S. R., 2005, Major and trace element composition of the depleted MORB mantle (DMM): Earth and Planetary Science Letters, v. 231, p. 53-72.

Wörner, G., Lezaun, J., Beck, A., Heber, V., Lucassen, F., Zinngrebe, E., Rössling, R., and Wilke, H. G., 2000, Precambrian and early Paleozoic evolution of the Andean basement at Belen (northern Chile) and Cerro Uyarani (western Bolivia Altiplano): Journal of South American Earth Sciences, v. 13, p. 717-737.

Wright, K. E., McCurry, M., Hughes, S. S., Bonnichsen, B., and White, C., 2002, Petrology and geochemistry of the Miocene Tuff of McMullen Creek, central Snake River Plain, Idaho: Tectonic and magmatic evolution of the Snake River Plain volcanic province. Idaho Geol Surv Bull, v. 30, p. 177-194.

Wright, T. L., and Stewart, D. B., 1968, X-ray and optical study of alkali feldspar: I. Determination of composition and structural state from refined unit-cell parameters and 2V: American Mineralogist: Journal of Earth and Planetary Materials, v. 53, p. 38-87.

Wurst, A. T., 1994, Analyses of late stage, Mesoproterozoic, syn and post tectonic, magmatic events in the Moonta Sub-domain: Implications for Cu-Au mineralisation in the" Copper Triangle" of South Australia.

Wyborn, L. A. I., Page, R. W., and Parker, A. J., 1987, Geochemical and Geochronological Signatures in Australian Proterozoic Igneous Rocks: Geological Society, London, Special Publications, v. 33, p. 377-394.

Wyborn, L., and Page, R., 1983, THE PROTEROZOIC KALKADOON AND EWEN BATHOLITHS, MOUNT ISA INLIER, QUEENSLAND-SOURCE, CHEMISTRY, AGE, AND METAMORPHISM: BMR Journal of Australian Geology & Geophysics, v. 8, p. 53-69.

Yakymchuk, C., and Brown, M., 2014, Behaviour of zircon and monazite during crustal melting: Journal of the Geological Society, v. 171, p. 465-479.

York, D., 1968, Least squares fitting of a straight line with correlated errors: Earth and planetary science letters, v. 5, p. 320-324.

Zang, W. L., 2006, Maitland Special, South Australia, Map Sheets SI53-12 and portion SI53-16, Geological Atlas 1:250 000 Series, Explanatory Notes, *in* Australia, G. S. o. S., ed.: Adelaide.

Zartman, R. E., 1965, The isotopic composition of lead in microclines from the Llano uplift, Texas: Journal of Geophysical Research, v. 70, p. 965-975.

Zartman, R. E., and Doe, B. R., 1981, Plumbotectonics—the model: Tectonophysics, v. 75, p. 135-162.

Zartman, R. E., and Haines, S. M., 1988, The plumbotectonic model for Pb isotopic systematics among major terrestrial reservoirs—A case for bi-directional transport: Geochimica et Cosmochimica Acta, v. 52, p. 1327-1339.

Zhang, H., Harris, N., Parrish, R., Kelley, S., Zhang, L., Rogers, N., Argles, T., and King, J., 2004, Causes and consequences of protracted melting of the mid-crust exposed in the North Himalayan antiform: Earth and Planetary Science Letters, v. 228, p. 195-212.

Zhang, L., Li, J., Xu, Y.-G., and Ren, Z.-Y., 2018, The influence of the double spike proportion effect on stable isotope (Zn, Mo, Cd, and Sn) measurements by multicollector-inductively coupled plasma-mass spectrometry (MC-ICP-MS): Journal of Analytical Atomic Spectrometry, v. 33, p. 555-562.

Zhang, L., Ren, Z.-Y., Nichols, A. R. L., Zhang, Y.-H., Zhang, Y., Qian, S.-P., and Liu, J.-Q., 2014, Lead isotope analysis of melt inclusions by LA-MC-ICP-MS: Journal of Analytical Atomic Spectrometry, v. 29, p. 1393-1405.

Appendix A: Compilation of Historical Geochemical/ Isotopic Data for the Tunkillia Suite

Major and Trace Element Geochemistry for the Tunkillia Suite (1/3)

Sample Number	879-47	444825	444833	444834	WGC81	444835
Collector (Year)	Taylor (1997)	Ferris (2001)	Ferris (2001)	Ferris (2001)	Teasdale (1997)	Ferris (2001)
Name	Lake Ifould[1]	Barton	Tallacootra 1[5]	Tallacootra 2[5]	Wynbring	Mulgathing[1]
mE (UTM 53)	224020	283614	232451	231647	357085	399000
mN (UTM 53)	6580364	6619257	6567700	6564845	6618513	6653600
Major Oxides (Wt. %)						
SiO_2	72.10	72.03	71.39	75.71	73.10	75.90
Al_2O_3	13.80	15.31	14.28	13.01	12.50	13.10
Fe_2O_3	2.12	1.94	2.32	1.28	2.42	0.87
MnO	0.02	0.02	0.04	0.02	0.04	0.01
MgO	0.58	0.78	0.22	0.28	0.59	0.03
CaO	1.91	2.02	0.56	1.05	1.41	0.78
Na_2O	3.15	3.48	3.26	3.80	3.03	3.13
K_2O	4.46	4.06	6.53	4.40	4.77	5.57
TiO_2	0.34	0.20	0.21	0.22	0.36	0.05
P_2O_5	0.10	0.03	0.11	0.03	0.08	0.08
LOI	1.18	0.20	0.95	0.02	0.68	0.30
Trace Elements (ppm)						
Ba	3650.00	1422.00	1050.00	1100.00	900.00	290.00
Cr	20.00	31.00	4.00	10.00	30.00	9.00
Cu	7.00	13.00	4.00	10.50	2.50	23.00
Ga	17.00	15.20	18.50	23.50	18.00	15.00
Hf	-	3.40	5.50	4.70	-	2.00
Nb	7.00	5.20	9.50	15.00	15.50	20.00
Ni	2.00	10.10	-	4.00	4.00	4.00
Pb	19.00	40.90	15.50	16.00	21.50	28.00
Rb	39.00	93.90	31.50	35.00	110.00	220.00
Sr	750.00	385.90	240.00	340.00	155.00	58.00
Ta	0.01	0.50	0.60	1.10	0.01	3.00
Th	13.00	11.70	3.10	7.50	22.00	37.50
U	0.70	1.51	0.35	0.66	2.10	6.00
V	20.00	31.00	7.00	31.00	20.00	14.00
Y	12.00	14.20	26.00	31.50	29.00	33.00
Zn	29.50	29.20	60.00	125.00	43.00	31.00
Zr	310.00	122.00	252.00	176.00	280.00	80.00

Major and Trace Element Geochemistry for the Tunkillia Suite (2/3)

Sample Number	444824	350424	350428	363435	370932	378924
Collector (Year)	Ferris (2001)	Ferris (2001)	Ferris (2001)	Ferris (2001)	Ferris (2001)	Ferris (2001)
Name	Pinbong[1]	Airstrip	Airstrip	Airstrip	Lake Everard	Vermin Proof Fence
mE (UTM 53)	544165	466840	477797	480020	478400	484352
mN (UTM 53)	6367104	6500257	6490815	6490385	6503092	6536030
Major Oxides (Wt. %)						
SiO_2	76.46	72.00	76.40	67.70	68.90	73.00
Al_2O_3	12.10	14.90	11.50	15.60	14.00	14.20
Fe_2O_3	1.59	1.73	1.47	2.84	5.11	1.72
MnO	0.04	0.05	0.03	0.09	0.16	0.05
MgO	0.31	0.36	0.13	0.71	1.34	0.39
CaO	0.79	1.64	0.45	1.95	2.63	2.15
Na_2O	2.88	4.22	2.72	3.21	3.07	3.36
K_2O	5.38	4.15	5.41	6.05	3.70	3.95
TiO_2	0.27	0.21	0.14	0.49	0.64	0.17
P_2O_5	0.03	0.13	0.04	0.13	0.12	0.13
LOI	0.00	1.11	0.73	1.43	1.05	0.56
Trace Elements (ppm)						
Ba	289.00	1250.00	270.00	2950.00	700.00	1600.00
Cr	9.00	3.00	4.00	4.00	6.00	2.00
Cu	6.00	15.00	6.00	150.00	14.50	13.00
Ga	14.90	17.00	19.50	18.50	19.50	15.50
Hf	6.30	2.00	3.00	6.00	5.00	3.00
Nb	21.70	8.00	11.00	8.00	11.00	6.00
Ni	3.50		3.00		3.00	2.00
Pb	32.60	22.00	29.00	36.00	26.00	26.00
Rb	289.10	120.00	230.00	110.00	185.00	92.00
Sr	58.20	360.00	35.50	470.00	94.00	500.00
Ta	1.90	4.00	4.00	3.00	8.00	4.00
Th	35.90	13.00	26.00	14.50	23.00	10.00
U	6.56	3.30	4.70	1.65	3.20	0.90
V	14.00	15.00	3.00	23.00	16.00	10.00
Y	42.00	15.00	35.00	11.50	20.00	6.50
Zn	23.20	36.00	50.00	60.00	56.00	76.00
Zr	203.00	140.00	140.00	380.00	220.00	110.00

Major and Trace Element Geochemistry for the Tunkillia and St Peters Suites (3/3)

Sample Number	370938	HCB1b	CGPJ9	1096-11b	1096-22	879-29b
Collector (Year)	Ferris (2001)	Knight (1997)	Swain et al. (2008)	Dove (1997)	Dove (1997)	Taylor (1997)
Name	Childara	St Peters Grp 1	St Peters Grp 1	St Peters Grp 2	St Peters Grp 2	2446 Ma Gneiss
mE (UTM 53)	474771	363694	351494	412169	394676	226746
mN (UTM 53)	6494106	6439915	6436657	6357840	6400100	6583029
Major Oxides (Wt. %)						
SiO_2	72.90	76.20	75.70	73.70	70.90	69.80
Al_2O_3	13.10	12.20	12.50	12.70	13.90	15.90
Fe_2O_3	3.32	1.11	1.15	1.18	2.55	2.17
MnO	0.05	0.05	0.07	0.03	0.07	0.03
MgO	0.45	0.07	0.12	0.11	0.51	0.95
CaO	0.57	0.06	0.36	0.22	1.26	3.10
Na_2O	3.03	4.40	3.39	3.12	3.33	5.24
K_2O	5.93	4.62	5.97	6.32	6.12	1.13
TiO_2	0.43	0.18	0.20	0.18	0.42	0.33
P_2O_5	0.07	0.02	0.02	0.02	0.10	0.11
LOI	0.32	0.39	0.39	0.45	0.56	1.67
Trace Elements (ppm)						
Ba	1150.00	80.00	600.00	340.00	850.00	800.00
Cr	20.00	–	2.00	–	3.00	30.00
Cu	11.00	–	–	1.50	4.00	3.00
Ga	24.00	19.50	18.00	16.50	19.00	21.00
Hf	9.00	5.00	5.00	5.00	8.00	-
Nb	25.00	11.00	7.50	10.00	12.50	4.50
Ni	4.00	–	–	–	–	8.00
Pb	18.00	19.50	19.50	34.50	30.50	13.50
Rb	280.00	145.00	100.00	185.00	150.00	15.50
Sr	85.00	2.00	16.00	64.00	120.00	600.00
Ta	0.50	–	–	–	–	0.01
Th	11.70	16.00	11.50	27.50	27.00	13.00
U	1.51	1.50	1.10	2.20	2.80	0.46
V	10.00	10.00	3.00	–	23.00	20.00
Y	27.00	31.00	30.50	56.00	40.50	3.10
Zn	30.00	29.00	62.00	42.50	56.00	45.00
Zr	140.00	190.00	220.00	200.00	310.00	160.00

REE Geochemistry for the Tunkillia and St Peters Suites (1/3)

Sample Number	879-47	444825	444833	444834	WGC81	444835
Collector (Year)	Taylor (1997)	Ferris (2001)	Ferris (2001)	Ferris (2001)	Teasdale (1997)	Ferris (2001)
Name	Lake Ifould[1]	Barton	Tallacootra 1[5]	Tallacootra 2[5]	Wynbring	Mulgathing[1]
mE (UTM 53)	224020	283614	232451	231647	357085	399000
mN (UTM 53)	6580364	6619257	6567700	6564845	6618513	6653600
Rare Earth Elements (ppm)						
La	90.00	34.35	34.00	125.00	62.00	66.00
Ce	160.00	66.71	76.00	210.00	130.00	130.00
Pr	18.00	7.10	10.00	24.00	15.00	15.00
Nd	58.00	25.62	42.50	92.00	56.00	48.00
Sm	6.50	4.44	8.00	15.00	10.00	8.50
Eu	2.30	1.02	1.45	2.30	1.45	0.83
Gd	3.60	4.05	4.80	9.50	6.00	6.50
Tb	0.49	0.63	0.91	1.55	1.15	1.10
Dy	2.30	2.76	5.50	8.50	6.50	6.50
Ho	0.41	0.46	0.98	1.35	1.10	1.25
Er	1.10	1.15	3.10	3.70	2.80	4.10
Tm	0.15	-	0.45	0.45	0.40	0.60
Yb	1.10	0.77	3.10	2.70	2.50	4.40
Lu	0.20	0.12	0.40	0.36	0.40	0.63

REE Geochemistry for the Tunkillia and St Peters Suites (2/3)

Sample Number	444824	350424	350428	363435	370932	378924
Collector (Year)	Ferris (2001)	Ferris (2001)	Ferris (2001)	Ferris (2001)	Ferris (2001)	Ferris (2001)
Name	Pinbong[1]	Airstrip	Airstrip	Airstrip	Lake Everard	Vermin Proof Fence
mE (UTM 53)	544165	466840	477797	480020	478400	484352
mN (UTM 53)	6367104	6500257	6490815	6490385	6503092	6536030
Rare Earth Elements (ppm)						
La	65.77	26.00	78.00	43.00	68.00	31.00
Ce	137.80	46.50	140.00	88.00	115.00	54.00
Pr	14.45	5.50	16.00	9.50	12.50	6.00
Nd	48.71	19.00	60.00	30.50	46.50	20.00
Sm	8.16	3.20	10.50	4.30	7.00	2.80
Eu	0.71	1.05	0.59	2.60	1.20	1.35
Gd	6.37	3.10	6.50	3.50	4.40	2.30
Tb	1.11	0.49	1.25	0.49	0.74	0.30
Dy	5.96	2.90	8.00	2.40	4.60	1.45
Ho	1.29	0.58	1.40	0.43	0.80	0.26
Er	4.04	1.90	4.30	1.30	2.50	0.80
Tm	-	0.30	0.65	0.20	0.35	0.10
Yb	4.12	2.30	4.30	1.25	2.50	0.80
Lu	0.60	0.35	0.60	0.21	0.37	0.15

REE Geochemistry for the Tunkillia and St Peters Suites (3/3)

Sample Number	370938	HCB1b	CGPJ9	1096-11b	1096-22	879-29b
Collector (Year)	Ferris (2001)	Knight (1997)	Swain et al. (2008)	Dove (1997)	Dove (1997)	Taylor (1997)
Name	Childara	St Peters Group 1	St Peters Group 1	St Peters Group 2	St Peters Group 2	2446 Ma Gneiss
mE (UTM 53)	474771	363694	351494	412169	394676	226746
mN (UTM 53)	6494106	6439915	6436657	6357840	6400100	6583029
Rare Earth Elements (ppm)						
La	93.00	40.50	36.00	92.00	86.00	48.50
Ce	180.00	88.00	76.00	170.00	175.00	86.00
Pr	16.00	11.00	10.50	20.50	21.50	9.50
Nd	60.00	52.00	52.00	92.00	94.00	32.00
Sm	8.00	8.00	8.00	11.50	12.00	3.60
Eu	1.00	0.80	1.30	0.80	1.60	1.40
Gd	11.00	5.50	6.00	8.00	8.00	1.75
Tb	1.50	1.10	1.20	1.70	1.50	0.19
Dy	12.00	6.00	6.50	10.00	8.00	0.70
Ho	2.50	1.30	1.30	2.20	1.70	0.11
Er	7.00	3.80	3.70	6.50	4.80	0.30
Tm	1.00	0.60	0.50	1.00	0.70	0.05
Yb	7.00	4.00	3.50	6.00	4.60	0.25
Lu	1.00	0.60	0.50	0.70	0.60	0.05

Appendix B: Method for solution-based MC-ICP-MS analyses

Alkali-feldspar step-leach dissolution were performed at the School of Earth Sciences, University of Melbourne, following procedures adapted from (Maas et al., 2015; Woodhead, 2002). Pristine alkali feldspar grains were micro-drilled then lightly ground in an agate mortar & pestle to an approximate grainsize of less than 0.5 mm, before being weighed into a teflon beaker (sample weight 120.9 mg) and subjected to a four-stage acid leach protocol:

1) 6M HCl, 20°C, 3 hrs
2) 6M HNO_3, 20°C, 3hrs
3) 5M (ca. 20%) HF, 60°C, 3 hrs
4) 6M HNO_3, 60°C, 3 hrs

The leach solutions from each step (plus rinse water) were transferred into separate beakers. Where required, settling of the residual material was accelerated by centrifuging within the original beaker. The residue after the fourth-stage of leeching was then completely dissolved in 3:1 HF-HNO3 and pure HNO3 (120°C, 12 hrs each). Each solution was split to provide a small (~ 10%) aliquot for trace element analysis by quadrupole ICP-MS. The remainder of each solution was dried, picked up in 1 ml of 0.6M HBr and loaded onto a 0.1 ml bed of AG1-X8 (100 - 200 mesh) anion exchange resin. The loading HBr and subsequent HBr fractions were collected within the original beakers and stored. Pb was eluted from the resin using 6M HCl. This procedure was repeated on a smaller bed of anion resin. Several procedural blanks indicate Pb contributions from the combined step leach and extraction protocols of 0.1 ng or less. By comparison, samples sizes for Pb are 147 - 820 in the leachates but 2.2 ng in the residue.

Pb-isotope ratios were measured on a Nu Plasma multi-collector ICP-MS, with sample aspiration via a Glass Expansion OpalMist PFA nebuliser (~0.07 ml/min uptake) and a CETAC Aridus desolvator. Pb fractions were re-dissolved in 2% nitric acid doped with 10 ppb of thallium, to allow correction of instrumental mass bias using the Tl doping method (Woodhead, 2002). For samples

large enough to produce sustained signals near 10 V of total Pb (for a typical 5-minute mass spectrometer run this consumes ca. 20 ng of Pb), this correction protocol produces external precisions of ±0.05 - 0.09% (2σ). The long-term average for a Broken Hill galena solution is 16.004 ± 0.038% ($^{206}Pb/^{204}Pb$), 15.388 ± 0.057% ($^{207}Pb/^{204}Pb$) and 35.659 ± 0.076% ($^{208}Pb/^{204}Pb$) (n = 73, 2σ), consistent with TIMS reference values ($^{206}Pb/^{204}Pb$ = 16.004, $^{207}Pb/^{204}Pb$ = 15.389, $^{208}Pb/^{204}Pb$ = 35.651; Richards (1986)).

Appendix C: LA-ICP-MS Results for Tunkillia Suite alkali feldspars

LA-ICP-MS Pb-isotope Results from Tunkillia Suite (1/6)

Sample Number	Sample Name	Spot Size	Frequency	Fluence	207/206	+/-1s	208/206	+/-1s	206/204	+/-1s	207/204	+/-1s	208/204	+/-1s
444825	Barton	110µm	10.00Hz	3.5J/cm2	0.976	0.002	2.261	0.004	15.832	0.043	15.449	0.038	35.797	0.081
444825	Barton	110µm	10.00Hz	3.5J/cm2	0.976	0.001	2.265	0.005	15.824	0.040	15.441	0.040	35.837	0.094
444825	Barton	110µm	10.00Hz	3.5J/cm2	0.976	0.002	2.265	0.003	15.790	0.034	15.411	0.040	35.772	0.091
444825	Barton	110µm	10.00Hz	3.5J/cm2	0.977	0.003	2.266	0.005	15.790	0.031	15.420	0.047	35.778	0.098
444825	Barton	110µm	10.00Hz	3.5J/cm2	0.977	0.001	2.265	0.003	15.783	0.044	15.422	0.044	35.754	0.120
444825	Barton	110µm	10.00Hz	3.5J/cm2	0.979	0.002	2.266	0.004	15.775	0.040	15.438	0.042	35.741	0.090
444825	Barton	110µm	10.00Hz	3.5J/cm2	0.973	0.002	2.259	0.004	15.768	0.026	15.348	0.039	35.625	0.090
444825	Barton	110µm	10.00Hz	3.5J/cm2	0.976	0.002	2.263	0.004	15.766	0.038	15.389	0.040	35.680	0.097
444825	Barton	110µm	10.00Hz	3.5J/cm2	0.978	0.002	2.266	0.005	15.763	0.048	15.411	0.056	35.722	0.111
444825	Barton	110µm	10.00Hz	3.5J/cm2	0.984	0.001	2.277	0.004	15.762	0.050	15.512	0.046	35.885	0.122
444825	Barton	110µm	10.00Hz	3.5J/cm2	0.978	0.002	2.264	0.004	15.744	0.047	15.401	0.054	35.639	0.116
879-47	Lake Ifould	110µm	10.00Hz	3.5J/cm2	0.995	0.002	2.309	0.009	15.400	0.099	15.316	0.083	35.560	0.227
879-47	Lake Ifould	110µm	10.00Hz	3.5J/cm2	0.988	0.002	2.303	0.003	15.391	0.041	15.209	0.039	35.440	0.119
879-47	Lake Ifould	110µm	10.00Hz	3.5J/cm2	1.000	0.006	2.324	0.007	15.307	0.178	15.305	0.218	35.576	0.503
879-47	Lake Ifould	110µm	10.00Hz	3.5J/cm2	0.997	0.004	2.310	0.005	15.288	0.061	15.249	0.040	35.317	0.106
879-47	Lake Ifould	110µm	10.00Hz	3.5J/cm2	0.988	0.002	2.301	0.005	15.272	0.050	15.087	0.051	35.141	0.119
879-47	Lake Ifould	110µm	10.00Hz	3.5J/cm2	0.994	0.002	2.312	0.004	15.259	0.047	15.172	0.044	35.281	0.111
879-47	Lake Ifould	110µm	10.00Hz	3.5J/cm2	1.000	0.002	2.318	0.003	15.223	0.052	15.219	0.048	35.285	0.127
879-47	Lake Ifould	110µm	10.00Hz	3.5J/cm2	0.996	0.003	2.310	0.002	15.215	0.060	15.150	0.078	35.147	0.124
879-47	Lake Ifould	110µm	10.00Hz	3.5J/cm2	0.995	0.003	2.316	0.003	15.180	0.044	15.109	0.039	35.153	0.098
444835	Mulgathing	110µm	10.00Hz	3.5J/cm2	0.963	0.003	2.241	0.008	15.964	0.070	15.368	0.087	35.781	0.211
444835	Mulgathing	110µm	10.00Hz	3.5J/cm2	0.966	0.003	2.216	0.007	15.951	0.097	15.415	0.091	35.344	0.228
444835	Mulgathing	110µm	10.00Hz	3.5J/cm2	0.961	0.002	2.232	0.005	15.903	0.058	15.277	0.065	35.501	0.149
444835	Mulgathing	110µm	10.00Hz	3.5J/cm2	0.970	0.004	2.244	0.003	15.882	0.085	15.399	0.076	35.641	0.206
444835	Mulgathing	110µm	10.00Hz	3.5J/cm2	0.959	0.002	2.229	0.005	16.098	0.085	15.433	0.086	35.886	0.168

LA-ICP-MS Pb-isotope Results from Tunkillia Suite (2/6)

Sample Number	Sample Name	Spot Size	Frequency	Fluence	207/206	+/-1s	208/206	+/-1s	206/204	+/-1s	207/204	+/-1s	208/204	+/-1s
444835	Mulgathing	110µm	10.00Hz	3.5J/cm2	0.956	0.004	2.226	0.013	16.209	0.112	15.504	0.112	36.087	0.363
444835	Mulgathing	110µm	10.00Hz	3.5J/cm2	0.961	0.003	2.237	0.005	15.967	0.121	15.345	0.120	35.713	0.242
444835	Mulgathing	110µm	10.00Hz	3.5J/cm2	0.973	0.007	2.253	0.010	15.752	0.178	15.320	0.190	35.494	0.378
444824	Pinbong	110µm	10.00Hz	3.5J/cm2	0.956	0.002	2.205	0.004	16.068	0.083	15.363	0.073	35.432	0.132
444824	Pinbong	110µm	10.00Hz	3.5J/cm2	0.956	0.001	2.210	0.003	16.022	0.047	15.317	0.031	35.412	0.100
444824	Pinbong	110µm	10.00Hz	3.5J/cm2	0.963	0.002	2.219	0.003	16.007	0.075	15.416	0.078	35.524	0.162
444824	Pinbong	110µm	10.00Hz	3.5J/cm2	0.961	0.003	2.222	0.005	15.977	0.056	15.361	0.038	35.497	0.105
444824	Pinbong	110µm	10.00Hz	3.5J/cm2	0.960	0.002	2.211	0.004	15.971	0.043	15.335	0.066	35.312	0.106
444824	Pinbong	110µm	10.00Hz	3.5J/cm2	0.959	0.002	2.213	0.003	15.965	0.048	15.316	0.066	35.323	0.134
444824	Pinbong	110µm	10.00Hz	3.5J/cm2	0.962	0.002	2.214	0.003	15.921	0.048	15.316	0.064	35.250	0.120
444824	Pinbong	110µm	10.00Hz	3.5J/cm2	0.964	0.002	2.219	0.003	15.843	0.057	15.276	0.067	35.158	0.141
444824	Pinbong	110µm	10.00Hz	3.5J/cm2	0.965	0.003	2.215	0.005	15.825	0.047	15.273	0.046	35.047	0.118
444824	Pinbong	110µm	10.00Hz	3.5J/cm2	0.959	0.003	2.223	0.006	16.013	0.062	15.350	0.059	35.594	0.144
444824	Pinbong	110µm	10.00Hz	3.5J/cm2	0.959	0.003	2.220	0.003	15.971	0.049	15.311	0.039	35.451	0.109
444824	Pinbong	110µm	10.00Hz	3.5J/cm2	0.960	0.002	2.224	0.004	15.905	0.058	15.268	0.070	35.367	0.145
444824	Pinbong	110µm	10.00Hz	3.5J/cm2	0.963	0.001	2.230	0.004	15.929	0.045	15.345	0.044	35.518	0.088
444824	Pinbong	110µm	10.00Hz	3.5J/cm2	0.962	0.004	2.238	0.006	16.118	0.107	15.501	0.052	36.076	0.232
444824	Pinbong	110µm	10.00Hz	3.5J/cm2	0.954	0.003	2.249	0.006	16.139	0.082	15.400	0.073	36.291	0.236
444824	Pinbong	110µm	10.00Hz	3.5J/cm2	0.952	0.004	2.232	0.005	16.146	0.099	15.369	0.051	36.037	0.205
444833	Tallacootra	110µm	10.00Hz	3.5J/cm2	1.000	0.002	2.324	0.008	15.309	0.075	15.311	0.067	35.578	0.172
444833	Tallacootra	110µm	10.00Hz	3.5J/cm2	0.997	0.002	2.330	0.004	15.305	0.082	15.256	0.075	35.669	0.213
444833	Tallacootra	110µm	10.00Hz	3.5J/cm2	1.000	0.002	2.324	0.004	15.282	0.071	15.285	0.071	35.513	0.160
444833	Tallacootra	110µm	10.00Hz	3.5J/cm2	1.000	0.003	2.324	0.007	15.238	0.065	15.244	0.046	35.416	0.170
444833	Tallacootra	110µm	10.00Hz	3.5J/cm2	1.000	0.003	2.321	0.005	15.225	0.042	15.221	0.070	35.339	0.113

LA-ICP-MS Pb-isotope Results from Tunkillia Suite (3/6)

Sample Number	Sample Name	Spot Size	Frequency	Fluence	207/206	+/-1s	208/206	+/-1s	206/204	+/-1s	207/204	+/-1s	208/204	+/-1s
444833	Tallacootra	110µm	10.00Hz	3.5J/cm2	1.001	0.002	2.324	0.005	15.202	0.038	15.213	0.036	35.328	0.083
444833	Tallacootra	110µm	10.00Hz	3.5J/cm2	0.999	0.003	2.327	0.006	15.198	0.069	15.188	0.073	35.366	0.160
444833	Tallacootra	110µm	10.00Hz	3.5J/cm2	1.005	0.004	2.271	0.005	15.177	0.085	15.252	0.102	34.461	0.175
444833	Tallacootra	110µm	10.00Hz	3.5J/cm2	0.998	0.002	2.314	0.005	15.160	0.077	15.126	0.072	35.086	0.187
444833	Tallacootra	110µm	10.00Hz	3.5J/cm2	0.997	0.003	2.317	0.007	15.118	0.059	15.071	0.043	35.032	0.106
444834	Tallacootra	110µm	10.00Hz	3.5J/cm2	1.011	0.004	2.325	0.007	15.178	0.072	15.350	0.081	35.291	0.178
444834	Tallacootra	110µm	10.00Hz	3.5J/cm2	1.005	0.003	2.328	0.005	15.114	0.091	15.185	0.069	35.178	0.183
444834	Tallacootra	110µm	10.00Hz	3.5J/cm2	1.008	0.003	2.329	0.005	15.103	0.061	15.221	0.053	35.172	0.122
444834	Tallacootra	110µm	10.00Hz	3.5J/cm2	1.006	0.002	2.328	0.004	15.086	0.050	15.180	0.047	35.116	0.105
444834	Tallacootra	110µm	10.00Hz	3.5J/cm2	1.006	0.002	2.324	0.007	15.077	0.032	15.169	0.038	35.034	0.103
444834	Tallacootra	110µm	10.00Hz	3.5J/cm2	1.009	0.004	2.333	0.006	15.064	0.086	15.196	0.087	35.150	0.233
444834	Tallacootra	110µm	10.00Hz	3.5J/cm2	1.005	0.002	2.325	0.003	15.055	0.060	15.131	0.061	35.008	0.133
444834	Tallacootra	110µm	10.00Hz	3.5J/cm2	1.009	0.004	2.331	0.006	15.020	0.090	15.159	0.078	35.015	0.148
444834	Tallacootra	110µm	10.00Hz	3.5J/cm2	1.004	0.003	2.317	0.006	15.001	0.058	15.061	0.048	34.754	0.071
444834	Tallacootra	110µm	10.00Hz	3.5J/cm2	1.008	0.002	2.321	0.003	14.940	0.051	15.065	0.046	34.673	0.115
WGC81	Wynbring	110µm	10.00Hz	3.5J/cm2	0.996	0.004	2.312	0.008	15.213	0.119	15.159	0.111	35.179	0.250
WGC81	Wynbring	110µm	10.00Hz	3.5J/cm2	0.962	0.005	2.321	0.004	15.087	0.052	14.513	0.061	35.017	0.137
WGC81	Wynbring	110µm	10.00Hz	3.5J/cm2	0.997	0.003	2.311	0.004	15.067	0.170	15.021	0.158	34.820	0.385
WGC81	Wynbring	110µm	10.00Hz	3.5J/cm2	0.979	0.005	2.313	0.010	14.912	0.177	14.601	0.184	34.493	0.448
WGC81	Wynbring	110µm	10.00Hz	3.5J/cm2	1.012	0.003	2.344	0.007	14.887	0.146	15.061	0.165	34.890	0.371
350424	Airstrip	110µm	10.00Hz	3.5J/cm2	0.958	0.002	2.234	0.004	15.905	0.055	15.243	0.051	35.536	0.128
350424	Airstrip	110µm	10.00Hz	3.5J/cm2	0.961	0.002	2.218	0.005	15.953	0.070	15.336	0.074	35.380	0.145
350424	Airstrip	110µm	10.00Hz	3.5J/cm2	0.960	0.002	2.230	0.005	15.955	0.046	15.321	0.030	35.585	0.057
350424	Airstrip	110µm	10.00Hz	3.5J/cm2	0.959	0.002	2.227	0.004	15.964	0.040	15.318	0.038	35.556	0.082

LA-ICP-MS Pb-isotope Results from Tunkillia Suite (4/6)

Sample Number	Sample Name	Spot Size	Frequency	Fluence	207/206	+/-1s	208/206	+/-1s	206/204	+/-1s	207/204	+/-1s	208/204	+/-1s
350424	Airstrip	110µm	10.00Hz	3.5J/cm2	0.957	0.001	2.224	0.004	15.989	0.032	15.304	0.033	35.559	0.078
350424	Airstrip	110µm	10.00Hz	3.5J/cm2	0.960	0.002	2.230	0.003	16.007	0.066	15.367	0.070	35.703	0.146
350424	Airstrip	110µm	10.00Hz	3.5J/cm2	0.957	0.002	2.221	0.004	16.009	0.037	15.322	0.035	35.550	0.098
350424	Airstrip	110µm	10.00Hz	3.5J/cm2	0.959	0.001	2.225	0.002	16.029	0.026	15.376	0.021	35.666	0.064
350424	Airstrip	110µm	10.00Hz	3.5J/cm2	0.959	0.001	2.227	0.003	16.062	0.041	15.400	0.036	35.775	0.122
350424	Airstrip	110µm	10.00Hz	3.5J/cm2	0.959	0.001	2.221	0.003	16.073	0.027	15.410	0.029	35.700	0.077
350424	Airstrip	110µm	10.00Hz	3.5J/cm2	0.958	0.002	2.229	0.004	16.080	0.044	15.402	0.042	35.842	0.102
350424	Airstrip	110µm	10.00Hz	3.5J/cm2	0.958	0.002	2.221	0.004	16.089	0.066	15.407	0.061	35.727	0.138
350435	Airstrip	110µm	10.00Hz	3.5J/cm2	0.964	0.002	2.236	0.006	15.858	0.073	15.287	0.077	35.461	0.192
350435	Airstrip	110µm	10.00Hz	3.5J/cm2	0.966	0.001	2.230	0.003	15.903	0.025	15.360	0.025	35.458	0.052
350435	Airstrip	110µm	10.00Hz	3.5J/cm2	0.961	0.002	2.224	0.005	15.919	0.059	15.298	0.045	35.408	0.123
350435	Airstrip	110µm	10.00Hz	3.5J/cm2	0.959	0.002	2.219	0.003	16.074	0.034	15.407	0.038	35.666	0.058
350435	Airstrip	110µm	10.00Hz	3.5J/cm2	0.955	0.002	2.214	0.003	16.079	0.044	15.363	0.033	35.596	0.091
350435	Airstrip	110µm	10.00Hz	3.5J/cm2	0.965	0.002	2.234	0.003	15.968	0.026	15.415	0.021	35.670	0.067
350435	Airstrip	110µm	10.00Hz	3.5J/cm2	0.962	0.001	2.224	0.003	15.988	0.050	15.380	0.048	35.551	0.110
350435	Airstrip	110µm	10.00Hz	3.5J/cm2	0.958	0.002	2.219	0.004	16.155	0.046	15.482	0.052	35.844	0.096
350435	Airstrip	110µm	10.00Hz	3.5J/cm2	0.959	0.001	2.221	0.003	15.965	0.069	15.303	0.064	35.463	0.146
350428	Airstrip	110µm	10.00Hz	3.5J/cm2	0.956	0.001	2.222	0.004	16.084	0.031	15.372	0.030	35.746	0.087
350428	Airstrip	110µm	10.00Hz	3.5J/cm2	0.955	0.002	2.215	0.006	16.118	0.046	15.389	0.041	35.697	0.107
350428	Airstrip	110µm	10.00Hz	3.5J/cm2	0.953	0.002	2.213	0.004	16.147	0.035	15.390	0.030	35.740	0.045
350428	Airstrip	110µm	10.00Hz	3.5J/cm2	0.955	0.002	2.214	0.004	16.115	0.027	15.392	0.034	35.681	0.085
350428	Airstrip	110µm	10.00Hz	3.5J/cm2	0.953	0.001	2.213	0.002	16.148	0.027	15.394	0.030	35.731	0.054
350428	Airstrip	110µm	10.00Hz	3.5J/cm2	0.954	0.001	2.213	0.004	16.137	0.033	15.396	0.036	35.714	0.065
350428	Airstrip	110µm	10.00Hz	3.5J/cm2	0.954	0.002	2.207	0.005	16.158	0.049	15.417	0.053	35.662	0.088

LA-ICP-MS Pb-isotope Results from Tunkillia Suite (5/6)

Sample Number	Sample Name	Spot Size	Frequency	Fluence	207/206	+/-1s	208/206	+/-1s	206/204	+/-1s	207/204	+/-1s	208/204	+/-1s
350428	Airstrip	110µm	10.00Hz	3.5J/cm2	0.958	0.001	2.218	0.003	16.099	0.027	15.418	0.017	35.714	0.081
350428	Airstrip	110µm	10.00Hz	3.5J/cm2	0.957	0.002	2.230	0.005	16.122	0.062	15.421	0.072	35.948	0.112
350428	Airstrip	110µm	10.00Hz	3.5J/cm2	0.954	0.002	2.216	0.004	16.169	0.042	15.427	0.044	35.830	0.076
350428	Airstrip	110µm	10.00Hz	3.5J/cm2	0.957	0.002	2.218	0.003	16.127	0.024	15.431	0.029	35.774	0.082
350428	Airstrip	110µm	10.00Hz	3.5J/cm2	0.952	0.003	2.207	0.004	16.247	0.034	15.469	0.040	35.849	0.069
350428	Airstrip	110µm	10.00Hz	3.5J/cm2	0.955	0.001	2.208	0.006	16.251	0.035	15.521	0.041	35.890	0.098
370932	Lake Everard	110µm	10.00Hz	3.5J/cm2	0.954	0.001	2.216	0.003	16.107	0.020	15.366	0.026	35.700	0.056
370932	Lake Everard	110µm	10.00Hz	3.5J/cm2	0.955	0.001	2.216	0.002	16.117	0.036	15.390	0.033	35.707	0.078
370932	Lake Everard	110µm	10.00Hz	3.5J/cm2	0.954	0.001	2.211	0.004	16.249	0.042	15.503	0.055	35.925	0.104
370932	Lake Everard	110µm	10.00Hz	3.5J/cm2	0.954	0.002	2.214	0.004	16.111	0.025	15.377	0.026	35.662	0.041
370936	Lake Everard	110µm	10.00Hz	3.5J/cm2	0.959	0.002	2.218	0.007	16.022	0.034	15.369	0.022	35.541	0.057
370936	Lake Everard	110µm	10.00Hz	3.5J/cm2	0.958	0.003	2.218	0.006	16.102	0.065	15.426	0.094	35.721	0.187
370936	Lake Everard	110µm	10.00Hz	3.5J/cm2	0.959	0.002	2.223	0.005	16.003	0.047	15.343	0.026	35.580	0.120
370936	Lake Everard	110µm	10.00Hz	3.5J/cm2	0.958	0.003	2.220	0.006	15.993	0.138	15.315	0.128	35.505	0.254
370936	Lake Everard	110µm	10.00Hz	3.5J/cm2	0.954	0.001	2.226	0.002	16.093	0.042	15.360	0.043	35.823	0.109
370936	Lake Everard	110µm	10.00Hz	3.5J/cm2	0.955	0.002	2.218	0.004	16.160	0.034	15.431	0.041	35.851	0.075
370938	Childara	110µm	10.00Hz	3.5J/cm2	0.959	0.001	2.223	0.002	16.021	0.026	15.366	0.027	35.622	0.064
370938	Childara	110µm	10.00Hz	3.5J/cm2	0.955	0.002	2.220	0.003	16.118	0.072	15.397	0.053	35.774	0.145
370938	Childara	110µm	10.00Hz	3.5J/cm2	0.955	0.003	2.211	0.005	16.097	0.049	15.381	0.025	35.594	0.085
370938	Childara	110µm	10.00Hz	3.5J/cm2	0.953	0.003	2.211	0.010	16.211	0.051	15.454	0.051	35.845	0.155
370938	Childara	110µm	10.00Hz	3.5J/cm2	0.958	0.002	2.223	0.003	16.026	0.029	15.358	0.037	35.628	0.062
370938	Childara	110µm	10.00Hz	3.5J/cm2	0.955	0.003	2.214	0.006	16.068	0.038	15.348	0.053	35.579	0.086
370938	Childara	110µm	10.00Hz	3.5J/cm2	0.957	0.001	2.217	0.005	16.094	0.030	15.397	0.026	35.679	0.101
370938	Childara	110µm	10.00Hz	3.5J/cm2	0.954	0.001	2.222	0.004	16.119	0.032	15.374	0.032	35.818	0.094

LA-ICP-MS Pb-isotope Results from Tunkillia Suite (6/6)

Sample Number	Sample Name	Spot Size	Frequency	Fluence	207/206	+/-1s	208/206	+/-1s	206/204	+/-1s	207/204	+/-1s	208/204	+/-1s
370938	Childara	110µm	10.00Hz	3.5J/cm2	0.953	0.002	2.217	0.004	16.151	0.043	15.393	0.036	35.804	0.063
378924	Vermin Proof Fence	110µm	10.00Hz	3.5J/cm2	0.958	0.001	2.223	0.003	16.051	0.022	15.380	0.022	35.685	0.053
378924	Vermin Proof Fence	110µm	10.00Hz	3.5J/cm2	0.956	0.001	2.212	0.004	16.058	0.030	15.354	0.021	35.514	0.077
378924	Vermin Proof Fence	110µm	10.00Hz	3.5J/cm2	0.960	0.004	2.225	0.005	15.962	0.076	15.324	0.045	35.519	0.148
378924	Vermin Proof Fence	110µm	10.00Hz	3.5J/cm2	0.957	0.002	2.220	0.004	16.125	0.019	15.429	0.032	35.794	0.069
378924	Vermin Proof Fence	110µm	10.00Hz	3.5J/cm2	0.956	0.003	2.228	0.005	16.037	0.042	15.338	0.052	35.734	0.153
378924	Vermin Proof Fence	110µm	10.00Hz	3.5J/cm2	0.956	0.001	2.218	0.003	16.065	0.039	15.364	0.037	35.631	0.086
378924	Vermin Proof Fence	110µm	10.00Hz	3.5J/cm2	0.958	0.002	2.226	0.003	16.072	0.022	15.397	0.041	35.769	0.068
378924	Vermin Proof Fence	110µm	10.00Hz	3.5J/cm2	0.962	0.002	2.228	0.007	16.003	0.044	15.396	0.034	35.660	0.120
378924	Vermin Proof Fence	110µm	10.00Hz	3.5J/cm2	0.956	0.001	2.227	0.003	16.072	0.032	15.370	0.028	35.785	0.080
378924	Vermin Proof Fence	110µm	10.00Hz	3.5J/cm2	0.956	0.003	2.230	0.008	16.080	0.066	15.377	0.051	35.862	0.110
378924	Vermin Proof Fence	110µm	10.00Hz	3.5J/cm2	0.959	0.001	2.222	0.003	16.030	0.044	15.365	0.048	35.626	0.085
378924	Vermin Proof Fence	110µm	10.00Hz	3.5J/cm2	0.960	0.002	2.230	0.007	16.103	0.068	15.464	0.041	35.906	0.075
378924	Vermin Proof Fence	110µm	10.00Hz	3.5J/cm2	0.960	0.001	2.225	0.002	15.990	0.028	15.347	0.033	35.575	0.077
378924	Vermin Proof Fence	110µm	10.00Hz	3.5J/cm2	0.958	0.001	2.224	0.003	16.034	0.026	15.353	0.031	35.652	0.045
378924	Vermin Proof Fence	110µm	10.00Hz	3.5J/cm2	0.956	0.002	2.218	0.003	16.023	0.024	15.313	0.044	35.532	0.070

LA-ICP-MS Pb-isotope Results from St Peters Suite

Sample Number	Sample Name	Spot Size	Frequency	Fluence	207/206	+/-1s	208/206	+/-1s	206/204	+/-1s	207/204	+/-1s	208/204	+/-1s
7563	St Peters	110µm	10.00Hz	3.5J/cm2	0.955	0.003	2.214	0.007	16.028	0.087	15.302	0.108	35.490	0.227
7563	St Peters	110µm	10.00Hz	3.5J/cm2	0.957	0.003	2.224	0.005	16.072	0.114	15.375	0.137	35.749	0.314
7563	St Peters	110µm	10.00Hz	3.5J/cm2	0.958	0.004	2.226	0.008	16.122	0.064	15.445	0.060	35.888	0.150
7563	St Peters	110µm	10.00Hz	3.5J/cm2	0.958	0.003	2.225	0.007	16.237	0.096	15.557	0.078	36.127	0.199
7563	St Peters	110µm	10.00Hz	3.5J/cm2	0.960	0.002	2.223	0.004	16.011	0.069	15.365	0.075	35.590	0.166
7563	St Peters	110µm	10.00Hz	3.5J/cm2	0.962	0.003	2.235	0.008	15.962	0.098	15.352	0.099	35.674	0.168
7563	St Peters	110µm	10.00Hz	3.5J/cm2	0.962	0.002	2.231	0.003	16.041	0.067	15.436	0.067	35.784	0.159
7563	St Peters	110µm	10.00Hz	3.5J/cm2	0.963	0.004	2.233	0.007	15.990	0.056	15.394	0.066	35.710	0.116
7563	St Peters	110µm	10.00Hz	3.5J/cm2	0.964	0.003	2.231	0.005	16.028	0.067	15.452	0.070	35.766	0.187
7563	St Peters	110µm	10.00Hz	3.5J/cm2	0.970	0.008	2.255	0.011	15.845	0.199	15.362	0.226	35.726	0.426
7580	St Peters	110µm	10.00Hz	3.5J/cm2	0.959	0.002	2.223	0.006	16.067	0.085	15.412	0.076	35.717	0.167
7580	St Peters	110µm	10.00Hz	3.5J/cm2	0.959	0.002	2.226	0.004	16.178	0.043	15.519	0.033	36.008	0.075
7580	St Peters	110µm	10.00Hz	3.5J/cm2	0.960	0.003	2.226	0.005	16.062	0.076	15.421	0.077	35.755	0.123
7580	St Peters	110µm	10.00Hz	3.5J/cm2	0.960	0.002	2.235	0.005	16.040	0.041	15.400	0.043	35.849	0.100
7580	St Peters	110µm	10.00Hz	3.5J/cm2	0.960	0.002	2.227	0.005	16.102	0.082	15.462	0.068	35.858	0.157
7580	St Peters	110µm	10.00Hz	3.5J/cm2	0.960	0.003	2.230	0.005	16.031	0.068	15.397	0.099	35.749	0.179
7580	St Peters	110µm	10.00Hz	3.5J/cm2	0.961	0.003	2.229	0.007	16.098	0.075	15.467	0.066	35.888	0.156
7580	St Peters	110µm	10.00Hz	3.5J/cm2	0.961	0.004	2.230	0.008	16.072	0.114	15.447	0.121	35.848	0.308
7580	St Peters	110µm	10.00Hz	3.5J/cm2	0.962	0.002	2.229	0.005	15.978	0.067	15.374	0.065	35.619	0.126
7580	St Peters	110µm	10.00Hz	3.5J/cm2	0.962	0.003	2.246	0.006	15.923	0.062	15.326	0.096	35.767	0.179

LA-ICP-MS Pb-isotope Results from Archean Gneiss

Sample Number	Sample Name	Spot Size	Frequency	Fluence	207/206	+/-1s	208/206	+/-1s	206/204	+/-1s	207/204	+/-1s	208/204	+/-1s
879-29b-1	Archean Gneiss	110µm	10.00Hz	3.5J/cm2	0.996	0.004	2.304	0.006	15.170	0.086	15.103	0.110	34.947	0.263
879-29b-2	Archean Gneiss	110µm	10.00Hz	3.5J/cm2	0.986	0.006	2.264	0.012	15.086	0.219	14.878	0.176	34.148	0.424
879-29b-3	Archean Gneiss	110µm	10.00Hz	3.5J/cm2	1.001	0.003	2.309	0.006	15.138	0.118	15.147	0.097	34.953	0.254
879-29b-4	Archean Gneiss	110µm	10.00Hz	3.5J/cm2	0.997	0.004	2.302	0.007	15.113	0.105	15.067	0.090	34.783	0.272
879-29b-5	Archean Gneiss	110µm	10.00Hz	3.5J/cm2	1.003	0.001	2.310	0.004	15.157	0.020	15.204	0.026	35.005	0.063
879-29b-6	Archean Gneiss	110µm	10.00Hz	3.5J/cm2	1.004	0.002	2.325	0.002	15.123	0.056	15.178	0.066	35.160	0.138
879-29b-7	Archean Gneiss	110µm	10.00Hz	3.5J/cm2	1.000	0.002	2.313	0.004	15.174	0.039	15.181	0.048	35.106	0.089
879-29b-8	Archean Gneiss	110µm	10.00Hz	3.5J/cm2	0.999	0.002	2.308	0.004	15.216	0.059	15.194	0.050	35.116	0.134
879-29b-9	Archean Gneiss	110µm	10.00Hz	3.5J/cm2	1.001	0.001	2.285	0.003	15.227	0.066	15.246	0.062	34.793	0.129
879-29b-10	Archean Gneiss	110µm	10.00Hz	3.5J/cm2	0.995	0.006	2.323	0.012	15.356	0.141	15.275	0.113	35.671	0.347
879-29b-11	Archean Gneiss	110µm	10.00Hz	3.5J/cm2	0.995	0.004	2.315	0.007	15.279	0.078	15.198	0.085	35.375	0.131

Appendix D: Compilation of Historical Geochemical/ Isotopic Data for the Hiltaba Suite/ GRV

Geochemical compilation of Hiltaba Suite and Gawler Range Volcanics Samples (1/2)

Informal Name	Pegler	Bulpara	Kychering	Pinding Rocks	Lake Gairdner Rhyolite	Konkaby West	Lyons	Pordia	Parla	Yantea Rhyolite
Source	Budd (2006)	Stewart and Foden (2003)	Budd (2006)	Budd (2006)	Agangi (2011)	Budd (2006)	Budd (2006)	Stewart and Foden (2003)	Stewart and Foden (2003)	Agangi (2011)
Major Oxides (Wt. %)										
SiO_2	67.9	65.8	74.8	74.0	77.0	74.2	76.5	74.6	70.7	70.9
Al_2O_3	15.2	14.3	13.0	12.7	12.1	13.0	12.4	13.3	14.5	14.5
CaO	2.5	2.5	0.1	0.7	0.5	0.1	0.3	0.1	0.1	0.1
Na_2O_3	3.9	3.6	4.1	3.6	1.9	3.1	3.1	3.4	3.8	3.8
K_2O	4.6	4.3	4.9	4.8	6.6	5.7	5.8	5.0	5.9	4.6
FeO(tot.)	3.2	5.0	0.9	1.3	2.0	1.5	0.9	1.3	3.2	3.3
MgO	1.2	1.2	0.4	0.4	0.2	0.3	0.1	0.3	0.4	0.8
MnO	0.1	0.1	0.1	0.0	0.1	0.0	0.0	0.1	0.1	0.1
Trace Elements (ppm)										
Ga	17.6	22.0	19.3	18.0	18.0	15.0	13.8	18.0	20.0	20.3
Nb	21.8	20.0	25.4	16.6	11.2	22.0	18.7	18.0	18.0	13.3
Pb	22.4	25.0	32.6	15.0	42.0	47.2	43.6	40.0	40.0	
Rb	147.0	154.0	346.0	301.0	226.0	318.0	219.0	301.0	214.0	123.0
Sr	301.0	247.0	8.9	42.0	50.0	93.7	41.9	87.0	133.0	191.0
Ta	1.3	2.9	3.7	3.4	1.3	1.0	1.0	2.0	2.0	0.9
Th	22.2	28.0	37.8	40.0	19.3	50.5	24.5	33.0	17.0	-
U	4.0	4.0	5.6	10.0	3.8	15.8	3.4	4.0	3.0	-
Y	27.9	48.0	21.9	30.8	26.2	27.0	21.1	22.0	48.0	37.7
Zr	267.0	385.0	199.0	212.0	293.0	209.0	183.0	138.0	340.0	442.0
Rare Earth Elements (ppm)										
La	68.1	63.0	73.6	72.2	67.0	71.0	51.3	46.0	80.0	54.4
Ce	142.0	133.0	122.0	142.0	131.0	139.0	108.0	82.0	157.0	
Sm	8.5	11.0	5.4	8.7	8.2	6.9	7.8	5.0	11.2	11.6
Nd	52.7	31.0	36.6	53.6	51.5	51.3	43.3	24.0	56.0	6.7
Eu	1.7	2.3	0.9	0.8	1.1	0.7	0.8	0.7	1.4	3.2
Gd	6.4	-	3.9	7.2	-	5.6	5.6	-	-	-
Tb	1.0	1.8	0.6	1.1	0.9	0.8	0.8	0.9	1.6	1.4
Yb	2.7	4.5	2.5	2.7	0.9	2.4	2.1	2.9	5.1	3.6
Lu	0.4	0.7	0.4	0.4	0.6	0.4	0.3	0.5	0.8	1.3
Zircon Sat. Temp. (T°C)	819.0	855.1	811.8	815.9	855.2	823.7	804.6	789.4	864.2	891.0

Geochemical compilation of Hiltaba Suite and Gawler Range Volcanics Samples (2/2)

Informal Name	Kokatha	Frogs Eyes	Buckleboo	Cunyarie	Tyringa	Charleston	Yardea Dacite	Opal Fields	Arthurton	Eucarro
Source	Stewart and Foden (2003)	Stewart and Foden (2003)	Stewart and Foden (2003)	Stewart and Foden (2003)	Stewart and Foden (2003)	Stewart and Foden (2003)	Stewart (1994)	BHP	Stewart and Foden (2003)	Stewart (1994)
Major Oxides (Wt. %)										
SiO_2	76.3	74.7	75.8	74.7	75.0	73.2	67.8	69.5	70.7	67.9
Al_2O_3	12.2	13.8	12.4	13.3	12.3	12.9	13.5	14.1	13.4	13.4
CaO	0.5	0.1	0.1	0.1	0.5	0.1	0.9	0.6	1.0	1.3
Na_2O_3	2.7	3.8	3.2	3.3	3.4	3.0	3.0	3.6	3.7	3.1
K_2O	5.2	5.9	5.2	5.2	5.3	5.5	5.9	5.4	4.7	5.3
FeO(tot.)	1.6	2.0	1.6	1.4	1.8	1.8	3.7	9.4	3.5	4.4
MgO	0.2	0.7	0.2	0.3	0.2	0.4	0.7	1.5	-	0.9
MnO	0.0	0.0	0.0	0.0	0.1	0.1	0.1	0.0	0.0	0.1
Trace Elements (ppm)										
Ga	18.0	16.0	22.0	18.0	20.0	19.0	21.0	22.0	18.0	19.0
Nb	23.0	11.0	24.0	12.0	26.0	21.0	23.0	21.0	-	20.0
Pb	38.9	12.0	25.0	28.0	4.3	39.0	30.0	24.0	9.0	31.0
Rb	341.0	159.0	343.0	180.0	302.0	367.0	237.0	127.0	235.0	216.0
Sr	47.0	261.0	26.0	149.0	51.0	102.0	131.0	291.0	86.0	127.0
Ta	3.0	1.6	3.6	2.1	2.5	2.8	2.0	1.7	-	1.7
Th	36.8	27.0	28.0	18.0	30.0	70.0	33.0	19.0	50.0	33.0
U	8.5	8.0	4.0	4.0	5.0	15.0	7.0	7.0	26.0	7.3
Y	68.0	20.0	60.0	14.0	74.0	49.0	59.0	53.0	-	60.0
Zr	185.0	288.0	135.0	128.0	296.0	199.0	451.0	440.0	285.0	399.0
Rare Earth Elements (ppm)										
La	77.0	79.0	50.0	48.0	86.0	112.0	93.0	79.0	84.0	91.0
Ce	157.0	129.0	116.0	92.0	175.0	203.0	179.0	156.0	178.0	170.0
Sm	10.6	8.7	11.5	5.3	12.8	10.8	13.8	12.7	15.8	12.7
Nd	53.0	55.0	48.0	53.0	65.0	65.0	73.0	67.7	66.0	77.0
Eu	0.6	1.2	0.6	0.9	0.8	1.2	2.6	3.5	2.4	2.7
Gd	-	-	-	-	-	-	12.1	11.7	-	11.0
Tb	1.4	1.4	1.9	0.7	2.1	1.4	1.9	1.7	1.6	1.9
Yb	5.9	1.5	5.9	1.3	8.2	5.2	6.2	5.0	5.6	5.9
Lu	0.9	0.4	0.8	0.2	1.2	0.8	0.9	0.6	0.9	0.9
Zircon Sat. Temp. (T°C)	814.3	845.4	783.3	782.9	843.9	822.3	886.9	888.5	841.6	869.6

Appendix E: LA-ICP-MS Results for SRM's used during Hiltaba Suite/ GRV Analyses

LA-ICP-MS Pb-isotopic results of Primary SRM (NIST610)

Name	Spot Size (µm)	Frequency (Hz)	Fluence (mJ/cm2)	207/206	+/-1s	208/206	+/-1s	206/204	+/-1s	207/204	+/-1s	208/204	+/-1s	206/238	+/-1s	208/232	+/-1s
NIST610	74	10	3.45	0.911	0.001	2.171	0.002	17.059	0.042	15.543	0.042	37.028	0.068	0.244	0.012	0.521	0.027
NIST610	74	10	3.45	0.910	0.001	2.169	0.003	17.057	0.036	15.517	0.025	36.997	0.046	0.250	0.007	0.534	0.017
NIST610	74	10	3.45	0.911	0.001	2.168	0.002	17.057	0.013	15.532	0.013	36.977	0.045	0.250	0.002	0.533	0.004
NIST610	74	10	3.45	0.908	0.001	2.168	0.002	17.059	0.022	15.497	0.021	36.978	0.042	0.253	0.001	0.538	0.003
NIST610	74	10	3.45	0.911	0.001	2.172	0.002	17.056	0.042	15.542	0.043	37.054	0.115	0.254	0.007	0.543	0.016
NIST610	74	10	3.45	0.909	0.002	2.170	0.003	17.056	0.039	15.510	0.030	37.005	0.076	0.249	0.012	0.537	0.024
NIST610	74	10	3.45	0.908	0.002	2.171	0.003	17.056	0.040	15.487	0.035	37.020	0.072	0.251	0.012	0.532	0.027
NIST610	74	10	3.45	0.909	0.001	2.166	0.003	17.056	0.051	15.496	0.042	36.947	0.097	0.250	0.013	0.538	0.026
NIST610	74	10	3.45	0.909	0.001	2.169	0.001	17.055	0.030	15.510	0.024	36.984	0.053	0.251	0.001	0.538	0.002
NIST610	74	10	3.45	0.912	0.001	2.168	0.003	17.054	0.023	15.548	0.030	36.977	0.074	0.248	0.007	0.531	0.017
NIST610	74	10	3.45	0.909	0.001	2.170	0.002	17.053	0.015	15.504	0.025	36.997	0.043	0.252	0.001	0.538	0.003
NIST610	74	10	3.45	0.912	0.002	2.168	0.004	17.053	0.032	15.546	0.036	36.976	0.076	0.252	0.009	0.540	0.025
NIST610	74	10	3.45	0.911	0.001	2.168	0.002	17.048	0.041	15.529	0.040	36.967	0.091	0.254	0.010	0.544	0.022
NIST610	74	10	3.45	0.909	0.001	2.171	0.003	17.047	0.017	15.498	0.020	37.003	0.059	0.251	0.002	0.537	0.004
NIST610	74	10	3.45	0.910	0.001	2.163	0.002	17.045	0.016	15.509	0.019	36.871	0.037	0.252	0.001	0.537	0.002
NIST610	74	10	3.45	0.911	0.001	2.171	0.001	17.044	0.024	15.534	0.025	37.003	0.050	0.249	0.001	0.537	0.002
NIST610	74	10	3.45	0.910	0.001	2.172	0.002	17.044	0.035	15.503	0.042	37.024	0.076	0.248	0.007	0.531	0.017
NIST610	74	10	3.45	0.911	0.002	2.169	0.003	17.040	0.031	15.519	0.022	36.962	0.046	0.249	0.012	0.533	0.025
NIST610	74	10	3.45	0.910	0.001	2.172	0.002	17.038	0.017	15.512	0.022	36.998	0.042	0.249	0.001	0.531	0.003
NIST610	74	10	3.45	0.909	0.001	2.169	0.002	17.038	0.037	15.484	0.037	36.949	0.086	0.248	0.002	0.545	0.003
NIST610	74	10	3.45	0.913	0.001	2.175	0.002	17.027	0.029	15.540	0.028	37.038	0.054	0.248	0.002	0.529	0.006
NIST610	74	10	3.45	0.911	0.001	2.171	0.002	17.025	0.021	15.516	0.024	36.958	0.048	0.249	0.001	0.531	0.002
NIST610	74	10	3.45	0.910	0.001	2.168	0.002	17.034	0.026	15.493	0.029	36.934	0.065	0.250	0.001	0.530	0.003
NIST610	74	10	3.45	0.911	0.001	2.170	0.004	17.033	0.030	15.521	0.035	36.960	0.059	0.251	0.012	0.534	0.027

LA-ICP-MS Pb-isotopic results of Secondary Check SRM's

Name	Spot Size (µm)	Frequency (Hz)	Fluence (mJ/cm2)	207/206	+/-1s	208/206	+/-1s	206/204	+/-1s	207/204	+/-1s	208/204	+/-1s	206/238	+/-1s	208/232	+/-1s
BCR-2G	110	10	3.45	0.835	0.003	2.073	0.005	18.702	0.088	15.620	0.105	38.763	0.203	1.607	0.007	0.923	0.005
BCR-2G	110	10	3.45	0.830	0.003	2.066	0.005	18.706	0.109	15.529	0.075	38.648	0.174	1.632	0.008	0.928	0.003
BCR-2G	110	10	3.45	0.838	0.003	2.068	0.006	18.721	0.109	15.683	0.111	38.708	0.184	1.757	0.017	1.078	0.010
BCR-2G	110	10	3.45	0.835	0.003	2.051	0.005	18.733	0.170	15.633	0.120	38.412	0.339	1.724	0.017	1.052	0.011
BCR-2G	110	10	3.45	0.834	0.003	2.071	0.007	18.763	0.111	15.652	0.077	38.850	0.186	1.833	0.021	1.117	0.017
BCR-2G	110	10	3.45	0.837	0.004	2.067	0.006	18.768	0.196	15.712	0.168	38.798	0.405	1.394	0.024	0.867	0.010
BCR-2G	110	10	3.45	0.836	0.003	2.069	0.006	18.784	0.120	15.708	0.135	38.864	0.235	1.618	0.010	0.941	0.008
BCR-2G	110	10	3.45	0.832	0.004	2.047	0.005	18.795	0.167	15.629	0.120	38.472	0.357	1.744	0.015	1.060	0.011
BCR-2G	110	10	3.45	0.832	0.002	2.063	0.005	18.813	0.143	15.661	0.114	38.814	0.237	1.725	0.010	1.002	0.004
BCR-2G	110	10	3.45	0.833	0.002	2.064	0.006	18.870	0.120	15.712	0.106	38.953	0.266	1.453	0.020	0.893	0.011
BCR-2G	110	10	3.45	0.832	0.002	2.043	0.004	18.941	0.141	15.751	0.116	38.691	0.246	1.752	0.019	1.045	0.013
BCR-2G	110	10	3.45	0.833	0.002	2.062	0.005	18.890	0.214	15.735	0.154	38.952	0.382	1.721	0.008	0.988	0.004
GSD-1G	74	10	3.45	0.804	0.002	1.988	0.004	19.507	0.058	15.676	0.052	38.780	0.121	0.366	0.005	0.720	0.011
GSD-1G	74	10	3.45	0.804	0.002	1.988	0.003	19.542	0.109	15.718	0.085	38.848	0.186	0.361	0.004	0.727	0.012
GSD-1G	74	10	3.45	0.807	0.003	1.980	0.008	19.544	0.146	15.763	0.083	38.701	0.204	0.384	0.004	0.770	0.011
GSD-1G	74	10	3.45	0.806	0.002	1.988	0.002	19.555	0.097	15.765	0.082	38.882	0.197	0.361	0.004	0.625	0.004
GSD-1G	74	10	3.45	0.804	0.002	1.990	0.006	19.561	0.086	15.729	0.064	38.920	0.222	0.363	0.004	0.703	0.014
GSD-1G	74	10	3.45	0.805	0.001	1.986	0.004	19.576	0.117	15.749	0.103	38.872	0.255	0.361	0.004	0.710	0.011
GSD-1G	74	10	3.45	0.801	0.002	1.980	0.004	19.595	0.072	15.696	0.059	38.789	0.157	0.344	0.005	0.720	0.015
GSD-1G	74	10	3.45	0.802	0.002	1.983	0.004	19.601	0.095	15.728	0.049	38.866	0.142	0.365	0.004	0.680	0.009
GSD-1G	74	10	3.45	0.805	0.003	1.982	0.003	19.605	0.116	15.791	0.076	38.865	0.195	0.337	0.006	0.724	0.017
GSD-1G	74	10	3.45	0.804	0.001	1.985	0.003	19.611	0.072	15.777	0.052	38.931	0.142	0.364	0.004	0.732	0.010
GSD-1G	74	10	3.45	0.806	0.001	1.983	0.003	19.620	0.056	15.818	0.052	38.915	0.134	0.358	0.004	0.729	0.012
GSD-1G	74	10	3.45	0.803	0.002	1.984	0.007	19.631	0.154	15.763	0.130	38.953	0.292	0.340	0.006	0.686	0.013

Appendix F: LA-ICP-MS Pb-isotope Results for Hiltaba Suite/ GRV alkali feldspars

LA-ICP-MS Pb-isotopic results of alkali feldspars from the Hiltaba Suite/ GRV (1/7)

Sample No.	Strat. Name	Spot Size (µm)	Frequency (Hz)	Fluence (mJ/cm2)	207/206	+/-1s	208/206	+/-1s	206/204	+/-1s	207/204	+/-1s	208/204	+/-1s
2167	Kychering	110	10	3.45	0.964	0.005	2.245	0.013	16.033	0.118	15.451	0.102	36.000	0.169
2167	Kychering	110	10	3.45	0.966	0.003	2.249	0.005	15.977	0.073	15.430	0.033	35.933	0.127
2167	Kychering	110	10	3.45	0.963	0.002	2.245	0.004	15.938	0.036	15.352	0.039	35.777	0.059
2167	Kychering	110	10	3.45	0.966	0.002	2.251	0.004	15.933	0.039	15.393	0.037	35.862	0.099
2167	Kychering	110	10	3.45	0.969	0.002	2.255	0.002	15.927	0.051	15.440	0.055	35.922	0.115
2167	Kychering	110	10	3.45	0.964	0.002	2.245	0.003	15.927	0.075	15.351	0.061	35.759	0.137
2167	Kychering	110	10	3.45	0.968	0.001	2.251	0.003	15.884	0.032	15.371	0.048	35.752	0.084
2167	Kychering	110	10	3.45	0.966	0.003	2.253	0.009	15.846	0.058	15.314	0.039	35.693	0.123
2167	Kychering	110	10	3.45	0.966	0.002	2.253	0.002	15.821	0.038	15.290	0.066	35.637	0.092
2193	Pegler	110	10	3.45	0.973	0.007	2.245	0.015	15.997	0.252	15.565	0.219	35.905	0.485
2193	Pegler	110	10	3.45	0.980	0.008	2.291	0.017	15.857	0.104	15.536	0.157	36.333	0.352
2193	Pegler	110	10	3.45	0.979	0.004	2.275	0.003	15.761	0.060	15.434	0.076	35.848	0.142
2193	Pegler	110	10	3.45	0.985	0.002	2.281	0.005	15.705	0.073	15.469	0.077	35.818	0.212
2193	Pegler	110	10	3.45	0.983	0.003	2.287	0.003	15.688	0.057	15.422	0.081	35.884	0.141
2193	Pegler	110	10	3.45	0.976	0.002	2.274	0.005	15.639	0.044	15.267	0.039	35.562	0.109
2193	Pegler	110	10	3.45	0.974	0.004	2.283	0.005	15.621	0.099	15.216	0.088	35.658	0.195
2193	Pegler	110	10	3.45	0.982	0.002	2.281	0.005	15.537	0.065	15.263	0.059	35.443	0.111
2193	Pegler	110	10	3.45	0.973	0.007	2.245	0.015	15.997	0.252	15.565	0.219	35.905	0.485
8910	Pinding	110	10	3.45	0.962	0.002	2.234	0.002	15.957	0.072	15.352	0.049	35.641	0.144
8910	Pinding	110	10	3.45	0.956	0.004	2.221	0.009	15.952	0.076	15.252	0.023	35.429	0.047
8910	Pinding	110	10	3.45	0.963	0.002	2.230	0.003	15.891	0.028	15.295	0.033	35.443	0.074
8910	Pinding	110	10	3.45	0.963	0.004	2.227	0.005	15.869	0.091	15.285	0.085	35.336	0.198
8910	Pinding	110	10	3.45	0.966	0.003	2.233	0.004	15.820	0.043	15.287	0.035	35.326	0.099
8910	Pinding	110	10	3.45	0.964	0.002	2.232	0.003	15.815	0.053	15.238	0.055	35.300	0.101

LA-ICP-MS Pb-isotopic results of alkali feldspars from the Hiltaba Suite/ GRV (2/7)

Sample No.	Strat. Name	Spot Size (µm)	Frequency (Hz)	Fluence (mJ/cm2)	207/206	+/-1s	208/206	+/-1s	206/204	+/-1s	207/204	+/-1s	208/204	+/-1s
8910	Pinding	110	10	3.45	0.963	0.002	2.236	0.003	15.796	0.084	15.209	0.080	35.312	0.194
8910	Pinding	110	10	3.45	0.964	0.001	2.244	0.003	15.767	0.048	15.199	0.044	35.375	0.098
8910	Pinding	110	10	3.45	0.967	0.002	2.244	0.004	15.744	0.057	15.225	0.041	35.335	0.125
8910	Pinding	110	10	3.45	0.974	0.001	2.254	0.004	15.651	0.058	15.237	0.051	35.282	0.138
8934	Lyons	110	10	3.45	0.960	0.002	2.223	0.007	16.019	0.066	15.382	0.060	35.608	0.156
8934	Lyons	110	10	3.45	0.963	0.002	2.225	0.006	16.006	0.112	15.413	0.129	35.617	0.312
8934	Lyons	110	10	3.45	0.948	0.003	2.213	0.006	15.988	0.125	15.152	0.136	35.386	0.268
8934	Lyons	110	10	3.45	0.963	0.002	2.229	0.005	15.985	0.088	15.388	0.069	35.630	0.164
8934	Lyons	110	10	3.45	0.943	0.003	2.209	0.010	15.951	0.097	15.036	0.068	35.239	0.122
8934	Lyons	110	10	3.45	0.957	0.005	2.217	0.010	15.950	0.075	15.260	0.096	35.366	0.200
8934	Lyons	110	10	3.45	0.957	0.004	2.179	0.008	15.937	0.095	15.245	0.093	34.732	0.173
8934	Lyons	110	10	3.45	0.965	0.002	2.221	0.005	15.857	0.088	15.308	0.087	35.212	0.167
8934	Lyons	110	10	3.45	0.949	0.004	2.205	0.005	15.827	0.097	15.016	0.057	34.892	0.171
8934	Lyons	110	10	3.45	0.961	0.002	2.233	0.005	15.816	0.079	15.205	0.065	35.313	0.170
8973	Konkaby West	110	10	3.45	0.946	0.005	2.227	0.004	16.097	0.098	15.221	0.077	35.850	0.213
8973	Konkaby West	110	10	3.45	0.958	0.004	2.225	0.003	16.004	0.034	15.336	0.051	35.605	0.069
8973	Konkaby West	110	10	3.45	0.944	0.003	2.217	0.007	15.983	0.071	15.092	0.039	35.430	0.079
8973	Konkaby West	110	10	3.45	0.965	0.003	2.235	0.006	15.961	0.055	15.404	0.043	35.677	0.128
8973	Konkaby West	110	10	3.45	0.967	0.003	2.233	0.004	15.959	0.063	15.426	0.074	35.638	0.142
8973	Konkaby West	110	10	3.45	0.963	0.002	2.230	0.004	15.915	0.052	15.329	0.052	35.492	0.111
8973	Konkaby West	110	10	3.45	0.960	0.003	2.235	0.005	15.912	0.087	15.282	0.090	35.565	0.146
8973	Konkaby West	110	10	3.45	0.958	0.002	2.231	0.004	15.886	0.094	15.223	0.071	35.438	0.198
9388	Tyringa	110	10	3.45	0.944	0.003	2.219	0.005	16.434	0.100	15.511	0.073	36.474	0.232
9388	Tyringa	110	10	3.45	0.945	0.003	2.217	0.011	16.434	0.101	15.531	0.075	36.438	0.304

LA-ICP-MS Pb-isotopic results of alkali feldspars from the Hiltaba Suite/ GRV (3/7)

Sample No.	Strat. Name	Spot Size (µm)	Frequency (Hz)	Fluence (mJ/cm2)	207/206	+/-1s	208/206	+/-1s	206/204	+/-1s	207/204	+/-1s	208/204	+/-1s
9388	Tyringa	110	10	3.45	0.934	0.005	2.238	0.011	16.595	0.097	15.500	0.049	37.135	0.215
9436	Parla	110	10	3.45	0.944	0.005	2.214	0.007	16.291	0.102	15.386	0.042	36.063	0.167
9436	Parla	110	10	3.45	0.957	0.002	2.212	0.004	16.054	0.074	15.371	0.088	35.517	0.180
9436	Parla	110	10	3.45	0.955	0.003	2.211	0.005	16.044	0.033	15.315	0.055	35.473	0.116
9436	Parla	110	10	3.45	0.954	0.005	2.210	0.008	16.014	0.107	15.283	0.146	35.389	0.324
9436	Parla	110	10	3.45	0.961	0.002	2.221	0.005	15.957	0.108	15.341	0.100	35.441	0.207
9436	Parla	110	10	3.45	0.956	0.003	2.214	0.010	15.944	0.082	15.250	0.069	35.297	0.149
9436	Parla	110	10	3.45	0.973	0.003	2.254	0.005	15.809	0.094	15.385	0.073	35.640	0.209
10911	Pordia	110	10	3.45	0.955	0.002	2.215	0.005	16.020	0.060	15.299	0.066	35.478	0.148
10911	Pordia	110	10	3.45	0.959	0.004	2.214	0.005	16.001	0.063	15.337	0.033	35.425	0.100
10911	Pordia	110	10	3.45	0.957	0.004	2.218	0.005	15.994	0.063	15.300	0.054	35.467	0.115
10911	Pordia	110	10	3.45	0.962	0.002	2.217	0.004	15.991	0.055	15.390	0.062	35.460	0.136
10911	Pordia	110	10	3.45	0.966	0.002	2.243	0.003	15.971	0.051	15.428	0.050	35.816	0.085
10911	Pordia	110	10	3.45	0.957	0.003	2.227	0.004	15.959	0.063	15.275	0.034	35.542	0.107
10911	Pordia	110	10	3.45	0.956	0.002	2.215	0.006	15.957	0.043	15.254	0.046	35.351	0.131
10911	Pordia	110	10	3.45	0.950	0.002	2.222	0.004	15.945	0.066	15.149	0.052	35.426	0.160
10911	Pordia	110	10	3.45	0.956	0.002	2.217	0.004	15.872	0.074	15.180	0.070	35.184	0.138
10911	Pordia	110	10	3.45	0.974	0.004	2.239	0.009	15.724	0.088	15.314	0.068	35.208	0.161
11303	Kokatha	110	10	3.45	0.942	0.005	2.187	0.010	16.378	0.089	15.434	0.071	35.815	0.130
11303	Kokatha	110	10	3.45	0.942	0.002	2.192	0.005	16.290	0.070	15.350	0.079	35.712	0.117
11303	Kokatha	110	10	3.45	0.944	0.006	2.198	0.011	16.159	0.121	15.257	0.048	35.509	0.148
11303	Kokatha	110	10	3.45	0.952	0.002	2.212	0.004	16.158	0.042	15.385	0.059	35.748	0.121
11303	Kokatha	110	10	3.45	0.954	0.002	2.217	0.004	16.113	0.058	15.370	0.051	35.720	0.137
11303	Kokatha	110	10	3.45	0.962	0.004	2.223	0.006	15.949	0.096	15.341	0.072	35.455	0.157

LA-ICP-MS Pb-isotopic results of alkali feldspars from the Hiltaba Suite/ GRV (4/7)

Sample No.	Strat. Name	Spot Size (µm)	Frequency (Hz)	Fluence (mJ/cm2)	207/206	+/-1s	208/206	+/-1s	206/204	+/-1s	207/204	+/-1s	208/204	+/-1s
11303	Kokatha	110	10	3.45	0.920	0.004	2.141	0.012	16.655	0.104	15.328	0.054	35.666	0.109
18703	Charleston	110	10	3.45	0.951	0.003	2.243	0.004	16.212	0.066	15.422	0.066	36.359	0.115
18703	Charleston	110	10	3.45	0.960	0.004	2.270	0.012	16.060	0.047	15.413	0.046	36.450	0.154
18703	Charleston	110	10	3.45	0.957	0.002	2.246	0.005	16.042	0.065	15.360	0.050	36.037	0.130
18703	Charleston	110	10	3.45	0.950	0.003	2.189	0.005	16.034	0.072	15.230	0.067	35.093	0.130
18703	Charleston	110	10	3.45	0.960	0.002	2.244	0.004	16.018	0.060	15.374	0.068	35.938	0.138
18703	Charleston	110	10	3.45	0.956	0.002	2.239	0.007	16.013	0.045	15.313	0.057	35.851	0.129
18703	Charleston	110	10	3.45	0.948	0.002	2.238	0.006	15.974	0.053	15.149	0.066	35.748	0.162
18703	Charleston	110	10	3.45	0.959	0.003	2.237	0.006	15.894	0.045	15.244	0.064	35.554	0.140
18804	Charleston	110	10	3.45	0.954	0.002	2.247	0.009	16.241	0.073	15.500	0.045	36.495	0.132
18804	Charleston	110	10	3.45	0.951	0.003	2.230	0.004	16.172	0.082	15.385	0.087	36.068	0.177
18804	Charleston	110	10	3.45	0.960	0.002	2.244	0.007	16.165	0.109	15.515	0.092	36.272	0.196
18804	Charleston	110	10	3.45	0.963	0.002	2.245	0.004	16.107	0.084	15.517	0.072	36.155	0.180
18804	Charleston	110	10	3.45	0.956	0.002	2.248	0.005	16.032	0.085	15.326	0.079	36.041	0.186
18804	Charleston	110	10	3.45	0.949	0.003	2.266	0.006	16.026	0.045	15.214	0.065	36.319	0.147
18804	Charleston	110	10	3.45	0.963	0.005	2.258	0.011	15.999	0.060	15.404	0.060	36.127	0.125
168732	Yantea Rhyolite	110	10	3.45	0.938	0.004	2.187	0.008	16.416	0.121	15.396	0.098	35.909	0.275
168732	Yantea Rhyolite	110	10	3.45	0.933	0.003	2.199	0.006	16.396	0.140	15.298	0.108	36.058	0.316
168732	Yantea Rhyolite	110	10	3.45	0.930	0.004	2.179	0.008	16.275	0.198	15.135	0.177	35.460	0.469
168732	Yantea Rhyolite	110	10	3.45	0.940	0.006	2.187	0.008	16.242	0.133	15.272	0.081	35.516	0.216
168732	Yantea Rhyolite	110	10	3.45	0.975	0.006	2.304	0.008	15.807	0.193	15.407	0.186	36.413	0.452
168790	Lake Gairdner Rhyolite	110	10	3.45	0.960	0.002	2.184	0.004	15.820	0.074	15.188	0.084	34.544	0.159
168790	Lake Gairdner Rhyolite	110	10	3.45	0.965	0.002	2.218	0.004	15.823	0.067	15.263	0.049	35.097	0.138
168790	Lake Gairdner Rhyolite	110	10	3.45	0.971	0.003	2.245	0.004	15.826	0.086	15.361	0.050	35.534	0.157

LA-ICP-MS Pb-isotopic results of alkali feldspars from the Hiltaba Suite/ GRV (5/7)

Sample No.	Strat. Name	Spot Size (µm)	Frequency (Hz)	Fluence (mJ/cm2)	207/206	+/-1s	208/206	+/-1s	206/204	+/-1s	207/204	+/-1s	208/204	+/-1s
168790	Lake Gairdner Rhyolite	110	10	3.45	0.966	0.001	2.233	0.004	15.838	0.060	15.297	0.056	35.366	0.133
168790	Lake Gairdner Rhyolite	110	10	3.45	0.965	0.003	2.236	0.005	15.846	0.045	15.285	0.076	35.435	0.114
168790	Lake Gairdner Rhyolite	110	10	3.45	0.963	0.002	2.242	0.004	15.859	0.081	15.273	0.068	35.558	0.138
168790	Lake Gairdner Rhyolite	110	10	3.45	0.965	0.001	2.231	0.004	15.902	0.071	15.341	0.063	35.476	0.142
168790	Lake Gairdner Rhyolite	110	10	3.45	0.962	0.003	2.230	0.004	15.914	0.082	15.307	0.070	35.485	0.150
168790	Lake Gairdner Rhyolite	110	10	3.45	0.964	0.002	2.228	0.002	15.922	0.064	15.348	0.066	35.482	0.163
168790	Lake Gairdner Rhyolite	110	10	3.45	0.962	0.003	2.225	0.006	15.937	0.058	15.328	0.042	35.454	0.106
18708-1	Charleston	110	10	3.45	0.963	0.002	2.260	0.003	16.064	0.092	15.471	0.097	36.302	0.212
18708-2	Charleston	110	10	3.45	0.961	0.003	2.252	0.004	16.044	0.091	15.416	0.102	36.130	0.219
18708-3	Charleston	110	10	3.45	0.967	0.002	2.272	0.013	16.040	0.063	15.507	0.068	36.449	0.179
2193 plag	Pegler	110	10	3.45	0.984	0.004	2.279	0.004	15.894	0.074	15.642	0.061	36.225	0.136
2193 plag	Pegler	110	10	3.45	0.974	0.006	2.260	0.008	15.824	0.092	15.405	0.052	35.760	0.108
2193 plag	Pegler	110	10	3.45	0.972	0.002	2.266	0.007	15.715	0.076	15.279	0.062	35.604	0.200
2193 plag	Pegler	110	10	3.45	0.975	0.007	2.271	0.010	15.629	0.095	15.245	0.108	35.485	0.233
2193 plag	Pegler	110	10	3.45	0.940	0.005	2.243	0.011	16.430	0.324	15.444	0.351	36.848	0.757
658673-1	Buckleboo	110	10	3.45	0.954	0.002	2.222	0.004	16.160	0.047	15.423	0.045	35.915	0.082
658673-2	Buckleboo	110	10	3.45	0.944	0.001	2.197	0.002	16.340	0.041	15.426	0.048	35.899	0.081
658673-3	Buckleboo	110	10	3.45	0.946	0.002	2.198	0.003	16.344	0.079	15.455	0.070	35.933	0.151
658673-4	Buckleboo	110	10	3.45	0.945	0.001	2.196	0.002	16.470	0.046	15.571	0.039	36.172	0.086
658673-5	Buckleboo	110	10	3.45	0.943	0.001	2.200	0.002	16.351	0.021	15.416	0.026	35.971	0.055
658673-6	Buckleboo	110	10	3.45	0.945	0.002	2.193	0.002	16.389	0.041	15.482	0.046	35.943	0.081
658673-7	Buckleboo	110	10	3.45	0.946	0.001	2.203	0.004	16.251	0.036	15.371	0.033	35.807	0.090
658673-8	Buckleboo	110	10	3.45	0.944	0.001	2.198	0.003	16.292	0.063	15.388	0.056	35.807	0.143
8832-1	Tyringa	110	10	3.45	0.952	0.002	2.222	0.003	16.205	0.030	15.421	0.038	36.011	0.070

LA-ICP-MS Pb-isotopic results of alkali feldspars from the Hiltaba Suite/ GRV (6/7)

Sample No.	Strat. Name	Spot Size (µm)	Frequency (Hz)	Fluence (mJ/cm2)	207/206	+/-1s	208/206	+/-1s	206/204	+/-1s	207/204	+/-1s	208/204	+/-1s
8832-2	Tyringa	110	10	3.45	0.958	0.002	2.225	0.005	16.181	0.039	15.509	0.032	36.001	0.126
8832-3	Tyringa	110	10	3.45	0.957	0.003	2.225	0.005	16.051	0.096	15.362	0.121	35.705	0.212
884-Y10-1	Yardea Dacite	110	10	3.45	0.954	0.003	2.224	0.008	16.272	0.077	15.530	0.090	36.192	0.145
884-Y10-10	Yardea Dacite	110	10	3.45	0.947	0.005	2.206	0.009	16.313	0.095	15.452	0.065	35.985	0.118
884-Y10-2	Yardea Dacite	110	10	3.45	0.952	0.002	2.217	0.005	16.182	0.090	15.399	0.075	35.880	0.160
884-Y10-3	Yardea Dacite	110	10	3.45	0.954	0.002	2.224	0.007	16.166	0.049	15.430	0.054	35.958	0.111
884-Y10-6	Yardea Dacite	110	10	3.45	0.895	0.005	2.157	0.017	16.938	0.633	15.153	0.607	36.534	1.360
884-Y10-8	Yardea Dacite	110	10	3.45	0.958	0.003	2.220	0.006	16.210	0.130	15.521	0.126	35.980	0.268
884-Y10-9	Yardea Dacite	110	10	3.45	0.953	0.003	2.229	0.007	16.271	0.069	15.514	0.084	36.269	0.218
8902-1	Frogs Eyes	110	10	3.45	0.956	0.004	2.235	0.006	15.928	0.076	15.221	0.060	35.603	0.152
8902-2	Frogs Eyes	110	10	3.45	0.959	0.002	2.227	0.004	16.100	0.034	15.442	0.035	35.850	0.060
8902-3	Frogs Eyes	110	10	3.45	0.954	0.002	2.222	0.007	16.078	0.039	15.345	0.036	35.723	0.084
9674-1	Childara	110	10	3.45	0.971	0.004	2.252	0.009	16.036	0.124	15.576	0.127	36.112	0.319
9674-2	Childara	110	10	3.45	0.972	0.002	2.271	0.008	15.889	0.096	15.451	0.088	36.083	0.210
9674-3	Childara	110	10	3.45	0.970	0.002	2.257	0.006	15.908	0.049	15.431	0.030	35.898	0.047
Arth2	Arthurton Granite	110	10	3.45	0.849	0.003	2.125	0.008	18.880	0.129	16.032	0.097	40.113	0.221
Arth2	Arthurton Granite	110	10	3.45	0.880	0.007	2.105	0.016	17.827	0.181	15.689	0.070	37.528	0.171
PD4-1	Phillips Dam	110	10	3.45	0.944	0.003	2.201	0.007	16.440	0.131	15.526	0.102	36.179	0.254
PD4-2	Phillips Dam	110	10	3.45	0.939	0.002	2.194	0.004	16.464	0.097	15.452	0.064	36.127	0.169
PD4-3	Phillips Dam	110	10	3.45	0.948	0.006	2.225	0.010	16.324	0.097	15.481	0.142	36.316	0.261
PW20	Eucarro Rhyolite	110	10	3.45	0.950	0.002	2.212	0.007	16.080	0.058	15.274	0.041	35.568	0.140
PW20	Eucarro Rhyolite	110	10	3.45	0.950	0.002	2.215	0.004	16.176	0.083	15.353	0.096	35.826	0.188
PW20	Eucarro Rhyolite	110	10	3.45	0.949	0.005	2.216	0.010	16.135	0.054	15.309	0.075	35.753	0.190
PW20	Eucarro Rhyolite	110	10	3.45	0.948	0.004	2.222	0.007	16.356	0.114	15.502	0.095	36.339	0.209
PW20	Eucarro Rhyolite	110	10	3.45	0.950	0.004	2.216	0.006	16.260	0.088	15.445	0.064	36.031	0.139
PW20	Eucarro Rhyolite	110	10	3.45	0.947	0.002	2.221	0.008	15.997	0.054	15.140	0.046	35.536	0.128
PW20	Eucarro Rhyolite	110	10	3.45	0.946	0.003	2.221	0.007	16.368	0.109	15.486	0.101	36.359	0.224

LA-ICP-MS Pb-isotopic results of alkali feldspars from the Hiltaba Suite/ GRV (7/7)

Sample No.	Strat. Name	Spot Size (µm)	Frequency (Hz)	Fluence (mJ/cm2)	207/206	+/-1s	208/206	+/-1s	206/204	+/-1s	207/204	+/-1s	208/204	+/-1s
PW20	Eucarro Rhyolite	110	10	3.45	0.949	0.003	2.218	0.005	16.303	0.095	15.468	0.078	36.161	0.163
PW20	Eucarro Rhyolite	110	10	3.45	0.955	0.004	2.216	0.011	16.247	0.081	15.516	0.055	35.997	0.221
PW20	Eucarro Rhyolite	110	10	3.45	0.952	0.002	2.217	0.007	16.228	0.105	15.451	0.083	35.970	0.160
PW20	Eucarro Rhyolite	110	10	3.45	0.951	0.002	2.225	0.009	16.188	0.087	15.398	0.085	36.015	0.283
PW20	Eucarro Rhyolite	110	10	3.45	0.952	0.004	2.225	0.005	16.207	0.087	15.430	0.061	36.057	0.182
PW20	Eucarro Rhyolite	110	10	3.45	0.950	0.003	2.222	0.005	16.260	0.088	15.438	0.061	36.137	0.146
PW20	Eucarro Rhyolite	110	10	3.45	0.953	0.002	2.226	0.004	16.237	0.081	15.466	0.051	36.137	0.157
PW20	Eucarro Rhyolite	110	10	3.45	0.952	0.002	2.222	0.007	16.244	0.085	15.455	0.085	36.095	0.212
PW20	Eucarro Rhyolite	110	10	3.45	0.949	0.002	2.211	0.006	16.356	0.109	15.513	0.081	36.169	0.245
PW20 -1	Eucarro Rhyolite	110	10	3.45	0.952	0.002	2.220	0.004	16.317	0.054	15.539	0.051	36.221	0.107
PW20 -2	Eucarro Rhyolite	110	10	3.45	0.964	0.001	2.236	0.005	16.377	0.105	15.791	0.104	36.611	0.213
PW20 -3	Eucarro Rhyolite	110	10	3.45	0.959	0.003	2.227	0.005	16.295	0.184	15.628	0.183	36.285	0.423
R360345	Buckleboo	110	10	3.45	0.948	0.003	2.215	0.005	16.335	0.062	15.478	0.050	36.184	0.124
R650345-11	Buckleboo	110	10	3.45	0.954	0.004	2.232	0.006	16.054	0.075	15.314	0.088	35.838	0.145
R650345-18	Buckleboo	110	10	3.45	0.938	0.004	2.200	0.011	16.484	0.151	15.468	0.142	36.272	0.310
R650345-23	Buckleboo	110	10	3.45	0.936	0.005	2.222	0.013	16.472	0.105	15.416	0.137	36.603	0.328
R650345-26	Buckleboo	110	10	3.45	0.952	0.002	2.225	0.004	16.298	0.052	15.511	0.051	36.270	0.125
R650345-27	Buckleboo	110	10	3.45	0.956	0.004	2.227	0.007	16.357	0.076	15.637	0.119	36.429	0.172
yd20-m7	Yardea Dacite	110	10	3.45	0.946	0.004	2.218	0.014	16.343	0.124	15.459	0.102	36.252	0.228
yd20-m7	Yardea Dacite	110	10	3.45	0.955	0.005	2.226	0.009	16.279	0.160	15.546	0.175	36.241	0.296
yd20-m7	Yardea Dacite	110	10	3.45	0.954	0.006	2.228	0.013	16.234	0.049	15.492	0.099	36.170	0.192
yd20-m7	Yardea Dacite	110	10	3.45	0.957	0.006	2.239	0.010	16.147	0.145	15.451	0.137	36.151	0.255
yd20-m7	Yardea Dacite	110	10	3.45	0.965	0.005	2.244	0.009	16.108	0.207	15.537	0.213	36.143	0.403
yd20-m7	Yardea Dacite	110	10	3.45	0.957	0.004	2.220	0.009	16.096	0.169	15.411	0.146	35.737	0.283
yd20-m7	Yardea Dacite	110	10	3.45	0.959	0.004	2.226	0.010	16.005	0.157	15.357	0.157	35.627	0.359
yd20-m7	Yardea Dacite	110	10	3.45	0.965	0.006	2.231	0.011	15.967	0.125	15.413	0.137	35.625	0.362
yd20-m7	Yardea Dacite	110	10	3.45	0.958	0.007	2.213	0.017	15.880	0.304	15.207	0.211	35.147	0.517

Appendix G: LA-ICP-MS Zircon Geochronology Results for Select Hiltaba Suite

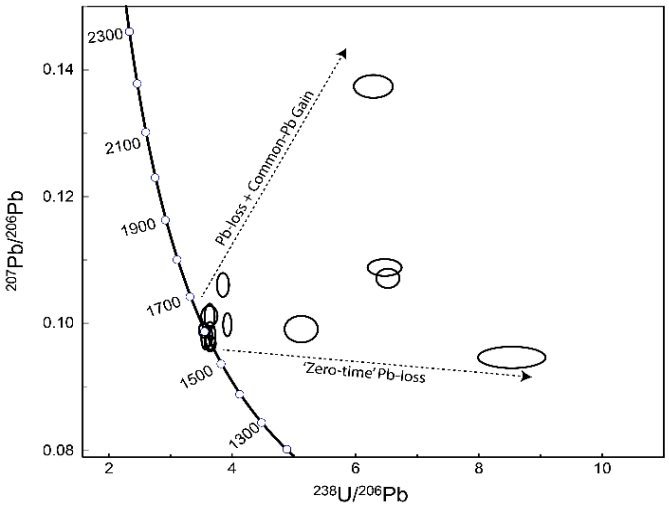

Results of zircon U-Pb dating undertaken on a sample of the Bulpara Pluton confirm a 1590 Ma magmatic crystallisation age. Analyses was undertaken in light of non-radiogenic initial Pb-isotopic ratios obtained from alkali feldspars indicated a model Pb-Pb age of c.1760 Ma.

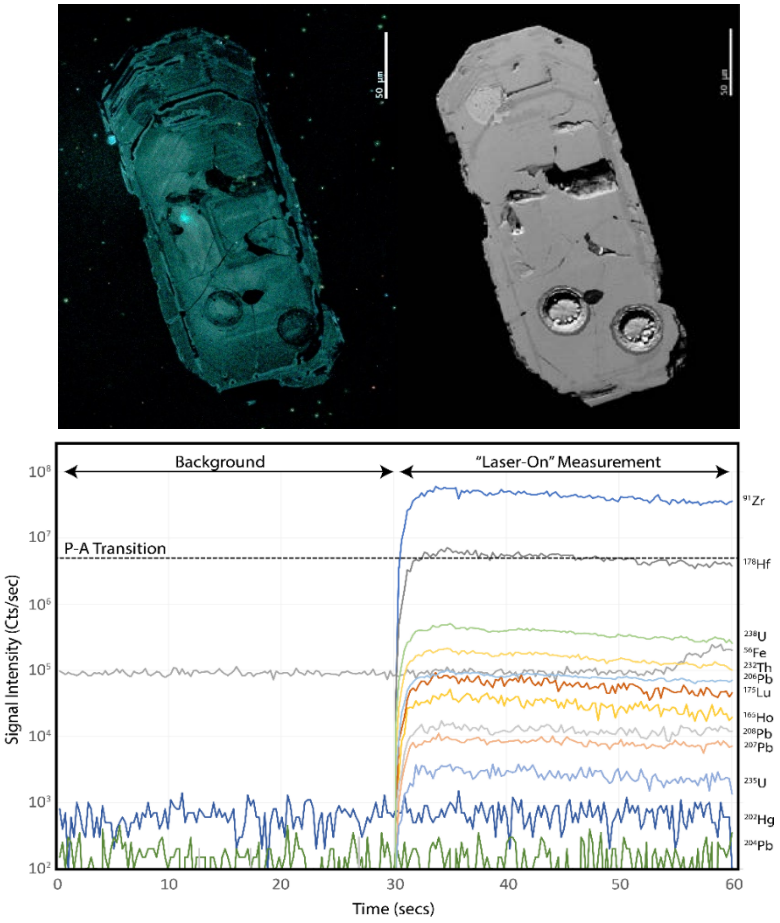

Cathodoluminence (top left) and BSE (top right) images of a Hiltaba Suite zircon analysed for U-Pb dating using LA-ICP-MS. Follow up zircon dating was undertaken for samples where no recent ages are present in the literature, and Pb-isotopic signatures indicated the potential for incorrect ages (i.e. non-radiogenic Pb-Pb). Respective spectra below, showing 13 of the 30 masses routinely collected for both U-Pb dating and QA/QC (i.e. ^{56}Fe, ^{140}Ce and ^{139}La etc).

LA-ICP-MS U-Pb Zircon Geochronology from the Bulpara Pluton (Unradiogenic Pb-Pb)

		207 corr. 206Pb/238U		206Pb/238U		206Pb/238U		208Pb/232Th		207Pb/206Pb		% concord.	238U/206Pb		207Pb/206Pb		common Pb at age of zirc
Sample #	Strat. Name	AGE (Ma)	+/-1	AGE (Ma)	+/-1	ratio	+/-1 RSE	ratio	+/-1 RSE	ratio	+/-1 RSE		ratio	+/-1 s	ratio	+/-1 s	
9674	Bulpara	1668	33	1668	34	0.295	0.020	0.107	0.025	0.101	0.011	1.011	3.386	0.069	0.101	0.001	0.969
9674	Bulpara	1640	21	1640	22	0.290	0.013	0.093	0.019	0.100	0.007	1.014	3.451	0.045	0.100	0.001	0.966
9674	Bulpara	1605	25	1605	26	0.283	0.016	0.087	0.018	0.099	0.008	1.002	3.537	0.058	0.099	0.001	0.963
9674	Bulpara	1603	16	1606	17	0.283	0.010	0.088	0.016	0.100	0.008	0.985	3.535	0.036	0.100	0.001	0.963
9674	Bulpara	1600	14	1600	15	0.282	0.009	0.083	0.018	0.099	0.009	0.998	3.549	0.032	0.099	0.001	0.962
9674	Bulpara	1575	21	1579	22	0.278	0.014	0.085	0.022	0.100	0.014	0.974	3.602	0.050	0.100	0.001	0.960
9674	Bulpara	1574	16	1576	17	0.277	0.010	0.082	0.018	0.099	0.011	0.985	3.610	0.038	0.099	0.001	0.960
9674	Bulpara	1464	20	1486	21	0.259	0.014	0.093	0.024	0.106	0.009	0.859	3.858	0.056	0.106	0.001	0.952
9674	Bulpara	1461	30	1473	31	0.257	0.021	0.085	0.024	0.099	0.024	0.913	3.895	0.083	0.099	0.002	0.950
9674	Bulpara	939	14	978	15	0.164	0.016	0.092	0.024	0.106	0.011	0.562	6.105	0.095	0.106	0.001	0.907
9674	Bulpara	884	24	925	26	0.154	0.028	0.064	0.022	0.109	0.008	0.520	6.477	0.183	0.109	0.001	0.903
9674	Bulpara	874	28	947	32	0.158	0.033	0.085	0.027	0.138	0.009	0.431	6.316	0.210	0.138	0.001	0.904
9674	Bulpara	869	14	918	15	0.153	0.017	0.106	0.024	0.116	0.007	0.486	6.534	0.108	0.116	0.001	0.902

Appendix H: Pb-isotopic Results for Olympic Dam carbonates, pyrite, Pb-chalcogenides and whole-rock RDG

RDG Whole-Rock Pb-isotopic Results

Name	Mineral	207/206	+/-2s	208/206	+/-2s	204/206	+/-2s	206/204	+/-2s	207/204	+/-2s	208/204	+/-2s
RD2488_576	WR RDG	0.7463	0.0149	1.8400	0.0368	0.0468	0.0009	21.38	0.43	15.95	0.32	39.33	0.79
HRD002_438	WR RDG	0.7027	0.0141	1.8370	0.0367	0.0437	0.0009	22.90	0.46	16.11	0.32	42.08	0.84
HRD001_382	WR RDG	0.6173	0.0123	1.6770	0.0335	0.0375	0.0007	26.67	0.53	16.40	0.33	44.72	0.89
RD2488_491.9	WR RDG	0.5995	0.0120	1.7770	0.0355	0.0363	0.0007	27.53	0.55	16.50	0.33	48.91	0.98
RD2274_342	WR RDG	0.5605	0.0112	1.7640	0.0353	0.0336	0.0007	29.74	0.59	16.66	0.33	52.47	1.05
RD2488_513.7	WR RDG	0.5325	0.0106	1.7310	0.0346	0.0318	0.0006	31.44	0.63	16.70	0.33	54.42	1.09
RD2323_446.1	WR RDG	0.4294	0.0086	1.5100	0.0302	0.0241	0.0005	41.41	0.83	17.74	0.35	62.51	1.25
RD2488_369.3	WR RDG	0.4088	0.0082	1.5030	0.0301	0.0229	0.0005	43.71	0.87	17.90	0.36	65.68	1.31
RD2326_444.6	WR RDG	0.3932	0.0079	1.4770	0.0295	0.0221	0.0004	45.18	0.90	17.82	0.36	66.75	1.34
RD2336_428.8	WR RDG	0.3662	0.0073	1.4660	0.0293	0.0199	0.0004	50.21	1.00	18.38	0.37	73.61	1.47
RD2499_499.3	WR RDG	0.3618	0.0072	1.3860	0.0277	0.0199	0.0004	50.30	1.01	18.22	0.36	69.74	1.39
RD2280_452.2	WR RDG	0.3595	0.0072	1.3600	0.0272	0.0196	0.0004	51.14	1.02	18.36	0.37	69.54	1.39
RD2347_533.6	WR RDG	0.3131	0.0063	1.3750	0.0275	0.0164	0.0003	61.01	1.22	19.08	0.38	83.88	1.68

LA-ICP-MS Pb-isotope Results for Calcites

Name	Mineral	207/206	+/-1s	208/206	+/-1s	204/206	+/-1s	206/204	+/-1s	207/204	+/-1s	208/204	+/-1s
OD827	Cal	0.925	0.003	2.163	0.009	0.0596	0.0005	16.781	0.154	15.519	0.142	36.304	0.327
OD827	Cal	0.923	0.005	2.145	0.008	0.0601	0.0003	16.647	0.076	15.367	0.071	35.71	0.136
OD827	Cal	0.927	0.004	2.168	0.011	0.0604	0.0003	16.556	0.08	15.354	0.055	35.888	0.191
OD827	Cal	0.919	0.003	2.148	0.008	0.0591	0.0004	16.93	0.117	15.561	0.103	36.374	0.278
OD827	Cal	0.922	0.004	2.146	0.007	0.0594	0.0002	16.847	0.065	15.53	0.1	36.161	0.183
OD827	Cal	0.922	0.005	2.156	0.008	0.0593	0.0004	16.875	0.105	15.561	0.127	36.385	0.262
OD827	Cal	0.919	0.004	2.15	0.008	0.0596	0.0003	16.791	0.073	15.427	0.088	36.104	0.197
OD827	Cal	0.917	0.002	2.141	0.006	0.0592	0.0006	16.903	0.173	15.499	0.148	36.193	0.388
OD827	Cal	0.917	0.002	2.143	0.007	0.0593	0.0002	16.859	0.067	15.473	0.051	36.124	0.194
OD827	Cal	0.928	0.003	2.163	0.008	0.0595	0.0003	16.802	0.073	15.594	0.066	36.337	0.165
OD827	Cal	0.925	0.002	2.157	0.011	0.0592	0.0004	16.897	0.113	15.633	0.113	36.445	0.189
OD827	Cal	0.93	0.002	2.17	0.009	0.0606	0.0004	16.513	0.101	15.359	0.092	35.827	0.263
OD827	Cal	0.919	0.002	2.141	0.008	0.0589	0.0004	16.99	0.111	15.625	0.109	36.383	0.246
OD827	Cal	0.919	0.003	2.163	0.013	0.0595	0.0006	16.796	0.178	15.448	0.158	36.323	0.491
OD827	Cal	0.928	0.002	2.163	0.009	0.06	0.0004	16.679	0.099	15.486	0.089	36.082	0.259
OD827	Cal	0.925	0.004	2.162	0.013	0.0593	0.0003	16.875	0.094	15.626	0.084	36.48	0.241
OD827	Cal	0.922	0.004	2.15	0.01	0.0599	0.0003	16.693	0.072	15.399	0.061	35.884	0.227
RD2775	Cal	0.901	0.005	2.096	0.014	0.0586	0.0005	17.067	0.134	15.381	0.124	35.771	0.369
RD2775	Cal	0.903	0.005	2.122	0.009	0.0586	0.0005	17.06	0.134	15.401	0.129	36.202	0.31
RD2775	Cal	0.92	0.003	2.144	0.011	0.0597	0.0005	16.751	0.132	15.405	0.112	35.917	0.262
RD2775	Cal	0.918	0.004	2.143	0.01	0.0594	0.0007	16.833	0.205	15.456	0.154	36.08	0.427
RD2775	Cal	0.929	0.008	2.159	0.014	0.0601	0.0003	16.647	0.087	15.46	0.109	35.944	0.217
RD2775	Cal	0.915	0.003	2.123	0.011	0.0591	0.0004	16.907	0.128	15.476	0.123	35.892	0.264
RD2775	Cal	0.929	0.005	2.161	0.013	0.0599	0.0006	16.7	0.154	15.51	0.133	36.091	0.44
RD2775	Cal	0.927	0.004	2.153	0.01	0.0597	0.0007	16.747	0.191	15.522	0.173	36.051	0.41
RD2775	Cal	0.924	0.006	2.16	0.011	0.0595	0.0006	16.8	0.18	15.523	0.166	36.279	0.457
RD2775	Cal	0.921	0.005	2.146	0.012	0.0593	0.0005	16.877	0.146	15.549	0.169	36.215	0.271

LA-ICP-MS Pb-isotope Results for Siderite

Name	Mineral	207/206	+/-1s	208/206	+/-1s	204/206	+/-1s	206/204	+/-1s	207/204	+/-1s	208/204	+/-1s
OD1050	Sd	0.935	0.002	2.181	0.004	0.06	0.0001	16.6	0.037	15.523	0.045	36.197	0.101
OD1050	Sd	0.934	0.002	2.181	0.005	0.06	0.0002	16.568	0.058	15.48	0.053	36.142	0.153
OD1050	Sd	0.932	0.004	2.175	0.009	0.061	0.0003	16.513	0.07	15.396	0.118	35.92	0.262
OD1050	Sd	0.925	0.004	2.15	0.007	0.059	0.0002	16.874	0.054	15.6	0.068	36.278	0.121
OD1050	Sd	0.914	0.003	2.146	0.01	0.059	0.0004	16.915	0.103	15.455	0.092	36.293	0.204
OD1050	Sd	0.909	0.004	2.109	0.006	0.057	0.0005	17.518	0.153	15.931	0.152	36.942	0.275
OD1050	Sd	0.907	0.004	2.105	0.012	0.058	0.0003	17.152	0.094	15.55	0.052	36.101	0.097
OD1050	Sd	0.897	0.001	2.086	0.002	0.058	0.0002	17.35	0.046	15.571	0.044	36.188	0.103
OD1047	Sd	0.927	0.002	2.171	0.004	0.06	0.0003	16.742	0.071	15.526	0.082	36.353	0.151
OD1047	Sd	0.923	0.002	2.153	0.008	0.059	0.0003	16.894	0.081	15.6	0.058	36.372	0.132
OD1047	Sd	0.922	0.003	2.143	0.008	0.059	0.0003	17.026	0.073	15.707	0.032	36.486	0.094
OD1047	Sd	0.906	0.002	2.107	0.004	0.058	0.0001	17.287	0.025	15.659	0.033	36.428	0.058
OD1047	Sd	0.89	0.002	2.069	0.004	0.057	0.0001	17.547	0.042	15.625	0.042	36.3	0.084
OD1047	Sd	0.863	0.002	1.995	0.006	0.055	0.0003	18.092	0.091	15.622	0.065	36.091	0.108
OD1047	Sd	0.862	0.004	1.991	0.009	0.055	0.0004	18.25	0.124	15.734	0.08	36.337	0.145
OD1047	Sd	0.856	0.003	1.981	0.007	0.055	0.0003	18.239	0.094	15.606	0.071	36.135	0.188
OD1047	Sd	0.843	0.001	1.957	0.006	0.053	0.0003	18.783	0.111	15.834	0.096	36.751	0.265

LA-ICP-MS Pb-isotope Results for Galena from High-Pb zone

Name	Mineral	207/206	+/-1s	208/206	+/-1s	204/206	+/-1s	206/204	+/-1s	207/204	+/-1s	208/204	+/-1s
OD218	Gn	0.834	0.004	1.944	0.009	0.0523	0.0003	19.134	0.117	15.99	0.095	37.205	0.271
OD218	Gn	0.825	0.003	1.932	0.014	0.0523	0.0005	19.134	0.196	15.816	0.123	36.962	0.212
OD218	Gn	0.83	0.003	1.934	0.013	0.0529	0.0003	18.915	0.12	15.73	0.102	36.576	0.234
OD218	Gn	0.853	0.001	1.982	0.006	0.0544	0.0001	18.383	0.031	15.705	0.035	36.431	0.152
OD218	Gn	0.853	0.001	1.991	0.006	0.0541	0.0001	18.481	0.035	15.798	0.026	36.8	0.105
OD218	Gn	0.926	0.002	2.151	0.008	0.0597	0.0003	16.743	0.073	15.514	0.062	35.987	0.144
OD218	Gn	0.893	0.004	2.079	0.011	0.0572	0.0004	17.469	0.108	15.601	0.053	36.291	0.118
OD218	Gn	0.864	0.006	2.01	0.015	0.0551	0.0005	18.161	0.161	15.695	0.026	36.479	0.081
OD218	Gn	0.909	0.003	2.119	0.007	0.0584	0.0002	17.127	0.053	15.57	0.018	36.27	0.078
OD218	Gn	0.881	0.004	2.057	0.013	0.0563	0.0004	17.754	0.121	15.648	0.038	36.505	0.172
OD218	Gn	0.828	0.002	1.929	0.009	0.0527	0.0001	18.97	0.042	15.715	0.022	36.576	0.117
OD827	Gn	0.901	0.005	2.144	0.013	0.0558	0.0006	17.931	0.19	16.241	0.12	38.439	0.346
OD827	Gn	0.909	0.004	2.168	0.01	0.0567	0.0002	17.643	0.068	16.127	0.095	38.241	0.265
OD827	Gn	0.915	0.002	2.191	0.007	0.0567	0.0002	17.651	0.068	16.244	0.05	38.658	0.148

LA-ICP-MS Pb-isotope Results of Pyrite

Name	Mineral	207/206	+/-1s	208/206	+/-1s	204/206	+/-1s	206/204	+/-1s	207/204	+/-1s	208/204	+/-1s
RD2775	Py	0.9	0.005	2.141	0.014	0.057	0.0005	17.665	0.168	15.897	0.143	37.814	0.371
OD211	Py	0.895	0.004	2.118	0.012	0.056	0.0004	17.902	0.113	16.06	0.059	37.912	0.203
OD211	Py	0.92	0.003	2.201	0.008	0.059	0.0005	17.069	0.159	15.752	0.142	37.568	0.374
OD211	Py	0.882	0.005	2.075	0.011	0.054	0.0004	18.373	0.124	16.261	0.113	38.125	0.276
OD211	Py	0.908	0.004	2.162	0.009	0.057	0.0003	17.628	0.089	16.061	0.072	38.111	0.281
OD211	Py	0.903	0.003	2.14	0.013	0.056	0.0004	17.705	0.124	16.038	0.107	37.891	0.277
OD211	Py	0.885	0.002	2.091	0.007	0.055	0.0003	18.104	0.085	16.081	0.074	37.853	0.21
RD2775	Py	0.909	0.007	2.165	0.011	0.056	0.0003	17.75	0.086	16.233	0.14	38.402	0.273
OD827	Py	0.901	0.005	2.144	0.013	0.056	0.0006	17.931	0.19	16.241	0.12	38.439	0.346
OD827	Py	0.909	0.004	2.168	0.01	0.057	0.0002	17.643	0.068	16.127	0.095	38.241	0.265
OD827	Py	0.915	0.002	2.191	0.007	0.057	0.0002	17.651	0.068	16.244	0.05	38.658	0.148
FCO276	Py	0.761	0.009	1.713	0.018	0.048	0.0011	20.965	0.503	15.965	0.366	35.901	0.613
FCO276	Py	0.687	0.016	1.5	0.018	0.04	0.0012	24.92	0.757	17.109	0.341	37.383	0.859
FCO276	Py	0.738	0.007	1.701	0.032	0.048	0.0009	20.788	0.396	15.35	0.335	35.362	0.631
FCO276	Py	0.181	0.003	0.441	0.006	0.007	0.0002	135.375	3.211	24.541	0.355	59.678	0.858
FCO276	Py	0.151	0.001	0.321	0.003	0.006	0.0003	170.752	7.741	25.699	1.091	54.863	2.416
FCO371	Py	0.318	0.006	0.71	0.01	0.016	0.0002	61.156	0.835	19.437	0.403	43.398	0.923
FCO371	Py	0.64	0.01	1.393	0.024	0.038	0.0006	26.634	0.452	17.051	0.294	37.093	0.613
FCO371	Py	0.681	0.008	1.611	0.031	0.043	0.0009	23.115	0.47	15.742	0.277	37.219	0.851
FCO371	Py	0.495	0.01	1.157	0.021	0.03	0.0004	33.557	0.473	16.611	0.354	38.831	0.679
FCO371	Py	0.376	0.008	0.835	0.013	0.02	0.0008	48.939	1.8	18.413	0.598	40.831	1.491
FCO386	Py	0.653	0.011	0.27	0.008	0.013	0.0006	75.584	3.427	20.422	0.587	49.354	1.511
FCO386	Py	0.588	0.014	0.234	0.006	0.012	0.0004	84.578	2.793	19.802	0.618	49.692	1.342
FCO386	Py	0.679	0.005	0.269	0.001	0.012	0.0004	80.72	2.515	21.716	0.678	54.833	1.585

LA-ICP-MS Pb-isotope Results for Pb-chalcogenides associate with Chalcopyrite-Dominant Ores (1/6)

Name	Cu-ore Type	207/206	+/-1s	208/206	+/-1s	204/206	+/-1s	206/204	+/-1s	207/204	+/-1s	208/204	+/-1s
FCO072	Cpy	0.513	0.009	1.098	0.008	0.029	0.0005	34.198	0.535	17.533	0.374	37.554	0.591
FCO072	Cpy	0.263	0.002	0.687	0.009	0.013	0.0001	75.755	0.782	19.887	0.213	52.066	0.789
FCO072	Cpy	0.253	0.001	0.638	0.006	0.012	0.0001	84.737	0.611	21.404	0.183	54.022	0.608
FCO072	Cpy	0.239	0.009	0.592	0.012	0.011	0.0003	88.943	2.708	21.285	0.589	52.672	1.086
FCO072	Cpy	0.191	0.002	0.467	0.007	0.008	0.0002	119.056	3.002	22.692	0.62	55.572	1.169
FCO099	Cpy	0.118	0.002	0.182	0.003	0.003	0.0001	298.79	9.877	35.383	0.873	54.25	1.062
FCO099	Cpy	0.321	0.006	0.653	0.01	0.016	0.0005	62.728	1.781	20.131	0.683	40.974	1.608
FCO103	Cpy	0.24	0.004	0.571	0.016	0.011	0.0002	89.452	1.641	21.453	0.29	51.055	0.944
FCO103	Cpy	0.12	0.001	0.198	0.003	0.004	0.0001	275.695	4.28	33.164	0.487	54.546	1.239
FCO103	Cpy	0.184	0.006	0.369	0.009	0.008	0.0002	127.207	2.988	23.372	0.884	46.888	1.633
FCO103	Cpy	0.211	0.002	0.423	0.005	0.011	0.0002	93.96	1.854	19.807	0.332	39.744	0.848
FCO103	Cpy	0.198	0.002	0.39	0.008	0.009	0.0004	106.347	3.985	21.081	0.682	41.466	1.148
FCO103	Cpy	0.093	0.002	0.125	0.002	0.002	0.0001	440.535	15.172	40.89	1.42	55.207	1.951
FCO103	Cpy	0.203	0.003	0.282	0.005	0.006	0.0002	167.235	6.419	33.931	1.206	47.196	1.724
FCO104	Cpy	0.172	0.002	0.349	0.002	0.007	0.0001	147.706	2.082	25.474	0.612	51.526	0.572
FCO118	Cpy	0.239	0.003	0.618	0.016	0.011	0.0003	87.498	2.315	20.888	0.716	54.024	1.484
FCO118	Cpy	0.239	0.003	0.617	0.016	0.011	0.0003	87.292	2.349	20.826	0.718	53.864	1.49
FCO118	Cpy	0.145	0.001	0.248	0.003	0.005	0.0002	215.529	9.172	31.352	1.247	53.501	2.172
FCO118	Cpy	0.145	0.001	0.248	0.003	0.005	0.0002	214.946	9.208	31.249	1.249	53.326	2.172
FCO118	Cpy	0.332	0.008	0.805	0.015	0.017	0.0006	60.52	2.338	20.088	0.577	48.685	1.393
FCO118	Cpy	0.332	0.008	0.804	0.015	0.017	0.0006	60.305	2.349	20.006	0.58	48.487	1.396
FCO118	Cpy	0.181	0.001	0.355	0.002	0.007	0.0003	152.366	6.771	27.538	1.111	54.05	2.109
FCO118	Cpy	0.181	0.002	0.355	0.003	0.007	0.0003	151.771	6.785	27.416	1.111	53.812	2.107
FCO118	Cpy	0.21	0.003	0.513	0.005	0.011	0.0005	94.263	4.057	19.818	0.669	48.316	2.001

LA-ICP-MS Pb-isotope Results for Pb-chalcogenides associate with Chalcopyrite-Dominant Ores Continued (2/6)

Name	Cu-ore Type	207/206	+/-1s	208/206	+/-1s	204/206	+/-1s	206/204	+/-1s	207/204	+/-1s	208/204	+/-1s
FCO118	Cpy	0.21	0.003	0.513	0.006	0.011	0.0005	93.782	4.062	19.708	0.669	48.05	1.996
FCO118	Cpy	0.344	0.006	0.856	0.025	0.019	0.0005	53.208	1.478	18.317	0.378	45.546	1.922
FCO118	Cpy	0.344	0.006	0.856	0.026	0.019	0.0005	52.818	1.49	18.175	0.381	45.201	1.913
FCO118	Cpy	0.301	0.007	0.769	0.015	0.015	0.0006	66.797	2.486	20.118	0.487	51.384	1.46
FCO118	Cpy	0.301	0.007	0.769	0.015	0.015	0.0006	66.272	2.488	19.953	0.489	50.971	1.457
FCO118	Cpy	0.249	0.005	0.632	0.023	0.013	0.0002	79.784	1.462	19.867	0.331	50.445	1.756
FCO118	Cpy	0.249	0.005	0.632	0.023	0.013	0.0002	78.978	1.497	19.662	0.335	49.935	1.746
FCO161	Cpy	0.116	0.002	0.16	0.004	0.003	0.0001	363.26	12.564	42.07	1.337	57.978	2.194
FCO161	Cpy	0.109	0.001	0.156	0.001	0.003	0.0001	356.114	11.324	38.794	1.279	55.389	1.883
FCO161	Cpy	0.288	0.002	0.708	0.003	0.014	0.0002	72.054	0.852	20.786	0.244	50.988	0.581
FCO161	Cpy	0.204	0.005	0.495	0.02	0.009	0.0002	113.84	2.69	23.184	0.545	56.378	2.379
FCO178	Cpy	0.083	0.002	0.106	0.002	0.002	0.0001	663.356	15.865	54.892	2.012	70.346	1.85
FCO183	Cpy	0.241	0.003	0.46	0.004	0.01	0.0002	95.857	1.536	23.083	0.308	44.105	0.703
FCO192	Cpy	0.109	0.001	0.16	0.002	0.003	0.0001	356.428	8.8	38.737	0.86	56.986	1.021
FCO192	Cpy	0.109	0.001	0.156	0.003	0.003	0.0001	352.699	7.679	38.421	0.848	55.018	1.302
FCO192	Cpy	0.188	0.004	0.342	0.012	0.009	0.0005	106.411	5.572	19.969	1.113	36.38	2.181
FCO192	Cpy	0.162	0.006	0.234	0.01	0.005	0.0001	192.705	5.196	31.288	0.834	44.991	1.671
FCO192	Cpy	0.164	0.006	0.232	0.011	0.005	0.0002	184.722	7.833	30.255	1.146	42.953	2.294
FCO192	Cpy	0.178	0.005	0.277	0.006	0.006	0.0005	153.965	11.741	27.433	1.815	42.708	2.997
FCO192	Cpy	0.091	0.002	0.109	0.003	0.002	0.0001	456.371	26.774	41.46	2.101	49.855	2.972
FCO193	Cpy	0.247	0.008	0.581	0.016	0.012	0.0003	81.87	2.292	20.206	0.454	47.577	1.684
FCO193	Cpy	0.247	0.008	0.581	0.016	0.012	0.0004	80.62	2.291	19.897	0.453	46.868	1.666
FCO193	Cpy	0.262	0.004	0.613	0.009	0.012	0.0002	85.203	1.204	22.345	0.356	52.192	1.025
FCO193	Cpy	0.262	0.004	0.613	0.009	0.012	0.0002	83.887	1.254	21.999	0.359	51.406	1.023

LA-ICP-MS Pb-isotope Results for Pb-chalcogenides associate with Chalcopyrite-Dominant Ores Continued (3/6)

Name	Cu-ore Type	207/206	+/-1s	208/206	+/-1s	204/206	+/-1s	206/204	+/-1s	207/204	+/-1s	208/204	+/-1s
FCO193	Cpy	0.275	0.003	0.632	0.012	0.013	0.0006	75.272	3.383	20.672	0.8	47.525	2.562
FCO193	Cpy	0.275	0.003	0.632	0.012	0.014	0.0006	73.771	3.335	20.264	0.788	46.612	2.517
FCO193	Cpy	0.246	0.004	0.581	0.019	0.011	0.0003	91.588	2.364	22.502	0.753	53.242	1.17
FCO193	Cpy	0.246	0.004	0.582	0.019	0.011	0.0003	89.54	2.352	22.005	0.74	52.1	1.157
FCO193	Cpy	0.235	0.002	0.569	0.005	0.011	0.0001	90.704	1.013	21.322	0.32	51.64	0.94
FCO194	Cpy	0.292	0.008	0.705	0.012	0.014	0.0003	71.716	1.583	20.954	0.789	50.582	1.654
FCO194	Cpy	0.124	0.001	0.261	0.005	0.004	0.0002	260.015	11.322	32.316	1.205	67.909	2.119
FCO194	Cpy	0.284	0.004	0.692	0.01	0.013	0.0005	77.915	3.282	22.109	0.814	53.883	2.042
FCO194	Cpy	0.129	0.006	0.261	0.018	0.004	0.0002	249.895	13.478	32.205	1.216	65.152	2.619
FCO194	Cpy	0.302	0.003	0.725	0.008	0.016	0.0003	63.295	1.176	19.137	0.357	45.872	0.726
FCO230	Cpy	0.095	0.001	0.09	0.001	0.001	0.0001	698.358	7.77	66.574	0.6	62.946	0.739
FCO230	Cpy	0.099	0.001	0.099	0.002	0.002	0.0001	596.518	9.899	59.079	0.514	58.789	0.407
FCO235	Cpy	0.081	0.001	0.062	0.004	0.002	0.0002	646.983	75.798	52.12	6.08	40.244	2.924
FCO235	Cpy	0.101	0.001	0.053	0.003	0.001	0.0001	830.41	59.008	83.502	5.912	44.353	2.256
FCO235	Cpy	0.195	0.004	0.401	0.005	0.008	0.0003	122.894	4.552	23.928	0.66	49.259	1.568
FCO235	Cpy	0.18	0.004	0.345	0.009	0.007	0.0002	145.829	4.546	26.304	0.562	50.267	1.372
FCO235	Cpy	0.137	0.001	0.228	0.005	0.004	0.0001	235.137	3.153	32.176	0.499	53.583	1.719
FCO235	Cpy	0.12	0.003	0.185	0.005	0.004	0.0001	266.854	10.358	32.032	1.371	49.298	2.808
FCO237	Cpy	0.116	0.002	0.154	0.002	0.003	0.0001	334.142	12.53	38.843	1.279	51.461	2.012
FCO237	Cpy	0.114	0.001	0.157	0.001	0.003	0	369.941	3.163	42.221	0.43	57.91	0.471
FCO237	Cpy	0.113	0.002	0.142	0.004	0.002	0.0002	414.912	29.878	46.837	3.566	58.921	5.294
FCO237	Cpy	0.087	0.003	0.074	0.002	0.001	0.0001	778.123	35.818	67.94	2.873	57.245	2.409
FCO237	Cpy	0.181	0.006	0.266	0.01	0.006	0.0002	179.577	5.757	32.456	1.627	47.773	1.86
FCO237	Cpy	0.126	0.002	0.087	0.004	0.002	0.0001	478.279	28.285	60.131	3.146	41.818	3.253

LA-ICP-MS Pb-isotope Results for Pb-chalcogenides associate with Chalcopyrite-Dominant Ores Continued (4/6)

Name	Cu-ore Type	207/206	+/-1s	208/206	+/-1s	204/206	+/-1s	206/204	+/-1s	207/204	+/-1s	208/204	+/-1s
FCO237	Cpy	**0.144**	0.002	0.237	0.002	0.004	0.0001	236.261	7.148	34.019	1.358	56.06	1.857
FCO237	Cpy	0.139	0.002	0.222	0.005	0.004	0.0001	247.915	5.48	34.519	0.581	55.063	1.145
FCO238	Cpy	0.09	0.001	0.102	0.002	0.002	0.0001	598.372	21.497	53.868	1.627	61.299	0.925
FCO238	Cpy	0.084	0.001	0.089	0.001	0.001	0.0001	676.301	28.218	57.063	2.254	60.092	2.132
FCO238	Cpy	0.102	0.001	0.137	0.003	0.002	0.0001	403.788	12.64	41.143	1.255	55.459	1.044
FCO238	Cpy	0.1	0.002	0.132	0.004	0.002	0.0001	473.399	25.827	47.194	1.897	62.563	1.864
FCO238	Cpy	0.222	0.006	0.388	0.012	0.009	0.0002	107.884	2.872	24	0.374	41.861	0.743
FCO238	Cpy	0.087	0.001	0.089	0.001	0.001	0.0001	687.518	11.962	59.7	0.81	61.001	0.813
FCO238	Cpy	0.082	0.001	0.079	0.001	0.001	0.0001	784.087	17.385	64.229	1.358	61.949	1.448
FCO238	Cpy	0.093	0.001	0.124	0.003	0.002	0.0001	483.89	22.78	44.897	1.743	60.151	1.932
FCO239	Cpy	0.212	0.003	0.523	0.019	0.009	0.0002	106.573	2.742	22.54	0.701	55.691	3.039
FCO241	Cpy	0.12	0.001	0.198	0.002	0.004	0.0001	268.644	4.026	32.349	0.521	53.161	1.054
FCO249	Cpy	0.273	0.006	0.649	0.014	0.013	0.0002	78.007	1.344	21.324	0.44	50.559	1.011
FCO249	Cpy	0.274	0.006	0.65	0.014	0.013	0.0002	76.796	1.269	21.021	0.427	49.871	0.984
FCO249	Cpy	0.305	0.006	0.747	0.014	0.016	0.0002	61.712	0.719	18.795	0.479	46.078	1.165
FCO249	Cpy	0.305	0.006	0.748	0.014	0.016	0.0002	60.815	0.643	18.546	0.467	45.494	1.14
FCO249	Cpy	0.765	0.035	1.845	0.052	0.046	0.0023	21.697	1.074	16.586	0.179	40.014	1.055
FCO249	Cpy	0.766	0.035	1.848	0.052	0.047	0.0023	21.447	1.056	16.414	0.166	39.618	1.037
FCO249	Cpy	0.312	0.001	0.738	0.004	0.016	0.0002	64.41	0.769	20.101	0.221	47.52	0.438
FCO249	Cpy	0.312	0.001	0.739	0.004	0.016	0.0002	63.893	0.696	19.96	0.207	47.204	0.408
FCO249	Cpy	0.457	0.011	1.086	0.029	0.028	0.0005	36.065	0.696	16.491	0.258	39.149	0.577
FCO249	Cpy	0.458	0.011	1.087	0.028	0.028	0.0005	35.8	0.669	16.387	0.249	38.913	0.56
FCO276	Cpy	0.311	0.005	0.8	0.014	0.016	0.0004	62.052	1.351	19.323	0.463	49.669	1.095
FCO276	Cpy	0.317	0.004	0.783	0.008	0.017	0.0005	59.225	1.611	18.807	0.595	46.386	1.224

LA-ICP-MS Pb-isotope Results for Pb-chalcogenides associate with Chalcopyrite-Dominant Ores Continued (5/6)

Name	Cu-ore Type	207/206	+/-1s	208/206	+/-1s	204/206	+/-1s	206/204	+/-1s	207/204	+/-1s	208/204	+/-1s
FCO276	Cpy	0.289	0.002	0.756	0.015	0.015	0.0002	67.604	1.142	19.563	0.334	51.138	1.092
FCO276	Cpy	0.358	0.007	0.893	0.008	0.02	0.0007	48.878	1.675	17.519	0.453	43.648	1.602
FCO276	Cpy	0.245	0.003	0.612	0.006	0.011	0.0003	90.49	2.089	22.223	0.597	55.39	1.559
FCO276	Cpy	0.22	0.002	0.52	0.008	0.01	0.0003	97.539	3.248	21.509	0.879	50.714	1.995
FCO276	Cpy	0.104	0.001	0.175	0.003	0.003	0.0001	340.273	12.47	35.643	1.463	59.713	1.577
FCO276	Cpy	0.364	0.005	0.904	0.011	0.02	0.0006	50.949	1.462	18.614	0.512	46.077	1.241
FCO276	Cpy	0.292	0.003	0.747	0.005	0.014	0.0003	69.807	1.522	20.435	0.517	52.145	1.24
FCO276	Cpy	0.292	0.002	0.761	0.009	0.015	0.0002	68.855	1.054	20.184	0.244	52.403	0.789
FCO276	Cpy	0.181	0.002	0.433	0.005	0.008	0.0001	118.901	2.073	21.564	0.209	51.47	0.687
FCO355	Cpy	0.145	0.001	0.239	0.002	0.005	0.0002	184.663	6.484	26.563	0.875	44.093	1.79
FCO355	Cpy	0.313	0.009	0.634	0.015	0.015	0.0007	65.92	3.165	20.481	0.757	41.75	1.603
FCO355	Cpy	0.439	0.01	0.879	0.033	0.023	0.0007	43.742	1.384	19.043	0.57	38.453	1.017
FCO355	Cpy	0.311	0.008	0.617	0.012	0.018	0.0007	55.096	2.051	17	0.628	33.992	1.214
FCO371	Cpy	0.292	0.005	0.567	0.014	0.016	0.0007	61.706	2.585	18.004	0.745	34.954	1.068
FCO371	Cpy	0.29	0.006	0.581	0.009	0.015	0.0002	68.589	0.807	19.921	0.409	39.813	0.879
FCO371	Cpy	0.26	0.002	0.498	0.011	0.013	0.0003	75.959	1.515	19.767	0.425	37.839	1.418
FCO371	Cpy	0.265	0.006	0.583	0.017	0.015	0.0004	67.42	1.632	17.888	0.502	39.304	1.082
FCO371	Cpy	0.32	0.007	0.653	0.019	0.019	0.0004	53.195	1.062	16.975	0.354	34.709	0.723
FCO371	Cpy	0.434	0.01	0.902	0.032	0.024	0.0006	42.024	1.077	18.219	0.416	37.896	0.793
FCO384	Cpy	0.218	0.005	0.542	0.018	0.009	0.0002	110.573	2.424	23.797	0.848	59.926	2.748
FCO384	Cpy	0.262	0.002	0.614	0.009	0.012	0.0002	82.061	1.327	21.165	0.449	50.356	1.215
FCO384	Cpy	0.231	0.002	0.554	0.004	0.011	0.0005	94.953	4.162	21.65	1	52.623	2.478
FCO384	Cpy	0.235	0.002	0.551	0.003	0.012	0.0003	84.625	1.792	19.518	0.387	46.619	0.938
FCO384	Cpy	0.239	0.005	0.562	0.016	0.011	0.0004	87.699	2.945	20.561	0.54	49.283	1.244

LA-ICP-MS Pb-isotope Results for Pb-chalcogenides associate with Chalcopyrite-Dominant Ores Continued (6/6)

Name	Cu-ore Type	207/206	+/-1s	208/206	+/-1s	204/206	+/-1s	206/204	+/-1s	207/204	+/-1s	208/204	+/-1s
FCO384	Cpy	0.25	0.003	0.593	0.005	0.012	0.0002	83.28	1.155	20.436	0.417	49.378	0.802
FCO384	Cpy	0.256	0.004	0.603	0.006	0.011	0.0003	89.669	2.405	22.49	0.633	54.097	1.476
FCO384	Cpy	0.239	0.002	0.582	0.011	0.011	0.0003	91.42	2.639	21.389	0.595	53.221	1.266
FCO384	Cpy	0.273	0.005	0.63	0.007	0.013	0.0004	74.662	2.304	19.977	0.63	47.002	1.734
FCO384	Cpy	0.218	0.003	0.509	0.008	0.009	0.0002	105.287	2.638	22.494	0.445	53.577	1.264
FCO384	Cpy	0.105	0.001	0.151	0.001	0.003	0.0001	385.969	8.812	39.575	1.012	58.164	1.423
FCO385	Cpy	0.14	0.002	0.172	0.004	0.004	0.0001	228.422	7.797	31.855	1.329	39.362	1.909
FCO386	Cpy	0.13	0.004	0.175	0.001	0.004	0.0002	227.078	9.758	29.519	1.085	39.699	1.612
FCO386	Cpy	0.183	0.001	0.433	0.005	0.008	0.0003	127.569	4.818	23.364	0.977	55.258	2.363
FCO392	Cpy	0.145	0.002	0.297	0.007	0.005	0.0001	196.35	4.2	28.477	0.448	58.201	0.952
FCO392	Cpy	0.16	0.002	0.35	0.008	0.006	0.0001	166.371	3.636	26.49	0.438	58.081	1.039
FCO392	Cpy	0.152	0.002	0.327	0.008	0.006	0.0002	174.162	5.821	26.378	0.824	56.804	1.582
FCO400	Cpy	0.111	0.001	0.183	0.001	0.003	0.0002	313.73	3.883	34.819	0.286	57.259	0.924
FCO400	Cpy	0.11	0.001	0.18	0.001	0.003	0.0001	297.769	4.906	32.739	0.567	53.53	0.846
FCO400	Cpy	0.113	0.001	0.174	0.002	0.003	0.0001	325.226	7.526	36.888	1.048	56.61	1.343
FCO411	Cpy	0.105	0.002	0.125	0.001	0.002	0.0001	503.876	7.916	52.86	0.912	63.104	1.243

LA-ICP-MS Pb-isotope Results for Pb-chalcogenides associate with Bornite-Dominant Ores Continued (1/5)

Sample No.	Cu-ore Type	207/206	+/-1s	208/206	+/-1s	204/206	+/-1s	206/204	+/-1s	207/204	+/-1s	208/204	+/-1s
FCO138	brn	0.173	0.002	0.415	0.006	0.007	0.0001	138.624	1.988	23.961	0.234	57.472	0.695
FCO138	brn	0.116	0.001	0.202	0.001	0.004	0.0001	281.926	2.383	32.648	0.234	56.908	0.408
FCO138	brn	0.117	0.001	0.207	0.001	0.004	0.0001	275.994	2.122	32.348	0.227	57.105	0.426
FCO138	brn	0.118	0.003	0.204	0.002	0.003	0.0001	292.824	5.76	34.646	0.964	59.817	1.301
FCO139	brn	0.175	0.002	0.348	0.008	0.007	0.0002	136.633	3.677	23.855	0.467	47.529	0.909
FCO139	brn	0.146	0.001	0.164	0.003	0.003	0.0001	286.337	8.004	41.66	1.091	47.024	1.148
FCO139	brn	0.231	0.004	0.448	0.012	0.011	0.0005	89.032	3.637	20.523	0.75	39.856	1.588
FCO139	brn	0.104	0.002	0.148	0.004	0.003	0.0001	316.506	7.701	32.863	0.683	46.878	0.842
FCO139	brn	0.42	0.007	0.987	0.018	0.023	0.0004	43.754	0.829	18.347	0.392	43.174	0.983
FCO139	brn	0.453	0.004	1.084	0.008	0.026	0.0006	38.085	0.846	17.238	0.358	41.296	0.813
FCO139	brn	0.4	0.007	0.84	0.016	0.022	0.0004	45.743	0.824	18.272	0.309	38.406	0.693
FCO139	brn	0.355	0.002	0.733	0.004	0.02	0.0005	51.171	1.279	18.132	0.426	37.498	0.888
FCO139	brn	0.261	0.004	0.523	0.009	0.013	0.0003	79.626	1.754	20.771	0.427	41.662	0.823
FCO139	brn	0.172	0.002	0.348	0.005	0.007	0.0001	135.671	2.458	23.361	0.544	47.159	1.304
FCO139	brn	0.103	0.001	0.136	0.002	0.003	0.0001	345.273	7.676	35.697	0.82	46.927	0.876
FCO156	brn	0.336	0.007	0.74	0.016	0.019	0.0007	53.278	1.932	17.91	0.673	39.455	1.488
FCO156	brn	0.112	0.001	0.149	0.002	0.003	0.0001	311.223	6.739	34.955	0.721	46.261	1.039
FCO162	brn	0.356	0.005	0.762	0.013	0.021	0.001	47.458	2.273	16.904	0.74	36.173	1.436
FCO162	brn	0.474	0.007	0.996	0.01	0.029	0.0009	34.29	1.037	16.25	0.381	34.158	0.922
FCO162	brn	0.852	0.008	1.946	0.02	0.053	0.0013	18.84	0.472	16.06	0.449	36.666	0.95
FCO162	brn	0.124	0.004	0.224	0.007	0.005	0.0003	206.322	13.752	25.647	1.144	46.121	2.532
FCO162	brn	0.186	0.003	0.435	0.007	0.007	0.0002	134.784	4.324	25.127	0.521	58.567	1.406
FCO162	brn	0.263	0.002	0.45	0.006	0.011	0.0004	89.39	3.066	23.495	0.798	40.217	1.221
FCO162	brn	0.277	0.003	0.523	0.015	0.013	0.0004	74.125	2.448	20.514	0.721	38.742	1.433

LA-ICP-MS Pb-isotope Results for Pb-chalcogenides associate with Bornite-Dominant Ores Continued (2/5)

Sample No.	Cu-ore Type	207/206	+/-1s	208/206	+/-1s	204/206	+/-1s	206/204	+/-1s	207/204	+/-1s	208/204	+/-1s
FCO162	brn	0.214	0.006	0.433	0.015	0.01	0.0005	97.555	4.906	20.88	0.475	42.237	0.741
FCO162	brn	0.143	0.003	0.264	0.004	0.005	0.0002	186.236	6.317	26.647	0.45	49.177	1.461
FCO162	brn	0.172	0.003	0.321	0.008	0.008	0.0002	125.118	3.368	21.519	0.518	40.12	0.855
FCO162	brn	0.562	0.022	1.27	0.041	0.034	0.0017	29.802	1.5	16.747	0.321	37.846	1.069
FCO162	brn	0.338	0.008	0.73	0.011	0.02	0.001	49.217	2.453	16.636	0.682	35.908	1.599
FCO162	brn	0.53	0.006	1.183	0.009	0.033	0.0008	30.745	0.79	16.287	0.422	36.37	1.042
FCO162	brn	0.251	0.005	0.451	0.013	0.012	0.0003	85.625	2.355	21.525	0.37	38.648	0.638
FCO177	brn	0.104	0.001	0.121	0.001	0.002	0.0001	461.496	9.034	47.733	0.952	55.698	1.141
FCO192	brn	0.157	0.002	0.278	0.005	0.005	0.0003	186.196	11.552	29.157	2.168	51.842	4.017
FCO192	brn	0.211	0.013	0.342	0.01	0.008	0.0005	119.91	7.903	25.346	1.232	40.993	3.193
FCO192	brn	0.156	0.003	0.279	0.007	0.007	0.0002	151.228	5.7	23.583	0.933	42.194	2.189
FCO192	brn	0.263	0.008	0.523	0.02	0.013	0.0005	75.829	2.628	19.94	0.608	39.681	0.8
FCO192	brn	0.193	0.006	0.349	0.011	0.008	0.0005	122.751	7.064	23.633	0.819	42.824	2.458
FCO192	brn	0.349	0.015	0.676	0.015	0.018	0.0011	56.801	3.554	19.849	1.433	38.378	1.872
FCO192	brn	0.162	0.003	0.346	0.004	0.007	0.0004	141.585	8.091	22.955	1.127	49.044	2.999
FCO192	brn	0.19	0.003	0.326	0.007	0.008	0.0004	120.49	6.184	22.856	1.275	39.332	1.974
FCO192	brn	**0.127**	0.001	0.217	0.002	0.005	0.0002	203.364	9.218	25.904	1.14	44.216	2.073
FCO192	brn	0.112	0.051	0.165	0.009	0.004	0.0043	240.525	246.205	26.897	23.653	39.616	34.761
FCO192	brn	0.175	0.003	0.322	0.005	0.007	0.0006	136.58	11.138	23.881	1.97	43.913	2.922
FCO192	brn	0.22	0.005	0.471	0.015	0.009	0.0005	107.286	6.21	23.547	1.457	50.541	2.784
FCO192	brn	0.22	0.003	0.55	0.011	0.012	0.0007	80.124	4.225	17.615	0.801	44.049	1.998
FCO199	brn	0.148	0.001	0.166	0.003	0.004	0.0001	281.038	7.737	41.716	1.079	46.725	1.121
FCO209	brn	0.27	0.007	0.572	0.018	0.013	0.0004	76.886	2.637	20.768	0.745	43.977	0.828
FCO209	brn	0.126	0.001	0.186	0.001	0.004	0.0001	243.721	3.961	30.789	0.497	45.273	0.64

LA-ICP-MS Pb-isotope Results for Pb-chalcogenides associate with Bornite-Dominant Ores Continued (3/5)

Sample No.	Cu-ore Type	207/206	+/-1s	208/206	+/-1s	204/206	+/-1s	206/204	+/-1s	207/204	+/-1s	208/204	+/-1s
FCO209	brn	0.274	0.004	0.609	0.008	0.014	0.0003	71.347	1.293	19.525	0.486	43.444	0.545
FCO209	brn	0.279	0.005	0.595	0.008	0.015	0.0005	65.419	2.217	18.247	0.68	38.904	1.17
FCO212	brn	0.097	0.001	0.143	0.001	0.002	0.0001	484.173	18.487	47.046	1.515	69.185	2.833
FCO212	brn	0.088	0.002	0.122	0.002	0.002	0.0001	549.594	20.84	48.457	1.377	67.073	2.337
FCO212	brn	0.085	0.001	0.087	0.002	0.001	0.0001	800.963	31.939	67.719	2.615	69.821	3.089
FCO212	brn	0.089	0.001	0.101	0.003	0.002	0.0001	559.374	14.854	49.667	1.257	56.244	1.052
FCO212	brn	0.084	0.001	0.103	0.001	0.001	0.0001	751.724	26.485	62.904	1.91	77.68	2.478
FCO212	brn	0.213	0.006	0.437	0.015	0.011	0.0004	94.609	3.946	20.111	0.979	41.335	0.928
FCO221	brn	0.11	0.002	0.152	0.003	0.003	0.0001	366.114	14.704	40.164	1.137	55.771	1.855
FCO221	brn	0.197	0.004	0.33	0.01	0.008	0.0002	122.648	3.695	24.099	0.574	40.497	1.051
FCO232	brn	0.18	0.001	0.465	0.003	0.007	0.0001	139.347	1.831	25.139	0.387	64.808	0.701
FCO232	brn	0.17	0.001	0.434	0.01	0.007	0.0001	152.952	2.114	25.955	0.295	66.336	1.314
FCO232	brn	0.177	0.001	0.456	0.006	0.007	0.0002	135.843	2.883	24.047	0.413	62.005	1.027
FCO232	brn	0.112	0.001	0.206	0.003	0.003	0.0001	296.214	10.14	33.208	1.075	61.066	1.671
FCO232	brn	0.095	0.001	0.123	0.006	0.002	0.0001	527.215	28.129	50.19	2.153	64.599	1.85
FCO232	brn	0.097	0.002	0.143	0.006	0.002	0.0001	450.126	24.456	43.526	1.251	64.366	1.008
FCO232	brn	0.086	0.001	0.104	0.003	0.002	0.0001	622.491	14.991	53.391	0.843	64.883	0.626
FCO232	brn	0.089	0.001	0.112	0.002	0.002	0.0001	583.235	7.512	51.623	0.651	65.087	1.248
FCO232	brn	0.086	0.001	0.106	0.003	0.002	0.0001	592.76	21.488	51.199	1.508	62.705	0.622
FCO232	brn	0.179	0.002	0.463	0.007	0.007	0.0001	136.83	2.221	24.49	0.226	63.331	0.502
FCO232	brn	0.145	0.002	0.337	0.008	0.005	0.0001	191.82	4.61	27.84	0.288	64.687	0.489
FCO232	brn	0.158	0.001	0.384	0.005	0.006	0.0001	165.227	2.152	26.164	0.284	63.476	0.655
FCO232	brn	0.157	0.002	0.377	0.008	0.006	0.0001	174.292	4.22	27.343	0.368	65.721	0.488
FCO232	brn	0.173	0.003	0.459	0.009	0.007	0.0001	143.037	2.441	24.711	0.268	65.689	0.847

LA-ICP-MS Pb-isotope Results for Pb-chalcogenides associate with Bornite-Dominant Ores Continued (4/5)

Sample No.	Cu-ore Type	207/206	+/-1s	208/206	+/-1s	204/206	+/-1s	206/204	+/-1s	207/204	+/-1s	208/204	+/-1s
FCO238	brn	0.087	0.001	0.069	0	0.001	0.0001	800.161	20.553	69.245	2.309	54.93	1.43
FCO238	brn	0.142	0.002	0.187	0.002	0.004	0.0002	260.614	11.307	37.114	1.624	48.732	2.318
FCO238	brn	0.099	0.001	0.127	0.002	0.003	0.0002	373.049	25.573	37.074	2.391	47.493	3.358
FCO238	brn	0.123	0.002	0.155	0.004	0.004	0.0002	282.532	16.633	34.733	1.953	43.885	2.193
FCO238	brn	0.113	0.006	0.154	0.004	0.002	0.0002	437.554	35.867	49.494	5.769	67.44	4.261
FCO238	brn	0.114	0.002	0.158	0.003	0.003	0.0001	380.935	15.779	43.356	1.388	60.112	1.79
FCO238	brn	0.11	0.003	0.154	0.004	0.004	0.0002	271.049	14.937	29.734	1.197	41.751	2.023
FCO238	brn	0.098	0.001	0.113	0.002	0.002	0.0001	476.329	23.082	46.778	2.505	53.732	2.958
FCO238	brn	0.111	0.002	0.142	0.002	0.003	0.0002	355.232	26.758	39.368	3.221	50.354	3.795
FCO238	brn	0.082	0.002	0.078	0.002	0.001	0.0001	810.747	15.358	66.396	1.16	63.19	1
FCO238	brn	0.085	0.001	0.09	0.001	0.001	0.0001	706.696	24.008	59.719	2.089	63.774	2.269
FCO238	brn	0.085	0.001	0.088	0.001	0.002	0.0001	634.31	18.9	53.665	1.624	55.862	1.214
FCO238	brn	0.085	0.001	0.085	0.003	0.001	0.0001	683.682	20.618	58.37	1.85	58.138	2.412
FCO241	brn	0.144	0.001	0.233	0.003	0.006	0.0002	171.23	4.457	24.733	0.586	39.906	1.195
FCO241	brn	0.102	0.001	0.105	0.003	0.002	0.0001	523.222	12.352	53.489	0.99	54.992	1.237
FCO287	brn	0.184	0.005	0.385	0.012	0.008	0.0003	118.896	4.256	21.919	0.492	45.736	1.752
FCO287	brn	0.181	0.004	0.36	0.006	0.008	0.0003	128.571	4.136	23.289	0.535	46.325	1.498
FCO287	brn	0.512	0.006	1.178	0.013	0.029	0.0008	34.614	0.971	17.726	0.51	40.761	0.911
FCO287	brn	0.202	0.002	0.441	0.009	0.009	0.0002	108.459	2.1	21.874	0.339	47.781	1.109
FCO287	brn	0.112	0.001	0.164	0.002	0.003	0.0001	336.552	8.177	37.757	0.891	55.23	1.643
FCO287	brn	0.263	0.007	0.73	0.021	0.014	0.0004	69.043	1.978	18.123	0.524	50.385	1.39
FCO287	brn	0.172	0.004	0.335	0.013	0.007	0.0003	138.891	5.011	23.883	0.518	46.578	0.615
FCO374	brn	0.195	0.004	0.436	0.015	0.009	0.0003	117.02	4.306	22.775	0.467	50.991	1.25
FCO374	brn	0.168	0.002	0.342	0.008	0.007	0.0002	150.221	4.931	25.177	0.71	51.313	1.8
FCO380	brn	0.264	0.009	0.508	0.027	0.013	0.0005	74.108	2.598	19.505	0.783	37.561	1.627

LA-ICP-MS Pb-isotope Results for Pb-chalcogenides associate with Bornite-Dominant Ores Continued (5/5)

Sample No.	Cu-ore Type	207/206	+/-1s	208/206	+/-1s	204/206	+/-1s	206/204	+/-1s	207/204	+/-1s	208/204	+/-1s
FCO380	brn	0.158	0.003	0.332	0.011	0.006	0.0002	162.473	5.577	25.634	0.662	53.785	1.234
FCO380	brn	0.404	0.011	0.843	0.03	0.024	0.0017	41.261	2.813	16.668	1.19	34.749	1.922
FCO380	brn	0.437	0.012	0.919	0.033	0.025	0.0015	39.766	2.385	17.374	0.614	36.51	1.45
FCO380	brn	0.591	0.016	1.337	0.052	0.038	0.0023	26.623	1.606	15.728	0.572	35.558	1.256
FCO380	brn	0.414	0.016	0.916	0.039	0.024	0.0011	42.164	1.971	17.45	0.373	38.588	0.932
FCO385	brn	0.272	0.002	0.497	0.005	0.014	0.0004	73.053	2.11	19.841	0.572	36.311	1.019
FCO385	brn	0.274	0.002	0.497	0.003	0.013	0.0005	74.629	2.733	20.414	0.765	37.057	1.241
FCO392	brn	0.153	0.002	0.294	0.008	0.006	0.0002	169.516	4.966	25.896	0.623	49.695	1.166
FCO392	brn	0.173	0.005	0.358	0.012	0.007	0.0003	137.354	5.626	23.657	1.064	49.033	1.515
FCO392	brn	0.179	0.007	0.344	0.011	0.006	0.0004	157.084	8.729	27.983	1.404	53.827	2.762
FCO400	brn	0.089	0.001	0.085	0.001	0.002	0.0001	637.192	6.923	56.631	0.693	53.858	0.976
FCO400	brn	0.193	0.002	0.441	0.004	0.008	0.0001	121.341	1.115	23.406	0.369	53.487	0.702
FCO400	brn	0.116	0.001	0.189	0.004	0.003	0.0001	304.341	6.371	35.392	0.565	57.431	0.47
FCO400	brn	0.115	0.002	0.168	0.002	0.003	0.0001	312.159	9.245	35.83	1.01	52.354	1.205

LA-ICP-MS Pb-isotope Results for Pb-chalcogenides associate with Chalcocite-Dominant Ores (1/3)

Name	Cu-ore Type	207/206	+/-1s	208/206	+/-1s	204/206	+/-1s	206/204	+/-1s	207/204	+/-1s	208/204	+/-1s
FCO126	Cc	0.108	0.001	0.164	0.003	0.003	0.0001	332.929	9.952	36.01	0.936	54.733	2.225
FCO126	Cc	0.095	0.001	0.156	0.004	0.002	0.0001	438.607	20.498	41.6	1.876	68.324	3.401
FCO126	Cc	0.314	0.004	0.654	0.009	0.016	0.0006	60.807	2.036	19.071	0.557	39.793	0.931
FCO126	Cc	0.199	0.004	0.434	0.007	0.01	0.0002	98.911	2.041	19.654	0.425	42.929	1.062
FCO126	Cc	0.129	0.002	0.204	0.003	0.004	0.0001	249.732	8.074	32.104	1.198	50.989	1.419
FCO127	Cc	0.157	0.002	0.332	0.005	0.006	0.0001	164.427	3.662	25.785	0.551	54.641	1.051
FCO127	Cc	0.153	0.002	0.334	0.004	0.006	0.0002	167.318	6.692	25.633	0.855	55.914	1.899
FCO127	Cc	0.138	0.002	0.281	0.006	0.005	0.0002	184.822	5.959	25.559	0.754	51.897	1.185
FCO127	Cc	0.144	0.002	0.311	0.007	0.006	0.0002	180.8	6.414	26.081	1.007	56.231	1.987
FCO127	Cc	0.143	0.002	0.283	0.006	0.005	0.0001	188.742	4.302	26.996	0.429	53.379	0.743
FCO127	Cc	0.131	0.001	0.257	0.003	0.005	0.0001	217.628	4.465	28.414	0.443	55.849	0.956
FCO127	Cc	0.133	0.001	0.25	0.002	0.004	0.0001	224.797	3.323	29.871	0.446	56.242	0.761
FCO127	Cc	0.309	0.008	0.625	0.025	0.015	0.0005	67.97	2.435	21.023	0.459	42.506	1.701
FCO127	Cc	0.259	0.004	0.543	0.01	0.013	0.0003	77.89	1.548	20.14	0.386	42.275	0.845
FCO127	Cc	0.305	0.006	0.642	0.014	0.016	0.0006	62.732	2.266	19.109	0.487	40.28	0.867
FCO127	Cc	0.182	0.001	0.431	0.009	0.008	0.0002	129.198	2.862	23.547	0.433	55.658	0.598
FCO127	Cc	0.183	0.002	0.413	0.004	0.007	0.0001	135.064	1.718	24.725	0.431	55.77	0.697
FCO128	Cc	0.682	0.017	1.559	0.039	0.043	0.0013	23.424	0.724	15.981	0.235	36.524	0.487
FCO128	Cc	0.157	0.002	0.343	0.007	0.006	0.0001	171.647	4.19	26.867	0.466	58.824	1.491
FCO128	Cc	0.157	0.003	0.36	0.011	0.006	0.0002	155.881	4.492	24.529	0.504	56.152	1.312
FCO128	Cc	0.134	0.002	0.268	0.008	0.005	0.0002	216.547	7.224	28.98	0.75	57.95	2.127
FCO128	Cc	0.872	0.005	2.035	0.014	0.055	0.0005	18.104	0.17	15.781	0.15	36.845	0.359
FCO128	Cc	0.479	0.011	1.049	0.03	0.026	0.0004	38.936	0.672	18.653	0.444	40.842	1.196
FCO128	Cc	0.812	0.008	1.867	0.015	0.052	0.0005	19.335	0.182	15.704	0.126	36.103	0.341

LA-ICP-MS Pb-isotope Results for Pb-chalcogenides associate with Chalcocite-Dominant Ores (2/3)

Name	Cu-ore Type	207/206	+/-1s	208/206	+/-1s	204/206	+/-1s	206/204	+/-1s	207/204	+/-1s	208/204	+/-1s
FCO128	Cc	0.131	0.002	0.259	0.008	0.004	0.0001	227.795	7.076	29.769	0.742	59.052	1.981
FCO128	Cc	0.156	0.002	0.336	0.003	0.006	0.0002	170.096	5.614	26.562	0.645	57.171	1.586
FCO128	Cc	0.383	0.013	0.868	0.017	0.023	0.001	43.689	1.854	16.74	0.4	37.906	1.099
FCO128	Cc	0.2	0.005	0.446	0.015	0.009	0.0004	111.425	4.843	22.306	0.569	49.642	1.307
FCO133	Cc	0.179	0.003	0.424	0.005	0.007	0.0002	142.937	3.578	25.53	0.733	60.62	1.608
FCO133	Cc	0.172	0.002	0.419	0.004	0.007	0.0002	137.279	3.434	23.544	0.666	57.515	1.526
FCO133	Cc	0.767	0.008	1.745	0.014	0.049	0.0009	20.554	0.4	15.754	0.286	35.861	0.686
FCO138	Cc	0.619	0.004	1.424	0.012	0.039	0.0007	25.777	0.44	15.948	0.266	36.703	0.654
FCO138	Cc	0.606	0.005	1.399	0.01	0.037	0.0004	26.946	0.305	16.323	0.178	37.697	0.377
FCO138	Cc	0.65	0.007	1.502	0.019	0.04	0.0009	24.839	0.567	16.117	0.271	37.309	0.539
FCO138	Cc	0.612	0.011	1.417	0.014	0.038	0.0009	26.232	0.648	16.027	0.454	37.162	1.044
FCO139	Cc	0.1	0.001	0.138	0.003	0.003	0.0001	372.34	6.439	37.077	0.915	51.244	1.484
FCO139	Cc	0.15	0.002	0.286	0.008	0.006	0.0002	166.567	4.188	25.012	0.346	47.556	0.597
FCO139	Cc	0.166	0.004	0.328	0.01	0.007	0.0002	145.547	3.831	24.185	0.431	47.805	0.9
FCO139	Cc	0.185	0.004	0.383	0.008	0.008	0.0002	119.956	3.388	22.222	0.627	45.891	1.231
FCO139	Cc	0.197	0.001	0.394	0.003	0.009	0.0002	112.449	3.113	22.184	0.621	44.292	1.191
FCO199	Cc	0.172	0.003	0.344	0.01	0.007	0.0003	149.624	5.95	25.725	0.88	51.523	2.332
FCO212	Cc	0.086	0.001	0.107	0.001	0.001	0	691.738	21.062	59.603	2.096	74.331	2.167
FCO212	Cc	0.132	0.001	0.266	0.004	0.004	0.0001	260.962	5.406	34.511	0.753	69.449	1.876
FCO212	Cc	0.083	0.001	0.094	0.001	0.001	0.0001	834.05	21.86	69.028	2.109	78.685	1.857
FCO212	Cc	0.101	0.002	0.137	0.003	0.003	0.0001	362.094	18.205	36.728	1.762	49.463	2.303
FCO212	Cc	0.127	0.002	0.255	0.003	0.004	0.0001	259.637	4.597	32.919	0.874	66.24	1.703
FCO221	Cc	0.267	0.004	0.51	0.009	0.013	0.0004	76.085	2.494	20.337	0.684	38.808	1.365
FCO221	Cc	0.109	0.002	0.145	0.004	0.003	0.0001	320.512	6.625	34.903	0.716	46.323	0.596
FCO221	Cc	0.104	0.001	0.119	0.002	0.003	0.0001	378.231	10.127	39.428	0.928	44.803	1.267

LA-ICP-MS Pb-isotope Results for Pb-chalcogenides associate with Chalcocite-Dominant Ores (3/3)

Name	Cu-ore Type	207/206	+/-1s	208/206	+/-1s	204/206	+/-1s	206/204	+/-1s	207/204	+/-1s	208/204	+/-1s
FCO230	Cc	0.098	0.003	0.093	0.003	0.002	0.0001	639.58	11.725	62.871	2.347	59.61	1.998
FCO230	Cc	0.096	0.001	0.112	0.002	0.001	0.0001	760.663	27.207	72.978	2.267	85.431	2.504
FCO230	Cc	0.098	0.001	0.098	0.001	0.002	0.0001	592.688	11.651	58.251	0.914	58.034	0.881
FCO230	Cc	0.105	0.001	0.115	0.001	0.002	0.0001	529.835	13.228	55.386	1.378	61.122	1.79
FCO243	Cc	0.078	0.001	0.075	0.001	0.001	0.0001	797.099	18.415	61.936	1.122	59.543	1.127
FCO243	Cc	0.088	0.001	0.106	0.002	0.002	0.0001	550.568	23.142	48.317	2.353	58.361	2.476
FCO314	Cc	0.079	0.001	0.062	0.001	0.001	0.0001	775.212	14.04	61.002	1.217	48.421	1.102
FCO314	Cc	0.529	0.018	1.273	0.062	0.031	0.0013	31.914	1.32	16.875	0.242	40.618	0.691
FCO374	Cc	0.232	0.005	0.537	0.013	0.011	0.0003	93.675	2.807	21.732	0.711	50.259	1.194
FCO374	Cc	0.174	0.004	0.362	0.009	0.007	0.0002	141.795	3.311	24.697	0.485	51.375	1.018
FCO392	Cc	0.141	0.002	0.261	0.006	0.005	0.0001	210.028	4.629	29.582	0.482	54.662	1.323
FCO392	Cc	0.136	0.002	0.263	0.007	0.005	0.0001	219.608	4.351	29.702	0.468	57.454	1.364
FCO392	Cc	0.135	0.003	0.244	0.006	0.005	0.0002	214.228	8.617	28.923	1.426	52.134	1.8
FCO392	Cc	0.362	0.009	0.806	0.028	0.02	0.0012	50.45	3.017	18.2	1.084	40.517	2.955
FCO392	Cc	0.135	0.002	0.258	0.007	0.005	0.0001	221.991	5.866	29.93	0.663	57.068	1.478
FCO400	Cc	0.113	0.001	0.197	0.003	0.003	0.0001	299.547	7.825	33.803	0.825	58.892	1.98
FCO407	Cc	0.115	0.001	0.2	0.003	0.003	0.0001	315.778	13.681	36.146	1.493	63.117	3.036